UNIVERSITY OF ADELAIDE
29-8-96
LIBRARY

SIGNAL ANALYSIS WITH APPLICATIONS TO ATMOSPHERIC RADARS

By

David A. Holdsworth, B.Sc. (Hons)

Thesis

submitted for the degree of

DOCTOR OF PHILOSOPHY

at the

UNIVERSITY OF ADELAIDE

(Department of Physics and Mathematical Physics)

December 22nd, 1995

This work contains no material which has been accepted for the award of any other degree or diploma in any university or other tertiary institution and, to the best of my knowledge and belief, contains no material previously published or written by another person, except where due reference has been made in the text.

I give consent to this copy of my thesis, when deposited in the University Library, being available for loan and photocopying.

Signed: dated: 22/12/95

David A. Holdsworth, B.Sc. (Hons)

Abstract

This thesis provides a systematic analysis of the performance of a number of spaced antenna (SA) radar processing techniques. These techniques include the full correlation analysis (FCA), the full spectral analysis (FSA), and a number of Doppler-selected imaging interferometry techniques. This analysis is performed using data generated by a "radar backscatter model". Where suitable, the results are supplemented using data collected by the Buckland Park 2 MHz MF radar operated by the Atmospheric Physics group of the Department of Physics and Mathematical Physics at the University of Adelaide.

The radar backscatter model is based on the volume scatter situation, whereby a number of randomly positioned scatterers with polar diagrams simulating horizontally extended regions of refractive index irregularities propagate through the volume illuminated by the radar. This model has been designed to be as simple and as realistic as possible, allowing the simulation of both spaced antenna and Doppler radars. The model includes features such as aspect sensitivity, gravity wave perturbations, turbulent motions, and finite scatterer lifetimes. The model is shown to simulate the characteristics of radar backscatter very well at both MF and VHF.

The FCA has been employed for the estimation of atmospheric wind velocities and scattering parameters using SA radar for the last forty years. Throughout this time the technique has been shown to produce biases in the wind velocity estimates, leading to speculation as to whether it accurately measures the mean wind velocity. The radar backscatter model has been used to investigate a number of these biases. The FCA is shown to account correctly for the effects of turbulent motions, scatterer anisometry, and monochromatic gravity waves. The triangle size effect is investigated, revealing a number of possible causes of bias which can be avoided in practice. The effects of the sampling time, time-series length, and wind field inhomogeneities arising from gravity waves are also investigated. A number of recently developed alternative correlation analyses are also investigated.

The FSA is the frequency-domain equivalent of the FCA. The results of the application of the FSA to individual time-series records reveals serious limitations in the technique. These limitations can be avoided using spectra calculated by the coherent average of the spectra obtained from the individual time-series records, at the cost of time resolution.

The Doppler-selected imaging interferometry techniques have been developed as alternatives to the FCA. These techniques are based on the assumption of discrete scatter. The application of these techniques to data generated using the radar backscatter model was found to produce results in good agreement with the results expected from volume scatter. The results are also in excellent agreement with the experimental results obtained in a number of different studies.

The results obtained in this thesis suggest that the FCA is the optimal technique for the estimation of atmospheric parameters provided all sources of instrumental bias can be effectively eliminated.

Acknowledgments

So here it is. At last. And here is the most eagerly awaited page. If you are reading these acknowledgments in the hope of stumbling upon something witty and profound then give up now. Go and read *Viz* instead. After four years of constantly questioning my sanity (not to mention those around me), the only semi-profound statement I can make is that finishing this thesis feels somewhat like giving birth! Albeit to a bloody ugly baby. And not as much fun in the conception either.

I would like to thank my supervisors, Dr. Iain Reid and Dr. Bob Vincent, for their assistance throughout the last four years, and for allowing me the opportunity of spending last summer at Davis, Antarctica. I would especially like to thank the late Dr. Basil Briggs for his assistance and patience throughout the early part of my candidature, and for encouraging me to investigate any idea I may have had no matter how ridiculous it may have initially sounded.

I would also like thank my colleagues past and present, most of whom have been a pleasure to work, fight, drink, party, philosophize, barrack, wreak general havoc with, give nicknames to, and obtain nicknames from. These reprobates include, in no particular order, Dr. Stephen "Rrrrrrrrrrrrrubberneck" Eckermann, Manuel "Alfie Slagger" Cervera, Dr. Brenton "Jana" Vandepeer, Dr. Deepak "Tough guy" Rajopadhyaya, David "Butterfingers Blowy Lowy" Low, Dr. Damian "Muphry" Murphy, Dr. Drazen "My engraving machine has no spell-checker" Lesicar, Dr. Trevor "not *another* procedure" Harris, Dorothy "Dozza Gibbo-Wildchild" Gibson-Wilde, Bridget Hobbs, Karen Berkefeld, Ali "How are you?" Kazempour, Scott "Slay the world" Dullaway, Sujata Kovalam, Laurence Campbell, and the honorable Mr. Simon J. Allen. Thanks also must go to Brian Fuller, Shane Dillon, Lesley Rutherford, Simon Ludborzs, Alex Didenko, Michael Smith and Mike Shorthose for those times when I had to deal with (god forbid!) experimental or computing equipment, and to Dallas Kirby and Lyn Birchby for help with anything and everything else. Thanks also must go to those

denizens of the "Anti-physics club" who made my studies all the more enjoyable.

I would especially like to thank my family, namely Mum, Dad, Paulus J., and Debbus A., for their support throughout the last four years, and for not asking when I was going to finish too often. Special thanks must go to the "mad gits" Benny and Toska, for being endless sources of amusement. Thanks also must go to all my friends, the Adelaide Uni cricket club (A-grade premiers 92/93 and 94/95), the guys from "The Curl", Cafe Michael, and everyone who made my stay at Davis so enjoyable. Thanks also to Nirvana, Smashing Pumpkins, REM, Pearl Jam, and all the other bands whose music I found myself playing during thesis pregnancy. Extra special thanks must go to the Maritime Operations Division (MOD) of the Defence Science and Technology Organisation (DSTO), who sponsored me throughout most of my candidature.

Contents

Abstract v

Acknowledgments vii

1 Introduction 1

1.1 Introduction 1

1.2 The atmosphere 1

1.2.1 Temperature structure 1

1.2.2 The ionosphere 3

1.2.3 Atmospheric measurements 5

1.3 Observations of atmospheric dynamics using radar techniques 6

1.3.1 Atmospheric radar 6

1.3.2 Altitudes observed by atmospheric radars 7

1.3.3 Scattering mechanisms 10

1.3.4 Spaced antenna radar techniques 11

1.3.5 The similar fades technique 14

1.3.6 The full correlation analysis 14

1.3.7 The spatial correlation analysis 15

1.3.8 Image forming 16

1.3.9 Interferometry 16

1.3.10 Beam steering techniques 17

1.4 Motivation and scope of this thesis 17

2 The Buckland Park field station 19

2.1 Introduction 19

2.2 The Buckland Park MF/HF radar 20

2.2.1 Spaced antenna operation 22
2.2.2 Doppler beam steering operation 23
2.3 Experimental data 24
2.3.1 BP930518 data-set 25
2.3.2 BP940527 data-set 27
2.4 Summary 30

3 The radar backscatter model **31**
3.1 Introduction 31
3.1.1 Analytical models 32
3.1.2 Numerical models 33
3.2 Description of the radar backscatter model 35
3.2.1 The nature of the scatterers 37
3.2.2 Signal returns 37
3.2.3 The radar volume 40
3.2.4 Scatterer motions 41
3.2.4.1 Turbulent random motions 42
3.2.4.2 Gravity-wave perturbations 44
3.3 Application of the radar backscatter model 46
3.3.1 Simulation parameters 46
3.3.2 Time series generation 49
3.3.3 The ground diffraction pattern 49
3.4 Verification of the model 60
3.4.1 The Full Correlation Analysis 60
3.4.2 Turbulent random motions estimation 60
3.4.3 Aspect sensitivity 63
3.4.4 Doppler analysis 65
3.5 Summary and conclusions 66

4 The Full Correlation Analysis **69**
4.1 Introduction 69
4.2 Theory of the FCA 72
4.2.1 Spatial characteristics of the ground diffraction pattern 72
4.2.2 Randomly changing ground diffraction pattern 73

4.2.3 Moving and randomly changing ground diffraction pattern 76
4.2.4 Ellipsoid parameter estimation 77
4.2.5 Determination of physical parameters 81
4.3 Application of the FCA 83
4.3.1 Calculation of the correlation functions 85
4.4 Application of the FCA to model-generated data 85
4.4.1 The effect of turbulent motions upon the FCA 85
4.4.2 The effect of anisometric scatter upon the FCA 90
4.4.3 Effects of gravity waves on the FCA 94
4.5 Application of the FCA to MF data 98
4.6 Effect of sampling time upon the FCA 102
4.6.1 Zero-lag auto-correlation function interpolation 102
4.6.2 Cross-correlation function Gaussian fit 105
4.6.3 Combined effects of the zero-lag auto-correlation interpolation and and the cross-correlation Gaussian fit 107
4.6.4 Summary 111
4.7 Effect of scattering mechanism upon the FCA 113
4.8 The effect of time-series length and coherent averaging upon the FCA 118
4.8.1 118
4.8.2 The effect of coherent averaging upon the FCA 122
4.8.3 Summary 125
4.9 Summary and conclusions 126

5 The Triangle Size Effect of the FCA **129**
5.1 Introduction 129
5.2 Magnitude biases 133
5.2.1 Magnitude biases in the noise-free situation 133
5.2.2 Magnitude biases in the presence of noise 138
5.2.3 Magnitude biases due to the effects of digitization and saturation . . . 141
5.2.4 Summary of TSE magnitude biases 148
5.3 Directional biases 150
5.4 Triangle size effect in experimental data 152
5.5 Summary and conclusions 155

6 Alternative Correlation Analyses **159**

6.1 Introduction 159

6.2 The slope-fitting correlation analysis 160

6.2.1 Theory of the slope fitting correlation analysis 160

6.2.2 Practical considerations for the RSFCA 164

6.2.3 Application of the RSFCA 166

6.2.4 Summary 167

6.3 The spatial correlation analysis 170

6.4 The three-antenna spatial correlation analysis 171

6.4.1 Theory of the three-antenna spatial correlation analysis 171

6.4.2 Application of the three-antenna spatial correlation analysis 173

6.4.3 The triangle size effect 176

6.4.4 Summary 179

6.5 The four-antenna spatial correlation analyses 179

6.5.1 Theory of the four-antenna spatial correlation analyses 179

6.5.2 Application of the four-antenna spatial correlation analyses 180

6.5.3 The triangle size effect 183

6.5.4 Summary 184

6.6 Experimental application of the spatial correlation analyses 185

6.7 Summary and conclusions 188

7 The Full Spectral Analysis **191**

7.1 Introduction 191

7.2 Theory of the Full Spectral Analysis 194

7.2.1 Experimental application of the FSA 196

7.3 Application of the FSA 199

7.3.1 The Gaussian fitting procedure 201

7.3.2 The linear fitting procedure 206

7.4 Application of the FSA to unaveraged spectra 211

7.4.1 Application to model generated-data 212

7.4.2 Explanation of results 216

7.4.3 Effects of time-series length upon the FSA 222

7.4.4 Effects of averaging over Doppler frequency 222

7.4.5 Summary of analysis of unaveraged spectra 226
7.5 Application of the FSA to averaged spectra 227
7.6 Summary and conclusions 232

8 Interferometry **235**
8.1 Introduction 235
8.2 Mean angle of arrival determination 237
8.2.1 Phase fitting radar interferometry 243
8.3 Doppler-selected imaging interferometry 247
8.3.1 Theory of the Doppler-selected imaging interferometry 247
8.3.2 Theoretical analysis of Doppler-selected imaging interferometry 249
8.4 Model analysis of Doppler-selected imaging interferometry 256
8.4.1 Effective scattering point determination 260
8.4.2 Velocity estimation in the volume scatter situation 271
8.4.3 Velocity estimation as a function of the number of model scatterers . . 273
8.4.4 The effects of noise on the interferometric analyses 276
8.4.5 The effects of thresholds 282
8.4.6 The multiple record analysis 283
8.4.7 Discussion 284
8.4.8 Notes on the interpretation of experimental results 287
8.5 Summary and conclusions 289

9 Summary and conclusions **293**
9.1 Summary 293
9.2 Conclusions 296
9.3 Suggestions for further work 297

A Model-generated data-sets **299**

B The time-displacement technique **305**

C Correlation functions **309**
C.1 The spatio-temporal correlation function 309
C.2 The spatial-correlation function 311
C.3 The auto-correlation function 311

C.4 The cross-correlation function 311
C.5 The effect of noise upon the correlation functions 312
C.6 Correction for the effects of noise 316
C.7 Application of correlation functions 317

D The FCA rejection criteria **319**
D.1 Record unsuitable for analysis 319
D.2 Unsuccessful correlation parameter estimation 319
D.3 Failure to satisfy theory of the FCA 321

E The FCA triangle size effect - directional biases **323**

F Spectra **335**
F.1 Definition of the spectra 335
F.2 The effect of noise upon the power-spectra 336
F.2.1 Estimation of the SNR 339
F.3 The effect of noise upon the cross-spectra 340
F.4 Summary 345

G The direction of the interferometric velocity **347**

H Thresholds and the imaging interferometric analyses **349**
H.1 Zenith angle threshold 349
H.2 Power threshold 353
H.3 Phase consistency threshold 356

I A simple model of atmospheric backscatter: Description and application to the full correlation analysis of spaced antenna data **359**

J Spaced antenna analysis of atmospheric radar backscatter model data **361**

References **363**

List of Tables

2.1 Parameters employed for the data-set BP930518. 28

2.2 Parameters employed for the data-set BP940527. 29

3.1 Standard atmospheric parameters employed for the radar backscatter model. 46

3.2 Standard sampling parameters employed for the radar backscatter model. . . 48

3.3 Standard polar diagram parameters used for SA radar simulation. 48

3.4 Standard polar diagram parameters used for Doppler radar simulation. 48

4.1 The FCA rejection criteria. 83

4.2 Estimates of the FCA velocities obtained over the period of the wave for various different wave parameters. 97

5.1 FCA outputs obtained as a function of antenna spacing 136

5.2 Triangles of antennae employed for TSE analysis using the BP MF data-set BP930518. 152

6.1 The RSFCA rejection criteria. 165

6.2 The SCA3 rejection criteria 175

7.1 The FSA rejection criteria 201

7.2 Estimates of the pattern scale $S_{0.5}$ and axial ratio R_{ax} obtained by applying the FCA and FSA techniques to the model-generated data-set MOD-MF-SA. 216

7.3 Estimates of A_{ij} and I_{ij}. 220

7.4 Cross-spectral magnitude maxima W_{0ij} estimated by Gaussian fits to the block averaged cross-spectra. 225

8.1 243

8.2 Receiver phase difference offsets obtained by applying Gaussian to the histograms of the receiver phase differences calculated in the frequency-domain. 245

8.3 Magnitude of the velocity estimates obtained for the IDI-like and MSIRI techniques for the individual and multiple record analyses
284

D.1 The FCA rejection criteria 320

H.1 Relationship between estimated velocity, average zenith angle and average radial velocity for different values of the zenith angle threshold for the UNSIRI and IDI-like analyses. 351

H.2 Relationship between estimated velocity, average zenith angle and average radial velocity for different values of the power threshold for the UNSIRI and IDI-like analyses. 354

List of Figures

1.1 Typical example of the temperature profile and the corresponding atmospheric nomenclature (adapted from *Brasseur and Solomon*, [1986]). 2

1.2 Stylized example of the electron concentration profile obtained for day and night and the corresponding ionospheric nomenclature. 4

1.3 Range-time plot illustrating the operation of an atmospheric radar (see text for details) (adapted from *Röttger*, [1984]). 7

1.4 The range of altitudes observed by atmospheric radars (revised from *Vandepeer*, [1993]). 9

1.5 Typical altitude profiles of the wet, dry and ionization terms of (1.1) (adapted from *Sato*, [1988]). 11

1.6 Illustration of the effects of Bragg scatter, Fresnel reflection and Bragg scatter upon the refractive index, n (adapted from *Röttger*, [1989]). 12

1.7 Taxonomy of spaced antenna analysis techniques (revised from Vandepeer [1993]). 13

2.1 Schematic illustration of the layout of the Buckland Park field station. 20

2.2 Schematic illustration of the configuration of "effective" antennae employed for the SA system at Buckland Park. 22

2.3 Schematic illustration of the configuration of effective antennae employed for the real-time SA system at Buckland Park (after *Reid et al.*, [1995]). 23

2.4 Schematic illustration of the configuration of the eight groups of three dipoles chosen for the May 1993 campaign. 26

2.5 Contour, cross-section, and surface plots of the polar diagram of the transmitted beam for the BP930518 data-set. 27

2.6 Average RMS signal amplitude and SNR profiles obtained for receiver 1 over the first four hours of the data-set BP930518. 28

2.7 Average RMS signal amplitude and SNR profiles obtained for receiver 1 over the first two hours of the data-set BP940527. 29

3.1 Geometry of radar backscatter model. 36

3.2 Example of the radar and enclosing volumes resulting from the use of the MF simulation parameters specified in Table 3.2 and 3.3. 41

3.3 Example of the horizontal turbulent velocity field obtained using a zonal and meridional rms velocity of 6 ms^{-1}. 42

3.4 Example of the vertical turbulent velocity field obtained using an rms vertical velocity of 6 ms^{-1}. 43

3.5 Standard antenna configuration employed for model data generated using the SA simulation. 47

3.6 Typical example of the time-series produced using the standard MF simulation parameters. 50

3.7 Typical example of the time-series obtained using the Buckland Park MF radar at a range of 90 km. 50

3.8 Typical example of the time-series produced using the standard VHF simulation parameters. 51

3.9 Typical example of the time-series obtained using the Buckland Park VHF radar at a range of 10 km. 51

3.10 Two examples of the evolution of the ground diffraction pattern image obtained by *Felgate and Golley* [1971]. 52

3.11 Ground diffraction patterns obtained using the model-generated data-set MOD-MF-GDP-V50. 55

3.12 Ground diffraction patterns obtained using the model-generated data-set MOD-MF-GDP-V0-T6. 57

3.13 Ground diffraction patterns obtained using the model-generated data-set MOD-MF-GDP-V50-T6. 59

3.14 Estimated ν values obtained using the FCA and spectral-width techniques for the model-generated data-set MOD-MF-TURB. 62

3.15 Estimated θ_s values obtained using the spatial-correlation and spectral-width techniques for the model-generated data-set MOD-MF-ASP-SEN. 64

3.16 Estimated θ_s values obtained using the spatial-correlation and spectral-width techniques as a function of the model turbulent random motions magnitude ν_{mod}. 65
3.17 MAOAs estimated using the model-generated data-set MOD-MF-DOPP. . . . 67

4.1 Example of the typical model-generated ground diffraction patterns resulting from the simulation of isometric and anisometric scatter. 74
4.2 Spatial correlation function obtained from the simulation of the anisometric scatter simulation. 75
4.3 Two-dimensional (ξ, τ) spatio-temporal correlation function obtained from the simulation of the isometric scatter situation in the presence of turbulent motions. 76
4.4 Two-dimensional (ξ, τ) and (η, τ) spatio-temporal correlation functions obtained from the simulation of the isometric scatter situation in the presence a mean background wind and turbulent motions 78
4.5 Schematic representation of the auto- and cross-correlation functions employed by the FCA for the determination of the correlation parameters. . . . 80
4.6 Typical examples of mean auto- and cross-correlation functions obtained using the Buckland Park MF SA system at 88 km. 86
4.7 The results obtained for the application of the FCA to the model-generated data-set MOD-MF-SA as a function of ν_{mod}. 87
4.8 Contours of the averaged radial velocity field resulting from a wind field both with and without isotropic turbulence motions. 88
4.9 Directions of the average true (θ_t) and apparent (θ_a) velocities as a function of model velocity direction (θ_{mod}). 91
4.10 Direction differences and as a function of θ_{mod} using various different anisometry parameters. 92
4.11 Histograms of the axial-ratio and axial-rotation obtained on applying the FCA to the model-generated data-set MOD-MF-ANISO using various different anisometry parameters. 93
4.12 Typical example of the zonal and meridional velocities obtained over the period of the wave for waves propagating parallel, perpendicular, and anti-parallel to the direction of the mean wind velocity. 95
4.13 Results of the application of the FCA to first two hours of the data-set BP940527. 99

4.14 Further results of the application of the FCA to first two hours of the data-set BP940527 100

4.15 Percentage of occurrence of error codes 0, 3, and 5 for the first two hours of the data-set BP940527. 101

4.16 Average cubic spline interpolated zero-lag auto-correlation using 3, 4, and 5 lags either side of zero-lag for the model-generated data-set MOD-VHF-SAMP.103

4.17 Average second-, fourth-, and sixth-order polynomial interpolated zero-lag auto-correlation using 4 lags either side of zero-lag for the model-generated data-set MOD-VHF-SAMP. 104

4.18 Variation of fading time and SNR as a function of sampling time for the model-generated data-set MOD-VHF-SAMP. 105

4.19 Average estimated cross-correlation maxima ρ_{0ij} as a function of sampling time for the model-generated data-set MOD-VHF-SAMP. 106

4.20 True velocity estimated by the OFCA and RFCA as a function of sampling time for the model-generated data-set MOD-VHF-SAMP. 109

4.21 True velocity estimated by the OFCA (solid line) and RFCA (dotted line) as a function of sampling time for the model-generated data-set MOD-VHF-VEL.111

4.22 Reproduction of Figure 5 of *Vincent et al.* [1987] and Figure B.3 of *Rajopadhyaya* [1994] illustrating the velocity fall-off sometimes seen in the application of the FCA to tropospheric VHF radar data. 112

4.23 Results of the application of the FCA to the model-generated data-set MOD-MF-IDI-NSCAT using $\nu_{\mathrm{mod}} = 0$ ms^{-1} as function of the number of model scatterers N_{scat}. 115

4.24 Results of the application of the FCA to the model-generated data-set MOD-MF-IDI-NSCAT using $\nu_{\mathrm{mod}} = 6$ ms^{-1} as function of the number of model scatterers N_{scat}. 117

4.25 Effect of time-series length upon the auto- and cross-correlation functions. . . 119

4.26 Results of the application of the FCA as a function of record length N for the model-generated data-set MOD-MF-4096. 121

4.27 Results of the application of the FCA to correlation functions obtained from the coherent average of N_{av} individual correlation functions for the model-generated data-set MOD-MF-SA. 123

4.28 Example of the effect of coherent averaging upon the auto- and cross-correlation functions. 124

5.1 True velocity magnitude V_t as a function of antenna spacing for four E-region records of the analysis of *Golley and Rossiter* [1970]. 131

5.2 Histograms of the true velocity magnitude estimated using the small and large spacings of the "main array" at Saskatoon (after *Meek*, [1990]), and profiles of the true velocity magnitude estimated using small and large spacings for the MU radar (after *Van Baelen et al.*, [1990]) 132

5.3 Averaged true velocity magnitude, apparent velocity magnitude, $T_{0.5}$, and $S_{0.5}$ obtained as a function of antenna spacing for the application of the FCA to the model-generated data-set MOD-MF-TSE. 134

5.4 Examples of typical cross-correlation functions obtained using the model-generated data-set MOD-MF-TSE. 135

5.5 Histograms of $S_{0.5}$ and $T_{0.5}$ obtained from the application of the FCA to model-generated data-set MOF-MF-TSE using antenna configurations with spacings 100 and 400 m. 138

5.6 Standard deviations of the true velocity magnitude, apparent velocity magnitude, $T_{0.5}$ and $S_{0.5}$ obtained as a function of antenna spacing for the application of the FCA and UFCA using rejection criteria 16 to the model-generated data-set MOD-MF-TSE. 139

5.7 Example of the effects of the addition of various different amounts of uncorrelated noise on the auto- and cross-correlation functions. 140

5.8 Average true velocity magnitude, $T_{0.5}$, and pattern scale as a function of antenna spacing obtained on the application of the FCA and UFCA to the model-generated data-set MOD-MF-TSE for various different SNRs of added receiver noise. 142

5.9 Example of the effects of the time-series digitization upon the auto- and cross-correlation functions, and the noise-corrected auto- and cross-correlation functions. 144

5.10 Average true velocity magnitude, $T_{0.5}$, and $S_{0.5}$ as a function of antenna spacing for the FCA and UFCA for various different numbers of digitization levels. 145

5.11 Example of the effects of the time-series saturation upon the auto- and cross-correlation functions, and the noise-corrected auto- and cross-correlation functions for various different "saturation percentages". 146

5.12 Average true velocity magnitude, $T_{0.5}$, and $S_{0.5}$ as a function of antenna spacing for the FCA and UFCA for various different "saturation percentages". . . 147

5.13 Results of the application of the FCA to the first four hours of the data-set BP930518. 153

5.14 One-dimensional spatial correlation function obtained using the aligned antenna trio 137 for heights 96, 92, 88 and 84 km for the first four hours of the BP MF data-set BP930518. 154

6.1 Meridional and zonal velocities estimated on the application of the SFCA to data collected by a 915 MHz SA profiler developed by the National center of atmospheric research (NCAR). 162

6.2 Typical example of the slopes obtained from the application of the zero-lag interpolation to the cross-correlation functions calculated using the data-set BP940527 at 90 km. 165

6.3 Results of the application of the FCA and RSFCA to the model-generated data-set MOD-MFSA. 168

6.4 Average velocity directions as a function of model velocity direction for the application of the anisometric and isometric formulations of the RSFCA to the model generated data-set MOD-MF-ANISO. 168

6.5 Profiles of the average velocity magnitude and standard deviation, and average velocity direction and standard deviation obtained applying the FCA and RSFCA to the data-set BP940527. 169

6.6 Example of the spatial correlation functions from the anisotropic scatter simulation at temporal lags $\tau = 0$ and $\tau = 2$ s. 172

6.7 Illustration of the technique used to estimate the position of the spatial correlation maxima $\rho(\xi, \eta, \Delta t)$ for three antennae $A_i = (\xi_i, \eta_i)$ arranged in an equilateral triangle. 174

6.8 A typical example of the application of the Gaussian fit to the spatial correlation values along the three arms of spatial lags obtained using an individual record of the model-generated data-set MOD-MF-SA with $\nu_{\text{mod}} = 6\ \text{ms}^{-1}$. . . 176

6.9 The estimation of the position of the spatial correlation maxima $\vec{D}_{\max}$ corresponding to the results illustrated in Figure 6.8. 177

6.10 Results of the application of the FCA and SCA3 to the model-generated data-set MOD-MF-SA. 178

6.11 Illustration of the SCA4S technique used to estimate the position of the spatial correlation maxima for four antennae arranged in a square. 181

6.12 Illustration of the SCA4T technique used to estimate the position of the spatial correlation maxima for four antennae arranged in a "Y" configuration. 182

6.13 Average velocity and standard deviation, and average direction and standard deviation obtained applying the FCA and SCA4S to the model-generated data-set MOD-MF-IDI. 183

6.14 Profiles of the results obtained on applying the FCA, SCA4S and SCA3 to the data-set BP930518. 186

6.15 Scatter plots of the magnitude and direction of the velocity estimates obtained for the application of the SCA4S and FCA-158 to the data-set BP930518. . . 187

7.1 Scatter plots of the true velocity magnitude and direction obtained on the application of the FCA and the FSA for data recorded using the BP MF radar (after *Briggs and Vincent*, [1992]). 192

7.2 Scatter plots of the zonal and meridional velocities estimated on the application of the FCA and the FSA to data recorded using the MU radar (after *Sheppard et al.*, [1993].) 193

7.3 Scatter plots of the zonal and meridional velocities estimated on the application of the FCA and FSA to data recorded using the Chung-Li VHF radar (after *Liu and Pan*, [1993]). 193

7.4 General form of the cross spectrum assumed by the FSA. 197

7.5 Typical three-receiver cross-spectral magnitude and phase pairs obtained using the BP MF radar in SA mode at 80 km. 198

7.6 Example of a typical cross-spectrum obtained at 80 km using the BP MF radar in SA mode before and after four point smoothing. 202

7.7 Example of the operation of the spike elimination procedure using a cross-spectrum obtained at 94 km using the BP MF radar in SA mode. 203

7.8 Scatter plots of the FCA and FSA estimates of $\tau_{0.5}$ obtained without and with use of the spike-elimination procedure for the first two hours of the BP MF SA data-set BP940527 205
7.9 Example of the operation of the phase unwrapping procedure. 208
7.10 Scatter plot of the FCA and FSA estimates of τ'_{ij} both without and with use of spectral magnitude weighting for the first two hours of the BP MF SA data-set BP940527. 210
7.11 Histogram of the σ_{ij} values obtained for "signal" and "noise" phase variations using the first two hours of the BP MF SA data-set BP940527. 211
7.12 Means and standard deviations of the apparent velocity magnitude (V_a) and direction (θ_a) obtained for the application of the FCA and BVFSA techniques to the model-generated data-set MOD-MF-SA. 213
7.13 Means and standard deviations of the true velocity magnitude (V_t) and direction (θ_t) obtained for the application of the FCA, BVFSA, SLFSA, and LPFSA techniques to the model-generated data-set MOD-MF-SA. 214
7.14 Means and standard deviations of the fading time $\tau_{0.5}$ and corrected fading time $T_{0.5}$ as a function of turbulent motions magnitude ν_{mod} obtained for the FCA, BVFSA, SLFSA, and LPFSA techniques to the model-generated data-set MOD-MF-SA. 215
7.15 Scatter plots of the FCA and FSA estimates of τ_{ij} obtained on applying the BVFSA and LPFSA to the first two hours of the BP MF SA data-set BP940527.217
7.16 Scatter plot of the FCA and SLFSA estimates of ρ_{0ij} obtained for the first two hours of the BP MF SA data-set BP940527. 218
7.17 Example of the contributions of the correlation function tails to the cross-spectra. 219
7.18 Scatter plot of the FCA and BVFSA estimates of τ_{ij} obtained using cross-spectra produced by the Fourier transform of the main peak of the cross-correlation functions for the first two hours of the BP MF SA data-set BP940527.221
7.19 Effect of time-series length upon the BVFSA and LPFSA. 223
7.20 Effect of coherent block averaging upon the cross-spectrum for an individual record of the BP MF SA data-set BP940527 at 80 km. 224
7.21 Average true velocity magnitude V_t estimated from the application of the BVFSA to the model-generated data-set MOD-MF-SA. 226

7.22 Scatter plots of the FCA and BVFSA estimates of τ_{ij} obtained using spectral averaging for the first two hour of the BP MF SA data-set BP940527. 228

7.23 Results of the application of the BVFSA and LPFSA to spectra and the FCA to spectra calculated using various different numbers of coherent averages for the model-generated data-set MOD-MF-SA with $\nu_{\mathrm{mod}} = 6\ \mathrm{ms}^{-1}$. 230

7.24 Standard deviation of the results of the application of the BVFSA and LPFSA to spectra and the FCA to correlation functions calculated using various different numbers of coherent averages for the model-generated data-set MOD-MF-SA with $\nu_{\mathrm{mod}} = 6\ \mathrm{ms}^{-1}$. 231

8.1 Two-dimensional representation of the phase difference ϕ_{ij} introduced between two receiving antenna i and j with separation d_{ij} due to reflection from a refractivity layer tilted at angle θ from the horizontal (adapted from *Röttger and Ierkic*, [1985]). 239

8.2 Histograms of the receiver phase differences obtained sing the phase of the zero-lag cross-correlation for the first 4 hours of the data-set BP930518. . . . 241

8.3 MAOAs obtained from the zero-lag cross-correlation phase after removal of the phase offsets as a function of height. 242

8.4 Relationship between the cross-correlation function and the cross-spectrum (adapted from *Briggs and Vincent*, [1992]) 244

8.5 Scatter plots of the zonal and meridional direction cosines obtained using the zero-lag cross-correlation phase and the cross-spectral phase at the Doppler offset. 246

8.6 Results obtained on the application of the MSIRI and FCA analyses to data recorded using the Saskatoon $1 - \lambda$ array (after *Meek and Manson*, [1987]). . 250

8.7 Results obtained on the application of the NSIRI and FCA analyses (after *Franke et al.*, [1990]) 251

8.8 Example of the effective scattering positions located by the imaging interferometry techniques in the volume-scatter situation using the cross-spectral phases at each Doppler frequency. 253

8.9 Relationship between the characteristic ellipse and the line of effective scattering positions obtained for isometric and anisometric scatter as a function of the direction of the actual wind velocity. 254

8.10 Preferred azimuth of effective scattering positions obtained in the IDI-like analysis (after *Vandepeer and Reid*, [1995a]). 256

8.11 Actual and estimated scattering positions located by the IDI technique (after *Adams et al.*, [1985]). 257

8.12 Example of the linear fits to the phase values along the meridional arm of the interferometer for the first record of the model generated data-set MOD-MF-IDI with $\nu_{\mathrm{mod}} = 0\ \mathrm{ms}^{-1}$. 260

8.13 Power spectrum and horizontal positions of the effective scattering positions located for the interferometric analyses using $N_{\mathrm{scat}} = 10$. 261

8.14 Power spectrum and horizontal positions of the effective scattering positions located for the interferometric analyses using $N_{\mathrm{scat}} = 20$. 262

8.15 Power spectrum and horizontal positions of the effective scattering positions located for the interferometric analyses using $N_{\mathrm{scat}} = 50$. 263

8.16 Power spectrum and horizontal positions of the effective scattering positions located for the interferometric analyses using $N_{\mathrm{scat}} = 100$. 264

8.17 Effective scattering positions located on applying the IDI-like technique to the model-generated data-set MOD-MF-IDI-NSCAT with $\nu_{\mathrm{mod}} = 0\mathrm{ms}^{-1}$ for various different values of N_{scat}. 266

8.18 Distribution of the preferred azimuths relative to the direction of the model input velocity θ_{mod} obtained on applying the IDI-like technique to the model-generated data-set MOD-MF-IDI-NSCAT with $\nu_{\mathrm{mod}} = 0\mathrm{ms}^{-1}$ for various different values of N_{scat}. 267

8.19 Distribution of the preferred azimuths relative to the direction of the model input velocity θ_t obtained using the model-generated data-set MOD-MF-IDI. 268

8.20 Distribution of the preferred azimuths relative to the direction α obtained relative to α, and relative to the direction of the model input velocity obtained on applying the IDI-like analysis to the model-generated data-set MOD-MF-IDI-ROTN2. 269

8.21 Average zenith angle and absolute radial velocity of the effective scattering points produced for the interferometric analyses. 270

8.22 Average horizontal velocity magnitudes estimated by the FCA and interferometric techniques as a function of model turbulent velocity. 272

8.23 Average horizontal velocity directions estimated from the application of the FCA and interferometric techniques to the model-generated data-sets MOD-MF-IDI-ROTN and MOD-MF-IDI-ROTN2. 274

8.24 Average horizontal velocities estimated by the FCA and interferometric techniques as a function of the number of model scatterers N_{scat} for a model turbulent velocity of 6 m s^{-1}. 275

8.25 Average horizontal velocity magnitude and direction estimated on applying the FCA and interferometric techniques to the model generated data-set MOD-MF-IDI with $\nu_{\mathrm{mod}} = 6$ ms^{-1} as a function of SNR. 278

8.26 Examples of the positional perturbations resulting from the addition of receiver noise of various different SNR. 279

8.27 Average horizontal velocity magnitude estimated on applying the UNSIRI technique to the model-generated data-set MOD-MF-IDI with $\nu_{\mathrm{mod}} = 6$ ms^{-1} as a function of the displacement of the direction cosines of the effective scattering positions. 280

8.28 Average horizontal velocity magnitude and direction estimated on applying the interferometric techniques to the model-generated data-set MOD-MF-IDI with $\nu_{\mathrm{mod}} = 6$ ms^{-1} as a function of receiver SNR using an antenna spacing of $d = \lambda$. 281

8.29 Effective scattering positions located on applying the IDI-like technique to the model-generated data-set MOD-MF-IDI for various different SNRs. 283

A.1 Antenna configuration employed for model-generated data-set MOD-MF-IDI. 300

A.2 Antenna configuration employed for model-generated data-set MOD-MF-TSE. 302

A.3 Antenna configuration employed for model-generated data-set MOD-MF-TSE. 303

B.1 Illustration of the derivation of (B.2). 306

B.2 Geometrical construction illustrating the calculation of the velocity $\vec{V}$ from the trace velocities V_x and V_y. 307

B.3 Geometrical construction illustrating the calculation of the velocity $\vec{V}$ from the trace velocities V_x and V_y for the general case of non right-angled triangle. 307

C.1 Example of the effects of the addition of various different amounts of uncorrelated noise on the auto- and cross-correlation functions. 315

E.1 Results of the application of the FCA to the smallest and largest equilateral triangles of the model-generated data-set MOD-MF-TSE-ROTN. 324

E.2 Results of the application of the FCA to the smallest and largest equilateral triangles of the model-generated data-set MOD-MF-TSE-ROTN with 4 dB added noise. 325

E.3 Results of the application of the UFCA to the smallest and largest equilateral triangles of the model-generated data-set MOD-MF-TSE-ROTN with 4 dB added noise. 326

E.4 Results of the application of the FCA to the smallest and largest right-angled triangles of the model-generated data-set MOD-MF-TSE-ROTN. 327

E.5 Acceptance rate for the application of the FCA to the largest right-angled triangle of the model-generated data-set MOD-MF-TSE-ROTN. 328

E.6 Results of the application of the FCA to the smallest and largest right-angled triangles of the model-generated data-set MOD-MF-TSE-ROTN with 4 dB added noise. 329

E.7 Results of the application of the UFCA to the smallest and largest right-angled triangles of the model-generated data-set MOD-MF-TSE-ROTN with 4 dB added noise. 330

E.8 Results of the application of the UFCA to the smallest and largest equilateral triangles of the model-generated data-set MOD-MF-TSE-ROTN for a saturation percentage of 100%. 331

E.9 Results of the application of the UFCA to the smallest and largest right-angled triangles of the model-generated data-set MOD-MF-TSE-ROTN for a saturation percentage of 100%. 332

F.1 Example of power-spectra obtained using various SNRs of added noise. 338

F.2 Illustration of the variation of the spectral parameters determined from the cross-spectrum for various different SNRs. 339

F.3 Example of cross-spectral magnitude and phase obtained using various SNRs of added noise. 343

F.4 Example of cross-spectral magnitude and phase obtained using various SNRs of added noise. 344

F.5 Illustration of the variation of the spectral parameters determined from the cross-spectrum for various different SNRs. 345

H.1 Average horizontal velocities estimated by the interferometric techniques as a function of zenith angle threshold for a model turbulent velocity of 6 ms^{-1}. . 350

H.2 Average horizontal velocities estimated by the interferometric techniques as a function of zenith angle threshold, for a model turbulent velocity of 6 ms^{-1}. . 351

H.3 Average horizontal velocities estimated by the interferometric techniques as a function of zenith angle threshold, for a model turbulent velocity of 6 ms^{-1}. . 352

H.4 Average horizontal velocities estimated by the interferometric techniques as a function of power threshold for a model turbulent velocity of 6 ms^{-1}. 353

H.5 Effective scattering positions located using Doppler frequencies with spectral powers below the 5 dB power threshold on applying the UNSIRI and IDI-like analyses to the model-generated data-set MOD-MF-IDI with $\nu_{mod} = 6$ ms^{-1}. 355

H.6 Magnitude of the average horizontal velocities obtained on the application of the IDI-like technique to the model-generated data set MOD-MF-IDI with $\nu_{mod} = 6$ ms^{-1} as a function of phase consistency threshold. 356

UNIVERSITY OF ADELAIDE LIBRARY

Chapter 1

Introduction

1.1 Introduction

This thesis provides a systematic evaluation of a range of spaced antenna (SA) radar analysis techniques developed for the estimation of atmospheric dynamics. The principal tool employed in this evaluation is a numerical model simulating the backscatter from a number of refractive index irregularities. This thesis has been structured such that the introductory material relevant to each individual topic is addressed at the commencement of the appropriate chapter. As a result, this introduction is necessarily brief. It is intended to provide a brief outline of the atmosphere, and the techniques employed to measure the physical properties of the atmosphere.

1.2 The atmosphere

1.2.1 Temperature structure

The atmosphere is usually classified according to the different physical properties observed as a function of the height above the surface of the Earth. The most common classification is based upon the temperature structure, as illustrated in Figure 1.1 (e.g. *Brasseur and Solomon*, [1986]). Although this structure is basically independent of latitude, longitude, and season, the individual profiles can vary considerably. The regions in ascending height are denoted the "troposphere", "stratosphere", "mesosphere", and "thermosphere". The transitions between these regions are denoted the "tropopause", "stratopause", and "mesopause".

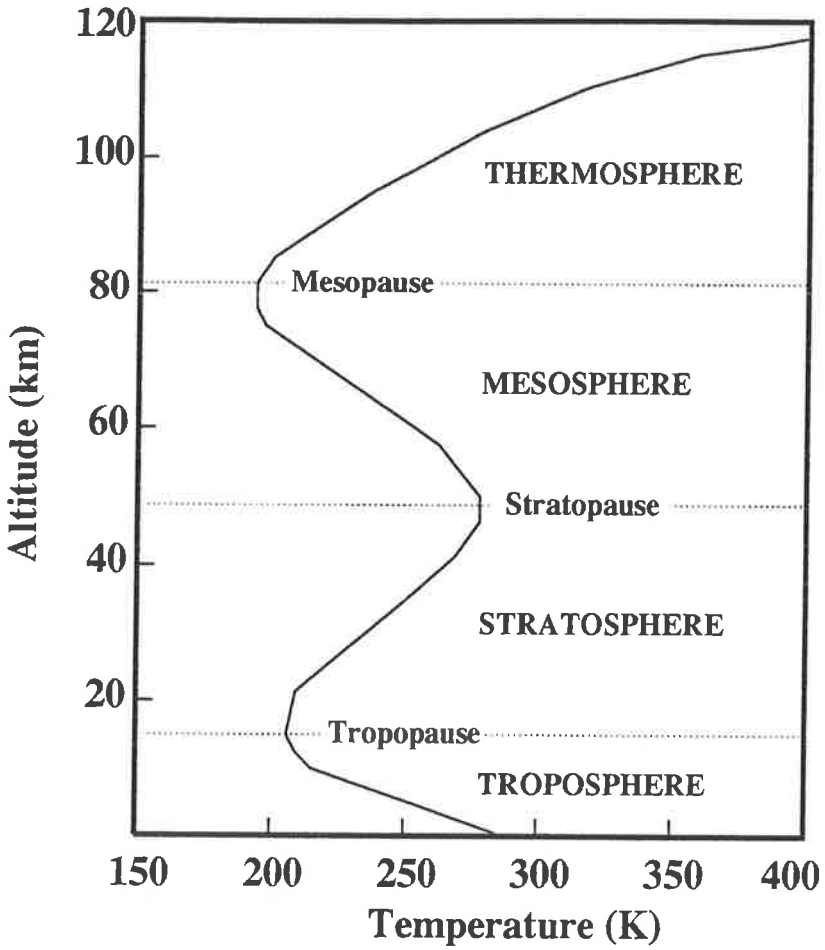

Figure 1.1: Typical example of the temperature profile and the corresponding atmospheric nomenclature (adapted from *Brasseur and Solomon*, [1986]).

The temperature structure illustrated in Figure 1.1 is a direct result of the interaction of solar electro-magnetic radiation with the atmosphere and the surface of the Earth. This interaction produces a number of competing dynamical and radiative processes local to individual regions of the atmosphere. The incoming solar radiation heats the surface of the Earth to approximately 280 K. The Earth then re-radiates as a black-body spectrum, peaking in the infra-red. The troposphere contains a number of gases which absorb infra-red radiation (e.g. H_2O, CO_2, and CH_4). This absorption results in the troposphere being heated. In an atmosphere devoid of liquid particles a vertically ascending parcel of air will cool at the dry "adiabatic lapse rate", which for the Earth is 9.8 K km^{-1}. The heating of the troposphere modifies the adiabatic lapse rate, producing an average value of about 6.6 K km^{-1}. The decrease in the rate of cooling at the tropopause results from the increase in the concentration of ozone, which maximizes at approximately 40 km. The incoming ultra-violet solar radiation dissociates the ozone, thereby heating the atmosphere. This

heating is responsible for the increasing temperature structure seen in the stratosphere. The concentration of ozone decrease significantly at the stratopause, where the emission of infrared radiation by carbon dioxide begins to cool the atmosphere. This cooling is responsible for the decreasing temperature structure seen in the mesosphere. The temperature structure in the mesosphere often departs significantly from radiative equilibrium. This behavior is the result of the deposition of energy and momentum by breaking internal atmospheric gravity waves. Above the mesopause both atomic and molecular oxygen absorb solar ultra-violet radiation, resulting in a subsequent increase in the temperature. This trend continues for several hundred kilometers until the *exosphere*, which is an essentially isothermal region.

1.2.2 The ionosphere

The ionosphere is the region of the atmosphere containing sufficient electron concentration to affect the propagation of radiowaves. The most common classification of the ionosphere is based upon the profile of the electron concentration (e.g. *Rishbeth and Garriot*, [1969]), as illustrated in Figure 1.2. The electrons are produced together with positive ions by the ionization of molecular oxygen and nitrogen, and nitrogen monoxide, by incoming short-wavelength solar-radiation and cosmic rays. The electron concentration is governed by a complex series of equations whose rates vary as a function of height, season, and time of day. The electron concentration is significantly greater during the day than at night, when the absence of solar radiation results in the recombination of the electrons and the positive ions.

The equations governing the propagation of radiowaves through the ionosphere can be derived by assuming the ionosphere acts as an ionized gas. In the absence of the Earth's geomagnetic field the refractive index n of the ionosphere for a transmitted signal of frequency ω is given by (e.g. *Rishbeth and Garriot*, [1969])

$$n = \sqrt{1 - \frac{\omega_N^2}{\omega^2}}, \tag{1.1}$$

where

$$\omega_N = \sqrt{\frac{Ne^2}{\epsilon_0 m}} \tag{1.2}$$

is denoted the "plasma frequency", N is the number density of electrons and positive ions, e is the electron charge (coulombs), ϵ_0 is electric permittivity of free space, and m is the mass of the particles (kg). Because the mass of the positive ions are at least three orders of magnitude larger than the mass of the electrons the effects of the positive ions can be

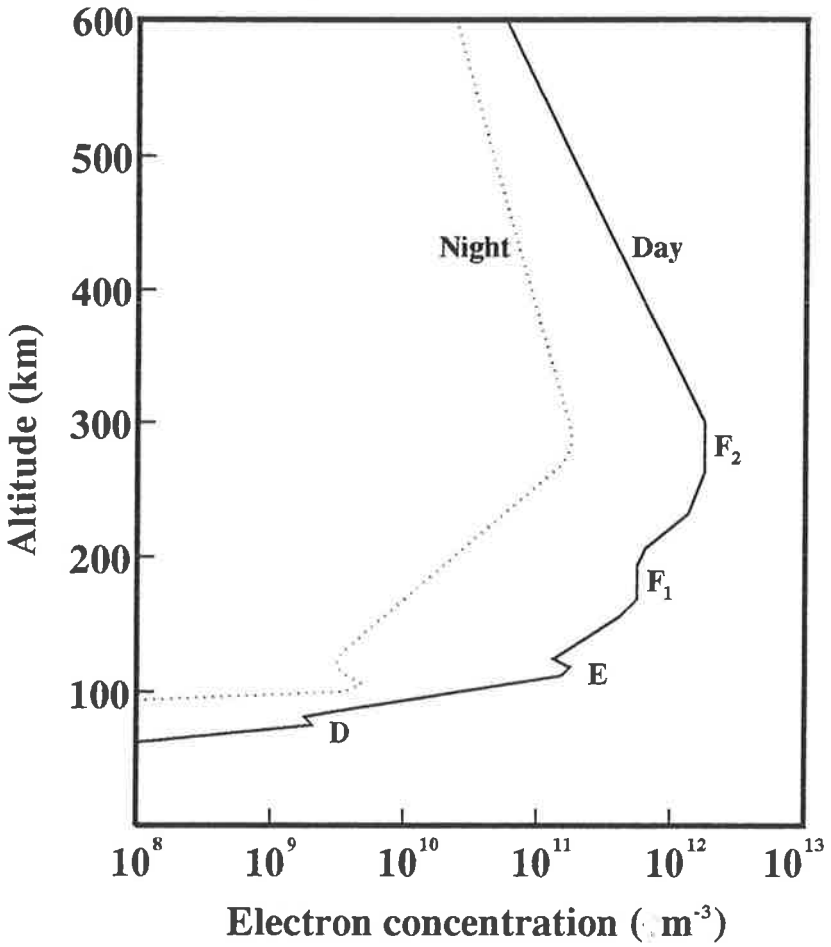

Figure 1.2: Stylized example of the electron concentration profile obtained for day (solid line) and night (dotted line) and the corresponding ionospheric nomenclature.

considered negligible. As the refractive index given by (1.1) is always less than unity the group velocity of the transmitted signal is always less than the speed of light throughout the ionosphere. The transmitted signal is therefore delayed as it propagates through the ionosphere. This effect is sometimes referred to as "group retardation", and must be taken into account in determining the height profiles of the various characteristics of the ionosphere under observation, such as the electron number density.

If the effects of the Earth's geomagnetic field are taken into account the ionosphere can be seen to act as a doubly refracting medium. The two modes of propagation are denoted the "ordinary" (O) and "extraordinary" (E or X) modes. The two modes are polarized in opposite senses, and propagate with different group velocities. The resulting expressions for the refractive index (see for e.g. *Rishbeth and Garriot*, [1969]) indicate that the refractive index can equal zero, in which case "total reflection" occurs. The electron concentration generally decreases with decreasing height because the majority of the ionizing radiation is

absorbed at the upper heights, thereby leaving less radiation for the ionization at the lower heights. As the refractive index for O-mode polarization is smaller than that for E-mode polarization it follows that total reflection for O-mode polarization occurs at a lower height than for E-mode polarization. Because linear polarization can be considered approximately to be the sum of the O- and E- modes the plane of polarization of a linearly polarized wave will rotate as the signal propagates. This effect is referred to as "Faraday rotation".

The individual regions of the ionosphere are denoted according to the peaks in the electron concentration profiles by, in ascending height, the D, E, F_1 and F_2 regions. The D-region lies between about 60 and 90 km, corresponding roughly with the mesosphere as defined in the temperature based nomenclature illustrated in Figure 1.1. As a result, the terms "D-region" and "mesosphere" are sometimes used interchangeably, as is the case throughout this thesis. The D-region is formed by the ionization of nitrous oxide by the Lyman-α Hydrogen emission line, and to a lesser extent by the ionization of molecular oxygen by the Lyman-β Hydrogen emission line and ultra-violet radiation. The D-region provides "partial reflection" radar returns from small discontinuities in the refractive index at both MF and VHF, allowing the application of the spaced antenna radar techniques described throughout this thesis. The E-region lies between about 90-150 km. The F-region is usually split into the F_1 region, which lies at an altitude of about 180 km, and the F_2 region, which lies at an altitude of about 280 km.

1.2.3 Atmospheric measurements

The measurement of the physical properties of the atmosphere can be divided into two separate groups, namely "in-situ" and "remote sensing" techniques. Examples of in-situ techniques include rocket and balloon borne techniques. These techniques have the advantage of providing a direct measurement of the physical properties of interest, such as pressure, density, temperature, electron concentration, chemical composition, and wind velocities. The remote sensing techniques require the estimation of the physical parameter of interest based on a theoretical model relating the physical parameter to some other measurable parameter. Examples of remote sensing techniques include radio techniques such as "radars" (Radio detection and ranging) and "ionosondes", and optical techniques such as "lidars" (Light detection and ranging), spectrometers and photometers. The remote-sensing techniques can be performed using both ground- and satellite-based radio and optical instruments, providing excellent temporal and spatial resolution of the physical parameter of interest.

1.3 Observations of atmospheric dynamics using radar techniques

1.3.1 Atmospheric radar

The origins of radar can arguably be traced back to work of Hertz, who in 1887 produced the first simulated radio-wave. This work led to the development of telecommunications through the work of Marconi, and the studies of communication at radio frequencies. The motivation for the understanding these communications provided the impetus for the initial investigations of the ionosphere. The height of the ionosphere was first measured by *Appleton and Barnet* [1926] using the "total-reflection" returns produced by a variable-frequency continuous electromagnetic wave emitter. The earliest partial reflections were observed in subsequent investigations (e.g. *Appleton*, [1930]). The ranging of detectable objects was enabled by the work of Watson-Watt, who in 1935 patented a pulsed monostatic radar which became the prototype for modern aviation, navigation, and atmospheric radars.

The operation of an atmospheric radar is summarized in Figure 1.3. Consider the situation where a radio frequency (RF) pulse of duration $\triangle T$ is transmitted at time T_0. The pulse shape is typically either Gaussian, triangular, boxcar or smoothed trapezoidal. The pulse propagates into the atmosphere at the speed of light, c, and is backscattered from various different ranges. The returns from the range R_a can be sampled by receiving the signal returns over the time interval T_a to $T_a + \triangle T$ after the time of transmission T_0, where $T_a = 2R_a/c$. The returns sampled over the time interval T_a to $T_a + \triangle T$ originate from the range of heights indicated by the shaded region. This region is typically referred to as a "range gate". The resolution $\triangle R$ of the range gate is given by $\triangle R = c \triangle T/2$. The range resolution can be increased by decreasing the pulse duration. The "bandwidth" of the receiving system provides a lower limit for the pulse duration, and therefore a lower limit for the range resolution $\triangle R$.

In order to sample the signal returns from each range gate with high temporal resolution the pulses are normally transmitted periodically. The period of the transmission is denoted the inter-pulse period T_{ipp}, while the reciprocal of T_{ipp} is denoted the pulse repetition frequency (PRF). The use of pulse repetition can introduce "range aliasing", whereby the returns from a larger range may also be sampled, thereby contaminating the resulting received signal. This effect is illustrated in Figure 1.3, where the returns from the range R_b resulting from the backscatter of a previously transmitted pulse are received at the same

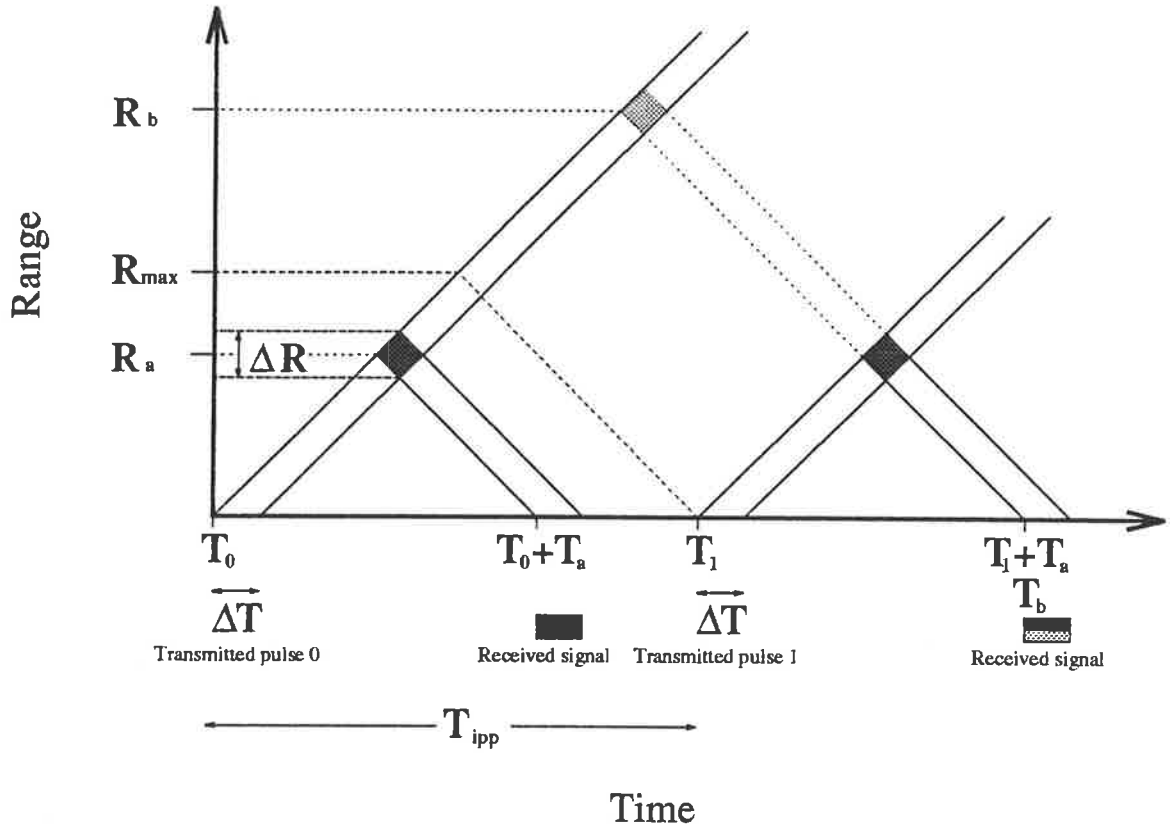

Figure 1.3: Range-time plot illustrating the operation of an atmospheric radar (see text for details) (adapted from *Röttger*, [1984]).

time as the returns from the range R_a. The effects of range-aliasing can be avoided by using "pulse coding", or by using a non-periodic $T_{\rm ipp}$. Pulse coding (e.g. *Woodman et al.*, [1980]) involves assigning a unique "code" to each transmitted pulse so that the receiving system can distinguish the signal returns from each pulse. The maximum unambiguous range of the radar is given by $R_{\rm max} = cT_{\rm ipp}/2$, while the minimum range is given by the pulse duration, plus any delays occurring in the propagation of the transmitted pulse through the transmitting system and the returned signal through the receiving system. The "duty cycle" D of the transmitter refers to the ratio of the pulse duration to the inter-pulse period, $D = \Delta T/T_{\rm ipp}$.

1.3.2 Altitudes observed by atmospheric radars

The range of altitudes observed by atmospheric radars is summarized in Figure 1.4. Medium (MF) and high frequency (HF) radars typically operate at frequencies between 2 and 6 MHz and receive partial-reflection returns from the region between about 60 and 100 km, which corresponds roughly with the mesosphere. The first systematic investigations of the returns from this region were made by *Gardner and Pawsey* [1953] and *Gregory* [1956]. The

backscatter results from ionization, and from refractive index discontinuities with vertical scales of the order of half the radar wavelength produced by turbulence and internal gravity waves. Recent results obtained by *Vandepeer* [1995] using the new Buckland Park MF radar described in Chapter 2 suggest that the height range can be extended below 60 km.

VHF radars typically operate at frequencies between 40 and 230 MHz, and provide consistent temporal coverage between about 1 and 20 km. VHF radars were first used in the late 60's and early 70's (e.g. *Flock and Balsley*, [1967]; *Woodman and Guillen*, [1974]). The backscatter in the troposphere and stratosphere is thought to result primarily from humidity and temperature variations. Ultra high frequency (UHF) radars operate at frequencies between 400 and 900 MHz. "Profiler" radars operate at the lower end of this frequency scale, providing consistent temporal coverage between about 500 m and 10 km. "Boundary layer" radars operate at the higher end of this frequency scale, providing consistent temporal coverage up to 4 km with high range resolution. The backscatter for these radars results from water vapor, precipitation, and aerosols. "Incoherent scatter" radars operate at VHF (e.g. Jicamarca - see for e.g. *Woodman and Guillen*, [1974]) and UHF (e.g. Arecibo - see for e.g. *Harper*, [1978]), and sometimes at both UHF and VHF (e.g. EISCAT - see for e.g. *Rishbeth and Van Eyken*, [1993]). These radars make use of "Thompson scatter" resulting from free electrons. Because the resulting scatter is extremely weak the radars require a large power-aperture product. The lowest observable height is usually between 65 and 70 km (e.g. *Harper and Gordon*, [1980]), and varies as a function of solar conditions. The Doppler shift of the resulting power spectrum can be employed to determine the wind velocity. Because the ion wind may depart from the neutral wind above 100 km due to the effects of the Earth's geomagnetic field the maximum observable height for the determination of the wind velocity is sometimes considered to be about 95 km (e.g. *Hines et al.*, [1993]).

Meteor radars operate at HF, MF, and VHF, and make use of the trail of ionization produced by meteors, which are fragments of extra-terrestrial material which enter the atmosphere at very high velocities (10 - 70 km s^{-1}). Signal returns are obtained from the portion of the trail perpendicular to the radar. The trail of ionization is rapidly diffused, and therefore produces very short-lived echoes. If the lifetime of the trail is sufficient the trail will drift with the mean wind, and the returned signal will be Doppler shifted from the transmitted frequency. The wind velocity can therefore be determined by estimating the Doppler shift. This technique was first employed by *Manning et al.* [1950], and is generally referred to as the "meteor winds" technique. Although meteors can be detected at altitudes

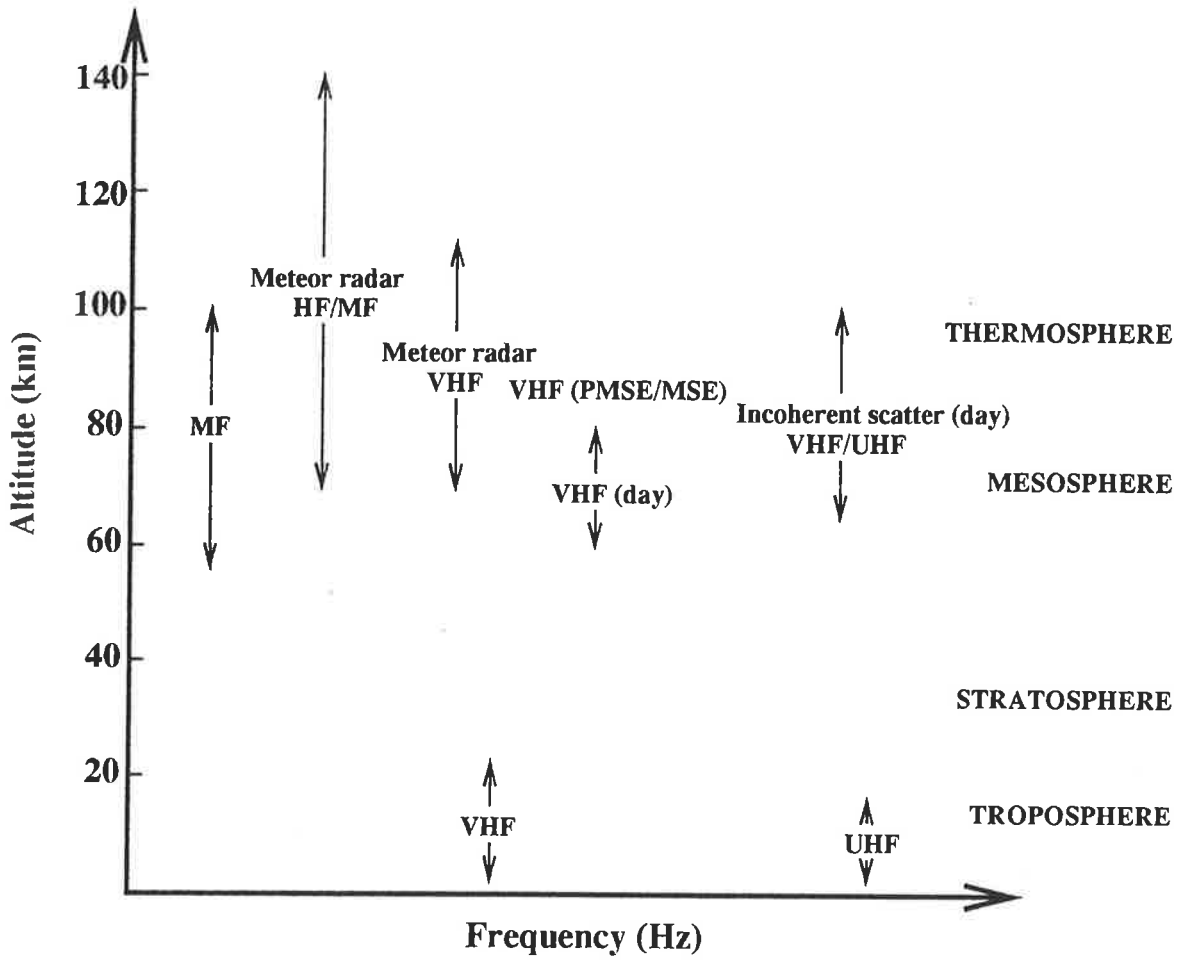

Figure 1.4: The range of altitudes observed by atmospheric radars (revised from *Vandepeer*, [1993]).

up to 120 km (e.g. *Steel and Elford*, [1991]) the meteor winds technique is generally only applied up to 100 km as the ion wind may depart from the neutral wind above this height.

MF/HF radars provide the only consistent temporal coverage of the mesosphere. Sporadic temporal coverage can be obtained using powerful very high frequency (VHF) radars, which are sometimes capable of obtaining returns from between 60 and 80 km during daytime, and can also obtain "polar mesopause summer echoes" (PMSE) at high latitudes (e.g. *Balsley et al.*, [1983]) and "mesopause summer echoes" at mid-latitudes (e.g. *Reid et al.*, [1989]) between 80 and 90 km during summer. Incoherent scatter radars are usually only capable of obtaining returns below 100 km during daylight hours, when there exists sufficient free electrons to produce Thompson scatter. On rare occasions however echoes can be obtained at night from intense layers of sporadic ionization below 100 km. Meteor radars are dependent on the existence of ionized trails perpendicular to the radar, which are produced sporadically. Nevertheless, meteor radars are capable of providing measurements with

a temporal resolution of at least one hour.

1.3.3 Scattering mechanisms

The partial reflection returns observed by atmospheric radars result from the backscatter from refractive index inhomogeneities. These inhomogeneities result from the mixing produced by the action of turbulence and internal gravity waves, and due to the existence of stable reflecting layers. The refractive index n for radiowaves propagating through the lower and middle atmosphere in the HF to UHF frequency range is given by (e.g. *Gage and Balsley*, [1980])

$$n - 1 = \frac{3.73 \times 10^{-1} e}{T^2} + \frac{77.6 \times 10^{-6} P}{T} - \frac{N_e}{2N_c}, \tag{1.3}$$

where e is the partial pressure of water vapor (millibars), T is the absolute temperature (Kelvins), P is the atmospheric pressure (millibars), N_e is the number density of electrons, and N_c is the critical plasma density. The first term on the right hand side of (1.3) is referred to as the "wet" term, and dominates in the lower troposphere due to the large concentration of water vapor. The second term is the "dry" term, and dominates between the mid-troposphere and the stratopause, where the effects of ionization begin to becomes significant. The final term is the "ionization" term, and dominates above the stratopause. The ionization term exhibits a diurnal variation, as a result of the ionization produced during the day and the recombination occurring at night. The height dependence of each of these terms is illustrated in Figure 1.5.

The scatter observed by atmospheric radars can be separated into four distinct categories. "Bragg scatter", or "turbulent scatter", results from refractive index irregularities with scales of the order of half the radar wavelength distributed randomly throughout the volume illuminated by the radar. A radar with operating wavelength λ will obtain signal returns from irregularities whose inner scale, l_0, and outer scale, L_0, obey the inequality $2\pi C_1 l_0 < \lambda/2 < 2\pi C_2 L_0$ (e.g. *Balsley and Gage*, [1980]), where the constants C_1 and C_2 have empirical values of 0.94 and 0.75, respectively (e.g. *Megaw*, [1957]). "Fresnel reflection", or "specular reflection", occurs from stable horizontal layers exhibiting sharp refractive index gradients, producing a slowly varying signal. "Fresnel scatter", or "diffuse reflection", occurs from collections of stable horizontal layers, producing strong, coherent scattered signals. The effects of these scattering mechanisms can be distinguished by examining the returned power profile, as illustrated in Figure 1.6. Fresnel reflection produces a sharp peak in the

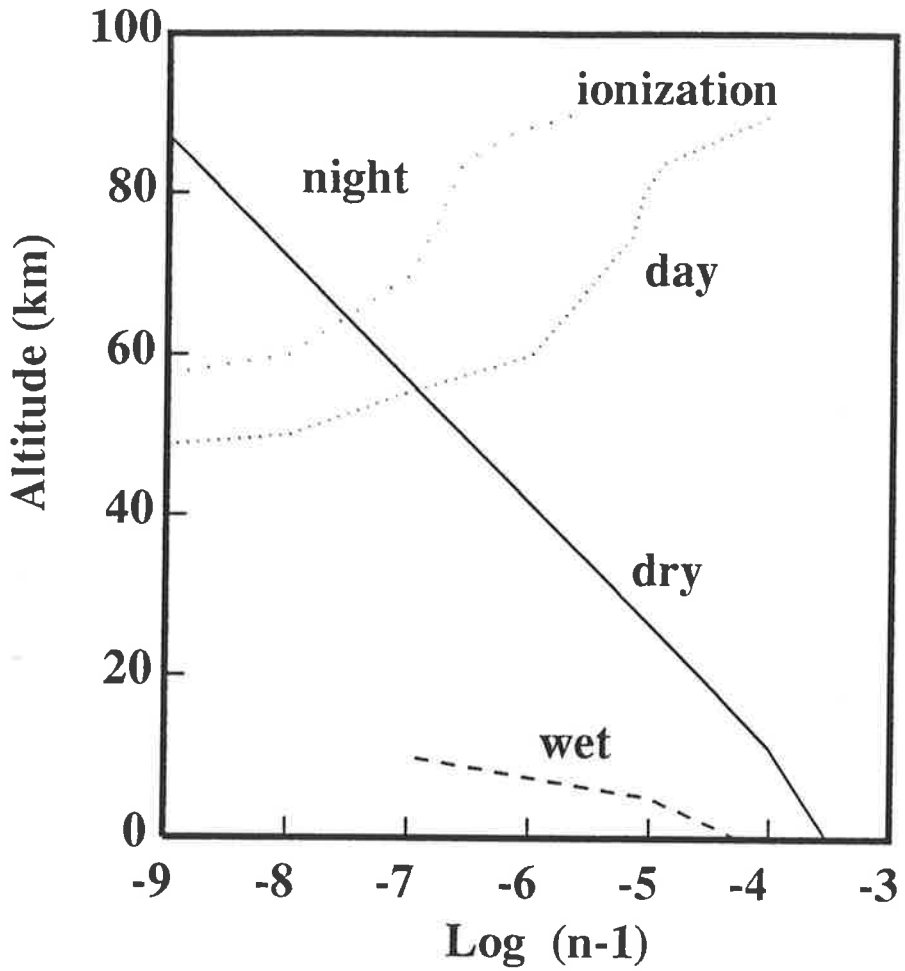

Figure 1.5: Typical altitude profiles of the wet, dry and ionization terms of (1.1) (adapted from *Sato*, [1988]).

vertical power profile which rapidly decreases as the zenith angle is increased. Fresnel scatter produces a series of smaller peaks, while Bragg scatter produces a slowly varying power profile. "Thompson" scatter results from the re-radiation of free electrons which are forced into oscillation by the incident transmitted signal. This scatter is distinct from the other three mechanisms described above in that it is "incoherent".

1.3.4 Spaced antenna radar techniques

The spaced antenna techniques are a family of analyses which make use of the signals recorded by a number of spatially separated receiving antennae. The history of spaced antenna radar observations has been reviewed recently by *Briggs* [1993]. This article provides the basis of the review presented in this section. The various spaced antenna techniques are summarized in the taxonomy of Figure 1.7.

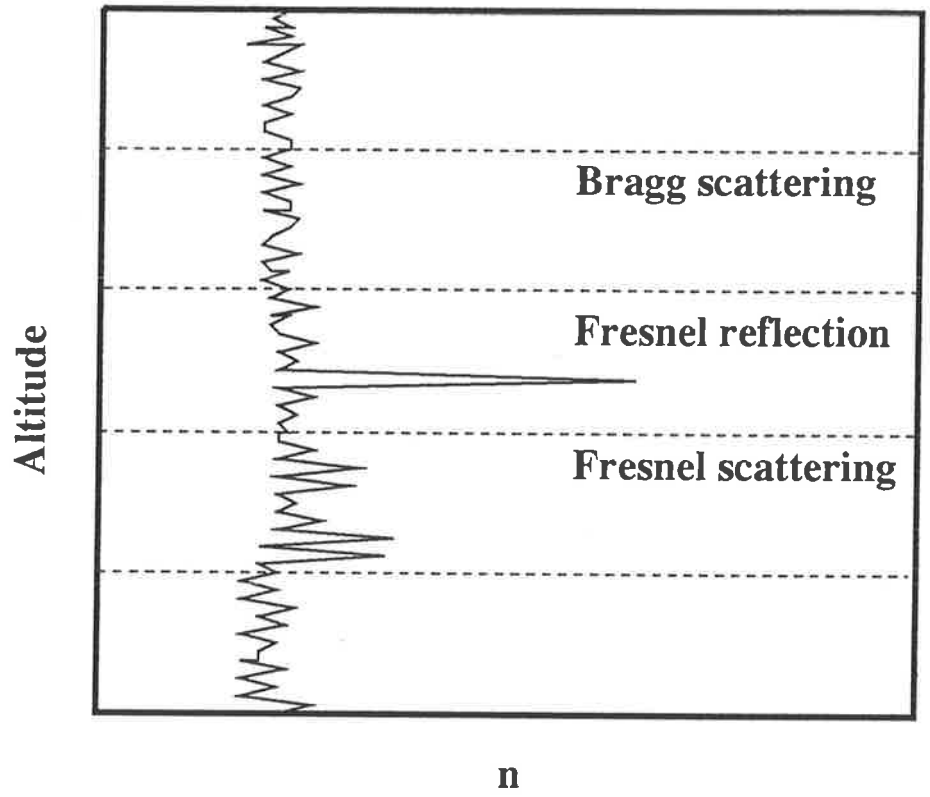

Figure 1.6: Illustration of the effects of Bragg scatter, Fresnel reflection and Bragg scatter upon the refractive index, n (adapted from *Röttger*, [1989]).

The origins of the spaced antenna techniques can be attributed to the work performed during the 1930s by Pawsey at the Cavendish laboratory, Cambridge University, and subsequently reported in *Pawsey* [1935]. The major aims of Pawsey's work were to determine the cause of the fading of signals backscattered from the ionosphere, and to determine whether any correlation existed between the signals recorded at spatially separated positions. On one particular occasion the recorded signals were found to be similar, but exhibited a consistent time displacement of the order of one second. This time displacement was interpreted as evidence of motion at the height of the backscatter. Using diffraction theory, Pawsey illustrated that if if the regions of backscatter were considered to behave as a random "screen" moving with velocity $\vec{V}$ that the resulting ground diffraction pattern would propagate at velocity $2\vec{V}$. This result was later verified by several authors (e.g. *Felgate*, [1970]) and denoted the "point-source effect". Pawsey further illustrated that the scale of the diffraction pattern formed over the ground could be used to determine the angular distribution of the regions responsible for the backscatter.

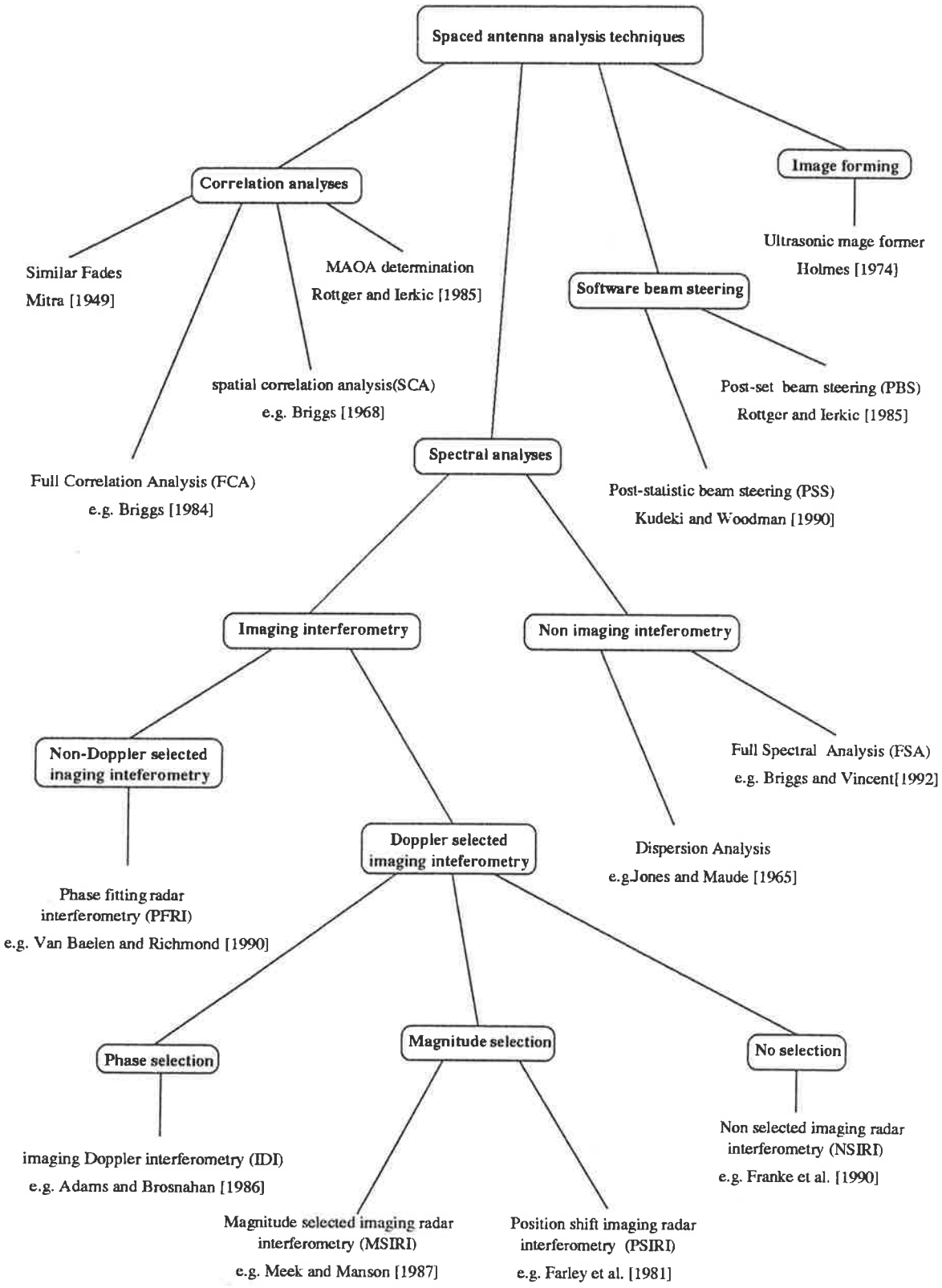

Figure 1.7: Taxonomy of spaced antenna analysis techniques (revised from Vandepeer [1993]).

1.3.5 The similar fades technique

The work of Pawsey was incorporated into the "similar fades" technique (e.g. *Mitra* , [1949]). This technique used the time-displacements measured between the amplitude of the signals recorded by three spatially separated receiving antennae to provide an estimate of the horizontal wind velocity in the E and F regions of the ionosphere. It soon become apparent that the velocity fluctuations seen between contiguous records on applying the similar fades analysis were inconsistent with the constant drift velocity assumed by the analysis. These velocity fluctuations could be explained however if the ground pattern was assumed to evolve randomly as a result of turbulent motions at the height of the backscatter (e.g. *Briggs et al.*, [1950]). The random changes result in the signal decorrelating faster, thereby resulting in a reduction in the estimated time-displacements. The similar fades analysis was also shown to be subject to directional biases if the ground diffraction pattern was anisometric (e.g. *Phillips and Spencer*, [1955]). The similar fades technique is described in Appendix B.

1.3.6 The full correlation analysis

The failure of the similar fades technique to compensate for the effects of random changes and pattern anisometry led to the development of the "full correlation analysis" (FCA) (e.g. *Briggs et al.*, [1950]). The basic assumption of the FCA is that the spatio-temporal correlation function of the ground diffraction pattern can be described by a family of ellipsoids. The FCA produces two velocity estimates. The "apparent" velocity is estimated using the similar fades technique. The "true" velocity includes corrections for the effects of random changes and anisometry in the ground diffraction pattern, and is thus generally considered the better velocity estimate.

The FCA also provides information on the spatial and temporal characteristics of the ground diffraction pattern. The FCA was originally applied to total reflection signals from the E and F regions of the ionosphere (e.g. *Briggs et al.*, [1950]). The technique was not universally accepted due to the somewhat arbitrary assumptions of the analysis, and due to controversy surrounding the origin of the refractive index irregularities responsible for the backscatter. The original idea was that the ionosphere contained small scale irregularities which caused the ionospheric reflecting layers to behave as diffuse scatterers rather than as specular reflectors (e.g. *Briggs*, [1977]). This mechanism later became known as "volume scatter", as backscatter is assumed to result from a larger number of randomly distributed

positions throughout the volume illuminated by the transmitted beam. It was later proposed that the backscatter may originate from undulations produced by the propagation of internal gravity waves (e.g. *Hines and Rao*, [1968]). In this situation the FCA would be expected to measure a velocity associated with the phase speed of the perturbing wave(s). The FCA was later applied to partial reflection returns from the D-region at MF (e.g. *Fraser* [1965]) and from the troposphere and lower stratosphere at VHF (e.g. *Röttger and Vincent*, [1978]), where the volume-scatter assumption is expected to hold more rigorously. The FCA is the subject of Chapters 4 and 5 of this thesis.

1.3.7 The spatial correlation analysis

The Buckland Park (BP) MF radar (e.g. *Briggs et al.*, [1969]) was constructed to address a number of issues surrounding the FCA. The radar is described in detail in Chapter 2. The receiving array consists of 89 pairs of crossed dipoles occupying a circular area of approximately 1 km diameter. This array allowed the production of images of the ground diffraction pattern, thereby allowing the calculation of the spatial and temporal correlation functions. The resulting spatial and temporal correlation functions were found to have a similar shape (e.g. *Golley and Rossiter*, [1970]), therefore verifying the use of this assumption in the model of the FCA. The array was also used to verify the point source effect (e.g. *Felgate*, [1970]). The ability to calculate spatial correlation functions led to the development of the "spatial correlation analysis" (SCA) (e.g. *Briggs*, [1968]). This technique provides an estimate of the velocity of the ground diffraction pattern by calculating the displacement of the spatial correlation function between sampling times. The technique was found to produce temporally consistent velocity estimates (e.g. *Briggs*, [1968]). The array also allowed the FCA to be applied to a number of different triangles of antennae with several different spacings. The results of *Golley and Rossiter* [1970] illustrated that the FCA true velocity gave a similar estimate to the SCA velocity if antenna spacings of the order of the scale of the ground diffraction pattern. The SCA is described in detail in Chapter 6. The technique was hitherto considered limited by the large number of antennae required for implementation. The results of Chapter 6 however suggest that a revised SCA can be implemented using a minimum of three receiving antennae.

1.3.8 Image forming

The use of both the amplitude and phase of the recorded signals allowed the development of a number of alternative spaced antenna techniques. Arguably the most ambitious of these techniques was the "ultrasonic image former" (e.g. *Briggs and Holmes*, [1973]; *Holmes*, [1974]), which was developed to determine the position and structure of the regions responsible for the backscattered signals. The ultrasonic image former was implemented using the BP MF array using processing by ultrasonic waves, and was successful in producing images of "glints" produced from totally reflecting ionospheric layers. The technique was limited by the need to have 89 receiving antennae with stable gains and phase shifts. There are currently tentative plans to implement a similar technique on the upgraded BP MF array using thirty receivers.

1.3.9 Interferometry

Among the analyses developed due to the availability of both amplitude and phase information are the "interferometric" and "beam steering" analyses. The interferometric techniques are descendents of the techniques described by *Pfister* [1971] and *Woodman* [1971]. The interferometric techniques can be separated into "imaging" and "non-imaging" techniques, depending upon whether the locations of apparent backscatter are determined during the analysis. The "imaging" techniques can be further separated into "Doppler selected" and "non-Doppler selected" techniques. The Doppler selected techniques (e.g. PSIRI, IDI, MSIRI and NSIRI) are based on the determination of the locations of the apparent backscatter for each individual Doppler frequency, while the non-Doppler selected techniques (e.g. MAOA, TDI, PFRI) are based on the determination of the mean location of the apparent backscatter over all Doppler frequencies. The Doppler selected techniques are based on the "discrete scatter" assumption, whereby the contributions to each Doppler frequency result from the backscatter from a single discrete region of the atmosphere. The individual techniques differ in their use of "single scatterer" criteria for the rejection of Doppler frequencies which do not satisfy the discrete scatter assumption. There has been some controversy of late as to validity of the discrete scatter assumption. The results of *Briggs* [1995] suggest that the Doppler selected imaging techniques will be influenced by the effects of random motions in the volume scatter situation assumed by the FCA. The experimental analysis of *Vandepeer and Reid* [1995a] and numerical model analysis of *Holdsworth and Reid* [1995b] further

confirm these results. The interferometry techniques are discussed in detail in Chapter 8.

The "full spectral analysis" (FSA) (e.g. *Briggs and Vincent*, [1992]) is a frequency-domain equivalent of the FCA. The FSA employs the same mathematical formulation as the FCA, but is based on the use of spectral parameters as opposed to correlation parameters. The FSA is sometimes referred to as a non-imaging interferometric technique. The FSA is discussed in Chapter 7.

1.3.10 Beam steering techniques

The "beam steering" techniques are employed to steer the direction of the radar beam on reception in software. These techniques are mathematically equivalent to the operation of a Doppler radar, whereby the radar beam is steered on transmission by the introduction of phase differences between the individual transmitting antennae. The phase differences can be introduced in hardware, or by using appropriate length cables. Doppler radars allow the application of the Doppler beam steering (DBS) technique (e.g. *Woodman and Guillen*, [1974]), whereby the line of sight velocity determined using a vertical beam and two orthogonal off-zenith beams can be used to determine the 3-dimensional wind vector.

The post-set beam steering (PBS) technique (e.g. *Röttger and Ierkic*, [1985]) involves multiplying the time-series by appropriate complex constants to introduce the appropriate phase shift, and adding the time-series to form a single time-series. This time-series is mathematically equivalent to the the time-series which would be measured by a Doppler radar. The post-statistics beam steering (PSS) technique (e.g. *Kudeki and Woodman*, [1990]) involves calculating the auto- and cross-correlation functions (or, alternatively, the auto- and cross-spectra) for each antenna pair, and multiplying these functions by the appropriate complex constants to introduce the appropriate phase shift. The PSS technique is computationally more efficient because the correlation functions (or spectra) need only be calculated once. The PBS and PSS yield very similar results.

1.4 Motivation and scope of this thesis

The motivation for the work presented in this thesis is the desire to better understand the performance of the spaced antenna (SA) radar analyses, as presented in section 1.3.4. The full correlation analysis (FCA) was first implemented in 1950, and is currently employed in a fundamentally identical manner. Despite the longevity of the technique the assumptions

of the analysis and the performance of the analysis under the variety of proposed scattering mechanisms have been consistently questioned. This speculation has intensified of late as a result of a number of comparisons suggesting that the FCA true velocity may actually underestimate the actual wind velocity in some circumstances (e.g. *Burrage et al.*, [1993]; *Cervera and Reid*, [1995]). The recently developed Doppler selected imaging interferometry techniques also produce velocities which consistently overestimate the FCA true velocity. The results of the recent AIDA (Arecibo Initiative in Dynamics of the Atmosphere) campaign have led *Hines et al.* [1993] to further speculate that MF radars may measure velocities related to the phase velocities of internal gravity waves as opposed to the background wind velocity.

The investigation of the SA analyses presented in this thesis are based principally upon the use of the "radar backscatter model", as described in Chapter 3. This model simulates the volume scatter conditions assumed by the full correlation analysis. The model is used to investigate a number of biases reported in the use of the FCA, such as those resulting from turbulent random motions, anisometry, gravity waves, sampling parameters, and antenna spacing, as presented in Chapters 4 and 5. These results lead to the investigation of two alternative correlation analyses, including a revised spatial correlation analysis, as presented in Chapter 6. The model is also employed to investigate the full spectral analysis (FSA) in Chapter 7, and the Doppler selected imaging interferometric techniques in Chapter 8. The results obtained using the model-generated data are supplemented by results obtained using data collected using the upgraded Buckland Park array, as described in Chapter 2.

Chapter 2

The Buckland Park field station

2.1 Introduction

The Buckland Park (BP) field station is located approximately 35 km north of Adelaide (34° 38′ S,138° 29′ E). The field station is operated by the Atmospheric Physics group of the University of Adelaide, and currently houses an MF/HF and a VHF radar, as well as a number of optical experiments, thereby providing coverage of the atmosphere from 2 - 20 km, and 60 - 100 km. This height coverage will be extended with the current installation of a VHF boundary layer radar capable of providing measurements from above 500 m. The ground layout of the Buckland Park site is schematically illustrated in Figure 2.1. The MF/HF array and the optical experiments are controlled from within the recently installed central laboratory. The VHF hut is linked to the central laboratory by an optical fibre link, enabling all experiments to be observed, and eventually controlled, from within the central laboratory.

As this thesis focuses upon the statistical aspects of the various spaced antenna analyses determined using model-generated data the description of the experimental aspects will be kept necessarily brief. The experimental analyses presented in this thesis were restricted to data collected using the MF radar. As a result, the discussion presented below will focus upon the MF radar and the modes of operation employed for the collection of the data used in this thesis. The MF radar was constructed in the mid-sixties (e.g. *Briggs et al.*, [1969]) to enable the investigation of a number of aspects concerning spaced antenna (SA) correlation analyses, as discussed in section 1.3.4. The radar has recently been upgraded to enable it's use as a true Doppler radar (e.g. *Reid et al.*, [1995]). The VHF radar was constructed in

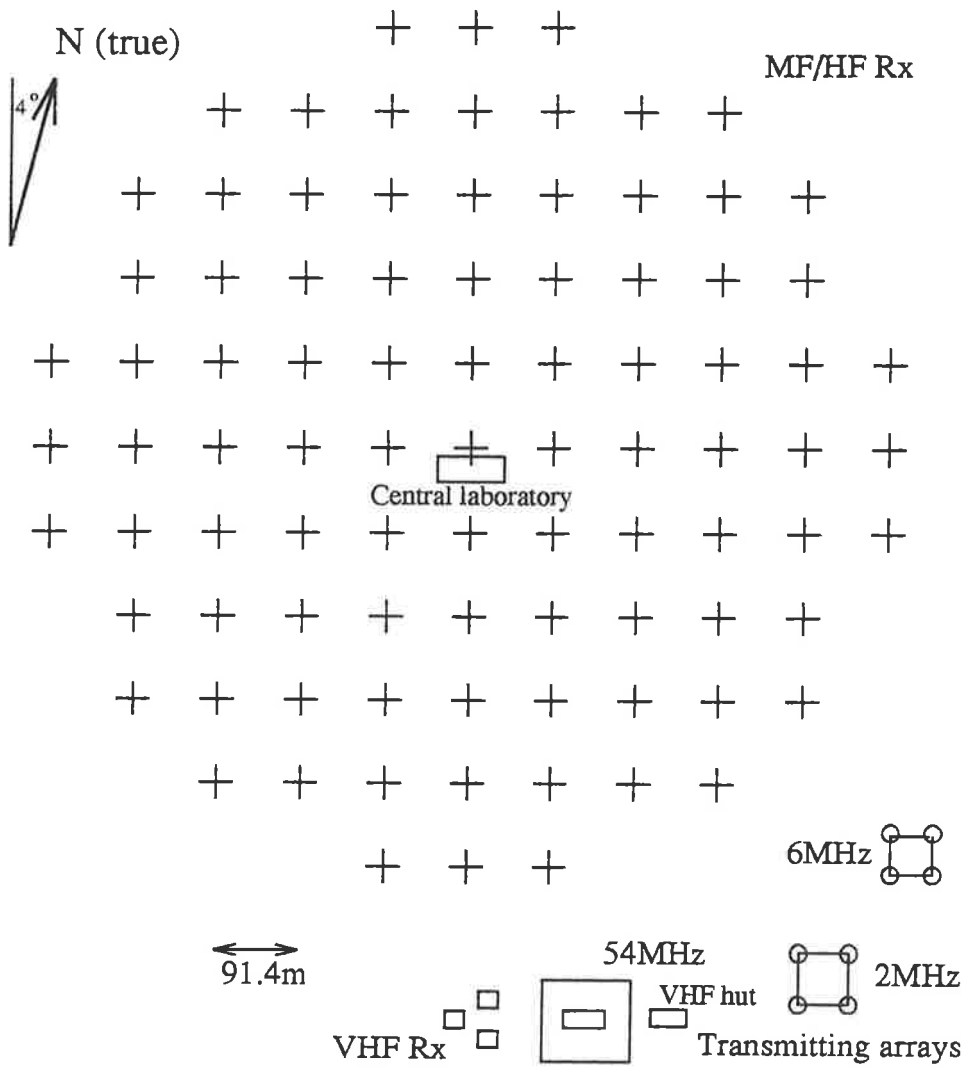

Figure 2.1: Schematic illustration of the layout of the Buckland Park field station.

the mid-eighties to operate both as a spaced antenna radar, and as a Doppler radar in the East-West plane (e.g. *Vincent et al.* [1987]). The radar has also been successfully employed for meteor work (e.g. *Cervera and Reid*, [1995]). The radar has recently been upgraded (e.g. *Cervera*, [1996]). Further upgrades are planned, including the ability to use Doppler mode in the North-South plane, and the delivery of a new 4-channel receiving system.

2.2 The Buckland Park MF/HF radar

The Buckland Park MF/HF radar is schematically illustrated in Figure 2.1. The MF transmitting array operates at a frequency of 1.98 MHz. The array consists of four center-fed half-wave dipoles which are arranged in a square and suspended approximately 27.4 m above

ground by four steel towers. The dipoles consist of a 71.6 m length of 2 mm diameter hard-drawn copper. A balun is hung at the center of each dipole to match the (nominally) 75 Ω antenna with the 75 Ω coaxial feeder cable. The polar diagram of the transmitting array has half-power half-width of approximately 40°. The dipoles are connected to a central transmitting hut by coaxial cable. The transmission of linear-, E-, or O-mode polarization is achieved by introducing the appropriate phase delays between the signal transmitted to the pairs of parallel dipoles. In practice, O-mode polarization is used during the day due to the strong absorption of E-mode polarization above 80 km. Conversely, E-mode polarization is preferred at night due the larger signal returns observed in comparison to O-mode polarization. The HF transmitting array operates at a frequency of 5.94 MHz. This array is currently not in use.

The MF transmitter consists of 10 solid-state modules each producing 2.5 kW nominal power. The RMS peak envelope power of the transmitter is therefore 25 kW. The transmitter is designed to produce amplitude-modulated Gaussian-shaped pulses. The exact shape and length of the pulse is adjustable. The half-width of the optimal pulse length is approximately 25 μs, thereby resulting in a range resolution of approximately 4 km (see section 1.3.1 for details on range resolution). In practice, a pulse repetition frequency (PRF) of 80 Hz is used during the day, while a PRF of 40 Hz is used at night in order to minimize problems arising from multiple reflections. The transmitter duty cycle is approximately 0.2 % when a PRF of 80 Hz is used.

The receiving array consists of 89 crossed half-wave dipoles arranged in a square grid, forming a filled circle of diameter 915 m. The array is aligned 4° East of North, which was the direction of magnetic North when the array was constructed in 1967. The array is located on an almost-flat coastal plane which drops by less than 2 m towards the South-West (e.g. *Reid*, [1984]). Each of the 178 individual dipoles are connected back to the central laboratory by 75 Ω coaxial cables whose electrical length are integer multiples of the wavelength of the main operating frequency of 1.98 MHz. The dipoles are cut to a resonant length of 71.6 m at 1.98 MHz, and are suspended approximately 10 m above ground by wooden poles. The dipoles are center fed by a balun mounted at the top of each pole to match the 28 Ω antenna with the 75 Ω coaxial feeder cable. The balun also serves as a passive switch between the 1.98 and 5.94 MHz modes of operation. The spacing between the grid points is approximately 91.4 m, corresponding to multiples of $\frac{3}{5}$ and $\frac{9}{5}$ of the wavelength of the operating frequencies of 1.98 and 5.94 MHz, respectively. The full receiving array has a half-power half-width of

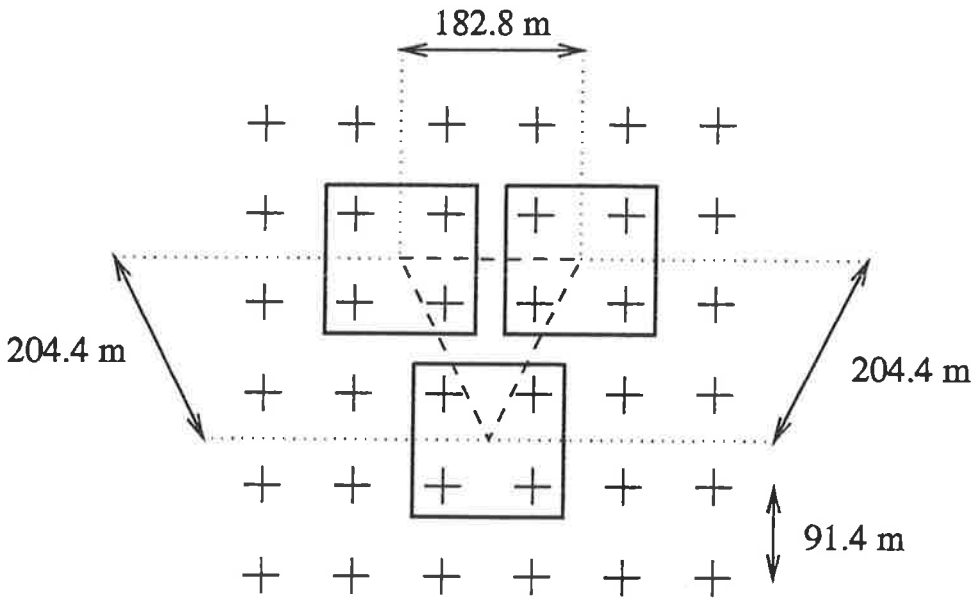

Figure 2.2: Schematic illustration of the configuration of "effective" antennae employed for the SA system at Buckland Park. Each antenna is formed by the combination of four similarly aligned dipoles.

approximately 4.5°, and exhibits no grating lobes in the radiation pattern when used at 1.98 MHz. If the array is used at 5.94 MHz grating lobes are evident at a zenith angle of 35°.

2.2.1 Spaced antenna operation

The BP MF radar has been operated as a real-time SA radar using the full correlation analysis (FCA) on an almost continuous basis since 1984. The antenna configuration used for the real-time analysis is shown in Figure 2.2. The "effective antennae" are arranged in an almost-equilateral isosceles triangle with separations 182.8 and 204.4 m. This configuration is employed to reduce directional biases that can result from the application of the FCA to antenna configurations containing one antenna pair separation considerable larger than the remaining two, such as a right-angled triangle configuration. These biases are addressed in Chapter 5. Each "effective" antenna is the combination of four similarly aligned dipoles, whose signals are combined to provide the input to an individual receiving channel of the radar and data acquisition system (RDAS). At the end of each acquisition period the resulting time-series record for each receiving channel are transferred from the RDAS to the host personal computer (PC), where the analysis is performed on-line. The raw time-series records can also be preserved for future off-line analysis.

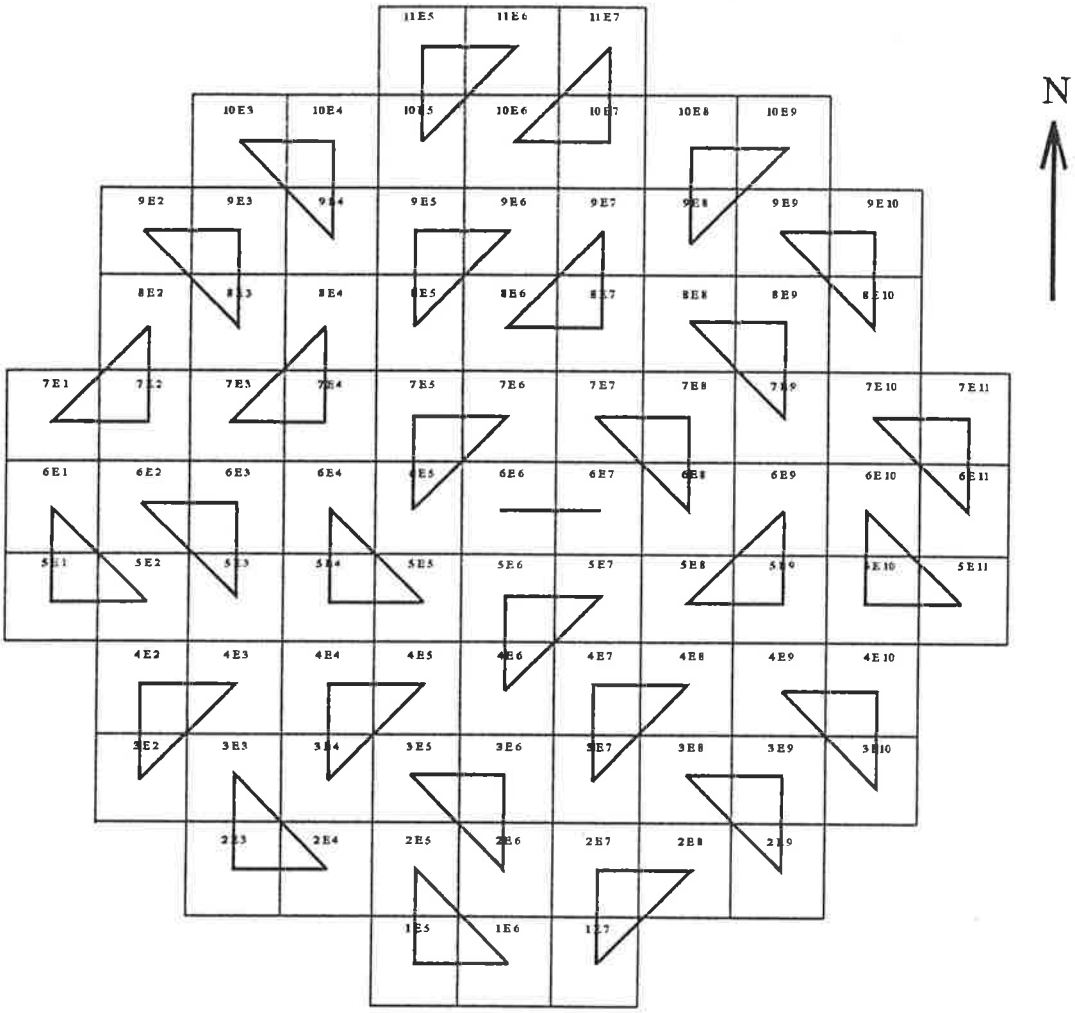

Figure 2.3: Schematic illustration of the configuration of effective antennae employed for the real-time SA system at Buckland Park (after *Reid et al.*, [1995]).

2.2.2 Doppler beam steering operation

Although the receiving array was originally designed principally for reception, the use the array for transmission was always considered realistic goal. The recent upgrade of the MF radar (e.g. *Reid et al.*, [1995]) has realized this goal, such that the array can now be used as a true Doppler radar. Design studies have illustrated that the use of 30 T/R channels connected to groups of three dipoles would provide satisfactory beam patterns for off zenith angles of at least 30°. The antenna configuration chosen for this implementation is illustrated in Figure 2.3.

The 30 channel transmitting system consists of three self-contained 10-channel subsystems. Each subsystems consist of 10 separate modules, each of which is portable and can be used as a stand-alone transmitting system. Each transmitting module consists of a power

amplification (PA) module, a phase control module, and a filter TR module, each of which delivers 2.3 kW RMS peak envelope power. Higher power versions of these transmitting modules delivering 4.6 kW RMS peak envelope power are currently being implemented. With all 30 channels operating at this higher power the total power of the transmitting system will be 148 kW RMS. The phase control modules are able to correct for phase drifts in the individual channels and allow the transmitted beam to be steered every inter-pulse period. The 30 channel RDAS is of modular design. Each module consists of a receiver with individual gain control, a signal processor which digitizes the in phase and quadrature components to 12-bit resolution, and recording and control hardware interfaced to a PC.

Preliminary results obtained using the radar in Doppler mode have been presented by *Vandepeer and Reid* [1995b]. This experiment was conducted during the upgrade of the MF system, using a pilot 10 channel transmitting system and interim 8 channel RDAS, as described in section 2.3. The transmitting system employed delivers a RMS peak envelope power of 25 kW, while the interim RDAS employed uses 8-bit digitization. More recent results obtained using a similar configuration but with the new 10 channel RDAS using 12-bit digitization have produced usable signal returns from as low as 56 km, where sensible FCA results have been obtained (e.g. *Vandepeer*, [1995]). It is envisaged that signal returns from as low as 50 km may be obtained when the transmitting power is extended to the intended maximum of 148 kW RMS peak envelope power.

2.3 Experimental data

The data employed for the analyses presented in this thesis was collected during two campaigns in May of 1993, and May of 1994. The upgrade of the MF system was only partially completed during these campaigns. Nevertheless, the system still provided sufficient flexibility to perform the desired experiments. At the time of the May 1993 campaign a pilot 10 channel transmitting system was available, and thirty of the crossed dipoles had been upgraded, allowing transmission on 10 groups of three dipoles. An interim 8-channel RDAS was also available, allowing reception on 8 groups of three dipoles. At the time of the May 1994 campaign the majority of the crossed dipoles had been upgraded.

The details of pilot 10 channel transmitting system and the interim 8-channel RDAS are beyond the scope of this thesis, and will not be described in detail. Both components are however described in detail by *Vandepeer* [1993]. The pilot 10 channel transmitting system

was an embryonic version of one of the 10 channel subsystems of the fully upgraded radar, as described above. The interim 8-channel RDAS was upgraded from a 5-channel system previously used by the Atmospheric physics group, and includes some of the features included in the newer 30 channel system.

The work described in this thesis uses two 24-hour data-sets taken during the two campaigns described above. The data-sets will hereafter be referred to as the BP930518 and BP940527 data-sets, where the "BP" indicates the location where the data-set was recorded, and the following six numbers give the year, month and day of creation.

2.3.1 BP930518 data-set

The available dipoles and the groups of three chosen for collection of the BP930518 data-set are illustrated in Figure 2.4. The antenna configuration was selected to allow a number of different analyses. A number of different triangles of antennae were also chosen to allow an investigation of the triangle size effect (e.g. *Golley and Rossiter*, [1970]), as discussed in Chapter 5. The configuration also allowed the determination of the one-dimensional spatial correlation function, as also discussed in Chapter 5. A square of antennae were chosen for the implementation of four channel FCA and Doppler-selected interferometry analyses. Although these analyses were eventually performed they have not been included in this thesis. This data has also been used to illustrate aspects of the determination of the MAOA (e.g. *Röttger and Ierkic* [1985]), as shown in Chapter 8. The configuration chosen implied that only eight of the ten available transmitting channels could be employed. The beam-steering facility was not employed. The polar diagram of the transmitting array is illustrated in Figure 2.5. This polar diagram has been calculated by taking into account the different attenuation factors for each dipole resulting from the different cable lengths, as described by *Reid et al.* [1995]. The zonal and meridional half-power half-widths of this polar diagram are 8.49° and 9.63°. The most shallow primary minima is located at a zenith angle of 20° and at azimuths of 80° and 260°, and are approximately 14 dB below the main-lobe. The most dominant secondary maxima are located at a zenith angle 28° at the same azimuths, and are approximately 13 dB below the main-lobe. As the major consideration in the collection of this data-set was the geometry of the antenna orientation for reception this polar diagram was considered suitable for the experiment.

The relevant radar parameters for the collection of the BP930518 are shown in Table 2.1. The "gain height" specifies the height used to determine the gain setting for the receivers.

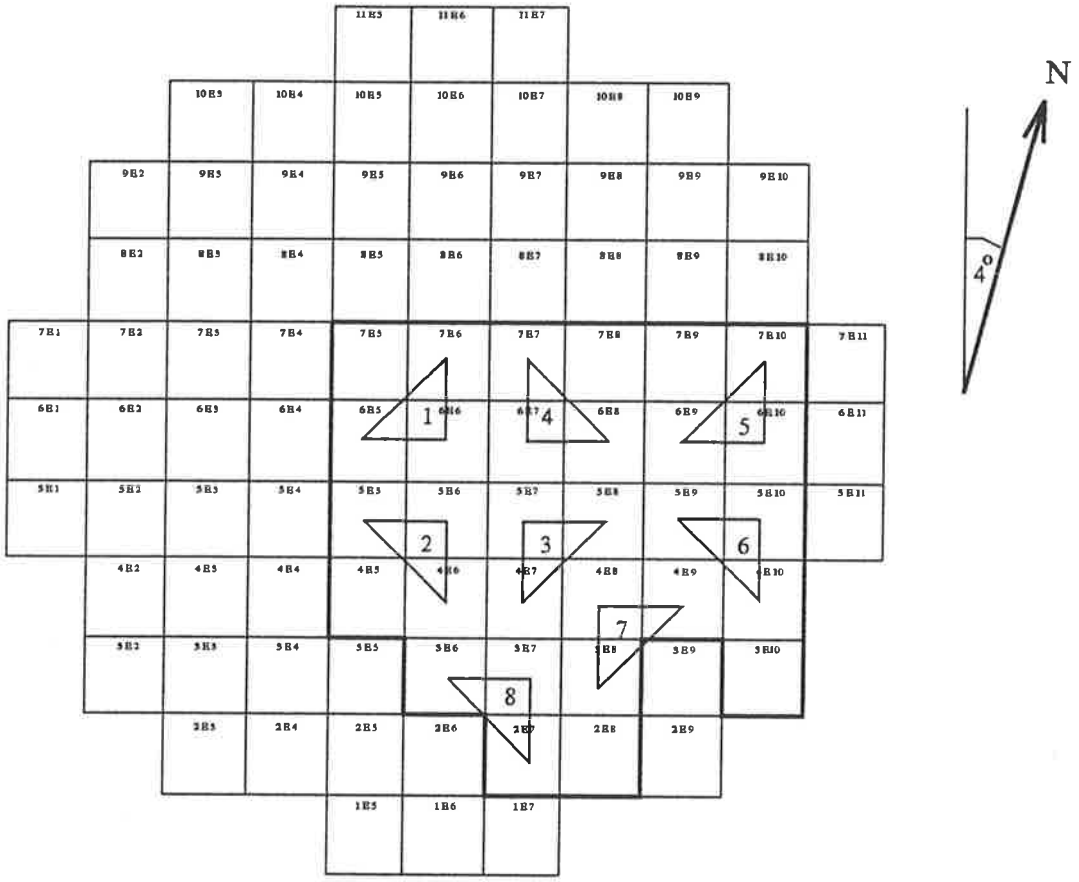

Figure 2.4: Schematic illustration of the configuration of the eight groups of three dipoles chosen for the May 1993 campaign. The available dipoles at the time of this campaign are denoted by dipoles enclosed by thick lines.

If the receiver output at the gain height is close to the dynamic range of the digitizers the gain is decreased for the next acquisition, while if the receiver output is using only a small portion of the total number of digitization levels the gain is increased. The gain height of 90 km used for this experiment sometimes resulted in the received signal below 70 km being very small. On the other hand, this setting produced very little receiver saturation at the upper heights. The average RMS signal amplitude and SNR profiles obtained for receiver 1 over the first four hours of the data-set are shown in Figure 2.6. The SNR is calculated using the zero-lag auto-correlation as discussed in Appendix C. The SNR profile indicates the data is not significantly affected by noise, except at the lower heights where the RMS signal amplitude is low, indicating that the dynamic range of the time-series occupies only a few digitization units. There is a small enhancement in the SNR at 84 and 86 km and in the RMS signal amplitude at 86 km, suggesting the possible existence of a reflecting layer at about these heights.

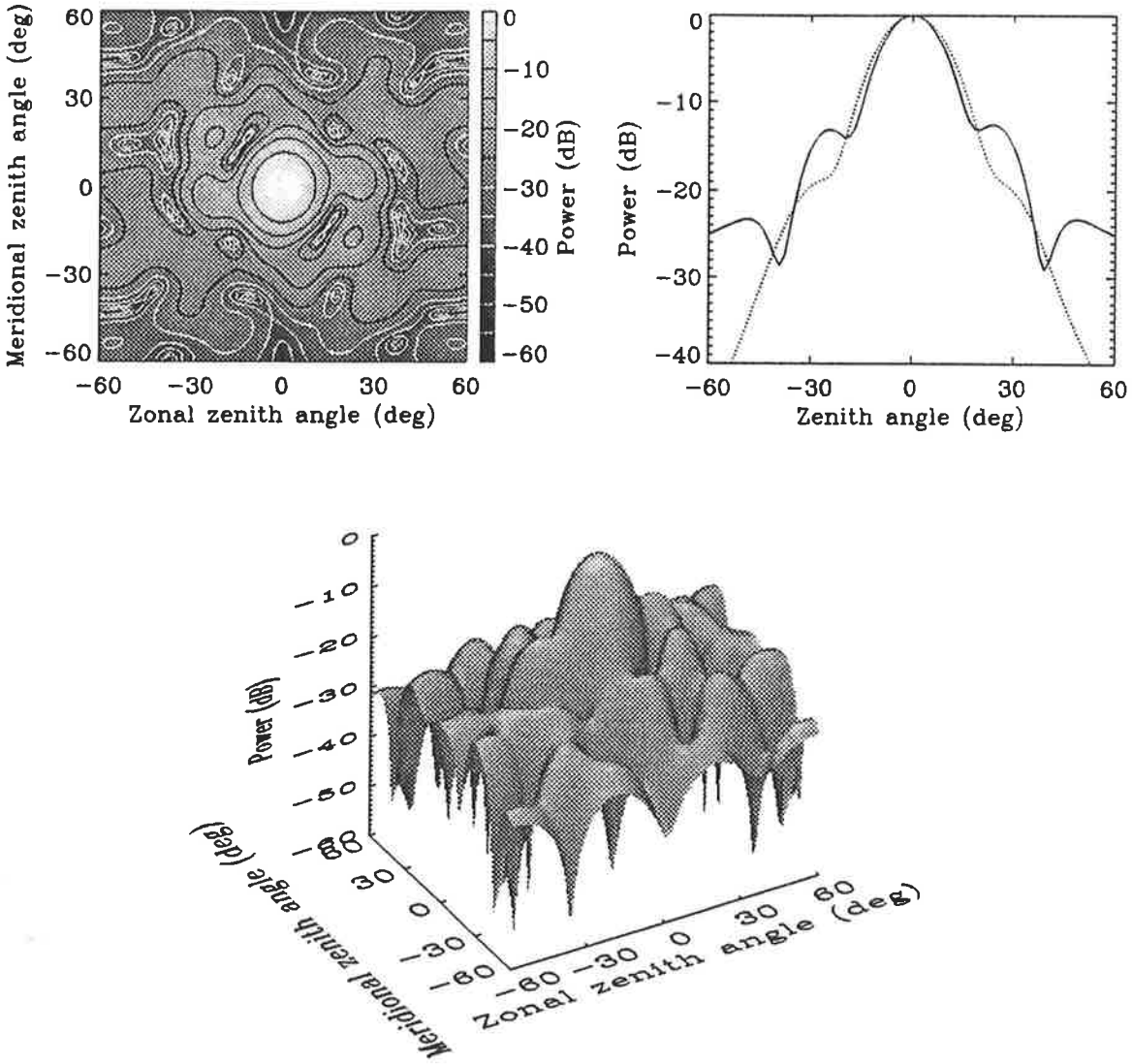

Figure 2.5: Contour (top left), cross-section, (top right) and surface (bottom) plots of the polar diagram of the transmitted beam for the BP930518 data-set. The lines in the cross-section plot indicate the zonal (solid) and meridional (dotted) cross-sections.

Investigation of the data later revealed that receiver 6 was not functioning properly throughout the campaign. The time-series recorded by this receiver where therefore deemed unsuitable for analysis. This restricted the number of triangles available for the triangle size effect analysis, but did not restrict any of the other planned analyses.

2.3.2 BP940527 data-set

The May 1994 campaign was conducted using the SA configuration, transmitting on the dipole array and receiving on three groups of four dipoles, as described in section 2.2.1. Two days of data were collected, using different temporal sampling parameters from which the

Table 2.1: Parameters employed for the data-set BP930518.

Parameter	Values
Receivers	8
Digitization resolution	8 bit
Height resolution	2 km
Number of height	20
Height range	day: 60-98 km night: 70-98 km
PRF	day: 80 Hz night: 40 Hz
Coherent integrations	day: 32 night: 16
Polarization	day: linear mode night: linear mode
Gain height:	90 km
Effective sampling time	0.4 s
Number of samples	256
Record length	102.4 s
Inter-record time	2 min

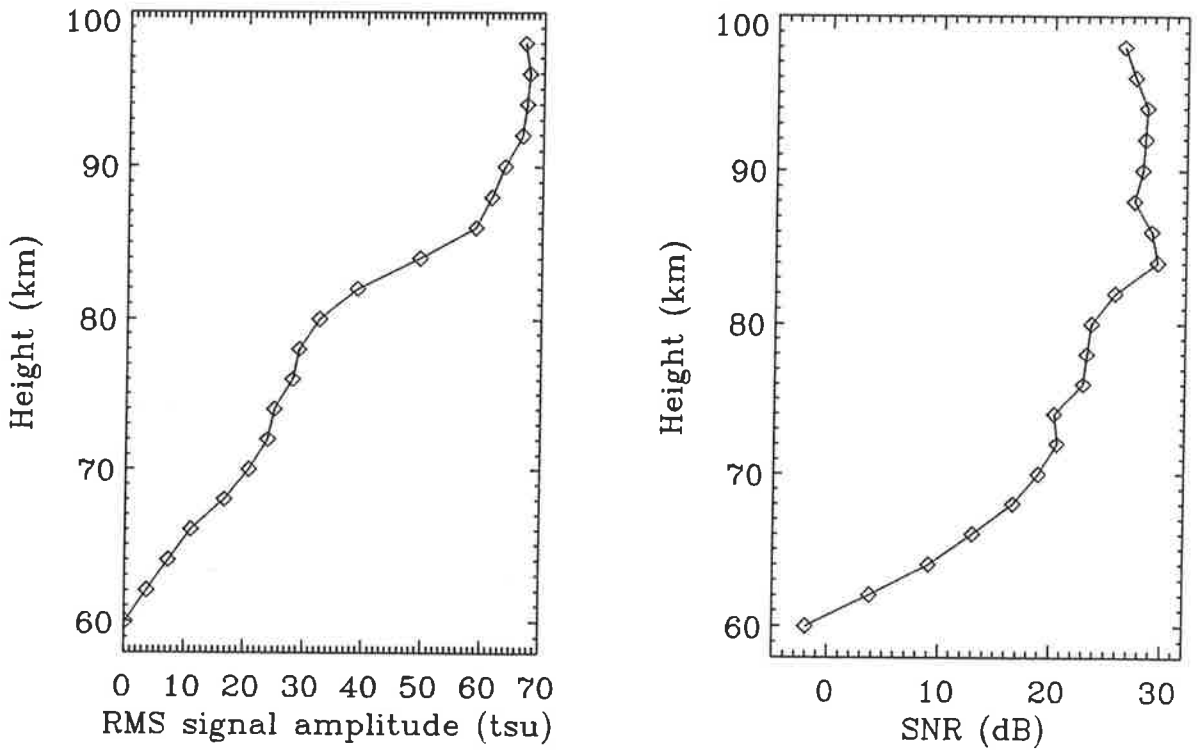

Figure 2.6: Average RMS signal amplitude (in time-series units) and SNR profiles obtained for receiver 1 over the first four hours of the data-set BP930518.

Table 2.2: Parameters employed for the data-set BP940527.

Parameter	Values
Receivers	3
Digitization resolution	8 bit
Height resolution	2 km
Number of height	20
Height range	day: 60-98 km night: 70-98 km
PRF	day: 80 Hz night: 40 Hz
Coherent integrations	day: 32 night: 16
Polarization	day: O-mode night: E-mode
Gain height:	86 km
Effective sampling time	0.4 s
Number of samples	1024
Record length	409.6 s
Inter-record time	7 min

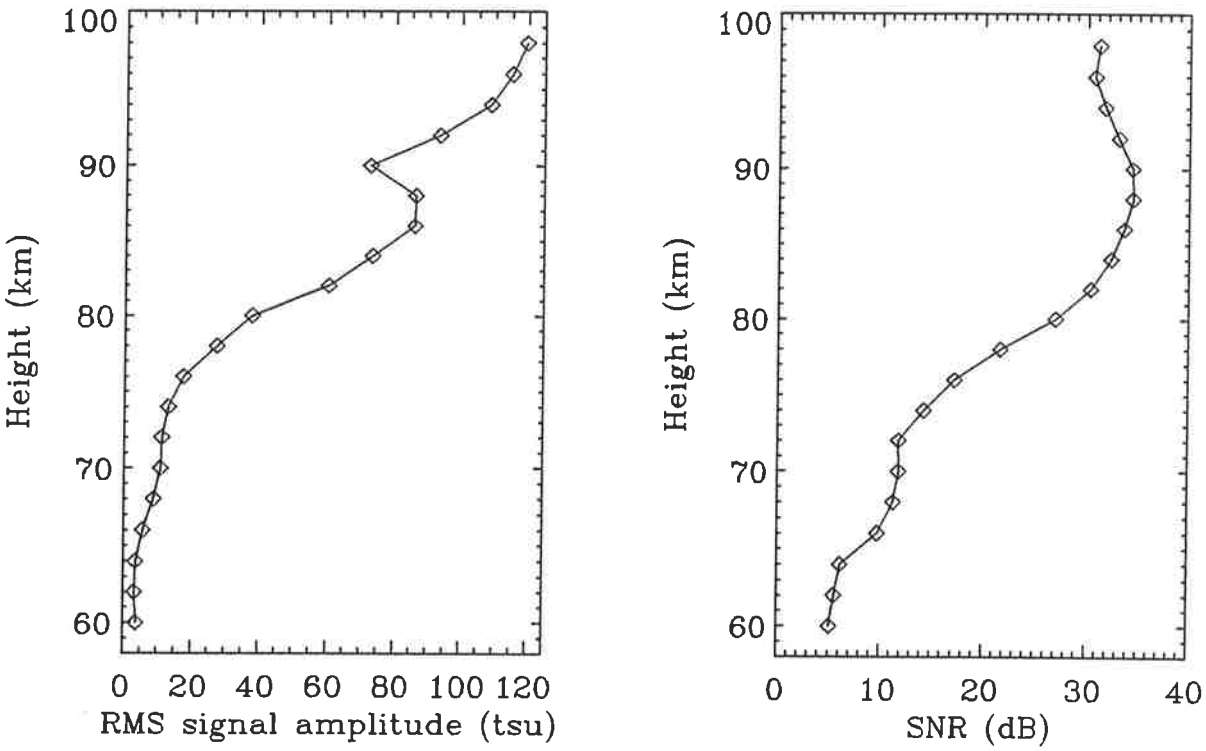

Figure 2.7: Average RMS signal amplitude (in time-series units) and SNR profiles obtained for receiver 1 over the first two hours of the data-set BP940527.

typical time-series employed for the SA analysis could be retrieved. The first day (26/5/94) involved maintaining the same record length, but reducing the number of coherent integrations by a factor of four to obtain an effective sampling time of 0.1 s. The second day (27/5/94) involved increasing the number of samples per record to 1024, such that each record was of length 409.6 s. These data-sets were collected to investigate the effects of the sampling parameters upon the FCA. Although preliminary analyses of these effects have been performed, the work is not described in this thesis. The data-set BP940527 represents the second day of this campaign. The time-series have however been split into the typical 256 sample record length employed for the routine FCA for the analysis described in this thesis.

The parameters employed for the collection of the BP940527 data-set are shown in Table 2.2. A gain height of 86 km used for this experiment, producing some saturation above 94 km and good signal returns at the lower heights. The average RMS signal amplitude and SNR profiles obtained for receiver 1 over the first two hours of the data-set are shown in Figure 2.7. There is a significant enhancement in the power profile between 86 and 88 km, suggesting the existence of a strongly reflecting layer. The SNRs are very good at all heights, suggesting the data is not significantly affected by noise.

2.4 Summary

In this chapter the Buckland Park field station and the various on-site experiments have been described. A number of recent and proposed upgrades have also been presented. The central laboratory provides the facility to observe all on-site experiments, and will eventually allow the full control of these experiments. The MF radar and it's modes of operation have been outlined, and the recent upgrades have been described. The modes of operation now include reception on selected dipoles of the main array, and transmission on the small dipole array or on the main array. The use of beam steering on transmission and reception on the main array allows the radar to operate as a Doppler radar. The two data-sets used throughout this thesis have been described. The power and SNR profiles for these data-sets have been presented, indicating the data provides excellent coverage of the 60 to 100 km height range of interest.

Chapter 3

The radar backscatter model

3.1 Introduction

A physically realistic model is an invaluable tool for scientific research. This is especially true in the field of radar processing, where there exists considerable debate over which of a number of techniques is the most suitable for the measurement of one the most fundamental of atmospheric properties, the wind velocity. Models offer several advantages over experimental observations. The most obvious advantage is that the atmospheric conditions can be controlled, thereby allowing the systematic evaluation of the performance of a variety of analyses. In addition, particular atmospheric conditions that may only occur irregularly in practice can be simulated at will. There are also no limits on the antenna configurations employed.

The "atmospheric radar backscatter" model described in this chapter extends the model first introduced by *Holdsworth and Reid* [1995a] (see Appendix I). This model has been designed to be both simple and realistic. The major motivation has been to provide a tool for the systematic evaluation and comparison of a number of analysis techniques employed by the atmospheric physics community. Such an evaluation has become especially important in light of suggestions by *Hines et al.* [1993] that MF partial reflection radars may measure the phase-speed of gravity-wave perturbations within the radar volume as opposed to the background wind velocity. A number of radar backscatter models of varying degrees of complexity have previously been developed to perform similar evaluations to the present model described in this chapter. Features of some of these models have also been incorporated into the present model.

An extensive compilation of the various radar backscatter models developed by the atmospheric physics community is beyond the scope of this thesis. As a result, only those models which have a direct relation to the work covered in this thesis will be discussed. These models can be divided into "analytical" and "numerical" models. Analytical models are developed in order to determine the general form of the mathematical functions employed by various analysis techniques, from which the average results of applying these analyses can be deduced. Numerical models are developed to simulate the actual backscatter, producing an ensemble of time-series records which can be analyzed in the same manner as experimental data. The model presented in this Chapter is a numerical model.

3.1.1 Analytical models

There have been a number of analytical models developed in order to evaluate the performance of a range of different analysis techniques. The analytical models most pertinent to this thesis are those developed by *Pfister* [1971], *Liu et al.* [1990], and *Kudeki et al.* [1993].

The models of *Pfister* [1971] were developed in an attempt to explain the linear phase behavior often exhibited in cross-spectra obtained from total reflection returns from the E-region. Using interferometric arguments, Pfister suggested that this behavior could be produced if the signal returns originated from a vertical or almost vertical plane. In order to fit this hypothesis Pfister proposed the situation of reflection from a distorted sinusoidal layer produced by the propagation of an internal gravity wave. Signal returns were assumed to result from regions of the layer perpendicular to transmitted signal. This model did produce formulae which could explain the linear behavior of the cross-spectral phase. The formulae also indicate that the full correlation analysis (FCA) true velocity will measure the phase velocity of the wave as opposed to the background wind velocity, as suggested by *Hines and Rao* [1968]. In order to more accurately explain the experimental results it was necessary to propose that the distorted layer contained a superposition of waves of various wavelengths. Nevertheless, it is still clear that the FCA would measure a velocity related to phase velocities of the various waves present as opposed to the background wind velocity.

A second model was also investigated, whereby the signal returns resulted from reflections from a small number of discrete scattering regions propagating with the background wind. This model did not produce linear cross-spectral phase behavior. However, Pfister suggested that in favorable circumstances that the phase information could be employed to determine

the location of the discrete scattering regions, thereby providing the basis for the Doppler-selected imaging interferometry techniques (e.g. *Adams et al.*, [1985]) presented in Chapter 8.

The model of *Liu et al.* [1990] was originally developed to evaluate the performance of the FCA and Doppler-selected imaging interferometry techniques. The model was then further developed to evaluate the performance of the the oblique spaced-antenna (OSA) technique (e.g. *Pan and Liu*, [1992]), and the full spectral analysis (FSA) and frequency-domain interferometry (FDI) techniques (e.g. *Liu and Pan*, [1993]). This model provides formulae for the correlation functions and spectra employed by these analyses, thereby allowing the results of the application of the analyses to be determined. The model is based on the volume scatter situation, and includes the effects of random motions, polar diagrams and range-gating. Formulae applicable to the discrete scatter situation are also approximated by decreasing the width of the polar diagram (e.g. *Liu et al.*, [1990]). The volume-scatter formulae suggest that the FCA true velocity will successfully estimate the mean wind velocity, while the Doppler-selected imaging interferometric techniques will produce spurious velocity estimates. Conversely, the discrete scatter formulae suggest that the interferometric techniques will successfully estimate the mean wind velocity, while the FCA true velocity will produce spurious estimates. The volume scatter situation also produces linear cross-spectral phase behavior akin to that seen in the experimental data of *Pfister* [1971].

The model of *Kudeki et al.* [1993] was developed to analyze the performance of the FCA, IDI, and Doppler beam steering techniques. The model is based on the volume scatter situation, and includes the effects of random motions and scatterer anisometry. The model has been employed to illustrate that all three techniques analyzed are influenced by horizontal gradients in the vertical wind component. The model has been further employed by *Sürücü et al.* [1995a] to illustrate that the FCA is also influenced by horizontal gradients in the horizontal wind component. Although the bias in the FCA apparent velocity is shown to be significant, the bias in the FCA true velocity is shown to be generally less than 4 ms^{-1}.

3.1.2 Numerical models

The numerical model of *Pitteway et al.* [1971] and *Wright and Pitteway* [1978] was developed to simulate the backscattered returns from a number of randomly positioned scatterers propagating across the field of the radar at a constant height. The effects of random motions, polar diagrams and scatterer anisotropy were also considered. The FCA was applied

to data generated using this model, illustrating that the true velocity correctly estimates the background wind velocity when the separation of the receiving antennae are matched to the scale of the ground diffraction pattern. Furthermore, the FCA was shown to produce characteristic velocities, and pattern axial-ratios and axial-rotations in excellent agreement with the model input parameters. The models of *Meek and Reid* [1984], *Van Baelen et al.* [1989], *Sheppard and Larsen* [1992], and *Holdsworth and Reid* [1995a] are all essentially based on this model, with the extension that the scatterers can occupy a range of heights, thereby simulating a range-gate.

The models of *Meek and Reid* [1984] and *Sürücü et al.* [1995b] were developed in order to determine the effects of short-period monochromatic gravity-waves upon the FCA. The difference in the models lies in the scattering mechanism simulated. The model of *Meek and Reid* [1984] simulates the propagation of a wave through a number of randomly distributed isotropic scatterers. In this situation the sole effect of the wave is to provide a velocity perturbation to each individual scatterer according to the phase of the wave at the scattering location. The isotropic scatterers are simulated by "point-scatterers" whose returned signal amplitudes vary independently of the scatterer location and the phase of the wave. The application of the FCA to data generated using this simulation produces true velocity estimates which consistently underestimate the model input velocity.

The model of *Sürücü et al.* [1995b] was developed in order to investigate whether the scenario proposed by *Hines et al.* [1993] could produce the wind velocity biases seen during the AIDA campaign. In this scenario the passage of a gravity wave produces "tilts" in the scatterers according to the phase of the wave at the scattering location, in addition to the velocity perturbations as described in the model of *Meek and Reid* [1984]. The tilts are proposed to result in the measurement of the phase speed of the wave as opposed to the mean wind velocity. In this model the scatterers are simulated by line segments. The anisotropy of the scatterers is increased by increasing the length of the line segments. The application of the FCA to data generated using this simulation reveals that the FCA true velocity is influenced by the passage of the wave. The average true velocity calculated over the period of the wave however shows good agreement with the model background wind velocity for both isotropic and anisotropic scatter.

The basic model of *Van Baelen et al.* [1989] is a three-dimensional equivalent of the model of *Wright and Pitteway* [1978]. This model has been used to investigate the FCA triangle size effect, whereby the FCA true velocity increases with increasing antenna spacing up to

a limit given by the actual wind velocity (e.g. *Golley and Rossiter*, [1970]). Two extensions on this basic model exist, these being the inclusion of a high-density region of scattering centers, and the inclusion of a tilted specular layer with both long- and short-wavelength structure. There appear to be no published results obtained from using these two extensions. The model of *Sheppard and Larsen* [1992] is also a three-dimensional equivalent of the model of *Wright and Pitteway* [1978], and has been used to illustrate that the FSA technique can successfully estimate the mean wind velocity if spectra obtained by the coherent average of the spectra determined from the individual time-series records are used.

The use of numerical models for the investigation of the Doppler-selected imaging interferometric techniques provides the additional advantage that the actual scattering positions are known, thereby allowing a comparison of the actual and located scattering positions. The model of *Adams et al.* [1985] was developed to evaluate the then embryonic imaging Doppler interferometry (IDI) technique. A number of point scatterers were placed in an "S" shape at a constant height and allowed to propagate with the background wind velocity. The results illustrate that both the scattering positions and the wind velocity could be successfully estimated. The model presented in this Chapter is employed for a more extensive analysis of the Doppler-selected imaging interferometric techniques in Chapter 8

3.2 Description of the radar backscatter model

The radar backscatter model has been programmed in Interactive Data Language (IDL). The program is run on a Dec Alpha 3000, and can be run overnight in order to provide a statistically suitable number of time-series realizations for each set of model input parameters selected. The model is based on the volume scatter situation, whereby signal returns originate from refractive index irregularities distributed randomly throughout the volume illuminated by the radar. The model incorporates the effects of transmitter polar diagrams, aspect sensitivity, finite scatterer lifetimes, turbulence and gravity waves perturbations, and can be used to simulate the operation of spaced antenna and Doppler radars.

The model geometry is illustrated in Figure 3.1. The "radar volume" indicates the volume illuminated by the transmitted radar pulse, as will be described in section 3.2.3. The radar volume is enclosed within a cylindrical "enclosing volume", throughout which a number of "scatterers" are initially randomly positioned. These scatterers simulate aspect sensitive regions of refractive index irregularity. At each sampling time the complex signal returns from

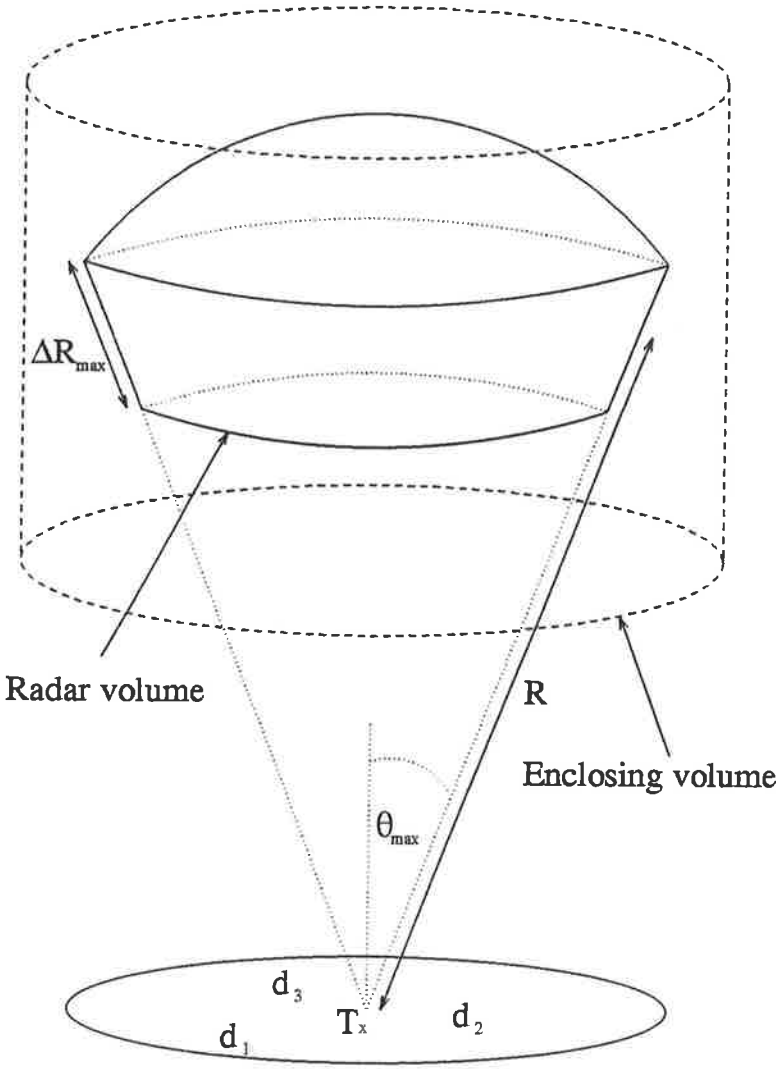

Figure 3.1: Geometry of radar backscatter model. The radar volume is defined in zenith by the zenith limit $\theta_{\mathbf{max}}$ and in range by the range limits $(R+0.5\triangle R_{\mathbf{max}}, R-0.5\triangle R_{\mathbf{max}})$. These limits are determined from the selected model parameters as discussed in section 3.3.1. The radar volume is contained within the enclosing volume (dashed lines). The effective center of the transmitting antennae (T_x) provides the origin of the coordinate system. Any number and configuration of receiving antennae d_i can be employed.

each scatterer are combined. The amplitudes of the signal returns are based on the combined polar-diagram of the transmitting and receiving antennae and the aspect-sensitivity of the scatterers, and the shape of the transmitted radar pulse. After each sampling time the scattering positions are updated, based on the mean background wind, as well as turbulent and gravity wave perturbations at the scattering position if required. Scatterers updated to positions outside the enclosing volume are re-admitted inside the opposite surface to which they left, thereby maintaining a constant number of scatterers.

3.2.1 The nature of the scatterers

The nature of the scatterers responsible for radiowave backscatter in the mesosphere at MF is still open to considerable speculation (e.g. *Lesicar and Hocking*, [1992]). It is generally considered that scatter below about 80 km is more specular, perhaps resulting from thin horizontal steps in refractive index, while scatter above 80 km results from more isotropic scatterers randomly distributed throughout the volume illuminated by the radar (e.g. *Reid*, [1988]).

The radar backscatter model is intended to simulate the scattering mechanism observed above 80 km. Each scatterer is represented by a single position in three dimensional space, but is intended to simulate a horizontally elongated Bragg scatterer. This is achieved by providing each scatterer with a polar diagram specified by the aspect sensitivity parameter θ_s. The θ_s values used can be related to the length-to-height (L/h) ratios of the scatterers (e.g. *Lesicar and Hocking*, [1992]) by

$$\frac{L}{h} = \sqrt{1 + \frac{\lambda}{8\pi^2 \sin^2 \theta_s}}, \tag{3.1}$$

where λ is the radar wavelength. Typical average weekly mesospheric L/h values of between 3 and 5 have been obtained using the Adelaide 2 MHz radar (e.g. *Lesicar and Hocking*, [1992]), corresponding to average weekly θ_s values ranging from 6 to 14 degrees. In using a large number of scatterers, returns will eventuate from a large number of positions distributed throughout the volume illuminated by the transmitted beam. Thus although individual scatterers are used, the model is not a "point scatterer" model. Because each scatterer has a polar diagram according to θ_s the model can be used to represent the "volume scatter" situation.

3.2.2 Signal returns

At each sampling time the complex signal returns from all scatterers within the radar volume are summed at the positions of the receiving antennae $\vec{d}_j$. The complex signal f_j recorded by the jth receiving antenna due to scatter from the ith scatterer located at position $\vec{r}_i$ is given by

$$f_j(\vec{r}_i) = a_j(\vec{r}_i) \exp(-i\phi_j(\vec{r}_i)) \tag{3.2}$$

where a_j is the amplitude of the signal and ϕ_j is the phase. The amplitude of the signal is defined by

$$a_j(\vec{r}_i) = \sqrt{p_i P(\vec{r}_i) S(\vec{r}_i) R(\vec{r}_i)}, \tag{3.3}$$

where p_i is the "reflectivity factor" of the scatterer, $P(\vec{r})$ is the combined polar-diagram of the transmitting and receiving antenna, $S(\vec{r})$ is the polar-diagram associated with the aspect sensitivity of the scatterers, and $R(\vec{r})$ is the range-weighting function. The phase of the signal at jth receiving antenna is given by

$$\phi_j(\vec{r}_i) = 2\pi \left(\frac{|\vec{r}_i - \vec{t}| + |\vec{r}_i - \vec{d}_j|}{\lambda} \right), \tag{3.4}$$

where $\vec{t}$ is the position of the effective center of the transmitting array and λ is the radar wavelength. As the origin of the coordinate system is set to the location of the effective center of the transmitting array it will hereafter be assumed that $\vec{t} = 0$.

The combined polar diagram of the transmitting and receiving antennae $P(\vec{r})$ is given by the product of the individual polar diagrams of the transmitting $T(\vec{r})$ and the receiving $D(\vec{r})$ antennae. Because these polar diagrams are often assumed in practice to be Gaussian (e.g. *Reid*, [1990]) the polar diagrams chosen for the model are also Gaussian. The general form of the polar diagram of the transmitting antennae is given by

$$T(\vec{r}_i) = \exp\left(-\frac{|\vec{r}_i|^2 - (\vec{r}_i \cdot \hat{r}_a)^2}{(|\vec{r}_i| \sin\theta_t)^2} \right), \tag{3.5}$$

where θ_t is the e^{-1} beam-width, and $\hat{r}_a$ is the unit vector in the direction of the beam tilt, which can be expressed in terms of the zenith angle θ_a and the azimuth angle clockwise from North ϕ_a of the tilt by $\hat{r}_a = (\sin\phi_a \sin\theta_a, \cos\phi_a \sin\theta_a, \cos\theta_a)$. The polar diagram of the receiving antennae is given by $D(\vec{r}_i) = 1$. This choice is based on the fact that the polar diagrams of the receiving antennae for SA systems are in general significantly larger than the polar diagrams of the backscatter resulting from the transmitting antennae and the aspect sensitivity of the scatterers. For Doppler systems, the two way polar diagram resulting from using the same antennae for transmission and reception can be simulated by using a transmitter polar diagram with an e^{-1} beam-width $\sqrt{2}$ times smaller than the individual transmitting and receiving polar diagrams.

The polar diagram resulting from the aspect sensitivity of the scatterers is given by

$$S(\vec{r}_i) = \exp\left(-\frac{|\vec{r}_i|^2 - (\vec{r}_i \cdot \hat{r}_{si})^2}{(|\vec{r}_i| \sin\theta_s)^2} \right), \tag{3.6}$$

where θ_s is the e^{-1} aspect sensitivity parameter and $\hat{r}_{si}$ is the unit vector in the direction of the tilt of the ith scatterer. In employing this formula each scatterer simulates a Bragg scatterer of wavelength $\frac{1}{2}\lambda$.

The effects of anisometric scatter have not been included in this model. These effects could easily be introduced by using an elliptical formulation of (3.6) incorporating a scale term, an axial-ratio and an axial-rotation. For the purposes of the work described in this thesis "artificial" anisometry has been introduced. For instance, in order to introduce anisometry along the zonal axis the zonal component of the scattering position x has been replaced by Ax in (3.5) and (3.6), where A is referred to as the "anisometry parameter". If $A = 1$ no anisometry is introduced. If $A > 1$ the combined polar diagram of the effects of the transmitted beam and the aspect sensitivity will be reduced along the zonal axis, thereby simulating scatterers which are elongated in the meridional direction.

The range-weighting function is dependent on the shape of the transmitted radar pulse, which is usually either Gaussian, triangular, boxcar or smoothed trapezoidal. The original range weighting function used for the model was a triangular function varying linearly from unity in the middle of the range gate to zero at the edges of the range gate, as employed by *Sheppard and Larsen* [1992]. This range weighting function was eventually abandoned in favor of a Gaussian function of the form

$$R(\vec{r}) = \exp\left(\frac{-(|\vec{r}| - r_0)^2}{r_e^2}\right) \tag{3.7}$$

where r_0 is the range in the center of the range gate, and r_e is the e^{-1} range-gate width.

The reflectivity factor p_i is employed to allow the simulation of varying scatterer reflectivities. This situation may for instance occur if the shapes of the scatterers evolve as a result of turbulent motions and gravity wave perturbations. The returned signal from each scatterer results from the addition of the rays reflected from the entire volume of the scattering region. As the shape of the scatterer evolves the amplitude of the returned signal will also evolve, passing through durations of constructive and destructive interference. The simulation employed by the model is defined in terms of the reflectivity lifetime, t_l, and the number of times during the acquisition period where the reflectivity will maximize, N_l. Prior to the production of a time-series record the times t_j where the N_l reflectivity maxima will occur are generated from a uniform distribution. The reflectivity factor is then defined by

$$p_i(t) = \sum_{j=0}^{N_l} \exp\left(-\frac{(t - t_j)^2}{t_l^2}\right), \tag{3.8}$$

Alternatively, the reflectivity factor can be defined as a constant in the range [0.5,1] for the entire duration of the passage of the scatterer through the enclosing volume.

3.2.3 The radar volume

Because the Gaussian functions used for $P(\vec{r})$, $S(\vec{r})$, and $R(\vec{r})$ do not fall-off to zero they must be artificially terminated. The zenith limit $\theta_{\max}$ illustrated in Figure 3.1 is defined by the positions $\vec{r}$ where

$$\theta_{\text{cut}} = \sqrt{P(\vec{r})S(\vec{r})}, \tag{3.9}$$

where θ_{cut} is the "angular cut-off amplitude". The range limit $\triangle R_{\max}$ is defined by the positions $\vec{r}$ where

$$R_{\text{cut}} = \sqrt{R(\vec{r})}, \tag{3.10}$$

where R_{cut} is the "range cut-off amplitude". The radar volume is defined by the positions $\vec{r}$ where $\theta_{\text{cut}} < \sqrt{P(\vec{r})S(\vec{r})}$ and $R_{\text{cut}} < \sqrt{R(\vec{r})}$. For all positions $\vec{r}$ outside the zenith and range limits the returned power is set to zero. This termination procedure is not ideal as it can produce discontinuities in the time-series records on a scatterer leaving the radar volume. This effect can produce discontinuities in time-series records, which can in turn produce auto- and cross-correlation functions with unsmooth behavior and zero-lag "spikes", thereby degrading the effective analysis of the data. The cut-off amplitudes must therefore be chosen as a compromise between minimizing such discontinuities and maximizing computational efficiency. It must be noted that no spurious effects have been detected using the cut-off amplitudes employed to produce the model-generated data used throughout this thesis. Because the maximum returned signal amplitude $A_{\max}$ is not always unity the cut-off amplitudes are usually expressed as "cut off ratios", which are the ratios of the cut-off amplitudes to $A_{\max}$.

The enclosing volume is selected to comfortably encompass the radar volume, as illustrated in Figure 3.1. The initial scattering positions are obtained by generating uniform random 3-dimensional positions within the enclosing volume. An example of the radar and enclosing volumes resulting from the use of the MF simulation parameters specified in Tables 3.2 and 3.3 is shown in Figure 3.2.

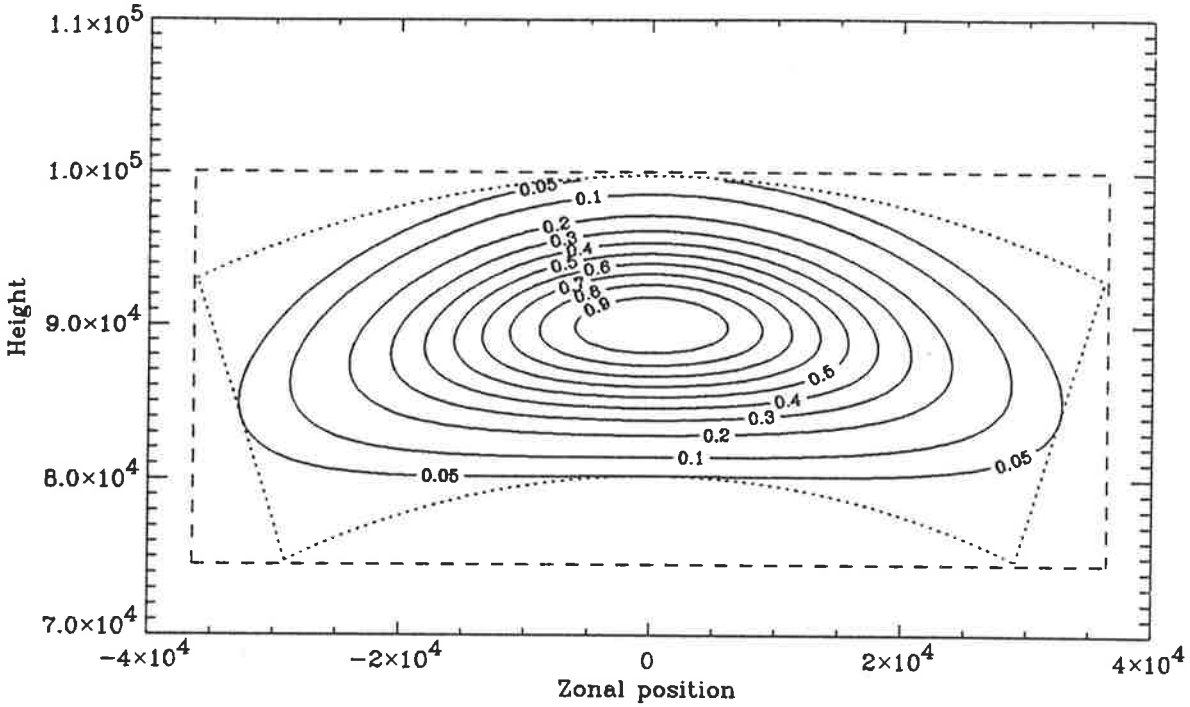

Figure 3.2: Example of the $y = 0$ cross-section of the radar (dotted line) and enclosing (dashed line) volumes resulting from the use of the MF simulation parameters specified in Table 3.2 and 3.3. The range gate is centered on the zenith at 90 km. The solid lines indicate the contours of constant signal amplitude for the product of the polar diagrams of the transmitting antenna and the aspect sensitivity, and the range weighting function.

3.2.4 Scatterer motions

After the signal returns from the scatterers are sampled the positions of the scatterers $\vec{r}_i$ are updated according to the equation

$$\vec{r}_i = \vec{r}_i + \vec{V}_i \, \Delta t, \tag{3.11}$$

where $\vec{V}_i$ is the velocity of the ith scatterer and Δt is the sampling time. The velocity $\vec{V}_i$ is given by

$$\vec{V}_i = \vec{V} + \vec{V}_{\text{turb}}(\vec{r}_i) + \vec{V}_{\text{gw}}(\vec{r}_i), \tag{3.12}$$

where $\vec{V}$ is the mean background wind velocity, $\vec{V}_{\text{turb}}(\vec{r}_i)$ is the turbulent random motion velocity at the position of the ith scatterer, and $\vec{V}_{\text{gw}}(\vec{r}_i)$ is gravity wave perturbation velocity at the position of the ith scatterer.

Scatterers updated to positions outside the cylindrical volume are readmitted in a manner similar to the model of *Meek and Reid* [1984] by placing the scatterer inside the opposite surface to which it left. On re-admission, both the reflectivity factor p_i and the turbulent velocity v_i' (as described in subsection 3.2.4.1) associated with the scatterer are regenerated,

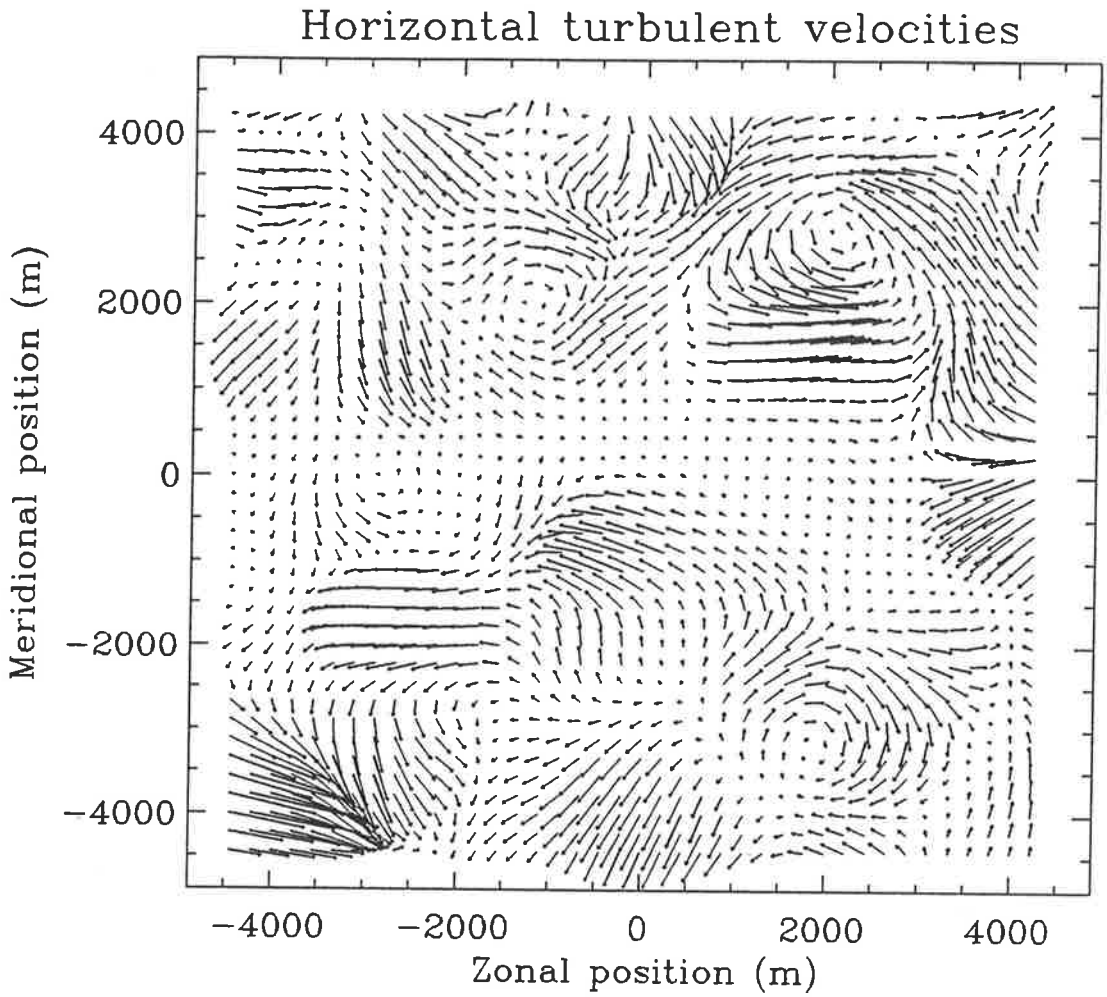

Figure 3.3: Example of the horizontal turbulent velocity field obtained using a zonal and meridional rms velocity of 6 ms^{-1}. The largest arrow indicates a velocity of 52 ms^{-1}.

as the readmitted scatterer is considered to be an entirely different scatterer to that leaving the enclosing volume.

3.2.4.1 Turbulent random motions

The scatterers employed by the model are intended to simulate refractive index irregularities produced by the action of turbulent random motions. The turbulent random motions introduce three-dimensional random components to the wind velocity of the irregularities. The components of the random motion evolve slowly over time.

The effects of turbulent random motions have been included in the models of *Wright and Pitteway* [1978] and *Sheppard and Larsen* [1992]. The model of *Wright and Pitteway* [1978] uses two different simulations. Because they use a grid of scatterers the motions are confined to two-dimensions. The first simulation technique ("explicit random motions")

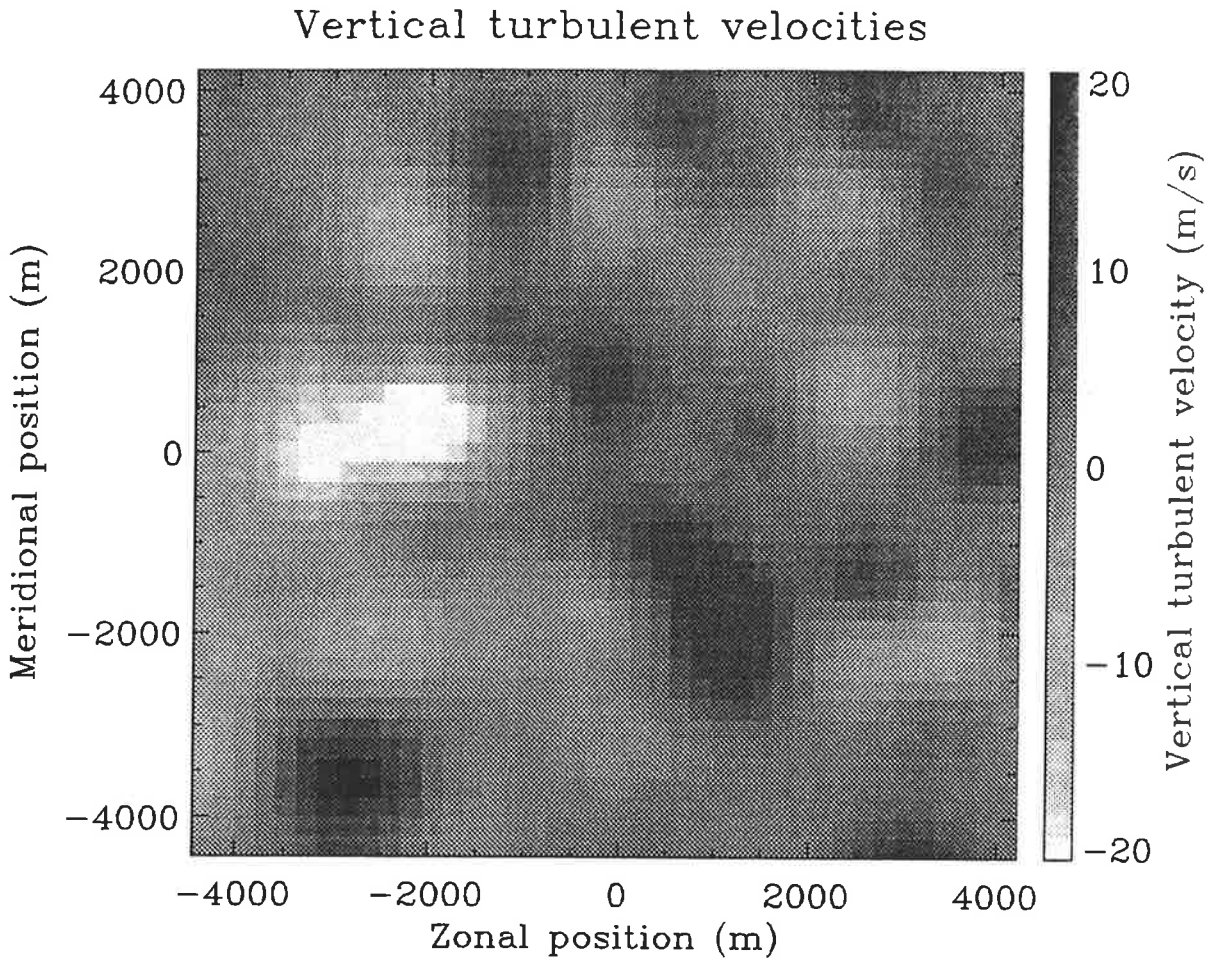

Figure 3.4: Example of the vertical turbulent velocity field obtained using an rms vertical velocity of 6 ms^{-1}.

involves generating a different set of random velocity components for each positional update of the scatterers. Although this simulation appears to produce the desired effect for their analysis, it obviously a poor simulation of what occurs in practice, and can introduce some undesirable effects. In the duration of the sampling time the random velocity components can change appreciably. Large random motion magnitudes can therefore produce abrupt changes in the positions of the scatterers. These abrupt changes can produce unsmooth time-series records, which can in turn produce auto- and cross-correlation functions with unsmooth behavior and zero-lag "spikes", thereby degrading the effective analysis of the data. The second technique ("fixed direction motions") involves assigning a fixed set of random velocity components to each scatterer. The fixed direction motions simulation avoids the problems described for the explicit random motions simulation but does allow the possibility that two different scatterers in close proximity can have significantly different random motions

random motions components. The technique used by *Sheppard and Larsen* [1992] is identical to the fixed direction motions simulation, except that the velocity components are derived from a Gaussian distribution.

The random motions are simulated in this model as follows. A three-dimensional vector $\vec{v}_i'$ is generated for each scatterer. The components of this vector are generated according to Gaussian distributions with specified zonal, meridional and vertical root-mean-square (rms) values. The turbulent velocity $\vec{V}_{\text{turb}}(\vec{r}_i)$ for the ith scatterer is determined using the equation

$$\vec{V}_{\text{turb}}(\vec{r}_i) = \sum_{j=0}^{N_{\text{scat}}-1} \vec{v}_j' \exp\left(-\left(\frac{|\vec{r}_i - \vec{r}_j|}{S_{\text{turb}}}\right)^2\right), \tag{3.13}$$

where N_{scat} is the number of model scatterers, and S_{turb} is a scale-factor used to vary the scale of the turbulence. This formulation produces random velocity velocity components with spatial and temporal correlation, thereby avoiding the deficiencies introduced by the simulations of *Wright and Pitteway* [1978] and *Sheppard and Larsen* [1992]. In practice, S_{turb} is usually set to be of the order of the average interscatterer separation r_{ij}. The spatial correlation can be seen in the results of Figures 3.3 and 3.4, which show typical horizontal and vertical turbulent velocity fields respectively for the application of (3.13) to mesospheric simulations using $S_{\text{turb}} = 0.5r_{ij}$. If the density within the radar volume is assumed constant the continuity equation is satisfied to within 2% when using a rectangular volume of the scale of the interscatterer spacing about each scattering position.

3.2.4.2 Gravity-wave perturbations

The implementation of gravity wave effects into the model has been restricted to the case of monochromatic waves. Although the effect of a spectrum of waves has not been implemented the turbulence random motions simulation can be regarded as the superposition of the effects of a combination of many waves with similar amplitudes.

The velocity perturbations resulting from monochromatic gravity-wave have been implemented in the same manner as in the model of *Meek and Reid* [1984], which was used to analyze the effects of short-period gravity waves upon FCA. At any position $\vec{r}$, the velocity perturbation resulting from a monochromatic gravity is given by

$$\vec{V}_{\text{gw}}(\vec{r}) = \vec{V}' \cos(\omega' t - \vec{k} \cdot \vec{r}), \tag{3.14}$$

where $\vec{V}'$ is the perturbation velocity, $\vec{k}$ is the wavenumber vector and ω' is the angular frequency in the frame of the radar.

The model input parameters used for the gravity wave simulations are the horizontal velocity perturbation V_h', the intrinsic gravity wave period T, the horizontal phase speed c_p and azimuth angle ϕ_p, and the Brunt Vaisala frequency ω_{bv}. The values of these parameters used in the model analyses described in this thesis have been taken from *Reid* [1989]. The horizontal wavelength λ_h is determined by

$$\lambda_h = c_p T, \tag{3.15}$$

from which the zonal k and meridional l wavenumbers are determined using the equation

$$k = 2\pi \sin\phi_p/\lambda_h, \tag{3.16}$$

$$l = 2\pi \cos\phi_p/\lambda_h. \tag{3.17}$$

The vertical wavelength m is determined using the dispersion relation

$$\omega = \frac{\omega_{bv}}{\sqrt{1+(\lambda_h/\lambda_z)^2}}, \tag{3.18}$$

from which the vertical wavenumber is determined using

$$m = 2\pi/\lambda_z. \tag{3.19}$$

The wavenumber vector is then given by $\vec{k} = (k, l, m)$. The vertical perturbation velocity w' is determined using the polarization relation

$$w' = -V_h'\lambda_z/\lambda_x. \tag{3.20}$$

The zonal and meridional perturbation velocities are determined using

$$u' = V_h' \sin\phi_p, \text{ and} \tag{3.21}$$

$$v' = V_h' \cos\phi_p, \tag{3.22}$$

thereby determining the perturbation velocity $\vec{V}' = (u', v', w')$. The ground based frequency of the wave is then given by

$$\omega' = \omega + \vec{k}\cdot\vec{V}, \tag{3.23}$$

where $\vec{V}$ is the background wind velocity.

The scatterer tilts simulation implemented by *Sürücü et al.* [1995b] has not been incorporated into the model. These tilts could be implemented in a similar manner by introducing an expression for the scatterer tilt of the same form as (3.14), which could then be converted into a unit vector $\hat{r}_{si}$ for use in (3.6).

Table 3.1: Standard atmospheric parameters employed for the radar backscatter model.

Model parameter	MF	VHF
Number of scatterers, N_{scat}	1000	200
Velocity magnitude, V (ms^{-1})	50	20
Velocity direction, θ (deg)	15	15
Horizontal rms turbulent velocity (ms^{-1})	6	0.5
Vertical rms turbulent velocity (ms^{-1})	6	0.5
Aspect sensitivity, θ_s (deg)	10.4	2
Scatterer tilt parameter, $\hat{r}_{si}$	0	0
Anisometry parameter, A	1	1

3.3 Application of the radar backscatter model

3.3.1 Simulation parameters

The simulation parameters used by the model can be divided into "atmospheric" and radar parameters. The atmospheric parameters are in general chosen to satisfy specific atmospheric conditions, while the radar parameters are in general chosen to simulate the operating characteristics of the BP MF and VHF radars.

The standard atmospheric parameters are shown in Table 3.1. Unless otherwise specified, these parameters are used for all simulations described in this thesis. The parameters are based on typically expected conditions at 90 km for MF, and at 10 km for VHF. The values of N_{scat} have been selected based on the results of the application of the FCA, as described in Chapter 4. The value of θ was initially chosen so that it was not aligned with any of the receiver separations employed for the SA simulations, and has thereafter been employed as the standard velocity direction. The θ_s values are taken from the results discussed in *Reid* [1990] at MF and *Hocking et al.* [1986] at VHF. The scatterer tilts unit vectors $\hat{r}_{si}$ are all set to zero, so that the scatterers are not tilted away form the horizontal. Isotropic turbulent rms velocities are chosen in order to yield FCA apparent velocity magnitudes approximately twice as large as the magnitude of the model input velocity. Gravity waves and variable reflectivity factors are not used in the standard implementation of the model.

The radar parameters can be separated into "sampling" and "polar diagram" parameters. The standard sampling parameters are shown in Table 3.2. Unless otherwise specified, these parameters are used for all simulations described in this thesis. As various noise sources seen in actual radar systems are absent from the model no temporal coherent averaging is

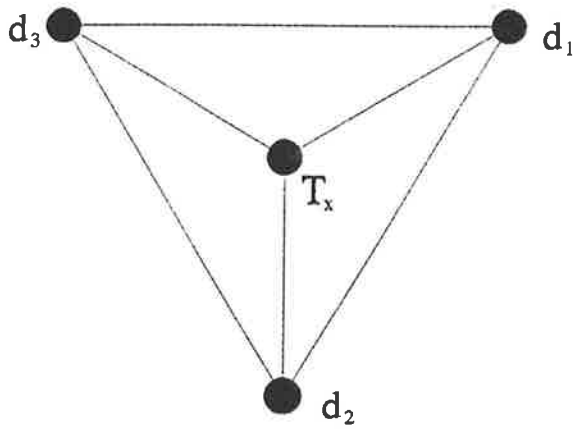

Figure 3.5: Standard antenna configuration employed for model data generated using the SA simulation. The receiving antenna d_j are arranged in an equilateral triangle with sides of length d_{ij} at angles 60°, 180° and 240° from the effective center of transmitting antennae at the origin of the coordinate system.

necessary. As a result, each time-series sample is given by the complex voltage induced at the particular sampling time rather than the coherent average over number of returned transmitter pulses.

The standard polar diagram parameters used for the simulation of MF and VHF SA radars are shown in Table 3.3. The configuration of the transmitting and receiving antennae are shown in Figure 3.5. The receiving antenna are arranged in an equilateral triangle at angles 60°, 180° and 240° from the effective center of transmitting antennae located at the origin of the coordinate system. Although the parameters in Table 3.3 are intended to represent the operating characteristics of the BP MF and VHF radars, an MF beam width of 15° has been chosen rather than the actual value of about 20°. The use of a 15° beam-width significantly reduces the radar and enclosing volumes. This results in the need for fewer scatterers which thereby reduces the computation time. As various noise sources seen in actual radar systems are absent from the model no temporal or spatial coherent averaging is necessary. Multi-antenna receiving arrays such as the 4-antennae and 16-antenna arrays used for the BP MF and VHF SA experiments are therefore simulated using a single antenna with the appropriate polar diagram. The effects of various noise contributions may be simulated after time-series generation.

The radar parameters used for the simulation of MF and VHF Doppler radars are shown in Table 3.4. The receiving antenna configuration is left open to the experimental requirements.

The angular and range cut-off ratios of 0.05 have been chosen based on observations of

Table 3.2: Standard sampling parameters employed for the radar backscatter model.

Model parameter	MF	VHF
Radar Frequency, f_0 (MHz)	2	50
Range, r_0 (km)	90	10
Range gate width, r_e (m)	2000	500
Range cut-off ratio, R_{cut}	0.05	0.05
Sampling time, Δt (s)	0.4	0.1
Pulse repetition frequency, PRF (Hz)	2.5	10
Coherent averages	1	1
Time series samples, N	256	1024
Time series duration, $N \Delta t$ (s)	102.4	256

Table 3.3: Standard polar diagram parameters used for SA radar simulation.

Model parameter	MF	VHF
Transmitter beamwidth, θ_t (deg)	15	2.5
Transmitter beam pointing angle, θ_a (deg)	0	0
Angular cut-off ratio, θ_{cut}	0.05	0.05
Receiving antenna separation, d_{ij} (m)	200	50

Table 3.4: Standard polar diagram parameters used for Doppler radar simulation.

Model parameter	MF	VHF
Transmitter beamwidth, θ_t (deg)	10	2
Transmitter beam pointing angle, θ_a (deg)	10	10
Angular cut-off ratio, θ_{cut}	0.05	0.05

the resulting time-series records. Values greater than 0.1 were found to produce time-series with small but noticeable discontinuities when the scatterers left the radar volume. On the other hand, the selected value of 0.05 produces no noticeable discontinuities. The model of *Sheppard and Larsen* [1992] used an angular cut-off ratio of $\sqrt{0.5}$. Despite this large cut-off ratio no spurious effects were reported. It is possible however that the large number of averages used to produced the correlation functions and spectra employed for their analyses may have minimized any spurious effects.

A complete description of the model-generated data-sets used in this thesis is given in Appendix A.

3.3.2 Time series generation

Typical examples of the time-series produced using the standard MF and VHF simulation parameters are shown in Figures 3.6 and 3.8, respectively. The MF time-series show considerable resemblance as the antennae separation (200 m) is of the order of the radar wavelength (150 m). On the other hand, the VHF time-series show little obvious resemblance as the antennae separation (50 m) is considerable larger than the radar wavelength ($\approx$ 6 m).

Typical examples of the time-series obtained using the BP MF and VHF radars at the heights simulated by the MF and VHF model parameters are shown in Figures 3.7 and 3.9, respectively. The model-generated time-series exhibit fading characteristics very similar to those exhibited in experimental data. The model-generated data illustrated here exhibits two distinct advantages over the experimental time-series. The first advantage is that the model-generated data is free from the effects of noise. The effects of noise result in the experimental time-series containing an additional random component. The effects of noise can however be included after the generation of the model time-series. The second advantage is that the model-generated data is free from the effects of phase differences introduced by the receivers or through the use of different cable lengths. The individual components of the BP MF time-series show little resemblance with each other as result of such phase differences. The existence of these phase differences can significantly affect the application of the Doppler-selected imaging interferometry techniques outlined in Chapter 8.

3.3.3 The ground diffraction pattern

The production of useful images of the ground diffraction pattern requires a large array of receiving antennae covering an area greater than the mean pattern scale, and with antenna

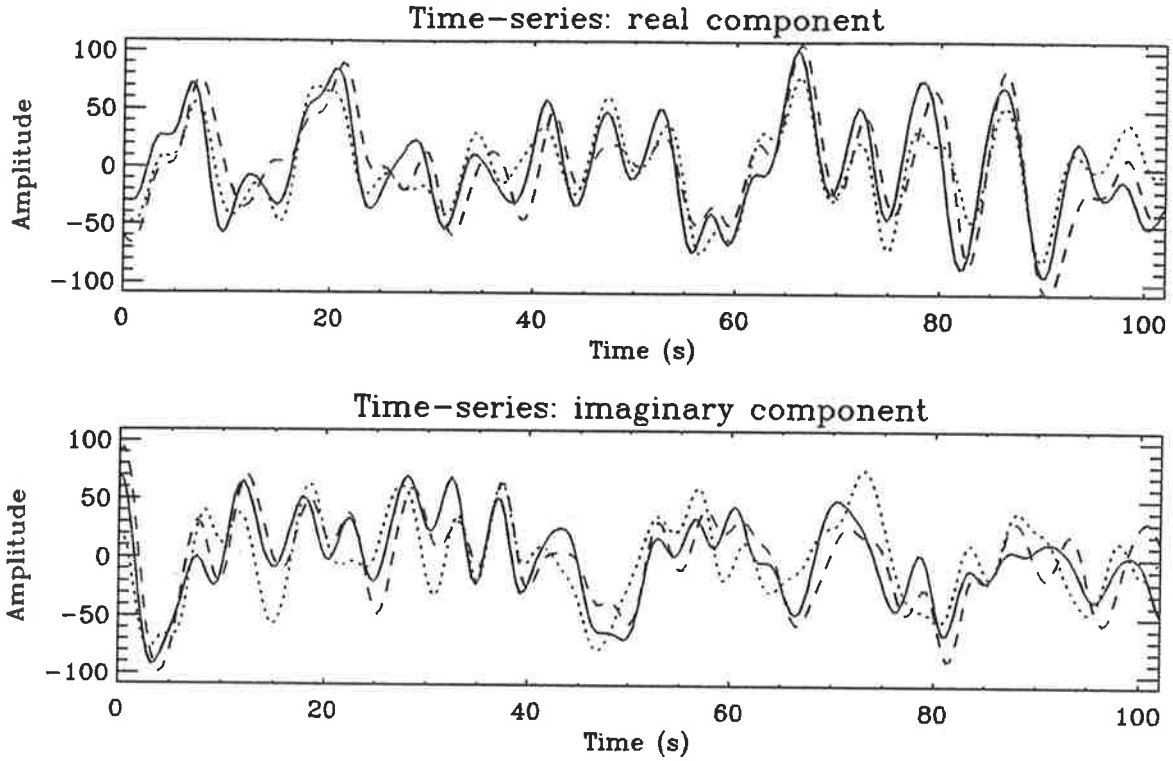

Figure 3.6: Typical example of the time-series produced using the standard MF simulation parameters.

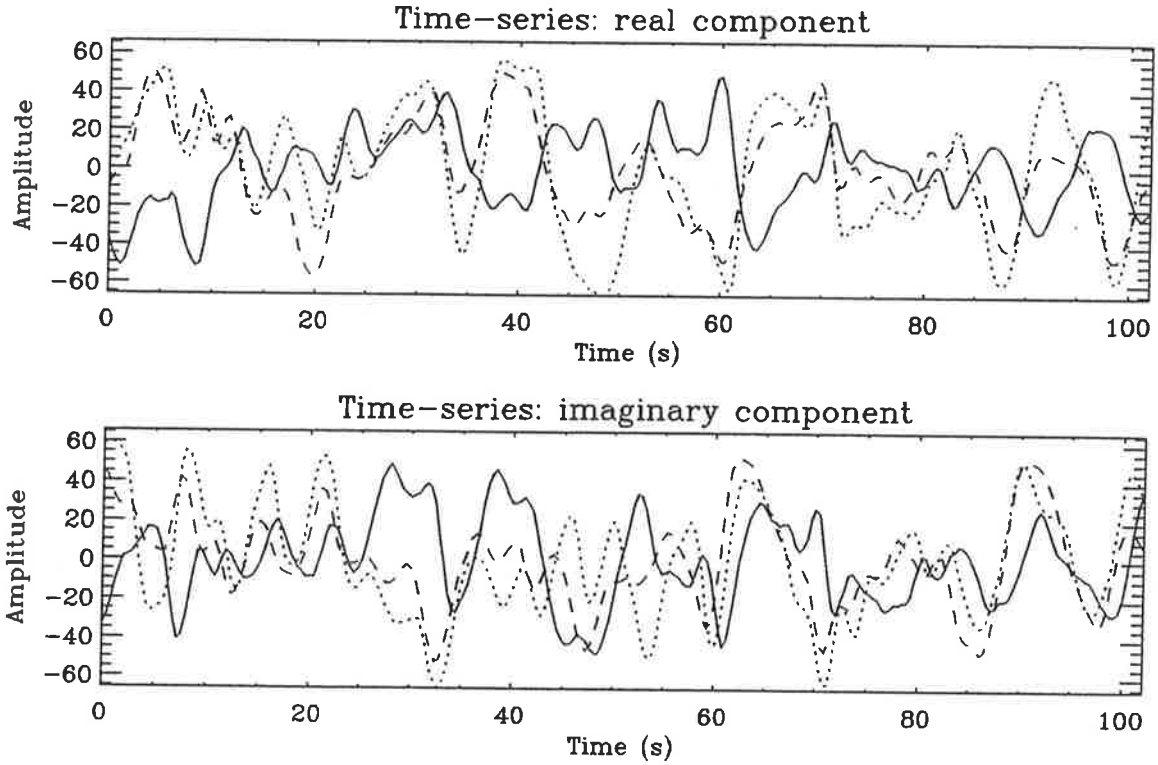

Figure 3.7: Typical example of the time-series obtained using the Buckland Park MF radar at a range of 90 km.

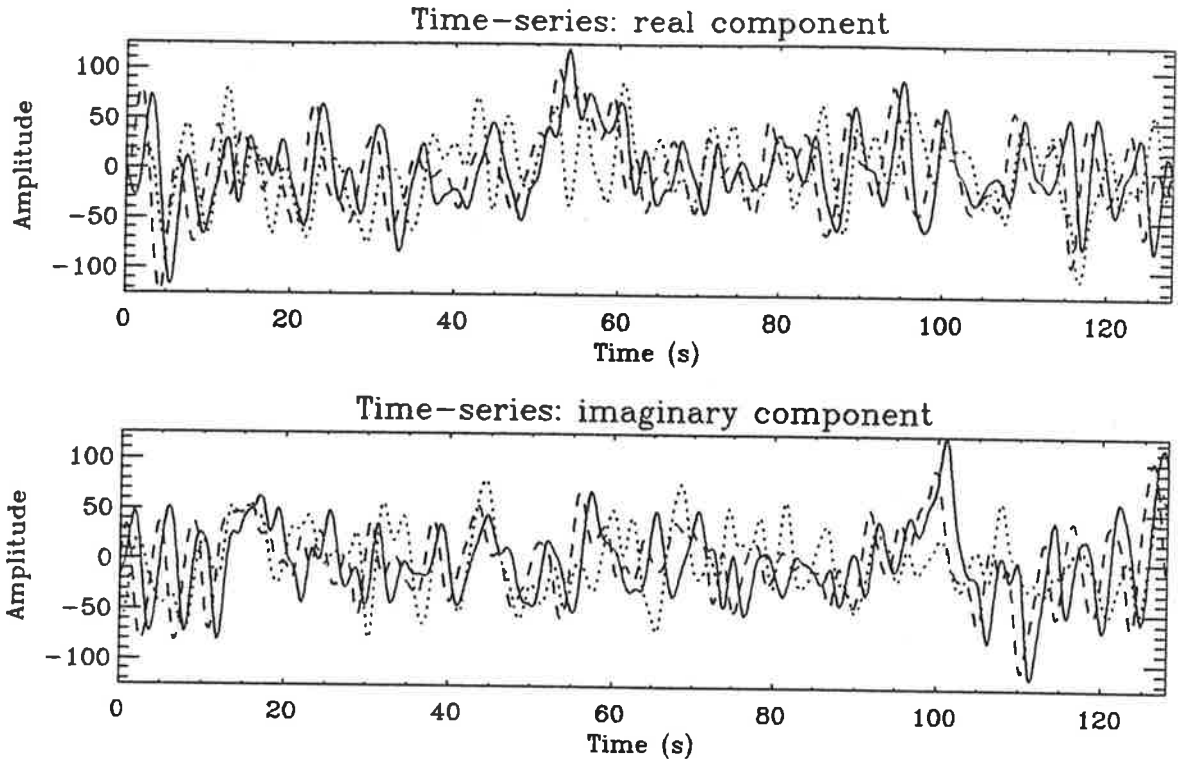

Figure 3.8: Typical example of the time-series produced using the standard VHF simulation parameters.

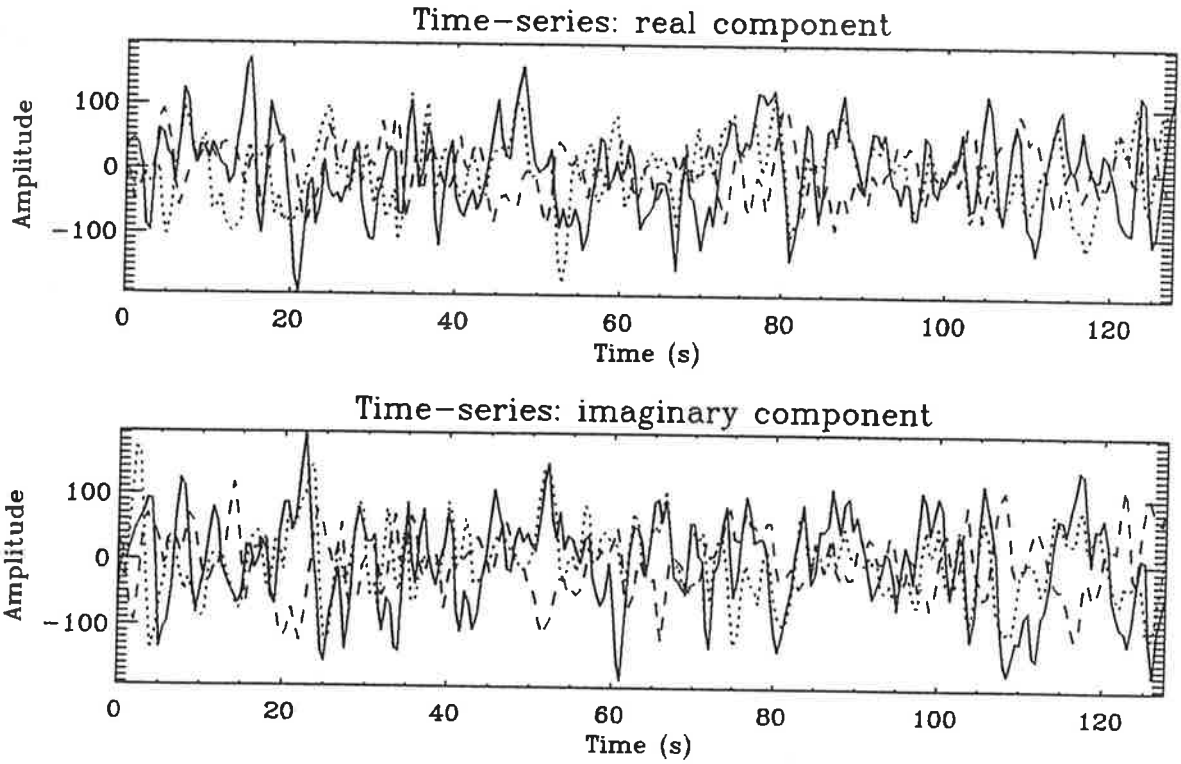

Figure 3.9: Typical example of the time-series obtained using the Buckland Park VHF radar at a range of 10 km.

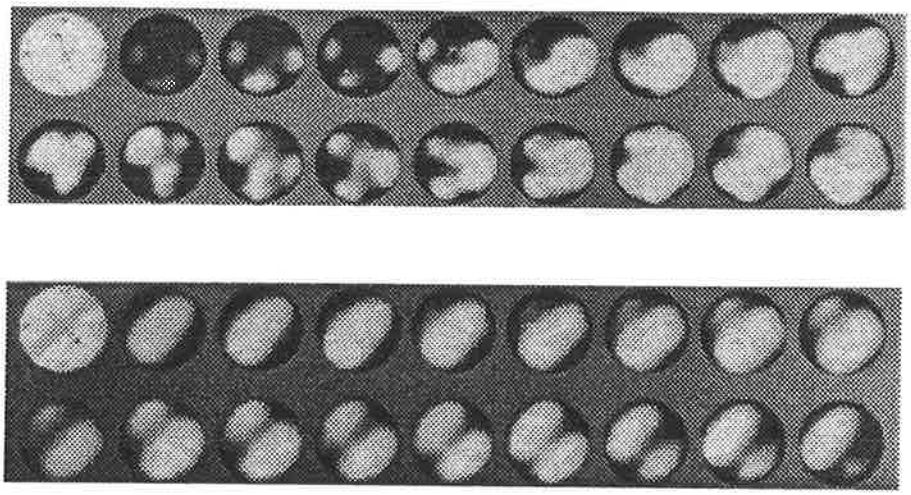

Figure 3.10: Two examples of the evolution of the ground diffraction pattern image obtained by *Felgate and Golley* [1971]. The top figure illustrates a random pattern from a night-time sporadic E-layer obtained at 0.5 s intervals. The bottom plot illustrates a periodic fringe pattern from a night-time F-region layer obtained at 0.75 s intervals.

spacings considerably shorter than the mean pattern scale. The Buckland Park MF array has been successfully employed for this purpose (e.g. *Felgate and Golley*, [1971]). The production of these images allows the application of the spatial correlation analysis (e.g. *Briggs*, [1968]. The production of such images are also especially important for the determination of the mechanisms responsible for the radiowave backscatter, and the verification of the assumptions made by the FCA and about the behavior of the ground diffraction pattern and the spatio-temporal correlation function.

The images of the ground diffraction pattern produced by *Felgate and Golley* [1971] were obtained using the 89 East-West aligned dipoles of the BP MF array. Each dipole was connected to a single receiver. The amplitude of the signal output of each receiver was used to vary the intensity of a small filament lamp. The lamps were arranged in the same configuration as the individual dipoles, and mounted behind a sheet of ground glass in order to smoothen the resulting image. Two examples of the evolution of the resulting ground diffraction pattern image are illustrated in Figure 3.10. The top figure illustrates a random pattern obtained from a night-time sporadic E-layer, while the bottom plot illustrates a periodic fringe pattern obtained from a night-time F-region layer.

The radar backscatter model has been employed to produce similar images of the ground diffraction pattern. The model-generated data-set MOD-MF-GDP-V50 has been produced using the MF simulation parameters without turbulent or gravity wave motions, with a model input velocity of 50 ms^{-1} eastwards. The resulting pattern has been sampled using a 60 by

60 array of receiving antennae with 50 m spacing. The evolution of the resulting ground diffraction pattern magnitude is shown in Figure 3.11. The pattern appears to propagate eastwards, which is consistent with the direction of the model input velocity. There appear to be no random changes in the pattern in the reference frame moving with the pattern, as expected for the case without turbulent or gravity wave motions. The pattern is also isometric, as expected due to the isometric scattering mechanism employed to generate the data.

The effects of random motions upon the ground diffraction pattern are illustrated in Figure 3.12, which shows the ground diffraction pattern obtained using the data-set MOD-MF-GDP-V0-T6, generated using a mean wind velocity of zero and $\nu_{\mathrm{mod}} = 6$ ms^{-1}. There is no distinct direction of pattern propagation. The individual features of the pattern change abruptly, such that the there is very little correspondence between the patterns obtained at intervals greater than 2 s.

The effects of random motions and a mean wind velocity upon the ground diffraction pattern can be seen in Figure 3.13, which illustrates the ground diffraction pattern obtained using the data-set MOD-MF-GDP-V0-T6, generated using a mean wind velocity of 50 ms^{-1} and a turbulent rms velocity of 6 ms^{-1}. The pattern appears to propagate eastwards, which is consistent with the direction of the model input velocity. However, because the individual features of the pattern change abruptly the propagation is only evident in comparing the patterns from contiguous samples.

The production of ground diffraction pattern images allows the application of the spatial correlation analysis (e.g. *Briggs*, [1968]). An example of the application of the spatial correlation analysis to model-generated images of the ground diffraction pattern is illustrated in Chapter 8. The model-generated ground diffraction patterns are also employed in Chapter 4 to illustrate the reasoning behind the assumptions employed by the FCA with respect to the spatial and temporal dependences of the spatio-temporal correlation function. The production of ground diffraction pattern images can also allow the imaging of the irregularities responsible for the radiowave backscatter in an computational analogue to the ultrasonic technique employed by *Briggs and Holmes* [1973]. The use of model generated ground diffraction pattern images could prove especially useful in the experimental implementation of such a technique.

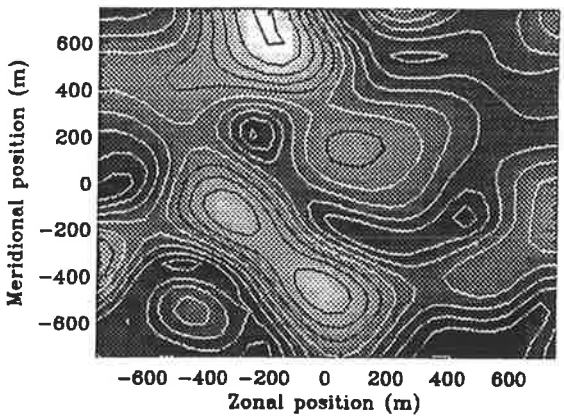
Meridional position (m)
600
400
200
0
−200
−400
−600
−600 −400 −200 0 200 400 600
Zonal position (m)

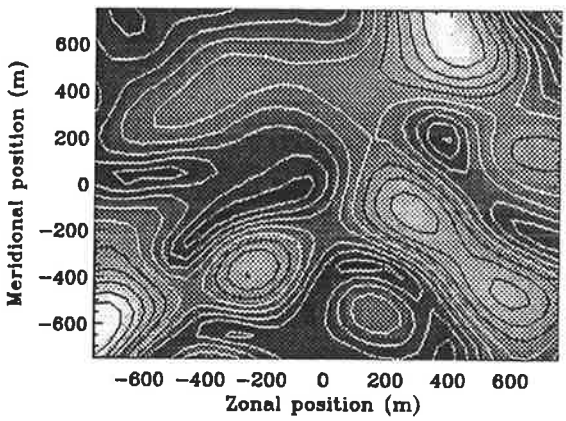
Meridional position (m)
600
400
200
0
−200
−400
−600
−600 −400 −200 0 200 400 600
Zonal position (m)

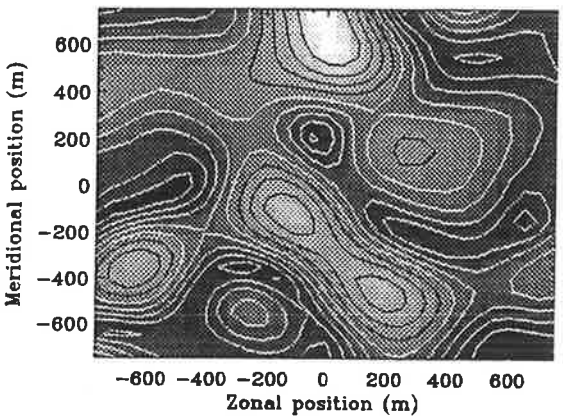
Meridional position (m)
600
400
200
0
−200
−400
−600
−600 −400 −200 0 200 400 600
Zonal position (m)

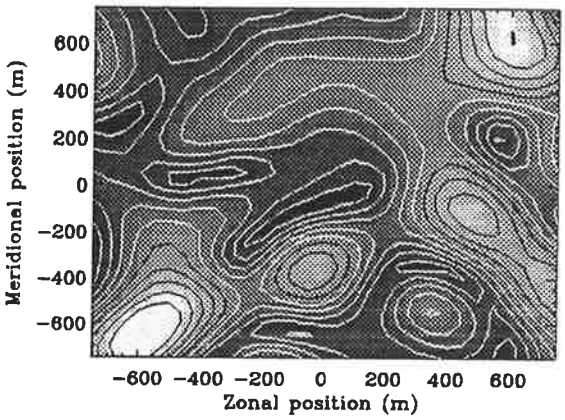
Meridional position (m)
600
400
200
0
−200
−400
−600
−600 −400 −200 0 200 400 600
Zonal position (m)

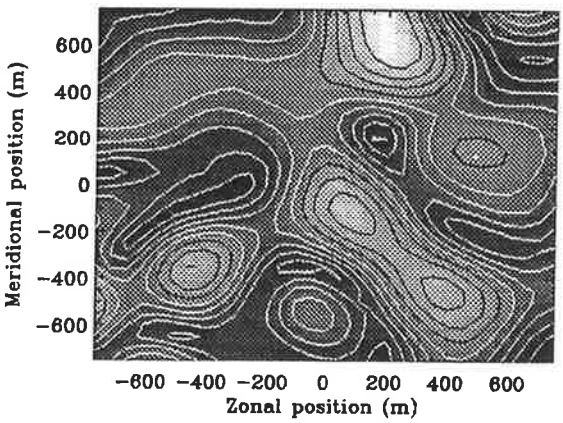
Meridional position (m)
600
400
200
0
−200
−400
−600
−600 −400 −200 0 200 400 600
Zonal position (m)

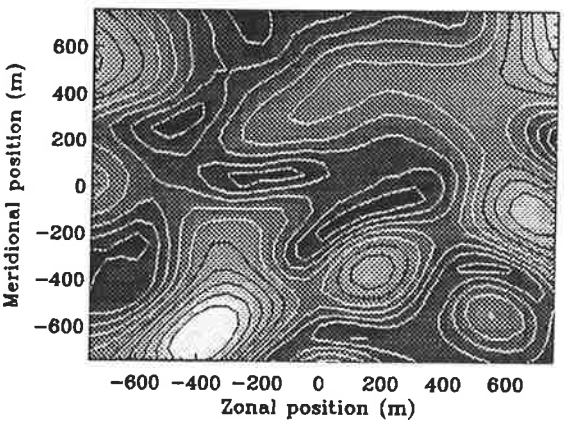
Meridional position (m)
600
400
200
0
−200
−400
−600
−600 −400 −200 0 200 400 600
Zonal position (m)

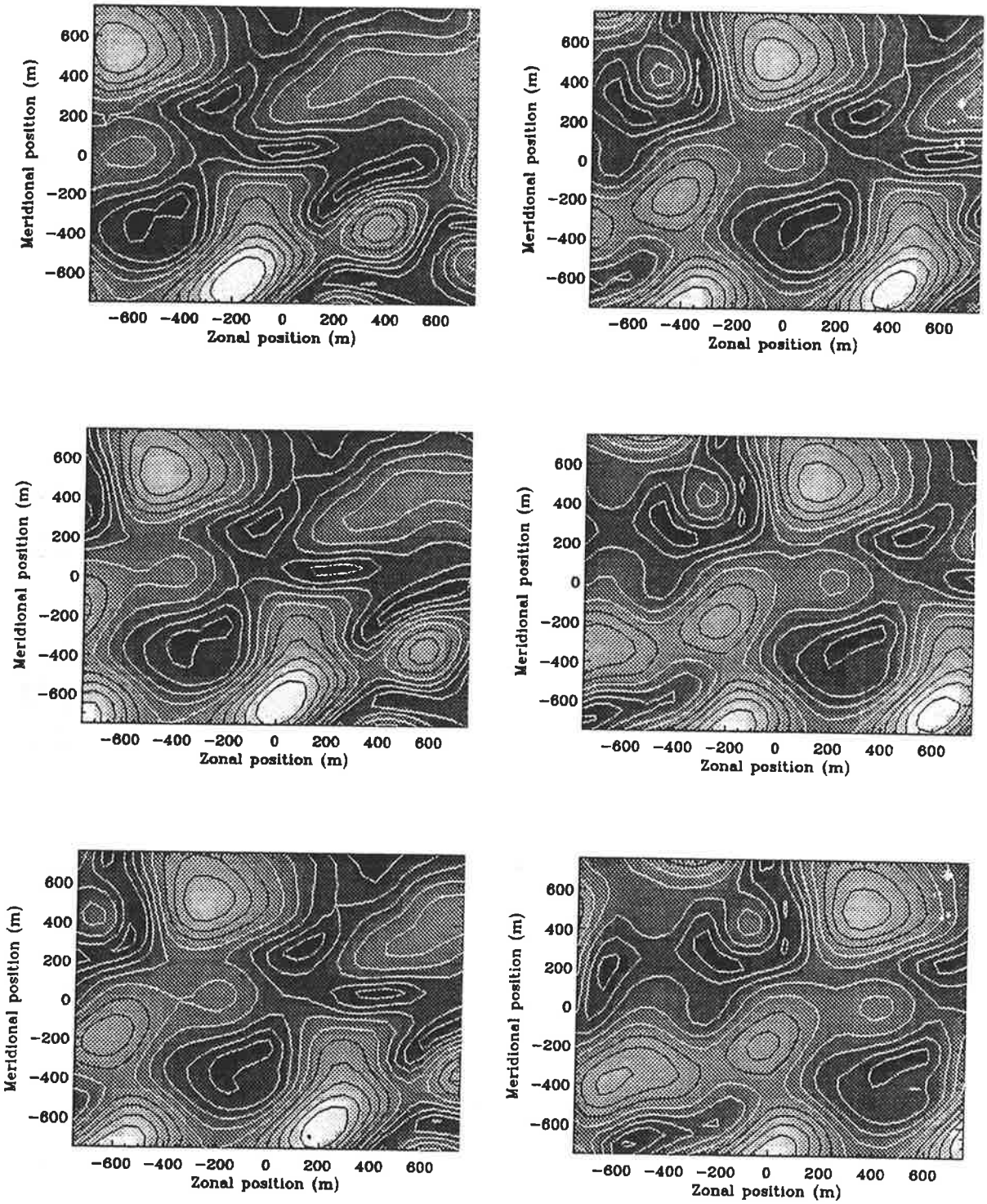

Figure 3.11: Ground diffraction patterns obtained using the model-generated data-set MOD-MF-GDP-V50, simulating the situation of a mean wind with velocity of 50 ms^{-1} propagating eastwards. The patterns are plotted in 2 second intervals starting from the top left plot, going from top to bottom and then left to right. The pattern appears to propagate eastwards no random changes. This is consistent with the model input parameters.

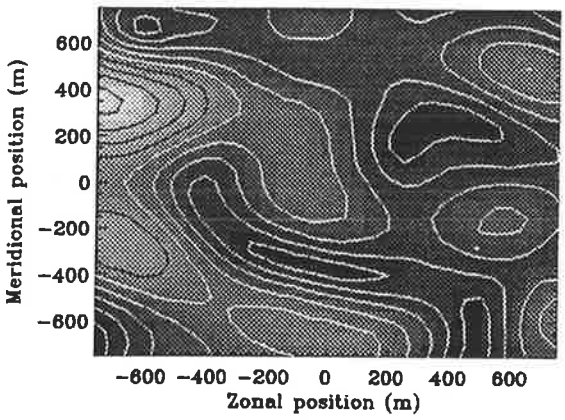
Meridional position (m)
600
400
200
0
−200
−400
−600
−600 −400 −200 0 200 400 600
Zonal position (m)

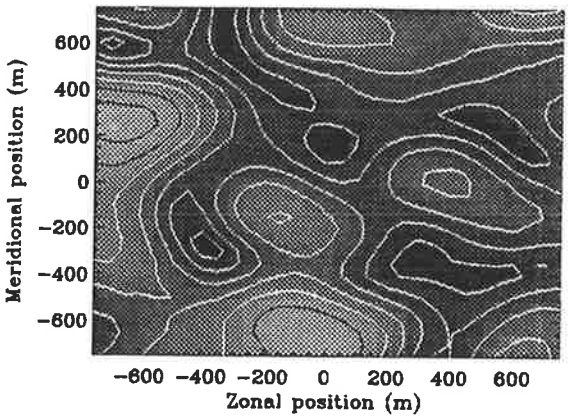
Meridional position (m)
600
400
200
0
−200
−400
−600
−600 −400 −200 0 200 400 600
Zonal position (m)

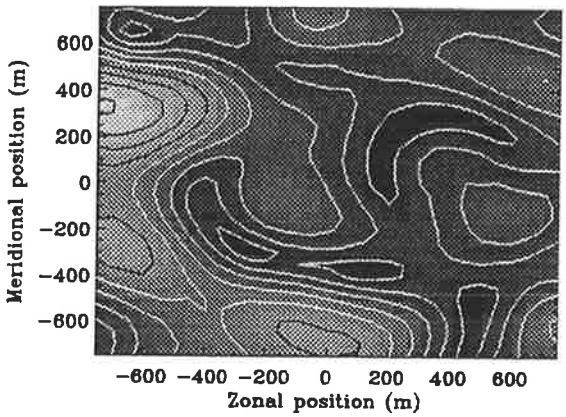
Meridional position (m)
600
400
200
0
−200
−400
−600
−600 −400 −200 0 200 400 600
Zonal position (m)

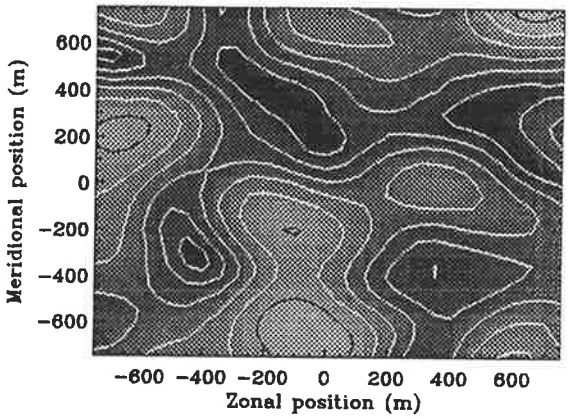
Meridional position (m)
600
400
200
0
−200
−400
−600
−600 −400 −200 0 200 400 600
Zonal position (m)

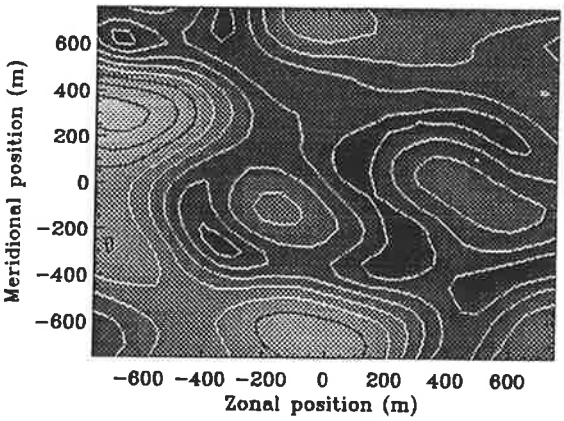
Meridional position (m)
600
400
200
0
−200
−400
−600
−600 −400 −200 0 200 400 600
Zonal position (m)

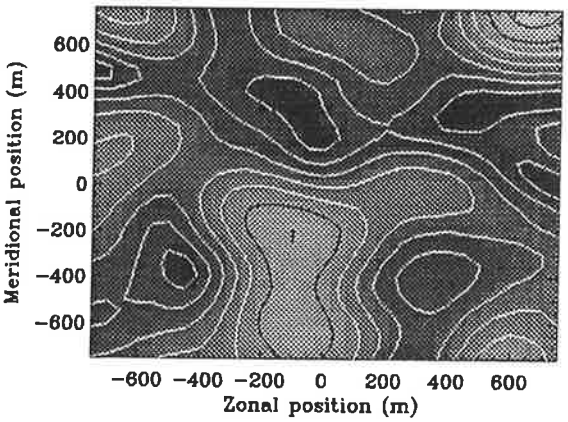
Meridional position (m)
600
400
200
0
−200
−400
−600
−600 −400 −200 0 200 400 600
Zonal position (m)

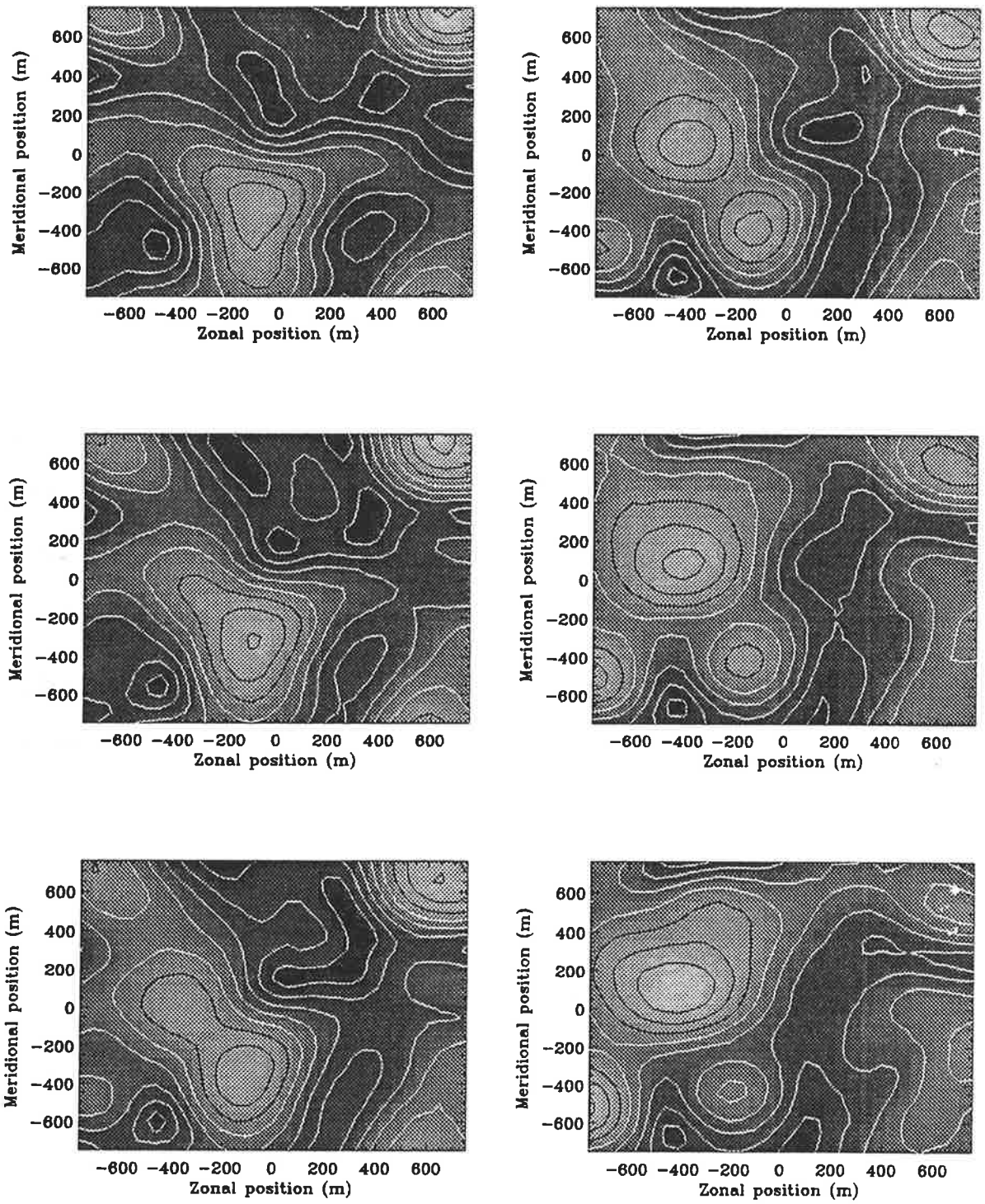

Figure 3.12: Ground diffraction patterns obtained using the model-generated data-set MOD-MF-GDP-V0-T6, which simulates the case of no mean wind and a turbulent motions velocity $v_{\text{mod}} = 6$ ms^{-1}. The patterns are plotted in 0.8 second intervals starting from the top left plot, going from top to bottom and then left to right. The turbulent motions result in the pattern evolving rapidly. The pattern appears to have no distinct direction of propagation, which is consistent with the model input velocity of zero.

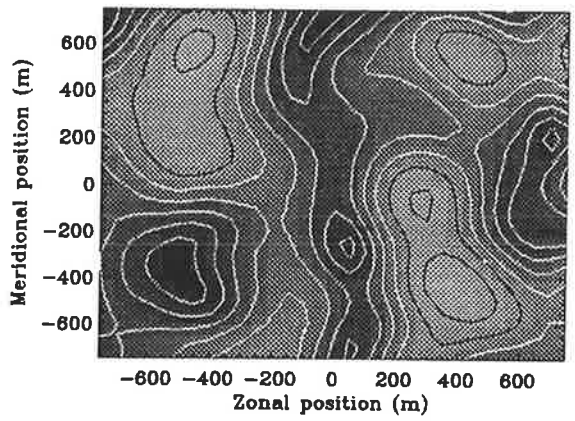
Meridional position (m)
600
400
200
0
−200
−400
−600
−600 −400 −200 0 200 400 600
Zonal position (m)

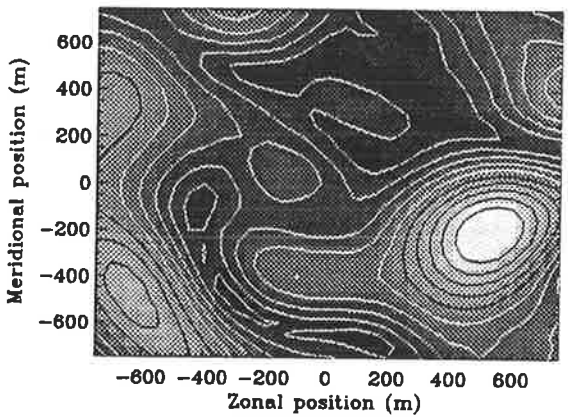
Meridional position (m)
600
400
200
0
−200
−400
−600
−600 −400 −200 0 200 400 600
Zonal position (m)

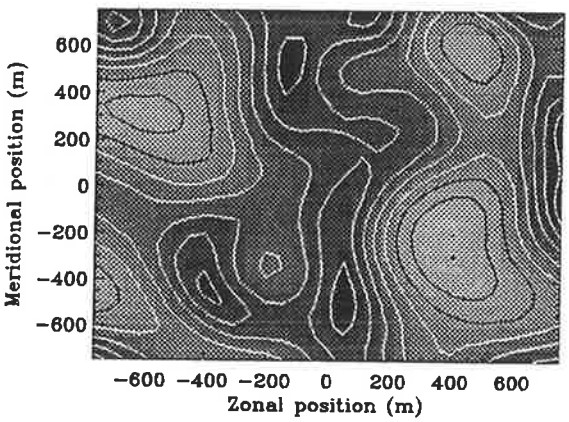
Meridional position (m)
600
400
200
0
−200
−400
−600
−600 −400 −200 0 200 400 600
Zonal position (m)

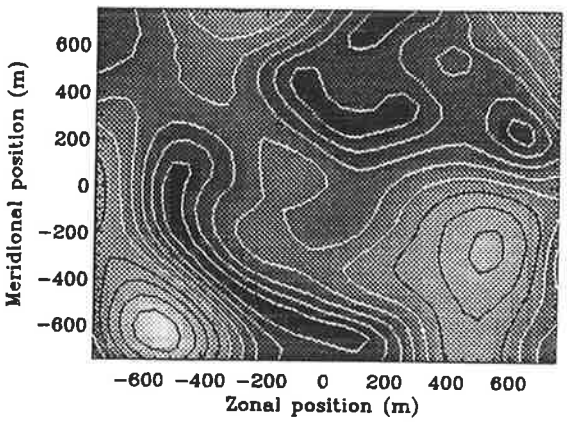
Meridional position (m)
600
400
200
0
−200
−400
−600
−600 −400 −200 0 200 400 600
Zonal position (m)

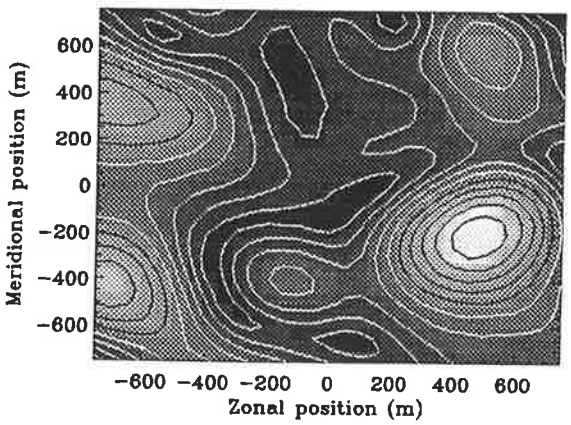
Meridional position (m)
600
400
200
0
−200
−400
−600
−600 −400 −200 0 200 400 600
Zonal position (m)

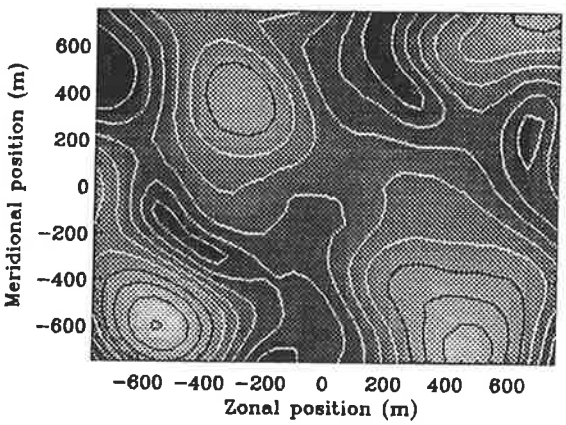
Meridional position (m)
600
400
200
0
−200
−400
−600
−600 −400 −200 0 200 400 600
Zonal position (m)

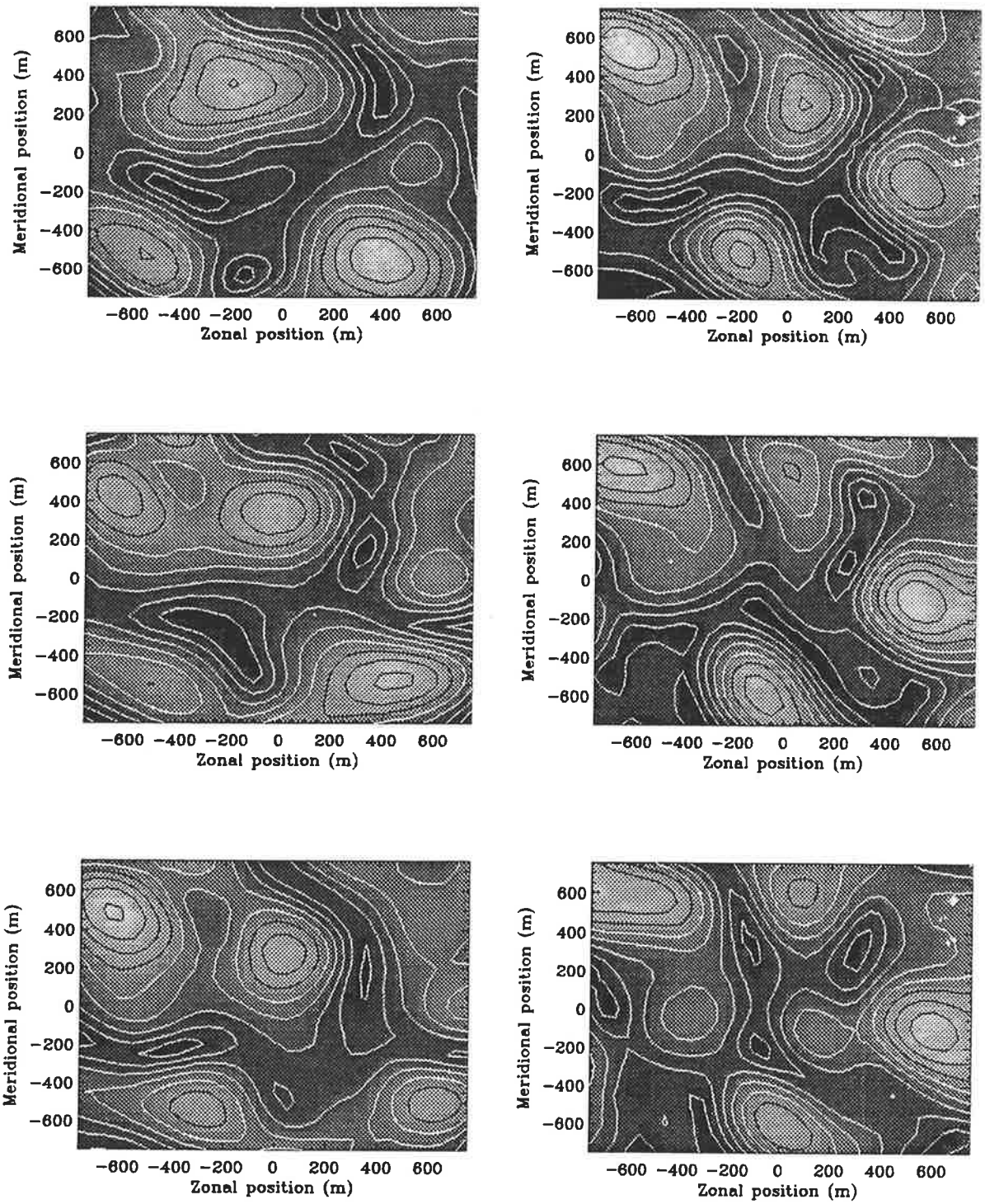

Figure 3.13: Ground diffraction patterns obtained using the model-generated data-set MOD-MF-GDP-V50-T6, which simulates the case of a mean wind velocity of 50 ms^{-1} propagating eastward, turbulent motions velocity $\nu_{mod} = 6$ ms^{-1}. The patterns are plotted in 2 second intervals, going from top to bottom and left to right. The pattern appears to propagate eastwards, which is consistent with the direction of the model input velocity. The turbulent motions result in the pattern evolving rapidly.

3.4 Verification of the model

In order to verify that the model is performing as expected a number of different analyses have been applied. These analyses have been used to check that the model input parameters are recoverable, thereby also verifying the analyses in the process.

3.4.1 The Full Correlation Analysis

The full correlation analysis (FCA) is described in detail in Chapter 4. The FCA provides two estimates of the wind velocity. The "apparent" velocity is estimated using the similar fades technique detailed in Appendix B. The "true" velocity includes corrections for the effects of random changes and anisometry in the ground diffraction pattern, and is thus generally considered the better velocity estimate. The FCA also provides information on the characteristics of the ground diffraction pattern, which can be used to obtain information on the nature of the irregularities responsible for the signal backscatter.

The results of the application of the FCA to a number of model-generated data-sets are presented in Chapter 4. The results of Figure 4.7 reveal that the "true" velocity provides an excellent estimate of the model input velocity for all magnitudes of model turbulent motions. On the other hand, the magnitude of the "apparent" velocity increases with increasing model turbulent motions. The results of Figure 4.9 reveal that the true velocity also provides an excellent estimate of the model input velocity for all values of pattern anisotropy, while the direction of the apparent velocity is biased towards the direction of pattern elongation.

These results suggest that the FCA true velocity is accurately measuring the model input velocity, thereby suggesting that the model is correctly simulating the effects of atmospheric wind motions.

3.4.2 Turbulent random motions estimation

The turbulent motions rms velocity magnitude ν can be estimated using a number of different techniques. These techniques can be roughly categorized into FCA techniques (e.g. *Briggs*, [1980]) and Doppler techniques (e.g. *Hocking et al.*, [1983a,b]). The verification of the turbulent motions simulation of the model presented in this section is confined to vertical beam techniques.

The turbulence simulation has been analyzed by comparing the model rms turbulent velocity ν_{mod} with values estimated by the FCA technique (e.g. *Briggs*, [1980]) and the

spectral-width technique (e.g. *Hocking*, [1983a]). The isotropic turbulent rms velocity predicted by the FCA technique is given by

$$\nu_{\text{fca}} = \frac{\lambda\sqrt{\ln 2}}{4\pi T_{0.5}}, \tag{3.24}$$

where $T_{0.5}$ is the fading time in the frame of the ground diffraction pattern. This fading time is attributed solely to the random motions of the pattern. The vertical turbulent rms velocity predicted by the spectral-width technique is given by

$$\nu_{\text{sw}} = \frac{\lambda}{2\sqrt{2\ln 2}}\sqrt{f_{0.5}^2 - f_{r0.5}^2}, \tag{3.25}$$

where $f_{0.5}$ is power-spectrum half-width and $f_{r0.5}$ is the theoretical "non-turbulent" power-spectrum half-width. The spectral half-width $f_{0.5}$ is the result of the combined effects of beam- and shear-broadening, and vertical oscillations of the wind velocity and turbulence. The term $\sqrt{f_{0.5}^2 - f_{r0.5}^2}$ gives "turbulent" power-spectrum half-width, resulting from the effects of turbulence alone. This technique requires the use of a narrow transmitting beam and a short pulse-width in order to eliminate the effects of beam- and shear-broadening. The data-set MOD-MF-TURB was generated using the standard MF Doppler parameters using turbulent rms velocities ν_{mod} ranging from 0 to 6 ms^{-1} with a beam pointing angle on the zenith. The requirements of the spectral width technique have therefore been partially met. As the model velocity is independent of range shear-broadening will not be encountered. The non-turbulent power-spectrum half-width was calculated using the $\nu_{\text{mod}} = 0$ ms^{-1} case.

The relationship between the average values of ν_{fca} and ν_{sw} as a function of ν_{mod} for the data-set MOD-MF-TURB are shown in in Figure 3.14. The non-zero value of ν_{fca} obtained when $\nu_{\text{mod}} = 0$ can be explained by taking into account the fact that the value of $T_{0.5}$ used to derive (3.24) is assumed to be solely due to turbulent fading. However, the variation in the reflectivity of the individual scatterers as they propagate through the beam contributes to $T_{0.5}$, as alluded to in *Briggs* [1984]. This fading results in ν_{fca} overestimating ν_{mod} when ν_{mod} is small. As ν_{mod} is increased turbulent fading gradually becomes the major contributor to $T_{0.5}$, and $\nu_{\text{fca}} \approx \nu_{\text{mod}}$. These results suggest that the model turbulence simulation approximates actual turbulence satisfactorily.

Despite these results, there are a number of factors that must be considered in determining the velocity magnitudes of the turbulent random motions. In developing the radar backscatter model it became clear that the vertical turbulent motions component contributed significantly greater random changes to the ground diffraction pattern than the horizontal

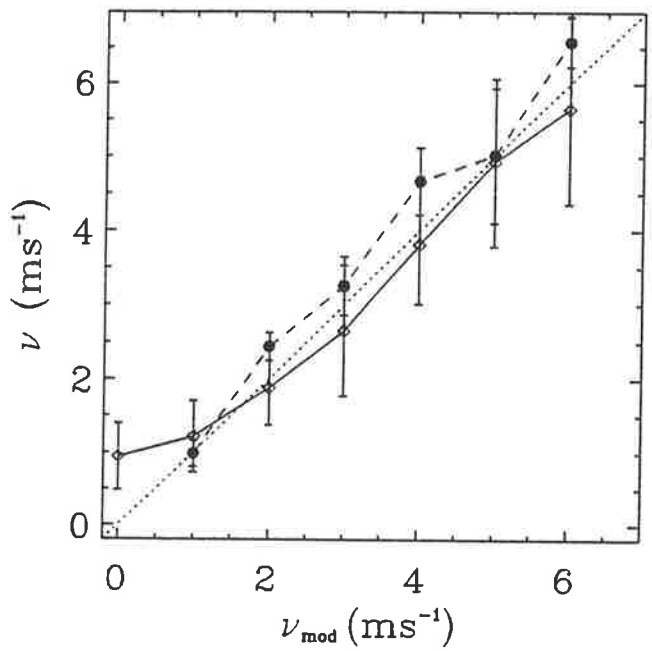

Figure 3.14: Estimated ν values obtained using the FCA ($\diamond$) and spectral-width ($\bullet$) techniques for the model-generated data-set MOD-MF-TURB.

component. For instance, the horizontal component of the random motions have to be up to 10 times larger than the vertical component to introduce the same amount of random changes. This result somewhat confirms the suggestion of *Røyrvik* [1983] that the horizontal variations in the vertical velocity resulting from internal gravity waves contribute greater random changes to the ground diffraction pattern than the variations in the horizontal velocity. As a result, it follows that (3.24) effectively measures the vertical component of the turbulent random motions rather than the isotropic motions, as specified by *Briggs* [1980]. This result appears to have been acknowledged by *Hocking* [1983a,b] who specifies formulae which predict the vertical component only.

Random changes in the ground diffraction pattern have sometimes previously been attributed solely to the random motions of the scatterers (e.g. *Briggs*, [1980]). The results of employing the varying scatterer reflectivity simulation of the radar backscatter model however reveal that the finite scatterer lifetimes act to increase the random changes in the ground diffraction pattern, and therefore to increase the magnitude of the apparent velocity. This result can be understood in terms of the fact that there will be little correlation between the ground diffraction patterns sampled at two times separated by an interval of the order of the scatterer lifetimes. The analytical model analysis of *Doviak et al.* [1995] suggests that the lifetimes of Bragg scatterers in the boundary layer with scales producing backscatter at UHF

can be as small as 1.6 s. It therefore follows that care should be taken in the interpretation of turbulent motions velocities obtained in this region of the atmosphere. The recent wind inhomogeneity analysis of *Sürücü et al.* [1995a] suggests that the apparent velocity can also be affected by horizontal gradients in the horizontal wind velocity. This result is clearly sensible as the ground diffraction pattern resulting from various regions of the atmosphere will move with different velocities, thereby giving the impression that the ground diffraction pattern is evolving randomly. The results of Chapter 4 also suggest that gravity waves can act to produce random changes in the ground diffraction. It therefore follows that finite scatterer lifetimes, horizontal gradients in the horizontal wind field, and gravity waves can produce an overestimation of the velocity magnitudes of the turbulent random motions.

3.4.3 Aspect sensitivity

The aspect sensitivity parameter θ_s can be estimated using a number of different techniques. These techniques can be roughly categorized into FCA techniques (e.g. *Lesicar and Hocking*, [1992]), Doppler techniques (e.g. *Hocking et al.*, [1986]) and poststatistic steering techniques (e.g. *Vandepeer and Reid*, [1995b]). The verification of the aspect sensitivity simulation of the model presented in this section is confined to the FCA techniques. Some aspects of the Doppler techniques will be discussed in the following section.

The FCA techniques used to verify the model are described in *Lesicar and Hocking* [1992]. The "spectral width" method relates the FCA fading time $\tau_{0.5}$ to the e^{-1} width of the effective polar-diagram θ_{sb} (in degrees) by the equation (after some manipulation)

$$\theta_{sb} = \frac{7.6\lambda}{|\vec{V}|\tau_{0.5}}, \tag{3.26}$$

where λ is the radar wavelength, and $\vec{V}$ is the horizontal wind velocity. This technique does not account for the effects of random changes in the diffraction pattern, which will tend to reduce the fading time. As a result, the aspect sensitivity estimated by this technique can be regarded as an upper limit. The "spatial correlation" method relates the FCA estimated pattern scale $S_{0.5}$ and axial ratio R_{ax} to θ_{sb} (in degrees) by the equation (after some manipulation)

$$\theta_{sb} = \frac{15.2\lambda\sqrt{R_{\mathrm{ax}}}}{S_{0.5}}. \tag{3.27}$$

The aspect sensitivity θ_s can be determined from θ_{sb} by using the equation (e.g. *Lesicar and Hocking* [1992])

$$\sin^{-2}\theta_s = \sin^{-2}\theta_{sb} - \sin^{-2}\theta_b, \tag{3.28}$$

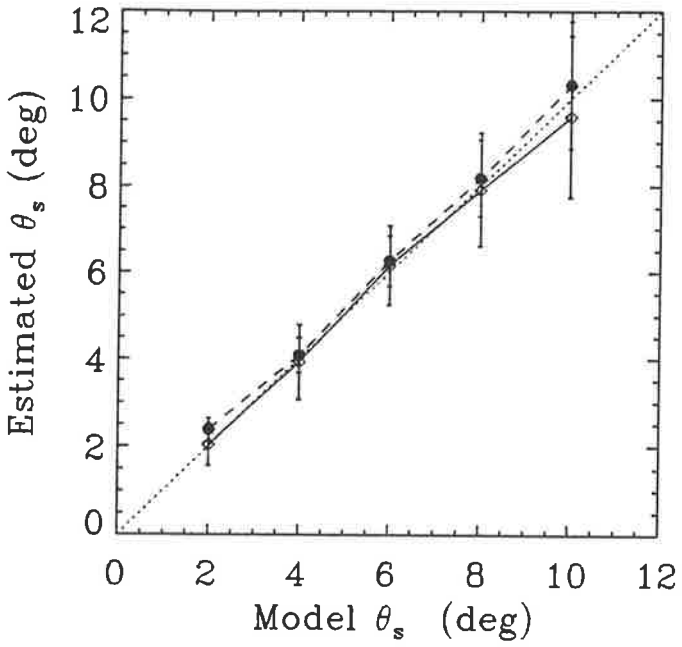

Figure 3.15: Estimated θ_s values obtained using the spatial-correlation ($\diamond$) and spectral-width ($\bullet$) techniques for the model-generated data-set MOD-MF-ASP-SEN.

where θ_b is the beam-width.

The model-generated data-set MOD-MF-ASP-SEN has been used to evaluate (3.27) and (3.28). This data consists of 100 time-series realizations generated using a range of different model aspect sensitivities without random motions. The θ_s values estimated using (3.27) and (3.27) are shown in Figure 3.15. These results suggest the aspect sensitivity simulation employed by the model approximates the realistic case well.

The model-generated data-set MOD-MF-SA has been used to evaluate the performance of these techniques in the presence of random motions. The results are shown in Figure 3.16. In this case the spectral-width technique increasingly overestimates θ_s as the magnitude of the random motions are increased. The spatial-correlation technique provides a good estimate of θ_s for all random motion magnitudes. These results are consistent with those obtained by *Lesicar and Hocking* [1992], who found the spectral-width technique produced θ_s values between 2 and 4 degrees larger than those produced by the spatial-correlation technique. As discussed above, the spectral-width technique does not allow for the effects of random motions, and consequently overestimates θ_s when random motions are present. There is a small decrease in the spatial-correlation estimate with increasing random motions. This decrease is a result of the increase in the pattern scale with increasing random motions as illustrated in the FCA results of Figure 4.7.

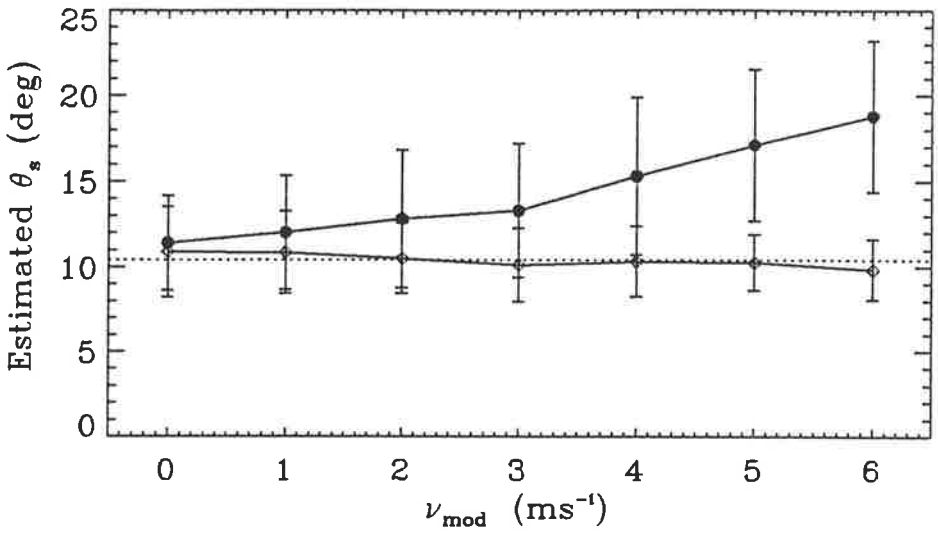

Figure 3.16: Estimated θ_s values obtained using the spatial-correlation ($\diamond$) and spectral-width ($\bullet$) techniques as a function of the model turbulent random motions magnitude ν_{mod} for the model-generated data-set MOD-MF-SA. The dotted line indicates the model input value of θ_s.

The results of Figures 3.15 and 3.16 suggest that the aspect sensitivity simulation employed by the model accurately simulates conditions generally seen experimentally. The results also reveal the limitations of the spectral-width technique in the presence of turbulent random motions.

3.4.4 Doppler analysis

The radar backscatter model allows the transmitted beam to be directed at any angle, thereby simulating the operation of a Doppler radar. The data-set MOD-MF-DOPP has been generated using the MF Doppler radar parameters specified in Table 3.4. This data was obtained using one vertical and two off-vertical beams. The off-vertical beams were tilted 10° off-zenith in the northward and eastward directions.

The Doppler beam steering (DBS) technique (e.g. *Woodman and Guillen*, [1974]) allows the determination of the atmospheric wind velocity using the radial velocities measured in a number of different beam directions. For a beam directed at zenith angle θ and azimuth angle ϕ clockwise from North the radial velocity V_r will be given by

$$V_r = u \sin\phi \sin\theta + v \cos\phi \sin\theta + w \cos\theta. \tag{3.29}$$

where $\vec{V} = (u, v, w)$ is the atmospheric wind velocity. Using the radial velocities determined from three different directions the wind velocity $\vec{V}$ can be therefore be determined using least

squares techniques. If the scatter is aspect sensitive the effective off-zenith beam pointing direction θ_e will be bought closer to the zenith for finite beam-widths (e.g. *Röttger*, [1981]). As a result, the substitution of the actual beam pointing direction θ_a into 3.29 will result in the wind velocity being underestimated.

The DBS technique therefore requires the estimation of the off-zenith beam pointing direction θ_e. This can be achieved in a number of different manners. If the aspect sensitivity parameter θ_s is known at the height of the backscatter θ_e can be determined using the equation (e.g. *Reid*, [1988])

$$\theta_e = \arcsin\left(\frac{\sin\theta_a \sin^2\theta_s}{\sin^2\theta_b + \sin^2\theta_s}\right), \tag{3.30}$$

where θ_b is the e^{-1} beam-width. The TDI analysis of *Vandepeer and Reid* [1995b] uses the mean angle of arrival (MAOA) (e.g. *Röttger and Ierkic*, [1985]) determined for each record to determine θ_e. The MAOA gives the power weighted location of the backscatter. The calculation of the MAOA is described extensively in Chapter 8. The MAOAs determined using the data-set MOD-MF-DOPP are shown in Figure 3.17. These results illustrate the reduction of the beam pointing angle by the aspect sensitive scatter. The θ_e estimates obtained from the average MAOAs for each beam direction are approximately 8.2° for both $\nu_{\text{mod}} = 0$ and 6 ms^{-1}. This value corresponds well with the estimate of 8.1° obtained using (3.30). Substitution of the MAOA θ_e estimates into (3.29) yields wind velocities of 49.1 ms^{-1} and 51.4 ms^{-1}, which are in good agreement with the model input value of 50 ms^{-1}. These results suggest that the model beam tilting simulation works satisfactorily, and further confirms the aspect sensitivity simulation.

3.5 Summary and conclusions

The radar backscatter model described in this chapter is an extension of the model first introduced by *Holdsworth and Reid* [1995a] (see Appendix I). The model was developed in order to allow the systematic evaluation of a number of spaced antenna (SA) radar processing techniques. The model is based on a number of previously developed models, and allows the simulation of both SA and Doppler radars.

The basis of the radar backscatter model is described in section 3.2. The model consists of a number of randomly distributed scatterers, each of which has it's own polar diagram based on the choice of transmitted beam-width and aspect sensitivity. Thus although each

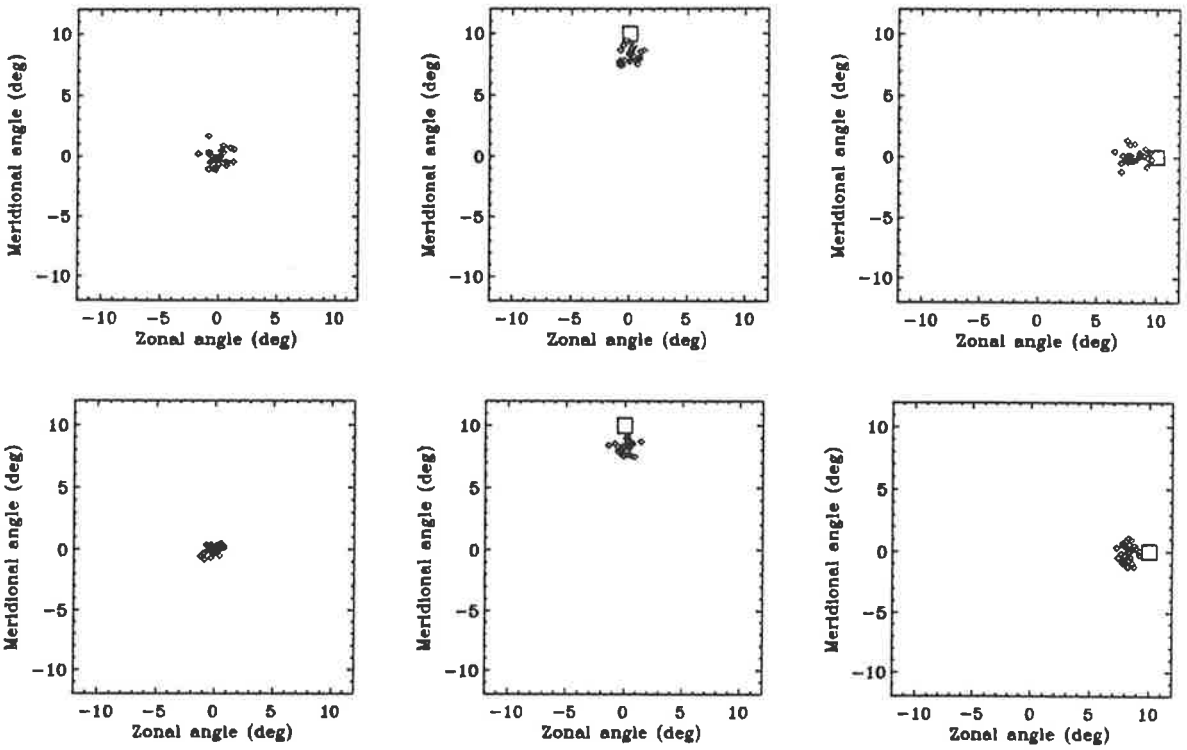

Figure 3.17: MAOAs estimated using the model-generated data-set MOD-MF-DOPP for turbulent rms velocities of 0 (top row), and 6 ms^{-1} (bottom row) using vertical (left), northward (middle), and eastward (right) directed beams. The squares in the northward and eastward plots denote the beam pointing direction. The MAOAs estimated for the off-zenith beams are brought back towards the zenith due to the aspect sensitivity of the scatterers.

scatterer is represented by a single position in three dimensional space it actually simulate a horizontally elongated Bragg scatterer. The model therefore simulates the "volume scatter" situation. The model includes the effects of turbulent random motions, gravity wave perturbations, and finite scatterer lifetimes. The resulting horizontal and turbulent velocity fields simulate those expected in practice.

The results of section 3.3 illustrate that the model-generated time-series records exhibit the same fading characteristics as seen in experimentally obtained time-series. Two major advantages of the use of model-generated time-series are also evident, in that the model-generated time-series are not subject to the effects of noise or receiver phase differences. The results of section 3.3.3 illustrate that the ground diffraction patterns exhibit the behavior expected from the simulation parameters. In the situation where turbulent motions are absent the pattern propagates without any random changes. In the situation where turbulent motions are present the pattern evolves rapidly, such that there is very little resemblance between the pattern images obtained over two second intervals.

The results of section 3.4 illustrate that standard analysis techniques, such as the full correlation analysis (FCA), and Doppler beam steering (DBS) technique in TDI mode (e.g. *Vandepeer and Reid*, [1995b]), are able to accurately recover the model input values of the mean wind velocity. The results also indicate that standard analysis techniques for the estimation of turbulence and aspect sensitivity satisfactorily estimate the model input parameters. The results suggest that finite scatterer lifetimes, horizontal gradients in the horizontal wind velocity, and gravity waves can be mistakenly interpreted as turbulent random motions. It therefore follows that some care should be taken in the interpretation of turbulent random motions magnitudes obtained experimentally. The spectral-width technique for the estimation of the aspect sensitivity parameter is also shown to overestimate θ_s in the presence of random motions, as suggested by *Lesicar and Hocking*, [1992].

The results obtained in Chapters 4 to 8 further verify that the model is performing as anticipated. The model has proven extremely beneficial for the determination of the optimal experimental conditions for the FCA, the development and verification of the revised spatial correlation analysis presented in Chapter 6, and the verification of the expected performance of the Doppler-selected imaging interferometry techniques in the volume scatter situation in Chapter 8. It is anticipated that the model will continue to be extremely beneficial for the verification of embryonic analysis techniques. This is especially true for the proposed implementation of the image forming technique using 30 channels of the upgraded BP MF array. The model provides the advantage that the actual scattering positions are known, therefore allowing the technique to be verified using model data prior to the experimental implementation. Future plans for improvements to the model include incorporating the effects of isotropic scatter, receiver polar diagrams and gravity wave spectra.

Chapter 4

The Full Correlation Analysis

4.1 Introduction

The full correlation analysis (FCA) (e.g. *Briggs et al.*, [1950]) was developed for the determination of atmospheric dynamics using the signals recorded at a number of spaced receiving antenna. The basic assumption of the FCA is that the spatio-temporal correlation function of the ground diffraction pattern can be described by a family of ellipsoids. The FCA produces two velocity estimates. The "apparent" velocity is estimated using the time-shift technique detailed in Appendix B. The "true" velocity accounts for the effects of random changes and anisometry in the ground diffraction pattern, and is thus generally considered the better velocity estimate. The FCA also provides information on the spatial and temporal characteristics of the ground diffraction pattern.

The FCA was originally applied to total reflection signals from the E and F regions of the ionosphere (e.g. *Briggs et al.*, [1950]), and for historical reasons was often referred to as the "spaced antenna drifts" (SAD) or "D1" technique. The application of the FCA to these regions was limited by the fact that a single frequency radar can only obtain returns from the height where the plasma frequency ω_N is equivalent to the operating frequency of the radar. The technique was also subject to some doubt caused by uncertainty with respect to the mechanism responsible for the fading. The initial idea was that the ionosphere contained small-scale irregularities which caused the reflecting surfaces to behave as diffuse scatterers rather than as specular reflectors (e.g. *Briggs*, [1977]). Later results however suggested that on some occasions that echoes appeared to originate from specular surfaces containing undulations with horizontal scales of approximately 20 km (e.g. *Felgate and*

Golley, [1971]). In this mechanism signal returns are produced from regions of the undulated surface perpendicular to the radar, as described by *Pfister* [1971]. This proposed mechanism led to suggestions that the FCA may not measure the wind velocity of the neutral air if the undulations were produced by the propagation of internal gravity waves (e.g. *Hines and Rao*, [1968]), as suggested by the result of *Vincent* [1972]. Despite this suggestion, comparisons between winds estimated using the FCA and meteor drift techniques (e.g. *Felgate et al.*, [1975]; *Wright et al.*, [1976]) and the FCA and incoherent scatter radar techniques (e.g. *Wright et al.*, [1976]) in the E-region showed good agreement.

The FCA was first applied to partial reflection returns from the D-region at MF by *Fraser* [1965]. The technique was also later applied to returns from the troposphere and stratosphere at VHF (e.g. *Röttger and Vincent*, [1978]). The application to partial reflection returns provided the ability to make simultaneous observations over a range of heights. Comparisons between winds estimated in the D-region by the FCA and alternative techniques such as Doppler beam swinging (DBS) (e.g. *Hocking*, [1983b]), meteor drifts (e.g. *Stubbs*, [1973]) and rocket measurements (e.g. *Vincent et al.*, [1977]) have in general shown good agreement. Similarly, comparisons in the troposphere and stratosphere with DBS radar (e.g. *Vincent et al.*, [1987]) and radiosondes (e.g. *Röttger and Vincent*, [1978]; *Vincent et al.*, [1987]) have also shown good agreement. Recent comparisons with winds estimated by satellite measurements (e.g. High Resolution Doppler Imaging (HRDI), *Burrage et al.*, [1993]), meteor drifts (e.g. *Cervera and Reid*, [1995]) and incoherent scatter radar (e.g. *Hines et al.*, [1993]) however suggest that the FCA may underestimate the wind velocity above about 90 km. Furthermore, the recently developed Doppler-selected imaging interferometry techniques (e.g. *Adams et al.*, [1986]) generally produce velocity estimates best agreeing with the FCA apparent velocity (e.g. *Meek and Manson*, [1987]), further fueling speculation that the FCA true velocity may underestimate the actual wind velocity.

The apparent underestimation of the FCA true velocity magnitude has been attributed to a number of possible effects. One of the most commonly accepted causes is the "triangle size effect" (e.g. *Golley and Rossiter*, [1970]), whereby the FCA true velocity can be shown to underestimate the actual wind velocity for antenna spacings less than the scale of the ground diffraction pattern. Other possible causes include low pass filtering (e.g. *Chandra and Briggs*, [1978]) and receiver saturation (see for e.g. Chapter 5). In addition, there have also been suggestions that the volume scatter mechanism assumed by the analysis does not always hold. The analytical model analysis of *Liu et al.* [1990] suggests that the FCA will break

down in the discrete scatter situation. The total reflection suggestions of *Hines and Rao* [1968] have been reapplied to the partial reflection situation by *Hines et al.* [1993], who have suggested that gravity waves may tilt the irregularities responsible for the scatter, thereby resulting in MF radars measuring the phase-speed of gravity-wave perturbations as opposed to the background wind velocity. This suggestion has gained considerable support of late, despite the claims of *Hocking et al.* [1990] and *Kudeki et al.* [1993] that no evidence for this proposed mechanism exists. The mean angle of arrival (MAOA) analysis of *Meek and Manson* [1992] suggests that the FCA true velocity can be underestimated in the presence of "glints' produced by backscatter from undulating specular layers distorted by the propagation of internal gravity waves. The underestimation was found to be independent of the direction of the phase velocity of the wave, leading the authors to conclude that the underestimation of the FCA true velocity was associated with the increase in the fading time associated with the glint. This result is consistent with the suggestion of *Røyrvik* [1983] that the existence of a strongly reflecting component will prohibit the FCA from accurately measuring the true velocity.

The work presented in this chapter and in the succeeding chapter detailing the triangle size effect is an attempt to address a number of biases reported by various authors in the application of the FCA. The theory of the FCA is presented in section 4.2. The assumptions upon which the analysis are based are verified with the use of spatial correlation functions calculated from images of the ground diffraction pattern produced using the radar backscatter model described in Chapter 3. The optimal experimental and sampling parameters for the the application of the FCA are discussed in section 4.3. The application of the FCA to model-generated data is presented in section 4.4. The effects of turbulent random motions, pattern anisometry, gravity waves, time series length, and the use of coherently averaged correlation functions upon the analysis are addressed. The application of the FCA to data collected using the BP MF SA system is presented in section 4.5. The performance of the FCA as a function of sampling time is presented in section 4.6, revealing that significant biases can result if the sampling time is too large. The performance of the FCA as a function of the number of scatterers employed in the generation of the model data is presented in section 4.7. The number of scatterers employed is intended to range from the discrete scatter to the volume scatter situation, thereby allowing an assessment of the performance of the FCA in the discrete scatter situation where there is some speculation that the technique will not accurately estimate the mean wind velocity. Unless otherwise specified, the use of the term

"correlation function" throughout the course of this chapter will refer to the "magnitude" of the correlation function.

4.2 Theory of the FCA

The FCA is based upon a analytical model describing the behavior of the spatio-temporal correlation function of the ground diffraction pattern (e.g. *Briggs*, [1984]). In order to obtain an accurate representation of the ground diffraction pattern it is necessary to use a large array of receiving antennae, such as the Buckland Park MF array. As this is generally not feasible in practice, the theory of the FCA is usually presented using analytical representations of the spatio-temporal correlation function. The radar backscatter model described in chapter 3 is capable of producing high resolution representations of the ground diffraction, therefore allowing the calculation of the spatio-temporal correlation function. The following discussion of the FCA is based on that of *Briggs* [1984], with the unique exception that the spatio-temporal correlation functions are calculated using model-generated data. The FCA is based upon the estimation of the spatio-temporal correlation function using the auto- and cross-correlation functions calculated from the signals recorded by a number of spaced receiving antennae. The FCA is most generally applied using three antennae. As a result, the following discussion will focus on the use of three antennae. The extension to the use of more than three antennae is relatively straightforward.

4.2.1 Spatial characteristics of the ground diffraction pattern

A typical example of the instantaneous pattern produced using the model-generated data-set MOD-MF-GDP-V50-T6 is illustrated in Figure 4.1. The contours of constant magnitude are approximately circular, as expected from the isometric scattering mechanism employed by the model to generate the data-set. The instantaneous pattern may sometimes be noticeably elongated in a particular azimuth. This effect usually results from scatter from regions elongated in a particular azimuth (e.g. *Lesicar and Hocking*, [1992]), thereby producing a pattern with elongation perpendicular to the elongation azimuth of the scattering regions. A typical example of the instantaneous pattern produced using the model-generated data-set MOD-MF-GDP-V50-T6-AN is also illustrated in Figure 4.1. The scatterers employed by the model to generate this data-set are elongated in the azimuth 135° clockwise from North. The resulting pattern is therefore elongated in the azimuth 45° clockwise from North,

perpendicular to the azimuth of the scatterers.

The spatial correlation function calculated from the antenna time-series used to produce the anisometric ground diffraction pattern of Figure 4.1 is illustrated in Figure 4.2. The spatial correlation function shows contours elongated in the same azimuth as the ground diffraction pattern. The contours of equal spatial correlation can be described by a family of ellipses. The general form of the spatial correlation function can therefore be approximated by

$$\rho(\xi,\eta) = \rho(A\xi^2 + B\eta^2 + 2H\xi\eta). \tag{4.1}$$

The ellipse described by $\rho(\xi,\eta) = 0.5$ is referred to as the "characteristic ellipse". The characteristic ellipse can be used to provide information on the nature of the regions of backscatter (e.g. *Lesicar and Hocking*, [1992]).

4.2.2 Randomly changing ground diffraction pattern

In the reference frame moving with the pattern the only temporal changes seen in the pattern result from turbulent random motions. The pattern obtained in the frame moving with the pattern can be simulated using the radar backscatter model by giving the scatterers turbulent random motions only, such that the mean drift velocity of the scatterers is zero. The model-generated data-set MOD-MF-GDP-V0-T6 simulates this situation, using a turbulent velocity of 6 ms^{-1} with zero mean wind. The two-dimensional (ξ,τ) spatio-temporal correlation function produced using this data-set is illustrated in Figure 4.3. This plot suggest that the contours of equal two-dimensional spatio-temporal correlation can be approximated by a family of ellipses. It must therefore follow that surfaces of equal spatio-temporal correlation can therefore be approximated by a family of ellipsoids, thereby suggesting that the spatial and temporal dependences of the spatio-temporal correlation function are identical. The form of the spatio-temporal correlation function in this situation can therefore be generalized by

$$\rho(\xi,\eta,\tau) = \rho(A\xi^2 + B\eta^2 + 2H\xi\eta + K\tau^2). \tag{4.2}$$

Terms of the form $\xi\tau$ or $\eta\tau$ are not introduced because there is no elongation of the contours of the two-dimensional spatio-temporal correlation functions away from either the spatial or temporal axes.

The assumption that the spatial and temporal dependences of the spatio-temporal correlation function are identical is generally considered the weakest assumption of the FCA (e.g. *Briggs*, [1984]). The results of *Golley and Rossiter* [1970] however indicate that the spatial

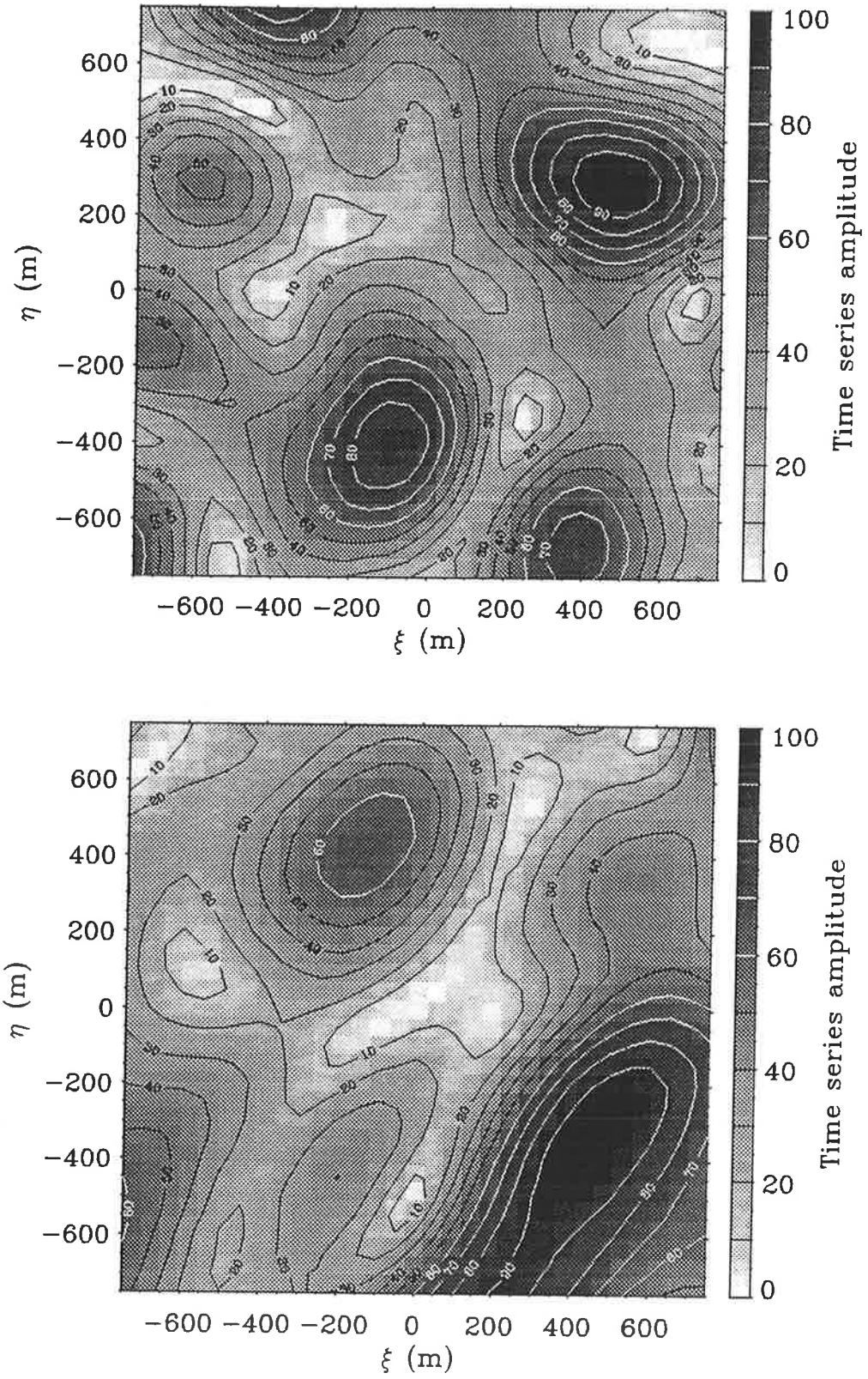

Figure 4.1: Example of the typical model-generated ground diffraction patterns resulting from the simulation of the isometric scatter situation using the model-generated data-set MOD-MF-GDP-V50-T6 (top), and the anisometric scatter situation using the model-generated data-set MOD-MF-GDP-V50-T6-AN (bottom). The isometric ground diffraction pattern has no preferential azimuth, while the anisometric ground diffraction pattern is elongated 45° clockwise from North, perpendicular to the azimuth of elongation of the model scatterers.

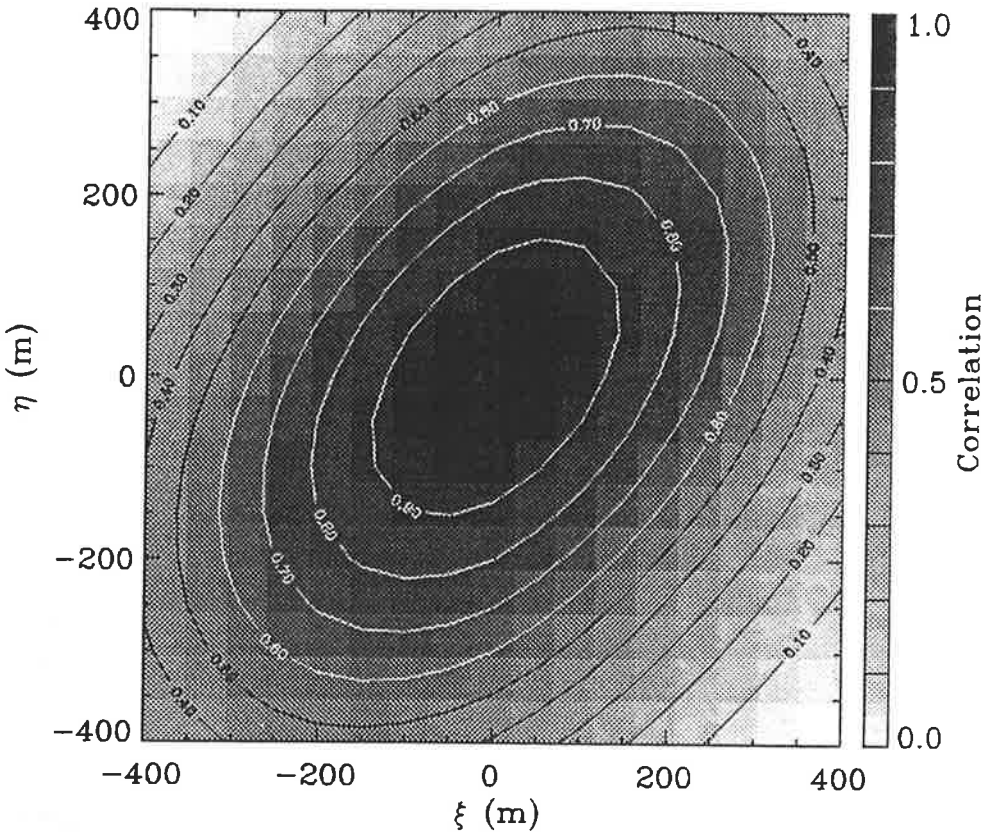

Figure 4.2: Spatial correlation function obtained from the simulation of the anisometric scatter situation using the model-generated data-set MOD-MF-GDP-V50-T6-AN. The spatial correlation function is elongated in the same azimuth as the ground diffraction pattern, as illustrated in the bottom plot of Figure 4.1.

and temporal dependences are essentially identical. Furthermore, comparison of the spatial and two-dimensional spatio-temporal correlation functions of Figure 4.2 and 4.3 generated by the radar backscatter model tend to suggest that the assumption of elliptical contours holds equally well for spatial and temporal dependences. There have been two variations of the FCA developed which do not incorporate this assumption. The FCA proposed by *Briggs and Maude* [1978] makes no assumptions about the temporal form of the spatio-temporal correlation functions, while the FCA of *Costa et al.* [1988] assumes a general form for the temporal dependence. However, neither of these techniques appear to have been applied experimentally and reported in the literature to date, let alone compared with the results of the standard FCA as described in this chapter.

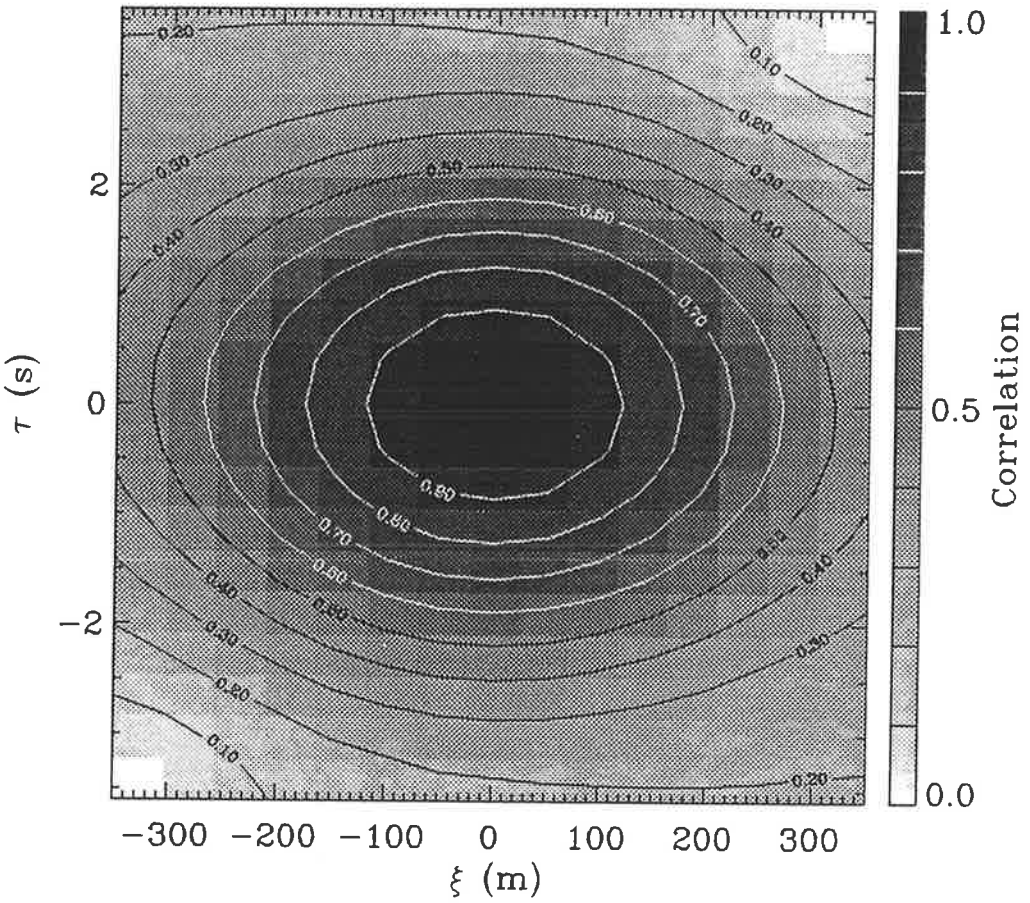

Figure 4.3: Two-dimensional (ξ, τ) spatio-temporal correlation function obtained from the simulation of the isometric scatter situation in the presence of turbulent motions only, using the model-generated data-set MOD-MF-GDP-V0-T6. The contours of constant spatio-temporal correlation have the same form as contours of constant spatial correlation in Figure 4.2, thereby suggesting that the spatial and temporal dependences of the spatio-temporal correlation function are identical.

4.2.3 Moving and randomly changing ground diffraction pattern

In a stationary reference frame the temporal changes in the pattern will result from both the mean wind velocity and turbulent motions. The model-generated data-set MOD-MF-GDP-V50-T6-AN simulates this situation, using a mean wind velocity of magnitude 50 ms^{-1} and direction 90° and a turbulent velocity of 6 ms^{-1} in the anisometric scatter situation. The two-dimensional (ξ, τ) and (η, τ) representations of the spatio-temporal correlation functions produced using this data-set are shown in Figure 4.4. In this case the correlation functions are elongated at an angle from the τ axis, so that terms of the form $\xi\tau$ or $\eta\tau$ are introduced into the spatio-temporal correlation function. The spatio-temporal correlation function is

more elongated in the zonal direction than in the meridional direction because the pattern is propagating in the zonal direction.

Consider the reference frame moving with the pattern, with coordinate system (ξ', η', τ'). The temporal changes in the pattern in this frame result solely from random changes. As illustrated above, the spatio-temporal correlation function in this frame is given by

$$\rho(\xi', \eta', \tau') = \rho(A\xi'^2 + B\eta'^2 + 2H\xi'\eta' + K\tau'^2). \tag{4.3}$$

If the pattern is moving with velocity $\vec{V} = (V_x, V_y)$ with respect to the stationary frame with coordinate system (ξ, η, τ), the coordinate systems of the two frames are related by the Galilean transformation

$$x = x' + V_x t, \tag{4.4}$$

$$y = y' + V_y t, \tag{4.5}$$

$$\tau = \tau', \tag{4.6}$$

from which it follows that

$$\xi = \xi' + V_x t \tag{4.7}$$

$$\eta = \eta' + V_y t. \tag{4.8}$$

The spatio-temporal correlation function in the stationary frame is therefore given by

$$\rho(\xi, \eta, \tau) = \rho(A(\xi - V_x t)^2 + B(\eta - V_y t)^2 + 2H(\xi - V_x t)(\eta - V_y t) + K\tau^2). \tag{4.9}$$

This can be rewritten in the general form

$$\rho(\xi, \eta, \tau) = \rho(A\xi^2 + B\eta^2 + C\tau^2 + 2F\xi\tau + 2G\eta\tau + 2H\eta\xi). \tag{4.10}$$

The spatio-temporal correlation function is therefore completely defined by the "ellipsoid parameters" A, B, C, F, G, and H.

4.2.4 Ellipsoid parameter estimation

The use of three receiving antennae prohibits the direct determination of the spatial characteristics of the spatio-temporal correlation function. The parameterization described by (4.10) however allows the spatial characteristics to be determined from the temporal characteristics, which can be determined from the auto- and cross-correlation functions calculated

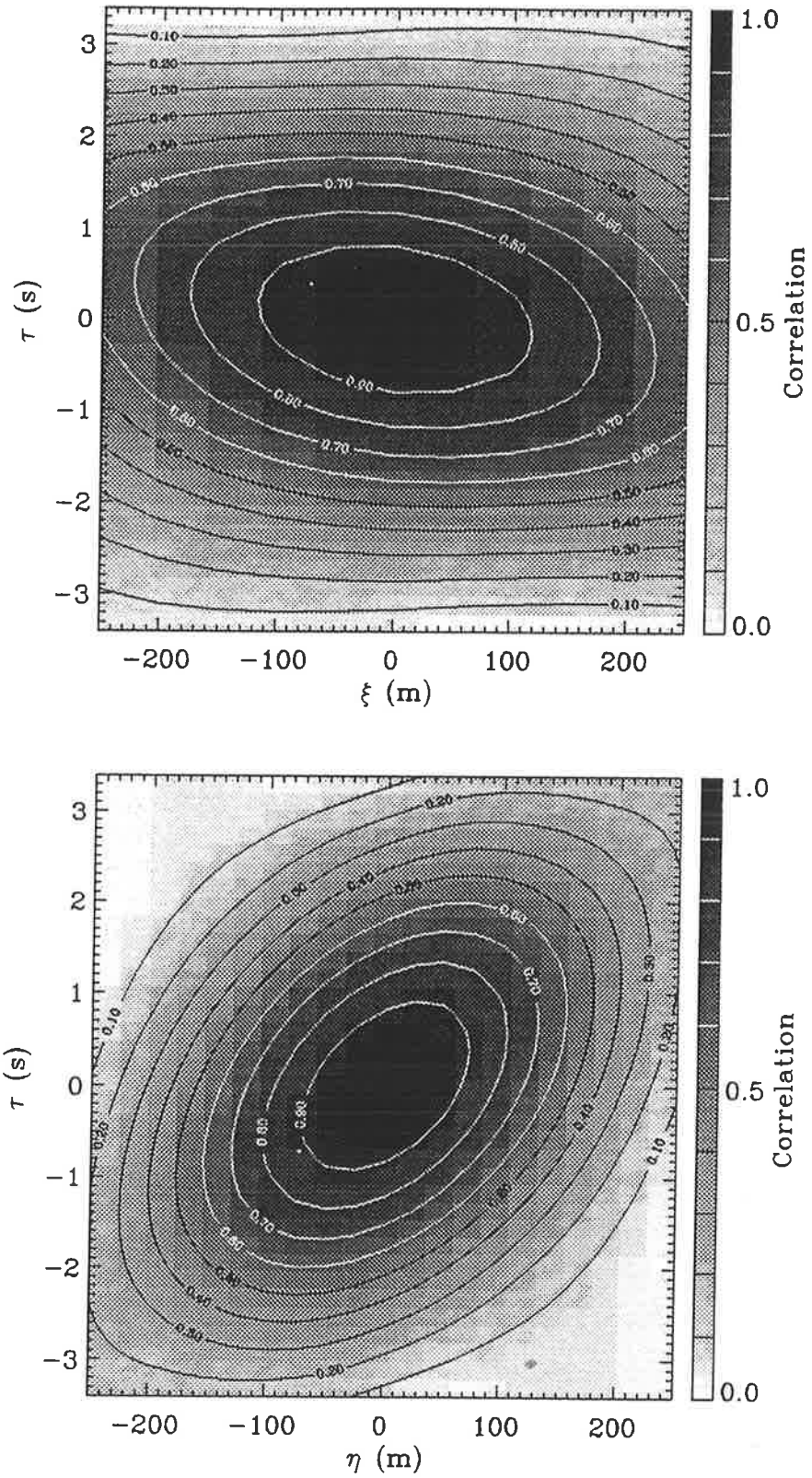

Figure 4.4: Two-dimensional (ξ, τ) and (η, τ) spatio-temporal correlation functions obtained from the simulation of the isometric scatter situation in the presence a mean background wind and turbulent motions using the model-generated data-set MOD-MF-GDP-V50-T6-AN. The correlation functions are elongated at an angle from the τ axis, suggesting that terms of the form $\xi\tau$ or $\eta\tau$ are introduced into the spatio-temporal correlation function.

from the time-series recorded at each antenna. The auto-correlation functions for each antenna are analytically identical, and are given by

$$\rho_i(\tau) = \rho(0,0,\tau) = \rho(C\tau^2). \tag{4.11}$$

In practice, small statistical differences are introduced because each antenna samples a different cross-section of the ground diffraction pattern. As a result, the mean auto-correlation function $\rho(\tau)$ is used in place of the individual auto-correlation functions throughout the analysis. The cross-correlation function for two receiving antennae i and j with spatial separation (ξ_{ij}, η_{ij}) is given by

$$\rho_{ij}(\tau) = \rho(\xi_{ij}, \eta_{ij}, \tau) = \rho(A\xi_{ij}^2 + B\eta_{ij}^2 + C\tau^2 + 2F\xi_{ij}\tau + 2G\eta_{ij}\tau + 2H\xi_{ij}\eta_{ij}). \tag{4.12}$$

The temporal characteristics of the spatio-temporal correlation function can be parameterized by the "correlation parameters", which are determined from the auto and cross-correlation as illustrated in Figure 4.5. The "fading time" $\tau_{0.5}$ is defined by the lag where the mean auto-correlation function equals 0.5,

$$\rho(\tau_{0.5}) = 0.5. \tag{4.13}$$

The parameter τ_{ij} is defined by the lag where the mean auto-correlation function equals the zero-lag cross-correlation,

$$\rho(\tau_{ij}) = \rho_{ij}(0). \tag{4.14}$$

The parameter τ'_{ij} is defined by the lag corresponding to the cross-correlation maxima ρ_{0ij}. The use of three antenna produces seven correlation parameters, as estimates of τ_{ij} and τ'_{ij} are produced for each antenna pair. The ellipsoid parameters are determined directly from the correlation parameters. For ease in deriving this relationship the parameters

$$a = \frac{A}{C},\ b = \frac{B}{C},\ f = \frac{F}{C},\ g = \frac{G}{C}\ h = \frac{H}{C},\ \text{and}\ k = \frac{K}{C} \tag{4.15}$$

are introduced.

The lag τ'_{ij} determined for each antenna pair ij can be obtained by solving the equation

$$\frac{\partial \rho_{ij}(\tau)}{\partial \tau} = 0. \tag{4.16}$$

Using the generalized form of the cross-correlation function (4.12),

$$\tau'_{ij} = -f\xi_{ij} - g\eta_{ij}. \tag{4.17}$$

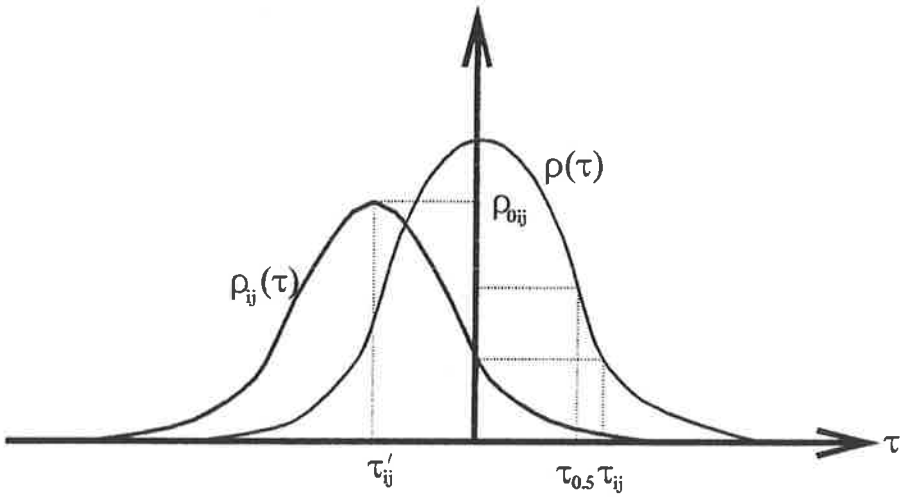

Figure 4.5: Schematic representation of the auto- ($\rho(\tau)$) and cross-correlation ($\rho_{ij}(\tau)$) functions employed by the FCA for the determination of correlation parameters, namely, the fading time $\tau_{0.5}$, the cross-correlation maxima ρ_{0ij} and corresponding lag τ'_{ij}, and the lag $\tau_{ij}$where the auto-correlation function equals the zero-lag cross-correlation.

The values of τ'_{ij} estimated from the three cross-correlation functions may then be used to determine the f and g. These parameters will be over-determined, and can be found using least-squares techniques. The zero-lag cross-correlation for each antenna pair ij is given by

$$\rho_{ij}(0) = \rho(A\xi_{ij}^2 + B\eta_{ij}^2 + 2H\xi_{ij}\eta_{ij}). \tag{4.18}$$

The lag τ_{ij} is therefore defined by

$$\tau_{ij}^2 = a\xi_{ij}^2 + b\eta_{ij}^2 + h\xi_{ij}\eta_{ij}. \tag{4.19}$$

The values of τ_{ij} estimated from the three cross-correlation functions may then be used to determine the ratios a, b, and h, which can be found using least-squares techniques. In practice, τ_{ij} is not calculated directly. It can be shown (e.g. *Briggs et al.*, [1950]) that

$$\tau_{ij}^2 = \tau_{ij}'^2 + \tau_{ij}''^2 \tag{4.20}$$

where τ''_{ij} is the lag at which the auto-correlation function equals the the cross-correlation maximum. This method is preferred over the direct method (e.g. *Fooks*, [1965]), as the lag-times τ'_{ij} and τ''_{ij} are closer to zero lag than τ_{ij}, and therefore less succeptible to statistical variation.

The parameters a, b, f, g and h are fixed by (4.17) and (4.19). The value of the parameter C is therefore arbitrary. It is usually expressed in terms of the lag $\tau_{0.5}$ where the mean auto-correlation function equals 0.5, given by

$$\rho(0, 0, \tau_{0.5}) = \rho(C\tau_{0.5}^2) = 0.5. \tag{4.21}$$

The characteristic ellipse can therefore be written

$$a\xi^2 + b\eta^2 + 2h\xi\eta = \tau_{0.5}^2. \tag{4.22}$$

4.2.5 Determination of physical parameters

The physical parameters estimated by the FCA are calculated directly from the ellipsoid parameters. These physical parameters include the true and apparent velocities, and parameters describing the spatial and temporal behavior of the ground diffraction pattern.

The "apparent" velocity $\vec{V}_a$ is calculated using the time-shift technique described in Appendix B, where the time-shifts are determined using the cross-correlation maxima delay-times τ'_{ij}. The apparent velocity does not account for the effects of random changes and anisometry in the ground diffraction pattern, and can therefore be subject to biases in magnitude and direction. The magnitude V_a and direction θ_a of the apparent velocity can be expressed in terms of the ellipsoid parameters f and g by

$$V_a = \sqrt{f^2 + g^2}, \text{ and} \tag{4.23}$$

$$\theta_a = \arctan\left(\frac{f}{g}\right). \tag{4.24}$$

The "true" velocity $\vec{V}_t$ incorporates corrections for the effects of random changes and anisometry in the ground diffraction pattern. Comparison of the spatio-temporal correlation functions (4.9) and (4.10) yields the equations

$$f = -aV_x - hV_y, \text{ and} \tag{4.25}$$

$$g = -hV_x - bV_y, \tag{4.26}$$

from which the zonal and meridional pattern velocity components V_x and V_y are determined by

$$V_x = \frac{hg - bf}{ab - h^2}, \text{ and} \tag{4.27}$$

$$V_y = \frac{hf - ag}{ab - h^2}. \tag{4.28}$$

The true velocity is given by

$$\vec{V}_t = \frac{1}{2}(V_x, V_y), \tag{4.29}$$

where the factor $\frac{1}{2}$ takes into account the point-source effect.

The random changes in the pattern seen in the frame moving with pattern velocity $\vec{V} = (V_x, V_y)$ result solely from the effects of turbulent motions. The "mean lifetime" $T_{0.5}$ of the pattern in this frame is defined by

$$\rho(T_{0.5}) = \rho(kT_{0.5}^2) = 0.5, \tag{4.30}$$

where

$$k = 1 - aV_x^2 - bV_y^2 - 2hV_xV_y \tag{4.31}$$

is referred to as the "turbulent motions parameter", determined from the comparison of (4.9) and (4.10). Comparing (4.11) and (4.31) yields

$$T_{0.5} = \frac{\tau_{0.5}}{\sqrt{k}}. \tag{4.32}$$

Large values of $T_{0.5}$, and hence small values of k, correspond to little random change in the reference frame of the pattern, and therefore small turbulent velocities. An estimate of the isotropic rms velocity of the turbulent motions can be obtained directly from $T_{0.5}$ (e.g. *Briggs*, [1980]), as discussed in chapter 3.

The effects of random changes upon V_a can be understood using the equation (e.g. *Vandepeer and Reid*, [1995a])

$$V_a = \frac{aV_x^2 + bV_y^2 + 2hV_xV_y + k}{2\sqrt{(aV_x + hV_y)^2 + (bV_y + hV_x)^2}}. \tag{4.33}$$

This equation suggests V_a increases with increasing k, and therefore, with increasing random changes in the ground diffraction pattern.

The spatial description of the pattern is provided in terms of the characteristic ellipse. The major $r_{\rm maj}$ and minor $r_{\rm min}$ axes of the characteristic ellipse are given by

$$r_{\rm maj} = \sqrt{\frac{2\tau_{0.5}^2}{a+b-r}}, \tag{4.34}$$

and

$$r_{\rm min} = \sqrt{\frac{2\tau_{0.5}^2}{a+b+r}}, \tag{4.35}$$

where

$$r = \sqrt{(a-b)^2 + 4h^2}. \tag{4.36}$$

The characteristic ellipse is usually specified in terms of the "axial-ratio", the "axial-rotation" and the "pattern scale". The axial-ratio $R_{\rm ax}$ measures the elongation of the characteristic ellipse

$$R_{\rm ax} = \frac{a+b+r}{a+b-r}. \tag{4.37}$$

Table 4.1: The FCA rejection criteria.

Code	Explanation
0	Record accepted
1	Low signal amplitude
2	SNR < -6 dB
3	$\tau_{0.5} > 6$ s Auto-correlation above 0.5 at greatest calculated lag Oscillatory Mean auto-correlation function
4	Slow fading
5	NTD > 0.5
6	$K < 0$
7	Breakdown in pattern analysis
8	$V_a > 250$ ms^{-1}
9	$\lvert\theta_t - \theta_a\rvert > 40°$
10	$V_a > 4\,V_t$
11	$V_t > 1.5\,V_a$
12	Poor fit to cross-correlation function
13	$\rho_{0ij} < 0.2$
14	Poor zero-lag auto-correlation interpolation
15	Maths error

The axial-rotation θ_{ax} is the orientation of the major axis

$$\theta_{\mathrm{ax}} = 0.5 \arctan\left(\frac{2h}{b-a}\right). \tag{4.38}$$

The pattern scale $S_{0.5}$ is usually defined by the length of the major axis, r_{maj}. The pattern scale is however sometimes defined by the "geometric mean" of the major and minor axes

$$S_{0.5} = \sqrt{r_{\mathrm{max}} r_{\mathrm{min}}} = \frac{r_{\mathrm{max}}}{\sqrt{R_{\mathrm{ax}}}}, \tag{4.39}$$

thereby providing an indication of the average "radius" of the characteristic ellipse.

4.3 Application of the FCA

There are several important factors that must be taken into account in applying the FCA experimentally. Failure to consider these factors can result in significant biases in the FCA output. The analysis employs a number of criteria to reject records which are either unsuitable for analysis or which does not satisfy the theory of the FCA, as shown in Table D. The explanation of these criteria is presented in Appendix D.

The time-series records employed must be of sufficient length such that the calculated correlation functions are statistically reliable. The generally accepted rule is that the record length should exceed $50\tau_{0.5}$ s (e.g. *May*, [1987]). The results of *Røyrvik* [1983] suggest that the acceptance rate is significantly enhanced by using longer time-series records. The sampling time must also be small enough to provide a sufficient number of lags on the main peak of the correlation functions for the successful estimation of the correlation parameters. The effects of the sampling time on the analysis are discussed in section 4.6.

The optimal receiver configuration for the application of the FCA is generally considered to be an equilateral triangle with antenna spacings the order of $S_{0.5}$ (e.g. *Briggs*, [1984]). The use of antenna spacings smaller than $S_{0.5}$ has been shown to result in the "triangle size effect", whereby the magnitude of the true velocity V_t increases with increasing antenna spacing up to the limit given by the magnitude of the actual wind velocity (e.g. *Golley and Rossiter*, [1970]). Similar biases are also seen in $T_{0.5}$ and $S_{0.5}$. The use of non-equilateral triangles has been shown to result in biases in the direction of the true velocity θ_t towards the azimuth perpendicular to the longest side of the triangle (e.g. *Briggs*, [1984]), as well as biases in θ_{ax} (e.g. *Golley and Rossiter*, [1970]) when the antenna spacing is less than the pattern scale. The use of antenna spacings larger than $S_{0.5}$ can result in the analysis breaking down due to low correlations between antenna pairs.

Although the use of antenna spacings of the order of $S_{0.5}$ are recommended to reduce the triangle size effect, the simple analytical model analysis of *Røyrvik* [1983] suggests that the errors in the FCA estimates will increase with increasing antenna spacing. This suggestion is confirmed by the results of *Meek* [1984a], who found that the distribution of NTD values increases with increasing antenna spacing, suggesting that the variation in the τ'_{ij} estimates increases with increasing antenna spacing. The model analysis of *Røyrvik* [1983] also suggests that the accuracy of the FCA increases with increasing transmitter beam-width. Increasing the beam-width results in a decrease in the scale of the ground diffraction pattern, therefore resulting in an decrease in the width of the correlation functions. The resulting τ'_{ij} estimates will therefore be determined with greater accuracy. The effects of the antenna configuration upon the FCA are discussed in more detail in Chapter 5.

4.3.1 Calculation of the correlation functions

The majority of the computation time for the application of the FCA is taken up with the calculation of the correlation functions. Typical examples of the mean auto- and cross-correlation functions obtained using the Adelaide MF SA system are illustrated in Figure 4.6. The mean auto-correlation functions is symmetric in magnitude and anti-symmetric in phase about zero-lag, thereby requiring the calculation of the non-negative lags only. The effects of noise produce a "spike" at zero-lag. The noise-removal procedure is detailed in appendix C. The "noise-free" zero-lag correlations are estimated by interpolating over zero-lag. The most common interpolation methods employed are cubic-spline, and even-powered low-order polynomial interpolations, such as parabolic and quartic interpolations. A detailed discussion of the interpolation procedures is presented in section 4.6.

The correlation parameters are determined from Gaussian fits to the mean auto and cross-correlation functions. The fading time $\tau_{0.5}$ is determined from the e^{-1} width resulting from the Gaussian fit to the mean auto-correlation function. The τ'_{ij} estimates are determined by Gaussian fits to the magnitude of the three cross-correlation functions. These Gaussian fits also provide estimates of the cross-correlation maxima ρ_{0ij}, which are used to estimate τ_{ij} by

$$\tau_{ij} = \sqrt{\frac{-\ln \rho_{0ij}}{\ln 2}}\tau_{0.5}. \tag{4.40}$$

This calculation is based on the assumption that the auto- and cross-correlation functions have the same width (e.g. *Meek*, [1980]). Examples of the application of Gaussian fits to the mean auto- and cross-correlation functions are illustrated in Figure 4.6. The statistical errors associated with the estimation of the correlation parameters has been addressed by *May* [1987].

4.4 Application of the FCA to model-generated data

4.4.1 The effect of turbulent motions upon the FCA

The FCA has been applied to the model-generated data-set MOD-MF-SA. This data was generated using a model input velocity of 50 ms^{-1} directed 15° clockwise from North for various different isotropic values of the model turbulent motions rms velocity ν_{mod}. Figure 4.7 illustrates the resultant average FCA outputs as a function of ν_{mod}. The error bars denote the standard deviations of each parameter. In the situation where $\nu_{\text{mod}} \to 0$, $\vec{V}_a \approx \vec{V}_t$, and $T_{0.5}$ is

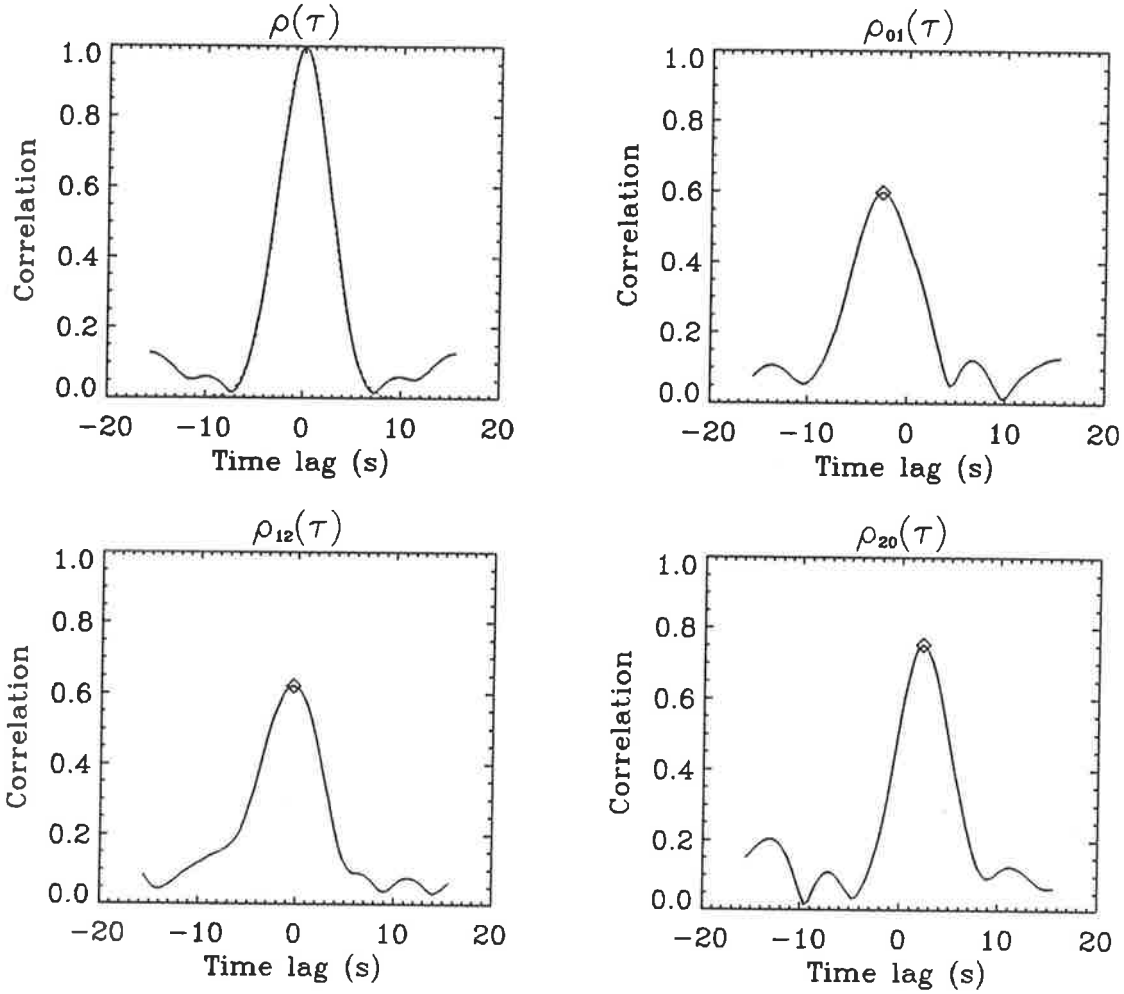

Figure 4.6: Typical examples of mean auto- (top left) and cross-correlation functions (top right and bottom left and right) obtained using the Buckland Park MF SA system at 88 km. The dotted line in the top left plot indicates the Gaussian fit to the mean auto-correlation function, while the diamonds in the cross-correlation function plots indicate the estimates of ρ_{0ij} and τ'_{ij} obtained from Gaussian fits to the cross-correlation functions.

large. As $\nu_{\rm mod}$ increases V_a increases, while $T_{0.5}$ and $\tau_{0.5}$ decrease. These effects are a direct result of the increasing random changes seen in the pattern, resulting in a reduction in the estimated time-displacements τ'_{ij} and the correlation widths. The true velocity magnitude V_t accurately estimates the magnitude of model input velocity $V_{\rm mod}$ for all values of $\nu_{\rm mod}$, although there is a slight tendency for V_t to overestimate $V_{\rm mod}$ for larger values of $\nu_{\rm mod}$. This is a consequence of the use of shorter than optimal time-series lengths and the use of the FCA rejection criteria 10. The effects of time-series length upon the FCA are discussed in subsection 4.8.1. The use of rejection criteria 10 tends to bias the average V_t towards larger absolute values by rejecting the smaller estimates. If this criteria is abandoned the

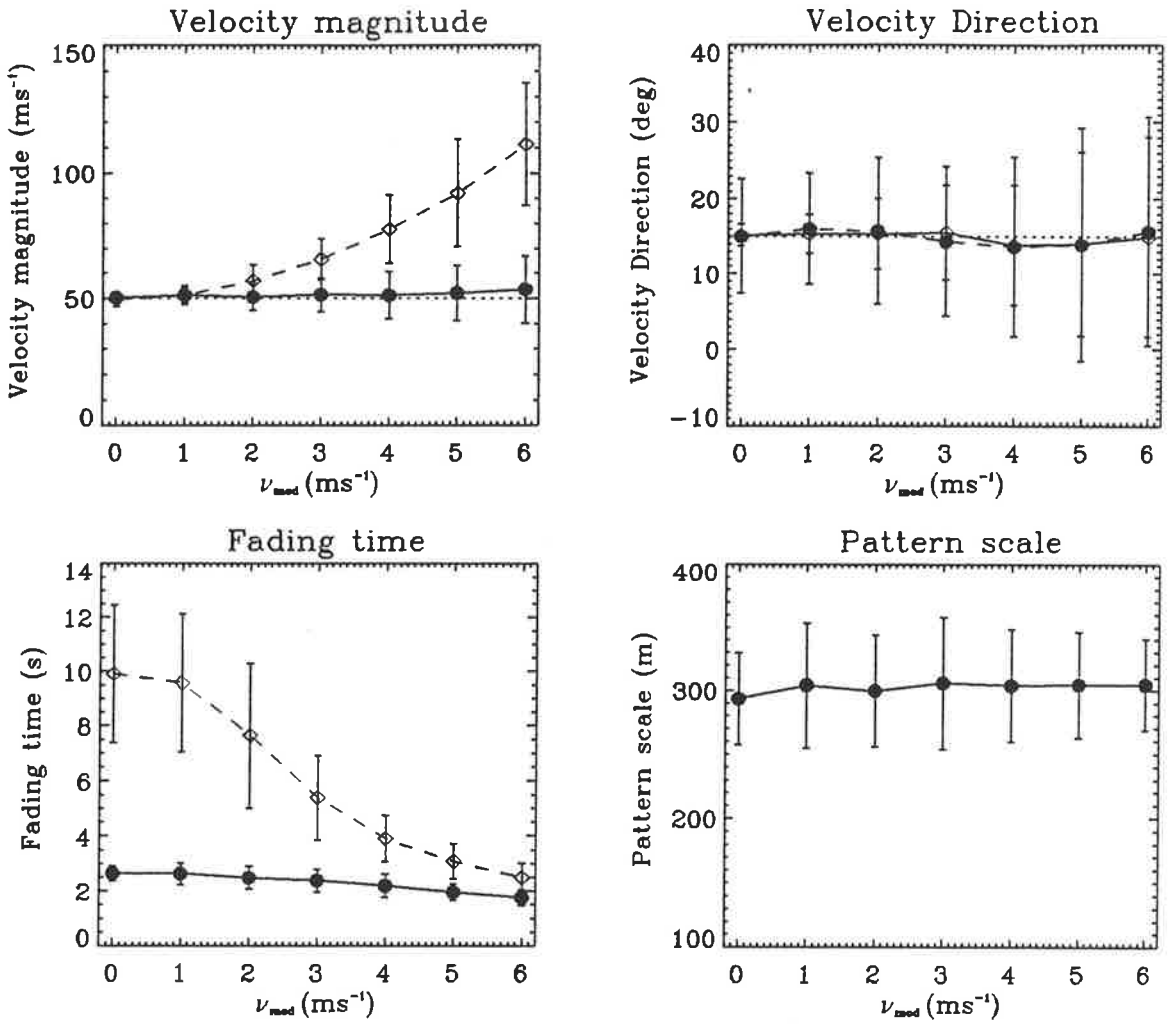

Figure 4.7: The results obtained for the application of the FCA to the model-generated data-set MOD-MF-SA as a function of ν_{mod}. The top plots show the magnitude (left) and direction (right) of the vector averaged true (•) and apparent (◇) velocities. The bottom left plot shows the fading time $\tau_{0.5}$ (•) and the corrected fading time $T_{0.5}$ (◇). The bottom right plot shows the pattern scale $S_{0.5}$.

overestimation is reduced significantly. For instance, for $\nu_{\text{mod}} = 6$ ms^{-1} the estimate of V_t is reduced from 53.5 ms^{-1} down to 50.7 ms^{-1}. The directions of the true θ_t and apparent θ_a velocities accurately estimate the direction of the model input velocity for all values of ν_{mod}. These results suggest that the FCA compensates correctly for the effects of the random changes.

The increase in the pattern scale $S_{0.5}$ seen with increasing ν_{mod} can be explained as follows. If the scattering regions propagate with respect to the radar the backscattered signal from any individual scattering region will be Doppler shifted from the transmitted

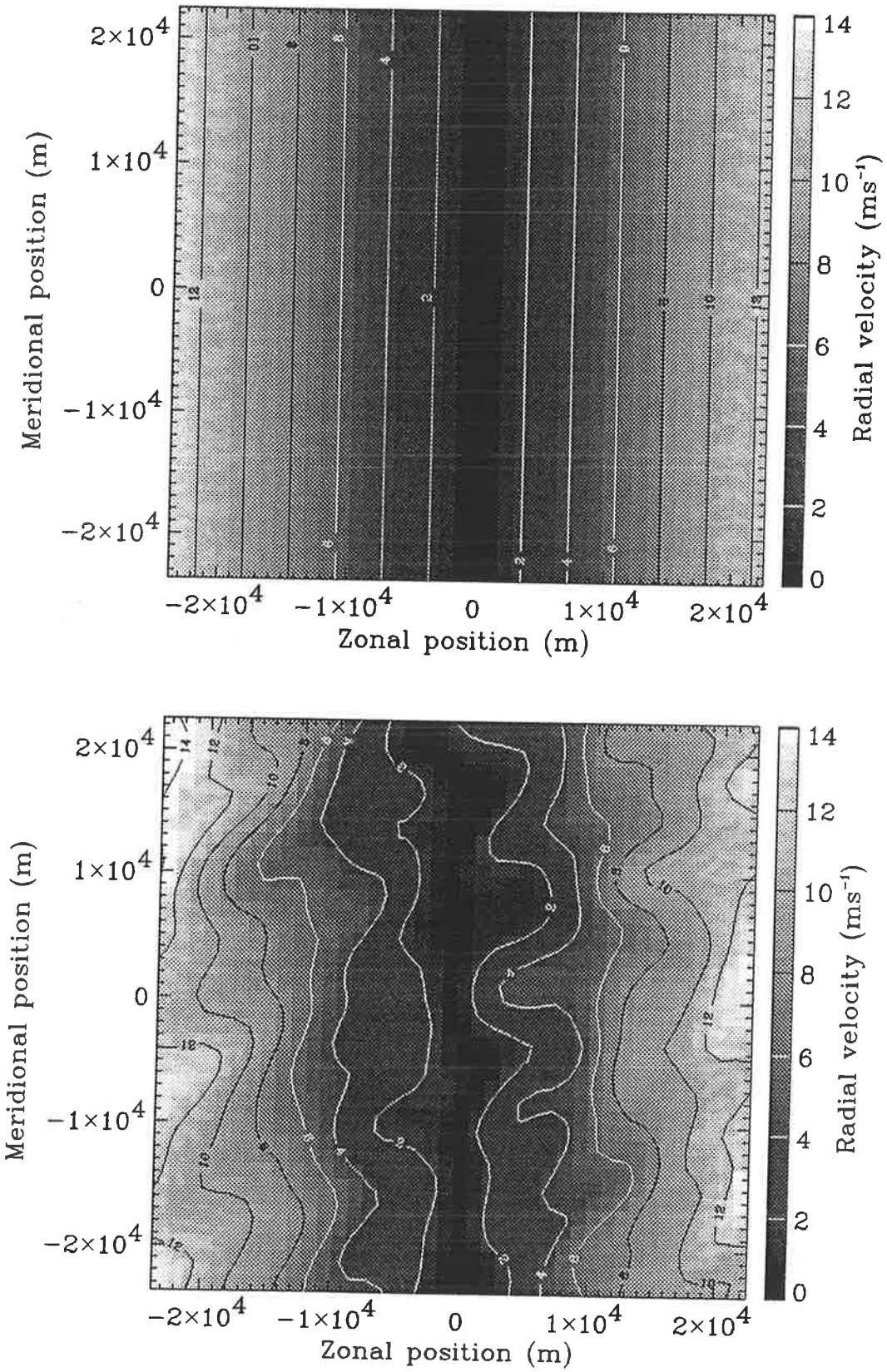

Figure 4.8: Contours of the averaged radial velocity field resulting from a wind field both with (bottom) and without (top) isotropic turbulence motions.

radar frequency f_0 by

$$\triangle f = \frac{-2V_r}{\lambda}, \tag{4.41}$$

where λ is the radar wavelength and V_r is the radial velocity, which is the component of the velocity in the direction of the scattering region. In the absence of turbulent motions the backscattered returns of a specific Doppler frequency can be shown to originate from a hyperbola which is symmetric about the direction of motion (e.g. *Briggs*, [1995]). As the turbulent motions are introduced the velocity field becomes randomized, and the returns will originate from a range of positions about this hyperbola, including positions closer to the zenith. Because the returned power decreases with increasing zenith angle the returns originating from closer to the zenith will be more dominant, thereby giving the impression that the hyperbola is located closer to the zenith than it actually is. This effect is illustrated in Figure 4.8, which shows contours of the hourly averaged radial velocity magnitude field resulting from the MF model simulation of a mean wind velocity of 50 ms^{-1} propagating eastwards at a height of 90 km, both with and without isotropic turbulent motions of magnitude 6 ms^{-1}. There clearly exist regions where the "turbulent" radial velocity contours are significantly closer to the zenith than the corresponding "non-turbulent" radial velocity contours. As the returns for each Doppler frequency appear to result from closer to the zenith the effective width of the "turbulent" polar-diagram is reduced, thereby resulting in an increased pattern scale. This effect will increase as the magnitude of the turbulent motions is increased, thereby resulting in $S_{0.5}$ increasing with increasing ν_{mod}. This is essentially the same effect that causes turbulent spectral broadening (e.g. *Hocking et al.*, [1983a]), and is an identical argument to that employed by *Briggs* [1995] to suggest that the Doppler-selected imaging radar interferometry techniques will break down in the volume scatter situation.

The results of Figure 4.7 clearly indicate the necessity for the corrections applied by the FCA for the effects of turbulent random motions. The true velocity correctly compensates for the effects of random motions which result in the magnitude of the apparent velocity V_a overestimating the magnitude of the model input velocity. The results of *Lesicar* [1993] suggest that the typical seasonal average values of $T_{0.5}$ observed in the mesosphere at Adelaide range from 3.5 to 9.5 s, corresponding the isotropic turbulent velocities ν ranging from 1.5 to 4.5 ms^{-1}. These values are in reasonable agreement with the vertical turbulent velocities ν_V obtained at Adelaide by *Hocking* [1983b], using the spectral width technique described in chapter 3. The typical seasonal average values of $T_{0.5}$ observed at both Christmas Island and Mawson range from 2.0 to 6.0 s, corresponding to values of ν ranging from 2.7 to beyond

6 ms^{-1}.

In quoting these values of ν from *Lesicar* [1993] however two factors must be considered. The first factor is best considered by defining the parameter

$$R_v = \frac{V_a}{V_t}, \tag{4.42}$$

which is the ratio of the magnitudes of the apparent V_a and true V_t velocity. If V_t is increased, the value of ν must be increased by the same multiplicative factor to maintain a constant value of R_v. Alternatively, if V_t is increased and ν is kept constant, the value of R_v must decrease. Thus the value of R_v obtained from Figure 4.7 is only applicable to the case where $V_t = 50$ ms^{-1}. It is therefore important to consider both V_t and ν when assessing the effects of turbulent motions upon the magnitude of the apparent velocities. Secondly, the triangle size effect (e.g. *Golley and Rossiter*, [1970]) can result in an underestimation of the magnitude of the true velocity V_t, thereby resulting in an increase in $T_{0.5}$, and a consequent overestimation of the effects of turbulent motions. It is therefore possible that the values of ν obtained by *Lesicar* [1993] may be underestimates. Despite these considerations, it is still fair to say that the effects of turbulent random motions can be significant in the mesosphere, and should be corrected for.

4.4.2 The effect of anisometric scatter upon the FCA

The effects of anisometric scatter upon the FCA have been investigated using the model-generated data-set MOD-MF-ANISO. The anisometry was introduced by decreasing the zonal component of the effective beam width θ_{bex} while keeping the meridional component θ_{bey} constant. This has the effect of producing a ground diffraction pattern with elongation along the zonal axis. The anisometry factor

$$A = \frac{\theta_{bey}}{\theta_{bex}} \tag{4.43}$$

was varied between unity and three, thereby ranging from isometric to extreme anisometric scatter. For each value of A the model velocity direction was varied between zero and 90° in steps of 5°, and for each direction 20 records were generated.

The directions of the vector averaged FCA true (θ_t) and apparent (θ_a) velocities produced using $A = 2$ are shown in Figure 4.9 as a function of the model velocity direction θ_{mod}. While θ_t shows excellent agreement with θ_{mod}, θ_a is biased towards zero degrees. This result is consistent with the predictions of *Phillips and Spencer* [1955] that anisometric scatter leads

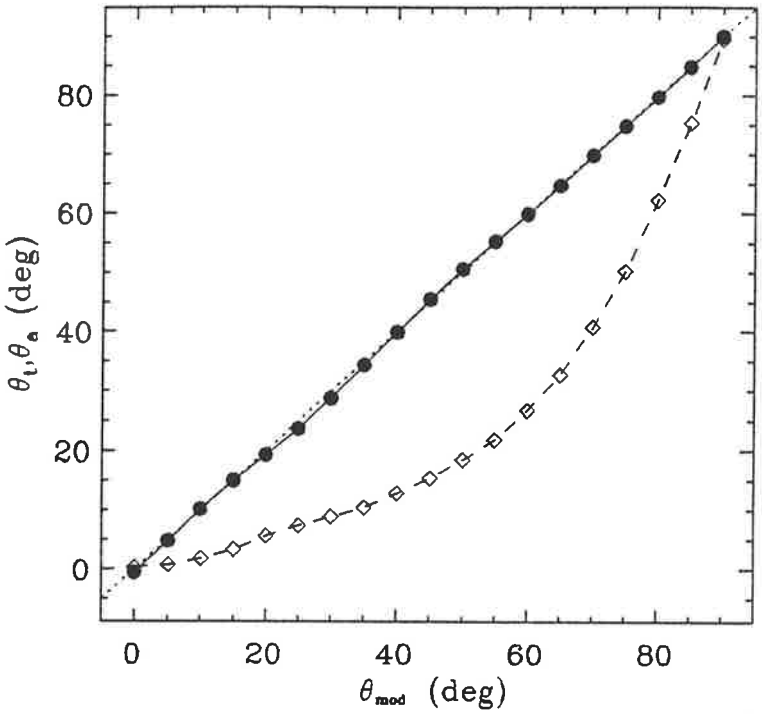

Figure 4.9: Directions of the average true (θ_t) (•) and apparent (θ_a) (◇) velocities as a function of model velocity direction ($\theta_{\rm mod}$). The dotted line indicates where $\theta = (\theta_{\rm mod})$.

to θ_a being biased towards the direction perpendicular to the pattern elongation $\theta_{\rm ax}$, which in this instance is zero degrees. Figure 4.10 shows plots of the parameters

$$\triangle \theta_t = \theta_t - \theta_{\rm mod}, \text{ and} \tag{4.44}$$

$$\triangle \theta_a = \theta_a - \theta_{\rm mod}, \tag{4.45}$$

as a function of $\theta_{\rm mod}$ for the various values of A. The FCA has been applied without rejection criteria number 9, allowing the difference in θ_t and θ_a to exceed 40°. These results suggest that θ_t proves an excellent estimate of $\theta_{\rm mod}$. except in the case of extreme anisometry, where there is a small bias of less than 6° towards the direction perpendicular to $\theta_{\rm ax}$. On the other hand, θ_a accurately estimates $\theta_{\rm mod}$ only in the isometric scatter situation, producing an increased bias towards the direction perpendicular to $\theta_{\rm ax}$ as A increases. It is apparent for large A that the difference in θ_t and θ_a can exceed 40°. Despite these directional biases, the magnitudes of both the true and apparent velocities agree well with the magnitude of the model velocity, as expected in the case where turbulent motions are not employed.

Figure 4.11 shows histograms of the axial-ratios $R_{\rm ax}$ and axial-rotations $\theta_{\rm ax}$ for each value of A using all values of $\theta_{\rm mod}$. The elongation of the characteristic ellipse should analytically be perpendicular to the elongation of the scatterers. Because $R_{\rm ax}$ is defined as the ratio of

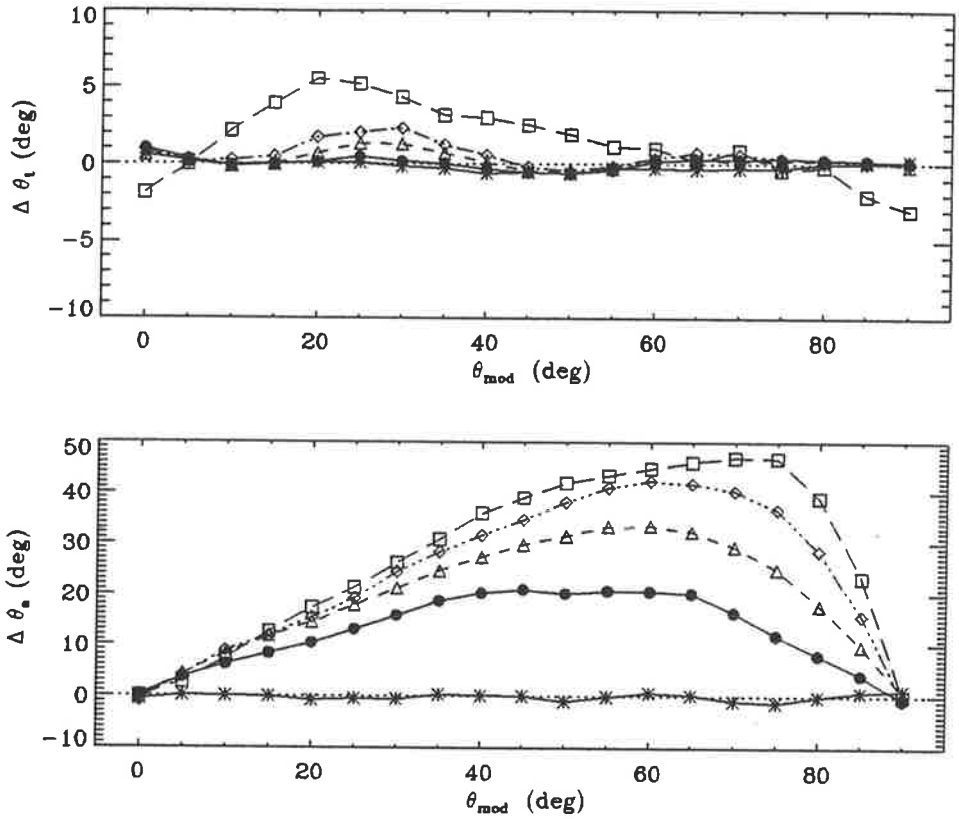

Figure 4.10: Direction differences $\triangle\theta_t$ (left) and $\triangle\theta_a$ (right) as a function of $\theta_{\rm mod}$ for A = 1 (∗), 1.5 (•), 2 (△), 2.5 (◇) and 3 (□). The dotted lines indicate a difference of zero degrees.

the major to minor axis it is necessarily greater than unity. The estimate of the average axial ratio $\bar{R}_{\rm ax}$ for $A = 1$ should therefore exceed unity, while the estimates for values of A exceeding unity the should be almost equal to A. The histogram of $R_{\rm ax}$ for $A = 1$ does not peak at unity because it is statistically unlikely that a perfectly isometric pattern will exist in practice. The histogram of $\theta_{\rm ax}$ for $A = 1$ shows no preferential direction, as expected in the isometric situation. For $A > 1$, $\bar{R}_{\rm ax}$ exceeds A by approximately 9%. The distribution of $R_{\rm ax}$ appears skewed towards larger values, giving the impression of a Raliegh distribution. The histograms of the $\theta_{\rm ax}$ values increasingly cluster about 90° as A increases. These results are consistent with those obtained in the numerical model analysis of *Wright and Pitteway* [1978], who found that $R_{\rm ax} > A$ for all values of A. This result was attributed to the inability of the FCA to separate the spatial and temporal properties of the ground diffraction pattern, resulting in the characteristic ellipse being foreshortened along the direction of motions. This result is discussed in more detail in Chapter 5. The results of *Røyrvik* [1983] suggest that $R_{\rm ax} \rightarrow A$ as the ratio of the time-series length T to the fading time $\tau_{0.5}$ is increased. This

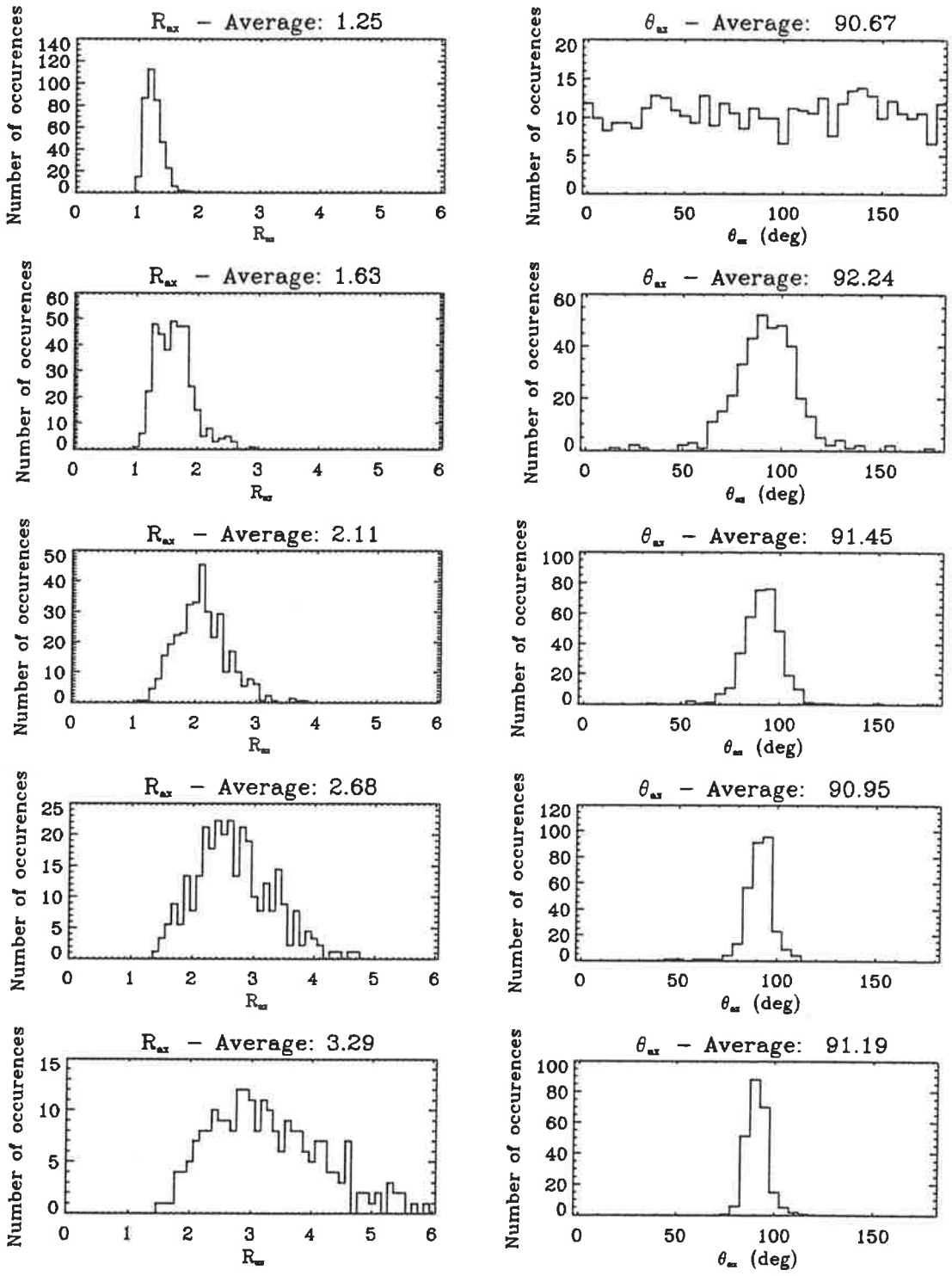

Figure 4.11: Histograms of the axial-ratio (R_{ax} - left column) and axial-rotation (θ_{ax} - right column) obtained on applying the FCA to the model-generated data-set MOD-MF-ANISO using anisometry parameters A of unity (top), 1.5 (second top), 2.0 (middle), 2.5 (second bottom) and 3 (bottom). The number at the top of each plot indicates the average of the distribution.

suggestion will be examined in 4.8.1.

The results of this subsection clearly indicate the necessity for the corrections applied by the FCA for the effects of anisometry. The results of Figure 4.11 indicate that average axial-ratios exceeding 1.5 can be regarded as evidence for anisometric scatter. In these circumstances the direction of the apparent velocity θ_a can be shown to be biased towards the direction perpendicular to the elongation of the ground diffraction pattern. The results of *Lesicar* [1993] suggest that typical seasonal average values of $R_{ax} = 1.6$ are observed at Adelaide, suggesting that on average there will be little anisometry, and consequently, little bias in θ_a. On the other hand, typical seasonal average values of $R_{ax} = 2.5$ are observed at the equatorial site of Christmas Island. The histograms of the axial-rotation θ_{ax} show significant peaks at approximately 0° above 90 km, suggesting that the scatterers are elongated in the East-West direction. Similar anisometry is seen in the E-region, where the scatterers are elongated in the direction of the equatorial electrojet (e.g. *Briggs*, [1977]). The presence of this anisometry suggests there will be significant biases in θ_a towards East-West, therefore emphasising the need for the correction inherent in the estimation of the true velocity at equatorial latitudes.

4.4.3 Effects of gravity waves on the FCA

The effects of internal gravity waves upon the FCA have been investigated using the radar backscatter model, using the simulation described in section 3.2.4.2. The effects of waves upon the FCA were initially addressed by *Hines and Rao* [1968], who proposed that the presence of the waves may act to perturb the layers responsible for total reflection returns from the ionosphere. In this situation the signal returns will eventuate from regions of the layer perpendicular to the transmitted signal, and the FCA would therefore be expected to measure a velocity related to the the phase velocity of the waves present rather than the mean background wind velocity. The results of *Meek and Manson* [1992] suggest that this argument is only applicable for the case of a single reflection, or "glint". As the fading period associated with a single glint is significantly larger than the fading periods generally observed in practice it follows that the arguments of *Hines and Rao* [1968] are most probably only rarely applicable. Nevertheless, *Meek and Manson* [1992] do suggest that the FCA true velocity can be underestimated in the presence of total reflection glints due to the increase in the fading period, rather than biased towards the phase speed of the perturbing waves.

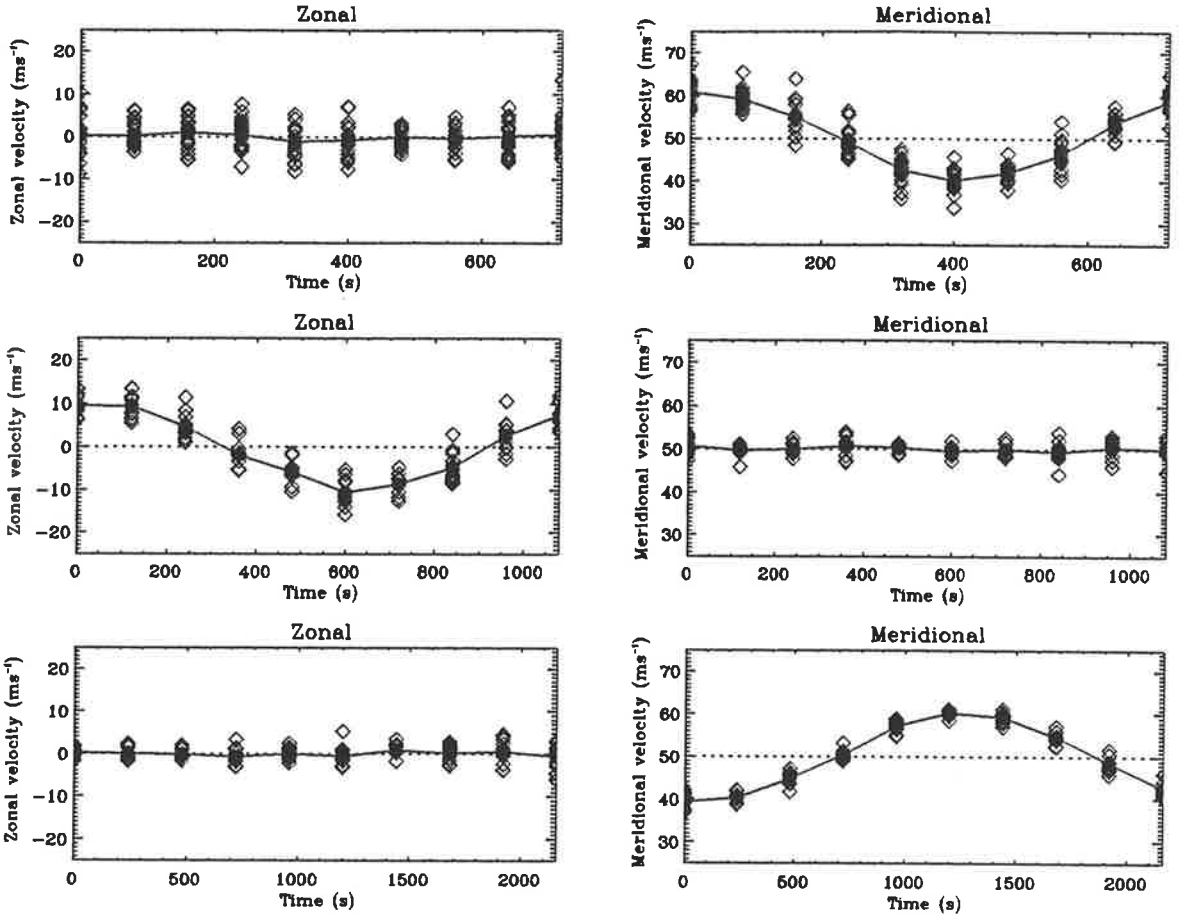

Figure 4.12: Typical example of the zonal (left) and meridional (right) velocities obtained over the period of the wave for waves propagating parallel (top), perpendicular (middle) and anti-parallel (bottom) to the direction of the mean wind velocity of 50 ms^{-1} N. The wave parameters employed are: period T = 20 min, horizontal phase speed c = 100 ms^{-1}, horizontal wavelength λ_h = 120 km, vertical wavelength λ_z = 31 km, horizontal perturbation velocity V_h' = 10 ms^{-1}, and vertical perturbation velocity V_z' = −2.5 ms^{-1}.

It was generally accepted throughout the atmospheric physics community that the arguments of *Hines and Rao* [1968] were inapplicable to the partial reflection returns (e.g. *Briggs*, [1977]; *Hocking et al.*, [1989]). In order to explain the results of the recent AIDA campaign however *Hines* [1993] have reapplied the arguments of *Hines and Rao* [1968], suggesting that the presence of waves may act to tilt the irregularities responsible for the backscatterer. It follows from these arguments that *all* MF radar techniques should measure a wind velocity related to the phase speed of the wave. This scenario was simulated numerically by *Sürücü et al.* [1995b], who illustrated that the average FCA true velocity calculated over the period of a monochromatic wave shows good agreement with the model background wind velocity, and is not influenced by the phase speed of the perturbing wave.

The gravity wave simulation employed by the radar backscatter model is identical to that employed by *Meek and Reid* [1984], and simulates the propagation of a monochromatic wave. The results of *Meek and Reid* [1984] suggest that for some sets of wave parameters that the FCA true velocity can underestimate the background wind velocity. The authors speculated that this effect may be the result of the model not fitting the assumptions of the FCA. The analysis of *Meek and Reid* [1984] has essentially been repeated in this section as part of a preliminary investigation into the effects of waves upon the FCA. An illustrated example of these results is shown in Figure 4.12, which shows the zonal and meridional velocities obtained over various phases of a wave over 20 periods for waves propagating parallel, perpendicular, and anti-parallel to the direction of the mean wind velocity, which is 50 ms^{-1} N. The average velocity estimated over each phase of the wave exhibits a clear sinusoidal perturbation about the average velocity obtained over the ground-based period of the wave, which is in excellent agreement with the model input velocity. The results obtained for a range of different wave parameters for short-period waves are shown in Table 4.2. These results indicate that the FCA true velocity accurately predicts the background wind velocity. The results also indicate that the FCA apparent velocity can be significantly influenced by the propagation of gravity waves, as discussed in section 3.4.2.

The analytical model analysis of *Røyrvik* [1983] suggests that the motion of the ground diffraction pattern can be significantly influenced by horizontal variations in the vertical velocity. It therefore follows that the instantaneous FCA true velocity will not necessarily measure the instantaneous horizontal velocity resulting from the addition of the background wind and the phase velocity of the wave. The velocity averaged over the period of the wave however should equal the background wind velocity. This result was also predicted by the analytical model analysis of *Kudeki et al.* [1993], and verified by the numerical model analysis of *Sürücü et al.* [1995b]. The same behavior was also observed using the radar backscatter model.

The results of this section indicate that the FCA true velocity successfully estimates the background wind velocity in the presence of a monochromatic wave if the results are averaged over the period of the wave. In some circumstances which are not illustrated in Table 4.2 however the velocity can be biased due to the application of FCA rejection criteria 8, 10, and 11. This result was also discussed in the wind field inhomogeneity analysis of *Sürücü et al.* [1995a], and suggests that these criteria should be applied with some care. As the effects of gravity wave spectra are soon to be included in the radar backscatter model

Table 4.2: Estimates of the FCA velocities obtained over the period of the wave for various different wave parameters. The wave parameters are the intrinsic wave period ω, the horizontal wavelength λ, the horizontal phase speed c_p, the azimuth of the horizontal phase velocity ϕ_p, the true velocity magnitude V_t, and the apparent velocity magnitude V_a. The horizontal perturbation velocity $V_h' = 10$ ms^{-1} for all cases.

ω (min)	λ_h (km)	c_p (ms^{-1})	ϕ_p (deg)	V_t (ms^{-1})	V_a (ms^{-1})
5.1	10	32.7	0	51.5	126.3
			90	54.5	128.2
			180	48.8	117.5
5.1	20	65.4	0	52.1	120.
			90	53.2	127.1
			180	47.9	131.2
5.1	50	163.4	0	52.7	108.2
			90	50.6	99.8
			180	46.2	94.6
5.1	100	326.8	0	50.7	122.4
			90	52.4	89.2
			180	52.3	102.3
10	10	16.7	0	52.3	72.0
			90	52.5	72.0
			180	52.2	71.7
10	20	33.3	0	52.3	72.0
			90	49.9	73.1
			180	50.6	71.0
10	50	83.3	0	47.2	66.5
			90	50.1	60.6
			180	48.2	65.7
10	100	166.7	0	48.9	54.9
			90	50.7	54.1
			180	50.8	55.5
20	10	8.3	0	50.8	55.5
			90	50.5	54.8
			180	50.9	56.3
20	20	16.7	0	51.0	56.3
			90	50.6	55.2
			180	49.9	57.2
20	50	41.7	0	50.0	58.1
			90	50.2	56.6
			180	50.5	54.1
20	100	83.3	0	50.5	56.3
			90	51.1	57.8
			180	50.1	54.4

the preliminary investigation presented in this section will be later supplemented by a more thorough investigation of the effects of gravity waves upon the FCA.

4.5 Application of the FCA to MF data

The FCA is employed by the Adelaide group for the realtime routine analysis of mesospheric and lower thermospheric using the BP MF SA configuration described in Chapter 2. The signal returns obtained in these regions are influenced by a combination of the effects of turbulent motions, gravity wave perturbations, and scatterer anisometry, as simulated in section 4.4. The data-set BP940527 was collected using the standard BP MF SA configuration, and can thus be regarded as a typical of the data employed during the routine analysis.

The results obtained on the application of the FCA to the first two hours of the data-set BP940527 are shown in Figures 4.13 and 4.14. The velocity profiles are typical of those observed during the month of May at Buckland Park, and are consistent with the seasonal results of *Lesicar* [1993]. The magnitude profiles increase with decreasing height, peaking at about 68 km, while the direction profiles indicate that the mean wind is predominantly zonal. At most heights V_a is significantly larger than V_t, suggesting that the ground diffraction pattern is evolving rapidly. This is confirmed by the fading time profiles, which reveal that $T_{0.5}$ is quite small, approximately twice as large as $\tau_{0.5}$. The average fading time $\tau_{0.5}$ lies between 2 and 4 s, while the average corrected fading time $T_{0.5}$ lies between 3 and 7 seconds. These fading times are again consistent with the seasonal results of *Lesicar* [1993]. The values of $T_{0.5}$ yield turbulent motion velocities ν_v of between 2 and 5 ms^{-1} if the formula of *Briggs* [1980], as presented in Chapter 3, is applied. The pattern scale $S_{0.5}$ varies between 200 and 550 m. The average antenna spacing for MF SA configuration is approximately 200 m, suggesting that the triangle size effect may cause some underestimation in V_t, $S_{0.5}$ and $T_{0.5}$ at the heights where the actual pattern scale is largest.

The results of section 4.4.2 suggest that axial-ratios R_{ax} exceeding approximately 1.5 are indicative of consistent ground diffraction pattern elongation, and therefore isometric scatter. The average values of R_{ax} exhibited in Figure 4.14 range from 1.3 and 2.3, suggesting that the ground diffraction pattern exhibits consistent elongation. The axial-rotation θ_{ax} by definition satisfies the relationship $0° < \theta_{\text{ax}} < 180°$. If the estimated pattern elongation is a statistical artifact of the analysis the individual estimates of θ_{ax} will be evenly distributed throughout this range, as illustrated in the top right panel of Figure 4.11. In this case the average θ_{ax}

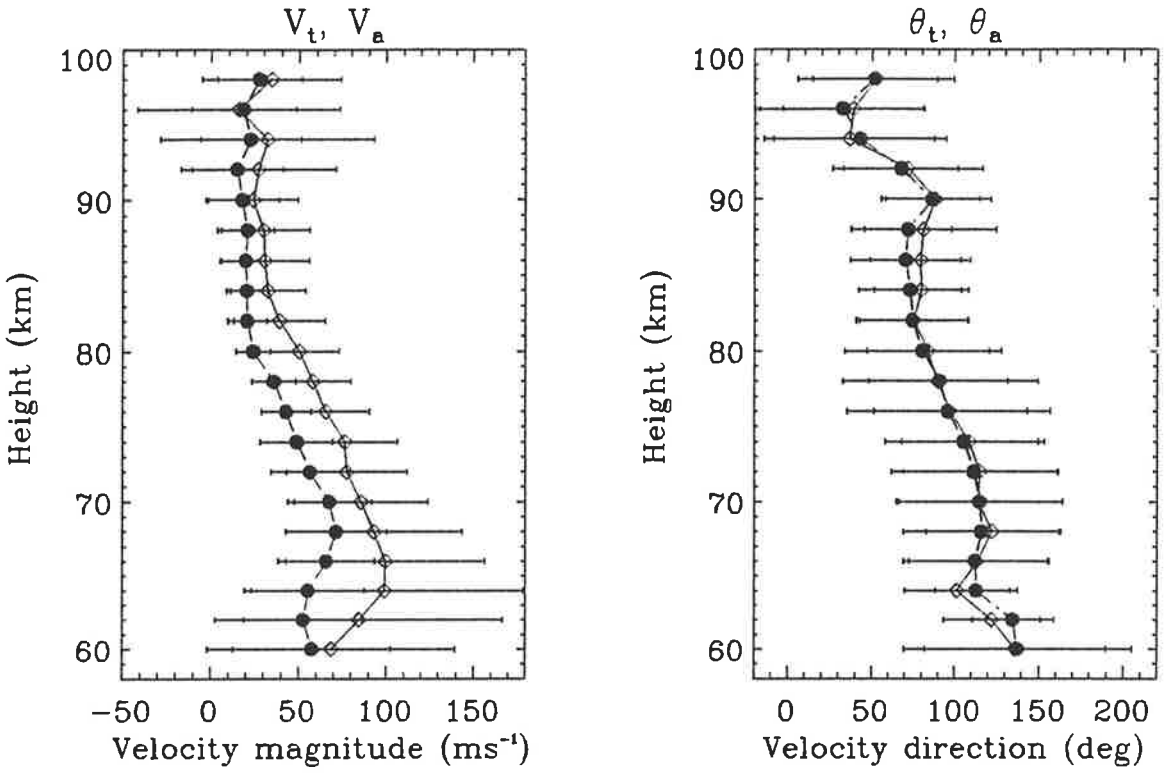

Figure 4.13: Results of the application of the FCA to first two hours of the data-set BP940527. The left plot shows the magnitude of the true (V_t) and apparent (V_a) velocity, while the right plot shows the direction of the true (θ_t) and apparent (θ_a) velocity.

should be close to 90°. If the estimated pattern elongation is on the other hand indicative of a consistent pattern elongation the estimates of $\theta_{\rm ax}$ will peak at the actual value of $\theta_{\rm ax}$. The average $\theta_{\rm ax}$ values illustrated in Figure 4.14 are determined using records where $R_{\rm ax} > 1.4$. This criterion precludes records with isometric estimated ground diffraction patterns from the averaging, thereby focusing on the orientation of the anisometric patterns. At some heights the average $\theta_{\rm ax}$ is up to 40° different from 90°, suggesting the existence of consistent pattern elongation. Below 82 km $\theta_{\rm ax}$ is within 15° of θ_t at all heights, suggesting that the pattern is either more isometric or is elongated along the direction of the wind velocity.

Profiles of the percentage of records yielding error codes 0, 3 and 5 are shown in Figure 4.15. The error code 0 indicates the record has passed all of the FCA rejection criteria. The acceptance rate between 68 and 86 km is approximately 70%. Above 86 km the acceptance rate decreases with increasing height, while below 68 km the the acceptance rate decreases of with decreasing height. The overall acceptance rate is approximately 54.6%. The majority of the rejections are due to criteria 3 (15.8%) and 5 (13.5%). The majority of rejection due to criterion 3 occur above 90 km. At 96 and 98 km almost half of the records are rejected

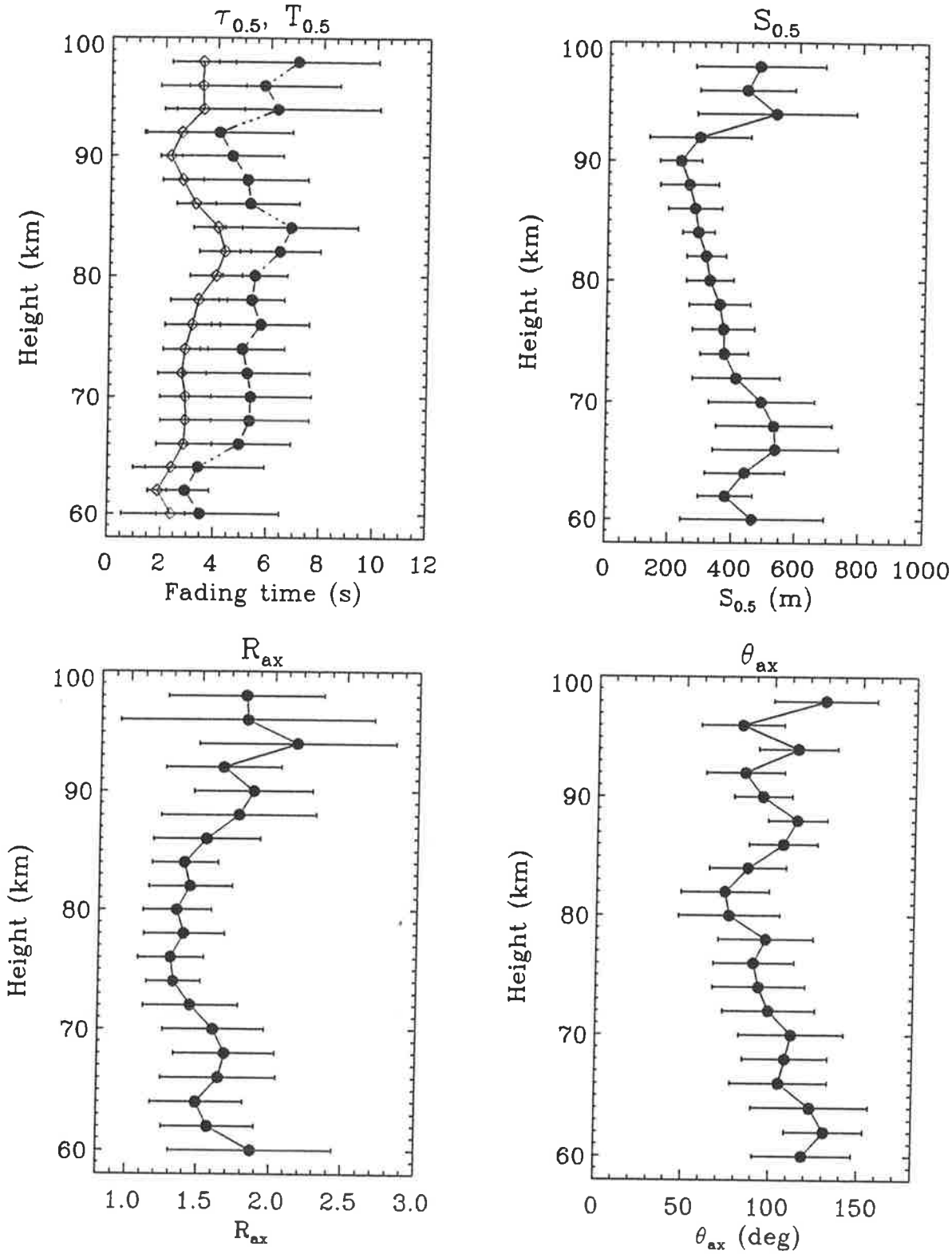

Figure 4.14: Further results of the application of the FCA to first two hours of the data-set BP940527. The top plots show the fading time $\tau_{0.5}$ ($\diamond$) and the corrected fading time $T_{0.5}$ ($\bullet$) (left) and the pattern scale $S_{0.5}$ (right), while the bottom plots show the axial-ratio R_{ax} (left) and axial rotation θ_{ax} (right).

UNIVERSITY OF ADELAIDE LIBRARY

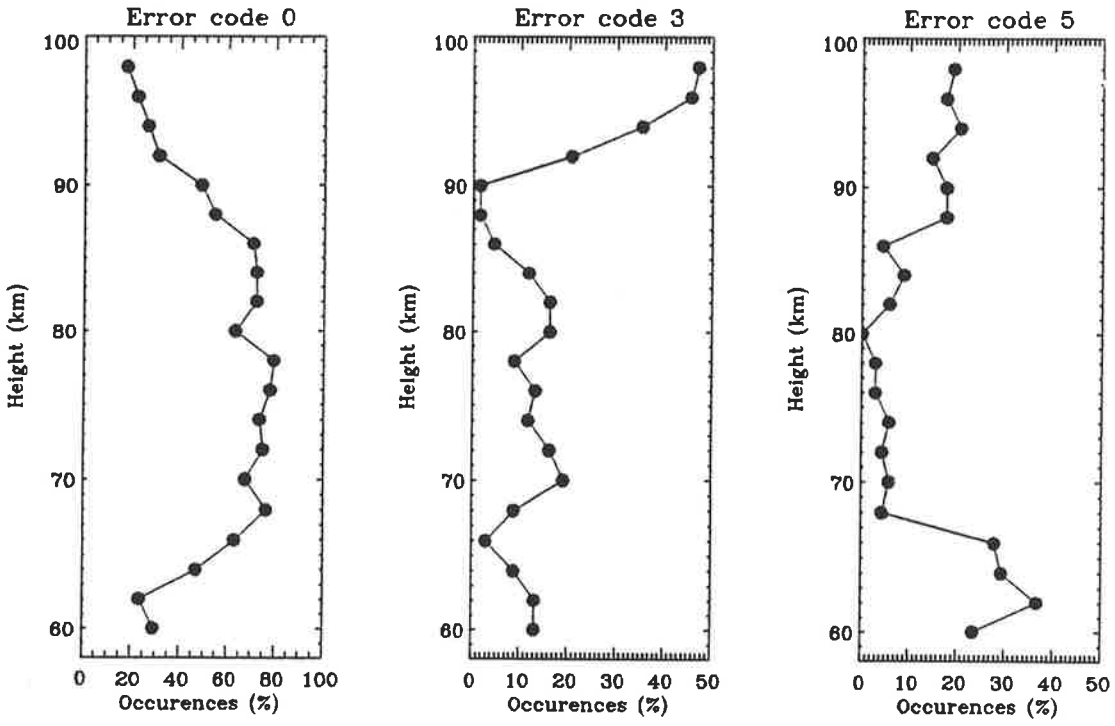

Figure 4.15: Percentage of occurrence of error codes 0 (no rejection - left), 3 (middle), and 5 (right) for the first two hours of the data-set BP940527.

by criterion 3, suggesting that there is considerable total-reflection occurring at these height producing slowly fading records. The profile of $S_{0.5}$ shown in Figure 4.13 exhibits a noticeable increase at these heights, which is consistent with a specular scattering mechanism. The majority of rejections due to criterion 5 occur above 86 km and below 68 km. The next most occurrent error codes are 4 (3.8%) and 10 (4.2%).

The results presented in this section are intended to provide an illustration of the application of the FCA to experimentally obtained data. The results obtained are typical of those obtained using the routine analysis as employed at Buckland Park. This analysis may be subject to biases such as the triangle size effect, which is discussed in chapter 4. The triangle size effect can result in underestimates in V_t, $T_{0.5}$, and $S_{0.5}$, as well as biases in θ_t and θ_{ax}. The returned power varies by over three orders of magnitude in the 60-100 km height range probed by the radar. The receiver gain is set in order to maximize the observable height range. As a result, the time-series records exhibit consistent saturation at heights above 90 km, and low numbers of digitization levels at heights below 70 km. These effects have previously been tolerated. The effects of saturation and coarse digitization upon the FCA are investigated in Chapter 5. These results indicate that saturation and coarse digitization can

contribute to the triangle size effect. The increase in the average R_{ax} values observed above 90 km in Figure 4.14 may therefore be introduced by the effects of saturation rather than indicative of consistent pattern elongation. This result is an important consideration in the examination of short and long term observations of the behavior of the output parameters of the FCA, such as those performed by *Lesicar* [1993].

4.6 Effect of sampling time upon the FCA

The FCA relies upon the accurate estimation of the correlation parameters. The sampling time Δt must therefore be small enough to provide a sufficient number of lags on the main peak of the correlation functions for the effective estimation of the correlation parameters. The effectiveness of the techniques used to extract the correlation parameters have therefore been analyzed as a function of Δt in order to determine the sampling time limits for the application of the FCA. The model-generated data-set MOD-VHF-SAMP has been employed for this purpose. This data consists of 100 time-series realizations of length 128 s and sampling time $\Delta t = 0.1$ s. Time-series records with sampling times of $N \Delta t$ are produced by coherently averaging N contiguous time-series samples.

4.6.1 Zero-lag auto-correlation function interpolation

The most common interpolations employed for the estimation of the noise-free zero-lag auto-correlation are cubic-spline and low-even-order polynomial interpolations. Polynomial interpolations have the limitation that the interpolation must be confined to the main peak of the auto-correlation functions, as spurious higher order polynomial powers may be introduced if the oscillations in the tails are included in the fit. The order of the polynomial interpolation is therefore limited by the number of lags on the main peak of the auto-correlation function. The same interpolation procedures are used to interpolate the zero-lag cross-correlation to correct for the effects of correlated noise seen simultaneously in each of the three receivers.

In the situation where a time-series record is noise-free the auto-correlation function will extrapolate smoothly to unity at zero-lag. This provides the ideal situation for the comparison of the effectiveness of the various interpolation procedures employed by various FCA analyses, as the correct value of the interpolation is known to be unity. The mean interpolated zero-lag auto-correlation obtained using the model-generated data-set MOD-VHF-SAMP using three-, four-, and five-lag cubic-spline interpolations as a function of the

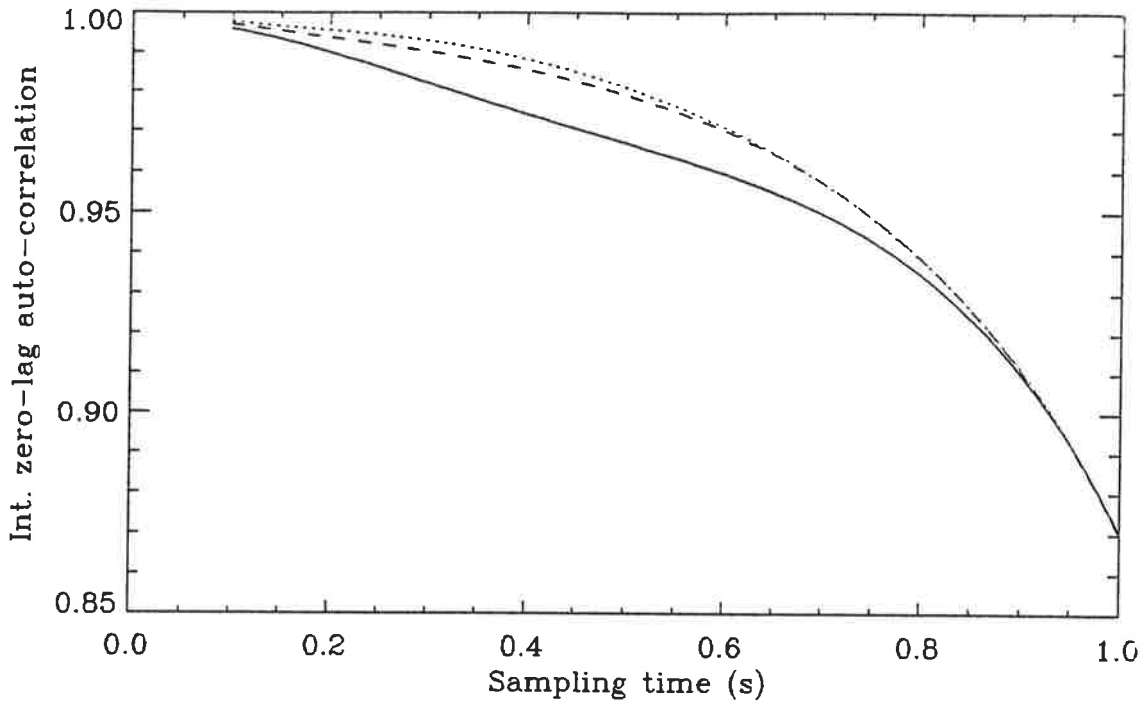

Figure 4.16: Average cubic spline interpolated zero-lag auto-correlation using 3 (solid line), 4 (dotted line), and 5 (dashed line) lags either side of zero-lag for the model-generated data-set MOD-VHF-SAMP.

sampling time are shown in Figure 4.16. The most obvious result is that the interpolated value decreases with increasing sampling time. This effect occurs because the first lag is being "pushed" further along the main peak of the auto-correlation function, thereby providing less reliable information on the actual behavior of the auto-correlation function about zero-lag. The four-lag interpolation produces the closest estimate to unity, suggesting that the accuracy of the interpolated value does not increase with the number of lags used. As the sampling time approaches 1 s the interpolations produce the same estimate. This is because any extra lags used in the interpolation lie outside the main peak of the auto-correlation function, and therefore provide no reliable information on the behavior of the auto-correlation function about zero-lag.

The average interpolated zero-lag auto-correlations obtained from the model-generated data-set MOD-VHF-SAMP using four-lag second-, fourth-, and sixth-order quadratic interpolations, and four-lag cubic-spline interpolations are shown in Figure 4.17 as a function of the sampling time. In the situation where the order of the quadratic interpolation exceeds the number of lags on the main peak of the correlation function with correlations exceeding 0.2 the interpolation is not performed. The accuracy of the interpolated value increases with the increasing order of the polynomial. Only the sixth-order polynomial interpolation

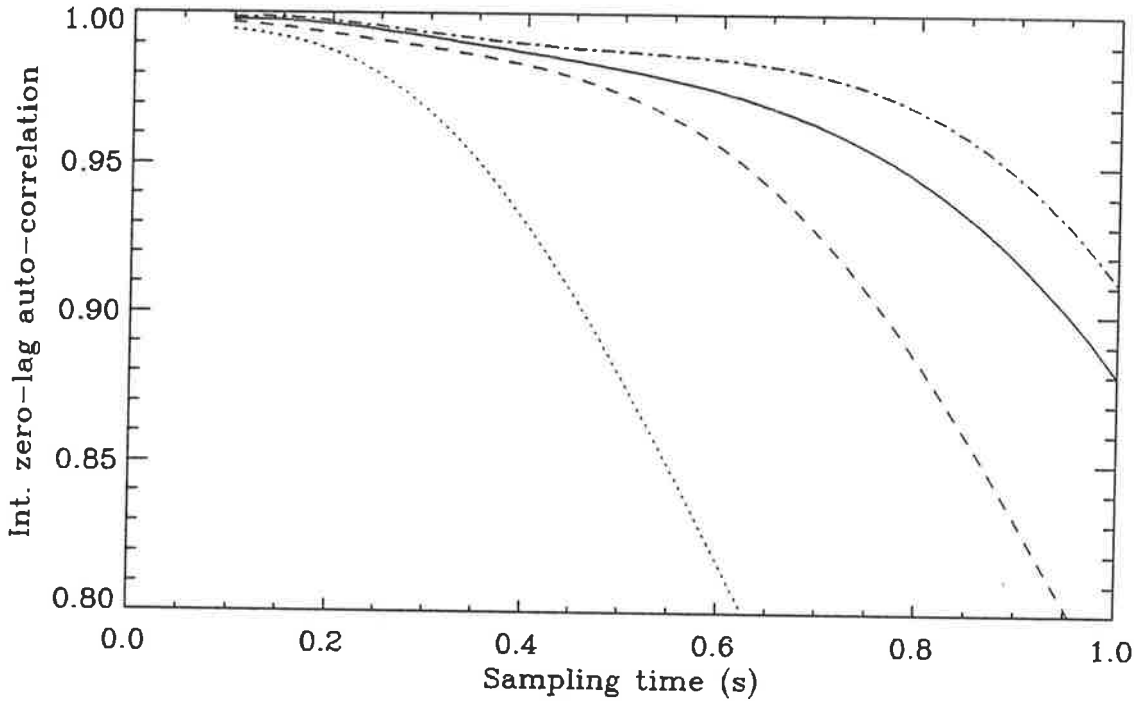

Figure 4.17: Average second- (dotted line), fourth- (dashed line), and sixth-order (dash-dotted line) polynomial interpolated zero-lag auto-correlation using 4 lags either side of zero-lag for the model-generated data-set MOD-VHF-SAMP. The solid line indicates the 4-lag cubic spline interpolated zero-lag auto-correlation.

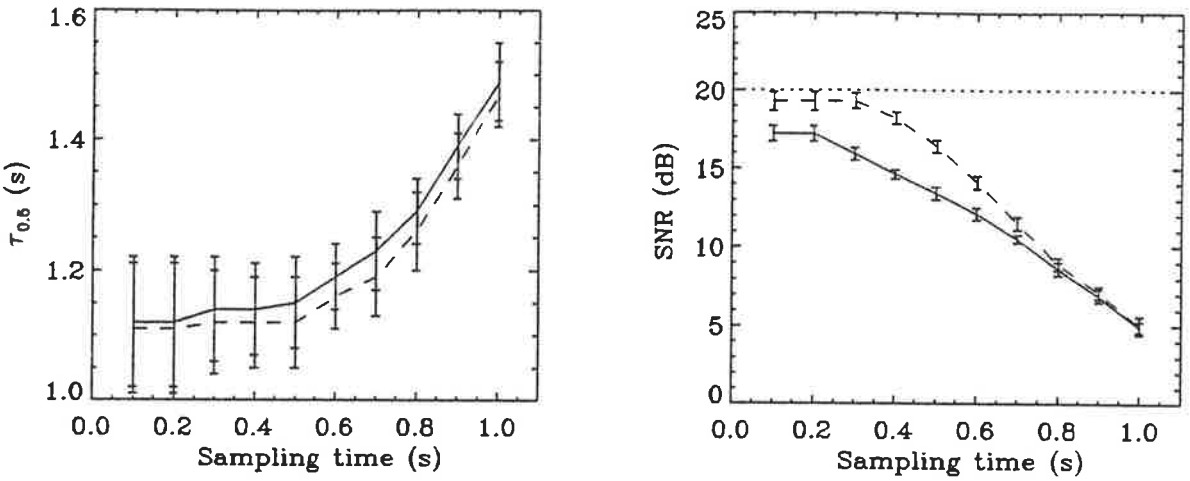

Figure 4.18: Variation of fading time and SNR as a function of sampling time for the model-generated data-set MOD-VHF-SAMP. The solid line indicates the results of the three-lag cubic-spline interpolation, while the dashed line indicates the results of the four-lag sixth-order polynomial interpolation. The dotted line on the SNR plot specifies the model input SNR. The error bars indicate the standard deviations of the distributions.

outperforms the four-lag cubic-spline interpolation, but still reveals a clear underestimation in the interpolated value for large sampling times.

The underestimation of the interpolated zero-lag auto-correlation has several consequences for the FCA. The underestimation results in the mean auto-correlation function becoming "flatter" about zero-lag. This subsequently results in an overestimation of the estimated fading time, $\tau_{0.5}$. The SNR is calculated using the ratio of the interpolated zero-lag auto-correlation to the difference between the interpolated and original zero-lag auto-correlation, as discussed in appendix C. The interpolation underestimation will therefore result in an underestimation of the SNR. The average $\tau_{0.5}$ and SNR estimate as a function of sampling time for the four-lag cubic-spline interpolation and four-lag sixth-order polynomial interpolation obtained using the model-generated data-set MOD-VHF-SAMP with 20 dB added receiver noise are shown in Figure 4.18.

4.6.2 Cross-correlation function Gaussian fit

The cross-correlation maxima ρ_{0ij} and the corresponding delay times τ'_{ij} are both used in the FCA. The cross-correlation maxima are employed to determine the lag-times τ_{ij} using (4.40), while the delay times τ'_{ij} are used directly. In the routine real-time FCA employed by the Adelaide group these parameters are estimated using a Gaussian fit over three lags either side of the estimated maximum position.

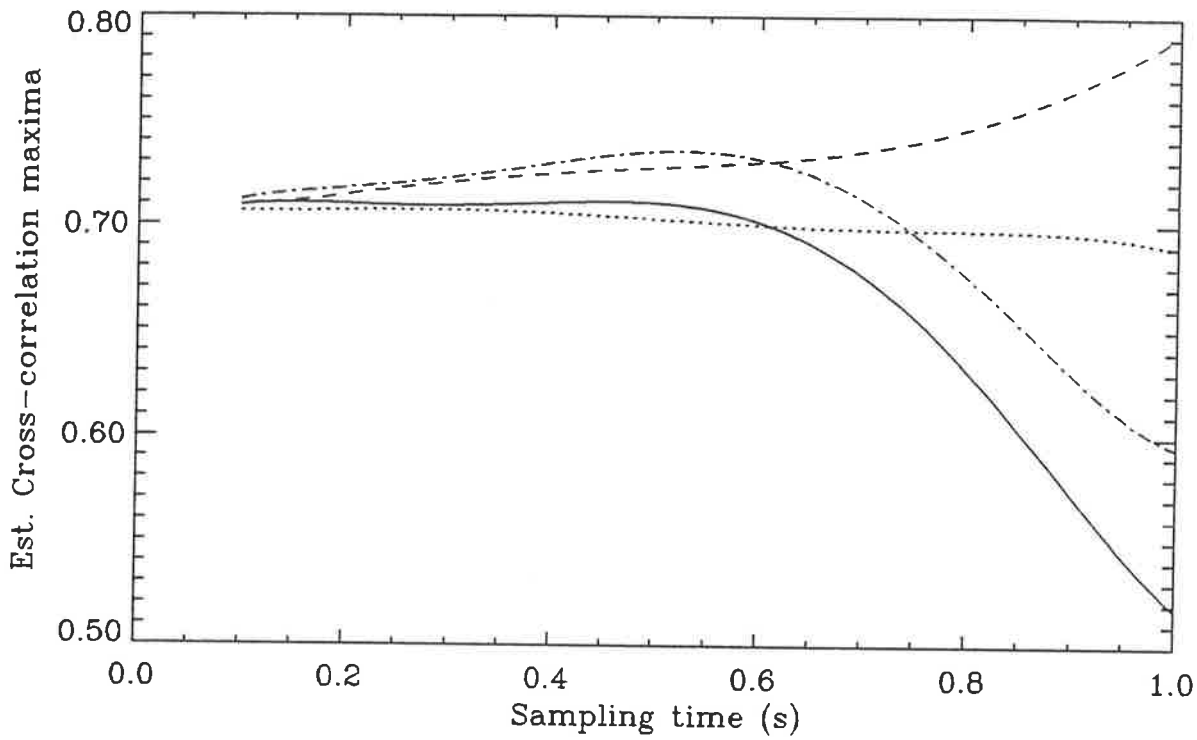

Figure 4.19: Average estimated cross-correlation maxima ρ_{0ij} as a function of sampling time for the model-generated data-set MOD-VHF-SAMP. The solid line indicates the estimate obtained without restricting the fit to the main peak of the cross-correlation function, while the dotted line indicates the estimate obtained by restricting to the fit to the main peak. The dot-dashed and dashed lines indicate the corresponding estimates obtained on applying the OFCA and RFCA procedures outlined in section 4.6.3, respectively.

The performance of the Gaussian fit has been investigated as a function of the sampling time using the model-generated data-set MOD-VHF-SAMP. In order to focus solely on the effects of the Gaussian fit the cross-correlation functions have not been re-normalized using the zero-lag auto-correlation interpolation, and have not used the zero-lag interpolation to remove the effects of correlated noise. The average fitted ρ_{0ij} as a function of sampling time for the three cross-correlation functions is shown in Figure 4.19. The rapid fall-off for sampling times above 0.6 s results from lags within the tails of the cross-correlation function being used in the fit. The Gaussian fit is biased away from the main peak of the correlation function towards the non-zero tails, and therefore underestimates ρ_{0ij}. The average τ'_{ij} however is not affected, although the variation of the individual estimates increases with increasing sampling time.

There is no simple solution to this problem. Alternative techniques do not estimate ρ_{0ij} with sufficient accuracy. The Gaussian fits employed by the FSA include the spectral

tails in the fit. However, the inclusion of the correlation function tails in the Gaussian fits generally results in poor estimation of the cross-correlation in the region of the maxima, even for sampling times where the six-lag Gaussian fit produces excellent estimation. Similarly, high even-order polynomial fits are susceptible to oscillations in the tails of the correlation functions, and therefore do not accurately estimate the behavior of the cross-correlation function in the region of the maxima. Limiting the polynomial fits to the main peak of the cross-correlation functions restricts the order of the polynomial, and therefore reduces the effectiveness of the fit. Limiting the Gaussian fit to lags within the main peak of the cross-correlation function appears to produce the best results. The results of applying this procedure, hereafter referred to as the "restricted Gaussian fit", are shown in Figure 4.19. There is a clear improvement on the results obtained using the six-lag fit, although there is still some underestimation of ρ_{0ij}.

4.6.3 Combined effects of the zero-lag auto-correlation interpolation and and the cross-correlation Gaussian fit

The inter-relation of the various correlation parameters makes it difficult to assess the effect of each individual parameter on the FCA output. As a result, the combined effect of the results discussed in the previous two subsections are difficult to predict. Two different analyses are employed in order to determine these effects. The OFCA refers to the "original" real-time analysis, as used by the Adelaide group. This analysis uses the three-lag cubic-spline interpolation and the six-lag cross-correlation function Gaussian fit. The RFCA refers to the "revised" analysis, using polynomial zero-lag interpolation of order equal to half the number of lags on the main peak of the auto-correlation function and cross-correlation Gaussian fits restricted to the main peak.

The OFCA and RFCA estimates of ρ_{0ij} for the model-generated data-set MOD-VHF-SAMP are shown in Figure 4.19. These values include the effects of the zero-lag auto-correlation renormalization. The OFCA estimates show a small increase with increasing sampling time followed by a sharp decrease. The initial increase results from the increase in the cross-correlation functions resulting from "over-normalization" due to the increasing underestimation of the zero-lag auto-correlation interpolation. The sharp decrease seen at larger sampling times results from the increasing underestimation of ρ_{0ij}. The RFCA estimate show a steady increase with increasing sampling time resulting from the increase in the cross-correlation "over-normalization".

The OFCA and RFCA true velocity magnitudes obtained using the model-generated data-set MOD-VHF-SAMP are shown as a function of sampling time in Figure 4.20. These velocities exhibit similar behavior to the corresponding ρ_{0ij} variations shown in Figure 4.19. The corrected fading time $T_{0.5}$ and pattern scale $S_{0.5}$ also show similar behavior. The apparent velocity however is calculated directly from the τ'_{ij} estimates, and is therefore approximately independent of the sampling time. These results suggest the need to establish a maximum sampling time $\Delta t_{\max}$ for the satisfactorily performance of the FCA. As $\tau_{0.5}$ is the half-width of the mean auto-correlation function it appears sensible to express $\Delta t_{\max}$ in terms of this quantity. The fading times corresponding to the velocity variations seen in Figure 4.20 are those shown in Figure 4.18, which suggest that $\tau_{0.5} \rightarrow 1.1$ s as $\Delta t \rightarrow 0$ s. If a maximum variation from the actual velocity magnitude of 10% is assumed acceptable, Figure 4.20 suggests $\Delta t_{\max} = 0.7$ s is the maximum sampling time for both the overestimation exhibited by the RFCA velocity and the underestimation exhibited by the OFCA velocity. This result suggests a maximum sampling time given by

$$\Delta t_{\max} = 0.63\tau_{0.5}. \tag{4.46}$$

Because the fading time decreases with increasing turbulent motions the maximum sampling time given by (4.46) will also decrease.

It is possible to proceed one step further and express $\Delta t_{\max}$ in terms of the radar operation parameters and the expected atmospheric conditions. The results of Chapter 3 indicate that in the absence of turbulent motions the aspect sensitivity parameter θ_s can be accurately estimated using both (3.26) and (3.28). Substituting these equations into (4.46) yields

$$\Delta t_{\max} = \frac{4.8\lambda}{|\vec{V}|}[\arcsin((\sin^{-2}\theta_s + \sin^{-2}\theta_b)^{-1/2})]^{-1}, \tag{4.47}$$

where λ is the radar wavelength, θ_s is the aspect sensitivity in degrees, and θ_b is the beamwidth in degrees. Because θ_s and θ_b are specified in degrees the result of the arcsin must also be specified in degrees. The maximum velocity magnitude $V_{\max}$ for the acceptable performance of the FCA can be expressed as a function of the sampling time Δt by the equation

$$\Delta V_{\max} = \frac{4.8\lambda}{\Delta t}[\arcsin((\sin^{-2}\theta_s + \sin^{-2}\theta_b)^{-1/2})]^{-1}. \tag{4.48}$$

These equations can be used to estimate the sampling time and velocity limits for specific radars. Given known values of λ, θ_b, and the expected maximum θ_s for the height range probed by the radar, (4.47) can be utilized to determine $\Delta t_{\max}$ using the maximum expected

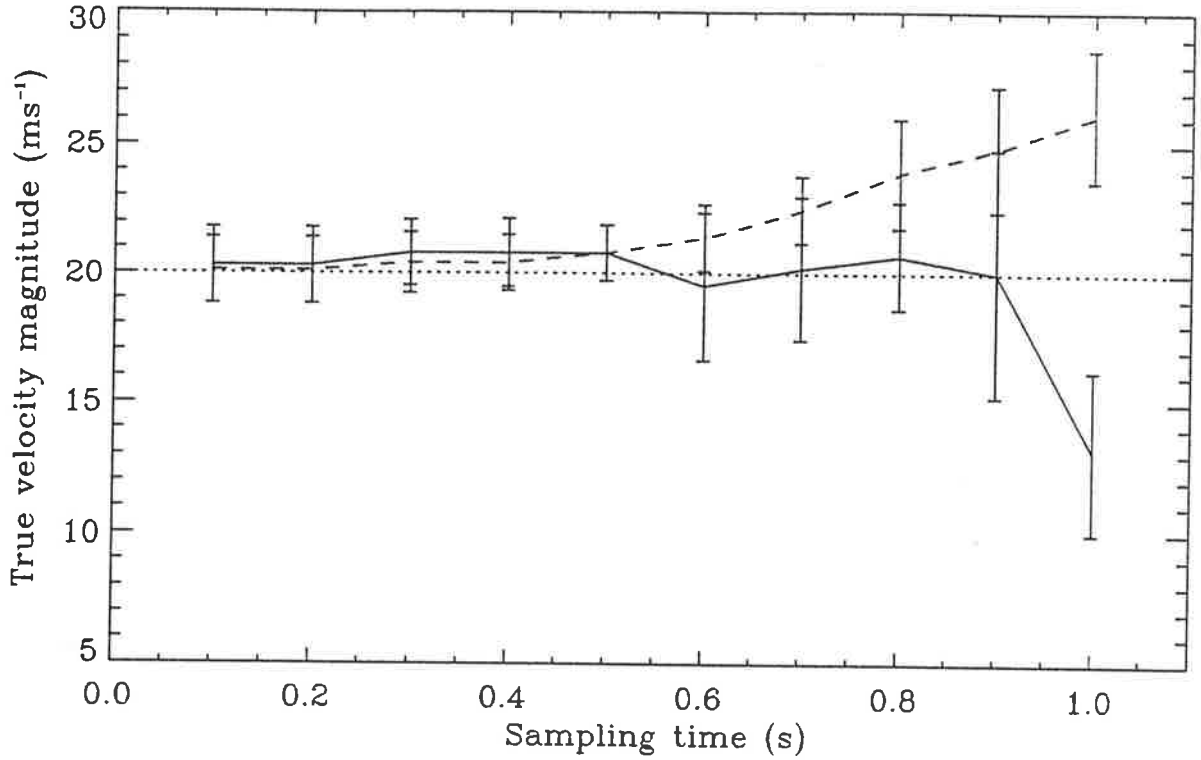

Figure 4.20: True velocity estimated by the OFCA (solid line) and RFCA (dashed line) as a function of sampling time for the model-generated data-set MOD-VHF-SAMP. The error bars indicate the standard deviations of the distributions, while the dotted line indicates the magnitude of the model input velocity.

velocity, and (4.48) can be employed to determine $V_{\max}$ using the sampling time. Because conditions of maximum velocity and maximum aspect sensitivity are seldom observed at the same height the values of $\Delta t_{\max}$ and $V_{\max}$ derived by these formulae may appear somewhat underestimated. However, turbulent motions are not accounted for in these formulae. Turbulent motions would result in a decrease in both $\Delta t_{\max}$ and $V_{\max}$, thereby compensating for the initial underestimation.

The BP VHF radar operates over a height range of 2-20 km. The half-power half-width of the transmitted beam has recently been calculated using two independent models to be approximately 1.65° (e.g. *Low*, [1995]; *Cervera*, [1996]). Over the height range of the radar the maximum θ_s encountered will be $\approx 10°$ (e.g. *Hocking et al.*, [1986]), while the maximum wind velocity magnitude encountered will be $\approx 80\text{ms}^{-1}$ (e.g. *Van Baelen et al.*, [1990]). Substituting these parameters into (4.47) yields a maximum sampling time of 0.17 s. This is significantly smaller than the effective sampling time of 0.5 s currently employed for the real-time analysis. The relevant $V_{\max}$ obtained using $\Delta t = 0.5$ s for these conditions is 27.3 ms^{-1}. These results suggest that the FCA will suffer from biases related to the sampling

time when applied to data obtained using the BP VHF radar in real-time analysis mode. The operational parameters for the BP MF radar in the SA configuration are shown in Table 2.2 of Chapter 2. Over the operating height range of 60-100 km, the maximum expected aspect sensitivity will be $\approx 10°$ (e.g. *Reid*, [1990]), while the maximum wind velocity magnitude maximum encountered will be $\approx 150\ \mathrm{ms}^{-1}$. Substituting these parameters into (4.47) yields a maximum sampling time of 0.5 s, which exceeds the present effective sampling time of 0.4 s. The relevant $V_{\max}$ obtained using $\Delta t = 0.4$ s is 187 ms^{-1}. These results suggest that the FCA will not suffer from biases related to the sampling time when applied to data obtained using the BP MF radar in the SA real-time analysis mode.

The velocity magnitude fall-off seen in Figure 4.20 can explain some results which suggest that the FCA may underestimate the actual wind velocity magnitude. The model-generated data-set MOD-VHF-VEL has been employed for this process. This data uses model velocity magnitudes ranging from 10 to 50 ms^{-1} and a sampling time of 0.5 s. The average OFCA and RFCA true velocity magnitudes estimated using the data-set MOD-VHF-VEL are shown in Figure 4.21 as a function of the model input velocity magnitude. Both the OFCA and RFCA accurately estimate the model velocity magnitude below 30 ms^{-1}. However, the FCA true velocity magnitude diverges from the model velocity magnitude above this value. The fall-off seen in the OFCA true velocity magnitude has also been seen in some comparisons of VHF radar FCA velocities and radiosonde wind velocities. In particular, Figure 5 of *Vincent et al.* [1987] and Figure B.3 of *Rajopadhyaya* [1994], which are reproduced in Figure 4.22, appear to show this effect. Both of these results were produced using the Adelaide VHF radar, the latter utilizing the OFCA technique. In general, the "fall-off" velocity will be greater than shown in Figure 4.21. These results were obtained using a constant θ_s value of 3°, corresponding to a pattern scale of 50 meters. However, larger velocities are usually seen at heights where $\theta_s < 3°$, corresponding to larger pattern scales, thereby resulting in larger estimated fall-off velocity magnitudes as derived from (4.48).

The true velocity magnitude fall-off observed in the application of the real-time FCA for the BP VHF radar could be eliminated by using sampling times less than 0.17 s. This could be achieved by reducing the number of coherent integrations by a factor of 4, thereby reducing the sampling time to 0.125 s. This will increase the volume of data recorded, which may require more efficient data handling. This will also result in a decrease in the SNR of the time-series records, which may lead to a decrease in the acceptance rate. On the positive side however, this will enable the accurate estimation of velocity magnitudes of up to 110

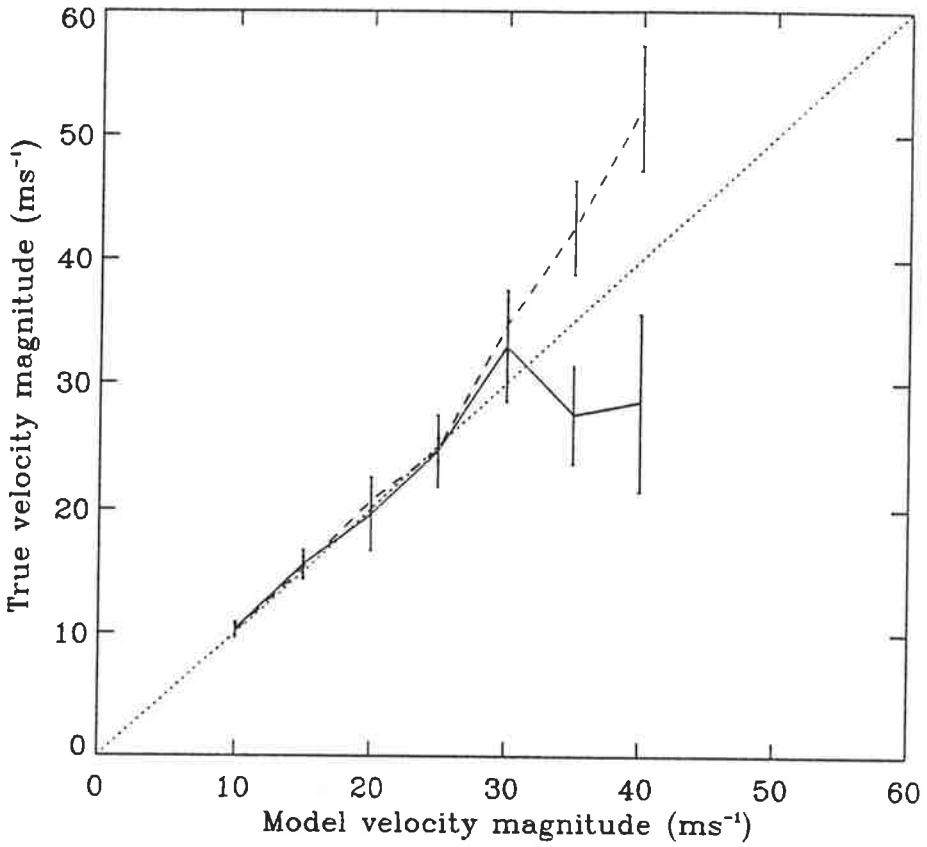

Figure 4.21: True velocity estimated by the OFCA (solid line) and RFCA (dotted line) as a function of sampling time for the model-generated data-set MOD-VHF-VEL. The error bars indicate the standard deviations of the distributions.

ms^{-1}.

4.6.4 Summary

The effects of the sampling time upon the interpolation and fitting procedures employed by the FCA have been investigated in this section. The results reveal that the accuracy of these procedures decreases with increasing sampling time. The zero-lag auto-correlation interpolation is employed to correct for the effects of noise, as described in Appendix C. The interpolated value is used to renormalize the cross-correlation function. As the sampling time is increased there is an increasing tendency for the zero-lag auto-correlation interpolation to underestimate the "noise-free" zero-lag auto-correlation, thereby resulting in an "over-normalization" of the cross-correlation function. The underestimation also results in an overestimation of the fading time $\tau_{0.5}$, and an underestimation of the SNR.

The cross-correlation Gaussian fit is employed to estimate the position τ'_{ij} and magnitude ρ_{0ij} of the maximum of the cross-correlation function. If the Gaussian fit employs a constant

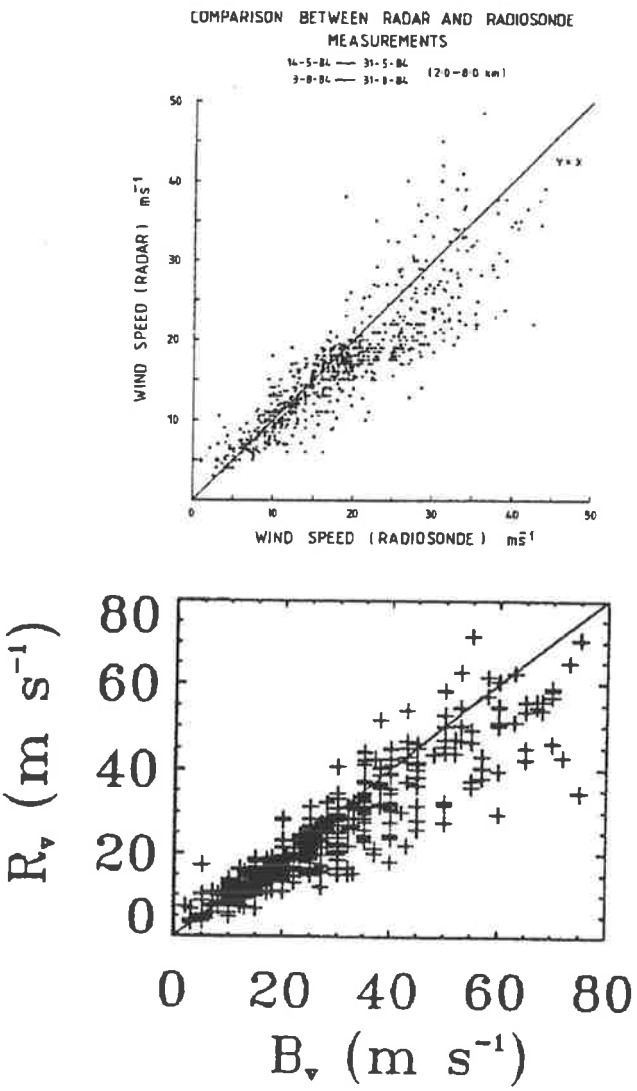

Figure 4.22: Reproduction of Figure 5 of *Vincent et al.* [1987] (top) and Figure B.3 of *Rajopadhyaya* [1994] (bottom) illustrating the velocity fall-off sometimes seen in the application of the FCA to tropospheric VHF radar data. The horizontal axis for each plot indicates the magnitude of the velocity estimated by radiosondes, while the vertical axis indicates the magnitude of the velocity estimated by the VHF radar.

number of lags the fitting region will extend further into the tails as the sampling time is increased ρ_{0ij}. The fit is therefore compromised between fitting the main peak and the tails, resulting in an underestimate of ρ_{0ij}. If the lags within the tails are precluded from the Gaussian fit this problem is reduced. However, in this case the FCA true velocity magnitude increases with sampling time as a result of the increasing underestimation of the zero-lag auto-correlation. In order to avoid these effects an expression for the maximum sampling time for the accurate application of the FCA has been derived. These results suggest that the

maximum sampling time for a typical VHF radar operating in the troposphere and stratosphere is approximately 0.17 s. The results obtained can explain a number of results which suggest that the FCA true velocity may underestimate the actual wind velocity magnitude.

4.7 Effect of scattering mechanism upon the FCA

The FCA is based upon the volume scatter assumption, whereby the entire volume illuminated by the transmitted beam is assumed to produce signal returns. In practice, the returns will result from Bragg scatter, Fresnel reflection, and Fresnel scatter from a number of irregularities which are randomly distributed throughout the radar volume. As a result, only a small percentage of the radar volume will actually produce signal returns. This is exactly the situation simulated by the radar backscatter model described in Chapter 3, which has been shown to produce results in very good agreement with those predicted by the "true" volume-scatter situation. The recently developed Doppler-selected imaging interferometry techniques which are discussed in Chapter 8 are based on the "discrete scatter" assumption, whereby the spectral information for each Doppler frequency is assumed to result from a single discrete scattering region. The analytical model of *Liu et al.* [1990] predicts that the FCA true velocity will not accurately estimate the wind velocity in the discrete scatter situation on the basis that the estimates of τ'_{ij} will differ from those expected in the volume-scatter situation.

The performance of the FCA in the transition between the discrete and volume scatter situations has been investigated using the model-generated data-set MOD-MF-IDI-NSCAT. This data was generated using 10, 20, 50, 100, 200, 500 and 1000 scatterers within the model enclosing volume, using turbulent motion velocities ν_{mod} of 0 and 6 ms^{-1}. Because this data-set was generated for the investigation of the Doppler-selected imaging interferometry techniques the antennae are arranged along two orthogonal arms, as illustrated in Figure A.1 of Appendix A. As a result, the antenna configuration employed for the FCA must necessarily be a right-angled triangle. This configuration is generally considered to be unideal for the FCA as directional biases in the true velocity and the characteristic ellipse can result. These biases are addressed in Chapter 5. The antennae 1, 3, and 6 have been chosen for the analysis as they provide the best match between antenna spacing and the expected pattern scale of $\approx$ 310 m. As the radar volume used for this simulation is approximately one quarter of the volume of the enclosing volume the average number of scatterers within the radar volume

is approximately one quarter of the number of scatterers N_{scat} within the enclosing volume. The returned power for any scatterer can vary by up to two orders of magnitude, depending on the position of the scatterer. This must be taken into account in the following results, as it is possible that the returned power from any individual scatterer may significantly exceed the returned power from the remaining scatterers within the radar volume, thereby giving the impression that the FCA is more susceptible to discrete scatter than is actually the case.

The results obtained on applying the FCA to the model-generated data-set MOD-MF-IDI-NSCAT with $\nu_{\text{mod}} = 0$ ms^{-1} are shown in 4.23. In this situation the true and apparent velocities should both be equivalent to the model input velocity. There are very few acceptances for smaller values of N_{scat}. The majority of rejections result from rejection criteria 3, due to slow fading and oscillatory correlation functions. For instance, 80% of records are rejected by this criteria for $N_{\text{scat}} = 10$. The time-series of these records exhibit strong sinusoidal behavior as they are comprised of the returns from a small number of scatterers. As a result, $\tau_{0.5}$ measures the period of the sinusoidal behavior rather than the fading period resulting from the interference of the returns from a larger number of scatterers. The 4% of records that do pass this rejection criterion also exhibit the same sinusoidal behavior. The inclusion of these records cannot be avoided, as reinforcing rejection criterion 3 to reject these records would result in the rejection of a significantly larger number of legitimate records for larger values of N_{scat}. As N_{scat} decreases the difference between the apparent and model input velocities increases. This result confirms the suggestions of *Liu et al.* [1990] that the estimates of τ'_{ij} obtained in the discrete scatter situation will differ from those obtained in the volume scatter situation situation. Despite this effect, the true velocity accurately predicts the model input velocity for $N_{\text{scat}} \geq 50$, corresponding to an average of 12 or more scatterers within the radar volume contributing signal returns.

The pattern scale $S_{0.5}$ and axial ratio R_{ax} show a significant increase with decreasing N_{scat}. These results can be explained by taking into account the ground diffraction pattern produced by a small number of scatterers, as considered by *Holmes* [1974]. The ground diffraction pattern produced by a single scatterer is approximately constant over spatial scales significantly smaller than the range of the scatterer. The ground diffraction pattern produced by two scatterers exhibits a "fringe" structure. The azimuth of the fringes is dependent upon the position of the two scatterers, and is therefore essentially random. The characteristic ellipse of the corresponding spatial correlation function is elongated along the direction of the fringes. The ground diffraction pattern produced by three non-colinear scatterers has three

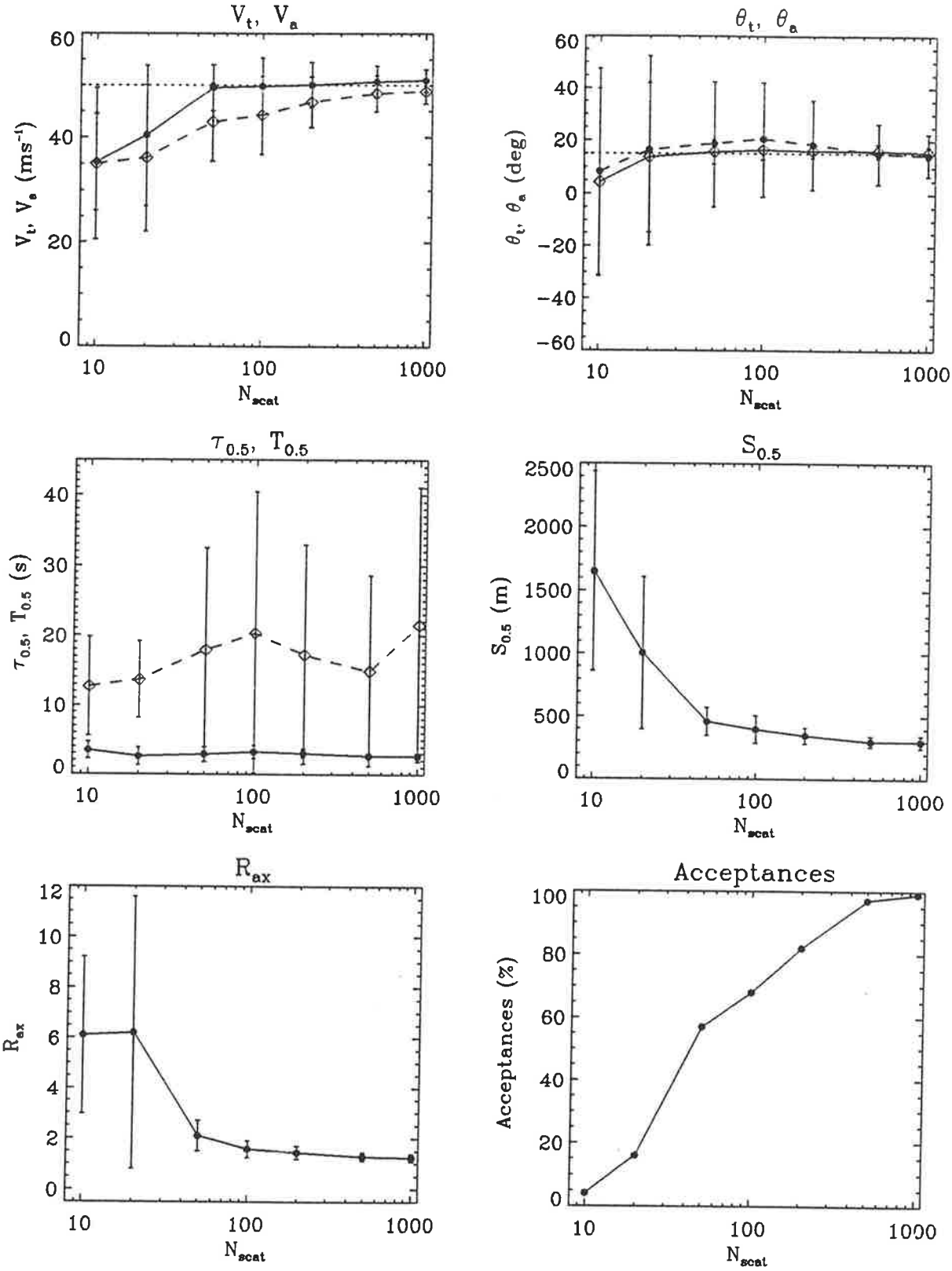

Figure 4.23: Results of the application of the FCA to the model-generated data-set MOD-MF-IDI-NSCAT using $\nu_{\mathrm{mod}} = 0$ ms^{-1} as function of the number of model scatterers N_{scat}. The top plots show the magnitude (left) and direction (right) of the vector averaged true ($\bullet$) and apparent ($\diamond$) velocities. The middle left plot shows the fading time $\tau_{0.5}$ ($\bullet$) and the corrected fading time $T_{0.5}$ ($\diamond$). The remaining plots show the pattern scale $S_{0.5}$ (middle right), axial ratio R_{ax} (bottom left) and acceptance percentage (bottom right). The error bars denote the standard deviations.

sets of fringe structures which combine to produce a ground diffraction pattern with elongated elliptical contours. The characteristic ellipse of the corresponding spatial correlation function is elongated in the same azimuth as the ground diffraction pattern. As the number of scatterers is gradually increased the elongation of the ground diffraction pattern and the corresponding characteristic ellipse is reduced, and the pattern becomes isometric. It follows from these arguments that R_{ax} and $S_{0.5}$ should increase as N_{scat} decreases, as is seen in Figure 4.23.

The results obtained on applying the FCA to the model-generated data-set MOD-MF-IDI-NSCAT with $v_{mod} = 6$ ms^{-1} are shown in 4.24. These results are very similar to those obtained for $v_{mod} = 0$ ms^{-1} as shown in Figure 4.23, with a few noticeable exceptions. The true velocity appears to provide a reasonable estimate of the model input velocity for $N_{scat} \geq 50$, although there is some tendency for V_t to overestimate the model input value, especially for $N_{scat} = 100$ and 200. This overestimation is reduced if rejection criteria 10 is abandoned, but is not totally removed. As N_{scat} is decreased the apparent velocity magnitude V_a decreases, while $T_{0.5}$ increases. This behavior can be understood in terms of the fact that decreasing the number of scatterers necessarily reduces the amount of random changes in the pattern, thereby decreasing V_a and increasing $T_{0.5}$. For smaller values of N_{scat} the dominating factor in the decrease in V_a is the "non volume scatter" estimate of τ'_{ij} described by *Liu et al.* [1990], as seen for the $v_{mod} = 0$ ms^{-1} case of Figure 4.23.

The results of the model analysis presented in this section suggest that the FCA true velocity will provide an acceptable estimate of the model input velocity if in excess of 50 scatterers are employed. This corresponds to an average of approximately 12 scatterers within the radar volume contributing signal returns. These scatterers will produce signal returns with powers varying over two orders of magnitude, suggesting that as few as 4 scatterers may actually be contributing significant signal returns. The corresponding scatterer number density for $N_{scat} = 50$ is only 7×10^{-3} km^{-3}. Thus although the FCA is based on the volume scatter assumption it can produce reasonably accurate estimates of the actual wind velocity for very small numbers of scatterers. The results also confirm the suggestions of the analytical model analysis of *Liu et al.* [1990] that the estimates of τ'_{ij} obtained in the discrete scatter situation will differ from those expected in the volume-scatter situation.

The acceptance rates for $N_{scat} = 50$ are $\approx 60\%$ for $v_{mod} = 0$ ms^{-1}, and $\approx 50\%$ for $v_{mod} = 6$ ms^{-1}. The most occurrent rejections are those due to criteria 3, 4, and 5. These rejections are also the most occurrent in the region above 90 km for the application of the

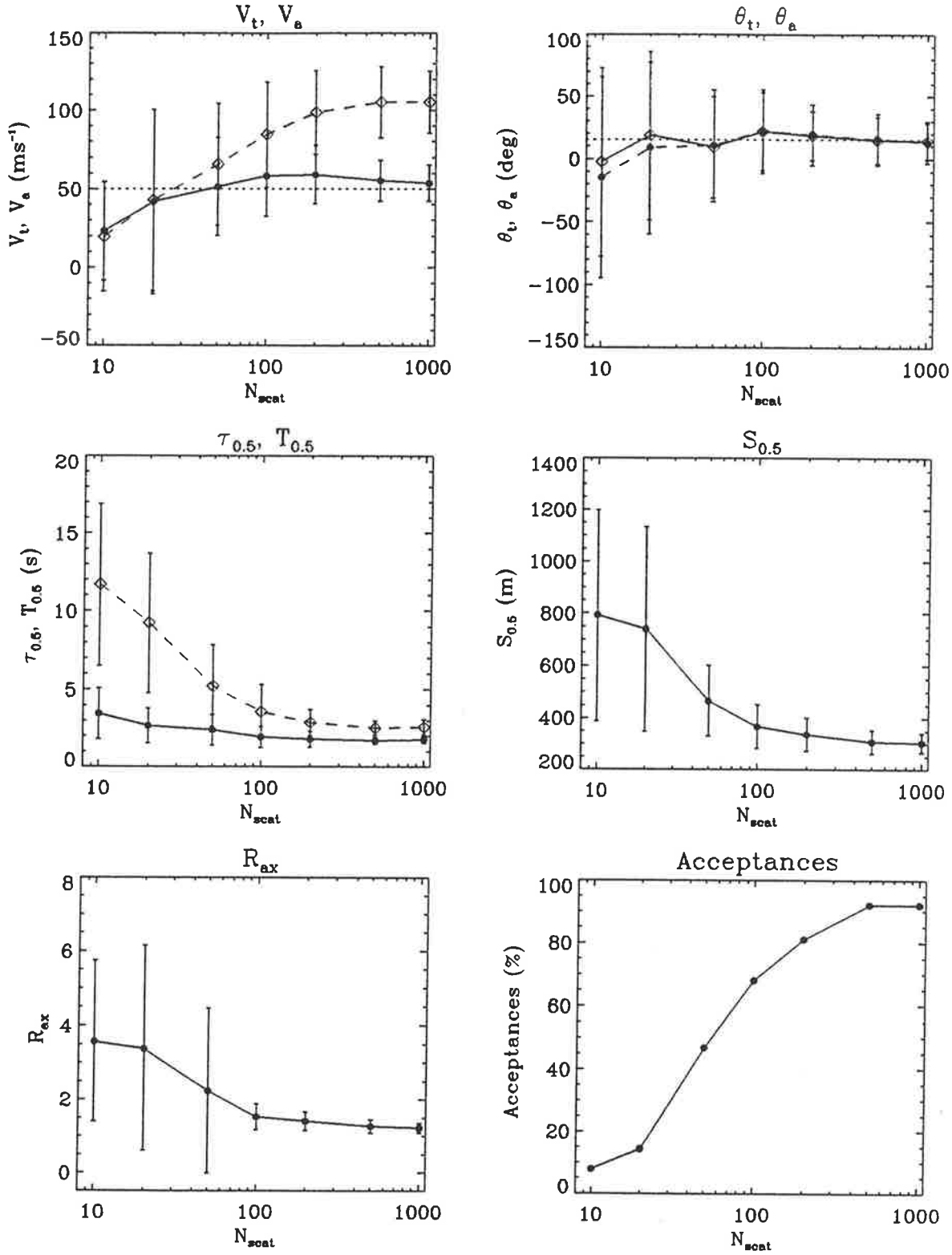

Figure 4.24: Results of the application of the FCA to the model-generated data-set MOD-MF-IDI-NSCAT using $\nu_{\mathrm{mod}} = 6$ ms^{-1} as function of the number of model scatterers N_{scat}. The top plots show the magnitude (left) and direction (right) of the vector averaged true ($\bullet$) and apparent ($\diamond$) velocities. The middle left plot shows the fading time $\tau_{0.5}$ ($\bullet$) and the corrected fading time $T_{0.5}$ ($\diamond$). The remaining plots show the pattern scale $S_{0.5}$ (middle right), axial ratio R_{ax} (bottom left) and acceptance percentage (bottom right). The error bars denote the standard deviations.

FCA to the BP data-set BP940527, as shown in Figure 4.13. These rejections have been attributed to the existence of total reflection "glints" resulting from regions of distorted specular layers which are perpendicular to the radar. The existence of these glints has been shown to result in an underestimation of the FCA true velocity in the experimental studies of *Meek and Manson* [1992]. The results also illustrate that $S_{0.5}$ and R_{ax} increase as N_{scat} decreases, suggesting the characteristic ellipse becomes more elongated. The axial rotation θ_{ax} of the characteristic ellipse obtained in these circumstances is dependent upon the positions of the scatterers contributing the signal returns, and is therefore random. This suggests that the discrete scatter situation assumed by the Doppler selected imaging interferometry techniques should produce small FCA acceptance rates, estimates of R_{ax} significantly greater than unity, and randomly distributed estimates of θ_{ax}. The observation of such results could confirm the applicability of the discrete scatter situation and therefore the Doppler-selected imaging interferometry techniques. This idea will be further extended in Chapter 8.

4.8 The effect of time-series length and coherent averaging upon the FCA

4.8.1 The effect of time-series length upon the FCA

The effects of the time-series length N upon the FCA have been investigated using the model generated data-set MOD-MF-4096. This data-set was generated using the standard MF simulation parameters, consisting of 30 records of 4096 samples. These records were divided into records of length 2048, 1024, 512, 256 and 128 for the application of the FCA.

The effects of the time-series length upon the magnitude of the auto- and cross-correlation functions employed by the FCA are illustrated in Figure 4.25. The main peak of the auto-correlation function does not appear to be influenced significantly by the time-series length. On the other hand, the main peak of the cross-correlation function appears to be located closer to zero-lag for larger N. This effect is seen in most of the cross-correlation functions studied, and leads to a decrease in the estimate of τ'_{ij} as N increases. The tails of the correlation functions decrease with increasing N. It appears that the increase in τ'_{ij} seen with decreasing N may be the result of the increasing prominence of these tails.

The results of the application of the FCA to the different record lengths are shown in

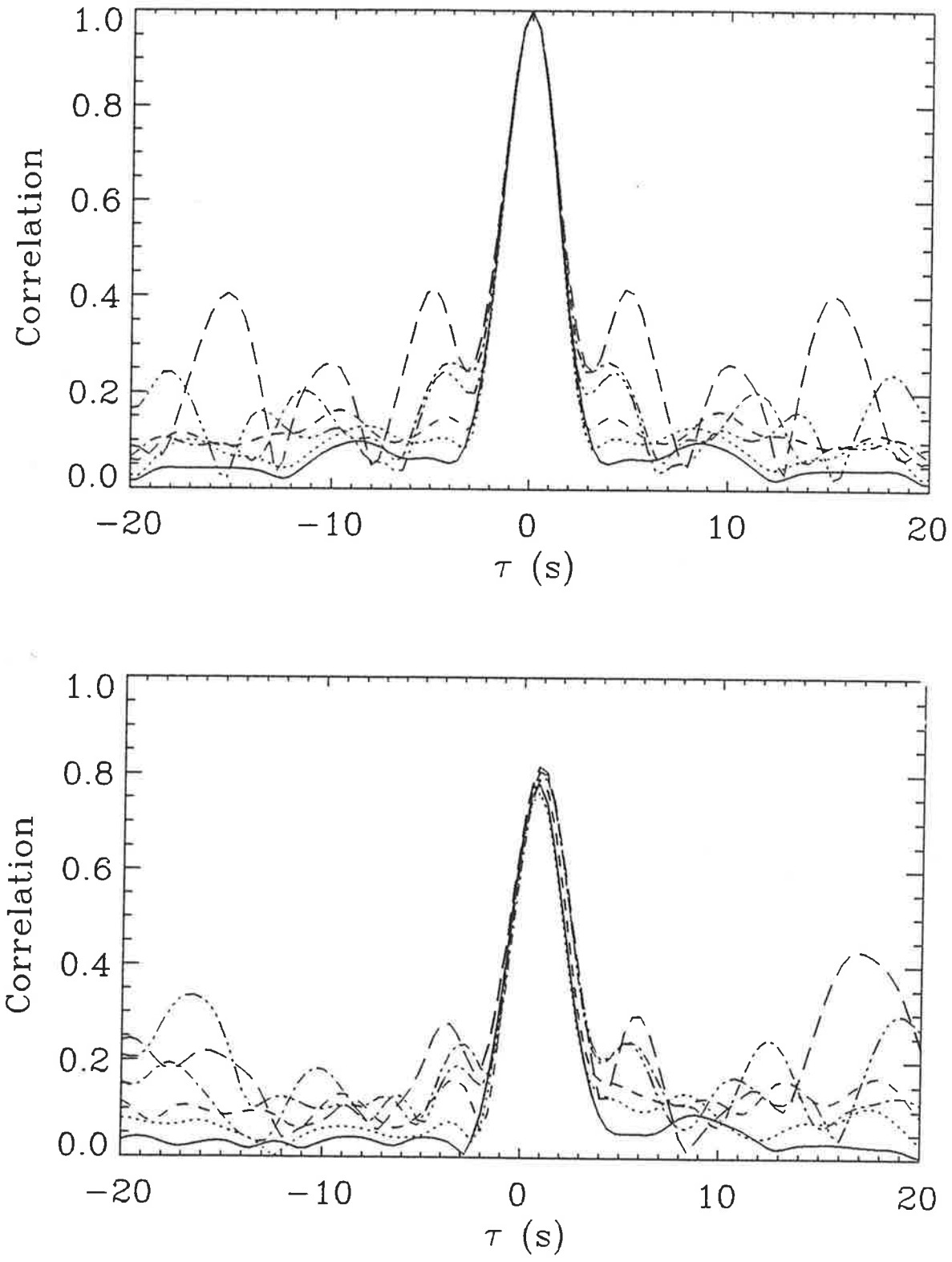

Figure 4.25: Effect of time-series length upon the auto- (top) and cross-correlation functions (bottom). The individual lines indicate the functions obtained using time-series lengths of 4096 (solid line), 2048 (dotted line), 1024 (dashed line), 512 (dash-dot line), 256 (dash-triple dot line) and 128 (long-dashed line).

Figure 4.26. The estimates of V_t show increasing agreement with the model input value as the length of the time-series N is increased. The estimates of V_a show a small increase with increasing N, as expected from the decrease in τ'_{ij} seen with increasing record length as suggested by the results of Figure 4.25. The decrease in τ'_{ij} is also directly responsible for the decrease seen in $T_{0.5}$ with increasing N. The estimates of $\tau_{0.5}$ are approximately constant, as expected from the results of Figure 4.25 which suggest that the width of the auto-correlation function is independent of N. The estimates of the axial ratio $R_{\rm ax}$ show increasing agreement with the value of unity expected for the isotropic scatter mechanism employed by the model to generate this data-set with increasing N. This behavior was predicted by *Røyrvik* [1993], and suggests the "false" anisometry exhibited in the isotropic scatter histogram of $R_{\rm ax}$ of Figure 4.11 is a result of using short time-series lengths. As discussed in Chapter 3, $T_{0.5}$ can be used to obtain an estimate of the turbulent motions velocity ν (e.g. *Briggs*, [1980]), while $S_{0.5}$ and $R_{\rm ax}$ can be used to obtain as estimate of the aspect sensitivity parameter θ_s (e.g. *Lesicar and Hocking*, [1992]). The estimates of ν and θ_s obtained on applying these techniques are shown in Figure 4.26. The agreement with the model input values increases with increasing N, as is also the case for V_t. The increasing agreement between the FCA and model input parameters observed with increasing N can be understood in terms of the fact that the total number of scatterers contributing to the time-series records is increased. The records therefore increasingly correspond with the "true" volume scatter situation described in section 4.7. The results obtained on applying the FCA to these records therefore show increasing agreement with the results expected in the volume scatter situation.

The results of Figure 4.26 suggest that the accuracy of the FCA estimates increase with increasing time-series length N. The results of Figure 4.25 suggest that this may be partially related to the reduction of the tails of the cross-correlation function. Although the FCA uses the information contained within the main peak of the correlation functions it is clear that the main peak of the cross-correlation functions can be influenced by the behavior in the tails. The overestimation of V_t exhibited for smaller values of N is a direct result of the underestimation of the effects of turbulent random motions. It is interesting to note that the spectral-width turbulent velocity estimation technique (e.g. *Hocking*, [1983b]) employed in Chapter 3 suffers the same limitations. The use of short time-series lengths results in spurious spikes in the power-spectra. These spikes result in the underestimation of the spectral width, and the subsequent underestimation of the turbulent velocity. These spectral spikes are directly related to the tails of the correlation functions (e.g. *May*, [1987]).

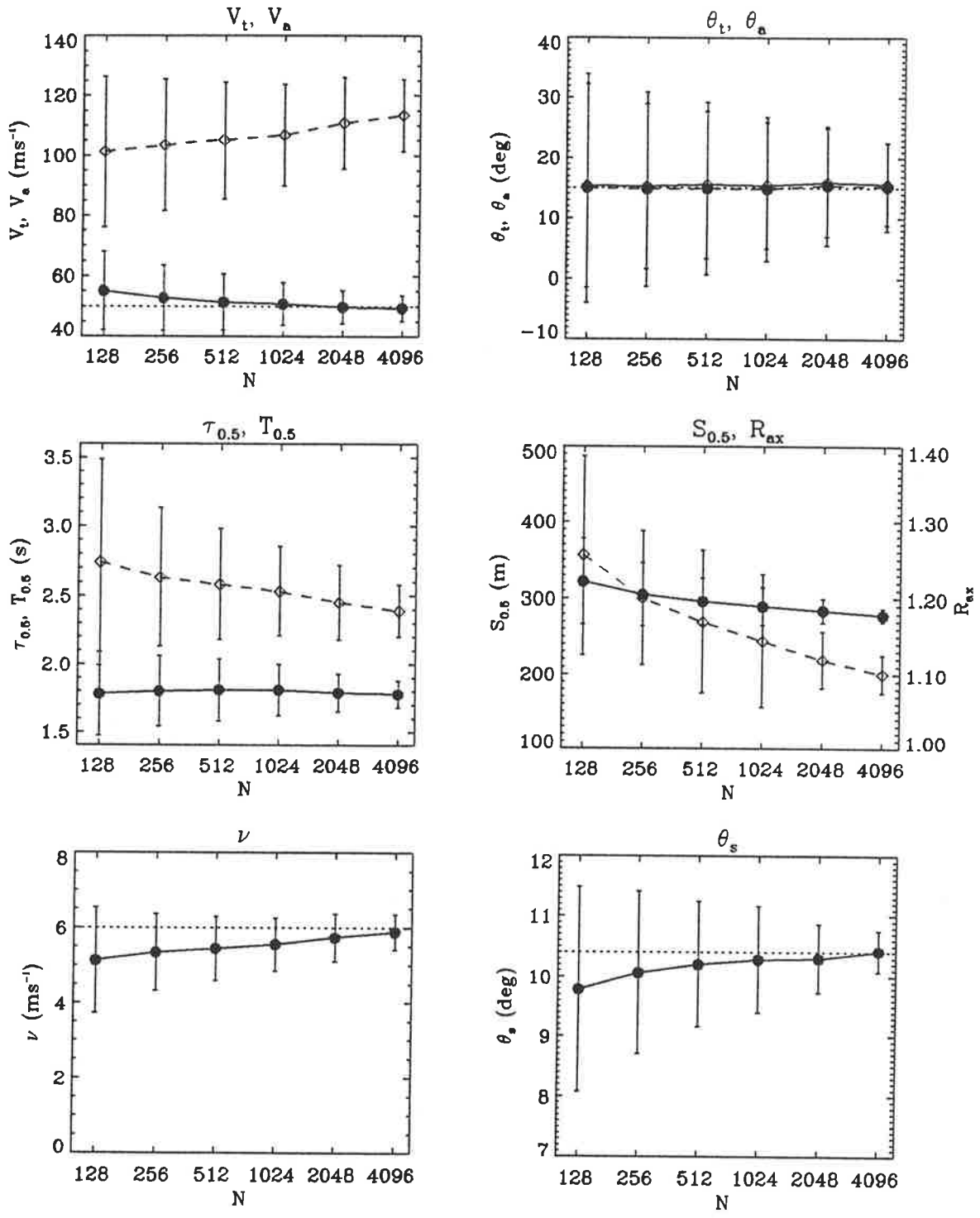

Figure 4.26: Results of the application of the FCA as a function of record length N for the model-generated data-set MOD-MF-4096. The top plots show the magnitude (left) and direction (right) of the vector averaged true (•) and apparent (◇) velocities. The middle left plot shows the fading time $\tau_{0.5}$ (•) and the corrected fading time $T_{0.5}$ (◇). The middle right plot shows the pattern scale $S_{0.5}$. The bottom plots show the estimates of ν (left) and θ_s (right).

The results of this analysis suggest that the record length should be made as long as possible for the application of the FCA. This assessment is based on the fact that the agreement between the FCA and model input parameters increases with record length. The variation in the individual estimates is also reduced significantly as the record length is increased. It is important to stress that it is the temporal duration of the record which is important factor rather than the number of samples. The results of *Awe*, [1964] suggest that basic shape of the correlation functions is approximately independent of the sampling time. The results of this section were obtained using a sampling time of 0.4 s. The 4096 sample time-series therefore corresponds to a duration of approximately 27 minutes. The use of such a time-series length may not be optimal in practice because the atmospheric dynamics can sometimes change appreciably over this time-scale. Furthermore, such a time-series length will preclude the determination of short-period fluctuations of the atmospheric dynamics, such as those resulting from short-period gravity waves.

4.8.2 The effect of coherent averaging upon the FCA

There has been an increasing tendency of late for some authors to apply the FCA to correlation functions obtained from the inverse Fourier transform of the spectra obtained by coherently averaging[1] the spectra obtained from individual records (e.g. *Liu and Pan*, [1993]). This technique produces correlation functions which are very similar to those obtained by coherently averaging the individual correlation functions. The effects of coherent averaging upon the FCA have been investigated using the model generated data-set MOD-MF-SA with $\nu_{\mathrm{mod}} = 6$ ms^{-1}. The results are shown in Figure 4.27. There is considerable similarity between the results of increasing the number of coherent averages N_{av} and the results of increasing the time-series record length N, as shown in Figure 4.26. The estimates of V_t show increasing agreement with the model input value as the number of averages N_{av} is increased. The estimates of V_a show a small increase with increasing N_{av}, while the estimates of $\tau_{0.5}$ show a small decrease with increasing N_{av}. The combination of these two effects results in an decrease in $T_{0.5}$. The pattern scale $S_{0.5}$ and axial-ratio R_{ax} also decrease with increasing N_{av}.

The decrease in $\tau_{0.5}$ can be understood by analyzing the effect of the averaging upon the auto-correlation function, as shown in Figure 4.28. At zero-lag the auto-correlation functions

[1]The term "coherent averaging" is used throughout this thesis to described complex averaging. This averaging is sometimes misleadingly described as "incoherent averaging" when applied to the averaging of spectra.

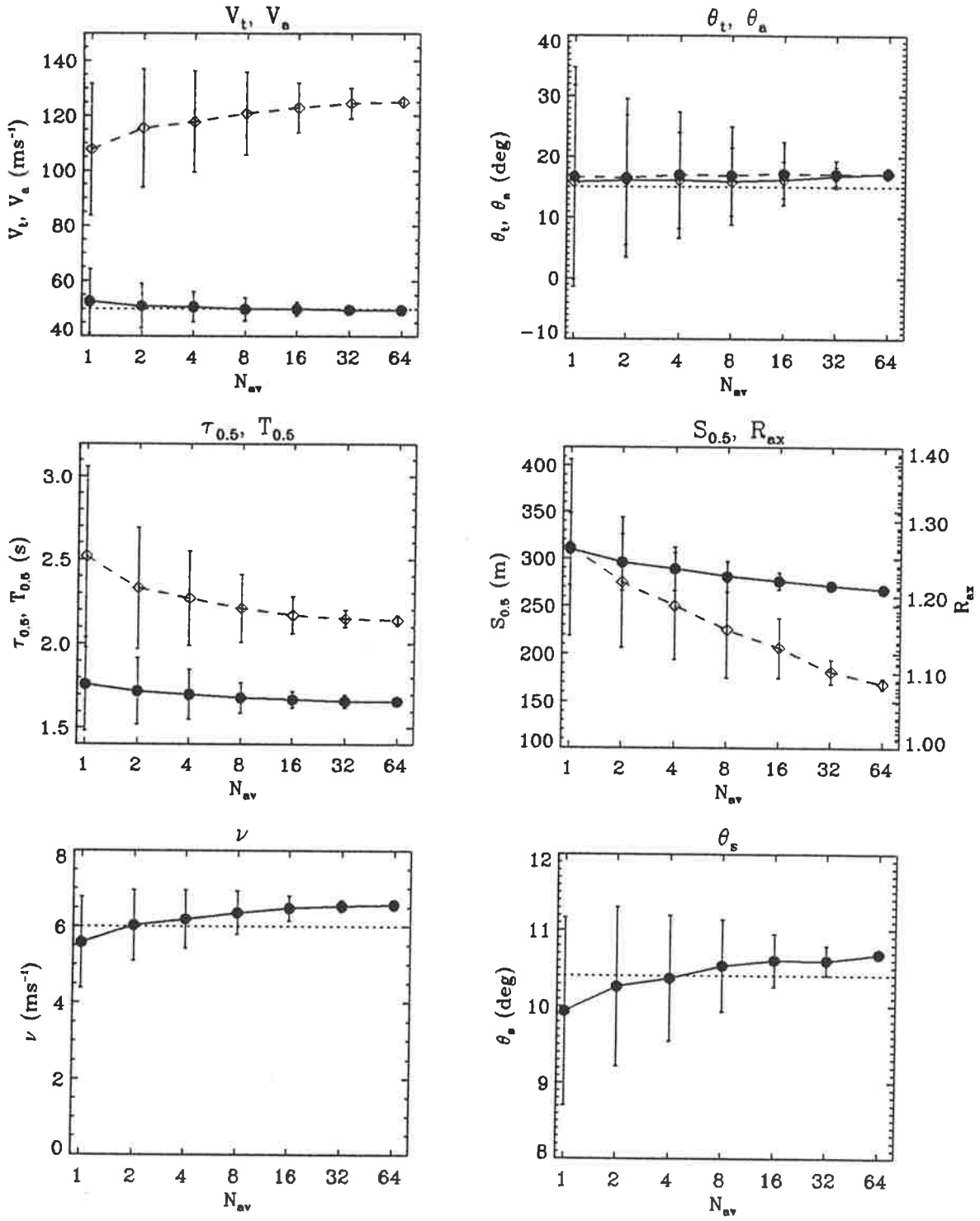

Figure 4.27: Results of the application of the FCA to correlation functions obtained from the coherent average of N_{av} individual correlation functions for the model-generated data-set MOD-MF-SA. The top plots show the magnitude (left) and direction (right) of the vector averaged true (•) and apparent (◇) velocities. The middle left plot shows the fading time $\tau_{0.5}$ (•) and the corrected fading time $T_{0.5}$ (◇). The middle right plot shows the pattern scale $S_{0.5}$. The bottom plots show the estimates of ν (left) and θ_s (right).

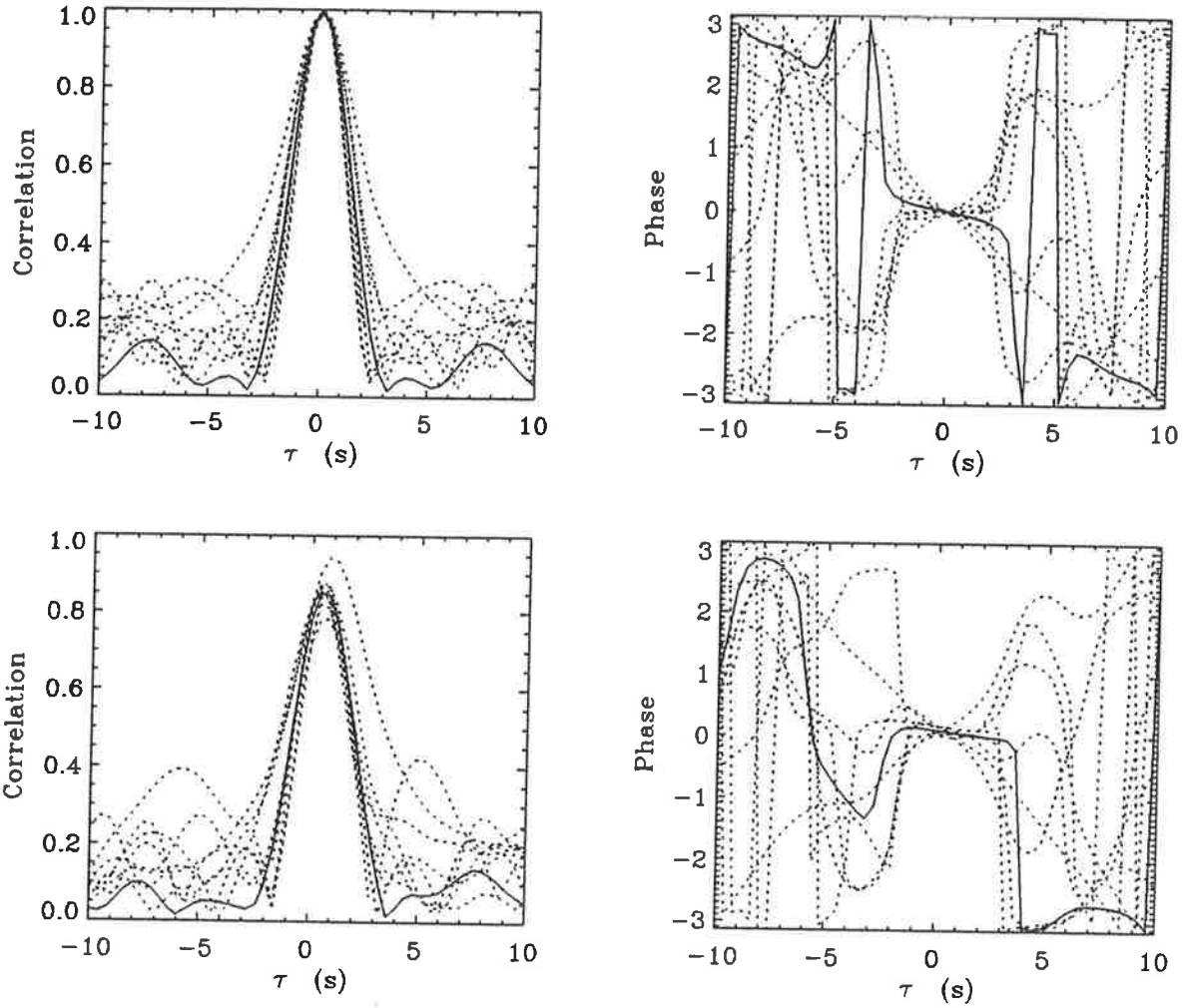

Figure 4.28: Example of the effect of coherent averaging upon the auto- (top) and cross-correlation (bottom) functions. The left plot shows the magnitude, while the right plot shows the phase. The dotted lines indicate the individual correlation functions while the solid line indicates the average correlation function.

are real, with a value of unity. It therefore follows that the averaged auto-correlation function will also be unity at zero-lag. At non-zero lags τ the auto-correlation functions become complex. This effect can be attributed to the effects of radial velocities and off-zenith scatter, as described in Chapter 8. Because the phase values of the individual auto-correlation functions vary it follows that the magnitude of the average auto-correlation function $|\overline{\rho}(\tau)|$ will be smaller than the average of the individual auto-correlation function magnitudes $\overline{|\rho(\tau)|}$ for non-zero lags τ. As the phase variation increases with increasing τ it follows that ratio of $|\overline{\rho}(\tau)|$ to $\overline{|\rho(\tau)|}$ must decrease with increasing τ. This results in the width of the averaged auto-correlation function being smaller than the average of the widths of the individual auto-correlation functions.

The decrease in τ'_{ij} can be understood using similar arguments. The effect of the averaging upon the cross-correlation function is also illustrated in Figure 4.28. The cross-correlation functions have non-zero phase values at all lags. The variation in the phase values of the individual cross-correlation functions increases with increasing lag τ. It therefore follows that the ratio of the magnitude of the average cross-correlation function $|\overline{\rho}_{ij}(\tau)|$ to the average of the magnitude of the individual cross-correlation functions $\overline{|\rho_{ij}(\tau)|}$ will decrease as τ decreases. This will result in the position of the maxima τ'_{ij} of the averaged cross-correlation function being closer to zero-lag.

The similarity between the effects of increasing the time-series record length N and increasing the number of coherent averages N_{av} is due to the fact that both techniques act to increases the number of scatterers contributing to the correlation functions employed by the analysis. The results therefore show a greater correspondence with the results expected in the volume scatter situation. The results of Figure 4.28 also reveal that averaging reduces the tails of the correlation functions. The estimates of ν and θ_s obtained from the estimates of $T_{0.5}$, $S_{0.5}$, and R_{ax} are also shown in Figure 4.27. Although V_t levels off to the model input value the estimates of $T_{0.5}$ and $S_{0.5}$ level off to values exceeding the model input values. This is a direct result of the decrease in $\tau_{0.5}$ as N_{av} is increased. This decrease is not seen with increasing time-series length N because $\tau_{0.5}$ is independent of N. The axial-ratio R_{ax} shows increasing agreement with the model input value of unity with increasing N_{av}.

4.8.3 Summary

The results obtained in this section suggest that the agreement between the FCA and model input parameters increases with increasing time-series length N and increasing number of coherent averages N_{av}. This result has been attributed to the fact that both techniques act to increase the number of scatterers contributing to the correlation functions employed by the analysis. The results obtained on applying the FCA to these correlation functions therefore show increasing agreement with the results expected in the volume scatter situation. The true velocity obtained on applying both techniques shows excellent agreement with the model input velocity. However, because the coherent averaging acts to reduce the fading time $\tau_{0.5}$, the estimates of ν and θ_s slightly overestimate the model input values.

The results therefore suggest that there is no significant difference in using longer time-series lengths and using coherently averaged spectra. It is clear however that both techniques appear to have a significant advantage over the application of the FCA to the typical 2-minute

length time-series. The estimates show better agreement with the model input values, and have significantly smaller errors. The "false" anisometry of the ground diffraction pattern seen using typical length time-series is also eliminated. The only apparent disadvantage in using longer time-series lengths and coherently averaged spectra in the analysis presented here is that the time-resolution of the results is reduced. An advantage of using typical length time-series may be that records failing the analysis are precluded from any averaging of the results. The inclusion of such a time-series within the length of a longer duration time-series may degrade the results, therefore nullifying any advantage gained in using the longer length time-series. Similarly, the inclusion of the correlation functions calculated from such a time-series in a coherent average may also degrade the results.

4.9 Summary and conclusions

In this chapter the full correlation analysis (FCA) technique has been investigated. The mathematical formulation of the FCA has been presented in section 4.2 using spatio-temporal correlation functions obtained using ground diffraction patterns generated by the radar backscatter model. The use of the model-generated data enables the simple visualization of the development of the FCA through the progressive inclusion of the effects of a mean background wind, scatterer anisometry, and turbulent random motions. The application of the FCA is described in section 4.3, which discusses the factors that must be taken into account in applying the experimental application of the FCA.

The effects of turbulent random motions, scatterer anisometry, and gravity waves have been investigated using the radar backscatter model in section 4.4. The effects of increasing the magnitudes of the turbulent random motions is to increase the magnitude of the apparent velocity V_a and decrease the corrected fading time $T_{0.5}$ in accordance with the model of the FCA. There is a slight tendency for the pattern scale $S_{0.5}$ to increase with increasing random motions that is not in accordance with the model of the FCA. This behavior however can be understood by taking into account the effects of the random motions upon the surfaces of constant radial velocity within the radar volume. The effects of increasing the anisometry of the scatterers results in the increase in the axial-ratio R_{ax} and $S_{0.5}$ and the bias of the direction of the apparent velocity θ_a in accordance with the model of the FCA. The estimates of R_{ax} overestimate the model input values by approximately 9%. The histograms of the axial-rotation θ_{ax} peak at an angle perpendicular to the elongation of the scatterers. The

effects of monochromatic gravity waves upon the FCA true velocity are shown to be negligible if the velocity is averaged over the period of the wave. The waves also result in an increase the magnitude of the apparent velocity V_a and decrease the corrected fading time $T_{0.5}$, suggesting that random changes in the ground diffraction cannot be solely attributed to turbulent random motions. The discussion of section 3.4.2 also points out that the effects of finite scatterer lifetimes and wind field inhomogeneities (e.g. *Sürücü et al.*, [1995a]) can also introduce random changes into the ground diffraction pattern.

The application of the FCA to experimentally obtained data is presented in section 4.5. The velocity profiles are typical of those observed during the month of May at Buckland Park, and are consistent with the seasonal results of *Lesicar* [1993]. The results indicate that there are a considerable number of rejections due to slow fading above 90 km, suggesting the existence of total reflection glints.

The effects of the sampling time upon the interpolation and fitting procedures employed by the FCA are investigated in section 4.6. The results reveal that the accuracy of these procedures decreases with increasing sampling time. As the sampling time is increased there is an increasing tendency for the zero-lag auto-correlation interpolation employed to correct for the effects of noise to underestimate the "noise-free" zero-lag auto-correlation, thereby resulting in an "over-normalization" of the cross-correlation function. The underestimation also results in an overestimation of the fading time $\tau_{0.5}$, and an underestimation of the SNR. The cross-correlation Gaussian fit employed to estimate the position τ'_{ij} and magnitude ρ_{0ij} of the maximum of the cross-correlation function is shown to increasingly underestimate ρ_{0ij} with increasing sampling time if the tails of the cross-correlation function are included in the fit. Precluding the tails from the fit removes this problem. In order to avoid these effects an expression for the maximum sampling time for the accurate application of the FCA has been derived. These results suggest that the maximum sampling time for a typical VHF radar operating in the troposphere and stratosphere is approximately 0.17 s. The results obtained can explain a number of results which suggest that the FCA true velocity may underestimate the actual wind velocity magnitude.

The effects of the scattering mechanism upon the FCA have been investigated in section 4.7. The results suggest that the FCA true velocity will provide an acceptable estimate of the model input velocity if in excess of 50 model scatterers are employed. This corresponds to an average of approximately 12 scatterers within the radar volume contributing signal returns. These scatterers will produce signal returns with powers varying over two orders of

magnitude, suggesting that as few as 4 scatterers may actually be contributing significant signal returns. Thus although the FCA is based on the volume scatter assumption it can produce reasonably accurate estimates of the actual wind velocity for very small numbers of scatterers. The results also confirm the suggestions of the analytical model analysis of *Liu et al.* [1990] that the estimates of τ'_{ij} obtained in the discrete scatter situation will differ from those expected in the volume-scatter situation. The results also illustrate that $S_{0.5}$ and R_{ax} increase as N_{scat} decreases, suggesting the characteristic ellipse becomes more elongated. The axial rotation θ_{ax} of the characteristic ellipse obtained in these circumstances is dependent upon the positions of the scatterers contributing the signal returns, and is therefore random.

The effects of the time-series length upon the FCA have been investigated in subsection 4.8.1. The results suggest that the record length should be made as long as possible for the application of the FCA, based on the fact that the agreement between the FCA and model input parameters increases with record length. The variation in the individual estimates is also reduced significantly as the record length is increased. The longer time-series lengths however may not be optimal in practice because the atmospheric dynamics may change appreciably over the time-series length. The effects of coherent averaging upon the FCA have been investigated in subsection 4.8.2. The effects of increasing the number of averages produces results very similar to increasing the time-series length.

The results of this chapter indicate that the FCA is a very robust technique. The analysis of model-generated data illustrates that the FCA true velocity provides an excellent estimate of the model input velocity over a number of different atmospheric conditions.

Chapter 5

The Triangle Size Effect of the FCA

5.1 Introduction

One of the major sources of bias encountered in the application of the FCA is the "triangle size effect" (TSE). The TSE refers to the decrease in the magnitude of the FCA true velocity V_t often seen with decreasing antenna spacing. Similar decreases are also seen in the corrected fading time $T_{0.5}$ and the pattern scale $S_{0.5}$. Additionally, increasing biases are also seen in the direction of the true velocity θ_t and the orientation of the characteristic ellipse θ_{ax} with decreasing antenna spacing. The TSE is still an ongoing concern, and has been recently been exhibited in the analyses of *Meek* [1990] and *Van Baelen et al.* [1990]. Although the term "triangle size effect" infers the results are seen for configurations involving three receiving antennae they are also seen for configurations involving four or more receiving antennae. Despite this inconsistency the effect will be hereafter addressed as the "triangle size effect" throughout the remainder of this thesis.

Although the TSE was initially observed by several authors (e.g. *Kelleher*, [1966]), the first extensive analysis was provided by *Golley and Rossiter* [1970] using the 89 east-west oriented receiving antennae of the BP MF array to produce a number of isosceles right-angle triangles with various different antenna spacings for the application of the FCA. They found that V_t approached an upper limit equivalent to the velocity estimated by the "spatial correlation analysis" (SCA) (e.g. *Briggs*, [1968]) as the antenna spacing was increased, as illustrated in Figure 5.1. The SCA is independent of assumptions about the form of

the temporal dependence of the spatio-temporal correlation function, and is considered to produce accurate estimates of the wind velocity. The SCA is described in more detail in chapter 6. The pattern scale $S_{0.5}$ was also shown to exhibit the same increase with increasing antenna spacing as seen for V_t. The upper limit of V_t was obtained at antenna spacings close to the upper limit of $S_{0.5}$. The characteristic ellipse was shown to be elongated in the direction of the hypotenuse for smaller antenna spacings. This elongation was also noted by *Benyon and Wright* [1969], who also found that θ_t was biased perpendicularly to the hypotenuse. Although this θ_t bias was not seen by *Golley and Rossiter* [1970], *Briggs* [1994] states that subsequent results obtained using the BP MF array did exhibit this bias. No biases in the magnitude V_a and direction θ_a of the apparent velocity were observed by *Golley and Rossiter* [1970].

The TSE seen by *Golley and Rossiter* [1970] was attributed to the fact that the spatial correlation function did not extrapolate to unity at zero-lag. This result was attributed to the effects of receiver noise and differences in the behavior of the receiving and digitization channels, both of which act to suppress the correlations at non-zero lags. This result was also seen by *Brown and Chapman* [1972], who further illustrated that the TSE was the direct result of the failure of the spatial correlation function to extrapolate to unity at zero spatial lag. The effects of receiver noise upon the FCA were analyzed by *Meek* [1990] using one-dimensional formulae for the auto- and cross-correlation functions. The resulting equations revealed that the failure to correct for noise produces estimates of V_t and $S_{0.5}$ which vary with antenna spacing in the same manner seen in the results of *Golley and Rossiter* [1970]. These equations also illustrated the fact that the failure to correct for the effects of noise accounted for the ratio of V_t estimates obtained using two different antenna spacings, as illustrated in Figure 5.2. This result led Meek to conclude that noise is the sole cause of the TSE. This result suggests that if the noise correction is applied then the TSE will not be seen. In addition to biases in V_t, $T_{0.5}$, and $S_{0.5}$, Meek also illustrates that the failure to correct for noise can produce the result noted by *Benyon and Wright* [1969] and *Golley and Rossiter* [1970] whereby θ_{ax} is biased towards the longest side of the triangle of receiving antennae used for the FCA. Although the one-dimensional theory employed by Meek prohibits the investigation of biases in θ_t, it is claimed that the failure to correct for noise results in θ_{ax} being biased perpendicularly to θ_t. Although Meek's equations are derived for the attenuation of the cross-correlation functions due to the effects of noise they are equally applicable to the case where the spatial correlation function does not extrapolate to unity at zero spatial lag, and

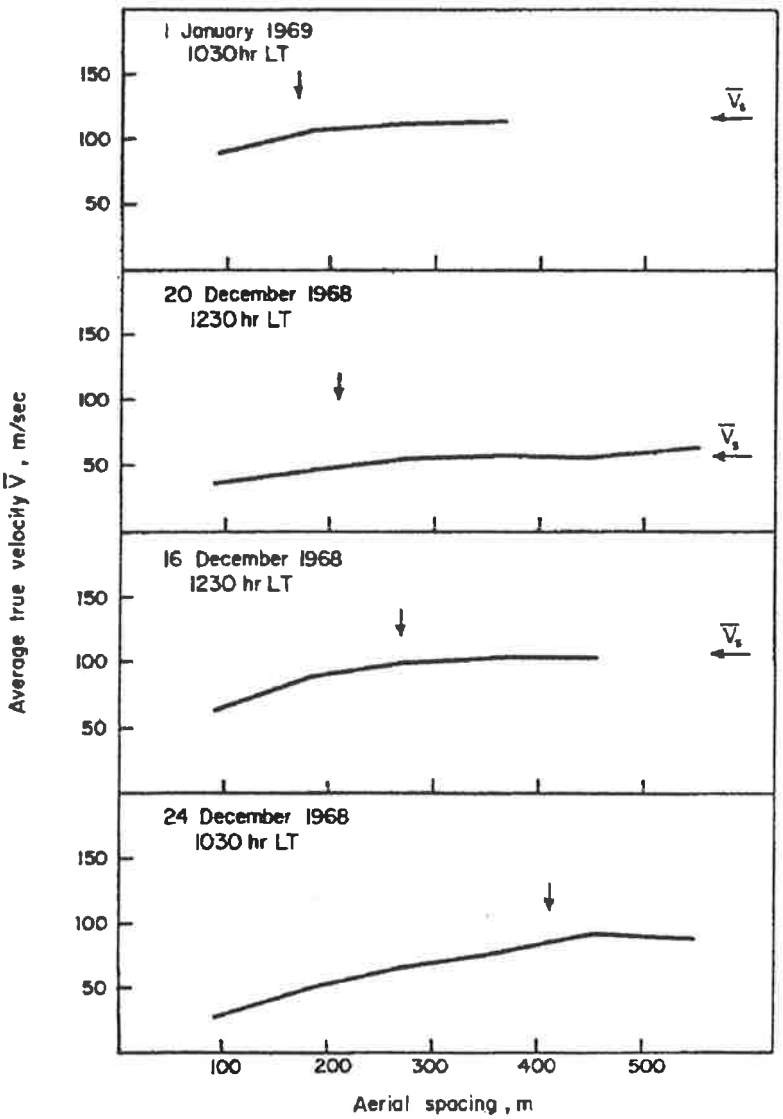

Figure 5.1: True velocity magnitude V_t as a function of antenna spacing for four E-region records of the analysis of *Golley and Rossiter* [1970]. The vertical arrow for each plot indicates the upper limit of the pattern scale $S_{0.5}$ estimated for each record, while $\vec{V}_s$ indicates the velocity magnitude estimated using the spatial correlation analysis if an estimate was available (after *Golley and Rossiter*, [1970]).

are therefore applicable to the effects of differences in the receiver characteristics.

The TSE has also been attributed to the effects of antenna coupling (e.g. *Fedor and Plywaski*, [1972]). The effect of antenna coupling would also be expected to result in an decrease in V_a with increasing antenna spacing. The results of *Golley and Rossiter* [1970] suggest that V_a is independent of antenna spacing. Furthermore, the results of *Rossiter* [1979] suggest that antenna coupling was negligible for the BP MF array employed by *Golley and Rossiter* [1970] for their analysis. The analysis of *Van Baelen et al.* [1990] suggests that

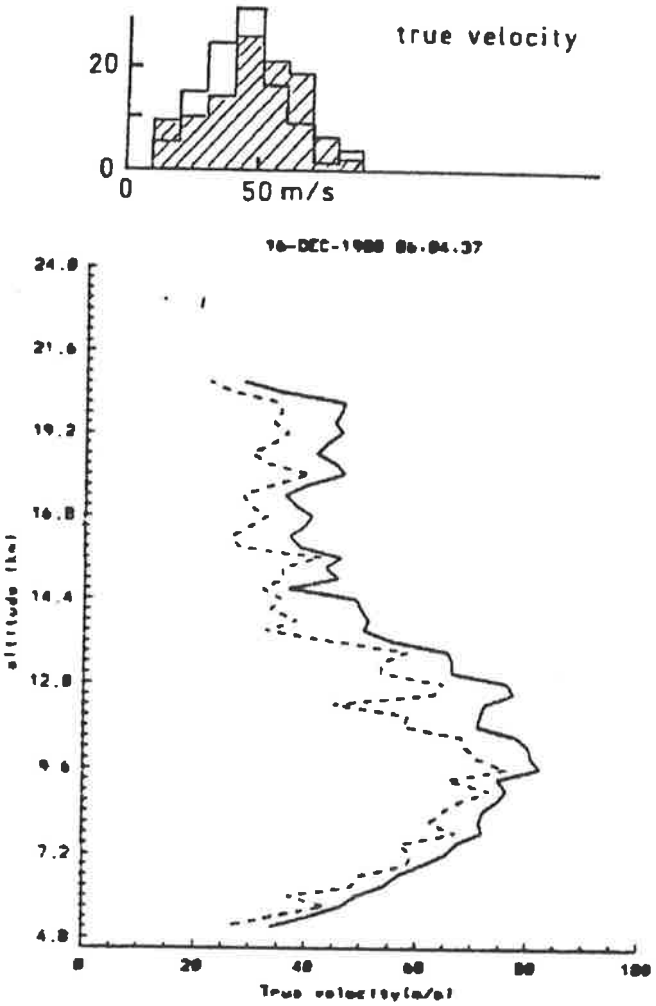

Figure 5.2: Top: Histograms of the true velocity magnitude estimated using the small (unshaded) and large (shaded) spacings of the "main array" at Saskatoon (after *Meek*, [1990]). Bottom: Profiles of the true velocity magnitude estimated using small (dashed) and large (solid) spacings for the MU radar (after *Van Baelen et al.*, [1990]).

V_a does decrease with increasing antenna spacing (Figure 7b, most heights). The simulated data analysis presented by *Van Baelen et al.* [1989] also exhibits this effect (their Figure 2), despite the fact that the effects of antenna coupling have not been simulated in their analysis.

The radar backscatter model of Chapter 3 has been used to investigate the TSE. Two data-sets have been generated for this purpose. The model-generated data-set MOD-MF-TSE has been employed to study "magnitude" biases, such as the biases in the true velocity magnitude V_t, the corrected fading time $T_{0.5}$ and the pattern scale $S_{0.5}$. This data-set uses the standard MF SA model input parameters, using a range of different antenna spacings. The model-generated data-set MOD-MF-TSE-ROTN has been used to investigate "directional"

biases, such as the biases in the true velocity direction θ_t and the axial-rotation of the characteristic ellipse θ_{ax}. This data-set uses the standard MF SA model input parameters, using a range of different model velocity directions and a range of different antenna spacings. The Buckland Park obtained data-set BP930518 is then investigated for the TSE. Because the systematic errors associated with the TSE are the major interest of this chapter little attempt is made to address the statistical errors that may also result.

5.2 Magnitude biases

5.2.1 Magnitude biases in the noise-free situation

The model-generated data-set MOD-MF-TSE has been used to investigate magnitude biases resulting from the TSE. This data consists of 100 time-series realizations obtained using seven different antenna spacings ranging from 100 to 400 m. This range of antenna spacings encompasses the average pattern scale resulting from this simulation of approximately 340 m. The FCA was employed both with and without the noise-correction specified in appendix C. The "uncorrected" analysis is hereafter referred to as the UFCA.

The results of applying the FCA and UFCA to time-series without added noise are illustrated in Figure 5.3. The true velocity magnitude V_t is approximately constant for antenna spacings between 100 and 250 m. The corrected fading time $T_{0.5}$ and pattern scale $S_{0.5}$ increase with increasing antenna spacing, while the apparent velocity magnitude V_a decreases with increasing antenna spacing. For spacings above 250 m V_t exhibits a sharp decrease with increasing antenna spacing. This decrease is accompanied by sharp increases in $T_{0.5}$ and $S_{0.5}$ and a sharp decrease in V_a. The decrease in V_a was not encountered by *Golley and Rossiter* [1970], but appears to be seen in the analyses of *Van Baelen et al.* [1989] and *Van Baelen et al.* [1990] using simulated and experimental data respectively. There appears to be little difference between the FCA and UFCA true velocity results. This is expected because noise effects have not been included, suggesting that the interpolated zero-lag auto-correlations should be close to unity. The FCA and UFCA apparent velocities are identical because the zero-lag auto-correlation renormalization does not alter the positions of the cross-correlation maxima, from which the apparent velocity is calculated.

Some aspects of the results of Figure 5.3 can be understood by examining the cross-correlation functions employed for the analysis. An example of the typical cross-correlation functions obtained using antennae with the same orientation but with spacings of 100, 200,

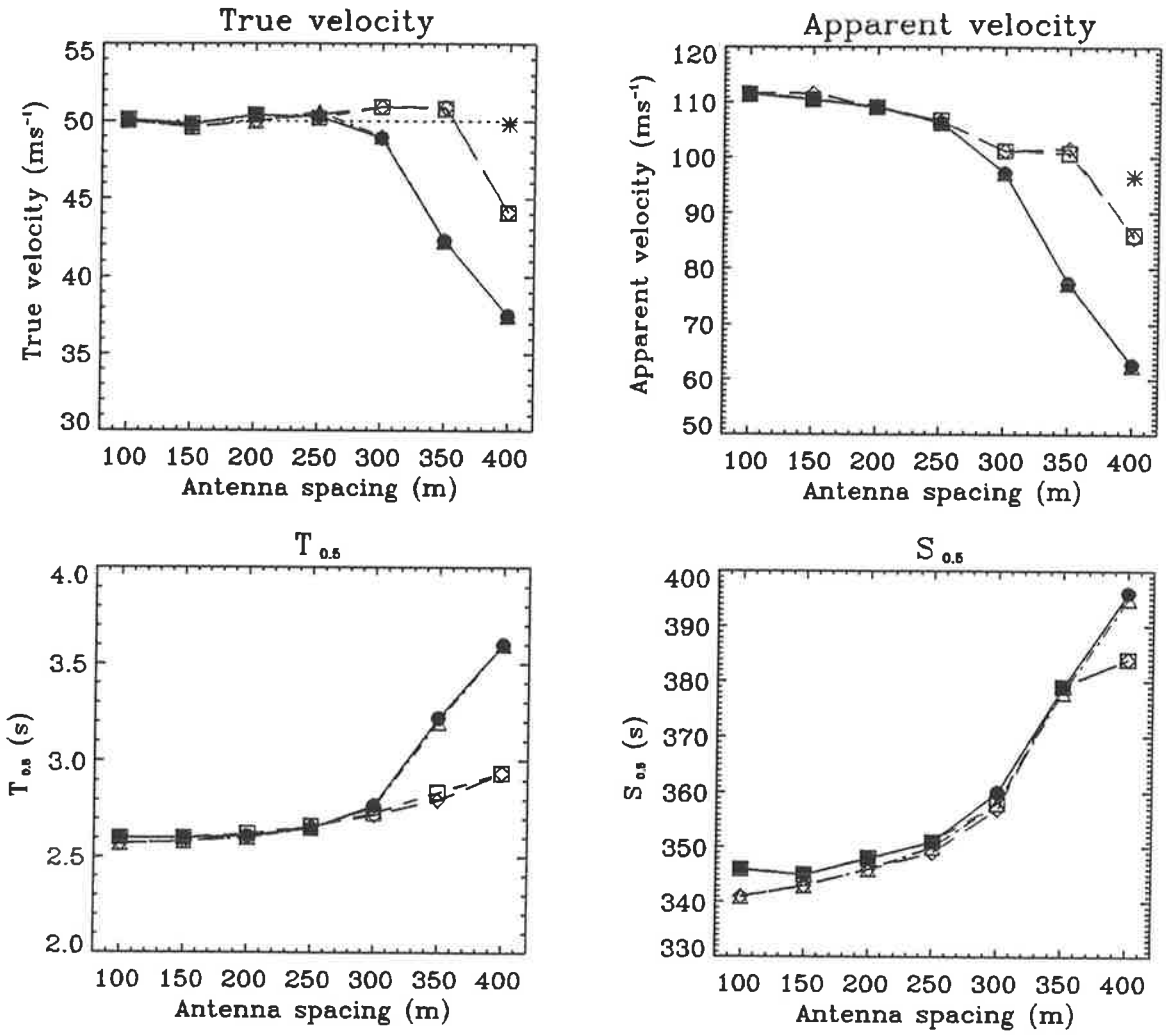

Figure 5.3: Averaged true velocity magnitude (top left), apparent velocity magnitude (top right), $T_{0.5}$ (bottom left), and $S_{0.5}$ (bottom right) obtained as a function of antenna spacing for the application of the FCA (•), UFCA (△), FCA using new rejection criteria (□) and UFCA using new rejection criteria (◇) to the model-generated data-set MOD-MF-TSE. The asterisk in the top plots indicates the averages obtained for the FCA using new rejection criteria with the "spurious" record removed from the averaging (see text).

300 and 400 m are illustrated in Figure 5.4. The results of applying the FCA to these particular correlation functions are shown in Table 5.1. As the antenna spacing is increased the cross-correlation maxima ρ_{0ij} decrease, while the positions of the maxima τ'_{ij} increase, thereby explaining the decrease in V_a and the increase in $S_{0.5}$ seen with increasing antenna spacing. For the smaller spacings the main peak of the cross-correlation function is prominent above the tails. At the largest spacing however the main peak is comparable in magnitude with the tails. This effect occurs because the antenna spacing exceeds the mean pattern scale of $\approx$ 340 m. As a result the antennae are not sampling the same "region" of the pattern,

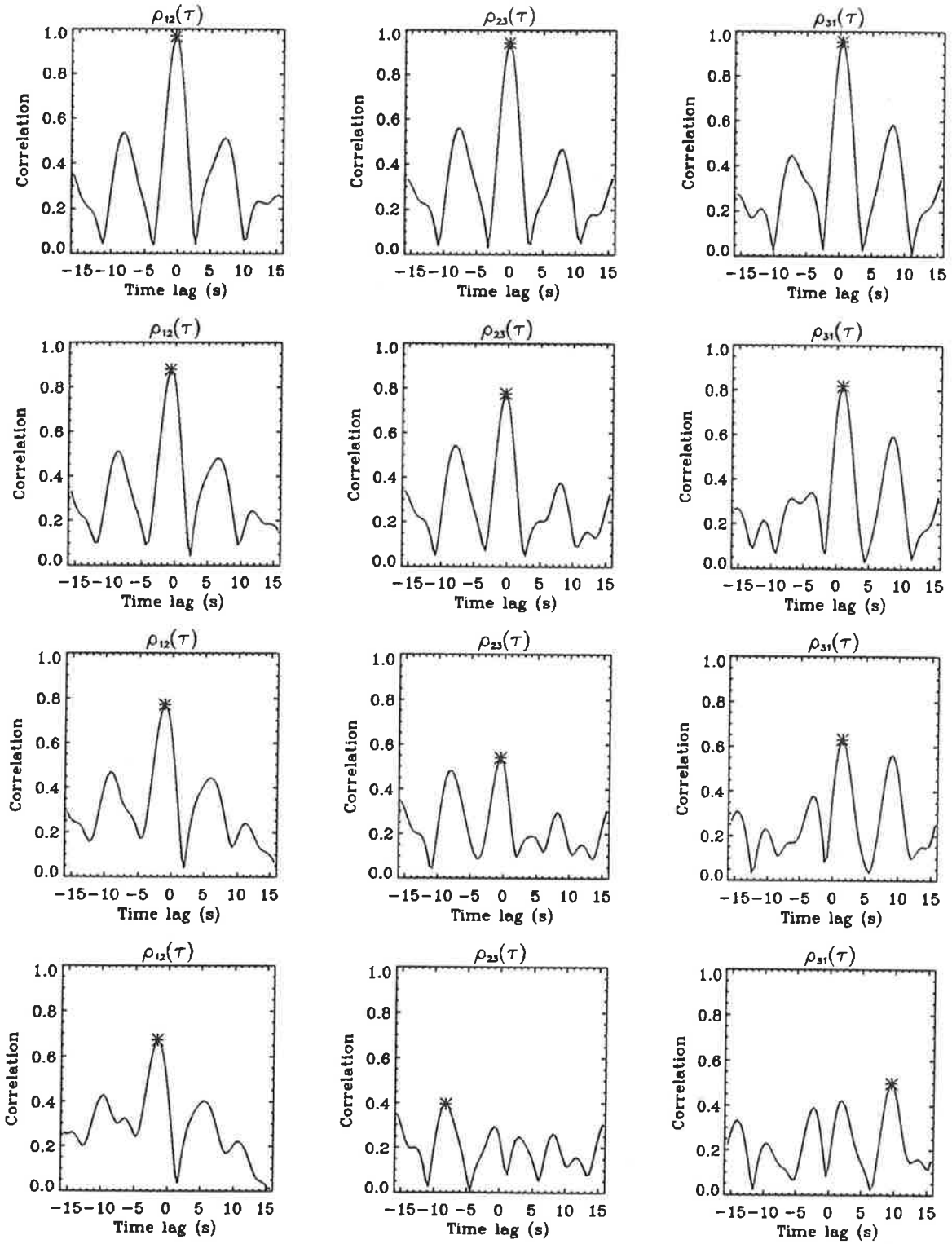

Figure 5.4: Examples of typical cross-correlation functions obtained using the model-generated data-set MOD-MF-TSE. Each column shows the functions obtained for each antenna orientation for antenna spacings of 100 (top), 200 (second from top), 300 (second from bottom) and 400 m (bottom). The asterisk for each plot denotes the estimates of ρ_{0ij} and τ'.

Table 5.1: FCA outputs obtained as a function of antenna spacing using cross-correlation functions illustrated in Figure 5.4.

Antenna spacing (m)	τ'_{12} (s)	τ'_{23} (s)	τ'_{31} (s)	$\lvert\vec{V}_a\rvert$ (ms^{-1})	$\lvert\vec{V}_t\rvert$ (ms^{-1})	$T_{0.5}$ (s)	$S_{0.5}$ (m)
100 m	-0.34	-0.12	0.45	108	61	2.70	367
200 m	-0.70	-0.29	0.92	102	62	2.79	367
300 m	-1.12	-0.52	1.43	96	65	2.97	360
400 m	-1.64	-8.22	9.52	19	27	37.7	416

thereby resulting in little correlation between the time-series recorded by each antenna. In this instance τ'_{ij} may be "detected" within the tails of the cross-correlation functions, as can be seen for τ'_{23} and τ'_{31} in Figure 5.4. This particular record is not rejected by the current FCA rejection criteria because criterion 13 is passed, as $\rho_{0ij} > 0.2 \ \forall ij$, and criterion 5 is passed, as NTD ≈ 0.01. This effect results in a decrease in the apparent and true velocity magnitude, and an increase $S_{0.5}$ and $T_{0.5}$, as illustrated in Table 5.1. This effect is the cause of the sharp decrease in V_a and V_t and the sharp increase in $T_{0.5}$ seen for the larger antenna spacings in Figure 5.3. It is interesting to note that the tails of the cross-correlation functions obtained for different antenna spacing exhibit very similar behavior.

In order to reject records where τ'_{ij} is located within the tails of the cross-correlation function a new rejection criterion has been implemented. This criterion is employed to reject records where $\tau'_{ij} > \tau_{0.1}$ for any ij, where $\tau_{0.1}$ is the lag where the mean auto-correlation function equals 0.1. This rejection criteria is hereafter referred to as FCA rejection criterion 16. The FCA results obtained using rejection criterion 16 are shown in Figure 5.3. The sharp decreases seen in V_t and V_a and the sharp increase seen in $T_{0.5}$ increases seen for antenna spacings above 300 m have been reduced significantly. The decrease in in V_t and V_a between 350 and 400 m results from a single spurious record. If this record is precluded from the averaging the decrease is reduced significantly. These results suggest that this new rejection criteria may be of importance in reducing any underestimation of V_t in instances where the antenna spacing exceeds the pattern scale. Unless otherwise specified, this rejection criterion is used for all remaining TSE analyses of model-generated data presented in this chapter.

The results obtained using rejection criterion 16 reveal that V_t shows a small increase of approximately 2% between antenna spacings of 100 and 350 m. This increase is significantly smaller than the increase seen in the experimental analyses of *Golley and Rossiter* [1970],

Meek [1990] and *Van Baelen et al.* [1990], and the simulated-data analysis of *Van Baelen et al.* [1989]. Furthermore, the estimate of V_t obtained at the smallest spacing is of the order of the model input velocity. However, V_a still shows a significant decrease with increasing antenna spacing, while $T_{0.5}$ and $S_{0.5}$ show significant increases.

The increase in $S_{0.5}$ seen with increasing antenna spacing results because patterns with scales smaller than the antenna spacing will produce time-series with very little correlation between the antennae, as seen in Figure 5.4. The majority of these records will therefore fail the FCA rejection criteria. As a result, the FCA will only produce acceptances for patterns with scales of the order of, or larger, than the antenna spacing. The decrease in V_a seen with increasing antenna spacing appears to be the result of two different effects. The first effect is a tendency for the τ'_{ij} estimates to increase non-linearly with increasing antenna spacing. This effect can be seen in the τ'_{ij} estimates in Table 5.1. The second effect results because the cross-correlation maxima ρ_{0ij} decrease as the random changes in the ground diffraction pattern increase. At larger spacings there is therefore a tendency for records with greater random changes to produce cross-correlation functions where the main peak is subdued, resulting in the record being rejected by the FCA rejection criteria. As a result, the number of records with greater random changes will decrease as the antenna spacing is increased. It therefore follows that the average V_a will decrease as the antenna spacing is increased, while the average $T_{0.5}$ will increase as the antenna spacing is increased. These arguments are confirmed by Figure 5.5. In practice, the acceptance of a record at larger spacings will depend on both the pattern size and the degree of random changes.

The standard deviation of the FCA parameters as a function of antenna spacing are illustrated in Figure 5.6. These results suggest that the statistical errors in the estimation of each parameter increase with increasing antenna spacing. This result agrees with the predictions of *Røyrvik* [1983], but contradicts the results of *Golley and Rossiter*, [1970], who found that the errors decreased with increasing antenna spacing. The results obtained here however are clearly sensible in terms of the fact that the error σ_ρ in any single correlation value ρ is given by (e.g. *Awe*, [1964])

$$\sigma_\rho = (1 - \rho^2) \left(\frac{\tau_{0.5}}{T} \right)^{0.5} \tag{5.1}$$

where T is the record length. The results of Figure 5.4 suggest that the correlation values on the main peak of the cross-correlation functions decrease with increasing antenna spacing. It therefore follows that the estimates of τ'_{ij} and ρ_{0ij} must also increase with increasing antenna

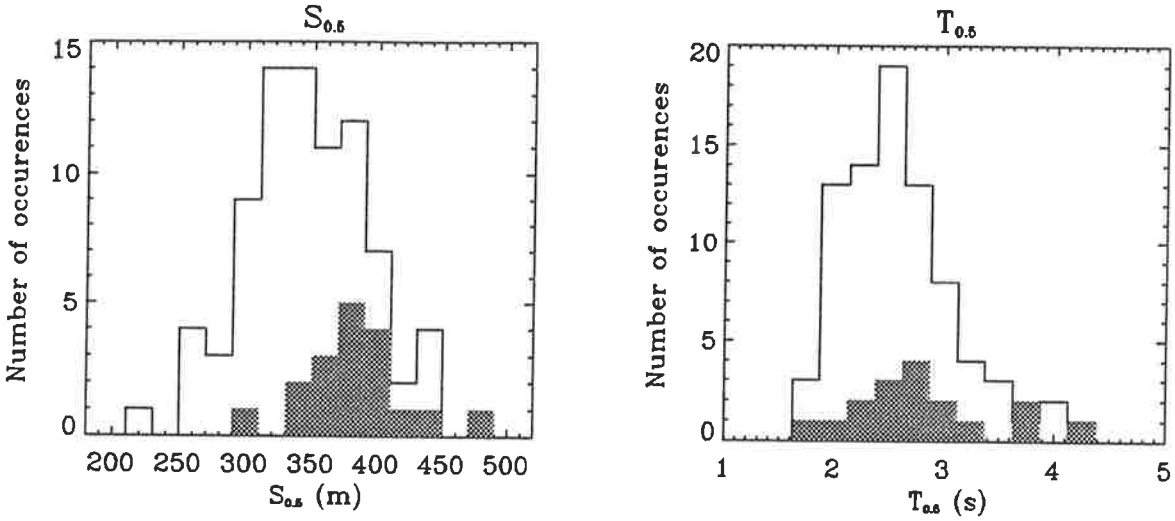

Figure 5.5: Histograms of $S_{0.5}$ and $T_{0.5}$ obtained from the application of the FCA to model-generated data-set MOF-MF-TSE using antenna configurations with spacings 100 (solid line) and 400 m (shaded).

spacing, suggesting that the FCA parameters must also should increase with increasing antenna spacing.

5.2.2 Magnitude biases in the presence of noise

The presence of noise in the time-series results in the failure of the spatial and temporal correlation functions to extrapolate to unity at zero-lag. This effect is illustrated in Figure 5.7, which shows the auto- and cross-correlation functions produced by the addition of random Gaussian distributed values to the real and imaginary components of the time-series. The added noise produces a zero-lag auto-correlation spike and attenuates the magnitude of the cross-correlation function. The noise-correction employed by the FCA removes these effects from the correlation functions.

The effects of receiver noise upon the FCA have been investigated by *Meek* [1990] using a one-dimensional formulation for the auto- and cross-correlation functions. If the correlation functions are not corrected for the effects of noise the resulting estimates of the FCA parameters V_t, $T_{0.5}$, and $S_{0.5}$ are shown to obey the equations

$$\frac{V_{t0}}{V_t} = 1 + \frac{2 \ln N S_0^2}{D^2}, \tag{5.2}$$

$$\frac{T_0}{T_{0.5}} = \sqrt{1 + \frac{2 \ln N T_0^2 V_0^2}{2 \ln N S_0 + D^2}}, \tag{5.3}$$

$$\frac{S_0}{S_{0.5}} = \sqrt{1 + \frac{2 \ln N S_0^2}{D^2}}, \tag{5.4}$$

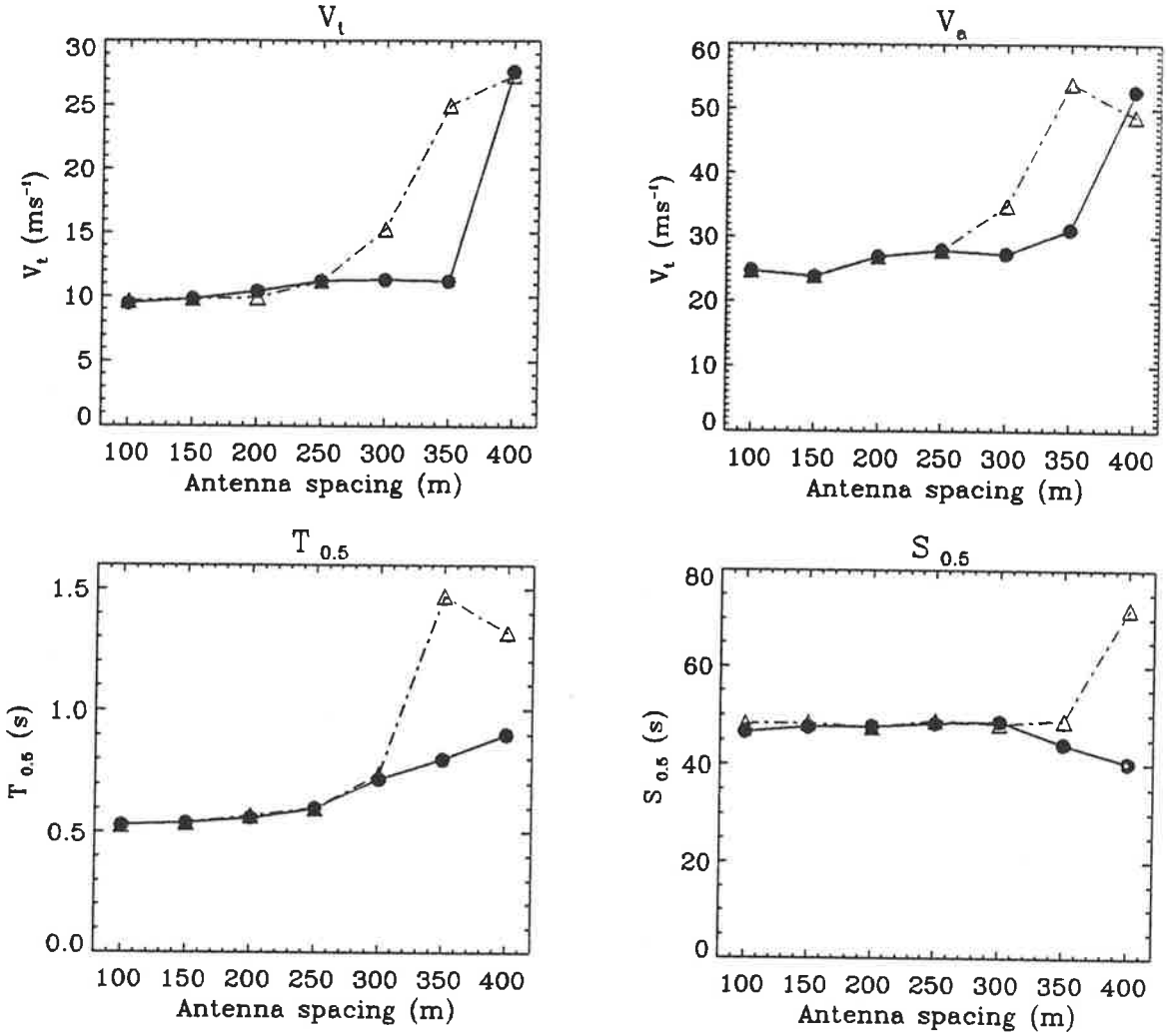

Figure 5.6: Standard deviations of the true velocity magnitude (top left), apparent velocity magnitude (top right), $T_{0.5}$ (bottom left) and $S_{0.5}$ (bottom right) obtained as a function of antenna spacing for the application of the FCA (•) and UFCA (△) using rejection criteria 16 to the model-generated data-set MOD-MF-TSE.

where V_{t0}, T_0, and S_0 are the corresponding "noise free" estimates of V_t, $T_{0.5}$, and $S_{0.5}$, respectively, D is the antenna spacing, and N is the "noise-factor", given by the ratio of the signal to noise contributions to the auto-correlation functions. These formulae indicate that V_t, $T_{0.5}$, and $S_{0.5}$ are monotonically increasing functions of D, producing the same behavior exhibited in the results of *Golley and Rossiter* [1970]. It is important to note that (5.2), (5.3), and (5.4) are applicable to the case where the spatial correlation function does not extrapolate to unity if

$$N = \frac{\rho_{ex0}}{(1 - \rho_{ex0})}, \tag{5.5}$$

where ρ_{ex0} is the extrapolated spatial correlation at zero spatial lag.

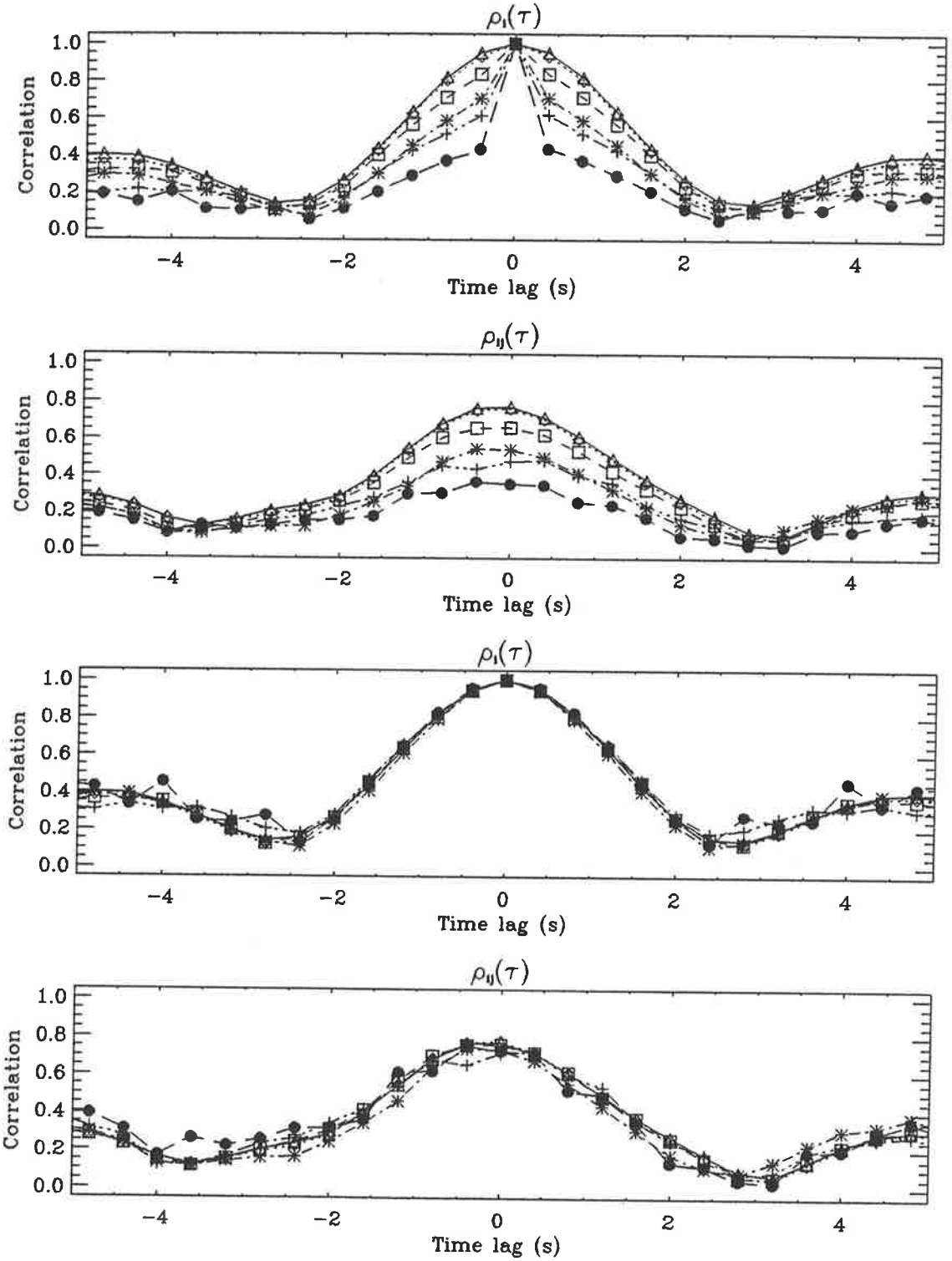

Figure 5.7: Example of the effects of the addition of various different amounts of uncorrelated noise on the auto- (top) and cross-correlation (second top) functions. The bottom plots show the corresponding noise corrected correlation functions. SNRs: 100 dB (△), 16 dB (◇), 8 dB (□), 4 dB (*), 2 dB (+), 0 dB (•).

The results of applying the FCA and UFCA to time-series with added receiver noise of various SNRs are shown in Figure 5.8. Rejection criteria 16 was abandoned for the UFCA as the presence of the noise-spike results in a decrease in the estimated width of the mean auto-correlation function, thereby resulting in the rejection of legitimate records at larger antenna spacings. The results of Figure 5.8 reveal a substantial decrease in the UFCA parameters as the antenna spacing is decreased. This decrease is of the form described by (5.2), (5.3), and (5.4). The application of FCA rejection criterion 10 results in the rejection of some of the smaller V_t estimates, thereby biasing the average of V_t to larger absolute values, especially for smaller antenna spacings. This effect is illustrated in Figure 5.8, which shows the average V_t obtained if this rejection criterion is abandoned. The average $T_{0.5}$ and $S_{0.5}$ are not altered significantly by abandoning criteria 10. These results are obtained because the UFCA does not compensate for the effects of noise. In some instances the compensation for noise effects can become difficult (e.g. *Meek*, [1990]). If, for instance, the main peak of the auto-correlation function is not sufficiently sampled the zero-lag auto-covariance can be underestimated, thereby resulting in significant biases in the application of the FCA (see section 4.6 for details).

The results of Figure 5.8 suggest there is some tendency for the FCA parameters to increase with decreasing SNR at all antenna spacings. This suggests that the zero-lag auto-covariance is being underestimated, resulting in the cross-correlation functions being "over-normalized" and the cross-correlation maxima ρ_{0ij} overestimated. This effect is understandable given the variation introduced into the correlation functions by the addition of noise, as shown in Figure 5.7. Apart from this effect at lower SNRs the FCA parameters appear very similar to those estimated without the addition of noise. The FCA and UFCA estimates of V_a (not shown) are essentially independent of SNR. The results of this section suggests that some care should be taken in the interpretation of the FCA results obtained using records where the SNR is less than 5 dB.

5.2.3 Magnitude biases due to the effects of digitization and saturation

The effects of using single-bit digitization upon the FCA have been considered by *Fraser* [1984]. Although there exists no simple relationship between the correlation functions obtained with and without single-bit digitization approximate expressions can be obtained. For instance, the auto-correlation function $\rho'(\tau)$ resulting from artificially saturating a time-series record with a Gaussian distribution of samples can be approximated by (e.g. *Fraser*

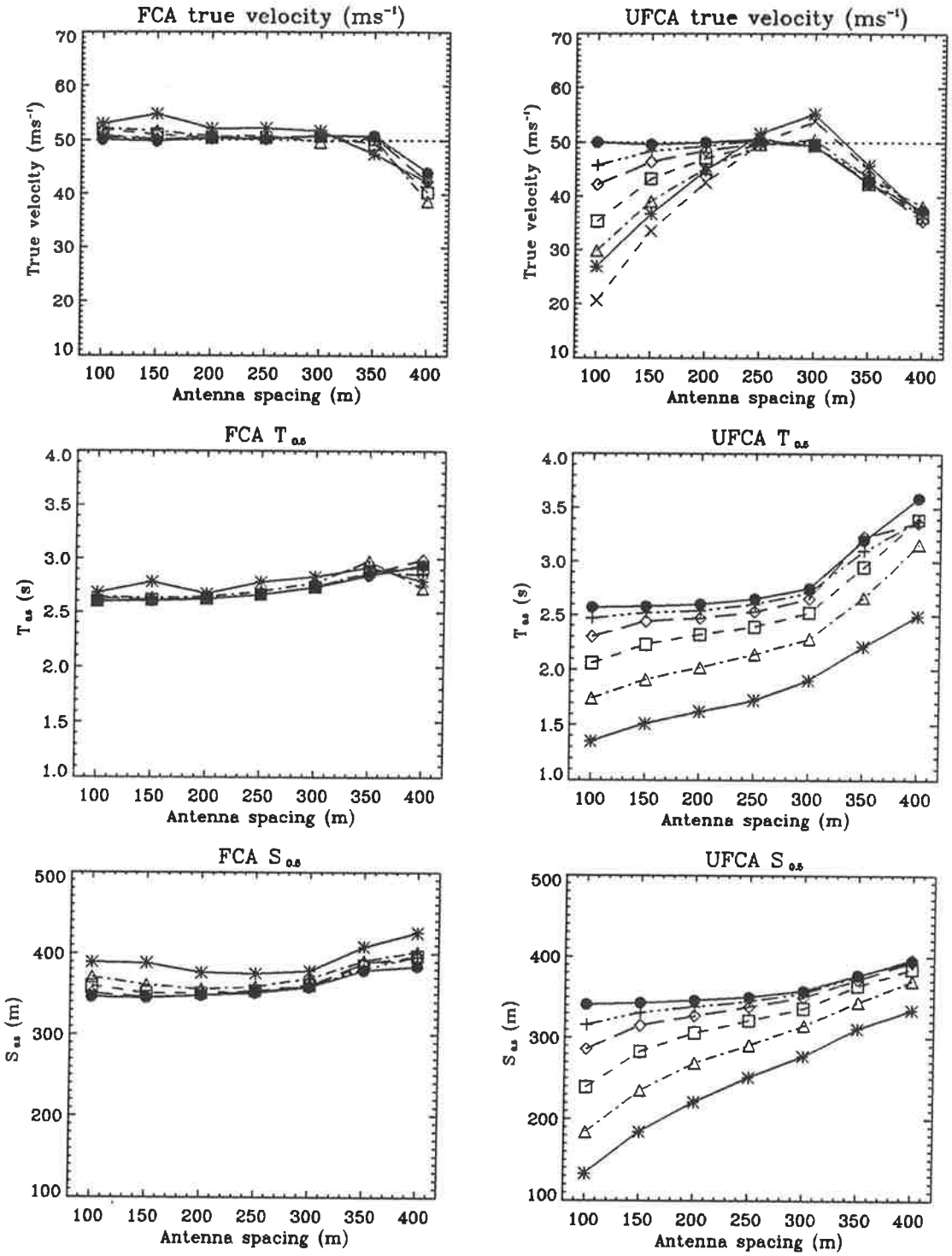

Figure 5.8: Average true velocity magnitude (top), $T_{0.5}$ (middle) and pattern scale (bottom) as a function of antenna spacing obtained on the application of the FCA (left) and UFCA (right) to the model-generated data-set MOD-MF-TSE for various different SNRs of added receiver noise: 100 dB (•), 20 dB (+), 16 dB (◇), 12 dB (□), 8 dB (△), 4 dB (*). The dotted line on the top plots indicates the model input velocity, while (x) on the top right hand plot indicates the true velocity obtained for the UFCA without applying FCA rejection criteria 10 (x).

[1984])

$$\rho'(\tau) = \frac{2 \arcsin \rho(\tau)}{\pi}, \tag{5.6}$$

where $\rho(\tau)$ is the auto-correlation function of the original time-series. This equation suggests the half-width of the resulting auto-correlation function is reduced considerably. The position of the cross-correlation maxima is not altered by digitization and saturation effects.

The effects of time-series digitization upon the auto- and cross-correlation functions were analyzed by digitizing the time-series into 256, 32, 16, 8, 4 and 2 digitization levels. A typical example of the auto- and cross-correlation functions obtained from an individual time-series record after application of these digitizations is shown in Figure 5.9. As the number of digitization levels is decreased the auto-correlation function becomes more triangular about zero-lag, while the cross-correlations decrease. The auto-correlation spike appears to exist over a number of lags about zero-lag, as distinct from the spike resulting from the effects of noise which only exists at zero-lag as illustrated in Figure 5.7. As a result, the application of the zero-lag noise-removal procedure produces corrected auto-correlation functions with widths which decrease as the number of digitization levels is decreased. The corrected cross-correlation functions still show a decrease with decreasing number of digitization levels despite the correction. The position of the cross-correlation maxima is not affected by the digitization, as suggested by *Fraser* [1984]. In order to avoid using lags influenced by the spike in determining the "digitization free" zero-lag auto-covariance some attempts were made at interpolating without using the first and second lags. However, these interpolations invariably underestimated the digitization free zero-lag auto-covariance estimates, as the resulting cross-correlation maxima often exceeding unity.

The effects of time-series digitization upon the FCA are shown in Figure 5.10. Rejection criteria 16 was abandoned for the UFCA because the digitization results in a decrease in the estimated width of the mean auto-correlation function, thereby resulting in the rejection of legitimate records at larger antenna spacings. There is a clear decrease in the FCA parameters with decreasing antenna spacing for smaller numbers of digitization levels for both the FCA and UFCA. The decrease is considerably more severe for the UFCA as no attempt has been made to account for the spike about zero-lag. It is interesting to note that despite the general decrease in V_t with decreasing number of digitization levels the estimate of V_t obtained using the 2-level digitization exceeds the estimate obtained using the 4-level digitization. The FCA and UFCA estimates of V_a (not shown) are essentially independent of the number of digitization levels employed.

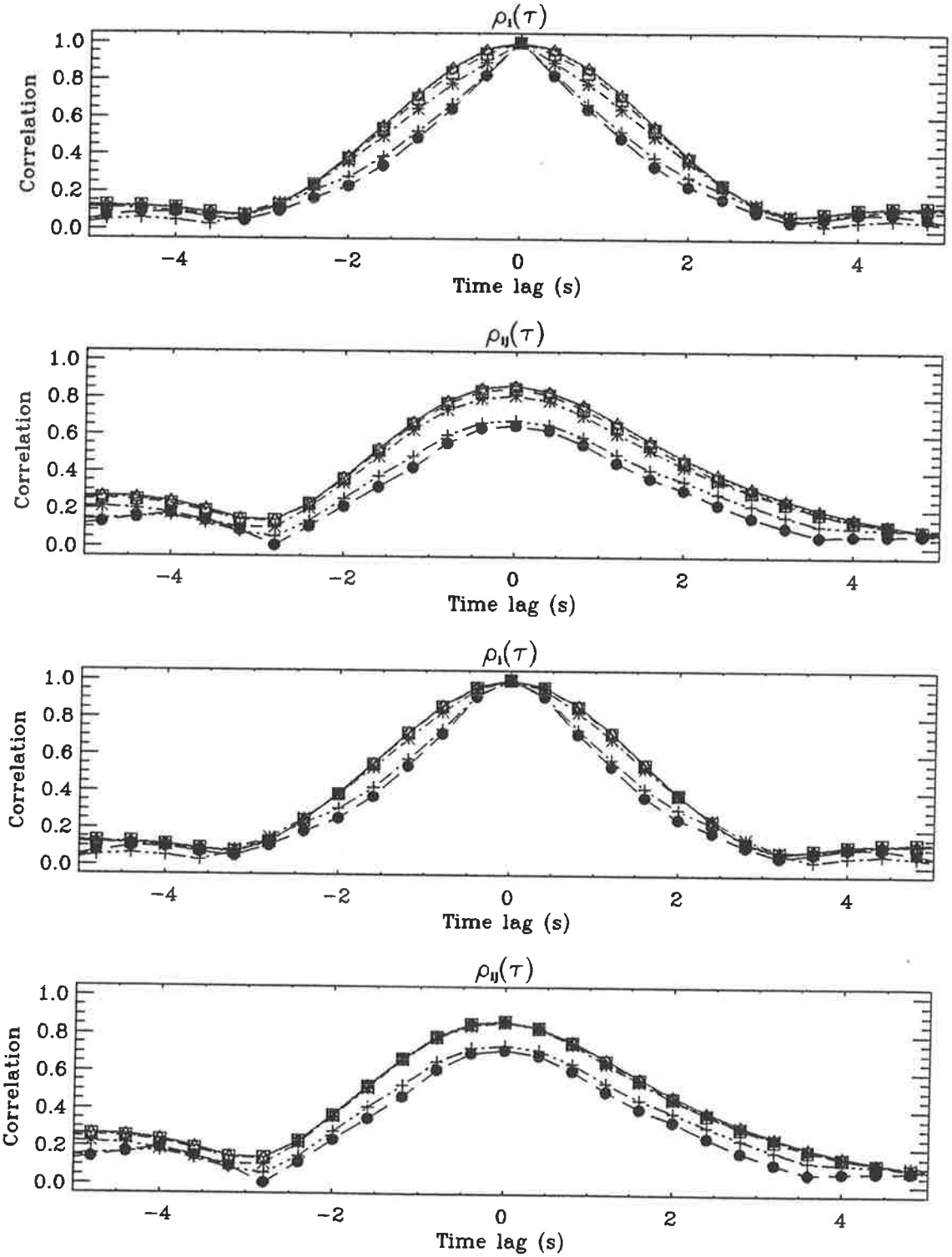

Figure 5.9: Example of the effects of the time-series digitization upon the auto- (top) and cross-correlation (second top) functions, and the noise-corrected auto- (second bottom) and cross-correlation (bottom) functions. Digitization levels: 256 (△), 32 (◇), 16 (□), 8 (*), 4 (+) and 2(•).

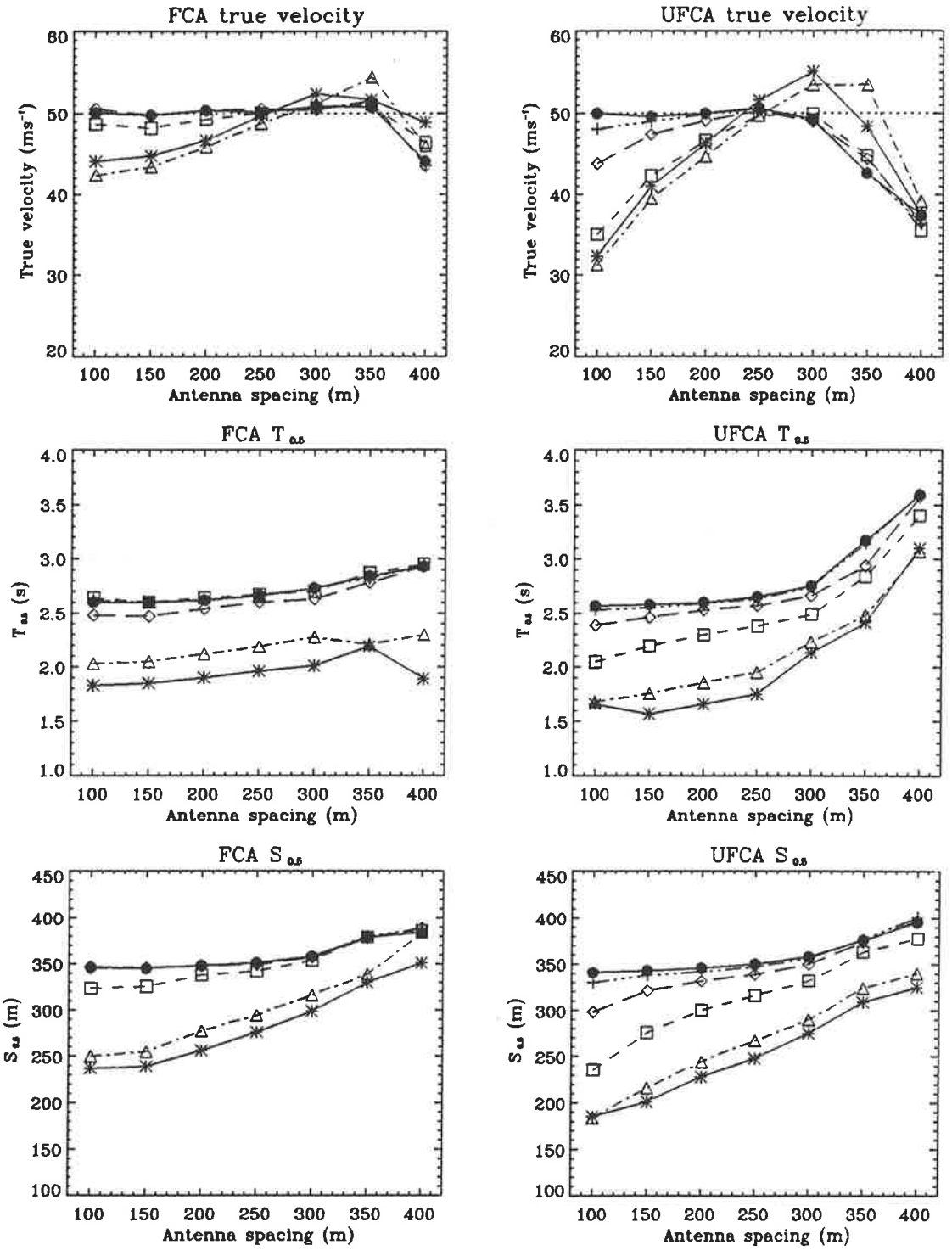

Figure 5.10: Average true velocity magnitude (top), $T_{0.5}$ (middle), and $S_{0.5}$ (bottom) as a function of antenna spacing for the FCA (left) and UFCA (right) for various different numbers of digitization levels: 256 (•), 32 (+), 16 (◇), 8 (□), 4 (△) and 2 (*). The dotted line on the top plots indicates the model input velocity.

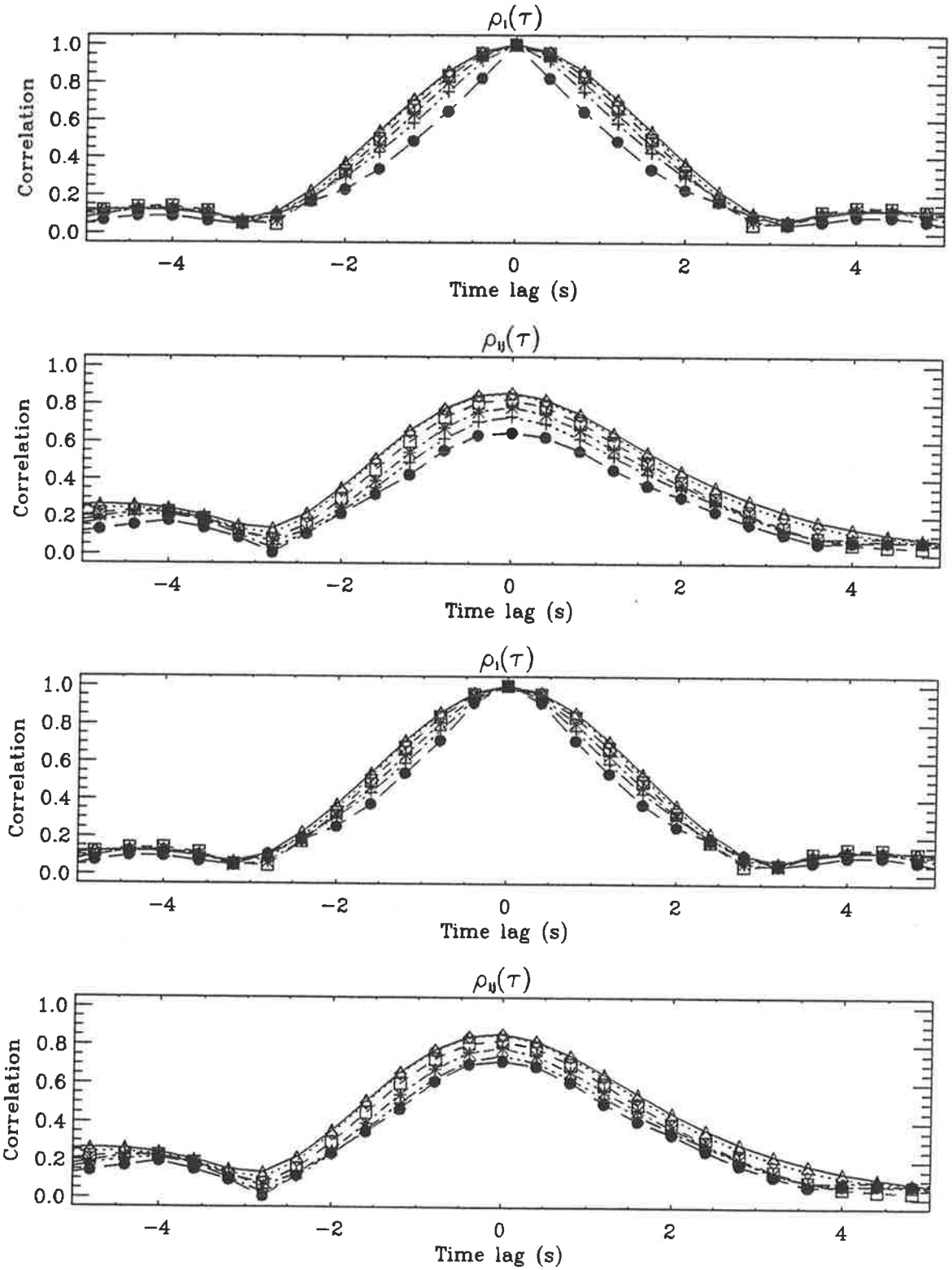

Figure 5.11: Example of the effects of the time-series saturation upon the auto- (top) and cross-correlation (second top) functions, and the noise-corrected auto- (second bottom) and cross-correlation (bottom) functions for various different "saturation percentages": 256 ($\triangle$), 32 ($\diamond$), 16 ($\square$), 8 (*), 4 (+) and 2($\bullet$).

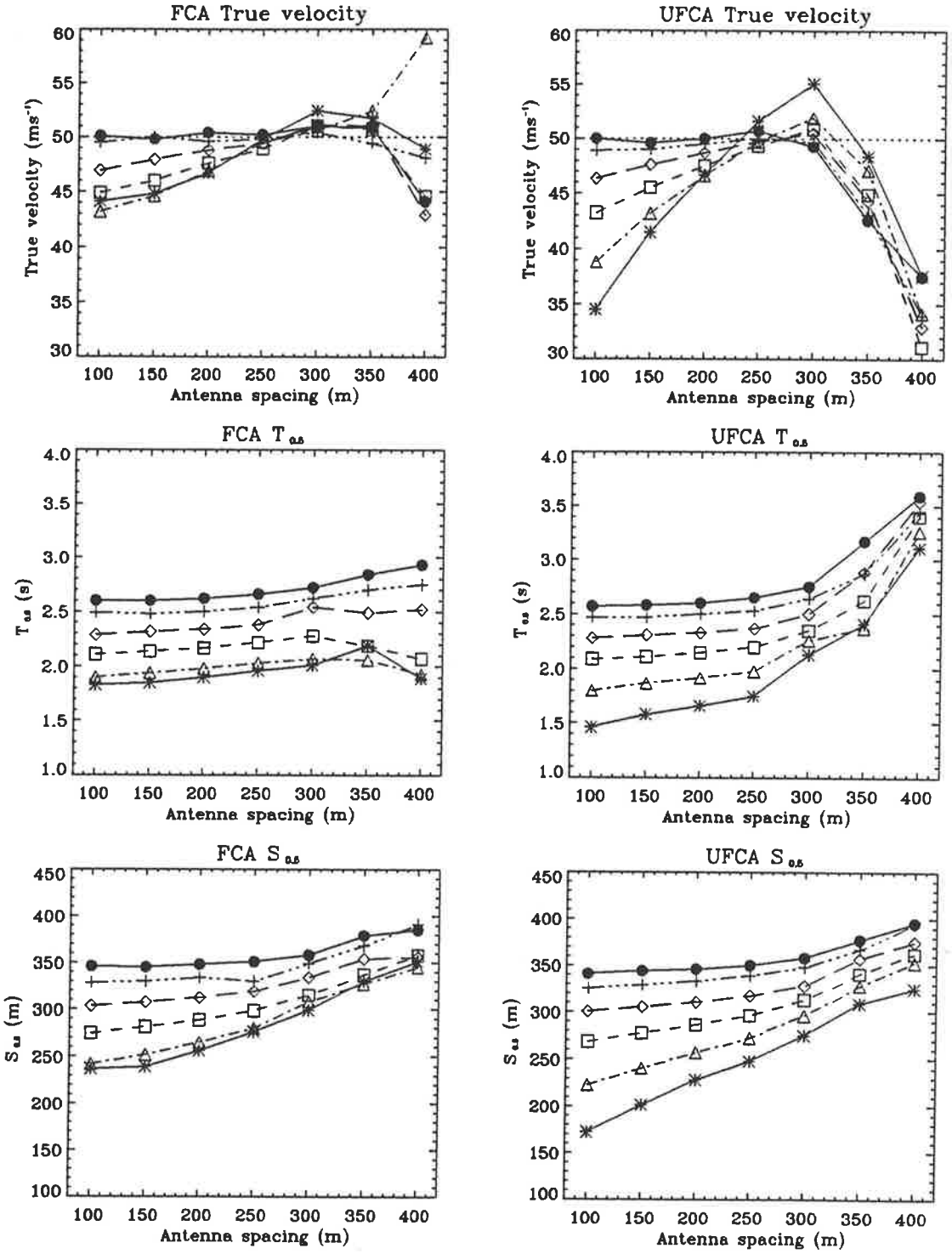

Figure 5.12: Average true velocity magnitude (top), $T_{0.5}$ (middle), and $S_{0.5}$ (bottom) as a function of antenna spacing for the FCA (left) and UFCA (right) for various different "saturation percentages": 0%(•), 20%(+), 40%(◇), 60%(□), 80%(△) and 100%(∗). The dotted line on the top plots indicates the model input velocity.

The effect of saturation upon the correlation functions is illustrated in Figure 5.11. The saturation was produced by artificially reducing the limits of the time-series. The "saturation percentage" refers to the percentage of time-series samples that lie on these limits. These results suggest that the effects of saturation are essentially identical to the effects of digitization, as illustrated in Figure 5.9. The effect of saturation upon the FCA is shown in Figure 5.12. Rejection criterion 16 was again abandoned for the UFCA. There is a clear decrease in the FCA parameters with decreasing antenna spacing and increasing saturation percentage for both the FCA and UFCA. The FCA and UFCA estimates of V_a (not shown) are essentially independent of the saturation percentage.

5.2.4 Summary of TSE magnitude biases

The TSE of the FCA results from the attenuation of the cross-correlation functions employed by the analysis. The results obtained in this section suggest that the TSE can be attributed to four possible causes:

- receiver noise
- the different characteristics of the individual receivers
- coarse digitization
- receiver saturation.

If receiver noise is the cause of the TSE the application of the noise-correction outlined in Appendix C will produce estimates equivalent to those obtained in the noise-free situation, except at small SNRs where there is some tendency to overestimate the noise-free estimates. If the TSE however is the result of the remaining three causes this noise correction will not prohibit the TSE, as the maximum of the noise-corrected cross-correlation functions will still be attenuated.

The TSE resulting from coarse digitization and receiver saturation has significant implications for the analysis of experimentally obtained data. The majority of MF and VHF radars can obtain useful partial reflections over a large range of heights. The returned power can vary by several orders of magnitude over this range of heights. For instance, the returned power for an MF radar at 60 km is usually several orders of magnitude smaller than the returned power at 100 km. In order to maximize the usable height range of the radar the receiver gains are usually set as a compromise between minimizing the receiver saturation at

the upper heights and maximizing the number of digitization levels at the lower heights. As a result there is usually some receiver saturation at the upper ranges and coarse digitization at the lower heights. The FCA may therefore produce the TSE in the lower and upper height ranges. If single-bit time-series are employed the correction outlined by *Meek and Soiferman* [1979] can be applied to determine the correct true velocity. However, if the number of digitization levels or amount of saturation is not known such a correction cannot be employed (e.g. *Vincent et al.*, [1994]).

The TSE resulting from receiver saturation may partially explain the results of recent comparisons between meteor drift velocities determined using the BP VHF radar and FCA true velocities determined using the colocated BP MF radar (e.g. *Cervera and Reid*, [1995]). These results suggest that the two techniques show reasonable agreement below 90 km, while the FCA true velocity magnitude underestimates the meteor drift velocity above 90 km. It was found that the receiver gain settings employed by the MF radar for this comparison resulted in significant receiver saturation at heights above 90 km. More recent comparisons made using receiver gain settings producing significantly less receiver saturation above 90 km reveal that the underestimation of the MF FCA true velocity magnitudes has been substantially reduced (e.g. *Vincent et al.*, [1994]).

The results obtained above appear to contradict the results of the model analysis of *Van Baelen et al.* [1989]. Although their analysis does not appear to have included the effects of receiver noise, receiver saturation, or digitization noise, they find a pronounced TSE. This may be a result of the conditions of their model, whereby scatterers leaving the radar volume are readmitted into the opposite surface to which they left. Because polar diagram and aspect sensitivity effects have not been included in their model any scatterers located at the edge of the radar volume will produce returned signal amplitudes of the same order as scatterers located about the zenith. Any scatterer leaving or entering the radar volume will therefore produce a small discontinuity in the time-series which produces a zero-lag spike in the auto- and cross-correlation functions. This behavior was in fact observed in the embryonic stages of the development of the radar backscatter model used for the current analysis. As the number of such discontinuities will increase with scatterer velocity the size of any such spike would therefore increase. As the analysis employed by *Van Baelen et al.* [1989] is essentially identical to the UFCA applied above the TSE would therefore increase with increasing velocity. This is exactly what their analysis shows. It is not explicitly stated whether the effects of noise are accounted for in the corresponding experimental results

which also exhibit the TSE (e.g. *Van Baelen et al*, [1990]). However, the significantly different behavior exhibited in the model and experimentally obtained TSEs may indicate some deficiency in their simplistic model.

These results also illustrate that V_t may be underestimated if the antenna spacing exceeds $S_{0.5}$. This underestimation results from a tendency for the analysis to locate τ'_{ij} outside the main peak of the correlation function due to the main peak being of the same order as the tails. The introduction of a new criterion was shown to reject such records and therefore remove the underestimation. The results also suggest that the average $S_{0.5}$ and $T_{0.5}$ will increase with increasing pattern scale regardless of whether the TSE is actually exhibited.

5.3 Directional biases

The model-generated data-set MOD-MF-TSE-ROTN has been employed to investigate the directional biases resulting from the TSE. This data-set consists of 100 time-series realizations obtained using model velocity directions ranging from 0° to 180° in 5° intervals. Both equilateral and right-angled triangles have been employed. Four different antenna spacings ranging from 150 to 350 m have been employed. For the right-angled triangles these spacings correspond to the lengths of the two shortest sides. This range of antenna spacings encompasses the average pattern scale resulting from this simulation, which is approximately 340 m.

The results of the investigation of the directional biases are presented in Appendix E. The results suggest that significant directional biases can result if the noise-correction described in Appendix C is not applied, or if receiver saturation or coarse digitization are present in the time-series records.

In the situation where the noise-correction is applied the biases are generally small, and increase with decreasing SNR. The bias in the direction of the true velocity θ_t for equilateral triangles is less than 2°, and is towards the azimuth perpendicular to the antenna separations. The bias for right-angled triangles is less than 4°. For smaller triangles the biases is towards the hypotenuse, while for larger triangles the bias is perpendicular to the antenna separations. There is a slight tendency for axial-rotation θ_{ax} to be biased perpendicular to the direction of the model input velocity θ_{mod} for both equilateral and right-angled antenna configurations. This behavior was also observed in the numerical model analysis of *Wright and Pitteway* [1978], who attributed the effect to the inability of the FCA to separate the

spatial and temporal properties of the ground diffraction pattern. This effect results in the characteristic ellipse being foreshortened along the direction of motion, resulting in the axial-rotation θ_{ax} being biased perpendicularly to the direction of motion. The results of section 4.8.1 suggest that this false "anisometry" is eliminated by using longer time-series lengths than the two-minute duration records employed for the analysis presented in this section.

In the situation where the noise-correction is not applied the biases become considerably more significant. The bias in θ_t for equilateral triangles is less than 3°, and is towards the azimuth perpendicular to the antenna separations. The axial-rotation θ_{ax} is biased perpendicularly to the direction of the model input velocity θ_{mod}, as suggested by *Meek* [1990]. The bias in θ_t for right-angled triangles θ_t is towards the hypotenuse of the triangle. The bias increases with decreasing antenna spacing, and can be as large as 25° for smaller antenna spacings. This bias can be understood using (5.2), as described in Appendix E. This result however contradicts those of *Benyon and Wright* [1969], who found that θ_t was biased perpendicular to the hypotenuse. The axial-rotation θ_{ax} for right-angled triangles is biased towards the hypotenuse for smaller antenna spacings, and is biased perpendicularly to the direction of the model input velocity θ_{mod} for larger spacings. This bias can be understood using (5.4), as described in Appendix E. The result for smaller spacings was also observed by *Golley and Rossiter* [1970], who found that θ_{ax} was biased towards the hypotenuse for smaller antenna spacings. The results obtained in the situation where the noise-correction is not applied are also directly applicable to the situation where differences exist in the receiving characteristics, as this effect results in the same attenuation of the cross-correlation functions.

In the situation where the time-series data contains receiver saturation or coarse digitization directional biases will result regardless of whether the noise correction is applied. The bias in θ_t is towards the directions of the antenna separations for both equilateral and right-angled triangles. The maximum bias for equilateral triangles is approximately 3°, while the maximum bias for right-angled triangles is approximately 8°. The bias in θ_{ax} is dependent upon the antenna spacing. The bias for equilateral triangles is in the direction of θ_{mod} for smaller spacings, and in the direction of perpendicular to θ_{mod} for larger spacings. The bias for right-angled is in the direction of the hypotenuse for smaller spacings, and in the direction of perpendicular to θ_{mod} for larger spacings.

The results of Appendix E suggest that the largest bias in direction of the true velocity θ_t observed upon using an equilateral triangle of receiving antennae is less than 4°. On the

Table 5.2: Triangles of antennae employed for TSE analysis using the BP MF data-set BP930518.

Triangle	Average Spacing (m)
378	167
124	173
238	183
247	245
457	248
157	328
158	382

other hand, the largest bias observed upon using an right-angled triangle is about 25°. These results suggest that an equilateral triangle is the optimal configuration for the minimization of biases in θ_t, as suggested by *Briggs* [1984]. The use of an equilateral triangle will however still result in significant biases in θ_{ax}. These biases should be taken into account in experimental studies such as those performed by *Lesicar* [1993].

5.4 Triangle size effect in experimental data

The BP MF data-set BP930518 has been employed for the experimental investigation of the TSE. This data-set is ideal for the investigation of the TSE as the half-width of the polar-diagram is small enough to give pattern scales of the order of 500 m, and the eight channels of data recorded provide a number of different triangle spacings and orientations. The analysis has been restricted to triangles where the three inter-antenna spacings are comparable. Table 5.2 shows a list of the triangles employed and their inter-antenna spacings.

The results obtained on the application the FCA to the triangles of antennae specified in Table 5.2 are shown in Figure 5.13 for the first 4 hours of the BP930518 data-set (13:30 - 17:30). All heights have been included in order to produce as large a range of velocity directions and pattern axial rotations as possible, and thereby reduce any directional biases that may result from the different antenna configurations employed. The results reveal that the estimates of V_t, $T_{0.5}$, and $S_{0.5}$ exhibit a pronounced TSE, while V_a is almost constant. These results are observed despite the fact that the noise-correction described in Appendix C has been employed, and receiver saturation and coarse digitization are almost nonexistent.

In order to determine the possible causes of this TSE the spatial correlation functions for

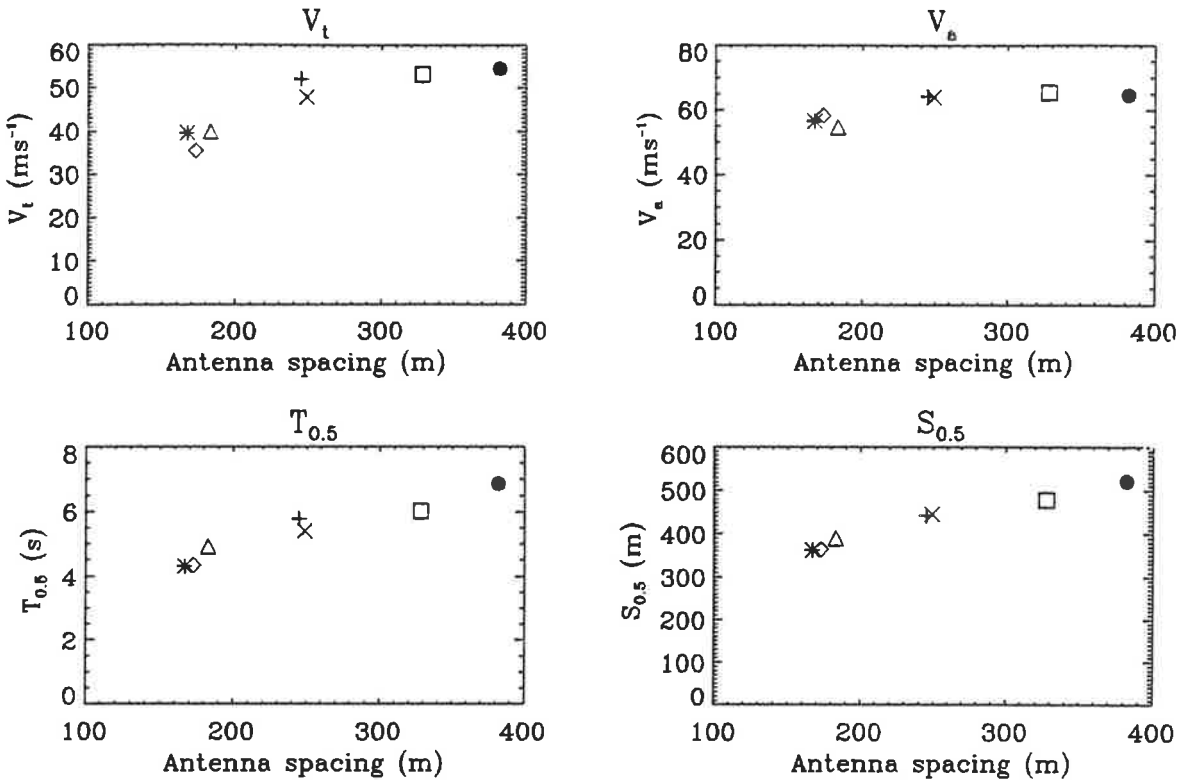

Figure 5.13: Results of the application of the FCA to the first four hours of the data-set BP930518 using the triangles of antennae listed in Table 5.2. The top plots show the true (left) and apparent (right) velocity magnitudes, while the bottom plots show the corrected fading time $T_{0.5}$ (left) and the pattern scale $S_{0.5}$ (right). Triangles: 378 ($*$), 124 ($\diamond$), 238 ($\triangle$), 247 ($+$), 457 ($\times$), 157 ($\square$) and 158 ($\bullet$).

the BP930518 data-set have been calculated. Although the antenna configuration employed for the TSE analysis provides insufficient spatial sampling for the calculation of the two-dimensional spatial correlation function, one-dimensional representations can be obtained using groups of aligned antennae, such as the antenna trios 137 and 145. It is clear from the discussion presented in Appendix C that the zero-lag cross-correlation $\rho_{ij}(0)$ between antennae i and j can be used to estimate the spatial correlation at the spatial lag (ξ_{ij}, η_{ij}) in the same manner employed by *Golley and Rossiter* [1970]. The antenna trios 137 and 145 therefore allow the determination of the one-dimensional spatial correlation function at three aligned spatial-lags.

The one-dimensional spatial correlation function obtained using the zero-lag cross-correlations averaged over 4 hours from antennae 137 at heights 96, 92, 88, and 84 km are shown in Figure 5.14. The spatial correlation function extrapolates to below unity at zero spatial lag for all heights. This result was also seen by *Golley and Rossiter* [1970] and *Brown and Chapman* [1972] for ground diffraction patterns resulting from E-region reflections. In order

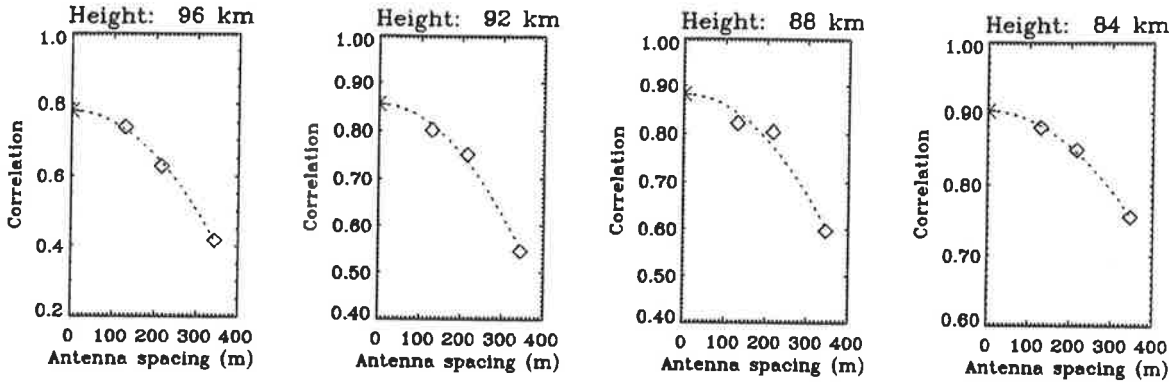

Figure 5.14: One-dimensional spatial correlation function obtained using the aligned antenna trio 137 for heights 96 (left), 92 (second left), 88 (second right), and 84 (right) km for the first four hours of the BP MF data-set BP930518. The diamonds denote the values determined from the zero-lag cross-correlations. The dotted line shows the Gaussian fit to the points, and the asterisks denote the zero-lag values estimated from the fit.

to determine the cause of this effect *Golley and Rossiter* [1970] fed the same antenna into ten different receivers, and found that the cross-correlations ranged from 0.86 to 0.96. This range of cross-correlations agreed well with the extrapolated zero-lag spatial correlations, leading to them to conclude that the cause was the different characteristics of the individual receivers. The spatial correlation functions obtained from E-region returns by *Brennan* [1960] and from tropospheric partial-reflection returns by *Vincent and Röttger* [1980] appear to extrapolate to unity. These authors however switched the individual antennae in turn into a single receiver, thereby avoiding any differences that may be introduced by different receiver characteristics.

Based on the cross-correlations obtained from feeding the same antenna into ten different receivers, *Golley and Rossiter* [1970] applied a correction to the cross-correlation function in a similar manner to the noise correction outlined in Appendix C. This correction however resulted in significant FCA rejections and had to be abandoned. Preliminary investigations to determine whether a similar correction could be applied using the BP930518 data-set also proved fruitless. The acceptance rate was less than 10%, and the variance of the FCA outputs was large. This result suggests there is no satisfactory correction that can be applied to correct for the failure of the spatial correlation to extrapolate to unity at zero-spatial lag. A possible solution to this problem is suggested by the results of *Brennan* [1960] and *Vincent and Röttger* [1980], and involves multiplexing the signals recorded by the individual receiving antennae into a single receiver. This solution has the added advantage of requiring only a single receiver, although additional hardware would obviously be required to perform the

multiplexing.

In situation where the receiver characteristics are sufficiently different to result in the spatial correlation function extrapolating to below unity at zero spatial lag the best solution is to use antenna spacings of the order of $S_{0.5}$. This is not always possible however because $S_{0.5}$ may vary considerably over the height range observed by the radar. For instance, the pattern scales obtained using the BP930518 data-set vary between 260 and 1000 m. Another possible solution to this problem may be to perform the analysis on triangles of different sizes. The analysis could then be applied to the various triangles, with the result taken from the largest triangle passing the rejection criteria. This solution would require significant data processing, and may not produce results significantly different from those obtained on applying the FCA to the largest triangle itself. If a number of different receivers are available an exercise similar to that carried out by *Golley and Rossiter* [1970] could be used to find receivers with high cross-correlations that could be used to reduce the problem. A further solution suggested by the results of Chapter 6 may be to employ the four-antenna spatial correlation analysis (SCA4), which appears to avoid the TSE.

5.5 Summary and conclusions

In this chapter the triangle size effect (TSE) of the full correlation analysis (FCA) has been investigated using both model-generated and experimentally obtained data. The results obtained are in very good agreement with those obtained in a number of different experimental studies, and indicate that the TSE results from the attenuation of the cross-correlation functions. This attenuation can result from four possible causes:

- receiver noise
- differences in the characteristics of the receivers
- coarse digitization
- receiver saturation.

If receiver noise is the sole cause of the attenuation the application of the noise-correction described in Appendix C will eliminate the TSE. If either of the remaining three causes produce the attenuation the TSE cannot be avoided.

The model-generated data-set MOD-MF-TSE has been employed to investigate the magnitude biases of the TSE. The results suggest that the FCA provides a very good estimate of

the model input velocity for antenna spacings less than the pattern scale. The results however suggest that the current analysis can produce true velocity magnitudes which underestimate the model input velocity magnitude for antenna spacings comparable to or greater than the pattern scale. In order to reduce this problem a new rejection criterion has been employed, whereby records with cross-correlation maxima delay-times τ'_{ij} exceeding the lag $\tau_{0.1}$ where the auto-correlation falls to 0.1 are rejected. This criterion has been shown to solve this underestimation. The estimates of $T_{0.5}$ and $S_{0.5}$ exhibit a small increase with increasing antenna spacing. This increase is a result of "selection effects" inherent in the use of different antenna spacings due to the observed range of turbulent random motions and pattern scales. The FCA is shown to be independent of the effects of noise for SNRs exceeding 5 dB if the noise-correction described in Appendix C is employed. If the noise-correction is not employed the results exhibit the TSE, whereby the estimates of V_t, $T_{0.5}$, and $S_{0.5}$ increase with increasing antenna spacing. If the effects of coarse digitization and receiver saturation are present the results also exhibit the TSE.

The model-generated data-set MOD-MF-TSE-ROTN has been employed to investigate the directional biases of the TSE. The results suggest that the FCA will only produce small biases if the noise-correction described in Appendix C is employed. If the noise-correction is not employed or the effects of coarse digitization and receiver saturation are present significant biases can result. The bias in the direction of the true velocity θ_t however will be less than 4° if an equilateral triangle of receiving antennae are employed. The bias in using a right-angled triangle however can be as large as 25°. This results confirms the suggestions of *Briggs* [1984] that an equilateral triangle is the optimal configuration for the minimization of biases in θ_t. The use of an equilateral triangle does not however reduce the biases in the axial-rotation $\theta_{\mathbf{ax}}$. The direction of the $\theta_{\mathbf{ax}}$ bias is shown to be dependent on the antenna spacing.

The application of the FCA to the experimentally obtained data-set BP930518 reveals a significant TSE. This result was observed despite the fact that the noise-correction described in Appendix C has been employed, while receiver saturation and coarse digitization are almost nonexistent. In order to determine the cause of this TSE one-dimensional representations of the spatial correlation function were calculated. The resulting spatial correlation functions were found to extrapolate to below unity at zero spatial lag. This result was attributed to differences in the characteristics of the individual receivers. Preliminary attempts

to account for these differences by correcting the cross-correlation functions for the attenuation have proven unsuccessful, as also found by *Golley and Rossiter* [1970]. The effects of differences in the receiver characteristics can be avoided by employing a single receiving antenna and using multiplexing in order to switch the signals recorded by the individual antennae in turn to this receiver. The TSE can alternatively be avoided by abandoning the FCA in favor of the four-antenna spatial correlation analysis (SCA4), which is introduced in Chapter 6.

Chapter 6

Alternative Correlation Analyses

6.1 Introduction

Although the full correlation analysis (FCA) was first implemented in the early fifties (e.g. *Briggs et al.*, [1950]) it is currently employed in a fundamentally identical manner. There exist a number of different descriptions of the FCA which are based on the same general assumptions, but employ different mathematical formulations to determine the FCA outputs. The most commonly referenced descriptions are those of *Brown and Chapman* [1972], *Meek* [1980], and *Briggs* [1984]. The description presented in Chapter 4 follows that of *Briggs* [1984], and is based on the determination of the FCA outputs from the estimated correlation parameters using a least squares analysis. The description presented by *Meek* [1980] on the other hand provides formulae for the direct estimation FCA outputs from the correlation parameters.

Despite the longevity of the FCA the assumptions of the analysis have consistently been questioned. The assumption that the spatial and temporal dependences of the spatio-temporal correlation function are identical is often considered the weakest assumption of the FCA (e.g. *Briggs*, [1984]). A number of alternative correlation analyses have been proposed which bypass the use of this assumption. The revised FCA of *Briggs and Maude* [1978] does not use any assumptions about the temporal form of the spatial correlation function. This technique relies on the determination of the lags where the auto- and cross-correlation function intersect. The analysis of *Costa* [1988] employs the same assumptions as the FCA for the spatial form of the spatio-temporal correlation function, but employs a general polynomial form for the temporal form. The spatial correlation analysis (SCA) (e.g. *Briggs*, [1968])

also employs the same assumptions as the FCA for the spatial form of the spatio-temporal correlation function, but does not require any assumptions about the temporal form. The implementation of the SCA has previously been limited by the belief that the ground diffraction pattern must be sampled at a large number of spatial positions. The SCA is described in section 6.3, where it is illustrated that the technique can be successfully implemented using a minimum of three receiving antennae.

A further alternative correlation analysis has recently been proposed by *Lataitas et al.* [1995]. This analysis is based on the determination of the wind velocity using the slope of the cross-correlation function about zero-lag. This analysis is described in section 6.2, where it is illustrated that the analysis is essentially a special case of the FCA for the situation of isotropic scatter.

6.2 The slope-fitting correlation analysis

6.2.1 Theory of the slope fitting correlation analysis

The use of correlation analyses has also extended into optical measurements of atmospheric velocities. The "laser velocimetry" technique of *Churnside and Yura* [1981] uses laser scattering from aerosols to provide estimates of the horizontal wind velocity. This technique is essentially an optical analogue of the FCA. The "laser scintillation" technique of *Wang et al.* [1981] uses the correlation of intensity fluctuations resulting from the propagation of turbulent irregularities across the optical path to provide estimates of the horizontal wind velocity. As a result of the rapid temporal evolution of the backscattered optical pattern the technique uses the slopes of the cross-correlation functions about zero-lag, which are demonstrated to be independent of the temporal evolution of the pattern.

The analysis presented by *Lataitas et al.* [1995], which is hereafter referred to as the slope-fitting correlation analysis (SFCA), is essentially the radar analogue of the optical slope fitting technique. The SFCA is based on the assumption of isotropic scatter, although the authors suggest that the technique should also be applicable to moderately anisotropic scatter. The mathematical formulation has been derived using an analytical model similar to that of *Liu et al.* [1990], confirming that the technique is independent of the effects of turbulent random motions.

To illustrate the technique, consider the situation where the ground diffraction pattern is propagating with velocity $\vec{V}$ at an angle θ to two receiving antennae i and j with separation

d_{ij}. In this situation the slope R_{ij} of the "renormalized" cross-correlation function

$$\rho'_{ij}(f) = \frac{\rho_{ij}(f)}{\rho_{ij}(0)} \tag{6.1}$$

at zero-lag is given by

$$R_{ij} = \frac{2d_{ij}V\cos\theta}{D^2_{\text{eff}}}, \tag{6.2}$$

where D_{eff} is the effective e^{-1} diameter of the polar diagram associated with the transmitting and receiving antennas. The slope R_{ij} is shown to be independent of the random changes in the ground diffraction pattern. Given three non-aligned receiving antennae, the horizontal wind velocity can be estimated using the values of R_{ij} determined from the three renormalized cross-correlation functions. The technique has been successfully implemented at UHF in the atmospheric boundary layer where isotropic scatter is considered the dominant scattering mechanism by *Lataitas et al.* [1995], as illustrated in Figure 6.1. In the literature to date the SFCA has not been applied at either MF or VHF where anisotropic scatter can occur.

The theoretical model of the spatio-temporal correlation function employed by the FCA has been used to investigate the SFCA. In this investigation the assumption that the spatial and temporal dependences of the spatio-temporal correlation function are identical has been abandoned by assuming a general form for the temporal dependence given by $T(\tau)$. The function $T(\tau)$ must have the properties $T(0) = 0$, $T(\tau) = T(-\tau)$, and $T(\tau) \to \infty$ as $\tau \to \infty$. As a result, it therefore follows that $(\partial T/\partial\tau)_{\tau=0} = 0$. The spatio-temporal correlation function of (4.9) can therefore be written

$$\rho(\xi,\eta,\tau) = \rho(A(\xi - V_x\tau)^2 + B(\eta - V_y\tau)^2 + 2H(\xi - V_x\tau)(\eta - V_y\tau) + T(\tau)). \tag{6.3}$$

The cross-correlation function for antennae i and j with vector separation (ξ_{ij},η_{ij}) is therefore given by

$$\rho_{ij}(\tau) = \rho(A(\xi_{ij} - V_x\tau)^2 + B(\eta_{ij} - V_y\tau)^2 + 2H(\xi_{ij} - V_x\tau)(\eta_{ij} - V_y\tau) + T(\tau)). \tag{6.4}$$

The temporal derivative of this equation is given by

$$\begin{aligned}\frac{\partial\rho_{ij}(\tau)}{\partial\tau} &= -(2AV_x(\xi_{ij} - V_x\tau) + 2BV_y(\eta_{ij} - V_y\tau) + \\ &\qquad 2HV_y(\xi_{ij} - V_x\tau) + 2HV_x(\eta_{ij} - V_y\tau) + \frac{\partial T(\tau)}{\partial\tau})\ \rho_{ij}(\tau).\end{aligned} \tag{6.5}$$

Substituting $\tau = 0$ into (6.5) yields

$$\left(\frac{\partial\rho_{ij}(\tau)}{\partial\tau}\right)_{\tau=0} = -(2AV_x\xi_{ij} + 2BV_y\eta_{ij} + 2HV_y\xi_{ij} + 2HV_x\eta_{ij} + \left(\frac{\partial T(\tau)}{\partial\tau}\right)_{\tau=0})\ \rho_{ij}(0). \tag{6.6}$$

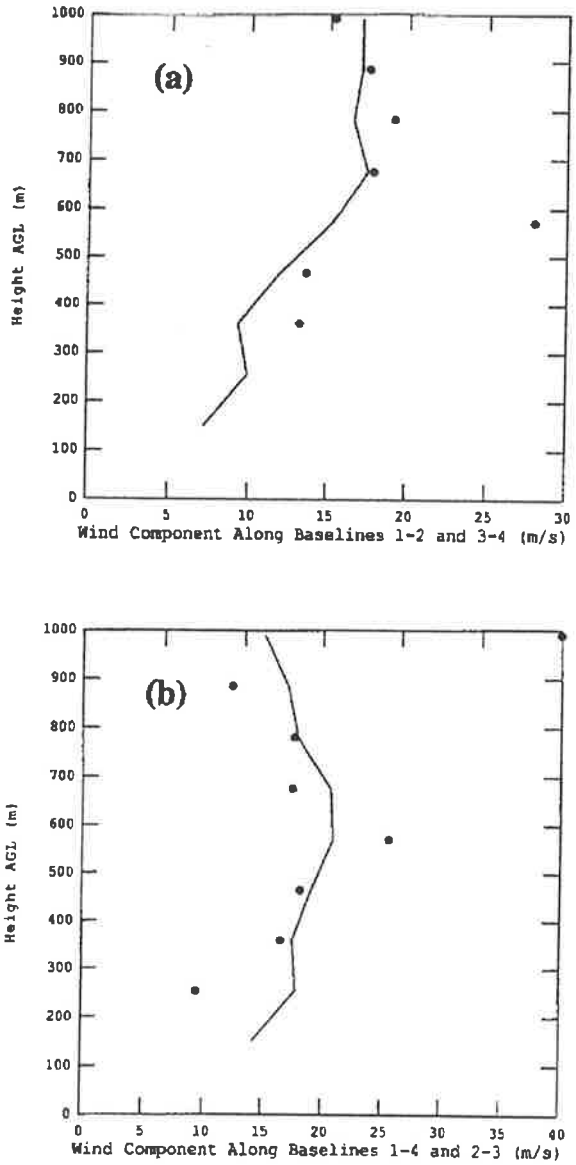

Figure 6.1: Meridional (top) and zonal velocities estimated on the application of the SFCA (•) to data collected by a 915 MHz SA profiler developed by the National center of atmospheric research (NCAR). The solid line denotes the wind velocity estimated from simultaneous rawinsonde measurements. (after *Lataitas et al.*, [1995]).

Using the condition $(\partial T/\partial \tau)_{\tau=0} = 0$, the slope of the renormalized cross-correlation function at zero-lag is given by

$$R_{ij} = -(2A\xi_{ij} + 2H\eta_{ij})V_x - (2B\eta_{ij} + 2H\xi_{ij})V_y. \tag{6.7}$$

This equation is independent of $T(\tau)$, and hence independent of the temporal form of the spatial correlation function. As a result, R_{ij} is independent of the random changes in the ground diffraction pattern, as also noted by *Lataitas et al.* [1995].

Consider the situation where two antennae are zonally aligned with spacing d_{ij}, such

that $\xi_{ij} = d_{ij}$ and $\eta_{ij} = 0$. If the pattern is isometric, $A = B$, and $H = 0$. In this case the e^{-1} pattern scale S_e, given by the spatial lag ξ where $A\xi^2 = -1$, is given by $S_e^2 = -A^{-1}$. If the velocity components are defined in terms of the angle from the zonal axis, $\vec{V} = (V_x, V_y) = (V\cos\theta, V\sin\theta)$, (6.7) becomes

$$R_{ij} = \frac{2d_{ij}V\cos\theta}{S_e^2}. \tag{6.8}$$

This equation is identical to (6.2) if $D_{\text{eff}} = S_e$. This is clearly sensible, as the e^{-1} pattern scale is equivalent to the effective e^{-1} width of the polar diagram in the anisotropic scatter situation. It therefore follows that (6.8) provides the extension of (6.2) to the anisotropic scatter situation for isometric ground diffraction patterns. As the characteristic ellipse incorporates the effects of pattern anisometry it is clear that (6.7) provides the full extension of (6.2) to the anisotropic scatter situation for anisometric ground diffraction patterns. The application of (6.7) will hereafter be referred to as the revised-SFCA, or RSFCA, in order to distinguish from the application of (6.2).

The RSFCA requires the determination of the characteristic ellipse parameters A, B, and H in order to determine the wind velocity. It is clear from the derivation of (6.8) that the ellipse parameters must be specified in terms of the e^{-1} pattern scale S_e, rather than half-width pattern scale $S_{0.5}$ as used by the FCA. The ellipse parameters can only be determined by assuming a functional form for the spatial correlation function. If a Gaussian form is assumed the procedure outlined in *Briggs* [1992] can be employed. In this situation the e^{-1} characteristic ellipse parameters are assumed to satisfy the equation

$$A\xi^2 + B\eta^2 + 2H\xi\eta = 1. \tag{6.9}$$

Consider two antenna i and j with vectorial separation $(\xi_{ij}, \eta_{ij}) = r_{ij}(\cos\theta_{ij}, \sin\theta_{ij})$. The spacing r'_{ij} which would yield a correlation of e^{-1} between these antennae is given by

$$r'_{ij} = r_{ij}(-\ln\rho_{ij}(0))^{-0.5}. \tag{6.10}$$

Substituting (6.10) into (6.9) yields

$$A\cos^2\theta_{ij} + B\sin^2\theta_{ij} + 2H\cos\theta_{ij}\sin\theta_{ij} = r'^{-2}_{ij}. \tag{6.11}$$

The ellipsoid parameters can be determined by the least squares solution to the series of equations produced by (6.11) for all combinations of antenna pairs.

6.2.2 Practical considerations for the RSFCA

There are a number of important factors that must be considered in applying the RSFCA experimentally. Because the RSFCA uses the zero-lag cross-correlations for the determination of the ellipsoid parameters the correlation functions must be corrected for the effects of noise. This can be achieved using the noise correction procedure outlined in Appendix C. The effects of noise can produce cross-correlation functions with a "ragged" appearance, as illustrated in Appendix C. The use of noisy cross-correlation functions can therefore significantly degrade the technique (e.g. *Lataitas et al.*, [1995]). The use of the ellipsoid parameters also implies that the RSFCA will be subject to the triangle size effect if any source of decorrelation exists (see Chapter 5). In general the pattern will be insufficiently temporally sampled to produce linear behavior in the cross-correlation function about zero-lag. This suggests that a linear fit over lags either side of zero-lag will not provide a satisfactory estimate of the slope of the renormalized cross-correlation at zero-lag. The errors inherent in using a linear fit have been investigated by *Lataitas et al.* [1995], who illustrate that accurate slope estimation can be obtained if the cross-correlation maximum delay-time τ'_{ij} exceeds sampling time by a factor of five.

For the present application of the RSFCA the slopes of the cross-correlation functions about zero-lag are obtained from the results of the interpolations used to correct the zero-lag cross-correlations for the effects of impulsive noise recorded simultaneously in each receiving channel. This allows the RSFCA to be applied using the minimum number of lags required to successfully perform the zero-lag auto- and cross-correlation interpolations. A typical example of the slopes obtained from the application of the interpolation to the cross-correlation functions calculated using the data-set BP940527 at 90 km are shown in Figure 6.2. The effective application of these interpolations is limited by the number of lags on the main peak of the correlation functions, and therefore by the sampling time Δt. An expression for the maximum sampling time $\Delta t_{\max}$ for the successful application of the FCA based on the zero-lag auto-correlation interpolation is given by (4.47). This expression is equally applicable for the RSFCA. If $\Delta t < \Delta t_{\max}$ the RSFCA can therefore be applied using correlation functions calculated to four-lags either side of zero-lag. As a result, there are considerably fewer calculations required for the application the RSFCA than for the FCA. On the other hand, the RSFCA does not provide any information on the random changes in the ground diffraction pattern.

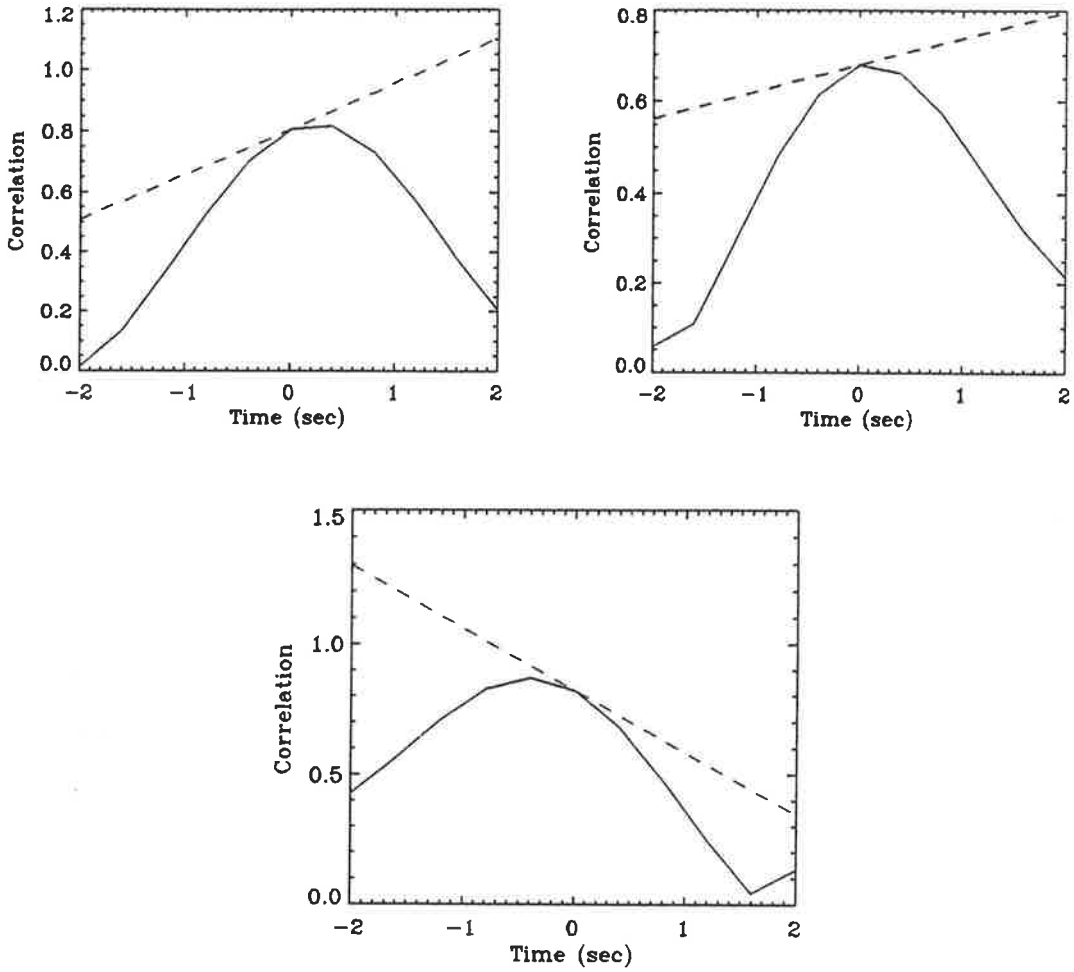

Figure 6.2: Typical example of the slopes obtained from the application of the zero-lag interpolation to the cross-correlation functions calculated using the data-set BP940527 at 90 km. The solid lines indicate the cross-correlation function, while the dashed lines indicate the estimated slope at zero-lag.

Table 6.1: The RSFCA rejection criteria.

Code	Explanation
0	Record accepted
1	Low signal amplitude
2	SNR < -6 dB
3	$\tau_{0.5} > 6$ s $\rho(\tau_{\max}) > 0.5$ $\rho(\tau)$ oscillatory
4	Slow fading
5	NTD > 0.5
6	Poor zero-lag interpolation
7	A or $B < 0$
8	$\tau'_{ij} < \tau_{0.1}$

In order to apply the RSFCA experimentally a number of rejection criteria have been developed. These criteria are shown in Table 6.1. The majority of these criteria are taken directly from the FCA rejection criteria shown in Appendix D. Where appropriate, the same rejection codes have been used. Criteria 2, 4, 6 and 8 are effectively applied by *Lataitas et al.* [1995], who only use records where the cross-correlations about zero-lag are sufficiently smooth and the main peak of the cross-correlation functions are distinct from the tails. Criterion 3 is employed to reject records indicative of specular scatter, as the RSFCA is essentially a volume-scatter technique. Criterion 5 is employed because (6.7) suggests that the sum of the R_{ij} values around a closed loop of antennae should sum to zero. In practice, statistical variations and noise can result in the sum being non-zero. As a result, the criterion is relaxed somewhat. This criterion is essentially identical to the FCA criterion 5, which applies the NTD to the cross-correlation maxima delay times τ'_{ij}, and was not employed by *Lataitas et al.* [1995]. Criterion 7 is employed because the RSFCA requires sensible parameterization of the characteristic ellipse, which is specified by the parameters A, B and H. The use of criterion 4 and 8 suggests that the correlation functions must be calculated to the same number of lags as for the FCA, and effectively rules out the possibility of applying the analysis using only the lags required for the zero-lag auto- and cross-correlation interpolation.

6.2.3 Application of the RSFCA

The velocity estimates obtained on the application of the FCA and RSFCA to the model-generated data-set MOD-MF-SA are illustrated in Figure 6.3 as a function of the model turbulent velocity v_{mod}. These results suggest that the RSFCA accurately estimates the model input velocity for all values of v_{mod}. The standard deviation of the FCA true and RSFCA velocity are also shown in Figure 6.3, revealing that the RSFCA produces a slightly larger standard deviation. This occurs because the zero-lag slope estimation is more susceptible to statistical errors than the Gaussian fits used for the estimation of the correlation parameters employed by the FCA, as suggested by *Lataitas et al.* [1995]. Nonetheless, the RSFCA appears to provide an excellent estimate of the model-input velocity. The importance of applying the anisometric formulation of the RSFCA provided by (6.7) is illustrated in Figure 6.4, which illustrates the velocity direction estimated by applying (6.7) and (6.8) to the model-generated data-set MOD-MF-ANISO which was generated using a model anisometry parameter $A = 2$ (see Chapter 3 for the details). The anisometric formulation of (6.7)

accurately reproduces the model input velocity direction, while the isometric formulation of (6.8) produces directions biased perpendicularly to the direction of elongation of the ground diffraction. This is the same bias produced by the FCA apparent velocity.

The results of the application of the FCA and RSFCA to the first two hours of the BP MF SA data-set BP940527 are shown in Figure 6.5. The velocities show good agreement at all heights except 90 km. There is some tendency for the magnitude of the RSFCA velocity to underestimate the magnitude of the FCA true velocity above 86 km. The cause of this underestimation is mainly due to the larger spread in the RSFCA velocity direction estimates. This effect was not seen in the analysis of the model-data. In addition, the fact that FCA rejection criterion 10 rejects some of the records with small V_t values biases the average V_t to larger absolute values at these heights. Approximately 15% of records are rejected by rejection criterion 5 for both the FCA and RSFCA. Of these records, approximately 50% are rejected by both criteria. This suggests that these criteria are similar, but not quite identical.

6.2.4 Summary

The slope fitting correlation analysis (SFCA) of *Lataitas et al.* [1995] has been presented. The theoretical model of the spatio-temporal correlation function employed for the FCA has been used to illustrate that the technique is essentially the isotropic scatter equivalent of the FCA. In order to apply the technique to anisometric patterns in the anisotropic scatter situation (6.7) must be employed. This formulation requires the determination of the characteristic ellipse, which is parameterized by the ellipsoid parameters A, B, and H. The ellipse parameters can be determined using the technique outlined by *Briggs* [1992]. The use of the ellipse parameters implies that the revised SFCA (or RSFCA) will be subject to the FCA triangle size effect, whereby any effect attenuating the magnitude of the cross-correlation function will result in an underestimation of the magnitude of the velocity estimate.

The results of Figures 6.3 and 6.5 suggest that the RSFCA produces velocity estimates in very good agreement with the FCA true velocity. This is clearly sensible given the fact that (6.7) is derived from the theoretical model of the spatio-temporal correlation function employed for the FCA. The importance of using the anisometric formulation of the SFCA is illustrated in Figure 6.4, which suggests that the velocity obtained on applying the isometric formulation is biased in the same direction as the FCA apparent velocity. The results of Figures 6.3 and 6.5 suggest that the RSFCA produces larger error estimates than the FCA.

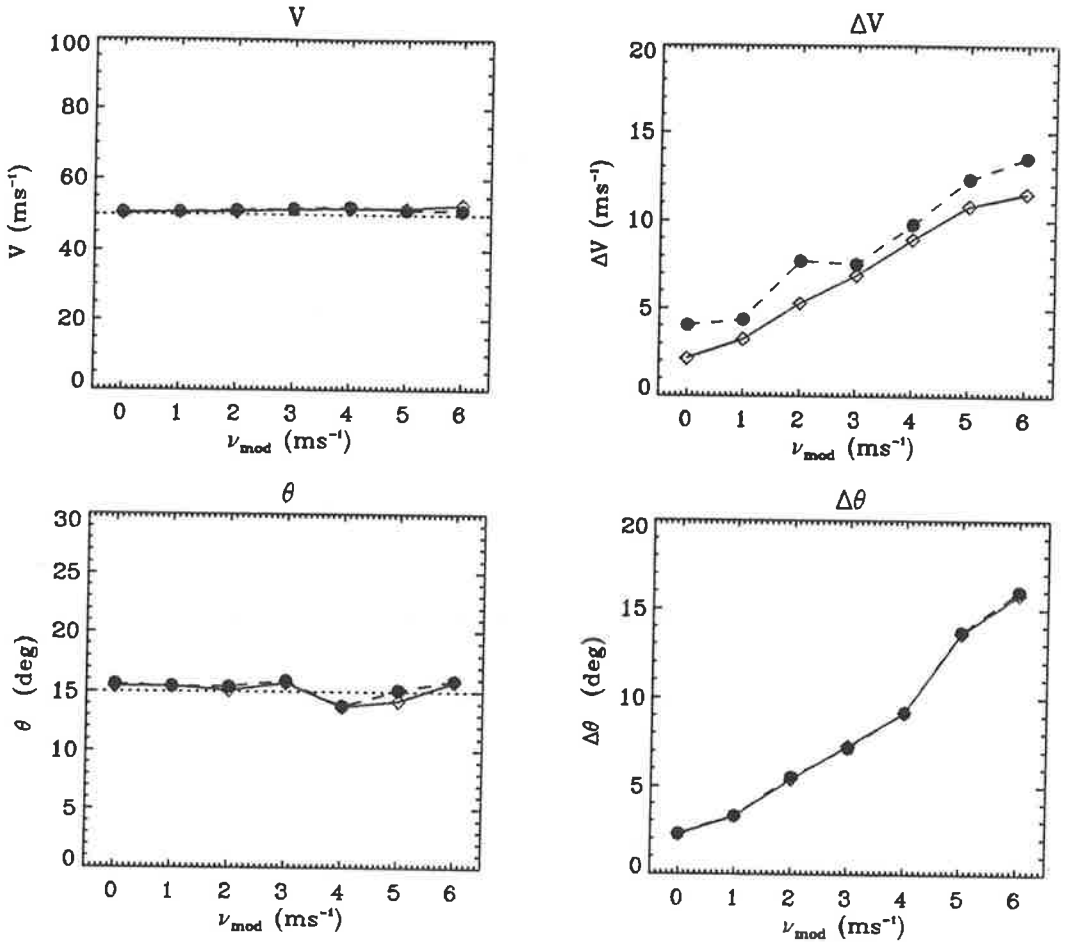

Figure 6.3: Results of the application of the FCA (◇) and RSFCA (•) to the model-generated data-set MOD-MFSA. The top plots show the average (left) and standard deviation (right) of the magnitude of the average velocity. The bottom plots show the average (left) and standard deviation (right) of the direction of the average velocity.

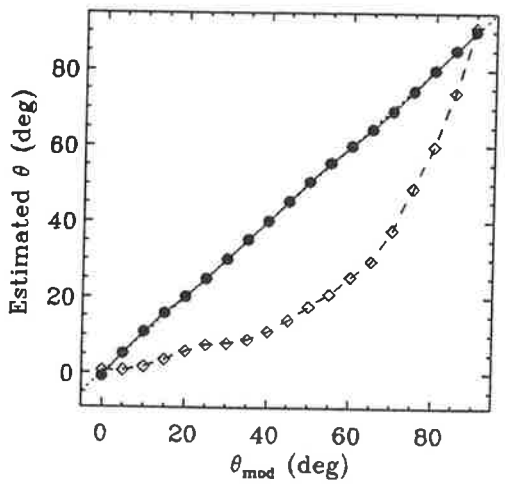

Figure 6.4: Average velocity directions as a function of model velocity direction (θ_m) for the application of the anisometric (◇) and isometric (•) formulations of the RSFCA to the model generated data-set MOD-MF-ANISO.

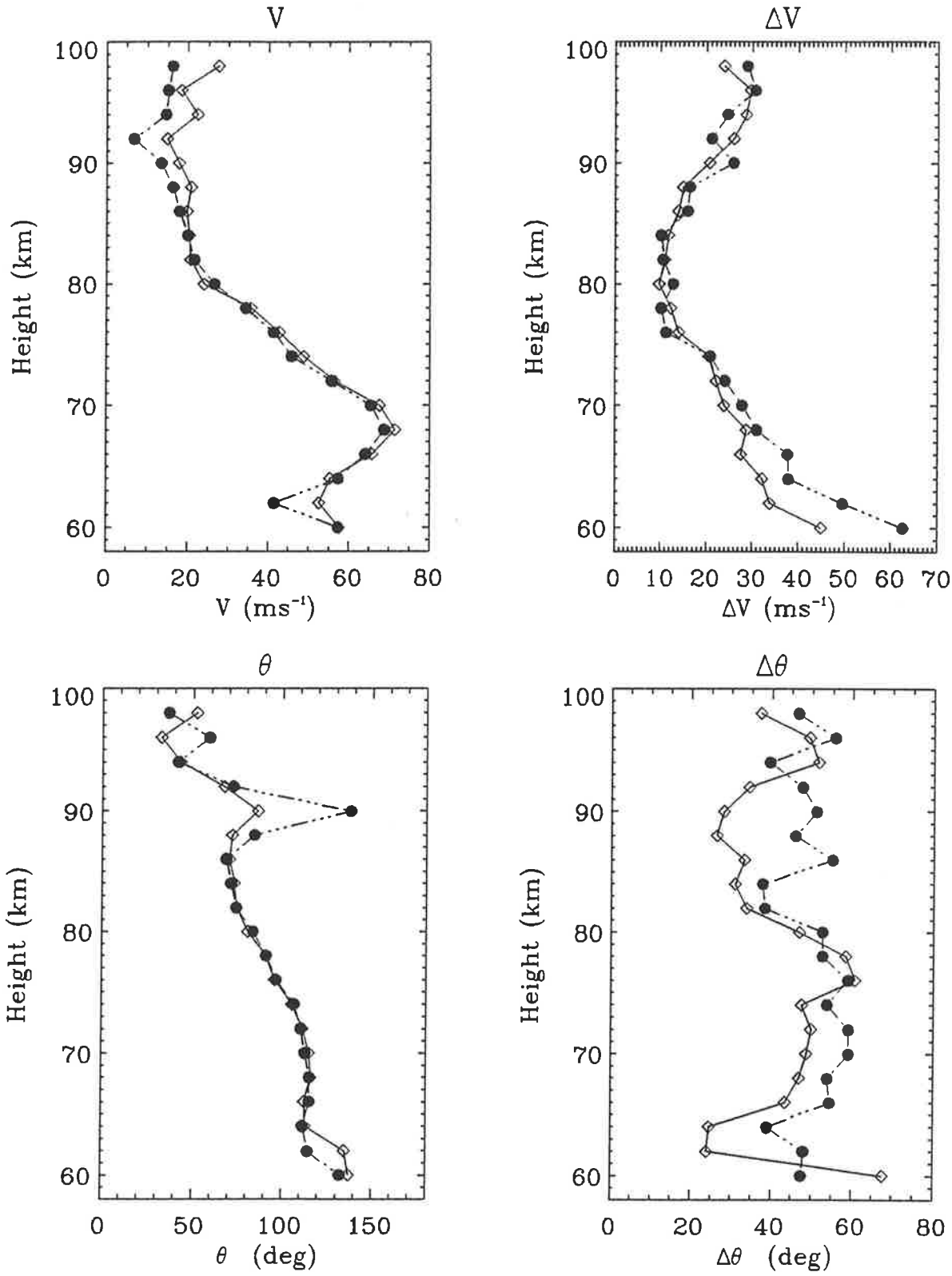

Figure 6.5: Profiles of the average velocity magnitude (top left) and standard deviation (top right), and average velocity direction (bottom left) and standard deviation (bottom right) obtained applying the FCA (◇) and RSFCA (•) to the data-set BP940527.

This is because the slope estimation procedure is more susceptible to statistical variations that the Gaussian fits employed by the FCA to determine the correlation parameters.

The analysis of the model-generated and experimental data-sets presented in this section suggest that the SFCA does not provide any advantage over the FCA. Although the technique can in theory be applied over the small number of lags required for the zero-lag auto- and cross-correlation interpolations the implementations described above and by *Lataitas et al.* [1995] both calculate the correlation functions out to a larger number of lags in order to apply the rejection criteria. Unlike the FCA, the SFCA does not provide any information on the temporal evolution of the ground diffraction pattern.

6.3 The spatial correlation analysis

The "spatial correlation analysis" (SCA) (e.g. *Briggs*, [1968]) is based upon the estimation of the displacement of the ground diffraction pattern between sampling times. In order to implement the technique experimentally it is necessary to be able to obtain instantaneous images of the ground diffraction pattern. This requires an array of receiving antennae covering an area exceeding the mean pattern scale, and with antenna spacings considerably shorter than the mean pattern scale in order to produce an image with sufficient spatial resolution.

The basis of the SCA is as follows. The displacement of the ground diffraction pattern in the duration of the sampling time Δt is first determined by estimating the position $\vec{D}_{\max}$ of the maximum of the spatial correlation function $\rho(\xi, \eta, \Delta t)$. This function is determined by substituting the temporal lag $\tau = \Delta t$ into the spatio-temporal correlation function $\rho(\xi, \eta, \tau)$. The position $\vec{D}_{\max}$ can be determined by applying a two-dimensional Gaussian fit to the spatial correlation function similar to that described by *Vandepeer and Reid* [1995b] for the determination of the direction of the power maximum obtained upon applying the PBS technique described in Chapter 1. The pattern velocity $\vec{V}$ is then determined by

$$\vec{V} = \frac{\vec{D}_{\max}}{\Delta t}. \tag{6.12}$$

The atmospheric velocity is obtained by halving the pattern velocity to account for the point-source effect (e.g. *Felgate*, [1970]). The position of the spatial correlation maximum $\vec{D}_{\max}$ can be shown to be independent of the effects of random changes in the ground diffraction pattern (e.g. *Briggs*, [1968]). The SCA therefore requires no assumptions about the temporal form of the spatio-temporal correlation function.

The SCA has been successfully implemented on the BP MF array using "amplitude-only" time-series (e.g. *Briggs et al*, [1969]). The application of the SCA to complex time-series records is complicated significantly by the need to account for any phase differences that may exist between the receivers employed for the analysis (see Chapter 8 for further details on receiver phase differences). The knowledge of these phase differences is critical to the calculation of the spatio-temporal correlation function detailed in Appendix C. The application of the SCA to complex time-series records is therefore best illustrated using model-generated data, where no receiver phase differences have been introduced. The spatial correlation functions obtained using the model-generated data-set MOD-MF-GDP-V50-T6-AN at the temporal lags $\tau = 0$ and $\tau = 2$ s are illustrated in Figure 6.6, together with the estimated position of the spatial correlation maxima $\vec{D}_{\max}$ for $\tau = 2$ s. The application of (6.12) yields an estimated velocity of 32 ms^{-1}, 87° clockwise from North, which shows reasonable agreement with the model input velocity of 50 ms^{-1}, 90° clockwise from North.

6.4 The three-antenna spatial correlation analysis

6.4.1 Theory of the three-antenna spatial correlation analysis

Because the majority of radars do not possess the spatial sampling capabilities suitable for the implementation of the SCA a preliminary attempt has been made to determine whether a revised analysis capable of working with a minimum of three receiving antennae could produce accurate velocity estimates.

Consider the situation illustrated in Figure 6.7 of three antennae A_i arranged in an equilateral triangle at positions (ξ_i, η_i). For each antenna pair ij the spatial correlation function at the non-zero temporal lag Δt can be evaluated at three spatial lags. The spatial correlation at zero spatial lag can be determined from the magnitude of the auto-correlation function by

$$\rho(0, 0, \Delta t) = \rho_i(\Delta t), \tag{6.13}$$

while the spatial correlation at spatial lags (η_{ij}, ξ_{ij}) and $(-\eta_{ij}, -\xi_{ij})$, where $(\xi_{ij}, \eta_{ij}) = (\xi_j, \eta_j) - (\xi_i, \eta_i)$, can be determined from the magnitude of the cross-correlation function by

$$\rho(\eta_{ij}, \xi_{ij}, \Delta t) = \rho_{ij}(\Delta t), \text{ and} \tag{6.14}$$

$$\rho(-\eta_{ij}, -\xi_{ij}, \Delta t) = \rho_{ij}(-\Delta t). \tag{6.15}$$

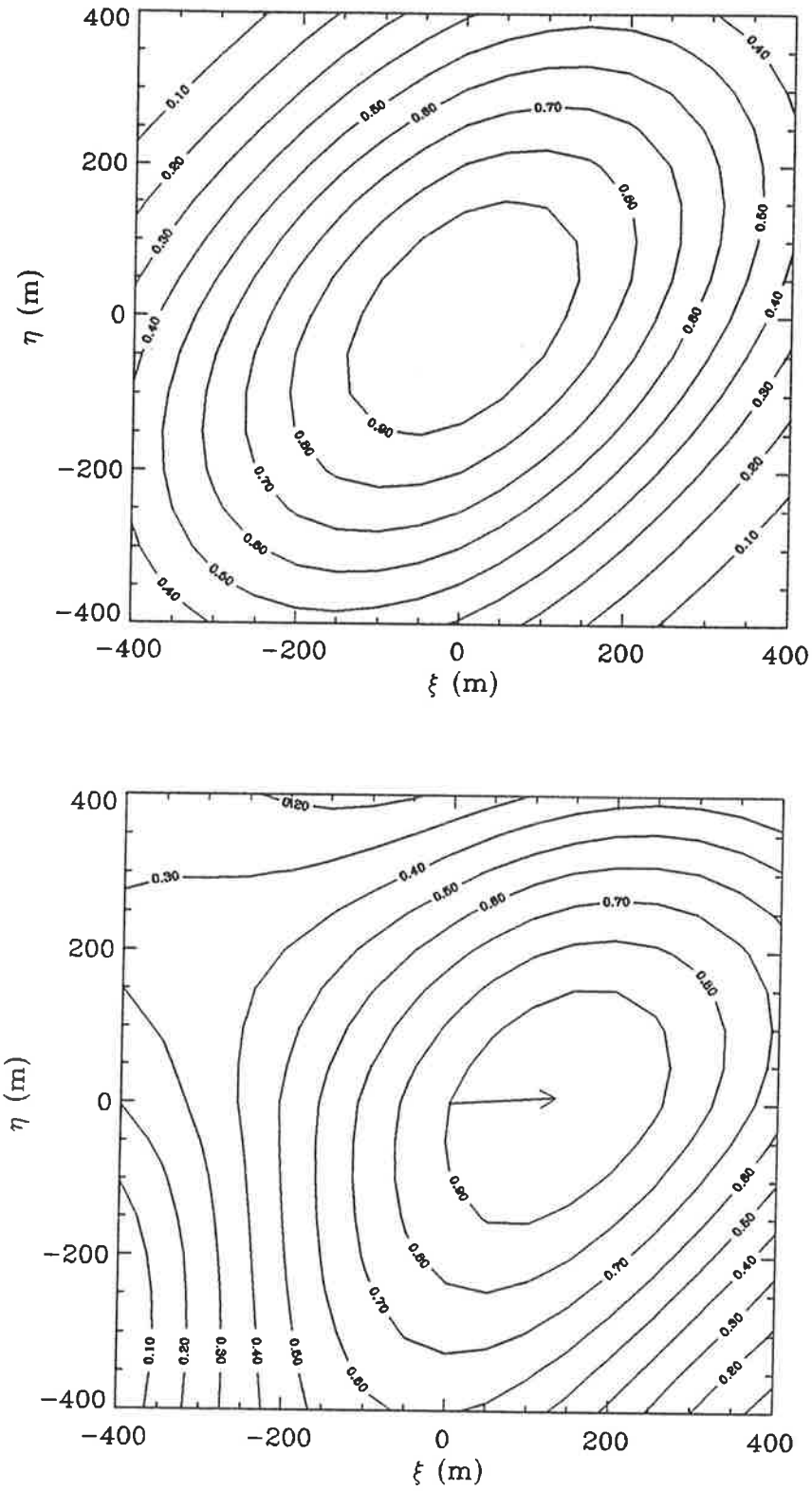

Figure 6.6: Example of the spatial correlation functions from the anisotropic scatter simulation at temporal lags $\tau = 0$ (left) and $\tau = 2$ s (right). The lines denote the contours of constant spatial correlation. The arrow in the right hand plot denotes the displacement of the spatial correlation function between these temporal lags.

Each antenna pair ij therefore yields one "arm" of three colinear spatial lags. As zero spatial lag is common to each antenna pair the spatial correlation function is evaluated at a total of seven spatial lags. The position of maximum spatial correlation I_{ij} along the arm of spatial-lags formed by each antenna pair ij occurs where one of the family of ellipses of constant spatial correlation touches the line (e.g. *Briggs*, [1968]). This position can be determined by applying a Gaussian fit over the spatial correlation values for the three spatial lags. The position of the spatial correlation maximum $\vec{D}_{\max}$ is given by the intercept of the three lines which pass through each I_{ij} with slopes tangential to the contours of constant zero temporal lag spatio-temporal correlation passing through I_{ij}, as illustrated in Figure 6.7. The velocity of the pattern can then be determined using (6.12). The application of this technique will be hereafter referred to as the three-antenna spatial correlation analysis, or the SCA3. The SCA3 can in theory be applied to any set of three non aligned receiving antennae provided that the antennae sample the same "region" of the pattern, as is the case for the FCA.

6.4.2 Application of the three-antenna spatial correlation analysis

The application of the SCA3 requires the determination of the contours of constant spatial correlation in order to estimate the slope of the lines through each I_{ij}. The contours of constant spatial correlation can be derived from the characteristic ellipse (see Chapter 4 for details), which can be estimated from the zero-lag cross-correlation values using the technique outlined by *Briggs* [1992]. This technique is presented in section 6.2. In order to apply this technique the zero-lag cross-correlation must be corrected for the effects of noise using the zero-lag interpolation procedure outlined in Appendix C. As the spatial correlation values along each arm of spatial lags are determined using the first lags of the auto- and cross-correlation functions the SCA3 can be applied using the minimum number of lags required for the application of the zero-lag interpolations.

The rejection criteria applied for the SCA3 analysis are shown in Table 6.2. Criteria 1, 2, 3, 4 and 8 have been taken directly from the RSFCA criteria described in section 6.2, as the SCA3 employs the same zero-lag auto- and cross-correlation interpolations and characteristic ellipse determination as the RSFCA. Criteria 5, 6, and 7 are applied to ensure the I_{ij} estimates are sensible. Criterion 5 is applied to reject records where at least one of the Gaussian fits to the arm of spatial lags produces a spatial correlation minimum rather than a maximum. Criterion 6 is applied to reject records where at least one of the I_{ij} estimates lies greater than one antenna spacing outside the maximum spatial lag for at least one arm

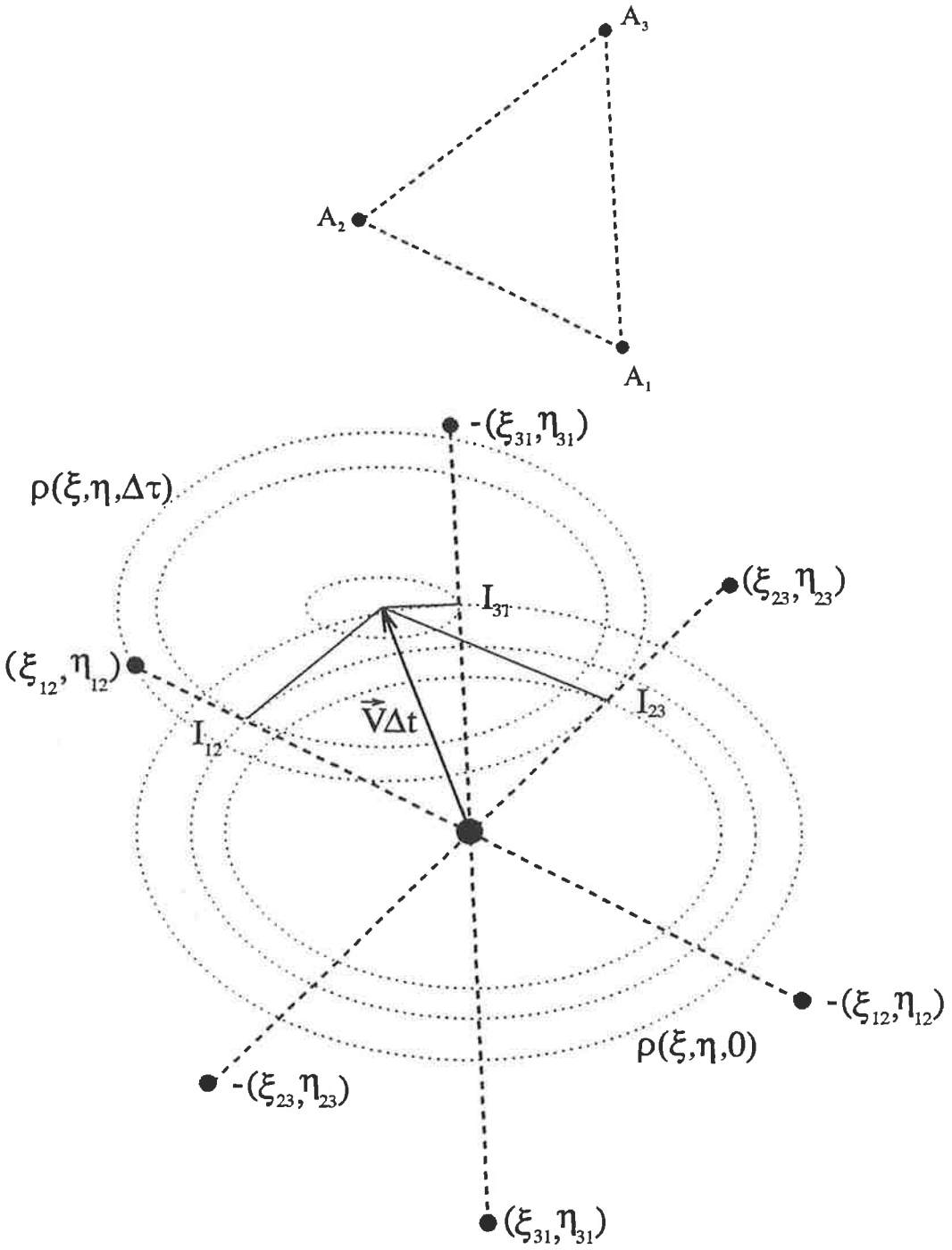

Figure 6.7: Illustration of the technique used to estimate the position of the spatial correlation maxima $\rho(\xi, \eta, \Delta t)$ for three antennae $A_i = (\xi_i, \eta_i)$ arranged in an equilateral triangle. The top plot illustrates the antenna configuration, while the bottom plot illustrates the spatial lags available using this antenna configuration, which produces three groups of three colinear spatial lags indicated by the thick dashed lines. The I_{ij} denote the positions of maximum spatial correlation along each line of spatial-lags. The dotted lines indicate the ellipses of constant spatial correlation $\rho(\xi, \eta, 0)$ and $\rho(\xi, \eta, \Delta\tau)$ passing through each I_{ij}. The position of the spatial correlation maxima $\vec{D}_{\max} = \vec{V} \triangle \tau$ is formed by the intersection of the three lines which pass through each I_{ij} tangentially to the ellipse of constant spatial correlation passing though I_{ij}.

Table 6.2: The SCA3 rejection criteria

Code	Explanation
0	Record accepted
1	Low signal amplitude
2	SNR < -6 dB
3	Poor zero-lag interpolation
4	$\rho_{ij}(0) < 0.2$
5	Poor Gaussian fit to at least one spatial lag arm
6	$I_{ij} >$ twice antenna spacing from zero spatial lag
7	Fitted spatial correlation maxima exceeds unity
8	A or B negative
9	Poor intersection of the lines through each I_{ij}

of spatial lags. In this situation there may be considerable inaccuracy in the I_{ij} estimate, thereby justifying the rejection of the record. If the SCA3 is applied using antenna spacings and sampling times typically employed for the FCA the maxima should lie within the spatial lag maxima. Criterion 7 is applied to reject records where the spatial correlation maxima exceeds unity on at least one arm. As the spatial correlation by definition cannot exceed unity it is unlikely that the I_{ij} value estimated in this instance will be accurately determined. Criterion 9 is employed to reject records where the variance of the $\vec{D}_{\max}$ estimate is large, as will be the case when the three lines produced for each arm of spatial lags do not come close to intersecting at one position.

The SCA3 has been applied to the model-generated data-set MOD-MF-SA with $\nu_{\text{mod}} = 6$ ms^{-1}. A typical example of the application of the Gaussian fits to the spatial correlation values along the three arms of spatial lags is shown in Figure 6.8. The estimation of the corresponding spatial correlation maxima $\vec{D}_{\max}$ are shown in Figure 6.9. In this situation the lines obtained from each value of I_{ij} intersect at a single point.

The results of the application of the SCA3 and the FCA to model-generated data-set MOD-MF-SA are illustrated in Figure 6.10 as a function of ν_{mod}. These results suggest that the SCA3 accurately estimates the model input velocity for all values of ν_{mod}. The standard deviation of the SCA3 results are slightly larger than those of the FCA. Nonetheless, the SCA3 provides an excellent estimate of the model-input velocity.

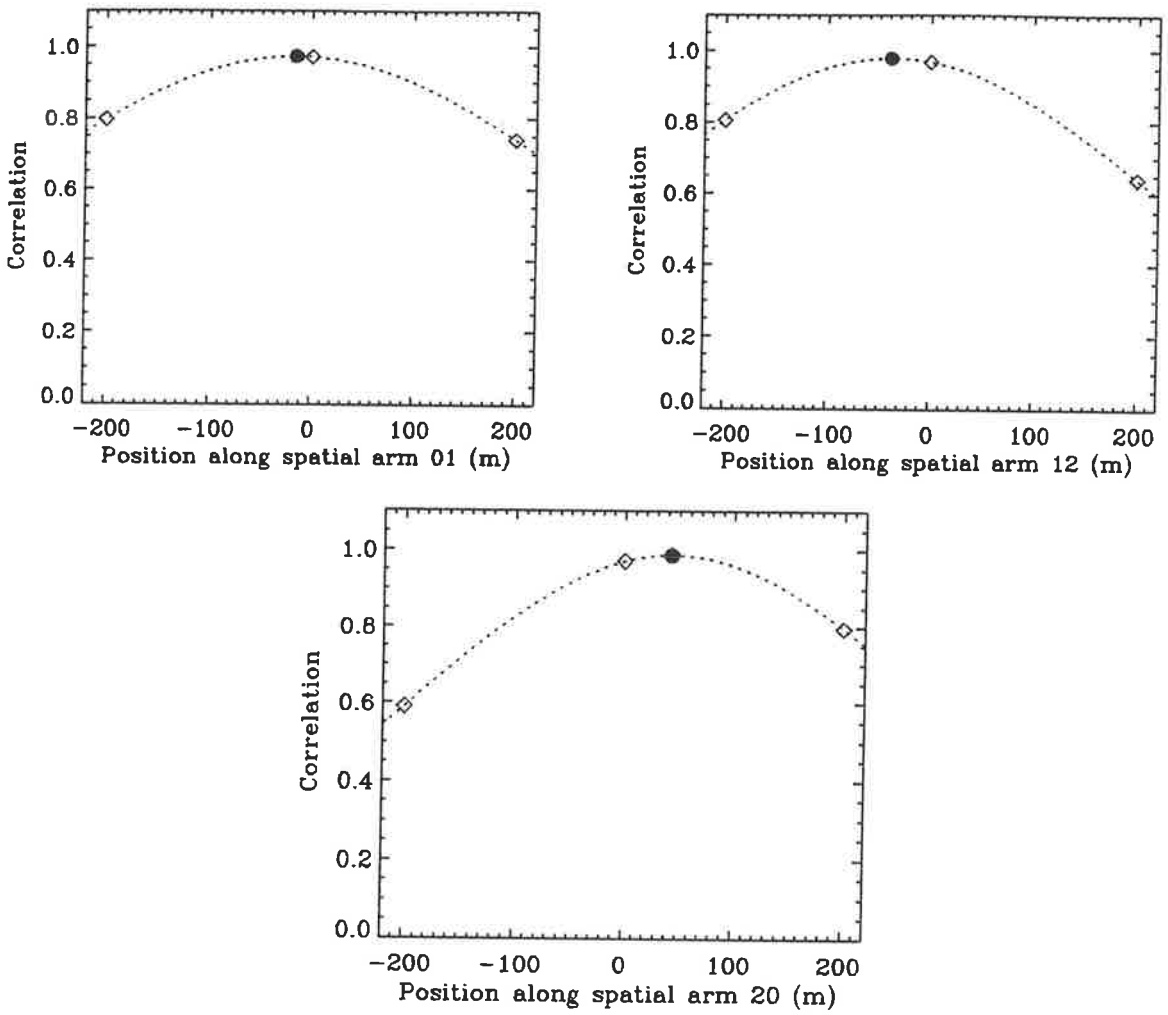

Figure 6.8: A typical example of the application of the Gaussian fit to the spatial correlation values along the three arms of spatial lags obtained using an individual record of the model-generated data-set MOD-MF-SA with $\nu_{\mathrm{mod}} = 6\ \mathrm{ms}^{-1}$. The diamonds ($\diamond$) denote the spatial correlation values. The resulting Gaussian fit is indicated by the dotted line, while the position of maximum correlation along each arm I_{ij} is denoted by ($\bullet$).

6.4.3 The triangle size effect

The FCA triangle size effect (TSE) occurs as a result of any attenuation introduced into the auto- and cross-correlation functions employed by the analysis. The analysis of Chapter 5 suggests that the TSE can result from the effects of noise, receiver saturation, coarse digitization, and differences in the characteristics of the receivers. The effect of noise can be easily removed from the correlation functions using the noise-correction procedure outlined in Appendix C.

The effects of receiver saturation and coarse digitization attenuate both the auto- and cross-correlation functions. The spatial correlation at zero spatial lag is calculated from

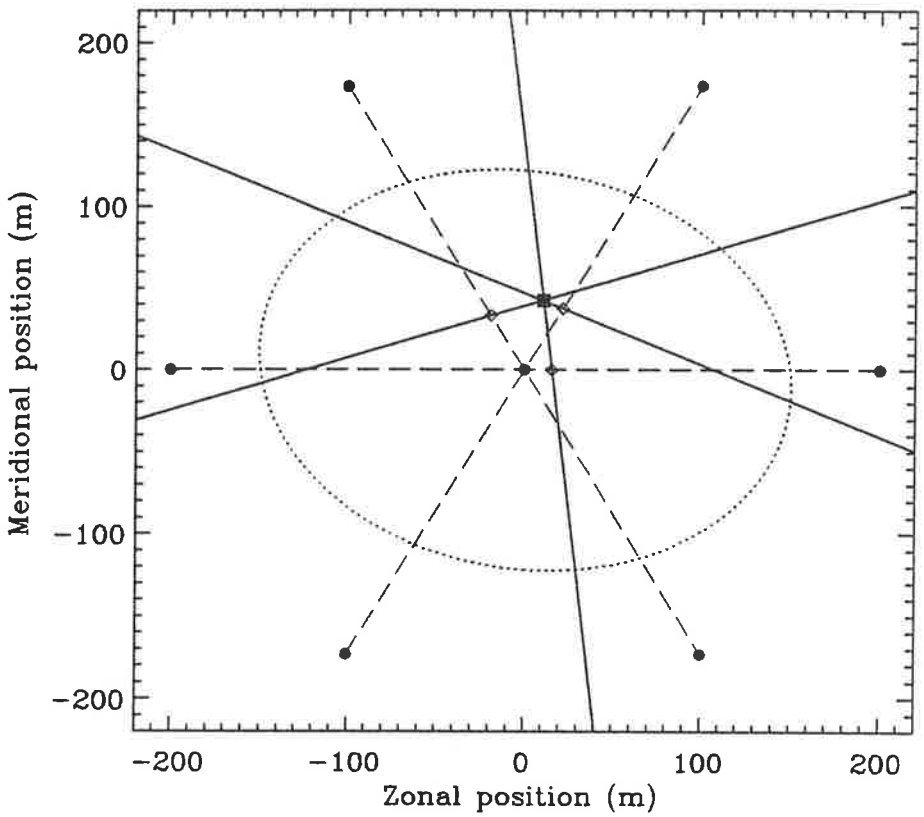

Figure 6.9: The estimation of the position of the spatial correlation maxima $\vec{D}_{\max}$ corresponding to the results illustrated in Figure 6.8. This figure is analogous to Figure 6.7, where the estimation process is explained in detail. The dotted line indicates the characteristic ellipse. The filled circles (•) denote the available spatial lags, while the dashed lines indicate the three arms of spatial lags corresponding to each receiver pair. The diamonds (◇) denote the positions of maximum correlation I_{ij} along each arm of spatial lags. The position $\vec{D}_{\max}$ is denoted by (□), which represents the intersection of the three solid lines passing through through the three I_{ij} positions.

the auto-correlation function, while the spatial correlation at the non-zero spatial lags is calculated from the cross-correlation function. It is evident from Figures 5.9 and 5.11 that the attenuation of the cross-correlation functions is greater than the attenuation of the auto-correlation functions. The spatial correlation at non-zero spatial lags are therefore suppressed more than the spatial correlation at non-zero spatial lags. It therefore follows that the position of maximum correlation I_{ij} along each arm of spatial lags will be biased towards zero-spatial lag. The resulting estimate of $\vec{D}_{\max}$ is therefore necessarily biased back towards zero-lag, resulting in the underestimation of the wind velocity. This decrease in analogous to the TSE.

The effects of differences in the receiver characteristics attenuates the cross-correlation functions only. The spatial correlation at zero spatial lag is therefore not suppressed. The

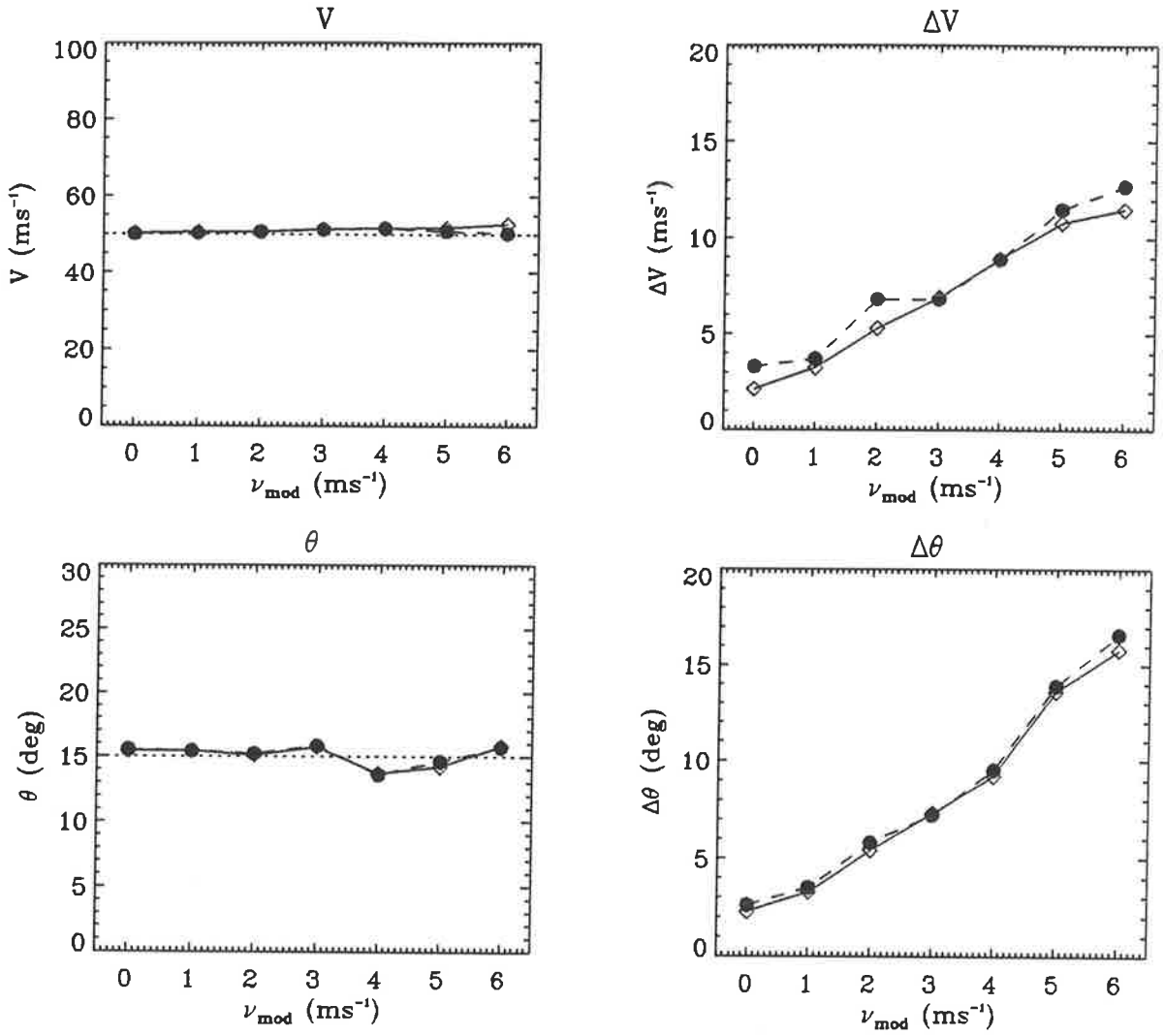

Figure 6.10: Results of the application of the FCA (◇) and SCA3 (•) to the model-generated data-set MOD-MF-SA. The top plots show the average (left) and standard deviation (right) of the magnitude of the average velocity. The bottom plots show the average (left) and standard deviation (right) of the direction of the average velocity.

spatial correlation at non-zero spatial lags however are suppressed, resulting in the position of maximum correlation I_{ij} along each arm of spatial lags being biased towards zero-spatial lag. The resulting estimate of $\vec{D}_{\max}$ is therefore necessarily biased back towards zero-lag, thereby resulting in the TSE.

These results suggest that receiver saturation, coarse digitization, and differences in the receiver characteristics will produce a triangle size effect in the SCA3. The triangle size effect can be directly attributed to the fact that the spatial correlation values at non-zero spatial lags are attenuated further than the spatial correlation value at zero spatial lags. This suggest that the preclusion of zero spatial lag from the analysis may eliminate the triangle

size effect. The use of zero spatial lag is however critical to any application of the spatial correlation analysis to three receiving antennae, such as the SCA3. Attempts to develop an analytical three-antenna spatial correlation analysis without the use of the spatial correlation value at zero spatial lag have proven unsuccessful.

6.4.4 Summary

In this section a three-antenna spatial correlation analysis (SCA3) has been presented. This analysis is based on the same fundamental idea as the spatial correlation analysis developed by *Briggs* [1968], whereby the atmospheric velocity is estimated by determining the displacement of the ground diffraction pattern $\vec{D}_{\mathbf{max}}$ in the duration of the sampling time. The use of three antennae allows the spatial correlation function to be evaluated along three "arms" of three colinear spatial lags. The position of the the spatial correlation maxima I_{ij} along each arm of spatial lags can be used to estimate $\vec{D}_{\mathbf{max}}$. This estimation require the parameterization of the contours of constant spatial correlation, which can be determined from the characteristic ellipse obtained using the technique presented by *Briggs* [1992].

The application of the SCA3 to the model generated data-set indicates that the technique provides an excellent estimate of the model input velocity for all values of the model turbulent velocity $\nu_{\mathbf{mod}}$. However, because the SCA3 is based upon the assumption that the spatial correlation function extrapolates to unity at zero-lag it will be subject to the triangle size effect. The application of the SCA3 to experimentally obtained data is presented in section 6.6.

6.5 The four-antenna spatial correlation analyses

6.5.1 Theory of the four-antenna spatial correlation analyses

In order for the spatial correlation analysis to avoid the TSE it is necessary to somehow bypass the fact that the spatio-temporal correlation function may not interpolate to unity at zero spatial lag. This can be achieved by precluding zero spatial lag from the analysis. In this case the estimate of $\vec{D}_{\mathbf{max}}$ will not be biased towards zero spatial lag, thereby eliminating the source of the TSE from the analysis. The use of zero spatial lag however is critical to any application of the spatial correlation analysis to three receiving antennae, such as the SCA3.

The application of the spatial correlation analysis to four receiving antennae does not

require the use of zero spatial lag. Figures 6.11 and 6.12 illustrate two techniques which can be applied using antenna arranged in a square and in a "Y" configuration, respectively, without using zero spatial lag. The use of a square of receiving antennae yields spatial lags at eight different positions, producing four "arms" of three spatial lags. Two different estimates are provided for the spatial correlation of the middle spatial lag of each arm. If the average of the two correlation values is employed for the analysis it is considerably simpler to use the average of the magnitudes as opposed to the magnitude of the averages, as the latter necessitates the knowledge of the existence of any phase differences between the antennae used to produce each correlation function. The use of a "Y" configuration of antennae yields spatial lags at twelve different positions, producing six arms of four spatial lags. The positions of the spatial correlation maxima I_i along each arm of spatial lags are determined by applying Gaussian fits to the spatial correlation values obtained along each arm in the same manner described for the SCA3 in section 6.4. The two-dimensional position of the spatial correlation maxima $\vec{D}_{\mathbf{max}}$ is given by the point of intersection of the lines which intersect the I_i positions from parallel arms. The four antennae spatial correlation analyses therefore do not require the estimation of the characteristic ellipse. The four-antenna spatial correlation analyses will be hereafter collectively referred to as the SCA4, or individually as the SCA4S and SCA4T, referring to the "square" and "triangular" antenna configurations, respectively.

6.5.2 Application of the four-antenna spatial correlation analyses

The four-antenna spatial correlation analyses employ essentially the same estimation procedures as the SCA3. As a result, the rejection criterion for the SCA3 shown in Table 6.2 are equally applicable to the SCA4, with the exception of criteria 8 and 9. Criterion 8 is not applicable to the SCA4 since the estimation of the characteristic ellipse is unnecessary. Criterion 9 is only applicable to the SCA4T as only two lines are available for the determination of $\vec{D}_{\mathbf{max}}$ for the SCA4S.

The results of the application of the FCA and SCA4S to the model-generated data-set MOD-MF-IDI are illustrated in Figure 6.13 as a function of the model turbulent velocity ν_{mod}. The SCA4S has been applied using antennae 1, 2, 6 and 10, while the FCA has been applied using antennae 1, 2 and 6. These results suggest that the SCA4S accurately estimates the model input velocity for all values of ν_{mod}. The standard deviations of the SCA4S results are noticeably smaller than those of the FCA results for $\nu_{\mathrm{mod}} < 6$ ms^{-1}.

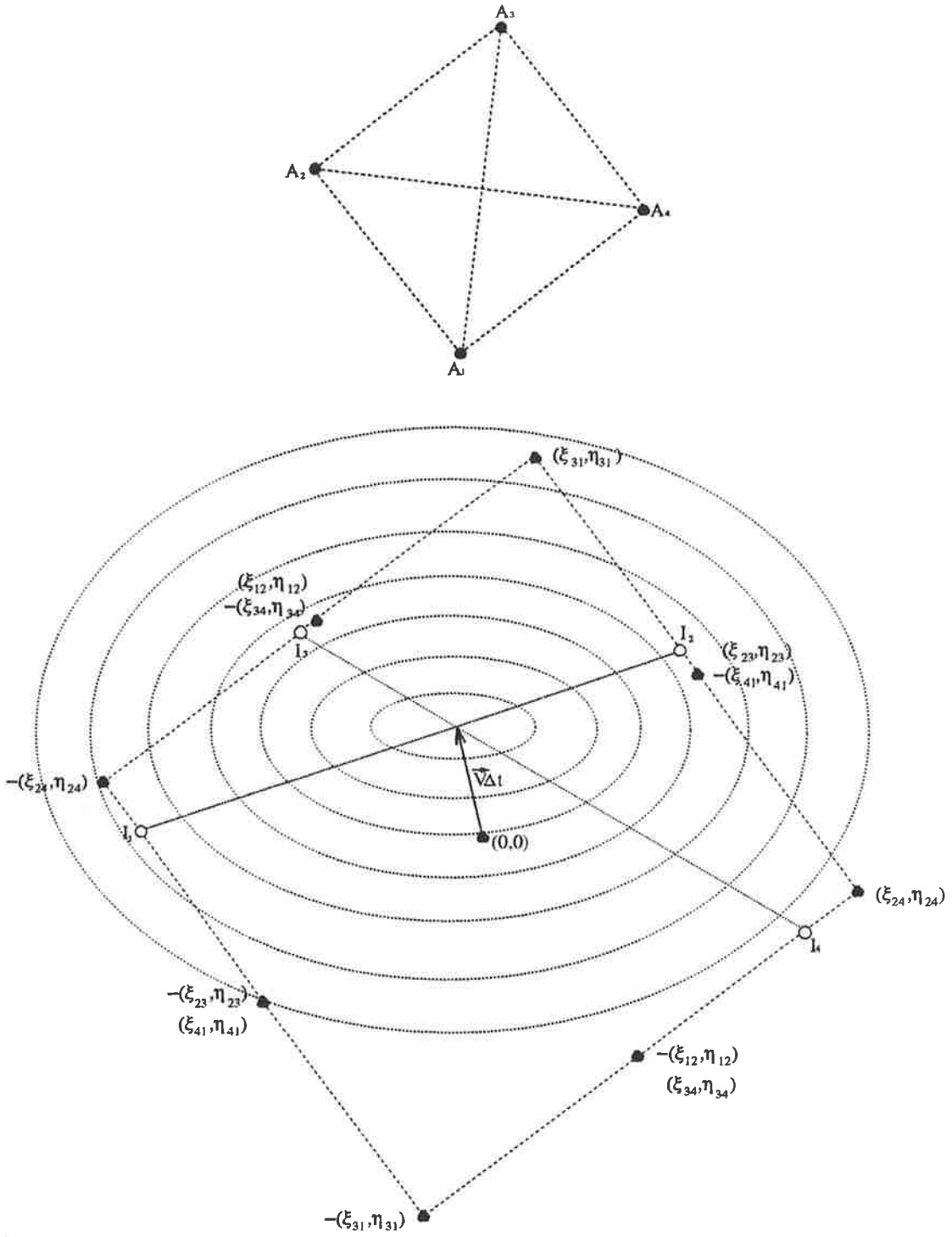

Figure 6.11: Illustration of the SCA4S technique used to estimate the position of the spatial correlation maxima for four antennae A_1, A_2, A_3 and A_4 arranged in a square (top). The bottom plot illustrates the spatial lags available using this antenna configuration, which produces four groups of three colinear spatial lags indicated by the dashed lines. The maximum spatial correlation along the ith group is indicated by an open circle and denoted I_i. The position of the maxima $\vec{D}_{\max} = \vec{V}\Delta t$ can be obtained by determining the intersection of the lines passing through the I_i determined from the two parallel groups of four colinear spatial lags, as indicated by the dotted lines.

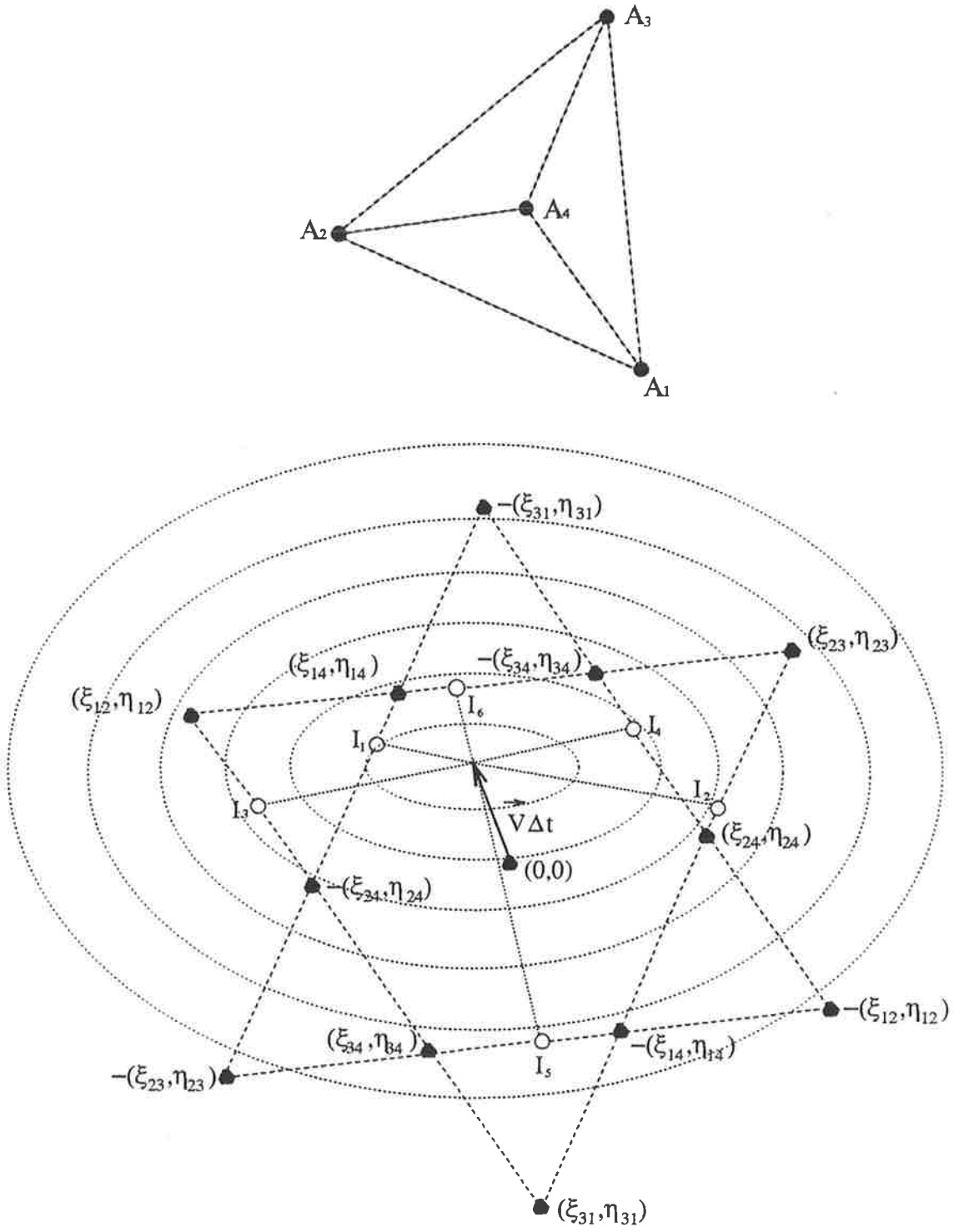

Figure 6.12: Illustration of the SCA4T technique used to estimate the position of the spatial correlation maxima for four antennae A_1, A_2, A_3 and A_4, where three antennae A_1, A_2 and A_3 form the vertices of an equilateral triangle and the A_4 is at the centre of this triangle (top). The bottom plot illustrates the spatial lags available using this antenna configuration, which produces six groups of four colinear spatial lags indicated by the dashed lines. The maximum spatial correlation along the ith group is indicated by an open circle and denoted I_i. The position of the maxima $\vec{D}_{\max} = \vec{V}\Delta t$ can be obtained by determining the intersection of the lines passing through the I_i determined from the three parallel groups of four colinear spatial lags, as indicated by the dotted lines.

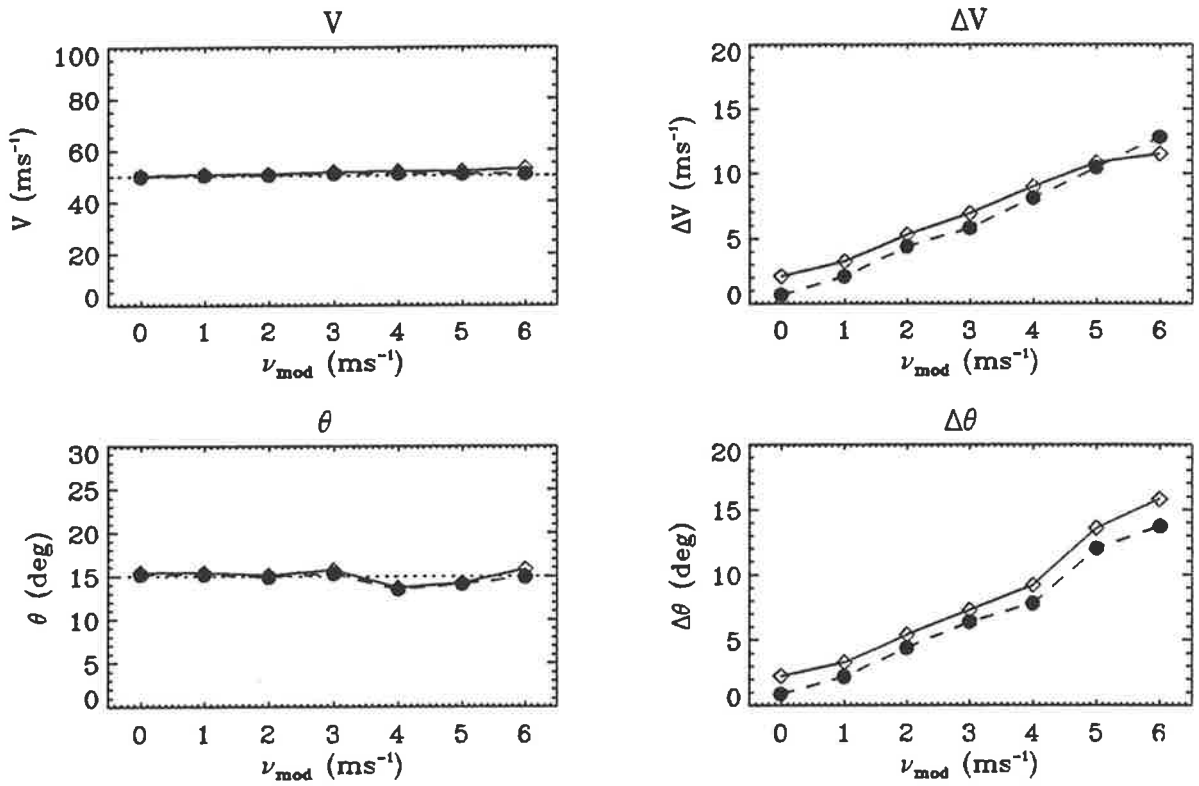

Figure 6.13: Average velocity (top left) and standard deviation (top right), and average direction (bottom left) and standard deviation (bottom right) obtained applying the FCA (◇) and SCA4S (•) to the model-generated data-set MOD-MF-IDI.

This result is somewhat surprising based on the fact that the Gaussian fits employed for the SCA4S use only three spatial correlation estimates, suggesting there may be some statistical variation introduced into the results. The Gaussian fits employed by the FCA are fitted over a minimum of six temporal lags. It was therefore envisaged that the SCA4S would produce larger errors than the FCA, as seen for the SCA3. On the other hand, the SCA4S uses an extra receiving antenna, and uses no assumptions about the temporal form of the spatio-temporal correlation function.

6.5.3 The triangle size effect

In the situation where the effects of receiver saturation, coarse digitization, and differences in the receiver characteristics are present the auto- and cross-correlation functions will be attenuated. The auto-correlation function is attenuated less than the cross-correlation functions, suggesting that the use of zero spatial lag will produce the triangle size effect.

The four-antenna spatial correlation analyses have been developed to avoid the use of zero spatial lag. If the cross-correlation functions employed for the determination of the spatial

correlation values at non-zero spatial lags are attenuated by the same factor the resulting spatial correlation values will be proportional to the non-attenuated spatial correlation values. In this situation the positions of I_i and $\vec{D}_{\max}$ will not be altered, suggesting that the SCA4 will produce the same velocity estimate as in the non-attenuated situation. It is unlikely however that the "attenuation factors" will be identical. If the attenuation is due to the effects of differences in the receiver characteristics there will most probably be a small range of attenuation factors. The range of factors can be determined in practice by performing the analysis described by *Golley and Rossiter* [1970], whereby the signal recorded by a single antenna was fed into a number of receivers. The attenuation factors obtained by *Golley and Rossiter* [1970] ranged from 0.86 to 0.96. This range is compatible with the zero-lag spatial correlation estimates obtained by interpolating the spatial correlation functions produced using the BP MF data-set BP930518 to unity. The knowledge of the attenuation factors may allow the SCA4 to correct for any biases that may result from any non uniformity of the attenuation factors.

6.5.4 Summary

In this section two four-antenna spatial correlation analyses (SCA4) have been presented. These analyses employ the same basic estimation procedures used for the SCA3, but do not make use of zero spatial lag. The SCA4S employs a square of receiving antennae, yielding four "arms" of three spatial lags. The SCA4T employs a "Y" configuration, yielding six arms of four spatial lags. The position of the spatial correlation maxima $\vec{D}_{\max}$ is determined by the intersection of the lines which pass through the positions of the spatial correlation maxima I_i along parallel arms of spatial lags. Unlike the SCA3, the SCA4 does not require the parameterization of the characteristic ellipse. However, this parameterization could be obtained if required using least squares techniques.

The application of the SCA4S to the model generated data-set indicates that the technique provides an excellent estimate of the model input velocity for all values of the model turbulent velocity v_{mod}. Because the SCA4 does not use zero spatial lag it will avoid major triangle size effect biases. There may however be some biases if the receiver characteristics exhibit significant differences as the resulting cross-correlation functions will have a range of attenuation factors. The application of the SCA4S to experimentally obtained data is presented in section 6.6.

6.6 Experimental application of the spatial correlation analyses

The spatial correlation analyses have been applied to the data-set BP930518. The application of the FCA to this data-set has been shown to exhibit the triangle size effect, as illustrated in Chapter 5. This triangle size effect is seen despite the application of the noise-correction outlined in Appendix C, and despite the absence of any receiver saturation or coarse digitization. This triangle size effect has been attributed to the different characteristics of the receivers, suggesting that the spatial correlation function will interpolate to below unity at zero spatial lag. The results of applying the FCA, SCA4S and SCA3 to this data-set are shown in Figure 6.14. The SCA4S has been applied using antennae 1, 2, 3, and 4, while the SCA3 has been applied using antennae 1, 2, and 3. The FCA has been applied using antennae 1, 2, and 3, and antennae 1, 5, and 8, which are the smallest and largest triangles of antennae available using this antenna configuration, respectively. The application of the FCA to these triangles will hereafter be referred to as the FCA-123 and FCA-158 analyses, respectively.

The SCA4S and FCA-158 results show excellent agreement, except above 90 km where the SCA4S velocity underestimates the FCA-158 true velocity. This agreement is further illustrated by Figure 6.15, which shows scatter plots of the FCA-158 and SCA4S velocity magnitude and direction. The cause of the SCA4S underestimation above 90 km is unclear. It must be pointed out that a large number of the FCA-158 records at these heights ($\approx 50\%$) are rejected by FCA criteria 4 and 5, suggesting that the antenna spacing may exceed the pattern scale. The triangle size effect analysis presented in Chapter 5 illustrates that there may be some overestimation of the true velocity magnitude in this circumstances, but generally not enough to explain the difference in the FCA-158 and SCA4S seen above 90 km in Figure 6.14. In addition, there is some tendency for the SCA4S to occasionally produce velocity magnitudes close to 0 ms^{-1} above 90 km . The preclusion of these records from the averaging increases the average SCA4S velocity magnitude by $\approx 2ms^{-1}$, which again is not sufficient to explain the difference in the FCA-158 and SCA4S seen above 90 km in Figure 6.14. There is a correspondence between records producing small SCA4S velocity estimates and those failing the FCA criteria 4 and 5 for the FCA-158 analysis. This is despite the fact that the analyses differ significantly, and use data from two significantly different antenna configurations with only one common antenna.

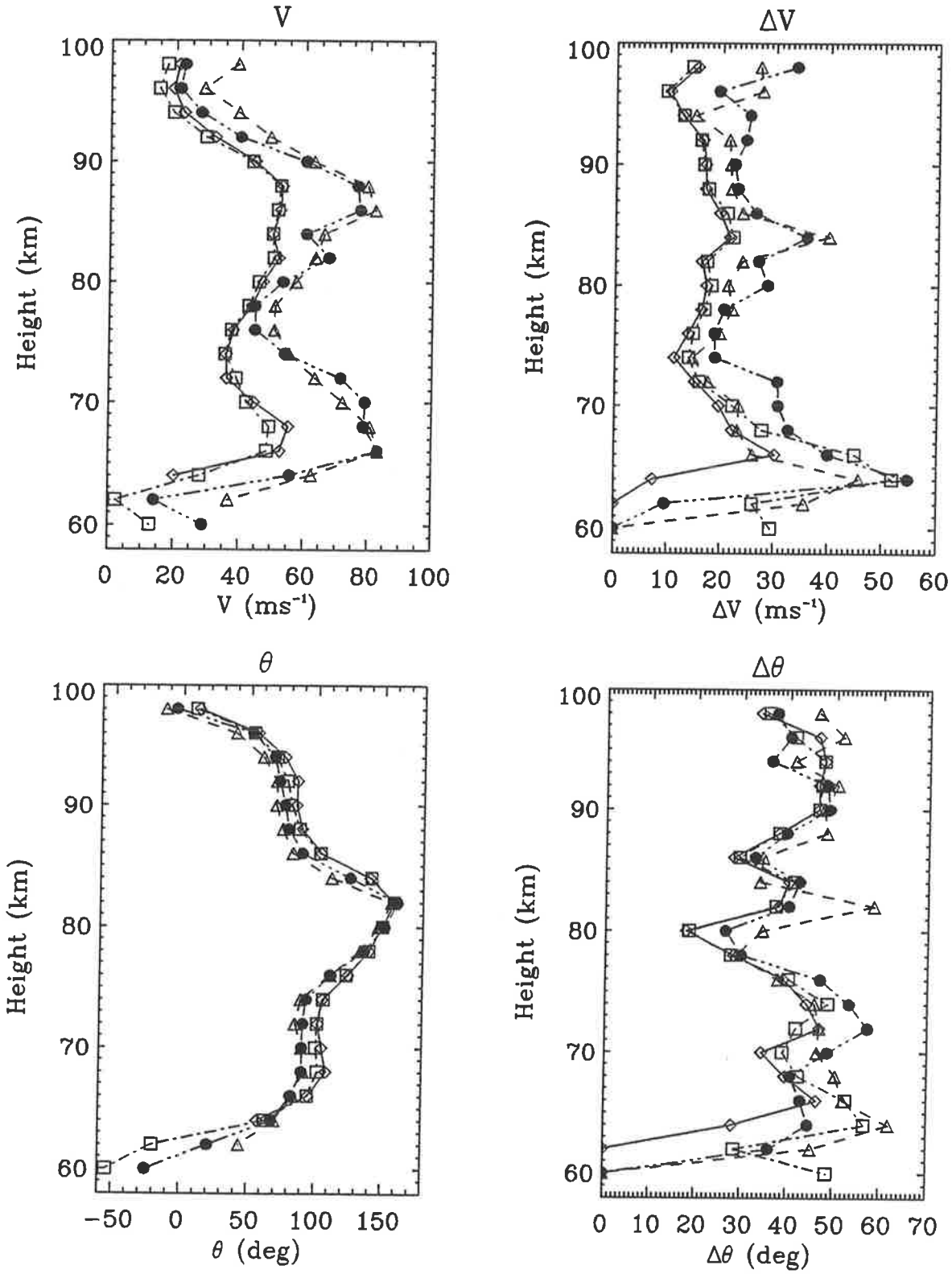

Figure 6.14: Profiles of the results obtained on applying the FCA, SCA4S and SCA3 to the data-set BP930518. The top plots illustrate the average (left) and standard deviation (right) of the velocity estimates, while the bottom plots illustrate the average (left) and standard deviation (right) of the velocity direction estimates for the SCA4S (•), SCA3 (□), FCA-158 (△) and the FCA-123 (◇).

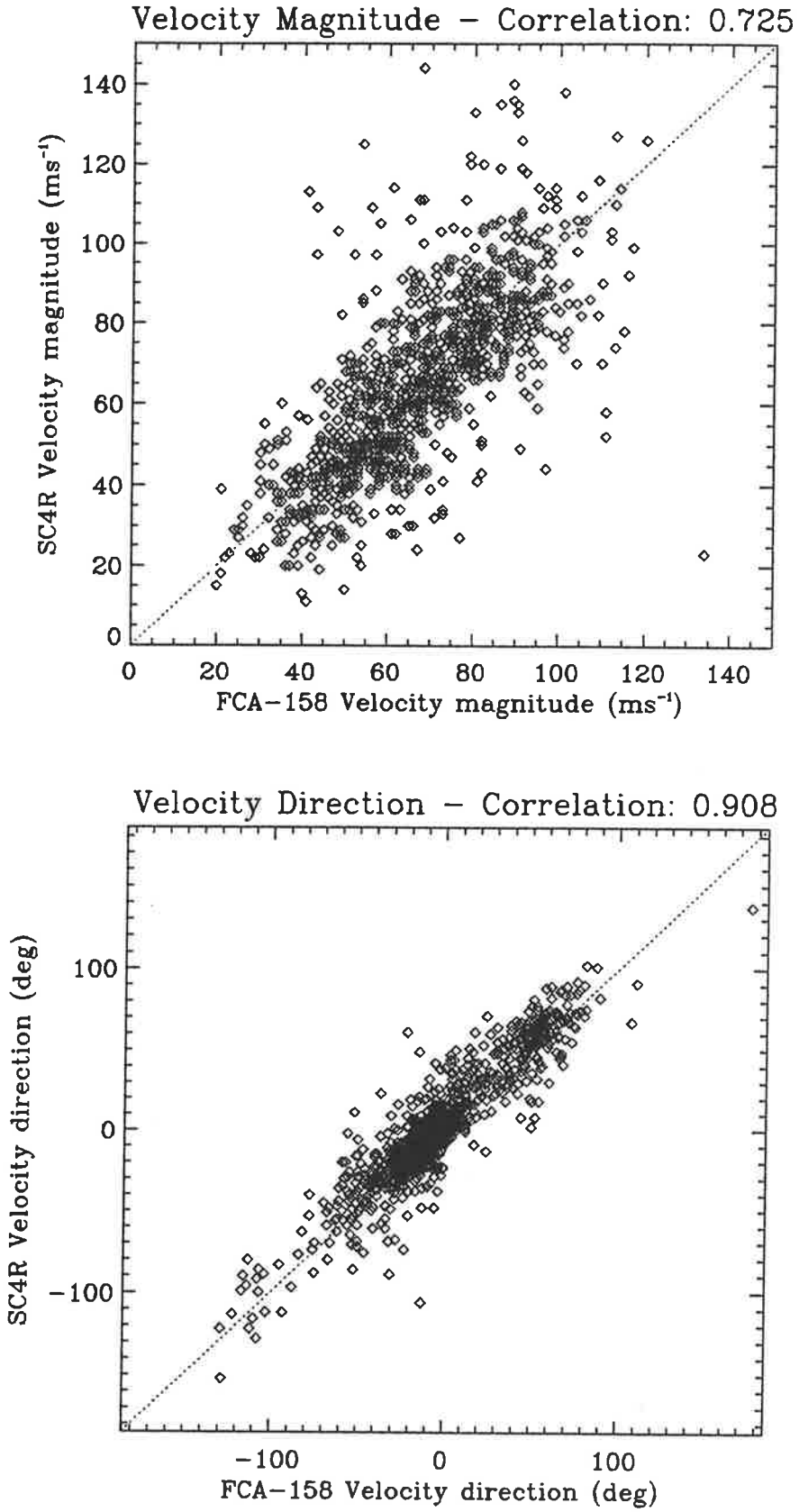

Figure 6.15: Scatter plots of the magnitude (left) and direction (right) of the velocity estimates obtained for the application of the SCA4S and FCA-158 to the data-set BP930518.

Although the antenna configuration employed to collect the BP930518 data-set does not allow the determination of the effect of antenna spacing upon the SCA4S there is evidence to suggest SCA4 will not be influenced by the antenna spacing, as suggested in section 6.5. The FCA-123 is applied using antennae arranged in a right angled triangle with spacing considerably smaller than the average pattern scale. The model analysis of the triangle size effect presented in Chapter 5 suggests that the magnitude of the FCA-123 true velocity will underestimated, while the direction of the true velocity will be biased towards the largest side of the triangle. On the other hand, the FCA-158 is applied using antennae arranged in an equilateral triangle with spacing comparable to the mean pattern scale, suggesting that no triangle size effect biases should be seen. The FCA-123 true velocity magnitude does underestimate the FCA-158 magnitude, and the FCA-123 true velocity direction is biased away from the FCA-158 true velocity direction towards the azimuth of the longest side of the triangle used for the FCA-123 analysis (135°) at most heights. The SCA3 results show the same biases as the FCA-123, suggesting the SCA3 is subject to the triangle size effect. The SCA4S results do not exhibit the same biases, despite using three of the same antennae as the FCA-123 and SCA3. This result suggests that the SCA4S is indeed independent of the triangle size effect.

6.7 Summary and conclusions

In this chapter two alternative correlation analyses to the FCA have been presented. The slope fitting correlation analysis (SFCA) (e.g. *Lataitas et al.*, [1995]) has been investigated, and an extension to the situation of anisotropic scatter has been proposed. The spatial correlation analysis (SCA) (e.g. *Briggs*, [1968]) has also been presented. Preliminary investigations to determine whether an analysis based on the same fundamental principles could be applied using a minimum of three receiving antennae have also been undertaken.

The slope fitting correlation analysis (SFCA) has been investigated using the theoretical model of the spatio-temporal correlation function employed by the FCA. The results illustrate that the technique is essentially the isotropic scatter equivalent of the FCA. The extension to anisotropic scatter requires the parameterization of the characteristic ellipse, which can be performed using the technique outlined by *Briggs* [1992]. The use of the characteristic ellipse parameters implies that the analysis will be subject to the same biases as the FCA triangle size effect. The application of the revised SFCA (or RSFCA) to model-generated

data produces velocity estimates in very good agreement with the model input velocity for a range of model turbulent velocities. The error estimates obtained using the RSFCA are slightly larger than those obtained using the FCA. This has been attributed to the larger errors inherent in the slope estimation procedure employed by the RSFCA. The application of the RSFCA to experimentally obtained data produces velocity estimates in very good agreement with the FCA true velocity.

The results obtained on the application of the RSFCA suggest that the analysis does not provide any apparent advantage over the FCA. Although the technique can in theory be applied over the small number of lags required for the zero-lag correlation function interpolations, a more rigorous analysis involving the calculation the correlation functions out to a larger number of lags is required in practice. The SFCA also provide no information on the temporal evolution of the ground diffraction pattern.

The spatial correlation analysis (SCA) is based on the estimation of the displacement of the ground diffraction pattern $\vec{D}_{\mathbf{max}}$ in the duration of the sampling time. The technique requires an array of receiving antennae covering an area exceeding the mean pattern scale, and with antenna spacings considerably shorter than the mean pattern scale in order to produce instantaneous high spatial resolution images of the ground diffraction pattern. As the application of the SCA is beyond the capability of the majority of radars the analysis has been demonstrated in this chapter using model-generated data. As a result of the limited applicability of the SCA preliminary investigations have been made to determine whether a revised spatial correlation analysis could be applied using antenna configurations generally employed experimentally, where typically three of four receiving antenna are used.

The three- (SCA3) and four-antenna (SCA4) spatial correlation analyses are based on the same fundamental idea as the SCA developed by *Briggs* [1968]. The SCA3 uses the spatial correlation values along three colinear "arms" of three spatial lags to estimate the position of the spatial correlation maxima $\vec{D}_{\mathbf{max}}$. The application of the SCA3 to model-generated data produces velocity estimates in very good agreement with the model input velocity for a range of model turbulent velocities. The error estimates obtained using the RSFCA are slightly larger than those obtained using the FCA. The application of the SCA3 to experimentally obtained data produces velocity estimates in very good agreement with the FCA true velocity. As the SCA3 technique uses zero spatial lag it will be subject to the same biases as the FCA triangle size effect. In order to avoid these biases it is necessary to avoid the use of zero spatial lag.

There exist two configuration for the SCA4 that avoid the use of zero spatial lag. These configuration consist of antennae arranged either in a square or a "Y" configuration. The SCA4S employs a square of antennae, yielding four "arms" of three colinear spatial lags. The SCA4T employs a "Y" configuration, yielding six arms of four colinear spatial lags. Unlike the SCA3, the SCA4 does not require the parameterization of the contours of constant spatial correlation. This parameterization could however be performed if required using least squares techniques. The application of the SCA4S to the model generated data-set indicates that the technique provides an excellent estimate of the model input velocity for all values of the model turbulent velocity ν_{mod}. The error in the SCA4S estimates are smaller than those in the FCA estimates for most values of ν_{mod}. The application of the SCA4S to experimentally obtained data produces velocity estimates in very good agreement with the FCA true velocity obtained for the largest possible antenna spacing. The results indicate that the SCA4S does not suffer from the same biases as the triangle size effect.

The investigations of the alternative correlation analyses presented in this Chapter suggest that the four-antenna spatial correlation analysis is the only technique that may offer advantages over the FCA. The major advantage is that the SCA4 does not produce the triangle size effect. Recent comparisons between the winds estimated using the FCA, the meteor drifts technique (e.g. *Cervera and Reid*, [1995]), and the high resolution Doppler imager (HRDI) (e.g. *Burrage et al.*, [1993]) suggest that the FCA true velocity magnitude underestimates the actual wind velocity. The triangle size effect is a likely contributor to this underestimation. The results of section 6.6 suggest that the SCA4 avoids triangle size effect biases, and should therefore be investigated more extensively than the preliminary investigation presented in this chapter. Although the implementation of the SCA4 described in this Chapter does not provide any information on the spatial and temporal properties of the ground diffraction pattern it is envisaged that these properties could be determined using a least squares analysis. The SCA4 would then provide the same parameters as the FCA without the biases inherent in the triangle size effect. Because the technique is independent of the triangle size effect the antenna spacing could be made significantly smaller than the typical spacings employed for the application of the FCA. The results of Chapter 5 suggest that the errors in the FCA are reduced by using smaller antenna spacings. It should therefore follow that the SCA4 produces smaller errors upon using smaller antenna spacings.

Chapter 7

The Full Spectral Analysis

7.1 Introduction

The conventional technique for the estimation of atmospheric parameters using spaced antenna (SA) radar is the full correlation analysis (FCA) (e.g., *Briggs*, [1984]), which is described in detail in Chapter 4. The FCA is performed entirely in the time-domain. It has long been realized that the cross-correlation delay-times employed by the FCA can be estimated directly from the phase-slopes of the corresponding cross-spectra (e.g., *Pfister*, [1971]). This has led to the development of a number of "phase fitting" interferometry techniques (e.g. *Kudeki*, [1988]; *Van Baelen and Richmond*, [1991]; *Larsen et al.*, [1992]), which produce velocities in good agreement with the FCA apparent velocity (e.g. *Van Baelen et al.*, [1991]). It has only recently been pointed out that the *entire* FCA can be performed in the frequency-domain (e.g., *Costa and Fougere* [1988]). This has led to the development of the full spectral analysis (FSA) technique (e.g., *Briggs and Vincent* [1992]; *Sheppard and Larsen* [1992]; *Liu and Pan* [1993]). The FSA is a frequency-domain analogue of the FCA, employing the same mathematical formulation based on the use of spectral parameters as opposed to correlation parameters.

The motivation for the investigation of the FSA is the belief that the FSA may offer several advantages over the FCA. Frequency domain analyses allows the simple removal of undesirable frequency contamination such as that resulting from sea echoes (e.g. *Briggs and Vincent*, [1992]) and meteor echoes in the mesosphere at MF and precipitation echoes in the troposphere at VHF. The correction for the effects of noise is also significantly simpler in the frequency domain, provided temporal undersampling is avoided. In addition, the FSA may

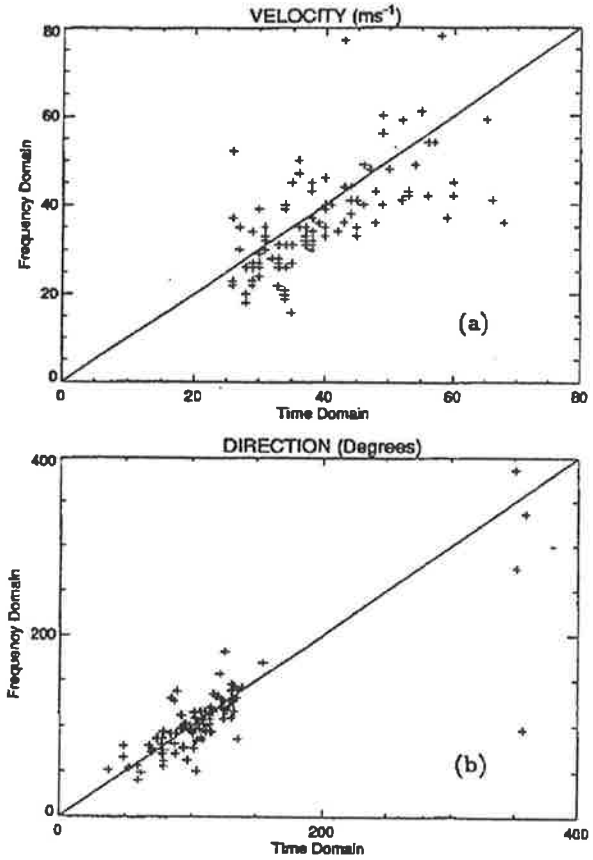

Figure 7.1: Scatter plots of the true velocity magnitude (top) and direction (bottom) obtained on the application of the FCA (horizontal axis) and the FSA (vertical axis) to individual two minute time-series records for data recorded between 60 and 100 km using the BP MF radar in SA mode (after *Briggs and Vincent*, [1992]).

also produce acceptances for records where the FCA fails, and vice-versa. The combination of the results obtained on applying the FCA and FSA may therefore result in an increase in the overall acceptance rate. The determination of spectra is also computationally more efficient than the determination of correlation functions.

The FSA has been shown to produce velocity estimates in good agreement with those produced by the FCA. The analysis of *Briggs and Vincent* [1992] suggests that the true velocity magnitude and direction obtained on applying the FCA and FSA to individual 2 minute time-series records produces good agreement. The analyses of *Liu and Pan* [1993] and *Sheppard et al.* [1993] suggest that the true velocity magnitude and direction obtained on applying the FCA and FSA to coherently averaged[1] correlation functions and spectra, respectively, produced excellent agreement. Furthermore, the model analysis of *Sheppard*

[1]The term "coherent averaging" is used throughout this thesis to described complex averaging. This averaging is sometimes misleadingly described as "incoherent averaging" when applied to the averaging of spectra.

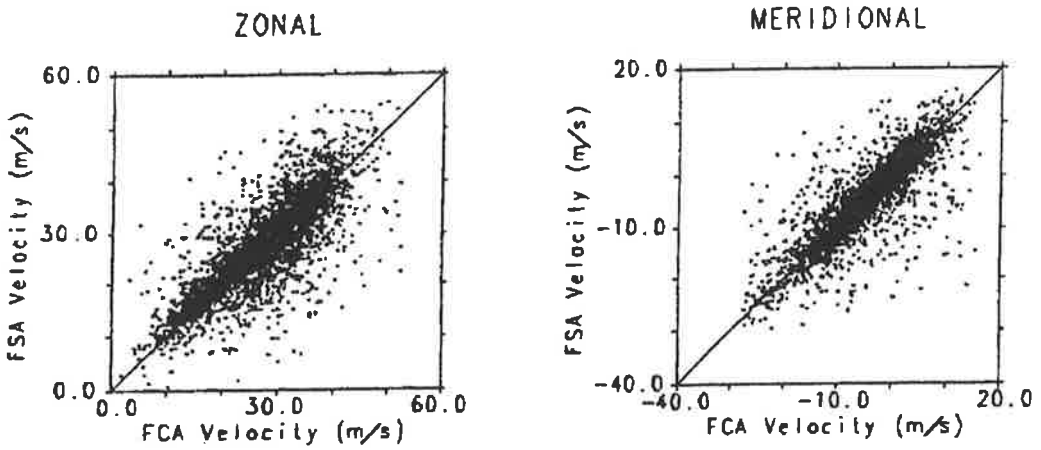

Figure 7.2: Scatter plots of the zonal (left) and meridional (right) velocities estimated on the application of the FCA to coherently averaged correlation functions (horizontal axis) and the FSA to coherently averaged spectra (vertical axis) to data recorded between 6 to 15 km using the MU VHF radar (after *Sheppard et al.*, [1993]).

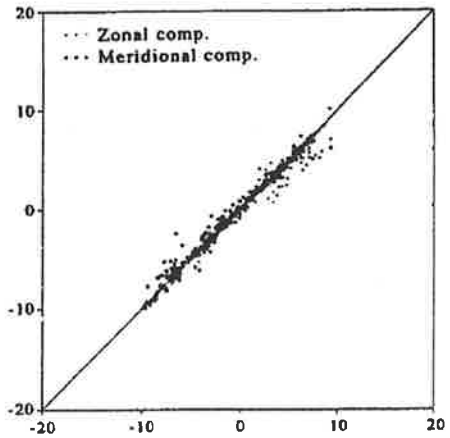

Figure 7.3: Scatter plots of the zonal and meridional velocities estimated on the application of the FCA to coherently averaged correlation functions (horizontal axis) and the FSA to coherently averaged spectra (vertical axis) for data recorded using the Chung-Li VHF radar (after *Liu and Pan*, [1993])

and Larsen [1992] suggests that the FSA correctly estimated the model input velocity when using coherently averaged spectra. Despite the encouraging results obtained in applying the FSA there appears to have been no further development of the technique in the literature of late. Because the FSA is the frequency domain equivalent of the FCA it is expected that the conditions for optimum performance should be the same as for the FCA, and that the technique should be subject to the same biases, such as the triangle size effect (e.g. *Golley and Rossiter*, [1970]).

The work presented in this chapter is an attempt to determine the advantages and disadvantages inherent in the application of the FSA. The theory of the FSA is presented in section 7.2, together with the modifications required to compensate for the effects of scatter centered off-zenith, non-zero vertical velocities, and noise. The application of the FSA to experimentally obtained data is addressed in section 7.2.1, together with the fitting techniques required for the estimation of the spectral parameters employed by the analysis. The FSA is applied to spectra calculated using individual time-series records in section 7.4.1. The effects of the time-series length and coherent block averaging upon the analysis are also discussed. The FSA is applied to spectra calculated from the coherent average of the spectra obtained using individual time-series records in section 7.5. As a result of the Fourier equivalence of the FCA and FSA techniques there has been little attempt to address any of the biases discussed in connection with the FCA, such as the triangle size effect.

7.2 Theory of the Full Spectral Analysis

There exist subtle yet important differences in the FSA techniques developed by the various authors. The techniques of *Briggs and Vincent* [1992] (hereafter denoted the BVFSA) and *Liu and Pan* [1993] (LPFSA) are based on the *Briggs* [1984] FCA, as described in Chapter 4. The technique of *Sheppard and Larsen* [1992] (SLFSA) is based on the *Meek* [1980] FCA, which produces very similar but not identical results to the *Briggs* [1984] FCA. Although the derivations of the formulae employed by the individual techniques differ the resulting formulae can be simply related, as discussed in 7.2.1. The derivation of the FSA formulae presented in this section follows that presented by *Briggs and Vincent* [1992] for the BVFSA technique, and is sufficient to illustrate the major points of the analysis.

The basic assumption of the FCA is that contours of equal spatio-temporal correlation can be approximated by a family of ellipsoids of the general form (e.g., *Briggs*, [1984])

$$\rho(\xi,\eta,\tau) = \rho(A\xi^2 + B\eta^2 + 2H\xi\eta + 2(F\xi + G\eta)\tau + C\tau^2), \tag{7.1}$$

where $[A,..,H]$ are referred to as the "ellipsoid parameters". In order to derive the frequency-domain analogue of (7.1) it is necessary to assume an explicit functional form for spatio-temporal correlation function. The real-time routine FCA programs employed by the Adelaide group are successfully based upon the assumption that the temporal dependence (and therefore, necessarily, the spatial dependence) of the correlation functions is of Gaussian

form. Using the assumption of Gaussian form, the spatio-temporal correlation function of (7.1) can be rewritten

$$\rho(\xi,\eta,\tau) = \exp -(A\xi^2 + B\eta^2 + 2H\xi\eta + 2(F\xi + G\eta)\tau + C\tau^2). \tag{7.2}$$

Consider two spaced receivers (i,j) with vectorial separation (ξ_{ij},η_{ij}). The cross-correlation function for this pair of receivers is given by

$$\rho_{0ij}(\tau) = \exp -(A\xi_{ij}^2 + B\eta_{ij}^2 + 2H\xi_{ij}\eta_{ij} + 2(F\xi_{ij} + G\eta_{ij})\tau + C\tau^2). \tag{7.3}$$

The Fourier transform of (7.3) gives the cross-spectrum, which can be written in the form

$$W_{ij}(f) = W_{0ij}\ \exp\left(-\frac{f^2}{f_s^2}\right)\ \exp(im_{ij}f), \tag{7.4}$$

where the cross-spectral magnitude W_{0ij} is given by

$$W_{0ij} = \sqrt{\frac{\pi}{C}}\ \exp -\left(A\xi_{ij}^2 + B\eta_{ij}^2 + 2H\xi_{ij}\eta_{ij} - \frac{(F\xi_{ij} + G\eta_{ij})^2}{C}\right), \tag{7.5}$$

the cross-spectral e^{-1} width f_s is given by

$$f_s = \frac{\sqrt{C}}{\pi}, \tag{7.6}$$

and the cross-spectral phase slope m_{ij} is given by

$$m_{ij} = -2\pi\left(\frac{F\xi_{ij} + G\eta_{ij}}{C}\right). \tag{7.7}$$

The effects of scatter centered off-zenith and vertical velocities are not included in (7.4). The inclusion of these effects was discussed by *Briggs and Vincent* [1992] for the 2-dimensional situation. The extension to 3-dimensions follows similar arguments, yielding the revised cross-spectrum

$$W_{ij}(f) = W_{0ij}\ \exp\left(-\frac{(f-f_0)^2}{f_s^2}\right)\ \exp(i\phi_{ij}f). \tag{7.8}$$

The spectral magnitude is shifted by the frequency offset

$$f_0 = \frac{-2V_r}{\lambda}, \tag{7.9}$$

where λ is the radar wavelength, and

$$V_r = \vec{V}\cdot\hat{r} = ul_0 + vm_0 + wn_0 \tag{7.10}$$

is the radial velocity in the direction of the mean angle of arrival $\hat{r} = (l_0, m_0, n_0)$ (e.g. *Röttger and Ierkic*, [1985]) of the scatter, resulting from a mean atmospheric wind velocity $\vec{V} = (u, v, w)$. The cross-spectral phase is given by

$$\phi_{ij}(f) = m_{ij}(f - f_0) + \phi_{0ij} \tag{7.11}$$

where

$$\phi_{0ij} = \frac{2\pi}{\lambda}(\xi_{ij} l_0 + \eta_{ij} m_0) \tag{7.12}$$

is the cross-spectral phase at the frequency offset f_0. Note that the parameters f_s and f_0 are not subscripted with the antenna indices as they are theoretically identical for each cross-spectrum. The effects of noise upon the cross-spectrum are manifested by an offset in the cross-spectral magnitude n_{ij}, as discussed in Appendix F. The general form of the cross-spectrum resulting from the inclusion of these effects is shown in Figure 7.4.

7.2.1 Experimental application of the FSA

The cross-spectrum specified by (7.8) is derived from the normalized cross-correlation function. As a result, the experimentally determined cross-spectra must be normalized in the same manner as the cross-correlation functions employed by the FCA. The normalized cross-spectrum is given by (e.g., *Briggs and Vincent* [1992])

$$W_{ij}(f) = \frac{S_i^*(f) S_j(f)}{\sqrt{\int |S_i(f)|^2 df \int |S_j(f)|^2 df}}, \tag{7.13}$$

where S_i is the amplitude spectrum determined from the Fourier transform of the ith time-series. This expression can be rewritten

$$W_{ij}(f) = \frac{S_i^*(f) S_j(f)}{\sqrt{A_i A_j}}, \tag{7.14}$$

where

$$A_i = \int P_i(f) df \tag{7.15}$$

is the area under the unnormalized power-spectrum

$$P_i(f) = |S_i(f)|^2. \tag{7.16}$$

An example of the typical three receiver cross-spectral magnitude and phase obtained using an individual record of the data-set BP940527 at 86 km is shown in Figure 7.5. The cross-spectral magnitude maxima W_{0ij}, e^{-1} width f_s, and the frequency offset f_0 can be

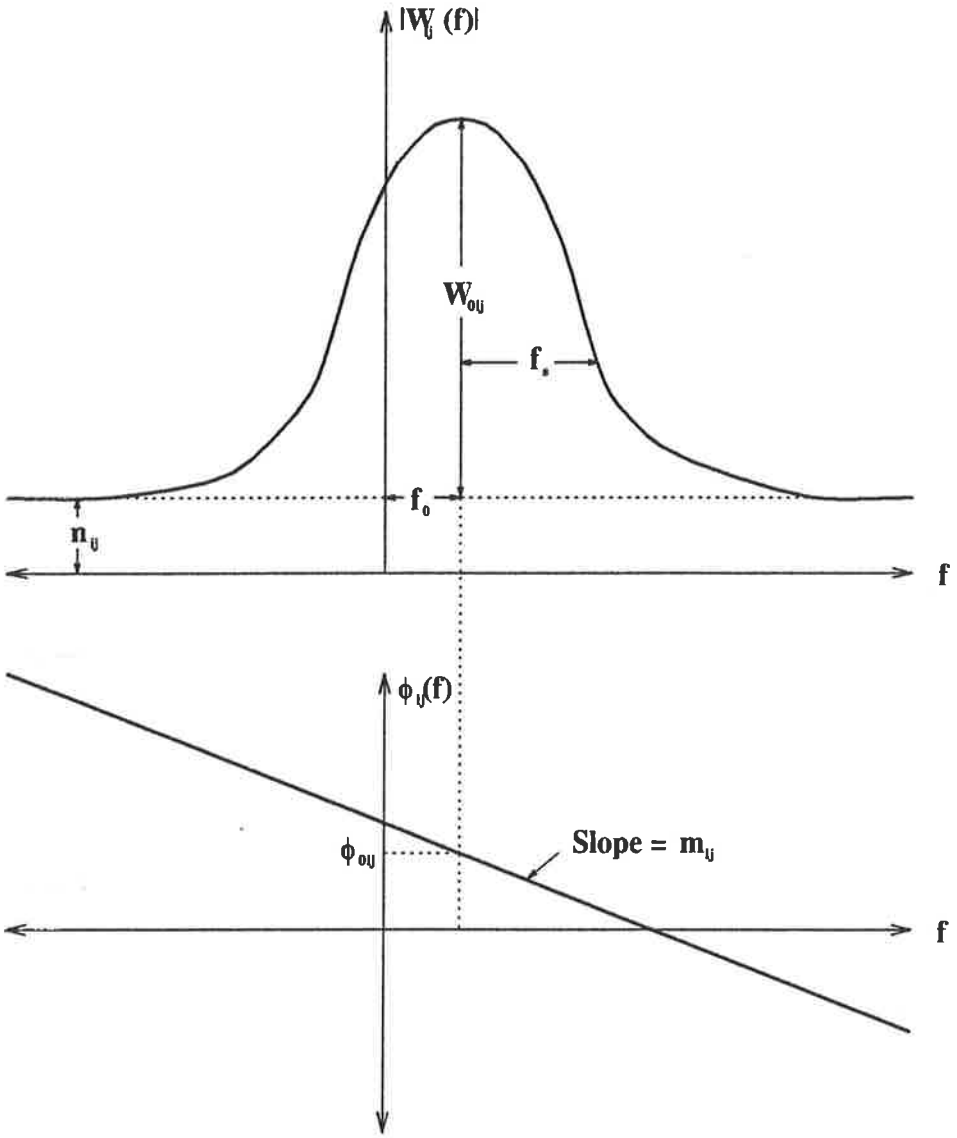

Figure 7.4: General form of the cross spectrum assumed by the FSA. Top: Cross-spectral magnitude $|W_{ij}(f)|$, defined by the maxima W_{0ij}, the e^{-1} width f_s, the noise offset n_{ij} and the frequency offset f_0. Bottom: Cross-spectral phase, defined by the phase slope m_{ij} and phase offset ϕ_{ij}. (adapted from *Briggs and Vincent*, [1992])

obtained by applying a Gaussian fit to the magnitude, while the cross-spectral phase slope m_{ij} and phase offset ϕ_{ij} can be obtained by applying a linear fit to the phase. The results of applying these fits are also illustrated in Figure 7.5.

Once the spectral parameters have been estimated the analysis can proceed along one of two different paths. The ellipsoid parameters can be estimated using (7.5), (7.6) and (7.7), from which the physical parameters estimated by the FSA can be estimated in the same manner as the FCA. Alternatively, the correlation parameters employed by the FCA may be estimated from the spectral parameters. These correlation parameters are the fading time

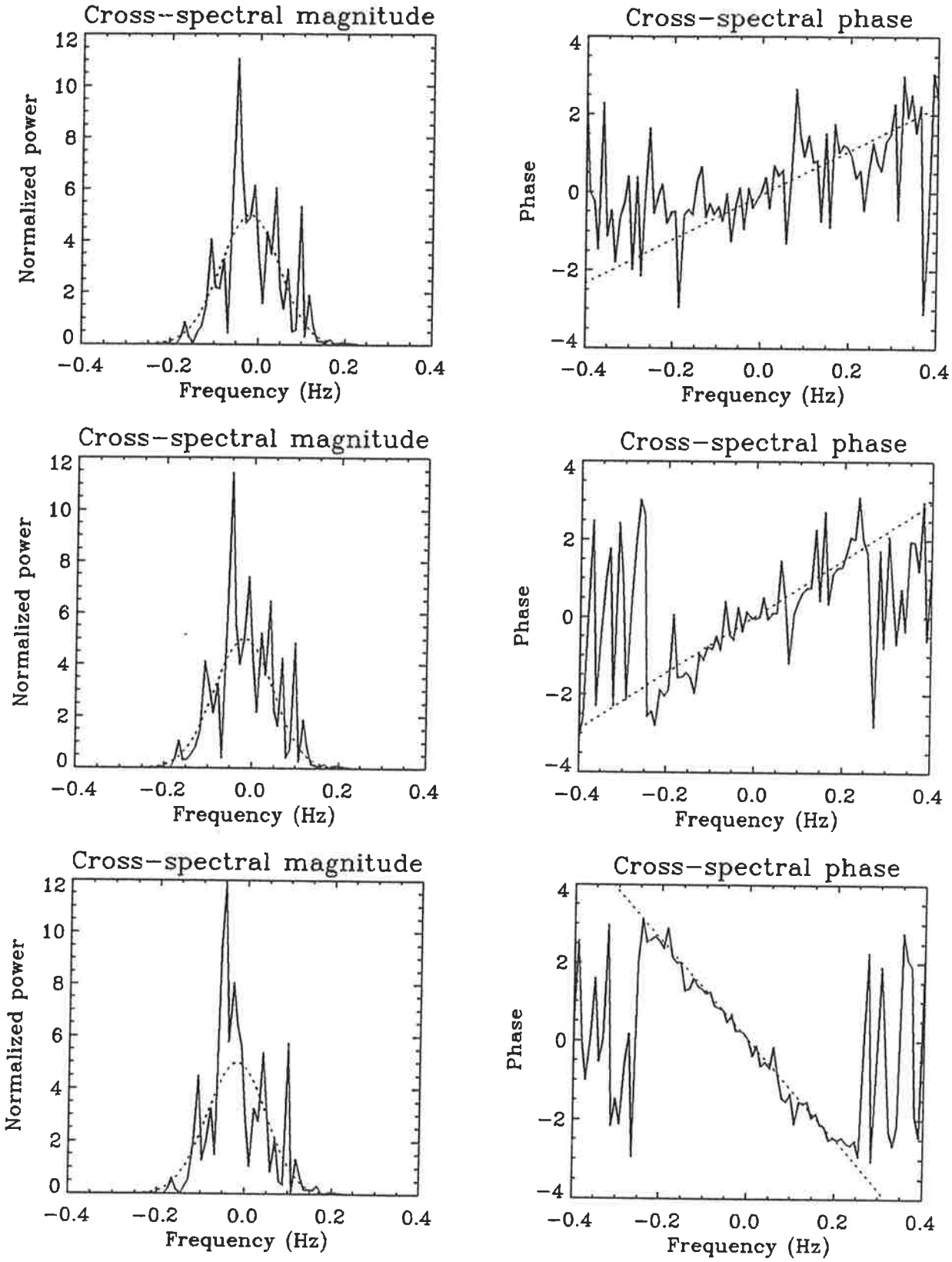

Figure 7.5: Typical three-receiver cross-spectral magnitude and phase pairs obtained using the BP MF radar in SA mode at 80 km. The dotted line indicates the resulting Gaussian and linear fits.

$\tau_{0.5}$, the cross-correlation maxima lag-times τ'_{ij}, and the lag times where the mean auto-correlation function equals the zero-lag cross-correlations, τ_{ij}. The spectral and correlation parameters are related by

$$\tau_{0.5} = \frac{\sqrt{\ln 2}}{\pi f_s}, \tag{7.17}$$

$$\tau'_{ij} = \frac{-m_{ij}}{2\pi}, \text{ and} \tag{7.18}$$

$$\tau^2_{ij} = \tau'^2_{ij} - \frac{\ln(A_{ij})\tau^2_{0.5}}{\ln 2}, \tag{7.19}$$

where A_{ij} is the area beneath the magnitude of the ijth cross-spectrum after the removal of the noise-offset n_{ij}. Because the cross-spectrum magnitude is of Gaussian form this area can be expressed as

$$A_{ij} = \pi^{\frac{1}{2}} W_{0ij} f_s \tag{7.20}$$

After some manipulation, and as shown in *Liu and Pan* [1993], (7.19) can also be written

$$\tau^2_{ij} = -\frac{\ln |I_{ij}| \tau^2_{0.5}}{\ln 2}, \tag{7.21}$$

where

$$I_{ij} = \int_{-\infty}^{\infty} W_{ij}(f) df. \tag{7.22}$$

The BVFSA, SLFSA and LPFSA techniques all employ (7.17) and (7.18) in order to estimate $\tau_{0.5}$ and τ'_{ij}. The difference in the techniques lies in the estimation of the third parameter. The BVFSA and LPFSA techniques are based on the *Briggs* [1984] FCA, which uses τ_{ij} as the third parameter. The two techniques differ in their estimation of the τ_{ij}, with the BVFSA using (7.19), and the LPFSA using (7.21). The SLFSA technique is based on the *Meek* [1980] FCA, which uses the cross-correlation maxima ρ_{0ij} in place of τ_{ij}. It can be easily shown (e.g. *Sheppard and Larsen*, [1992]) that the cross-correlation maxima ρ_{0ij} is equivalent to the area under the cross-spectral magnitude, A_{ij}.

7.3 Application of the FSA

Because the FSA is a relatively new technique there has been little attempt to determine the optimal experimental conditions for it's application. However, since the FSA is the frequency-domain analogue of the FCA it seems logical that the conditions for optimum performance of the FCA should also apply to the FSA. These conditions are addressed in Chapter 4. The FSA apparent velocity is determined directly from the phase slopes in the

same manner as the horizontal velocity is determined in the phase-slope fitting interferometry (PSFI) techniques (e.g. *Kudeki*, [1988], *Van Baelen et al.*, [1991]; *Larsen et al.*, [1992]). As a result, aspects of the optimal experimental conditions for the PFI techniques are also directly applicable to the FSA.

The effects of noise upon the spectra employed by the FSA are discussed in Appendix F. The FSA formulae derived in 7.2 are based on the assumption that noise is not present. The effects of noise must therefore be "removed" from the spectra prior to the analysis. The results of Appendix F suggest that the effects of noise can be effectively removed from the power-spectra by subtracting the noise-level. Because the power-spectrum has Gaussian form after the removal of the noise-level the area A_i can be estimated analytically using the equation

$$A_i = \sqrt{\pi} P_{0i} f_s. \tag{7.23}$$

where P_{0i} is the power-spectral maxima, and f_s is the e^{-1} width. The cross-spectrum defined by (7.13) requires that the denominator is calculated using the noise-removed power-spectra. This renormalization is identical to that used for the cross-spectrum for the correction for the effects of noise, as discussed in Appendix C. The results of Appendix F also illustrate that the effects of noise cannot be removed from the complex components of the cross-spectrum. Despite this result, the effects of noise can be effectively removed from the cross-spectral magnitude by subtracting the noise-level, provided the SNR exceeds approximately 5 dB. For SNRs below 5 dB there is a significant degradation in the parameters estimated from the cross-spectral magnitude, suggesting that the FSA should not be applied in these circumstances. This corresponds well with the results of Chapter 5, which suggest that the FCA should not be applied to time-series records with SNRs less than 5 dB.

The acceptance criteria employed for the application of the FSA are shown in Table 7.1. Because the FCA and FSA are based on the same mathematical formulation the majority of the FSA criteria are taken directly from the FCA. The FCA criteria not applicable to the frequency-domain have been replaced analogous frequency-domain criteria. The FCA criterion 4 is employed to reject records where the main peak of the cross-correlation function is indistinct. The FSA equivalent is employed to reject records where the error in the phase fit is large, suggesting there is no distinct linear trend in the phase. This criterion is discussed in more detail in section 7.3.2. The NTD employed for criterion 5 can be applied either to the cross-spectral phase slopes m_{ij} or the corresponding cross-correlation delay times τ'_{ij} calculated using 7.18. Criterion 13 is essentially identical to the FCA criterion 13, because,

Table 7.1: The FSA rejection criteria

Code	Explanation
0	Record accepted
1	Low signal amplitude
2	SNR < -6 dB
3	$\tau_{0.5} > 6$ s
4	Poor linear fit to $\phi_{ij}(f)$
5	$NTD > 0.5$
6	$K < 0$
7	Breakdown in pattern analysis
8	$V_a > 250$ ms^{-1}
9	$\lvert\theta_t - \theta_a\rvert > 40°$
10	$V_a > 4\,V_t$
11	$V_t > 1.5\,V_a$
12	Poor Gaussian fit to $W_{ij}(f)$
13	$A_{ij} < 0.2$
14	Maths errors

as discussed in 7.2, $A_{ij} = \rho_{0ij}$.

7.3.1 The Gaussian fitting procedure

The parameters W_{0ij} and f_s can be estimated directly from the application of Gaussian fits to the cross-spectral magnitude $|W_{ij}(f)|$. In practice, only the cross-spectral maxima W_{0ij} are estimated from the cross-spectral magnitude. The e^{-1} width f_s is calculated from the mean power-spectrum. This estimation is based on the assumption that the power- and cross-spectra have the same width. Although the three power-spectra are theoretically identical, statistical errors may introduce small differences between the individual power-spectra. As a result, the mean power-spectrum provides a more reliable estimate of f_s. This procedure is analogous to that employed for the FCA, whereby the e^{-1} width of the cross-correlation functions is estimated using the magnitude of the mean auto-correlation function. The frequency offset f_0 is also estimated from the Gaussian fit to the mean power-spectrum, and can be used to provide an estimate of the vertical velocity analogous to that obtained using the slope of the mean auto-correlation function about zero-lag (e.g. *Woodman and Guillen*, [1974]).

Prior to the application of the Gaussian fits the noise-offset must be removed from the spectral magnitude, as described in Appendix F. This process requires the sampling time

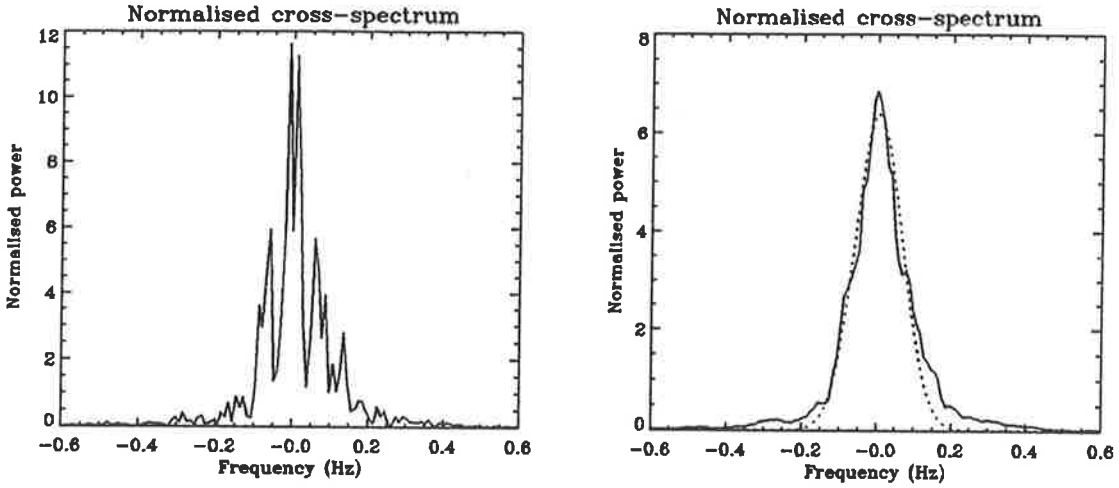

Figure 7.6: Example of a typical cross-spectrum obtained at 80 km using the BP MF radar in SA mode before (left) and after (right) four point smoothing. The dotted line shows the Gaussian fit to the smoothed spectrum.

to be sufficiently small such that the e^{-1} width of the power-spectra is considerably smaller than the Nyquist frequency. If this is not the case there may be appreciable spectral power at the Nyquist frequency. This can result in the noise-offset being overestimated, resulting in an underestimation in A_{ij} and a subsequent underestimation of the true velocity magnitude.

An example of a typical experimental cross-spectrum magnitude calculated using an individual 2-minute time-series record is shown in Figure 7.6. The unsmoothed spectrum appears to be composed of a collection of "spikes" superimposed upon a general Gaussian behavior. The Gaussian resemblance is enhanced considerably by smoothing, suggesting that the Gaussian fits should be applied to smoothed spectra. Dominant spikes are however not always entirely smoothed out, with the result that the Gaussian fit is biased towards fitting the spikes rather than the general Gaussian shape of the spectrum. This effect is illustrated in Figure 7.7. A number of different techniques have been employed in an attempt to counteract this problem. One such technique involved applying a parabolic fit to the natural logarithm of the spectral magnitude using only those Doppler frequencies where the spectral magnitude exceeded a selected threshold above the noise level. The exponential of the fitted parabola was then taken in order to produce the Gaussian fit to the spectrum. Another technique investigated involved applying a weighted Gaussian using weights which were inversely proportional to the spectral magnitude for Doppler frequencies exceeding a selected threshold above the noise level, thereby giving the spikes smaller weighting to reduce their effects upon the fit. These techniques both tended to produce Gaussian fits which

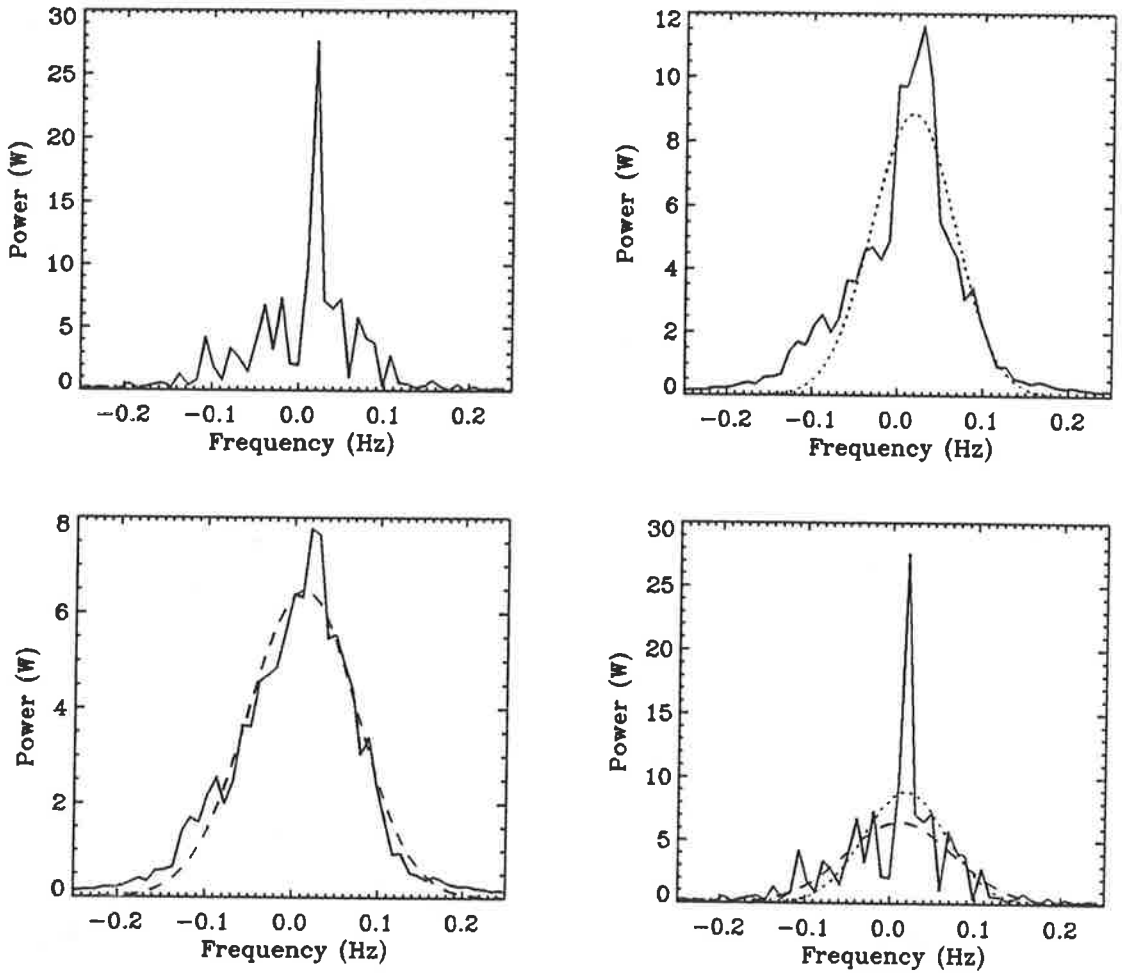

Figure 7.7: Example of the operation of the spike elimination procedure using a power-spectrum obtained at 94 km using the BP MF radar in SA mode. Top left: cross-spectrum with dominant spike close to zero Hz. Top right: smoothed spectrum and fitted Gaussian (dotted line). The smoothing has not smoothed out the spike, and the Gaussian fit has consequently been biased towards the spike, and away from the general Gaussian shape of the spectrum. Bottom left: smoothed spectrum with spike removed from the averaging and fitted Gaussian (dashed line). The Gaussian fits the general Gaussian shape of the spectrum. Bottom right: Unsmoothed spectrum with Gaussian fits obtained with (dashed line) and without (dotted line) use of spike elimination formula.

overestimated the spectral width, as well as producing a number of undesirable results.

The best solution to this problem was found using a procedure similar to that employed by *Hocking* [1983a] in the estimation of turbulent velocity magnitudes from power-spectral widths. This procedure involves the use of an iterative cycle of progressively eliminating the Doppler frequency with the largest spectral powers from the smoothing process until either the resulting Gaussian fit stabilizes or four Doppler frequencies have been eliminated. The stability criterion was chosen after observing many examples by hand, and can therefore

be applied with a high degree of confidence. An example of the operation of the spike elimination procedure is shown in Figure 7.7, revealing an improved Gaussian fit. The improvement obtained in employing the spike elimination procedure can be seen in Figure 7.8, which shows the scatter plots of the FCA and FSA estimates of $\tau_{0.5}$ obtained using the first two hours of the BP MF SA data-set BP940527 both with and without the spike elimination procedure. In the case where the spike elimination procedure is not employed the presence of dominant spikes often results in the underestimation of f_s, and consequently an overestimation of $\tau_{0.5}$. Although this effect is not entirely eliminated by the use of the spike elimination procedure it is significantly reduced. There are also a number of cases introduced where the FSA estimate of $\tau_{0.5}$ considerably underestimates the FCA estimate.

The use of the spike elimination procedure raises a number of important questions in respect to the application of the FCA and the FSA. The contributions of each individual Doppler frequency to the correlation functions employed by the FCA can be considered to be approximately proportional to the amplitude of the frequency component. It therefore follows that the Doppler frequencies with largest spectral powers will contribute the most information to the correlation functions. The spike elimination procedure effectively removes these frequencies from the Gaussian fit. The presence of dominant spectral components tends to result in an increase in the width of the correlation functions, as illustrated in section 4.7. The removal of these dominant spectral components by the spike elimination procedure will therefore result in the FSA estimate of $\tau_{0.5}$ underestimating the FCA estimate, as can be seen in Figure 7.8. This raises the question as to which is the best estimate of $\tau_{0.5}$. If the FSA is applied using the spectral parameters estimated by applying Gaussian fits using the spike elimination procedure the results may differ from those obtained using the FCA. If the spikes are the result of specular scatter their removal may actually be advantageous, as the FSA is based upon the assumption of volume scatter.

The FSA applied throughout this chapter uses the spike-removal procedure for the Gaussian fit to the mean power-spectrum in order to obtain an accurate estimate of $\tau_{0.5}$. The Gaussian fits applied to the power- and cross-spectral magnitudes do not use the spike-elimination procedure. The peak power- and cross-spectral magnitudes, P_{0i} and W_{0ij} respectively, are determined using the values of f_s and f_0 estimated from the mean power-spectrum. The spike elimination procedure is not employed for these fits because it has been designed specifically to obtain an accurate estimate of the spectral width and offset, rather than the peak amplitude. As a result, the spike-elimination procedure can produce an underestimate in

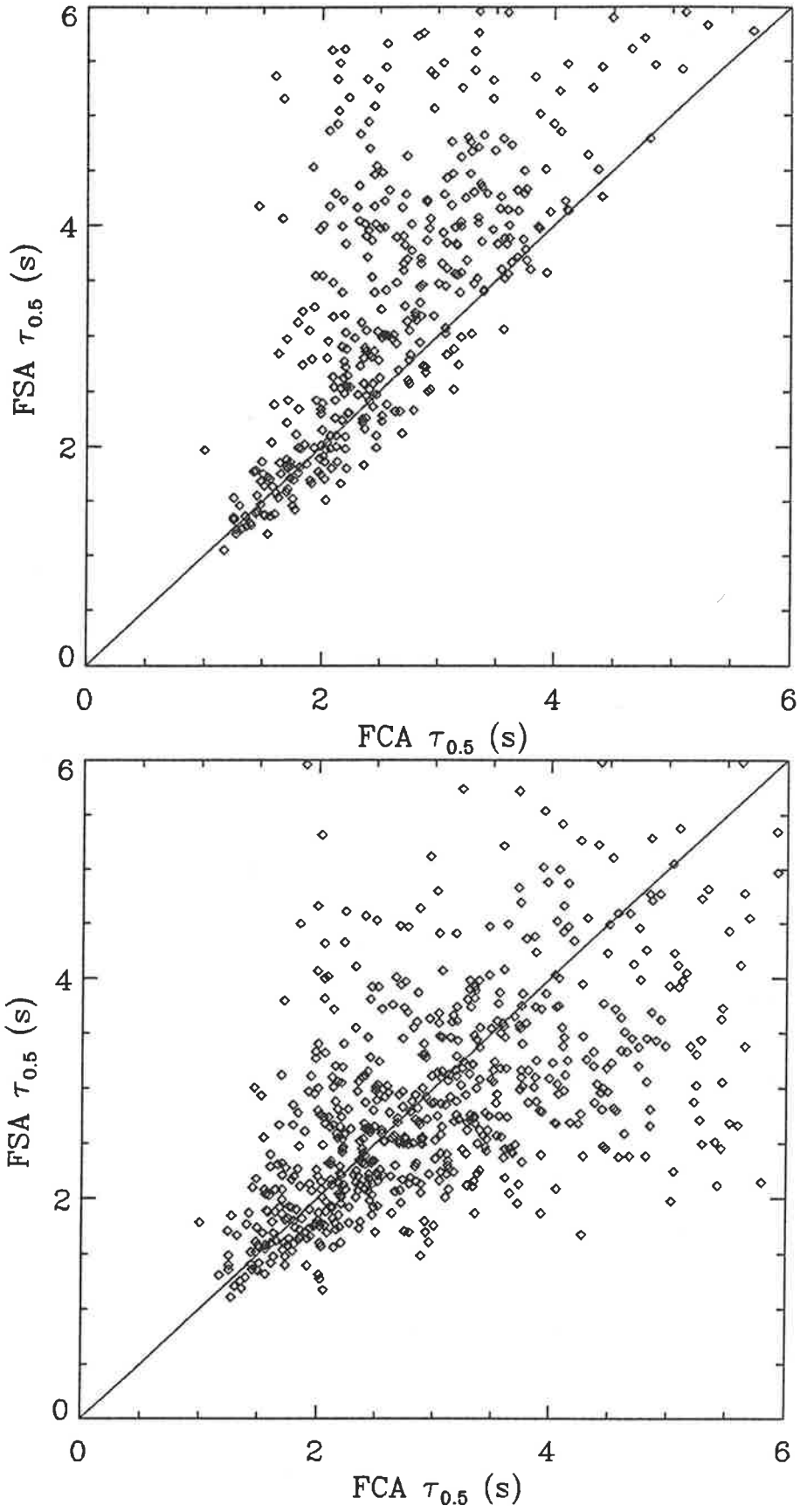

Figure 7.8: Scatter plots of the FCA and FSA estimates of $\tau_{0.5}$ obtained without (top) and with (bottom) use of the spike-elimination procedure for the first two hours of the BP MF SA data-set BP940527. The ratio of the average FSA to FCA estimates of $\tau_{0.5}$ are 1.26 (top) and 1.05 (bottom).

the peak amplitude, as is evident in Figure 7.7.

7.3.2 The linear fitting procedure

The cross-spectral phase slopes m_{ij} are estimated by applying linear fits to the cross-spectral phase. The cross-spectral magnitude and phase plots of Figure 7.5 illustrate that the phase usually shows a linear trend within the main peak of the cross-spectral magnitude, submerged in a random variation. If this random variation is sufficiently large the phase fit can be significantly affected by 2π ambiguities. This is especially true for cross-spectra with low SNR, as shown in Appendix F. Random variations can also be introduced by the effects of spatial decorrelation and turbulent random motions (e.g. *Sheppard and Larsen*, [1992]). These random variations can be significantly reduced by averaging over Doppler frequency, or by using coherently averaged spectra. The phase fit is also complicated by wraparound effects due the finite $\pm\pi$ domain of the phase. If the ground diffraction pattern velocity is sufficiently small the phase will go through several 2π cycles, thereby producing wraparound. The presence of instrumentally produced phase differences between receivers (e.g. *Vandepeer*, [1993]) can also produce wraparound. The phase differences result in the addition of a phase offset $\Delta\phi_{ij}$ to the cross-spectral phase of 7.11, producing the revised equation

$$\phi_{ij}(f) = m_{ij}(f - f_0) + \phi_{0ij} + \Delta\phi_{ij}. \tag{7.24}$$

If the phase difference between receivers is of the order of $\pm\pi$, phase wraparound will almost certainly result. If the receiver phase differences can be estimated they should be subtracted from the cross-spectral phase to reduce such ambiguities.

In order to reduce the problems associated with phase ambiguities and wraparound, a phase unwrapping procedure has been developed. The application of this procedure is illustrated in Figure 7.9, where $\phi_0(f)$ denotes the phase variation to be unwrapped. The first step involves calculating the phase differences between contiguous Doppler frequencies over the range of frequencies employed for the linear fit. Any absolute phase differences exceeding a pre-selected threshold are recorded as possible ambiguities. The phase ambiguities determined using $\phi_0(f)$ are denoted A_i. The first ambiguity A_1 is used to produce an alternative phase variation $\phi_1(f)$ by adding or subtracting 2π as appropriate to or from the phases at Doppler frequencies to the right of A_1. The second ambiguity is then used to produce alternative phase variations $\phi_2(f)$ and $\phi_3(f)$ by adding or subtracting 2π as appropriate to or from the phases at Doppler frequencies to the right of A_2 for $\phi_0(f)$ and

$\phi_1(f)$. This procedure is repeated until all possible phase variations have been determined. If n ambiguities are determined an ensemble of 2^n phase-variations are produced. The phase variation producing the linear fit with the smallest goodness-of-fit parameter is deemed the "unwrapped phase", and the slope of the fitted line is employed as the cross-spectral phase slope m_{ij} for the analysis. The phase variation $\phi_7(f)$ will obviously produce the smallest goodness-of-fit parameter, and the slope of this phase variation will subsequently be used in the analysis.

The cross-spectral phase associated with any particular Doppler frequency is in theory known with greater certainty the larger the cross-spectral magnitude is. This is verified by the fact that the phase associated with small cross-spectral magnitudes often appears to be random. The effect of including such random phases in the linear fit is to produce an underestimate of the phase slope, thereby producing an underestimate of τ'_{ij} and consequently an overestimation of the apparent velocity magnitude. This effect was also noted by *Sheppard et al.* [1993], who found that the phase slope decreased as the width of the fitting region was increased. This effect is also the cause of the result seen in Figure F.5 of Appendix F whereby the fitted phase slope decreases with decreasing SNR. As a result of this effect the phase slopes have been estimated by weighting the linear fit by the cross-spectral magnitudes of the Doppler frequencies within the e^{-1} values of the mean power-spectrum.

The justification for using the weighted fit is as follows. As has previously been discussed, the contributions of each Doppler frequency to the correlation functions used by the FCA can be considered to be approximately proportional to the spectral magnitude. It therefore follows that there is an implicit spectral magnitude weighting involved in the determination of the FCA cross-correlation delay times τ'_{ij}. It should therefore follow that the FSA will produce closer τ'_{ij} estimates to the FCA if weighting is employed. This is confirmed by the results of Figure 7.10, which shows the scatter plots of the FCA and FSA estimated values of τ'_{ij} both with and without spectral weighting for the first two hours of the BP MF SA data-set BP940527. The results illustrate that spectral weighting produces significantly less spread and a significantly larger correlation coefficient. The underestimate of τ'_{ij} resulting from the use of Doppler frequencies with small spectral magnitudes as discussed above is also evident. Unless otherwise stated, spectral magnitude weighting has been employed for all cross-spectral phase fits used to produce the results presented in this chapter. It is worth noting that weighting is also used in the linear fit to the cross-spectral phase employed during the PFI analysis described by *Van Baelen and Richmond* [1991], although they choose to

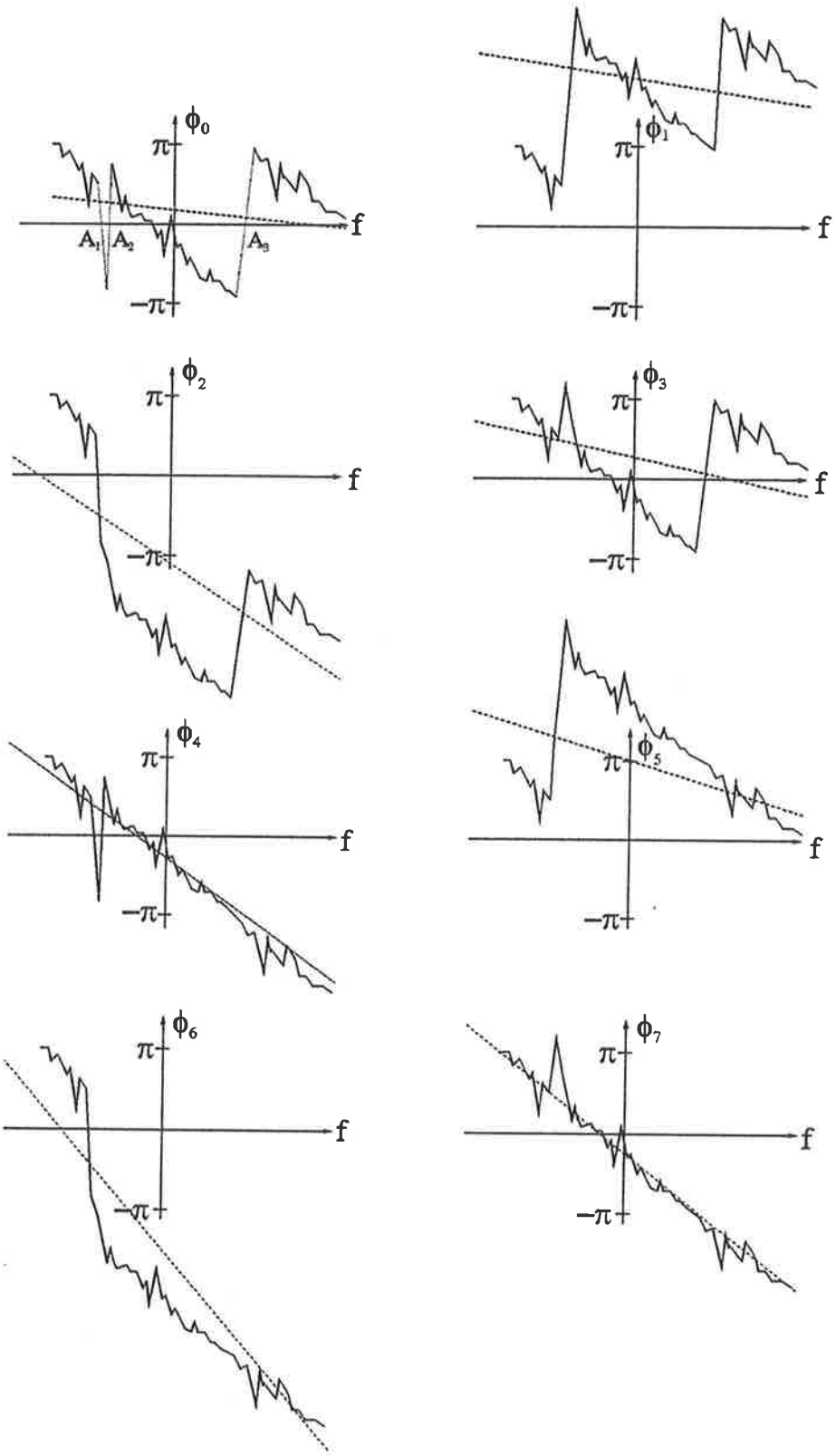

Figure 7.9: Example of the operation of the phase unwrapping procedure (see text for details). The ambiguities A_1, A_2, and A_3 are denoted by the dotted lines, while the linear fits to each phase variation are denoted by the dashed lines.

use the coherency rather than the cross-spectral magnitude.

In order to apply the FSA rejection criterion 4 it was necessary to determine an appropriate goodness-of-fit parameter σ_{ij} and threshold $\sigma_{ij\max}$. The technique used to estimate $\sigma_{ij\max}$ involved determining the "signal" and "noise" distributions of σ_{ij} obtained using the first two hours of the BP MF SA data-set BP940527. The signal distribution was obtained from the σ_{ij} values produced in determining the τ'_{ij} values shown in Figure 7.10 for the case of spectral weighting. The noise distribution was obtained from the σ_{ij} values produced using the same records with the actual phase variations replaced by randomly generated phase variations. The noise case was intended to simulate the case where there is on average no linear behavior. It was found for the noise case that the χ^2 parameter could vary depending on range of frequencies employed for the linear fit. The χ^2 parameter was therefore deemed an inappropriate goodness-of-fit parameter. The goodness-of-fit parameter chosen for the analysis is given by

$$\sigma_{ij} = \frac{\sum_{k=0}^{N_p-1} W_{ij}(f_k)(\phi'_{ij}(f_k) - \phi_{ij}(f_k))^2}{\sum_{k=0}^{N_p-1} W_{ij}(f_k)}. \tag{7.25}$$

where $(f_0, \ldots f_{N_p-1})$ are the N_p frequencies over which the fit is applied, $\phi'_{ij}(f)$ is the cross-spectral phase, $\phi'_{ij}(f)$ is the fitted phase, and $W_{ij}(f)$ is the cross-spectral magnitude. This parameter is a sensible choice based on the spectral magnitude weighting used for the phase fit, and was found to be independent of the range of frequencies employed for the linear fit for the noise case.

The signal and noise distributions of σ_{ij} resulting after the application of FSA rejection criterion 5 are shown in Figure 7.11. Approximately 30% of the noise records are rejected by criterion 5. The threshold $\sigma_{ij\max}$ must be picked as a compromise between minimizing the rejection of records with genuinely linear behavior and minimizing the number of "noisy" records. A threshold of $\sigma_{ij\max} = 1.5$ was selected. It was found that only 2% of the noise records which passed criteria 5 also passed the remaining FSA rejection criteria, thereby suggesting that random phase variations are almost entirely eliminated from the analysis. Unless otherwise specified, the threshold $\sigma_{ij\max} = 1.5$ has been applied for all cross-spectral phase fits used to produce the result presented in this chapter.

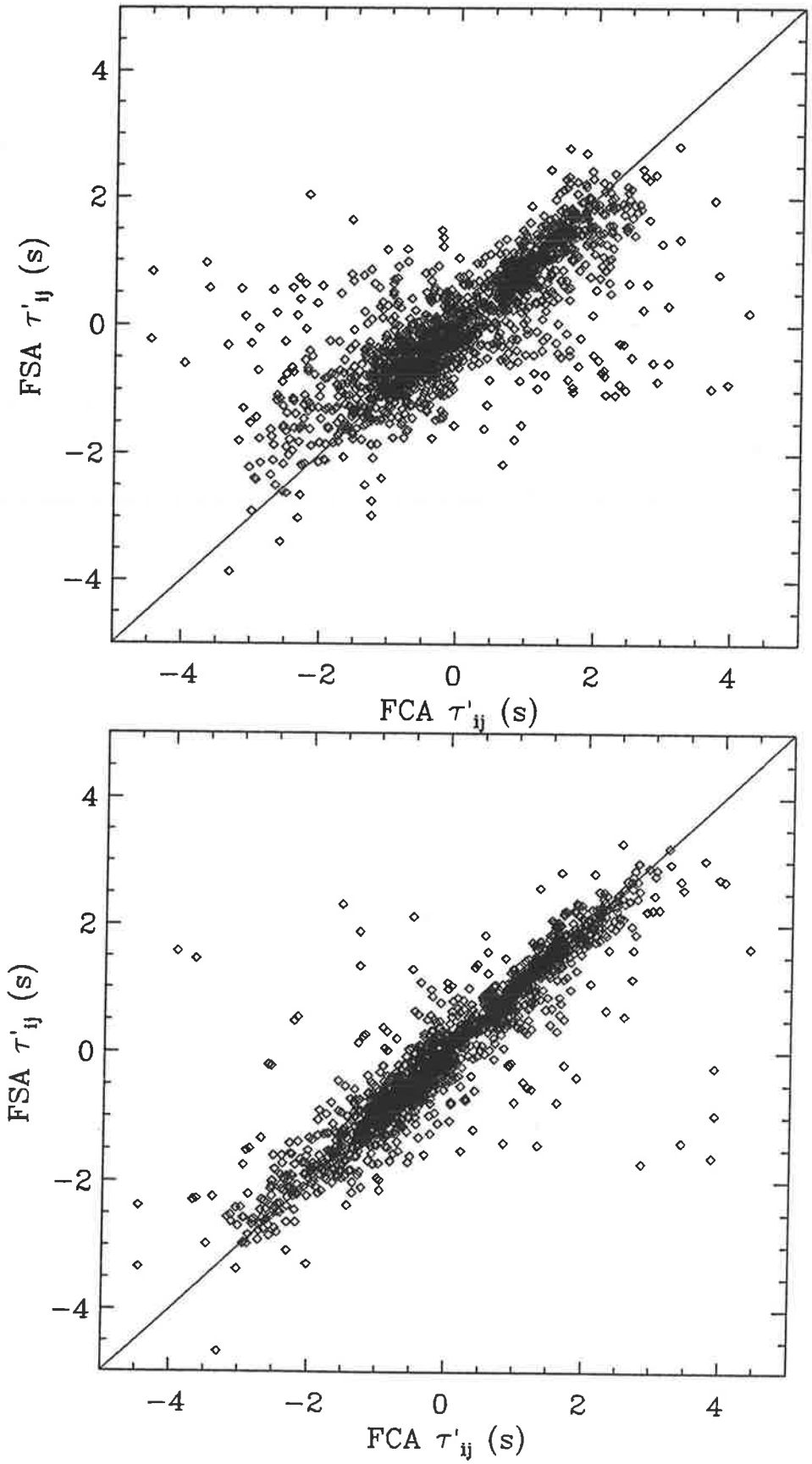

Figure 7.10: Scatter plot of the FCA and FSA estimates of τ'_{ij} both without (top) and with (bottom) use of spectral magnitude weighting for the first two hours of the BP MF SA dataset BP940527. The correlation coefficients for the plots are 0.76 (top) and 0.91 (bottom).

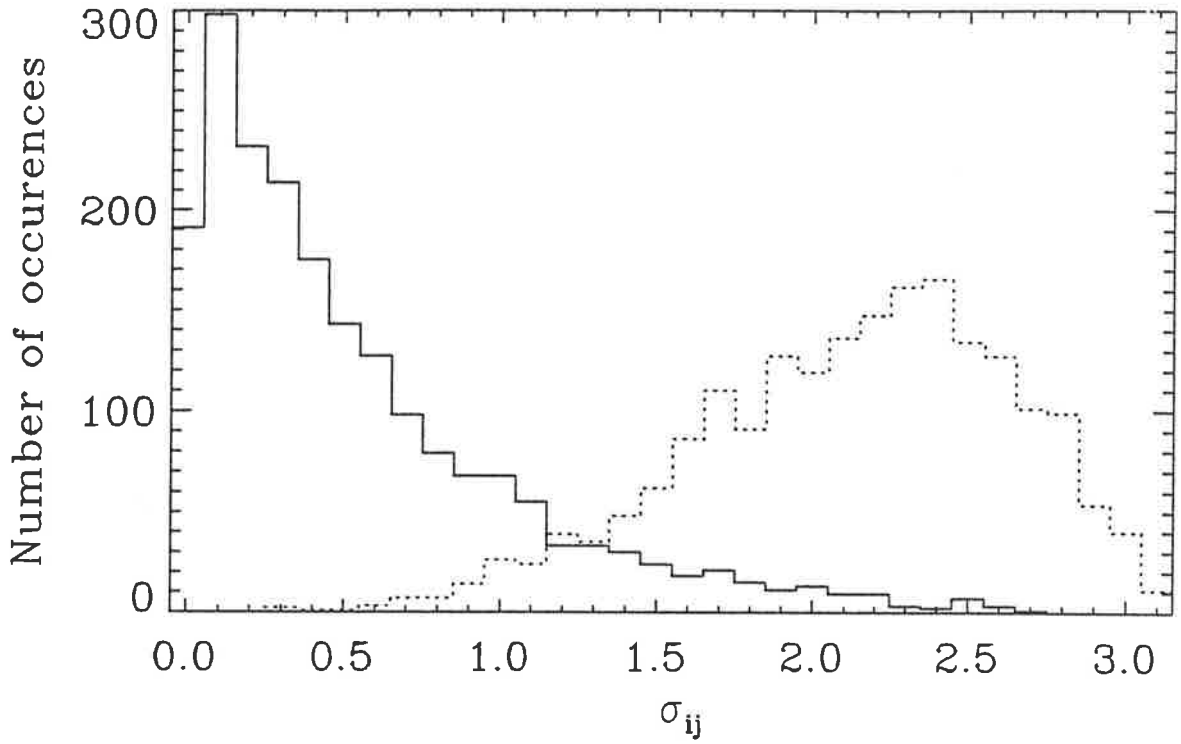

Figure 7.11: Histogram of the σ_{ij} values obtained for "signal" (solid line) and "noise" (dotted line) cross-spectral phase variations using the first two hours of the BP MF SA data-set BP940527. The signal values are obtained using the actual cross-spectral phase values, while the noise values are obtained using randomly generated cross-spectral phase values.

7.4 Application of the FSA to unaveraged spectra

The FCA is employed for the routine analysis of mesospheric and lower thermospheric winds by the Adelaide group using the BP MF SA. The analysis is performed on correlation functions calculated from the individual time-series records. The FSA results employed for the comparison of the FCA and FSA presented by *Briggs and Vincent* [1992] were based on spectra calculated from the individual time-series records. The comparison of the FCA and FSA results presented by *Sheppard et al.* [1993] and *Liu and Pan* [1993] were based on the average of the spectra calculated from the individual time-series records. This averaging is based on the idea that the correspondence between the experimental and theoretical spectral phase and magnitude increases with the number of averages performed (e.g. *Liu et al.*, [1990]).

In order to illustrate the differences between the use of unaveraged and averaged spectra this section will focus on the results obtained using spectra calculated from the individual time-series records, while the following section will focus on the results obtained using

averaged spectra.

7.4.1 Application to model generated-data

The three FSA techniques have been applied to the model-generated data-set MOD-MF-SA. This data was generated using a model input velocity of magnitude 50ms^{-1} and direction 15° clockwise from North for various different turbulent motion magnitudes ν_{mod}. A total of 200 realizations were generated for each value of ν_{mod}. For simplicity, all three FSA techniques have employed the rejection criteria discussed in section 7.3. The averages and standard deviations of the results of these analyses are shown in Figures 7.12 to 7.14, and Table 7.4.1, together with the results obtained on applying the FCA.

The BVFSA and FCA estimates of the apparent velocity magnitude V_a and direction θ_a are shown in Figure 7.12. The SLFSA and LPFSA estimates are not shown because they use the same estimates of τ'_{ij} as the BVFSA, and should therefore produce the same estimates of V_a and θ_a. In practice, small differences between the average FSA estimates will result due to the rejection criteria rejecting different records for each analysis. The BVFSA and FCA estimates show excellent agreement, as expected based on the agreement between the FCA and FSA estimates of τ'_{ij} shown in Figure 7.10. The errors in the FSA estimates are significantly larger for all values of ν_{mod}. This occurs because the random variation in the cross-spectral phase results in the estimation of the cross-spectral phase slope being more susceptible to errors than the estimation of the cross-correlation maxima, which is in general a simple process.

The FSA and FCA estimates of the true velocity magnitude V_t and direction θ_t are shown in Figure 7.13. The LPFSA and FCA estimates show excellent agreement with the model input velocity magnitude V_{mod} and direction θ_{mod} for all values of ν_{mod}. The errors of the LPFSA estimates are however considerably larger than those for the FCA estimates. The BVFSA estimates of V_t correctly estimate V_{mod} for small values of ν_{mod}, but increasingly overestimates V_{mod} with increasing ν_{mod}. The SLFSA estimates of V_t overestimate V_{mod} for all values of ν_{mod}, and the overestimation increases with increasing ν_{mod}. The BVFSA and SLFSA estimates of θ_t successfully estimate θ_{mod}, but produce significantly larger errors. These results appear to contradict the results of *Briggs and Vincent* [1992] and *Sheppard et al.* [1993], who found good agreement between the BVFSA and the FCA and the SLFCA and FCA, respectively. The reasons for these contradictions will be addressed later.

The FSA and FCA estimates of $\tau_{0.5}$ and $T_{0.5}$ are shown in Figure 7.14. As is the case for

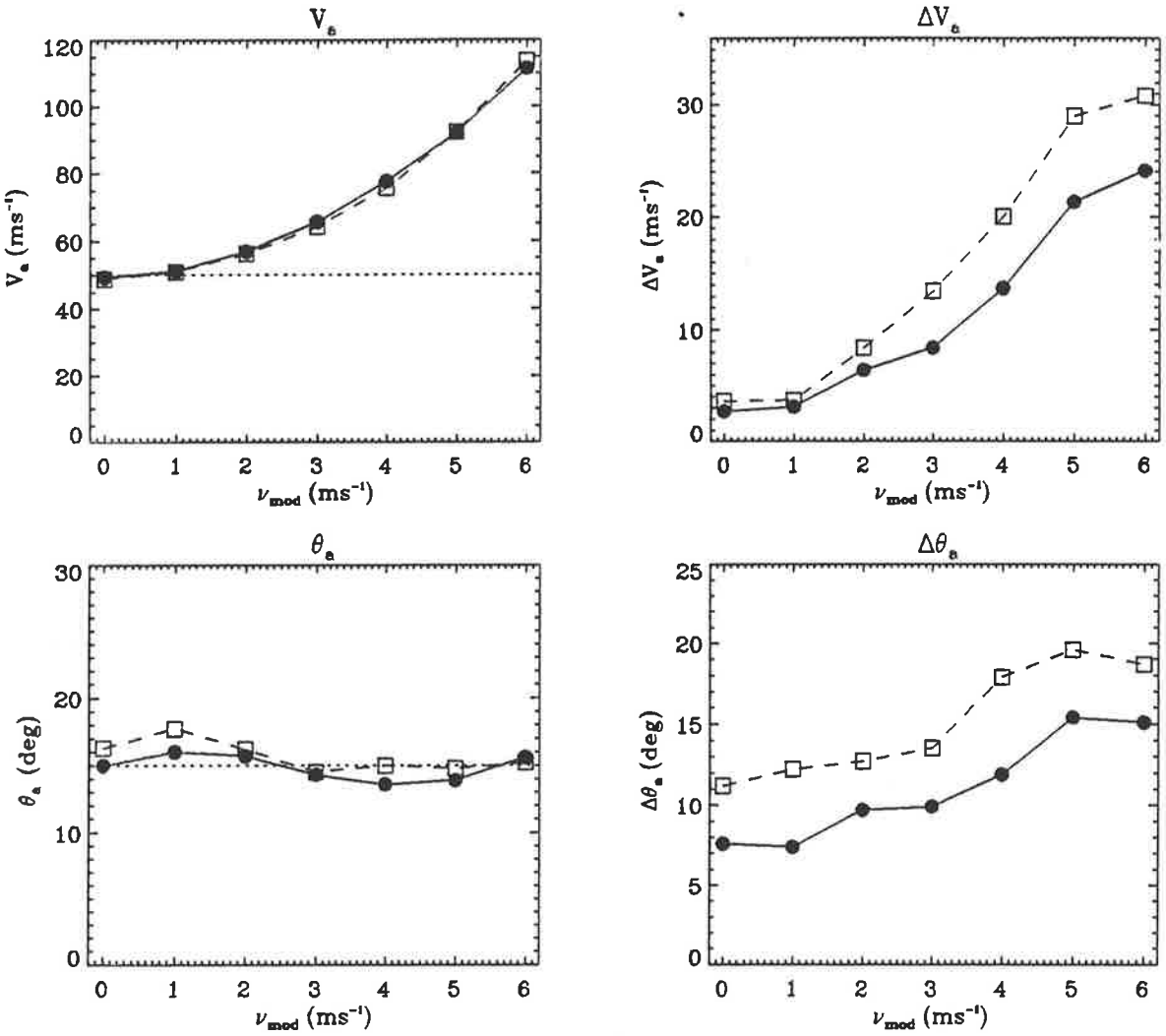

Figure 7.12: Means (left column) and standard deviations (right column) of the apparent velocity magnitude (V_a) and direction (θ_a) as a function of turbulent motions magnitude ν_{mod} for the application of the FCA (•) and BVFSA (□) techniques to the model-generated data-set MOD-MF-SA.

the apparent velocity, the SLFSA and LPFSA estimates of $\tau_{0.5}$ are not shown because all FSA techniques use the same estimation procedure. The BVFSA and FCA estimates of $\tau_{0.5}$ show good agreement, although there is a small underestimation in the BVFSA estimates for smaller values of ν_{mod}. The errors in the BVFSA estimate are consistently larger than the FCA estimates. This occurs because the "spiky" nature of the mean power-spectra results in the estimation of f_s being more susceptible to variation than the estimation of $\tau_{0.5}$ from the mean auto-correlation function. The LPFSA and FCA estimates of $T_{0.5}$ show good agreement for all values of ν_{mod}. The errors of the LPFSA estimates are again however considerably larger than those for the FCA estimates. The BVFSA and SLFCA estimates

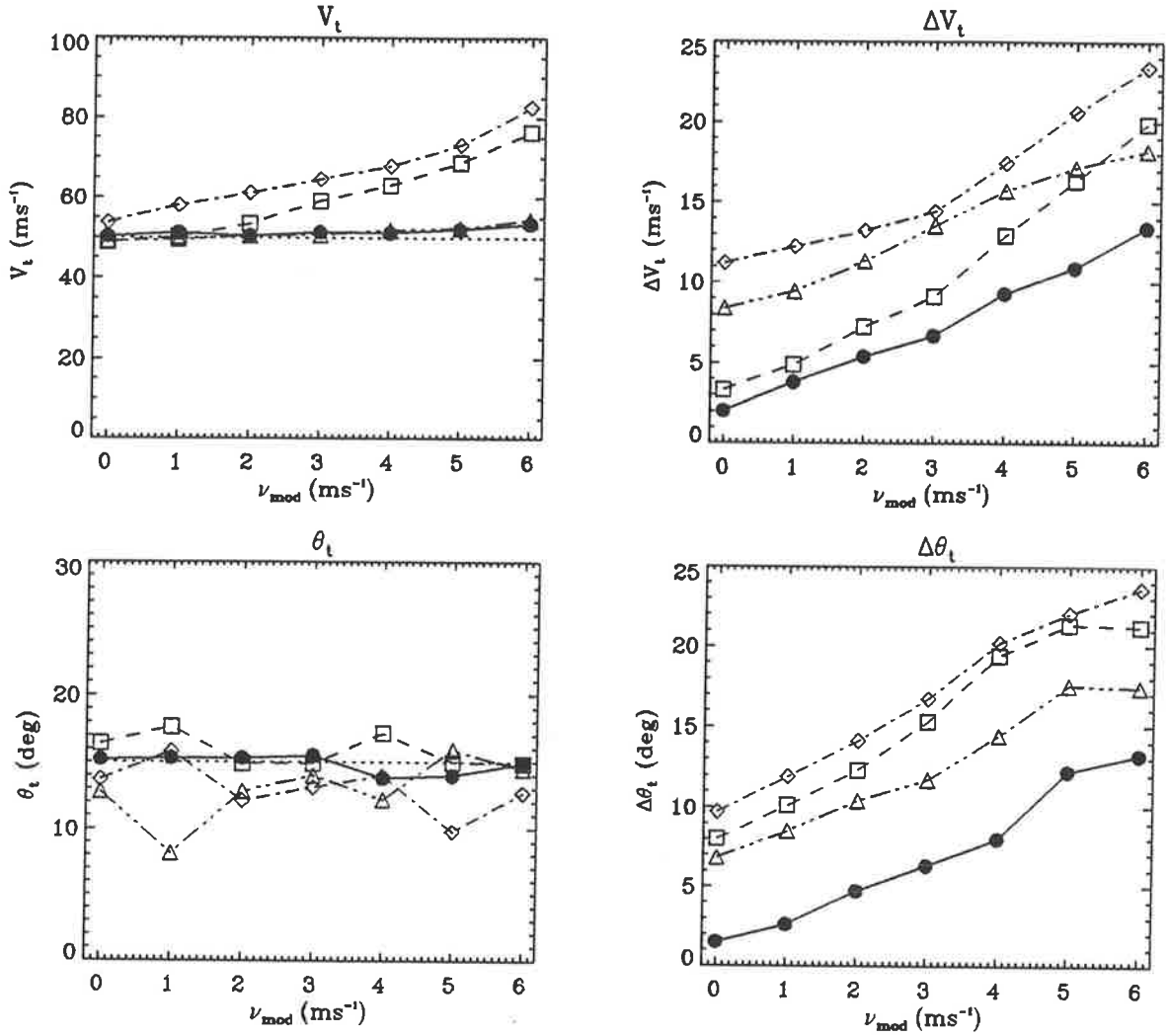

Figure 7.13: Means (left column) and standard deviations (right column) of the true velocity magnitude (V_t) and direction (θ_t) as a function of turbulent motions magnitude ν_{mod} obtained for the application of the FCA (•), BVFSA (□), SLFSA (◇), and LPFSA (△) techniques to the model-generated data-set MOD-MF-SA.

of $T_{0.5}$ again overestimate the FCA estimates.

The FSA and FCA estimates of the pattern scale $S_{0.5}$ and axial ratio R_{ax} are shown in Table 7.4.1. The FCA and LPFSA estimates of $S_{0.5}$ show good agreement, while the estimates of R_{ax} agree well with the value of about unity expected due to the isometric scatterers used to generate the data. The BVFSA and SLFSA estimates considerably overestimate the FCA and LPFSA estimates of each parameter. Histograms of the BVFSA and SLFSA estimates of the axial rotation θ_{ax} reveal a bias towards a direction of 105°, which is the direction perpendicular to the model input velocity direction θ_{mod}. On the other hand, the LPFSA estimates of θ_{ax} show no bias.

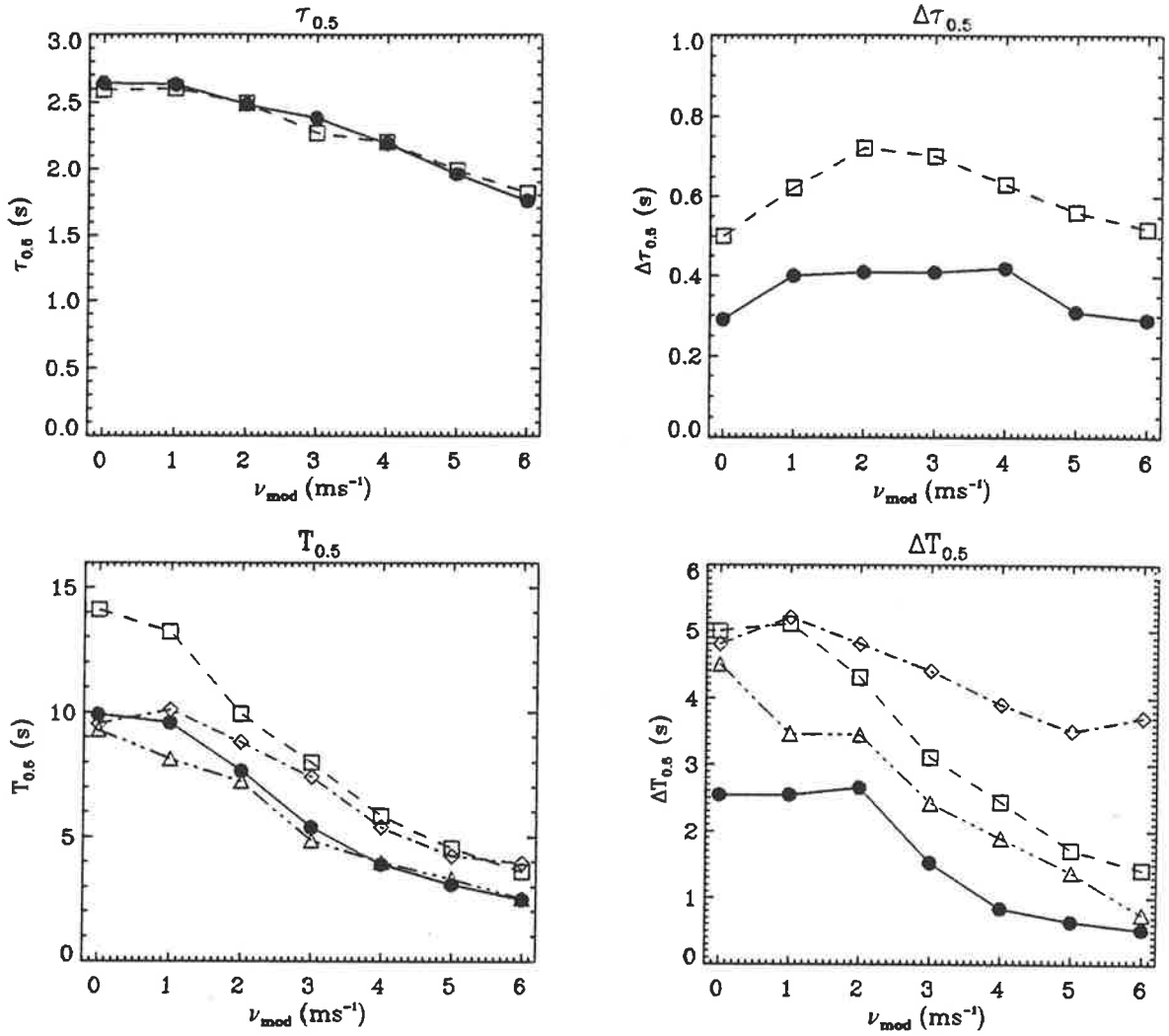

Figure 7.14: Means (left column) and standard deviations (right column) of the fading time $\tau_{0.5}$ (left) and corrected fading time $T_{0.5}$ (right) as a function of turbulent motions magnitude ν_{mod} obtained for the application of the FCA (•), BVFSA (□), SLFSA (◇) and LPFSA (△) techniques to the model-generated data-set MOD-MF-SA.

Despite the discrepancy in the BVFSA and SLFSA estimates of $T_{0.5}$ and $S_{0.5}$, the relative values agree with the results of *Meek* [1980], who found that the estimates of $T_{0.5}$ and $S_{0.5}$ obtained using the Meek FCA were consistently smaller than the results obtained using the FCA described by *Fedor* [1967], which uses essentially the same formulae as the Briggs FCA. Since the SLFSA uses the Meek FCA it follows that it should produce estimates of $T_{0.5}$ and $S_{0.5}$ smaller than those obtained using the BVFSA, which is based on the Briggs FCA.

The results of this section suggest that the BVFSA and SLFSA produce biases in the estimates of the FSA parameters. The LPFSA however produces results that agree well with those produced by the FCA. The errors obtained in applying the LPFSA are however

Table 7.2: Estimates of the pattern scale $S_{0.5}$ and axial ratio R_{ax} obtained by applying the FCA and FSA techniques to the model-generated data-set MOD-MF-SA.

Analysis	$S_{0.5}(m)$	R_{ax}
FCA	302 ± 44	1.22 ± 0.14
BVFSA	551 ± 145	2.01 ± 0.52
SLFSA	496 ± 97	1.97 ± 0.53
LPFSA	307 ± 64	1.32 ± 0.22

considerably larger than those produced by the FCA. This is a result of the larger variation inherent in the estimation of the spectral parameters required for the spectral analyses.

7.4.2 Explanation of results

In order to comprehend the results of 7.4.1 it is necessary to refer back to the individual parameters estimated in applying the FCA and FSA techniques. The results of Figures 7.8 and 7.10 illustrate that the FCA and FSA estimates of $\tau_{0.5}$ and τ'_{ij} show good agreement. It follows that the overestimation of the BVFSA and SLFSA estimates of V_t, $T_{0.5}$ and $S_{0.5}$ must lie in the estimation of the remaining parameter, namely τ_{ij} for the BVFSA and ρ_{0ij} for the SLFSA. This is verified by Figures 7.15 and 7.16, which shows scatter plots of the FCA and FSA estimates of these parameters for the first two hours of the data-set BP940527. The LPFSA estimate agrees well with the FCA estimate, while the BVFSA and SLFSA estimates show a marked discrepancy.

This discrepancy can be explained by taking into account the effects of the cross-correlation function tails upon the spectra used by the FSA. The FCA is performed solely on the main peak of the correlation functions. The tails therefore have little influence on the results. The FSA is performed on cross-spectra, which are related to the cross-correlation functions by the Fourier transform. As a result, the FSA is performed on cross-spectra containing the contributions from the cross-correlation function tails. Figure 7.17 illustrates a typical cross-correlation function magnitude and the corresponding cross-spectrum magnitude obtained by the Fourier transform. The spectrum obtained by Fourier transforming the cross-correlation function with all lags outside the e^{-1} width set to zero is also shown, along with the spectrum obtained using all lags inside the e^{-1} width set to zero. This plot clearly illustrates the separate contributions of the main peak and the tails of the cross-correlation function to the cross-spectra. The main peak produces the Gaussian base of the spectrum,

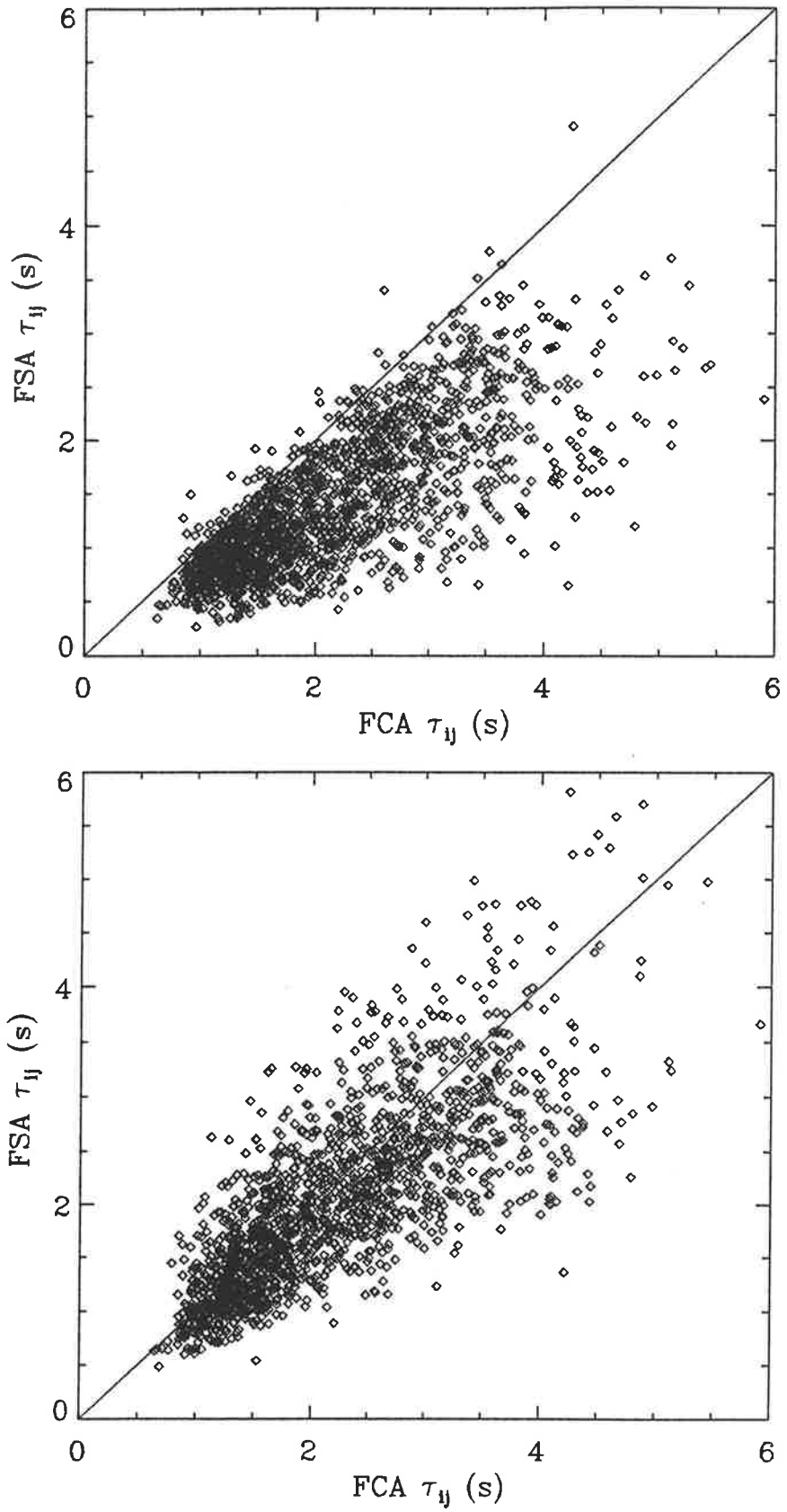

Figure 7.15: Scatter plots of the FCA and FSA estimates of τ_{ij} obtained on applying the BVFSA (top) and LPFSA (bottom) to the first two hours of the BP MF SA data-set BP940527.

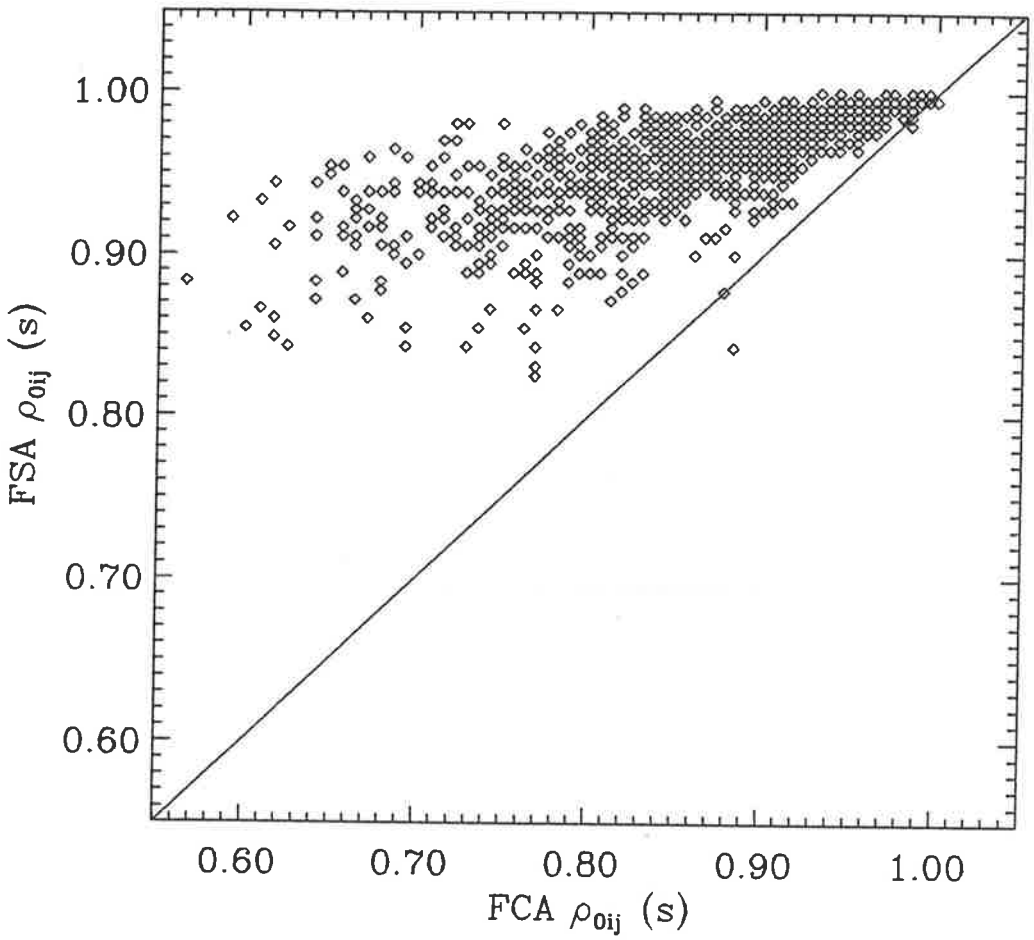

Figure 7.16: Scatter plot of the FCA and SLFSA estimates of ρ_{0ij} obtained for the first two hours of the BP MF SA data-set BP940527.

while the tails produce the spectral spikes. This is a well established result (e.g., *Awe*, [1964]; *May*, [1987]; *Sheppard et al.*, [1993]).

It is interesting to note that the cross-spectral magnitude produced using the tails of the cross-correlation function has the same width and offset as the spectral magnitude produced using both the entire correlation function and the main peak. This occurs because the fading period of the main peak and the oscillations in the tails of the cross-correlation are identical (e.g. *Awe*, [1964]). This result refutes the claims of *Sheppard et al.* [1993] that the major difference between the FCA and FSA lies in the different frequencies contributions inherently employed by the two analyses. They claim that the FSA is more dependent upon the higher frequency contributions than the FCA because the spectra include the effects of the tails of the correlation functions which are neglected by the FCA. It is clear from Figure 7.17 that the main peak and tails produce the same frequency distribution, and that both the FCA

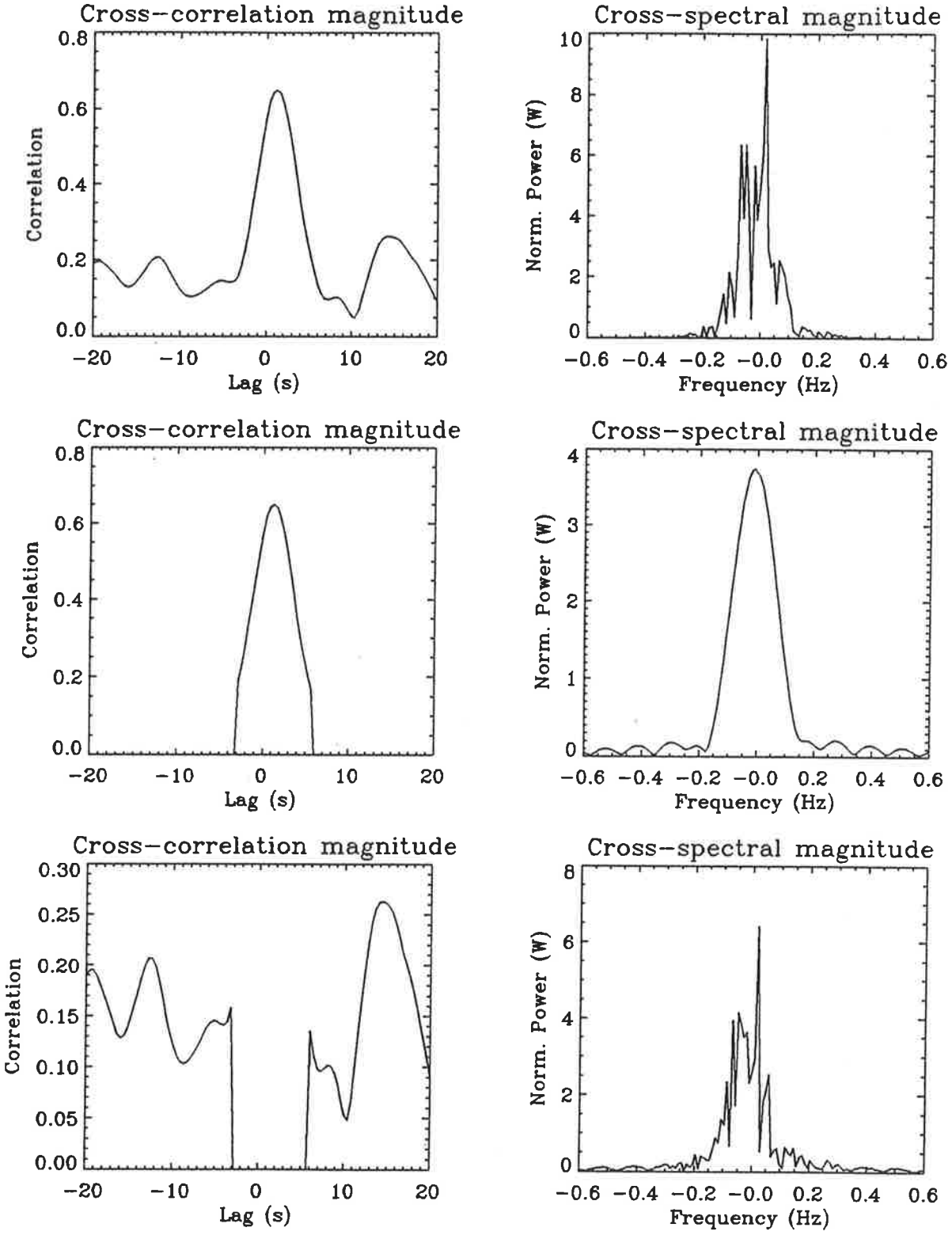

Figure 7.17: Example of the contributions of the correlation function tails to the cross-spectra. The top plot shows a typical cross-correlation function magnitude and cross-spectral magnitude pair. The middle plot shows the corresponding functions obtained using only the main peak of the cross-correlation function, while the bottom plot shows the corresponding functions obtained using only the tails of the cross-correlation function.

Table 7.3: Estimates of A_{ij} and I_{ij} obtained from the cross-spectra of Figure 7.17.

	A_{ij}	I_{ij}
entire ccf	0.821	0.317 + i 0.517
main peak	0.656	0.292 + i 0.499
tail	0.546	-0.003 - i 0.005

and FSA make use of the same frequency contributions.

The values of A_{ij} and I_{ij} estimated from the spectra shown in Figure 7.17 are shown in Table 7.3. As discussed in section 7.2.1, the estimate of A_{ij} should be identical to the cross-correlation maxima, ρ_{0ij}. In the case of Figure 7.17, $\rho_{0ij} \approx 0.65$. The value of A_{ij} obtained from the spectrum calculated using the main peak of the cross-correlation function agrees well with ρ_{0ij}. However, the value of A_{ij} obtained from the spectrum calculated using the entire cross-correlation function overestimates ρ_{0ij}, as shown in Figure 7.16. This effect also results in the underestimation of the BVFSA τ_{ij} estimates shown in Figure 7.15. On the other hand, the cross-correlation tails do not contribute to I_{ij}, explaining the good correspondence between the LPFSA and FCA τ_{ij} estimates. Figure 7.18 shows the scatter plot of the FCA and BVFSA estimates of τ_{ij} obtained using cross-spectra calculated using the main peak of the cross-correlation function. The underestimation of the BVFSA estimates of τ_{ij} seen in Figure 7.15 is no longer seen. In accord with this result, the application of the FSA to spectra calculated using the main peak of the correlations function produces estimates in excellent agreement with the FCA.

These results can be explained as follows. The real and imaginary components of the tails of the cross-correlation function are essentially random. As a result they must integrate to zero. It therefore follows that the real and imaginary components of the spectra resulting from the cross-correlation function tails must also integrate to zero, as confirmed by the results shown in Table 7.3. However, the magnitude of the spectral components are by definition positive, and must therefore integrate to a positive value. This is an analogous effect to that seen in the cross-spectrum magnitude due to the presence of noise, as discussed in Appendix F. The presence of noise results in a positive contribution to the cross-spectral magnitude, producing the noise floor, while the real and imaginary components of the noise integrate to zero. It is interesting to note that the tails of the cross-correlation function contribute almost as much "normalized power" to the cross-spectrum (0.546) as the main

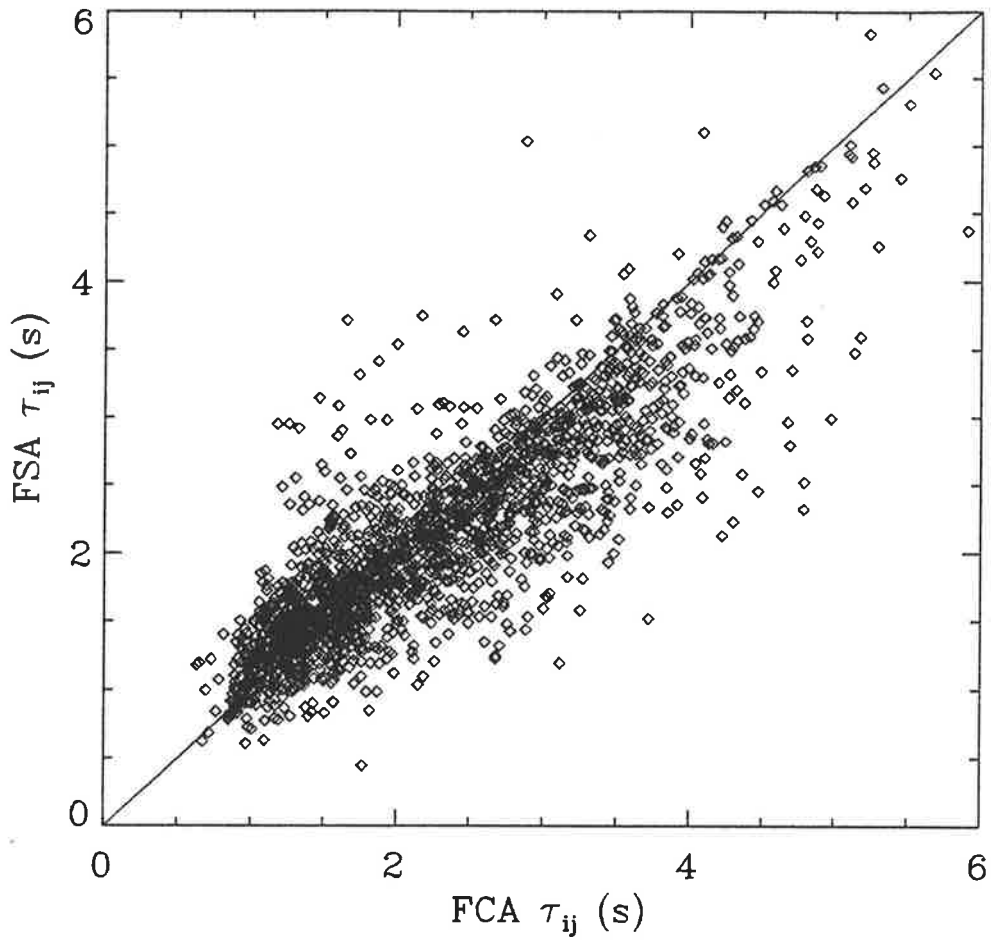

Figure 7.18: Scatter plot of the FCA and BVFSA estimates of τ_{ij} obtained using cross-spectra produced by the Fourier transform of the main peak of the cross-correlation functions for the first two hours of the BP MF SA data-set BP940527.

peak of the cross-correlation function (0.656). These figures of do not add up to the "total normalized power" (0.821) because the cross-spectrum is the complex addition of the contributions from the main peak and tails of the cross-correlation function.

The effect of the underestimation of the BVFSA τ_{ij} estimates upon the analysis can be understood by examining the FCA equations presented in Chapter 4. The ellipsoid parameters a, b, and h are related to τ_{ij} by (4.19). The underestimation of τ_{ij} results in the underestimation of a, b, and h, which leads to an overestimation of $S_{0.5}$ as described by (4.34). Because the BVFSA and FCA produce similar τ'_{ij} estimates, it follows from (4.17) that they must produce similar estimates of the ellipsoid parameters f and g. It therefore follows from (4.25) and (4.26) that the zonal and meridional components of the ground diffraction pattern velocity V_x and V_y must be overestimated, and that V_t must also be overestimated.

7.4.3 Effects of time-series length upon the FSA

The results obtained in the 7.4.2 suggest that the BVFSA and SLFSA techniques require the effects of the tails of the cross-correlation functions to be removed from the cross-spectra prior to analysis. The results of Chapter 4 illustrate that the tails of the correlation functions can be reduced by using longer time-series records (e.g. Figure 4.25), or by using correlation functions calculated from the coherent average of correlations functions obtained from individual time-series records (e.g. Figure 4.28). It may therefore follow that the cross-spectra obtained using longer time-series records or by the coherent average of the cross-spectra obtained using individual time-series records could have the effects of the correlation tails suppressed sufficiently to produce accurate BVFSA and SLFSA parameter estimation.

The model-generated data-set MOD-MF-4096 has been used to investigate the effects of the time-series length upon the FSA. The results of applying the BVFSA and LPFSA to various different time-series lengths are shown in Figure 7.19. The LPFSA results agree well with the FCA results shown in Figure 4.26. The estimates converge towards the model input values as the record length is increased. The estimate of V_a also shows the same increase with record length seen in the FCA results. The BVFSA estimates show a significant decrease with increasing record length. The decrease however is not sufficient to produce agreement with the LPFSA estimates which agree well with the model input values. The decrease in the BVFSA estimates suggests that the overestimation may be removed if time-series records longer than those used to produce Figure 4.26 are employed. The 4096 sample time-series corresponds to a time duration of approximately 27 minutes. The use of records longer than this duration is generally not advisable in practice because the characteristics of the atmospheric may vary significantly within the duration of the record. This suggests that the BVFSA and SLFSA cannot effectively be applied to individual time-series records. Although the cross-correlation function tails are suppressed by the use of longer time-series records the suppression is not sufficient to correct for the overestimation exhibited in the BVFSA and SLFSA results.

7.4.4 Effects of averaging over Doppler frequency

The results obtained in 7.4.1 appear to contradict the results of *Briggs and Vincent* [1992], who found good agreement between the FCA and BVFSA estimates of V_t and θ_t. Their

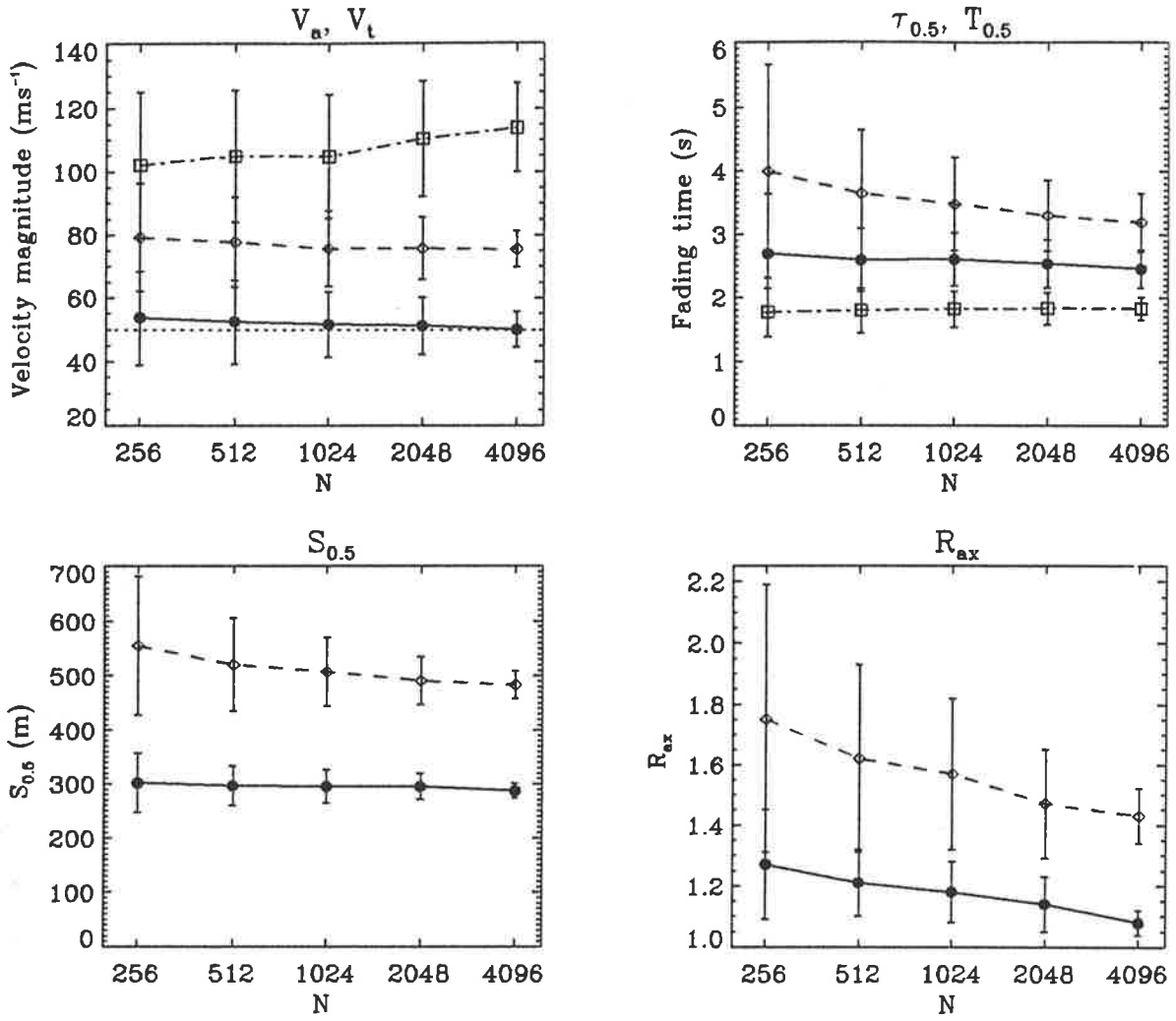

Figure 7.19: Effect of time-series length upon the BVFSA and LPFSA. The top left plot shows the BVFSA estimates of V_t (□) and V_a (◇) and the LPFSA estimate of V_t (•). The top right plot shows the BVFSA estimates of $\tau_{0.5}$ (•) and $T_{0.5}$ (◇) and the LPFSA estimate of $T_{0.5}$ (□). The bottom left and right plots show $S_{0.5}$ and θ_{ax} respectively for the LPFSA (•) and BVFSA (◇).

analysis used coherent "block" averaging to reduce the number of Doppler frequency components from 256 to 64 in order to simplify the Gaussian and linear fits used to estimate the cross-spectral magnitude maximum W_{0ij} and cross-spectral phase slope m_{ij}.

The effect of coherent block averaging upon the cross-spectrum magnitude is shown in Figure 7.20. The values of W_{0ij}, f_s and A_{ij} estimated from Gaussian fits to these spectra are shown in Table 7.4. The averaging results in a decrease in W_{0ij} and an increase in f_s, which results in an overall decrease in A_{ij}. The decrease in W_{0ij} can be explained by the fact that the magnitude of the average of a number of vectors with different directions must

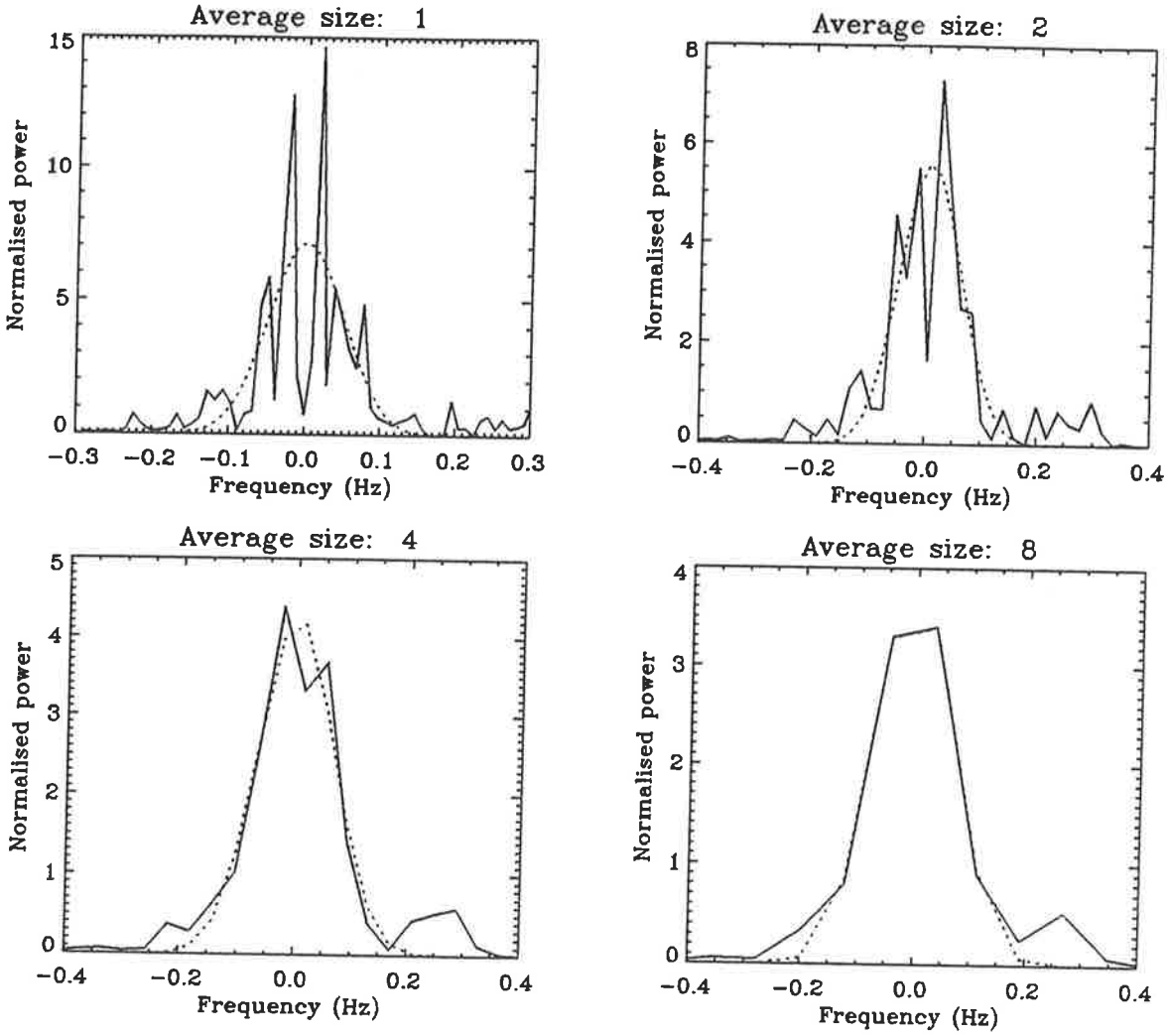

Figure 7.20: Effect of coherent block averaging upon the cross-spectrum, using block average sizes of one (unaveraged spectrum) (top left), two (top right), four (bottom left) and eight (bottom right) for an individual record of the BP MF SA data-set BP940527 at 80 km. The dotted line shows the Gaussian fit to each cross-spectrum.

be less than the average of the magnitudes of the individual vectors. Because the cross-spectral phases of the contiguous frequency components used in the block average will differ it follows that the resultant estimate of W_{0ij} must therefore decrease. The increase in f_s results because the averaging smears the spectral power over a range of frequencies. The resulting decrease in A_{ij} leads to an increase in τ_{ij}.

The BVFSA technique has been applied to the model-generated data-set MOD-MF-SA using cross-spectra produced using coherent block average sizes of 1, 2, 4 and 8 frequency components. In order to produce sensible results it was necessary to apply the same size block average to the power-spectra. This was because the analysis presented here is based

Table 7.4: Cross-spectral magnitude maxima W_{0ij} estimated by Gaussian fits to block averaged cross-spectra of Figure 7.20.

Block average size	W_{0ij}	f_s	A_{ij}
1	7.14	0.071	0.98
2	5.60	0.077	0.76
4	4.26	0.094	0.71
8	3.94	0.097	0.67

on using the estimate of f_s obtained from the Gaussian fit to the mean power-spectrum in order to estimate W_{0ij} from the cross-spectrum. The results of Table 7.4 illustrate that the values of f_s estimated from the Gaussian fit to the cross-spectra increase with increasing block average size. If the block average was not applied to the power-spectra the values of f_s estimated from the mean power-spectrum underestimated the actual value. This resulted in poor estimates of W_{0ij}, which resulted in a large number of rejections during the analysis. However, if the block average was also applied to the power-spectra these problems were not encountered.

The results of this revised analysis are shown in Figure 7.21. The results suggest that the estimate of V_t decreases with increasing block average size. This is a direct result of the decrease in the A_{ij} estimates as exhibited in Table 7.4. Similar decreases were also seen in $T_{0.5}$, and $S_{0.5}$ (not shown). The V_a estimates were found to be independent of the block averaging size, indicating that block averaging has a negligible influence upon the estimation of τ'_{ij}. This result is sensible based on the use of spectral magnitude weighting for phase fit, as the phase of any block averaged spectral component will be influenced to a greater extent by the phase of the component with the largest spectral magnitude (e.g. *Franke et al.*, [1990]). The SLFSA estimates of V_t, $T_{0.5}$, and $S_{0.5}$ were also found to decrease with increasing block average size. This result is in accord with the decrease in A_{ij} with increasing block average size shown in Table 7.4. The LPFSA estimates were found to be almost independent of the block average size. This is clearly sensible as coherent block averaging will not change the estimate of I_{ij}, suggesting that any difference introduced in the results must be due to the estimates of $\tau_{0.5}$ and τ'_{ij} used.

The results of Figure 7.21 suggest that the good agreement between the FCA and the BVFSA results exhibited in *Briggs and Vincent* [1992] may result from their use of a coherent block average size of four frequency components. In this instance, Figure 7.21 suggests that

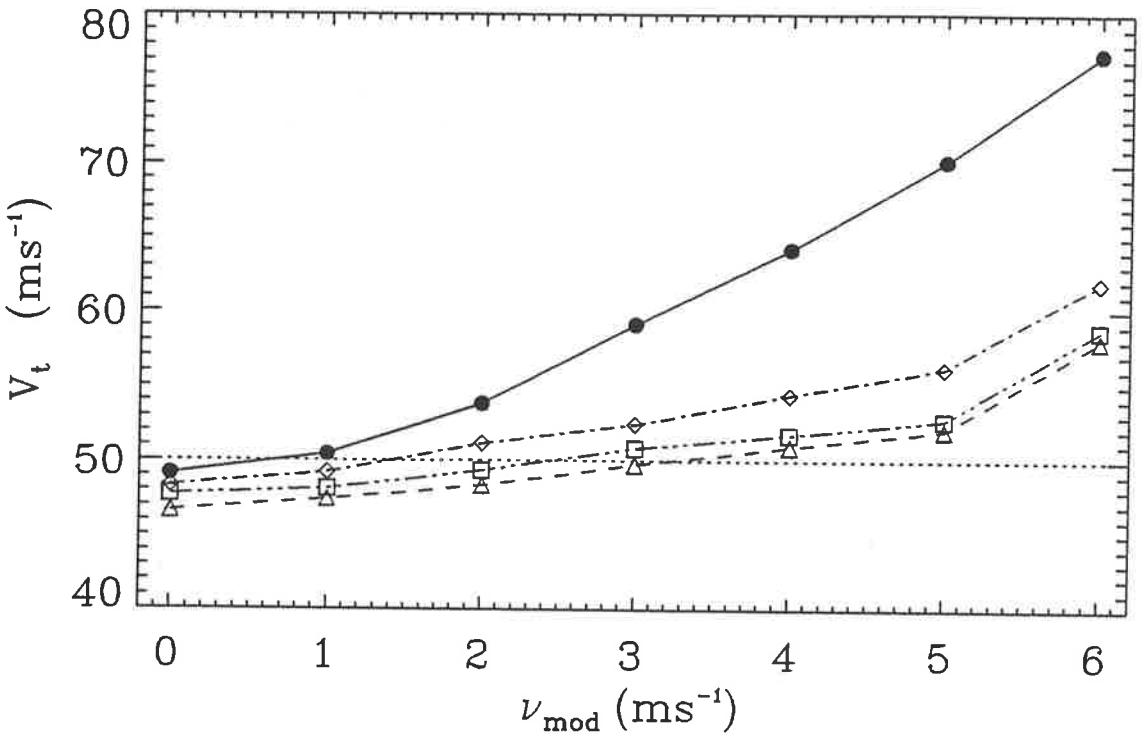

Figure 7.21: Average true velocity magnitude V_t estimated from the application of the BVFSA to the model-generated data-set MOD-MF-SA using coherent block averaging sizes of one (•), two (◇), four (□) and eight (△) frequency components.

records with small random changes will underestimate the actual wind velocity, while records with large random changes will overestimate the actual wind velocity. The net effect would be that the average V_t would be close to the actual wind velocity, as is the case for *Briggs and Vincent* [1992]. The results of Figure 7.21 also suggest that increasing the block average size beyond 8 frequency components would further reduce V_t. However, this is in general impractical as Figure 7.20 illustrates that the use of a block average size beyond 8 frequency components will produce cross-spectra only a few frequency components wide. However, the results of Figure 7.21 are equally applicable to cross-spectral magnitudes produced using a running coherent block average in order to preserve the number of frequency components.

7.4.5 Summary of analysis of unaveraged spectra

The results of this section suggest that the FSA techniques appear to have a number of disadvantages in comparison with the FCA for the analysis of individual time-series records. The spectral parameters are obtained by the application of Gaussian fits to the spectral

magnitudes and linear fits to the cross-spectral phase. The "spiky" nature of the spectral magnitudes necessitates the use of a spike elimination procedure for the application of the Gaussian fits. The random variations in cross-spectral phase necessitates the use of a phase unwrapping procedure for the application of linear fits. In comparison, the corresponding parameters for the FCA are obtained simply by applying a Gaussian fit to the magnitudes of the correlation functions. As a result, there are considerably larger error in the spectral estimates, which results in considerably larger errors in the FSA estimates. The FSA of *Briggs and Vincent* [1992] and *Sheppard and Larsen* [1992] produces parameters which overestimate those obtained using the FCA. This overestimation is a result of the contributions of the tails of the correlation functions to the cross-spectral magnitude. The FSA of *Liu and Pan* [1993] produces results that agree well with the FCA. The LPFSA is not affected by the contributions of the tails of the spectrum because it uses the complex components of the cross-spectrum rather than the magnitude of the cross-spectrum.

The results obtained for the BVFSA and SLFSA appear to contradict the results obtained in *Briggs and Vincent* [1992] and *Sheppard et al.* [1993], respectively. The disagreement with the results of *Briggs and Vincent* [1992] results due to their use of coherent block averaging to smooth the spectra prior to the Gaussian fit. This block averaging results in a decrease in the total cross-spectral magnitude, which results in a decrease in the BVFSA and SLFSA estimates. The results of *Sheppard et al.* [1993] were obtained using averaged spectra. The effects of spectral averaging upon the FSA are considered in 7.5.

7.5 Application of the FSA to averaged spectra

The results obtained in the previous section suggest that the cross-spectra employed for the application of the BVFSA and SLFSA require the removal of the effects of the tails of the cross-correlation functions prior to analysis. The tails can be reduced by using either longer duration time-series records, or by using cross-spectra produced by the coherent average of cross-spectra calculated using individual contiguous time series records. The equivalent process to coherently averaging cross-spectra in the frequency-domain is to coherently average cross-correlation functions in the time-domain. Because the cross-correlation functions tails are essentially random the coherent average reduces the magnitudes of the tails. This effect is illustrated in Figure 4.28 of Chapter 4, which shows the average cross-correlation function magnitude resulting from the coherent averaging of eight individual

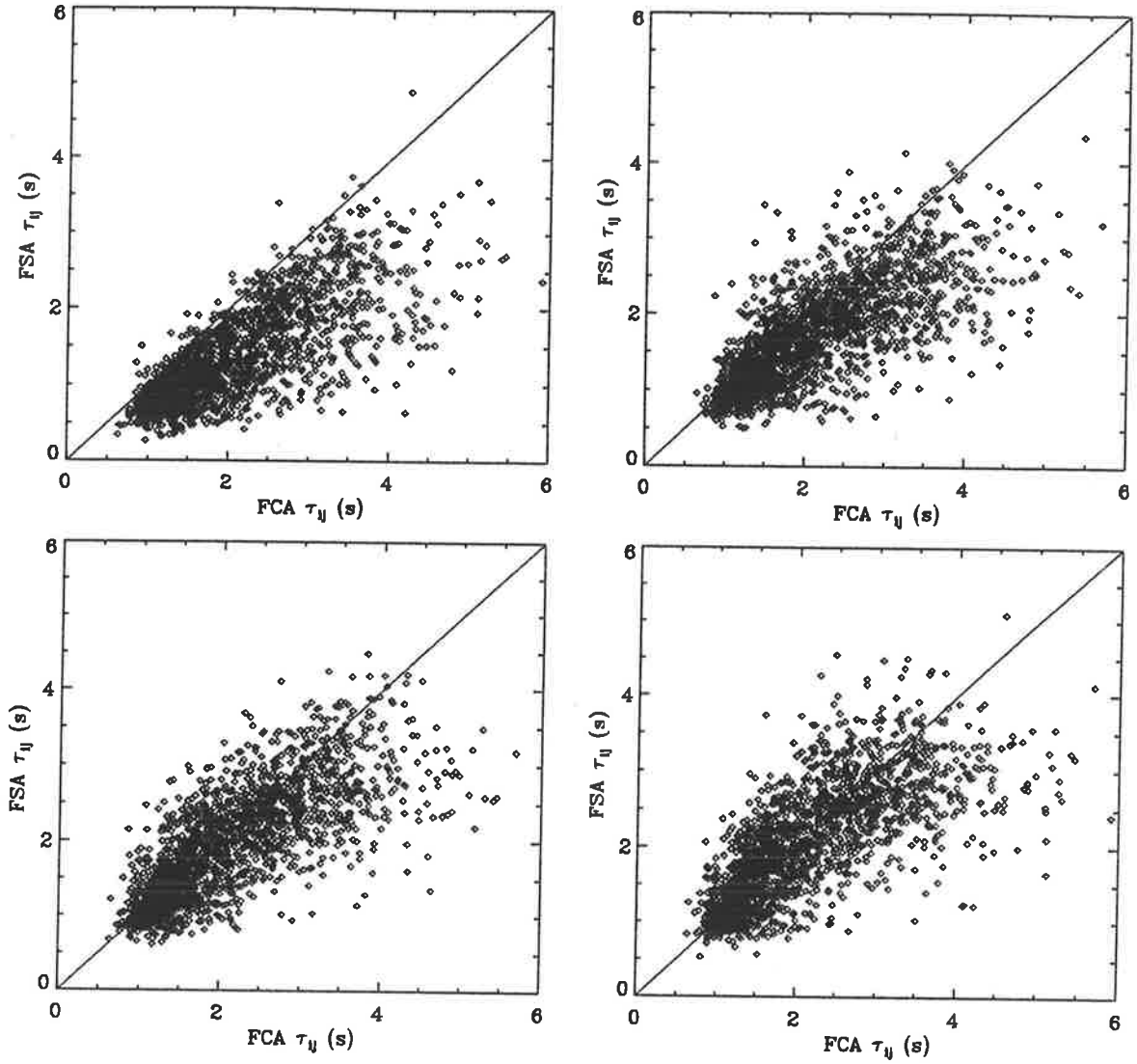

Figure 7.22: Scatter plots of the FCA and BVFSA estimates of τ_{ij} obtained using one (top left), 2 (top right), 4 (bottom right), and 8 (bottom left) spectral averages for the first two hour of the BP MF SA data-set BP940527.

cross-correlation functions calculated from contiguous time-series records. The tails of the averaged cross-correlation function are subdued considerably compared to the tails of the individual cross-correlation functions.

The relationship between the FCA and BVFSA estimates of τ_{ij} obtained by coherently averaging different numbers of cross-spectra calculated from contiguous time series records for the first two hours of the data-set BP940527 are shown in Figure 7.22. The agreement increases with the number of cross-spectra used in the coherent average as the effects of the cross-correlation function tails become more suppressed.

The results of applying the BVFSA and LPFSA to spectra and the FCA to correlation

functions calculated using various different numbers of coherent averages N_{av} using the model-generated data-set MOD-MF-SA with $\nu_{\mathrm{mod}} = 6$ ms^{-1} are shown in Figure 7.23. These results suggest that the estimates approach limiting values as N_{av} is increased. The limiting value of V_l corresponds well with the model input value $V_{\mathrm{mod}} = 50$ ms^{-1}, while the limiting values of ν and θ_s overestimate the model input values by a small amount. The results obtained on applying the SLFSA are not shown as they are very similar to those obtained on applying the BVFSA. The overestimation seen in the application of the BVFSA to individual records decreases significantly with increasing N_{av}. These results are in excellent agreement with those obtained by *Sheppard et al.* [1993] and *Liu and Pan* [1993], who found excellent agreement between the zonal and meridional components of true velocities estimated on applying the FCA and FSA to coherently averaged correlation functions and spectra, respectively.

The standard deviation of the FCA and FSA output parameters are shown in Figure 7.24. The errors in the FSA estimates are only slightly larger than the FCA estimates for larger values of N_{av}, suggesting that the difficulties encountered in the application of the FSA techniques to individual time-series records are reduced significantly. The spikes seen in the spectral magnitudes calculated using individual time-series are effectively smoothed by the use of coherently averaged spectra, thereby reducing the need for the spike elimination procedure. The random variations seen in the cross-spectral phase calculated using individual time-series are also effectively smoothed by coherently averaging. However, phase wrapping effects may still be present, suggesting that the phase unwrapping procedure must still be employed. The increasingly linear phase behavior seen with increasing N_{av} however allows the phase ambiguity threshold to be increased, thereby reducing the computation time associated with the phase unwrapping procedure. The application of the FSA techniques is therefore considerably simpler in the situation where coherently averaged spectra are employed, thus explaining the increased accuracy of the technique with respect to the FCA. The results of Figure 7.24 are consistent with those of *Sheppard et al.* [1993], who found that the standard deviation of the zonal and meridional components of the FSA true velocity were slightly larger than the FCA estimates.

Although the use of coherent averaging reduces the effects of the spectral tails, it has the disadvantage of reducing the time resolution, and thereby reducing the ability to discern any short-term velocity fluctuations such as those resulting from short period gravity waves. An alternative averaging method was investigated whereby the time-series of the individual

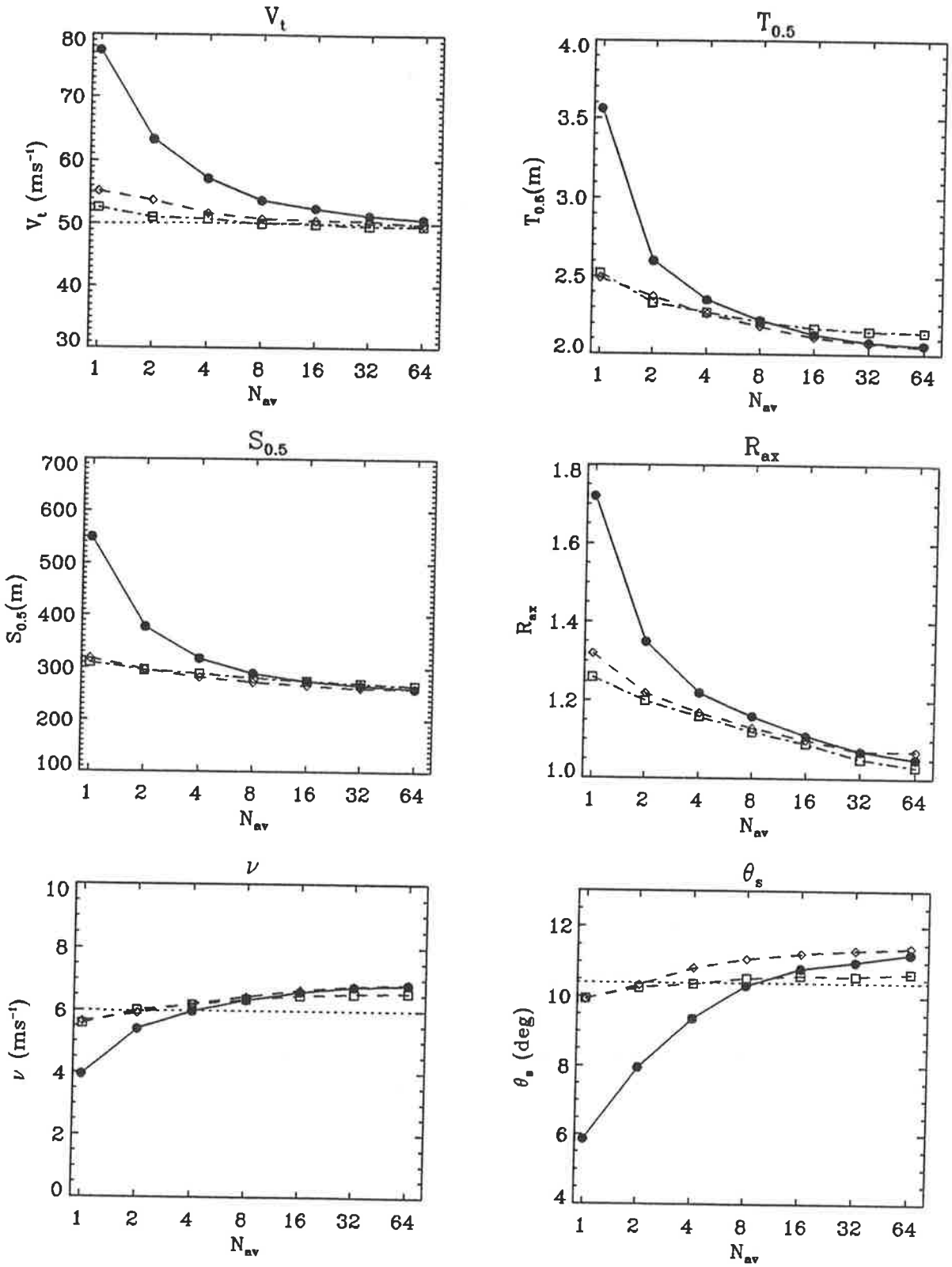

Figure 7.23: Results of the application of the BVFSA (•) and LPFSA (◇) to spectra and the FCA (□) to spectra calculated using various different numbers of coherent averages $N_{\rm av}$ using the model-generated data-set MOD-MF-SA with $\nu_{\rm mod} = 6$ ms^{-1}. The top left plot shows the magnitude of the vector averaged true velocity. The top right plot shows the corrected fading time $T_{0.5}$. The middle plots shows the pattern scale $S_{0.5}$ (left) and axial ratio $R_{\rm ax}$ (right). The bottom plots show the estimates of ν (left) and θ_s (right) obtained from the estimates of $T_{0.5}$ and $S_{0.5}$ respectively.

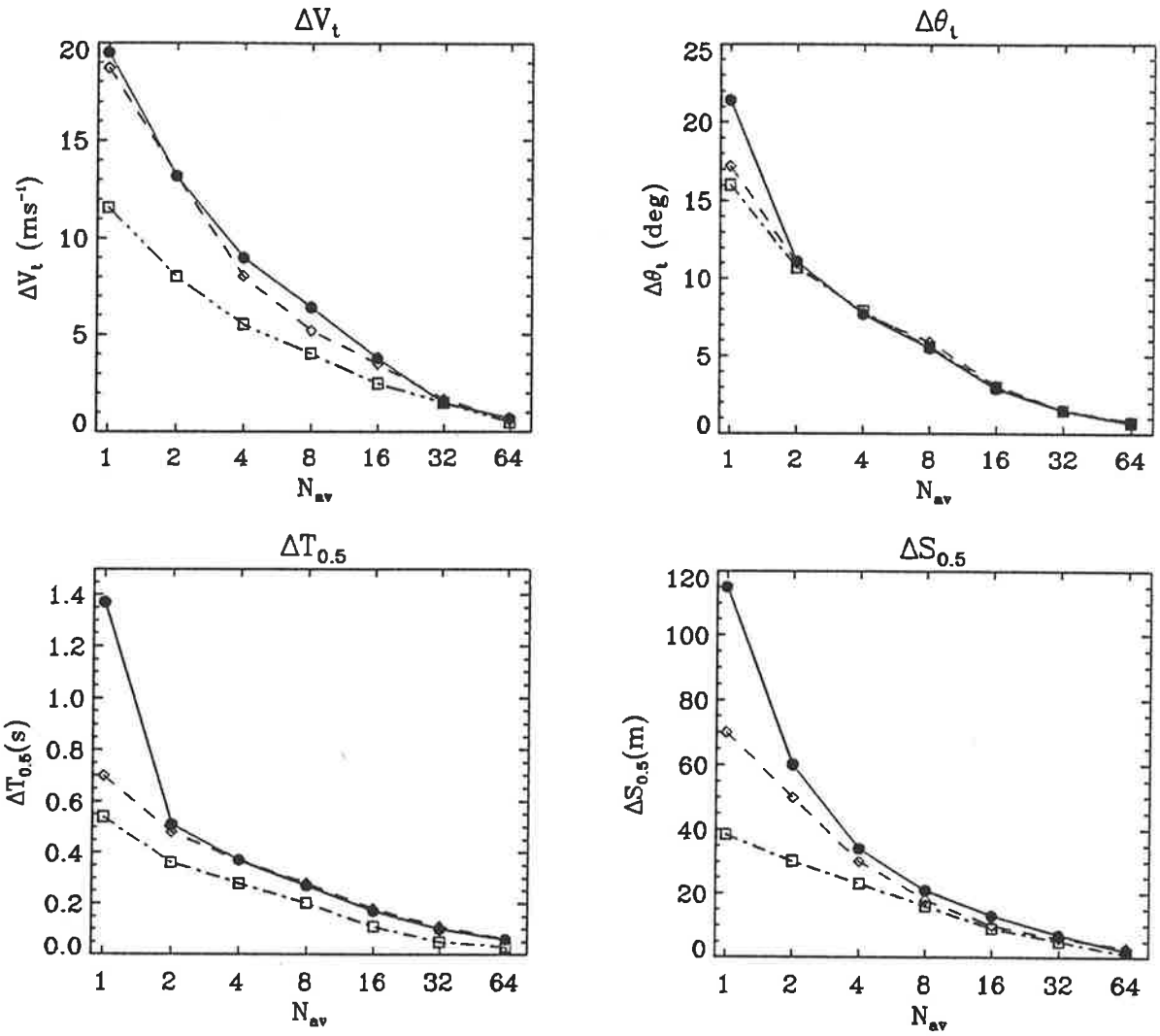

Figure 7.24: Standard deviation of the results of the application of the BVFSA (•) and LPFSA (◇) to spectra and the FCA (□) to correlation functions calculated using various different numbers of coherent averages $N_{\rm av}$ using the model-generated data-set MOD-MF-SA with $\nu_{\rm mod} = 6$ ms^{-1}. The bottom plots show the corrected fading time $T_{0.5}$ (left) and the pattern scale $S_{0.5}$ (right).

records were divided into a number $N_{\rm av}$ of equal length smaller time-series. The spectra calculated from these records were then averaged to produce a coherently averaged spectra for the original time-series. This method was also employed by *Franke et al* [1990] for the calculation of "smoothed" cross-spectra for the application of the NSIRI Doppler-selected imaging interferometry technique. It was found that the spectra obtained for $N_{\rm av} > 2$ contained dominant spikes which were somewhat difficult to fit with a Gaussian even if the spike elimination procedure described in 7.3.1 was employed. The use of larger values of $N_{\rm av}$ also produces the same problems encountered in the use of coherent block averaging

whereby the main peak of the spectrum is only a few frequency components wide. It is clear from the results of Figure 7.23 that the application of the BVFSA to individual time-series records requires $N_{av} > 16$ in order to remove the overestimations. As a result of these effects it is clear that the FSA is not suitable for the analysis of spectra calculated using divided records.

7.6 Summary and conclusions

In this chapter the full spectral analysis (FSA) technique has been investigated. The FSA is the frequency-domain analogue of the FCA, employing the same mathematical formulation based on the use of spectral parameters as opposed to correlation parameters. The spectral parameters are converted into the corresponding correlation parameters employed by the FCA, from which the analysis proceeds in the same manner as for the FCA. There exist three different variations of the FSA. The three techniques employ the same methods for the estimation of correlation parameters τ'_{ij} and $\tau_{0.5}$, but employ different techniques for the estimation of the remaining correlation parameter. The FSA of *Briggs and Vincent* [1992] (BVFSA) is based upon the FCA of *Briggs* [1984], which uses the correlation parameter τ_{ij}. The estimate of τ_{ij} is determined using the magnitude of the cross-spectrum. The FSA of *Liu and Pan* [1993] is also based upon the FCA of *Briggs* [1984]. The estimate of τ_{ij} however is determined using the real and imaginary components of the cross-spectrum. The FSA of *Sheppard and Larsen* [1992] is based upon the FCA of *Meek* [1980], which uses the correlation parameter ρ_{0ij} as the third parameter. The estimate of ρ_{0ij} is determined using the magnitude of the cross-spectrum.

The application of the FSA techniques to experimentally obtained data produces estimates of τ'_{ij} and $\tau_{0.5}$ in good agreement with the estimates produced by the FCA. The procedures employed to determine these estimates however are significantly more complicated than those employed by the FCA. Although the LPFSA estimate of the remaining correlation parameter τ_{ij} exhibits good agreement with the FCA estimate, the BVFSA and SLFSA estimates exhibit poor agreement. This is a result of the inclusion of the effects of tails of the cross-correlation functions in the cross-spectral magnitude. As the FCA is performed solely on the main peak of the correlation functions the tails have little influence on the analysis. The cross-spectra employed by the FCA are related to the cross-correlation

functions by the Fourier transform, and therefore include the effects of the tails of the cross-correlation function. If the FSA is applied using cross-spectra determined by the Fourier transform of the main-peak of the cross-correlation only the BVFSA and SLFSA estimates of τ_{ij} exhibits good agreement with the FCA estimate. The LPFSA estimate of τ_{ij} avoids the effects of the tails of the cross-correlation function because the sum of the real and imaginary components of the cross-spectra resulting from the tails sum to zero. The application of the LPFSA technique to model-generated data produces true velocity estimates in excellent agreement with the model input values for all values of the model turbulent velocity. The application of the BVFSA and SLFSA techniques produce true velocity estimates in excellent agreement with the model input values in the absence of turbulent motions. In the presence of turbulent motions however the estimates increasingly overestimate the model input values with increasing turbulent velocity.

The results obtained on the application of the BVFSA contradict those of *Briggs and Vincent* [1992], who found that the estimates of the BVFSA and FCA true velocity exhibit good agreement. These results were obtained using coherent block-averaging in order to smooth the cross-spectra prior to the application of the Gaussian fits employed to estimate the cross-spectral maxima. The application of coherent block averaging acts to reduce the magnitude of the cross-spectra. This result can be explained by the fact that the addition of a number of vectors with different directions will always produce a vector of magnitude less than the sum of the individual vector magnitudes. Coherent block-averaging therefore acts to reduce the area under the cross-spectra. This results in a decrease in the BVFSA true velocity magnitude, thereby explaining the good agreement between the FCA and BVFSA true velocities seen by *Briggs and Vincent* [1992].

The application of the BVFSA and SLFSA to spectra obtained by coherently averaging the spectra obtained from individual time-series records suggests that the estimates of the third correlation parameter exhibit increasing agreement with the FCA estimates as the number of spectra employed in the average is increased. This effect can be understood by taking into consideration the effects of coherent averaging upon the cross-correlation function. The coherent averaging acts to decrease the magnitude of the tails of the cross-correlation function. The act of coherently averaging the cross-correlation functions in the time-domain is analogous to the act of coherently averaging the cross-spectra in the frequency-domain. The coherently averaged cross-spectra therefore have the effects of tails of the correlation functions removed. The results suggest the BVFSA and SLFSA will accurately estimate the

model input velocity if greater than 16 averages are employed. The LPFSA true velocity provides an excellent estimate of the model input velocity for all numbers of averages.

The results of this chapter therefore suggest that the LPFSA technique is the only suitable technique for the use of individual time-series records. If sufficiently coherently averaged spectra are employed however the BVFSA and SLFSA techniques can be successfully applied. The results suggest however that the errors in the FSA output parameters are considerably larger than those of the corresponding FCA output parameters. The FSA however offers some advantage over the FCA in that contaminating frequency components such as those resulting from sea, meteor, and precipitation echoes are dealt with significantly easier in the frequency-domain.

Chapter 8

Interferometry

8.1 Introduction

The term "interferometry" was originally employed to denote those optical and radio techniques which make use of the interference produced on combining the signals incident on a number of spatially separated receiving sensors, such as Michelson stellar interferometry. In the context of modern radio physics the term is employed to denote those techniques which make use of the phase differences determined between the signals recorded at a number of spatially separated receiving antennae. The determination of these phase differences was enabled by the use of complex time-series data (e.g. *Pfister*, [1971]).

The techniques described by *Woodman* [1971] and *Pfister* [1971] are generally regarded as the pioneering radar interferometry works. Woodman illustrated that cross-correlation phase information could be employed to determine the position and velocity of highly localized scattering regions. The technique was successfully employed to determine the inclination of the geomagnetic field in the ionosphere above the Jicamarca radar observatory. Pfister illustrated that the cross-spectral phase at any particular Doppler frequency could be employed to determine the position of the region responsible for the backscatter of this Doppler frequency, provided that a single region was indeed responsible for the backscatter. Pfister further illustrated how this positional information could be used in conjunction with the Doppler frequency information to provide an estimate of the horizontal wind velocity. The various different interferometry techniques described in this chapter are all descendents of the techniques of *Woodman* [1971] and *Pfister* [1971]. The relationship between these techniques is outlined in the taxonomy shown in Figure 1.7 of Chapter 1. The various different

techniques will be referred to by the names and acronyms outlined in this taxonomy.

The phase shifting imaging radar interferometry (PSIRI) technique of *Farley et al.* [1981] combines aspects of the techniques described by *Woodman* [1971] and *Pfister* [1971]. The cross-spectral phase of Doppler frequencies exhibiting high coherency were employed to determine the individual regions responsible for the backscatter. The horizontal displacement of these regions over a number of contiguous time-series records was then employed to produce an estimate of the horizontal wind velocity. The mean angle of arrival (MAOA) technique developed by *Röttger and Ierkic* [1985] is essentially identical to the technique of *Woodman* [1971]. The technique determines the power weighted average position of the backscatter, referred to as the MAOA. It is sometimes evident that linear trends exist in the MAOAs located over a number of contiguous time-series records, allowing the estimation of the velocity of the regions responsible for the backscatter (e.g. *Röttger and Ierkic*, [1985]; *Vandepeer*, [1993]). The MAOAs can also be employed to determine the wind velocity using the TDI technique (e.g. *Vandepeer and Reid*, [1995b]). The MAOA technique is discussed in 8.2.

The imaging Doppler interferometry (IDI) technique (e.g. *Adams et al.* [1985,1986]; *Brosnahan and Adams*, [1993]) is essentially an extension of the technique described by *Pfister* [1971]. The extension is provided by the use of two orthogonal rows of receiving antenna. Doppler frequencies exhibiting linear phase variation over both rows of antennae are assumed indicative of scatter from an individual scattering region, and subsequently used in the analysis. The velocity of the scattering regions is determined using the positions of apparent backscatter and their associated radial velocity information. The magnitude selected imaging radar interferometry (MSIRI) technique of *Meek and Manson* [1987] employs a similar analysis, based on the use of an alternative single scatterer criterion. Doppler frequencies exhibiting simultaneous local maxima in the each power spectra are assumed indicative of scatter from an individual scattering region, and subsequently used in the analysis. The non-selected imaging interferometry technique of *Franke et al.* [1990] argues the merits of applying no single scatterer criterion on the basis that the velocity estimate exhibits reasonable agreement with the FCA true velocity. These techniques are discussed in detail in 8.3.2.

The phase fitting radar interferometry technique (e.g. *Kudeki*, [1988]; *Van Baelen et al.* [1990]; *Larsen et al.* [1992]) is based upon the determination of the 3-dimensional wind vector and the MAOA, using the parameters estimated on applying linear fits to the cross-spectral phase. The technique employed to estimate the MAOA is essentially the frequency-domain

analogue of the MAOA technique of *Röttger and Ierkic* [1985]. The horizontal velocity is estimated in the same manner as the FSA apparent velocity by using the slopes inferred from the linear fits. As a result, the FSA is sometimes referred to as an interferometry technique, despite it's Fourier equivalence with the FCA technique.

The various interferometric techniques can be separated into "imaging" and "non-imaging" techniques, depending upon whether the locations of apparent backscatter are determined during the analysis. The "imaging" techniques can be further separated into "Doppler selected" and "non-Doppler selected" techniques. The Doppler selected techniques (e.g. PSIRI, IDI, MSIRI and NSIRI) are based on determining the locations of the apparent backscatter for each individual Doppler frequency, while the non-Doppler selected techniques (e.g. MAOA, TDI, PFRI) are based on determining the mean location of the apparent backscatter over all Doppler frequencies. The non-imaging techniques (e.g. FSA) do not employ any imaging.

The work described in this chapter focuses mainly upon the Doppler selected imaging radar interferometry techniques, as described in 8.3.2. The non-Doppler selected techniques are described in 8.2 and 8.2.1, introducing some of the concepts important for the understanding of the Doppler selected techniques. The results of the theoretical analysis of the imaging techniques is presented in 8.3.2. These results are verified by the use of the radar backscatter model described in Chapter 3 in 8.4.

8.2 Mean angle of arrival determination

The concept of the mean angle of arrival (MAOA) was first introduced by *Röttger and Ierkic* [1985]. The MAOA corresponds to the power-weighted mean position of the radiowave backscatter. The interpretation of the MAOA is dependent upon the mechanism assumed responsible for the radiowave backscatter. If the backscatter is assumed to result from tilted refractivity layers (e.g. *Röttger and Ierkic*, [1985]) the MAOA will be given by the angle from where the largest returns will eventuate. This will be given approximately by the direction perpendicular to the tilt. In practice the finite beam-width of the transmitted signal may result in the MAOA underestimating this tilt angle. If the backscatter is assumed to result from a number of randomly-distributed horizontally-oriented scatterers the MAOA will be close to the zenith. It will not in practice be located directly on the zenith due to the random locations and reflectivities of the individual scatterers.

The effect of backscatter from a refractivity layer tilted at an angle θ from the horizontal is illustrated for the two-dimensional case in Figure 8.1 (e.g. *Röttger and Ierkic*, [1985]). The phase difference ϕ_{ij} introduced between two receiving antennae with separation d_{ij} is given by

$$\phi_{ij} = kd_{ij} \sin\theta, \tag{8.1}$$

where $k = 2\pi/\lambda$ is the radar wavenumber, and λ is the radar wavelength. The 3-dimensional extension of this equation can be obtained by defining the azimuth angle α of the tilt, clockwise from North. The phase difference ϕ_{ij} measured between two antennae with separation (ξ_{ij}, η_{ij}) is then given by

$$\phi_{ij} = k(\xi_{ij} l_0 + \eta_{ij} m_0), \tag{8.2}$$

where

$$l_0 = \sin\alpha \sin\theta, \text{ and} \tag{8.3}$$

$$m_0 = \cos\alpha \sin\theta \tag{8.4}$$

are the zonal and meridional direction cosines, respectively. A minimum of three receiving antennae are sufficient to allow a least squares estimate of l_0 and m_0. The phase differences ϕ_{ij} are determined from the phase of the zero-lag cross-correlations, $\psi_{ij}(0)$.

The radial velocity V_{r_0} resulting from scatter centered on the direction (l_0, m_0) is given by

$$V_{r_0} = \vec{V} \cdot \hat{r} = l_0 u + m_0 v + n_0 w, \tag{8.5}$$

where $\vec{V} = (u, v, w)$ is the background wind velocity, and n_0 is the vertical direction cosine, given by

$$n_0 = \cos\theta = (1 - l_0 - m_0)^{\frac{1}{2}}. \tag{8.6}$$

If the MAOA is centered on the zenith, $V_{r_0} = w$. However, if the MAOA is centered off-zenith the horizontal velocity components will contaminate V_{r_0}, and the vertical velocity must be calculated using estimates of the horizontal velocity components, using (e.g. *Röttger and Ierkic*, [1985])

$$w = \frac{V_{r_0} - u l_0 - v m_0}{n_o}. \tag{8.7}$$

The radial velocity is often estimated using the auto-correlation phase-slope about zero-lag (e.g. *Woodman and Guillen*, [1974]).

The formulae (8.2) and (8.7) have been employed by a number of authors to determine the MAOA and the corrected vertical velocity at VHF in the troposphere and stratosphere (e.g.

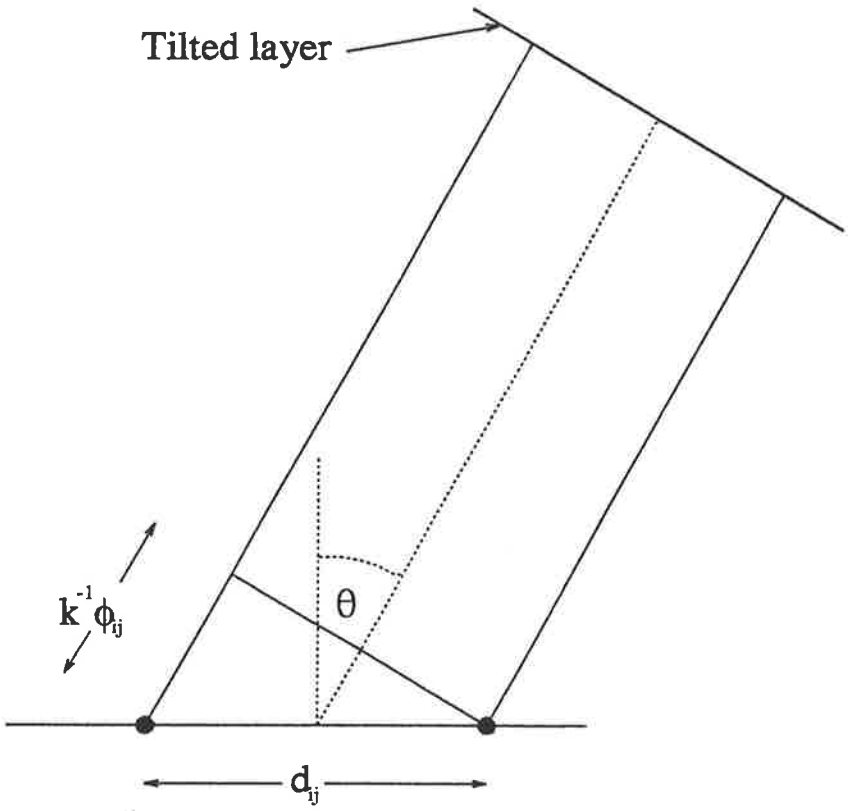

Figure 8.1: Two-dimensional representation of the phase difference ϕ_{ij} introduced between two receiving antenna i and j with separation d_{ij} due to reflection from a refractivity layer tilted at angle θ from the horizontal. The parameter k is the radar wavenumber (adapted from *Röttger and Ierkic*, [1985]).

Larsen and Röttger, [1991]; *Röttger et al.*, [1990]) and mesosphere (e.g. *Röttger and Ierkic*, [1985]) and at MF in the mesopshere (e.g. *Meek and Manson*, [1992]; *Vandepeer*, [1993]). The MAOAs determined by *Larsen and Röttger* [1991] in the troposphere and stratosphere for individual records were generally less than 2°, while the six-hourly averages were generally less than 1°. These MAOAs led to vertical velocity corrections as large as 200%. The corrected vertical velocities were found to be in better agreement with observed atmospheric conditions. The validity of the MAOAs calculated at VHF in the troposphere and lower stratosphere have come under question recently due to recent results suggesting that the vertical velocities obtained without the MAOA correction using colocated VHF and UHF radars produce long-term differences of less than 1 cm^{-1} (e.g. *McAfee et al.* [1994,1995]). This result suggests that the irregularities responsible for the backscatter at VHF and UHF must be tilted in the same sense. The irregularities responsible for the backscatter at UHF however are essentially isotropic, suggesting that the tilts of the irregularities responsible for the backscatter at VHF cannot be significant.

The validity of the MAOAs calculated at MF in the lower mesosphere have been questioned by *Meek et al.* [1989] on the basis of the normalized phase discrepancy (NTD). The "Y" array at Saskatoon comprises of four receiving antenna, three of which (antennae 1, 2 and 3) are arranged in an equilateral triangle with the fourth (antenna 4) placed at the center of the triangle. This configuration allows the MAOA to be determined using the phase differences ϕ_{14}, ϕ_{24} and ϕ_{34} measured between the inner and outer antennae. The NTD is calculated using the formula

$$NTD = \frac{|\sum_{i=1}^{3} \phi_{i4}|}{\sum_{i=1}^{3} |\phi_{i4}|}. \tag{8.8}$$

The concept of the MAOA is based on the idea that the returned signal can be considered to originate from the MAOA. In the far field the returned signal is therefore assumed to be plane wave incident. If this condition is true, NTD = 0. The results of *Meek et al.* [1989] suggest that the phase differences obtained between 64 and 73 km produce distributions of NTD values only marginally different from those obtained using randomly generated phase differences, thereby suggesting that the incident signal cannot necessarily be considered plane wave. The results of *Vandepeer* [1993] illustrate that the estimated MAOA can be significantly influenced at these heights by ground clutter.

The formulae (8.2) and (8.7) can also be used to determine the horizontal velocity components using the Time Domain Interferometry (TDI) technique (e.g. *Vandepeer and Reid*, [1995b]). This technique is essentially identical to the Doppler beam swinging (DBS) technique, with the exception that the effective beam pointing direction (e.g. *Röttger*, [1981]) for each beam direction is determined by the MAOA. The MAOA and the associated estimates of V_{r_0} obtained for each beam direction are then used to provide a least squares estimate of the 3-dimensional wind field using (8.5). The TDI technique has been shown to produce velocity estimates in good agreement with the FCA true velocity in the mesosphere (e.g. *Vandepeer and Reid*, [1995b]). Preliminary investigations to determine the feasibility of estimating the 3-dimensional wind field using an identical concept to TDI for vertical beams only have been made by the Adelaide group (e.g. *Berkefeld*, [1994]). This technique involves applying a least squares fit over the estimates of the MAOA and the associated V_{r_0} obtained from individual contiguous records in order to determine the 3-dimensional wind field.

In order to satisfactorily apply any of the various imaging interferometry techniques it is necessary to eliminate any systematic sources of phase error from the analysis. Phase errors can result in the angles of arrival being biased significantly off-zenith. Phase errors can be attributed to a number of factors such as unequal cable lengths, phase propagation delays

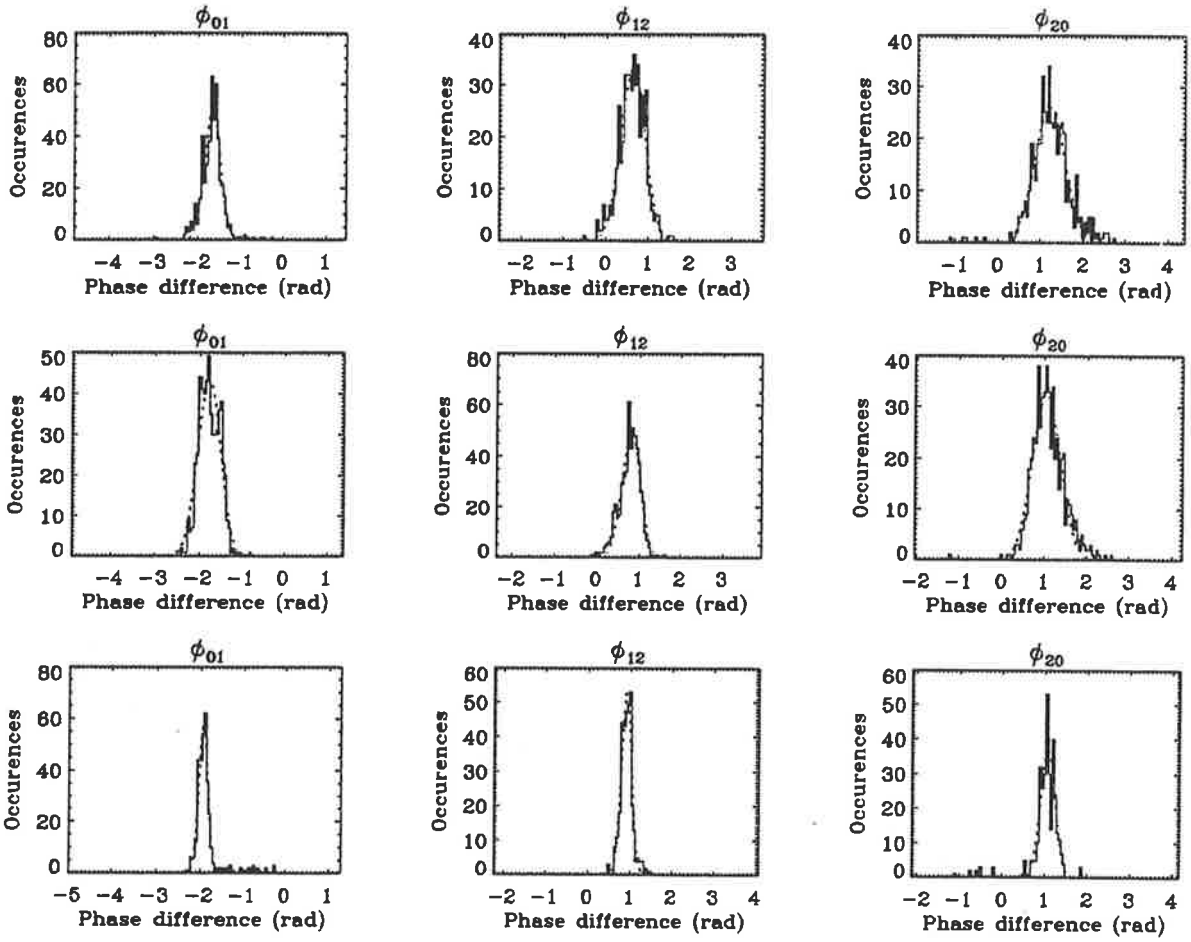

Figure 8.2: Histograms of the receiver phase differences obtained from the height ranges 90-98 km (top row), 80-88 km (middle row), and 70-78 km (bottom row) using the phase of the zero-lag cross-correlation for the first 4 hours of the data-set BP930518. The dotted line indicates the result of a Gaussian fir to each distribution.

through receivers, and variations in antenna impedance reactances, as discussed extensively by *Vandepeer* [1993]. The phase errors result in the addition of a constant offset $\Delta\phi_{ij}$ to the phase offsets ϕ_{ij}. If the average MAOA obtained over a larger number of records is assumed to be on the zenith the values of $\Delta\phi_{ij}$ can be determined from the mean values of the distributions of the antenna phase differences ϕ_{ij}. Histograms of the receiver phase differences obtained from various height ranges using the phase of the zero-lag cross-correlation for the first 4 hours of the data-set BP930518 are shown in Figure 8.2. The estimated offsets obtained from applying Gaussian fits to these histograms are shown in Table 8.1. The results indicate that the estimated offsets vary with the height range. This behavior was also seen in the results of *Meek* [1989].

The MAOAs obtained after the removal of the phase offsets given in Table 8.1 from the zero-lag cross-correlation phases are shown in Figure 8.3.

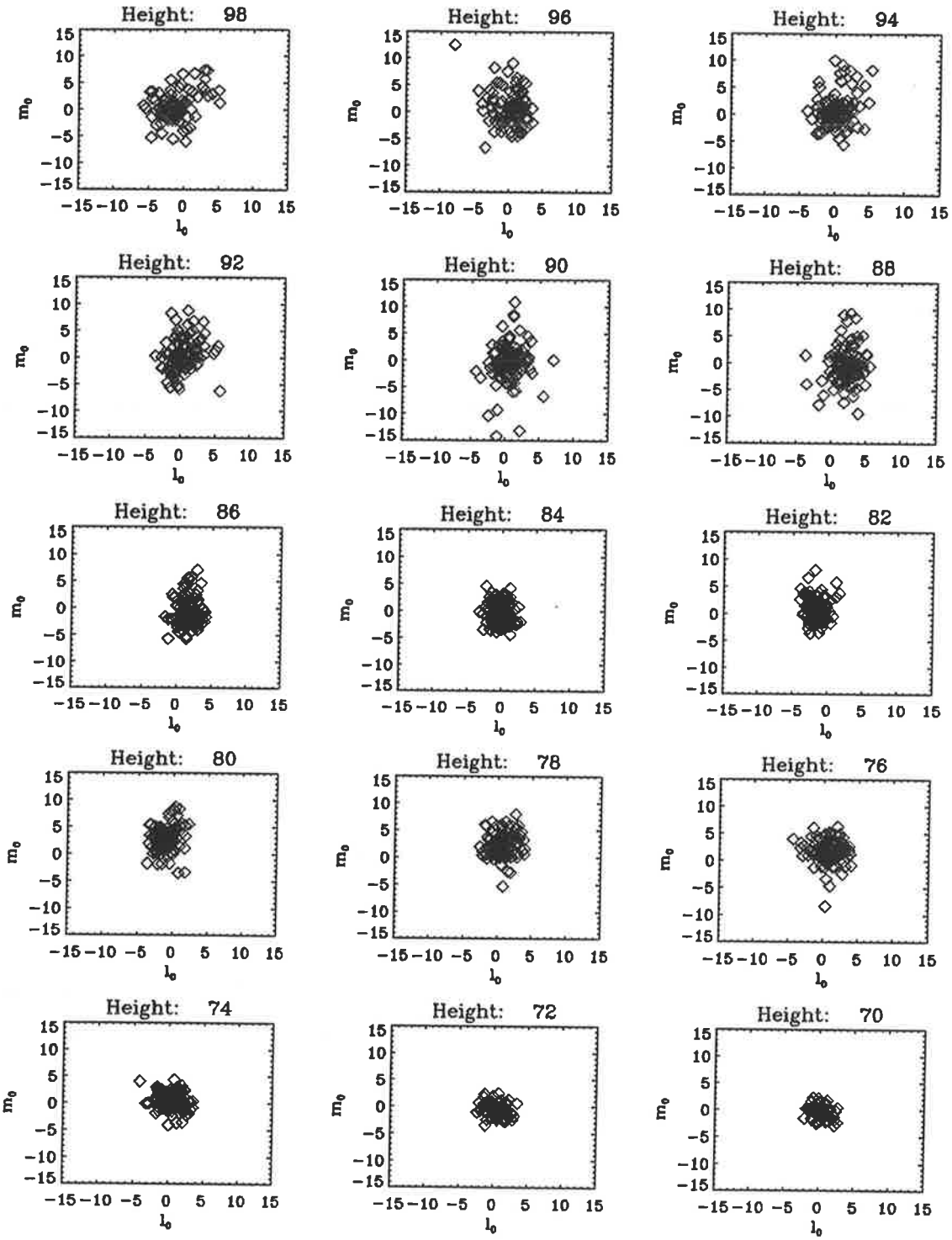

Figure 8.3: MAOAs obtained from the zero-lag cross-correlation phase after removal of the phase offsets as a function of height.

8.2.1 Phase fitting radar interferometry

The theory of the FCA can also be used to derive the MAOA formula of (8.2). The derivation for the two-dimensional case is given in *Briggs and Vincent* [1992]. The extension to three-dimensions is trivial, and follows identical arguments to those used to derive the two-dimensional case. The FCA derived cross-correlation function and the cross-spectrum resulting from off-zenith scatter are shown in Figure 8.4. The cross-correlation phase is given by

$$\psi_{ij}(\tau) = k(\xi_{ij} l_0 + \eta_{ij} m_0) - 2k\tau V_{\tau_0}. \tag{8.9}$$

The zero-lag cross-correlation phase is therefore given by

$$\psi_{ij}(0) = k(\xi_{ij} l_0 + \eta_{ij} m_0), \tag{8.10}$$

which is identical to (8.2). The cross-spectral phase is given by

$$\phi_{ij}(f) = k(\xi_{ij} l_0 + \eta_{ij} m_0) - 2\pi(f - f_0)\tau', \tag{8.11}$$

where τ' is the cross-correlation maxima delay time, and f_0 is the Doppler offset of the spectrum, which is given by

$$f_0 = \frac{-2V_{\tau_0}}{\lambda}. \tag{8.12}$$

The cross-spectral phase at the Doppler offset f_0 is therefore identical to the zero-lag cross-correlation phase.

It is clear from these results that the MAOA determination and vertical velocity correction can be applied entirely in the frequency-domain. This is the basis of the phase fitting interferometry (PFRI) techniques of *Van Baelen et al.* [1990] and *Larsen et al.* [1992]. The PFRI technique of *Van Baelen et al.* [1990] employs a least squares analysis in order to determine the 3-dimensional wind field and an "anisotropy parameter" δ using the parameters obtained by applying linear fits to the cross-spectral phase. The horizontal velocity is

Table 8.1: Receiver phase difference offsets obtained by applying Gaussian to the histograms of the receiver phase differences shown in Figure 8.2.

Height range	ϕ_{01}	ϕ_{12}	ϕ_{20}
90 - 98 km	-1.67	0.63	1.21
80 - 88 km	-1.78	0.81	1.04
70 - 78 km	-1.94	0.91	1.07

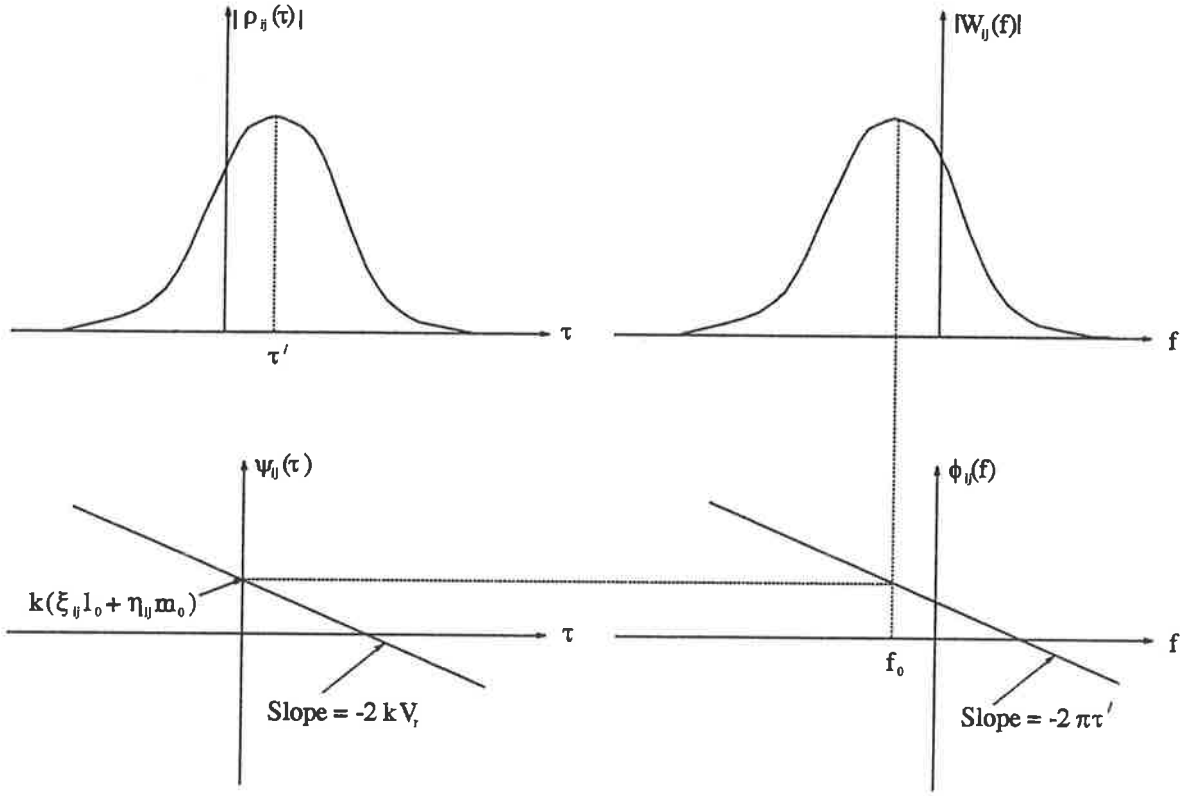

Figure 8.4: Relationship between the cross-correlation function and the cross-spectrum (adapted from *Briggs and Vincent*, [1992]).

determined using the cross-spectral phase slopes m_{ij} in an identical manner to that used to determine the FSA apparent velocity, thereby explaining the excellent agreement exhibited between the PFRI velocity and the FCA apparent velocity (e.g. *Van Baelen et al.*, [1990]). The vertical velocity w and δ are obtained using the phase intercepts b_{ij}. The vertical velocity exhibits excellent agreement with the corrected vertical velocity obtained by substituting the FCA apparent velocity into (8.7) (e.g. *Van Baelen et al.*, [1990]). This is simply a result of the equivalence of the time- and frequency-domain techniques as described by (8.9) and (8.11). The results of Chapters 4 and 7 indicate that the apparent velocity magnitude overestimates the actual wind velocity magnitude in the presence of turbulent random motions. It therefore follows that the vertical velocity estimated using the PFRI techniques of *Van Baelen et al.* [1990] and *Larsen et al.* [1992] will be over-corrected.

The PFRI anisometry parameter δ measures the displacement of the MAOA in the direction perpendicular to the direction of motion. In order to obtain the MAOA the displacement parallel to the direction of motion must also be obtained. This requires the estimation of the V_{r_0}. In the analysis of *Van Baelen et al.* [1990] V_{r_0} is obtained using the phase-slope

of the mean auto-correlation (e.g. *Woodman and Guillen*, [1974]). However, it is clear from Figure 8.4 that V_{r_0} could equally well be obtained from the Doppler frequency offset f_0. This parameter is estimated during the FSA by applying a Gaussian fit to the mean power-spectrum. The phase slopes m_{ij} and offsets b_{ij} are also obtained during the FSA, suggesting that the PFRI technique can be applied as an extension of the FSA. The main advantage of applying the PFRI in this manner is that a more accurate estimate of w can be obtained by substituting the FSA true velocity into (8.7), provided the FSA formulation of *Liu and Pan* [1993] is employed.

The estimated offsets of the antenna phase differences obtained from various height ranges using the phase offset estimated from a linear fit to the cross-spectral phase for the first 4 hours of the data-set BP930518 are shown in Table 8.2. These estimates are in excellent agreement with those obtained from the zero-lag cross-correlation phases, as shown in Table 8.1. Scatter plots of the time- and frequency-domain estimates of the direction cosines are shown in the Figure 8.5. The correlation coefficients for these scatter plots are 0.88 and 0.91, indicating that significant correlation exists.

The results of Figure 8.5 confirm that the MAOA can be calculated in either the time- or frequency-domain. The technique presented here differs from that employed by *Van Baelen et al.* [1990] in that it makes use of the Doppler offset of the spectra, and can thus be applied solely in the frequency-domain. The frequency-domain technique offers similar advantages to the FSA, in that it allows the simple removal of undesirable frequency contamination such as that resulting from sea echoes (e.g. *Briggs and Vincent*, [1992]) and meteor echoes in the mesosphere at MF and precipitation echoes in the troposphere at VHF (e.g. *Chilson et al.*, [1995]). The frequency-domain technique requires the use of a Gaussian fit to the spectral magnitude and linear fits to the cross-spectral phase. On the other hand, the time-domain technique can be applied using solely the zero-lag cross-correlation, and is therefore much

Table 8.2: Receiver phase difference offsets obtained by applying Gaussian to the histograms of the receiver phase differences calculated in the frequency-domain.

Height range	ϕ_{01}	ϕ_{12}	ϕ_{20}
90 - 98 km	-1.70	0.63	1.13
80 - 88 km	-1.76	0.80	1.03
70 - 78 km	-1.93	0.88	1.08

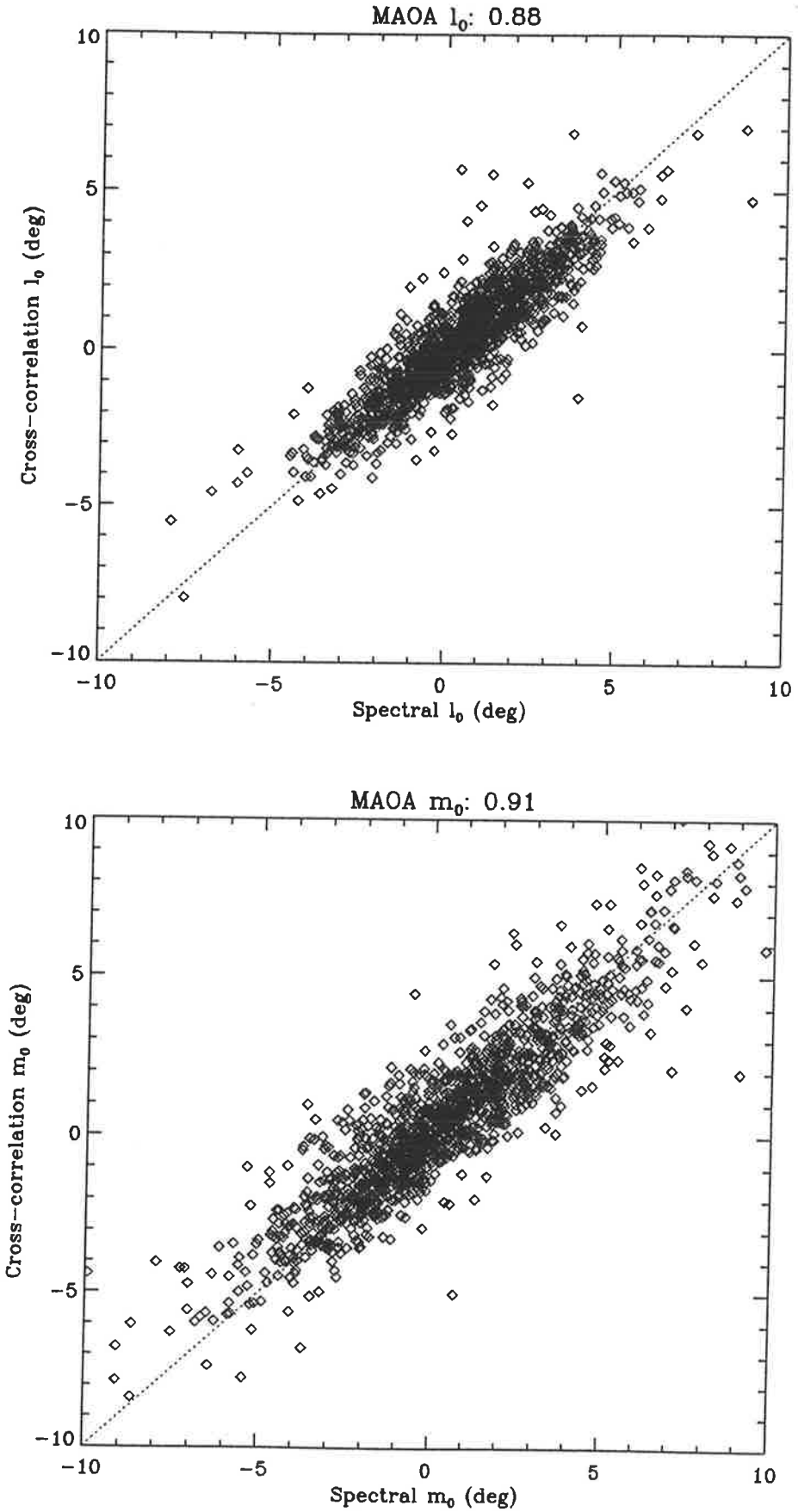

Figure 8.5: Scatter plots of the zonal (l_0 - top) and meridional (m_0 - bottom) direction cosines obtained using the zero-lag cross-correlation phase (vertical axis) and the cross-spectral phase at the Doppler offset (horizontal axis).

easier to implement. The results of Chapter 7 also indicate that there are significantly larger errors in spectral estimates, suggesting that the variance in the frequency-domain estimates of the MAOA will be larger than the time-domain estimates. This effect was evident in the results used to produce Figure 8.5.

8.3 Doppler-selected imaging interferometry

8.3.1 Theory of the Doppler-selected imaging interferometry

The Doppler-selected interferometry techniques make use of a two-step process first proposed by *Pfister* [1971] in order to estimate the background wind velocity. The first step involves the determination of the direction cosines $\hat{r}(f) = (l(f), m(f), n(f))$ of the apparent locations of radiowave backscatter for each Doppler frequency f. The zonal $l(f)$ and meridional $m(f)$ direction cosines are determined using the phase differences $\phi_{ij}(f)$ measured between a minimum of three non-colinear receiving antenna with separation (ξ_{ij}, η_{ij}) using the equation

$$\phi_{ij}(f) = k(\xi_{ij} l(f) + \eta_{ij} m(f)), \tag{8.13}$$

where k is the radar wavenumber. The vertical direction cosine $n(f)$ is determined using

$$n(f) = (1 - l(f) - m(f))^{\frac{1}{2}}. \tag{8.14}$$

The direction cosines are related to the zenith $\theta(f)$ and azimuth $\alpha(f)$ of the scattering locations by

$$l(f) = \sin\alpha(f) \sin\theta(f), \text{ and} \tag{8.15}$$

$$m(f) = \cos\alpha(f) \sin\theta(f). \tag{8.16}$$

The scattering locations are hereafter referred to as the "effective scattering positions" following the terminology of *Briggs* [1995]. The second step involves the determination of the velocity from the effective scattering positions. This can be achieved using a number of different techniques. The "individual record" analysis (e.g. *Adams et al.*, [1985,1986]; *Meek and Manson*, [1987]; *Franke et al.*, [1990]) involves using the radial velocity

$$V_r(f) = \frac{-\lambda f}{2} \tag{8.17}$$

associated with the effective scattering points to produce a least squares estimate of the mean wind field velocity $\vec{V} = (u, v, w)$ for each time-series record using

$$V_r(f) = \vec{V} \cdot \hat{r}(f) = l(f)u + m(f)v + n(f)w, \tag{8.18}$$

The "multiple record" analysis (e.g. *Brosnahan and Adams*, [1993]) involves combining the effective scattering positions and radial velocities from a number of records to produce a single least squares estimate of the mean wind field velocity over the duration of the combined records. The "contiguous records" technique (e.g. *Farley et al.* [1981]) involves determining the shift in the effective scattering positions between contiguous records in order to estimate the mean wind field velocity. The work presented in this Chapter focuses on the use of the individual and multiple record techniques only. As the "phase difference" between two antennae at a particular Doppler frequency is equivalent to the "cross-spectral phase" at that Doppler frequency, these two terms are used interchangeably throughout the remainder of this chapter.

The fundamental assumption of the Doppler-selected interferometric analyses is that the information associated with each Doppler frequency is the result of scatter from single discrete scattering point. If two or more scattering locations contribute to the same Doppler frequency the resultant "aliased" effective scattering position will not necessarily coincide with either of the actual scattering positions (e.g. *Adams et al.*, [1985]). *Meek and Manson* [1987] have suggested that the effective scattering positions resulting from aliasing do not necessarily propagate with the same speed as the individual scattering positions responsible for the aliasing. The inclusion of aliased effective scattering positions in the analysis may therefore result in velocity biases. It is also important that the effective scattering positions are unambiguously resolved. With certain combinations of antenna spacings and radar wavelengths however it is possible that this is not always the case. For instance, a spacing of $D = \lambda$ results in the zenith angles of all effective scattering positions lying within 30° of the zenith, despite the fact that some of the actual scattering locations may lie outside this zenith angle. This effect is hereafter referred to as "spatial aliasing" (e.g. *Franke et al.*, [1990]), and can be eliminated by using antenna spacings less than $D = \frac{1}{2}\lambda$ (e.g. *Adams et al.*, [1985]). It is impossible to determine whether an effective scattering positions has been spatially aliased (e.g. *Vandepeer*, [1993]). It is therefore often considered necessary to preclude effective scatterering positions with zenith angles exceeding a calculated spatial aliasing threshold from the analysis, even though not all of these scatterers are necessarily spatially aliased.

The basic difference between the various Doppler-selected interferometric techniques lies in the selection criteria used to determine whether the spectral information for each Doppler frequency satisfies the conditions for scatter from a single discrete scattering location. The

IDI technique (e.g. *Adams et al.*, [1985,1986]; *Brosnahan and Adams*, [1993]) uses two orthogonal rows of receiving antennae. Doppler frequencies exhibiting sufficiently linear phase variation along both rows of antennae are assumed indicative of plane-wave incidence, and therefore scatter from a single discrete location. These Doppler frequencies are subsequently used in the analysis. The phase differences between antennae used in (8.2) are determined from a linear fit to the power spectral phases each arm. The IDI technique has been shown to produce velocity estimates in good agreement with the FCA apparent velocity (e.g. *Vandepeer and Reid* [1995a]; *Turek et al.*, [1995]). The MSIRI technique (e.g. *Meek and Manson*, [1987]) uses a minimum of three receiving antennae. Doppler frequencies exhibiting local maxima in the power-spectra calculated for all receiving antennae are assumed indicative of scatter from a single discrete location, and subsequently used in the analysis. The use of a fourth receiving antennae allows the calculation of the normalized phase discrepancy (NPD) as further indication of scatter from a single discrete location. The MSIRI technique produces velocity estimates in excellent agreement with the FCA apparent velocity (e.g. *Meek and Manson*, [1987]; *Brown et al.*, [1995]). The results obtained by *Meek and Manson* [1987] are illustrated in Figure 8.6. The NSIRI technique used (e.g. *Franke et al.*, [1990]) uses three receiving antennae. The technique does not employ any single-scatterer criterion. The application of the NSIRI to unsmoothed (or unaveraged) data, hereafter referred to as the UNSIRI, produces velocity estimates in agreement with the FCA true velocity (e.g. *Franke et al.*, [1990]; *Sürücü et al.*, [1992]). The application of the NSIRI to smoothed (or averaged) data, hereafter referred to as the SNSIRI, produces velocity estimates in agreement with the FCA apparent velocity (e.g. *Franke et al.*, [1990]). The results obtained by *Franke et al.* [1990] are shown in Figure 8.7.

8.3.2 Theoretical analysis of Doppler-selected imaging interferometry

There has been little attempt to analytically analyze the performance of the Doppler-selected imaging interferometric techniques. This is a partially a result of the difficulty in analytically modeling unsmoothed cross-spectra (e.g. *Franke et al.*, [1990]). The analytical model analysis of *Liu et al.* [1990] indicates that (8.2) is applicable in the absence of turbulent random motions if the cross-spectral phase associated with each Doppler frequency is a result of scatter from an individual highly localized region within the radar volume. The analysis suggests that the FCA true velocity will not correctly estimate the actual wind velocity

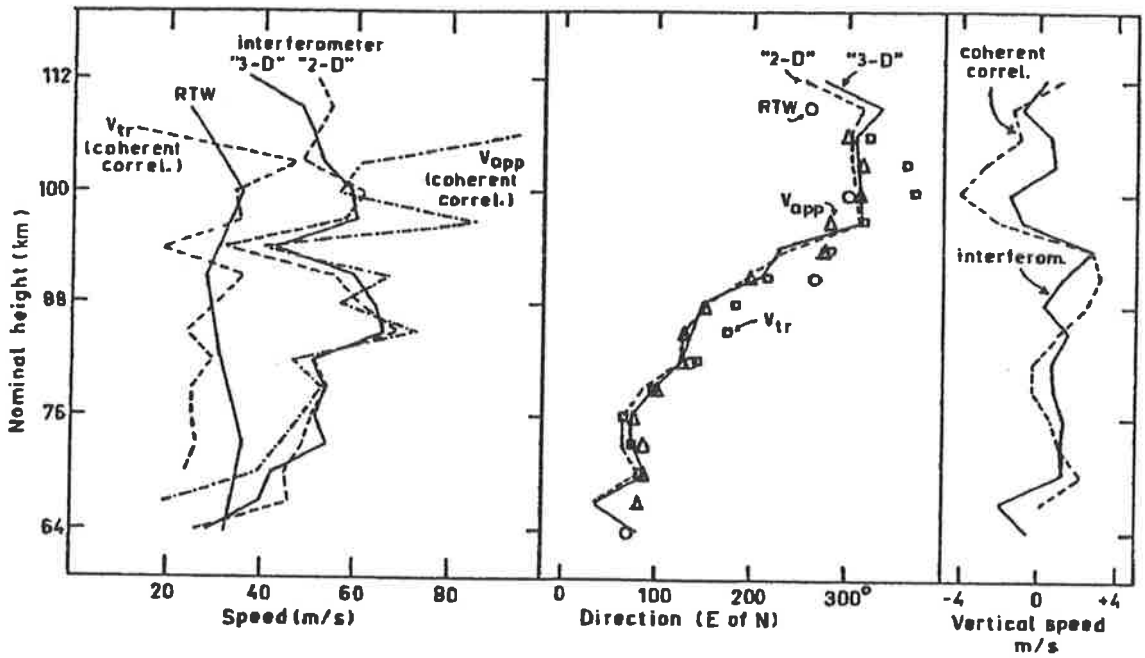

Figure 8.6: Results obtained on the application of the MSIRI and FCA analyses to data recorded using the Saskatoon $1-\lambda$ array. The labels $V_{\rm tr}$ and $V_{\rm ap}$ denote the FCA true and apparent velocity magnitudes, respectively. The terms "2D" and "3D" denote the velocity magnitudes obtained on applying the MSIRI using 2- and 3-dimensional analyses, respectively. The label RTW denotes the FCA true velocity magnitude obtained using single-bit time-series records produced by the non-coherent RTW system (after *Meek and Manson*, [1987]).

in this situation. It is not apparent that (8.2) will hold in the presence of turbulent random motions. Furthermore, the model analysis suggests that the Doppler-selected imaging interferometry techniques will not produce the correct velocity estimate if the background velocity is sufficient to smear the information from individual scatterers over a number of frequency bins. In this situation the model analysis predicts that the FCA true velocity will produce the correct velocity estimate.

A number of interesting results become apparent in considering the performance of the Doppler-selected imaging interferometry techniques in the volume-scatter situation. A number of these results have been described by *Briggs* [1995] and *Vandepeer and Reid* [1995a] for the situation where the MAOA is on the zenith and the vertical velocity is zero. The extension of these results to the situation where the MAOA is off-zenith and the vertical velocity is non-zero is trivial, and can be derived using the cross-spectral phase defined by (8.11). The cross-spectral phases derived by *Briggs* [1995] include a sign error due to the incorrect application of the shift theorem of the Fourier transform (e.g. *Bracewell*, [1965]).

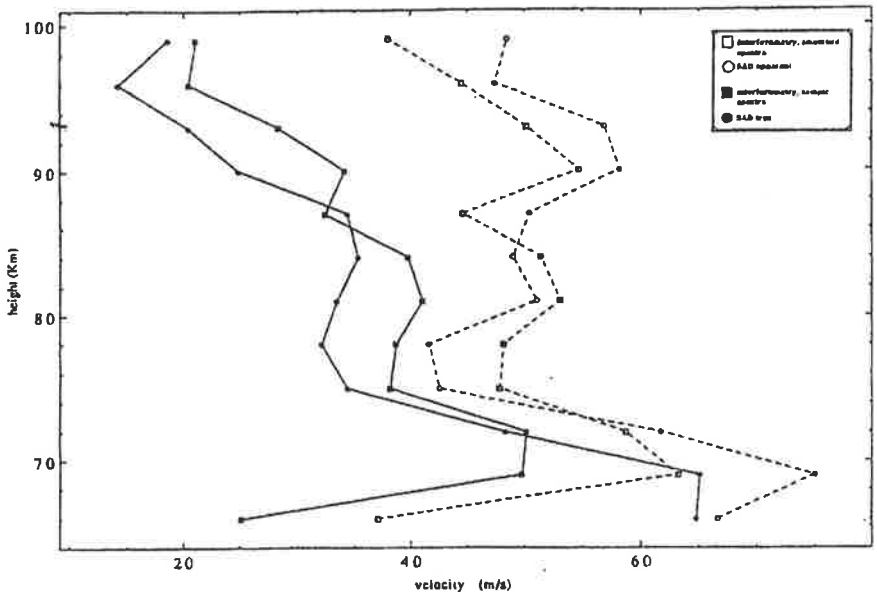

Figure 8.7: Results obtained on the application of the NSIRI and FCA analyses of *Franke et al.* [1990]. The symbols represent the FCA true (•) and apparent (○) velocity magnitudes, and the unsmoothed (UNSIRI - filled □) and smoothed (SNSIRI - □) NSIRI velocity magnitudes (after *Franke et al.*, [1990]).

This sign error also follows through into the results of *Vandepeer and Reid* [1995a]. The sign error does not affect any of the conclusions drawn by *Briggs* [1995] and *Vandepeer and Reid* [1995a], as can be deduced from the discussion presented below where the sign error is not present.

In the volume-scatter situation the cross-spectral phase is given by (8.11). For two antennae with zonal separation ξ_{ij} the cross-spectral phase becomes

$$\phi_\xi(f) = k\xi_{ij}l_0 - 2k\tau'_x V_{r_0} - 2\pi f\tau'_x, \tag{8.19}$$

where k is the radar wavenumber, l_0 is the zonal direction-cosine of the MAOA, and V_{r_0} is the radial velocity in the direction of the MAOA, as given by (8.5). The parameter τ'_x can be expressed (see Chapter 4)

$$\tau'_x = \frac{\xi_{ij}(aV_x + hV_y)}{aV_x^2 + bV_y^2 + 2hV_xV_y + k}, \tag{8.20}$$

where V_x and V_y are the zonal and meridional components of the ground diffraction pattern velocity. The "ellipsoid parameters" a, b, and h are determined by the contours of equal spatial correlation of the ground diffraction pattern

$$a\xi^2 + b\eta^2 + 2h\xi\eta = \text{const}, \tag{8.21}$$

and k is determined by the magnitude of the turbulent random motions, as described in detail in Chapter 4. The ellipse obtained for $const = 0.5$ is referred to as the "characteristic ellipse" (e.g. *Briggs*, [1984]), and can be related to the anisometry of the regions responsible for the radar backscatter (e.g. *Briggs*, [1992]). The cross-spectral phase for two antennae with meridional separation η_{ij} is given by

$$\phi_\eta(f) = k\eta_{ij}m_0 - 2k\tau'_y V_{r_0} - 2\pi f\tau'_y, \tag{8.22}$$

where m_0 is the meridional direction-cosine of the MAOA, and

$$\tau'_y = \frac{\eta_{ij}(bV_y + hV_x)}{aV_x^2 + bV_y^2 + 2hV_xV_y + k}. \tag{8.23}$$

Equations (8.19) and (8.22) suggest that the cross-spectral phases resulting from volume-scatter are linear functions of antenna separation. This is exactly the behavior assumed by the IDI to be indicative of plane wave incidence due to scatter from a single discrete location. This results however suggests that linear phase behavior does not necessarily imply discrete scatter.

The direction-cosines corresponding to the cross-spectral phases given by (8.19) and (8.22) can be determined from (8.13), yielding

$$l(f) = l_0 - \frac{\tau'_x(2V_{r_0} - \lambda f)}{\xi_{ij}} \tag{8.24}$$

and

$$m(f) = m_0 - \frac{\tau'_y(2V_{r_0} - \lambda f)}{\eta_{ij}}. \tag{8.25}$$

These equations suggest that the effective scattering positions lie along a line passing through the MAOA (l_0, m_0), as shown in Figure 8.8. If the range of MAOAs are distributed evenly about the zenith the effective scattering positions located over a number of individual records will form a "band" of points centered on the zenith.

The azimuth angle α of the line of effective scattering positions with respect to the MAOA is given by (e.g. *Briggs*, [1995])

$$\alpha = \arctan\left(\frac{l(f) - l_0}{m(f) - m_0}\right) \tag{8.26}$$

$$= \arctan\left(\frac{aV_x + hV_y}{bV_y + hV_x}\right). \tag{8.27}$$

If the scatterers are isometric the characteristic ellipse given by (8.21) will also be isometric (i.e. $a = b$, $h = 0$). In this case α will be in the direction of the background wind,

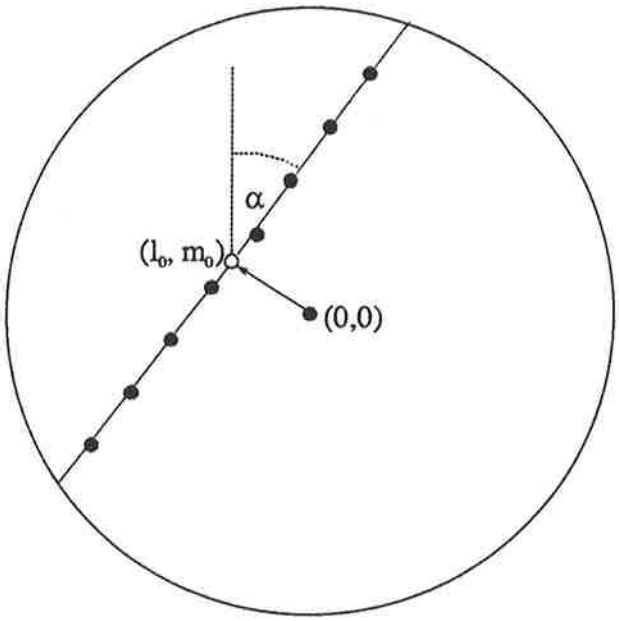

Figure 8.8: Example of the effective scattering positions (•) located by the imaging interferometry techniques in the volume-scatter situation using the cross-spectral phases at each Doppler frequency. The zenith is indicated by the position (0,0), while the MAOA is indicated by the open circle at the position (l_0, m_0).

as illustrated in Figure 8.9. This result is consistent with the suggestion of *Adams et al.* [1985] that aliasing will result in the effective scattering points being clustered about a line passing through the zenith in the direction of motion, as volume scatter can be considered to produce an extreme form of aliasing whereby the entire region contributing signal returns to a particular Doppler frequency is aliased to a single effective scattering position. If the scatterers are anisometric the characteristic ellipse will also be anisometric (i.e. $a \neq b$), with elongation perpendicular to the elongation of the scatterers (see Chapter 4). In this case α will be biased away from the direction of the background wind towards the direction perpendicular to the elongation of the characteristic ellipse, unless the direction of the background wind is either perpendicular or parallel to the direction of elongation of the scatterers. These results are summarized in Figure 8.9.

The zenith angle $\theta(f)$ of the effective scattering points at each Doppler frequency is given by

$$\sin^2 \theta(f) = l(f)^2 + m(f)^2. \tag{8.28}$$

In the situation where the MAOA is centered on the zenith ($l_0 = m_0 = 0$) and the vertical velocity is zero $w = 0$ it follows that $V_{r_0} = 0$. In this situation (8.28) can be written (e.g.

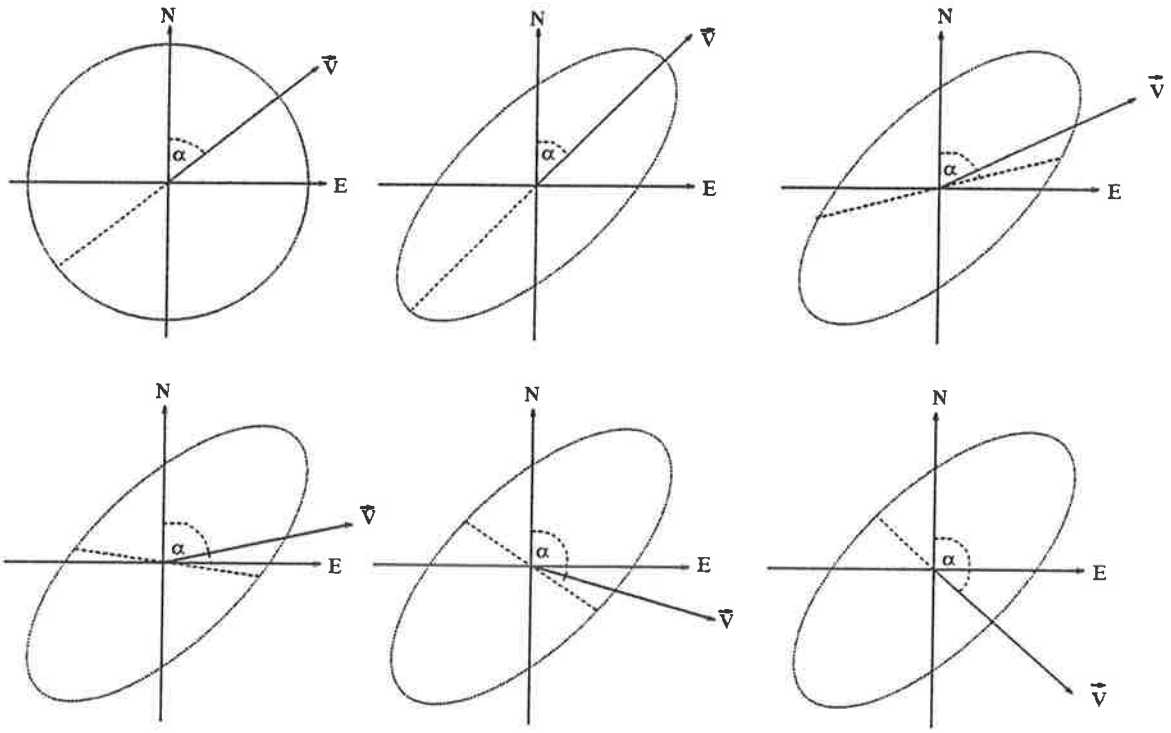

Figure 8.9: Relationship between the characteristic ellipse (dotted line) and the line of effective scattering positions (dashed lines) obtained for isometric scatter (top left), and anisometric scatter as a function of the direction of the actual wind velocity $\vec{V}$ (top middle to bottom right). The azimuth of the line of effective scattering positions is denoted by α. In the isometric scatter situation α is aligned in the direction of $\vec{V}$, while in the anisometric scatter situation α is biased towards the direction perpendicular to the elongation of the characteristic ellipse.

Briggs, [1995])

$$\sin^2\theta(f) = \frac{\lambda^2[(aV_x + hV_y)^2 + (bV_y + hV_x)^2]f^2}{(aV_x^2 + bV_y^2 + 2hV_xV_y + k)^2}. \tag{8.29}$$

The effective scattering positions will therefore approach the zenith as the effects of random changes, measured by the parameter k, increase. The magnitude of the horizontal velocity $V_h(f)$ inferred from an effective scattering position with zenith angle $\theta(f)$ and radial velocity $V_r(f)$ can be obtained by rearranging (8.18), yielding the equation (e.g. *Vandepeer and Reid*, [1995a])

$$V_h(f) = \frac{V_r(f)}{\sin\theta(f)}, \tag{8.30}$$

where θ is the zenith angle of the scatterer. This result suggests that the magnitude of the horizontal wind velocity must increase with increasing random motions. Substituting (8.17) and (8.29) into (8.30) yields

$$V_h(f) = \frac{aV_x^2 + bV_y^2 + 2hV_xV_y + k}{2\sqrt{(aV_x + hV_y)^2 + (bV_y + hV_x)^2}}, \tag{8.31}$$

which is identical to the magnitude of the FCA apparent velocity given by (4.33) from Chapter 4. This result suggests that the interferometric techniques do not implicitly employ a correction for the effects of random changes in the volume scatter situation akin to that employed to produce the FCA true velocity. In the situation where the MAOA is off-zenith and the vertical velocity is non-zero it is not possible to obtain a simple expression such as (8.31) for the interferometric velocity magnitude. However, it is not unreasonable to assume that the average interferometric velocity magnitude will be approximately equivalent to the FCA apparent velocity magnitude if the average MAOA is centered close to the zenith and the average vertical velocity is approximately zero.

The volume scatter situation also provides a number of additional results that are not reported by either *Briggs* [1995] or *Vandepeer and Reid* [1995a]. The direction of the FCA apparent velocity θ_a can be specified in terms of the parameters a, b, h, and k by substituting (4.25) and (4.26) into (4.24). This yields the result $\theta_a = \alpha$. This result suggests that the preferred azimuth of the effective scattering points will lie in the direction of the FCA apparent velocity in the volume scatter situation. The direction of the interferometric velocity is shown in Appendix G to be identical to the direction of the actual wind velocity if the MAOA is centered on the zenith and the vertical velocity is zero. Thus although the the magnitude of the interferometric velocity is affected by random changes and pattern anisometry the direction of the interferometric velocity is not. These result also suggests that the preferred azimuth will not necessarily be aligned in the direction of the interferometric velocity.

The volume scatter predictions are based on the use of idealized cross-correlation functions and cross-spectra such as those shown in Figure 8.4. These results are therefore somewhat difficult to relate to the "noisy" cross-spectral phase variations obtained in practice for unaveraged spectra. Despite this difficulty a number of experimental studies have produced results consistent with the volume scatter predictions. The IDI analysis of *Vandepeer and Reid* [1995a] produced velocities in good agreement with the apparent velocity magnitude, and distributions of effective scattering positions elongated in the direction predicted by (8.26), as illustrated in Figure 8.10. The technique employed by *Vandepeer and Reid* [1995a] to determine the preferred azimuths is outlined in 8.4, where it is applied to distributions of effective scattering positions obtained using model-generated data. The IDI analysis of *Turek et al.* [1995] and the MSIRI analyses of *Meek and Manson* [1987] and *Brown et al.* [1995] also produced velocities in good agreement with the apparent velocity. The analysis of *Brown*

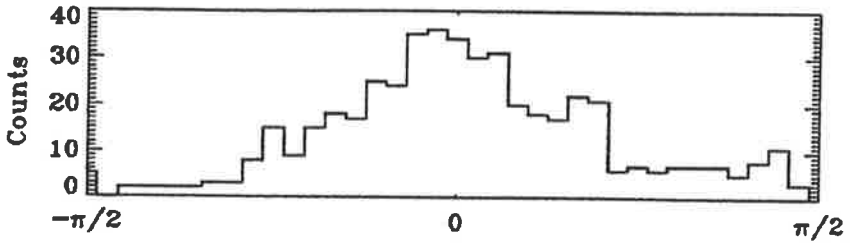

Figure 8.10: Preferred azimuth of effective scattering positions obtained in the IDI-like analysis of *Vandepeer and Reid* [1995a], relative to the azimuth predicted by 8.26 (after *Vandepeer and Reid*, [1995a]).

et al. [1995] also indicates that the agreement between the magnitudes of FCA apparent and MSIRI velocities is significantly greater than the agreement between the magnitudes of the FCA true and MSIRI velocities for large FCA estimated values of the turbulent random motions magnitude. In such instances the magnitude of the apparent velocity is usually significantly greater than the magnitude of the true velocity because the apparent velocity is not corrected for the effects of the random motions. Furthermore, the analysis of *Brown et al.* [1995] also indicates that the agreement between the apparent and interferometric velocities decreases as the anisometry of the ground diffraction pattern increases. On the other hand, the agreement between the true and interferometric velocities is almost independent of the anisometry of the ground diffraction pattern. This result suggests that the interferometric velocity estimates are not influenced by pattern anisometry.

8.4 Model analysis of Doppler-selected imaging interferometry

The Doppler-selected imaging interferometric techniques are particularly suited to numerical model analyses as the actual scattering positions are known, thereby allowing an assessment of the accuracy of the estimated wind velocity *and* the effective scattering positions. Despite this interesting situation only two numerical model analyses of the imaging interferometric techniques have been reported in the literature to date. The analysis of *Adams et al* [1985] focused upon the performance of the IDI technique using a limited number of model scatterers, and is therefore applicable to the discrete scatter situation. They found that the IDI technique was able to successfully estimate both the scattering positions and model velocity, as illustrated in Figure 8.11. The analysis of *Holdsworth and Reid* [1995b] focuses upon

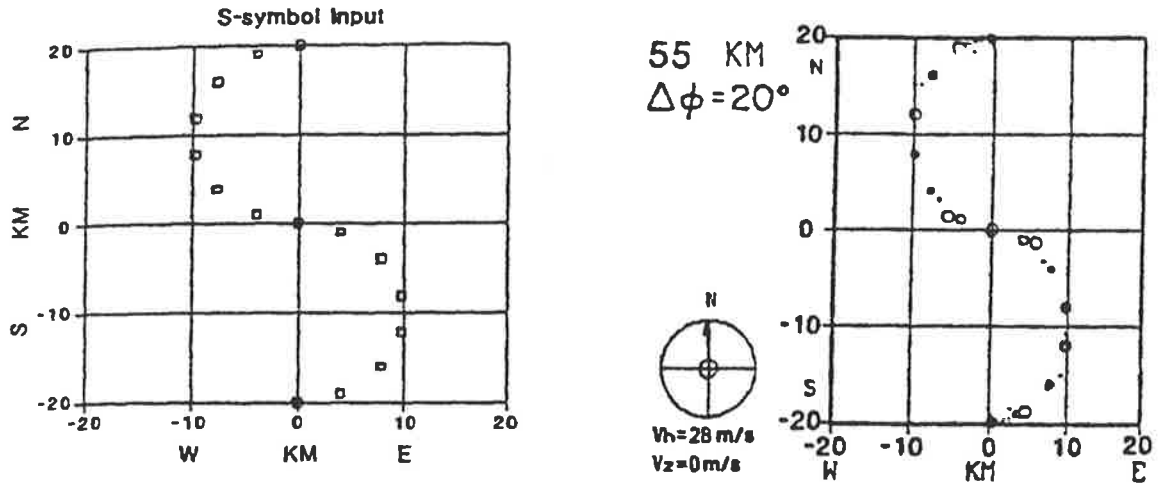

Figure 8.11: Actual (left) and estimated scattering positions located by the IDI technique (right) in the numerical model analysis of *Adams et al.* [1985]. The velocity estimate is of 28 ms^{-1} in the meridional direction is in good agreement with the model input value of 30 ms^{-1} (after *Adams et al.*, [1985]).

the performance of a number of imaging interferometric techniques in the volume scatter situation. The results presented in this section are an extension of those results.

The radar backscatter model described in Chapter 3 has been used to simulate the general configuration of an MF SA radar suitable for the application of the FCA and the three interferometric techniques under examination, namely the IDI, MSIRI and NSIRI techniques. Unless otherwise specified, the standard MF SA parameters described in Chapter 3 have been employed for this analysis. The transmitter beam-width of 15° results in a radar volume zenith cut-off of 22°. The antenna configuration employed for this analysis is illustrated in Figure A.1. The antenna spacing of $d = \frac{1}{2}\lambda$ eliminates spatial aliasing. The MSIRI, NSIRI and FCA techniques are applied using antennae 1, 2 and 6. The IDI technique is applied using antennae 1-5 as the zonal arm of the interferometer, and antennae 1 and 6-9 as the meridional arm. The actual phase differences between antenna pairs 1,2, and 1,6, are used in place of the phase differences estimated by the linear fit as employed by *Adams et al.* [1985,1986]. The technique is therefore hereafter referred to as the "IDI-like" technique. The actual phase differences are used so that the technique employs the same phase information as the MSIRI and NSIRI techniques, thereby allowing a direct comparison of the effects of the individual acceptance criterion employed. The average velocity estimates obtained on applying the IDI-like technique were found to be almost identical to those obtained using the IDI technique.

The radar backscatter model was employed to generate a number of different data-sets,

as described in Appendix A. The data-set MOD-MF-IDI was generated to examine the effects of turbulent random motions upon the interferometric analyses. The model turbulent random motions parameter ν_{mod} was varied between 0 and 6 ms^{-1} in intervals of 1 ms^{-1}, with 200 records generated at each value of ν_{mod}. The data-set MOD-MF-IDI-NSCAT was generated to examine the effects of the number of model scatterers N_{scat} upon the interferometric analyses. Values of N_{scat} ranging from 10 to 1000 have been employed, thereby covering the range from discrete scatter to (effectively) volume scatter. The data was generated using $\nu_{\mathrm{mod}} = 0$ and $6\mathrm{ms}^{-1}$. The data-set MOD-MF-IDI-ROTN was generated to examine the direction of the velocities estimated by the interferometric analyses. The direction of the model velocity θ_t was varied between $\pm 45°$ in intervals of 5°, with 20 records generated for each value of θ_t. The data-set MOD-MF-IDI-ROTN2 was generated to examine the effects of scatterer anisometry on the interferometric analyses. The model parameters employed were identical to those used to generate MOD-MF-IDI-ROTN, with the exception that scatterer anisometry was introduced using an anisometry parameter of $A = 2$, with a scatterer elongation of $-45°$.

The interferometry algorithms applied in this Chapter are similar to those employed in the analyses of *Adams et al.* [1985], *Meek and Manson* [1987], and *Franke et al.* [1990]. Two common acceptance criteria are employed for each technique.

The first of these criteria is that Doppler frequencies with spectral power less than 5 dB above the noise floor are precluded from the analysis. This criterion is employed to preclude Doppler frequencies within the spectral tails from the analysis on the basis that they contribute no useful information. The same criterion is employed by *Meek and Manson* [1987] and *Franke et al.* [1990] using thresholds of 5 dB and 15 dB, respectively, but is not employed in the IDI analyses of *Adams et al.* [1985,1986] and *Brosnahan and Adams* [1993].

The second common criterion is that effective scattering positions located outside the 22° zenith bound of the radar volume are precluded from the analysis on the basis that they must be spurious positions. This criterion is analogous to the upper limit zenith angle threshold employed in the IDI analysis of *Brosnahan and Adams* [1993] to exclude zenith angles outside the first minima in the transmitter polar diagram. A lower limit threshold was employed by *Meek and Manson* [1987] in order to minimize ambiguities associated with the correction for the phase differences between receivers (see for e.g. section 8.2). This is not necessary for the current analysis as there are no receiver phase differences in the model-generated data. An upper limit zenith angle thresholds was employed by *Adams et*

al. [1985,1986], *Meek and Manson* [1987] and *Franke et al.* [1990] in order to reduce the effects of spatial-aliasing. This is not necessary for the current analysis as the antenna spacing of $\frac{1}{2}\lambda$ eliminates spatial-aliasing.

The additional criteria employed are those specific to each particular technique. The IDI-like technique uses Doppler frequencies where the *rms* error of the linear fit to the phase variation along each antenna arm is less than 10°. The phase unwrapping algorithm described by *Adams et al.* [1985] is employed in this process. Examples of the phase fit over the meridional arm of the interferometer are shown in Figure 8.12. The MSIRI technique uses Doppler frequencies exhibiting local maxima in all three of the power-spectra employed for the analysis. The NSIRI techniques use no additional criteria. Spectral smoothing for the SNSIRI technique is performed in the manner described by *Franke et al.* [1990], whereby individual time series are divided into four segments and the cross-spectra obtained from each segment are averaged to produce an averaged, or smoothed, cross-spectrum. Since the model uses only one range gate, no range correction is used. Because the model does not incorporate velocity gradients this should not affect the analysis. Unless otherwise specified, all interferometric parameters are obtained from the average of the application of the individual record technique over 200 time-series records as described in section 8.3.1, and no Doppler frequency weighting is employed. The use of the multiple record analysis is described in 8.4.6. The effects of weighting are discussed by *Meek and Manson* [1987] and *Brosnahan and Adams* [1993].

The analysis presented in this section is an extension of that presented by *Holdsworth and Reid* [1995b] (see Appendix J), which will hereafter be referred to as the "initial analysis". The only major difference in the current analysis lies in the use of windowing functions in order to minimize effects associated with the use of finite length time-series. Windowing functions were not used in the initial analysis on the basis that the FSA results described in Chapter 7 were not influenced by the use of windowing. The major effect of windowing upon the spectra is to reduce the power of the Doppler frequencies in the transition between the main peak and the tails. The use of the power threshold therefore reduces the range of Doppler frequencies employed for the analysis, reducing the possibility of "noisy" Doppler frequencies being included in the analysis. The use of windowing significantly reduces the variance of the interferometric velocity estimates. Although the use of windowing does not alter any of the major conclusions made by *Holdsworth and Reid* [1995b], it can on occasions produce interferometric velocity estimates noticeably different from those obtained without

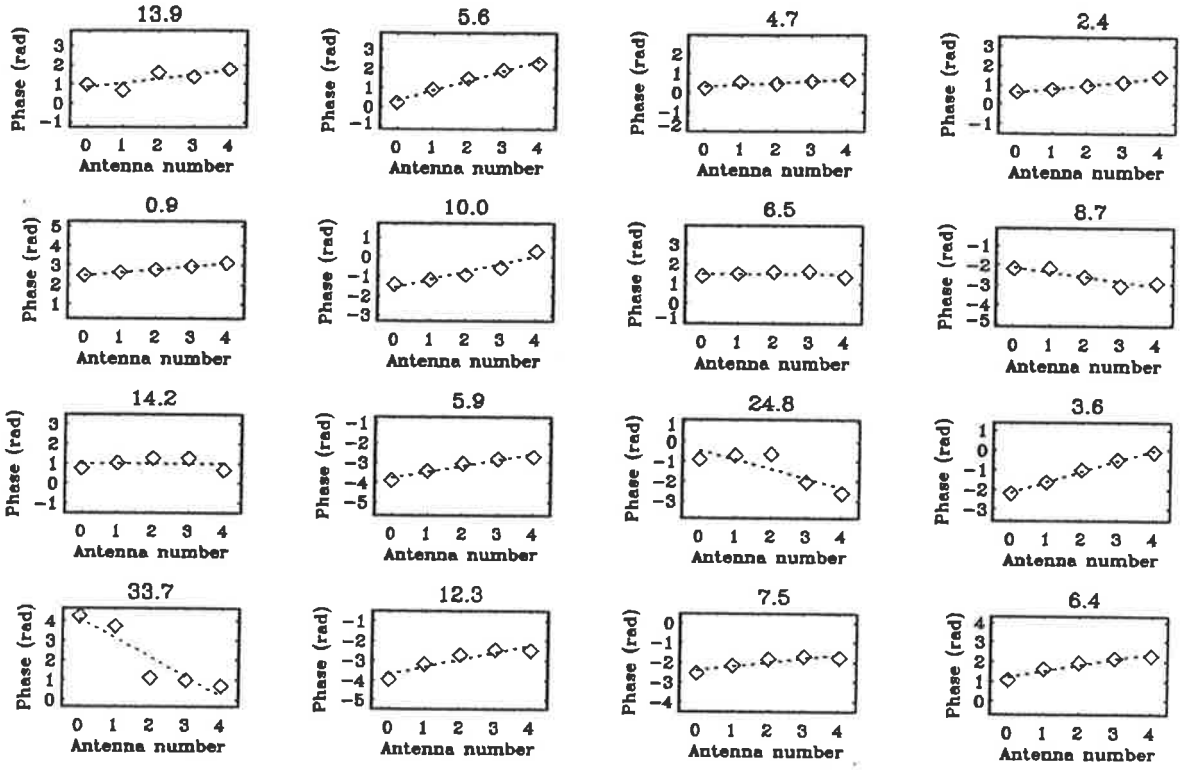

Figure 8.12: Example of the linear fits (dotted lines) to the phase values ($\diamond$) along the meridional arm of the interferometer for the first record of the model generated data-set MOD-MF-IDI with $\nu_{\text{mod}} = 0$ ms^{-1}. The number at the top of each plot denotes the RMS error of the fit. The range of the phase axis for each plot is constant, although the actual phase values may vary.

the use of windowing. The 22° zenith angle threshold was not employed in the initial analysis. The inclusion of this threshold does not significantly affect the analysis.

8.4.1 Effective scattering point determination

Typical examples of the log power spectra obtained and the horizontal effective scattering positions located using individual two minute record on employing the interferometric analyses are shown in Figures 8.13 to 8.16. The four plots correspond to N_{scat} values of 10, 20, 50 and 100, where N_{scat} denotes the number of scatterers within the enclosing volume. On average, approximately 25% of the scatterers within the enclosing volume will also occupy the radar volume, thereby producing signal returns. The unbroken lines indicate the actual locations occupied by the scatterers during the two minute record, while the dotted circle indicates the horizontal bound of the radar volume. Because the IDI-like and MSIRI techniques employ the same phase differences as the UNSIRI technique the effective scattering positions located for the IDI-like and MSIRI techniques must coincide with UNSIRI positions.

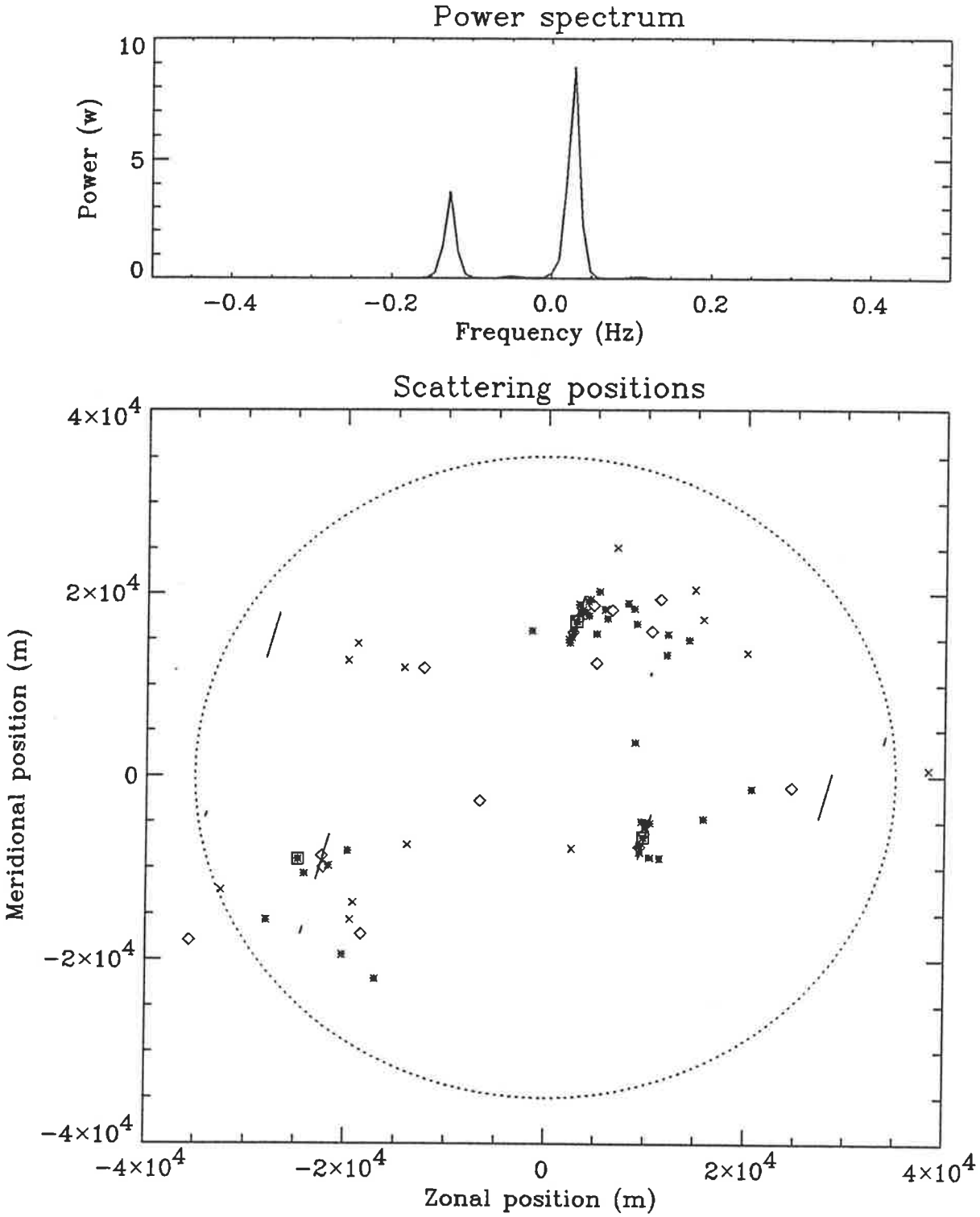

Figure 8.13: Power spectrum (top) and horizontal positions of the effective scattering positions located for the UNSIRI (×), SNSIRI (◇), IDI-like (+), and MSIRI (□) analyses (bottom) using $N_{\text{scat}} = 10$. The asterisks (∗) are formed by the overlap of the + and × symbols, thereby denoting effective scattering positions located for both the UNSIRI and IDI-like analyses. The dotted circle indicates the horizontal bounds of the radar volume, while the solid lines indicate the positions occupied by the model scatterers over the duration of the record.

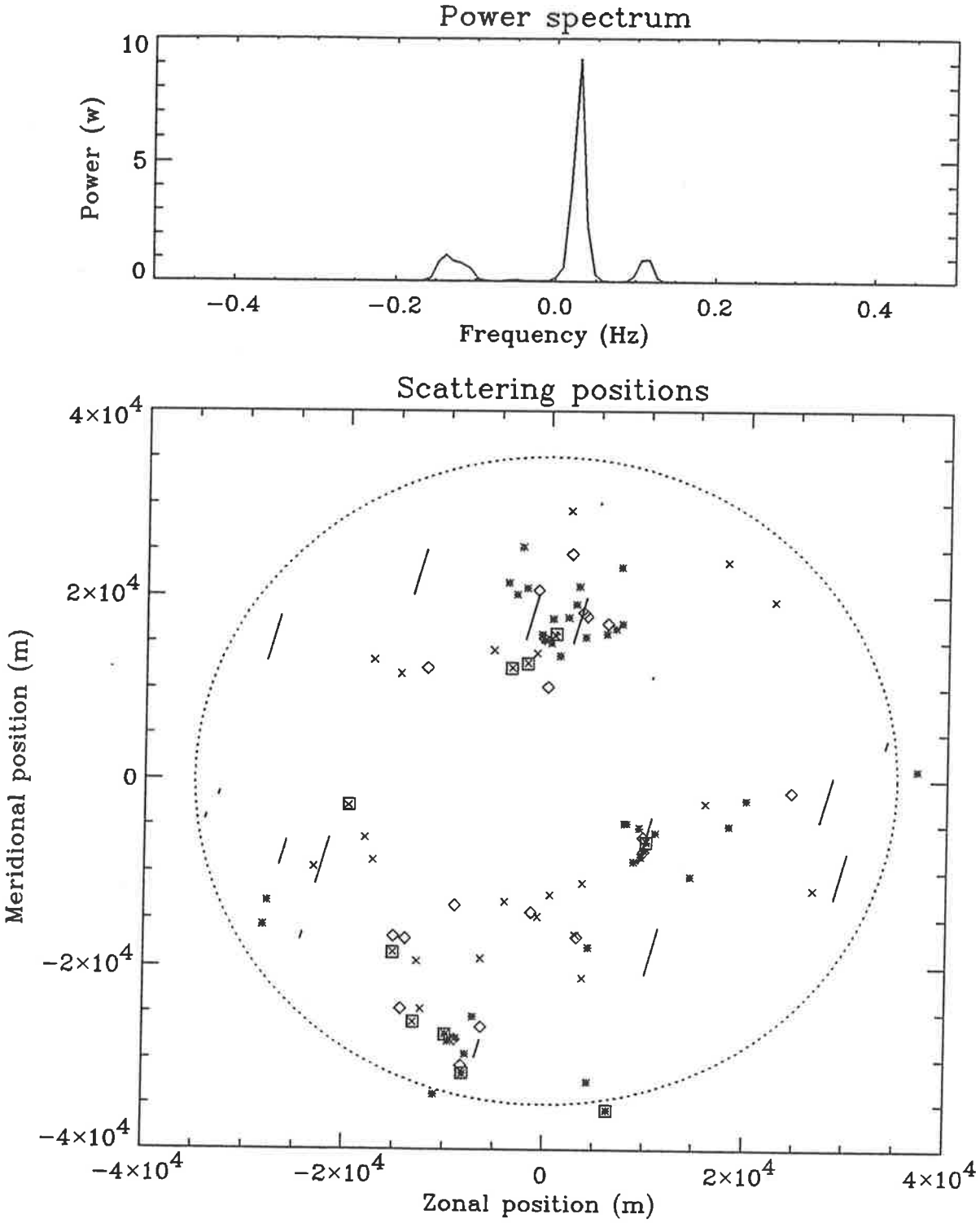

Figure 8.14: Power spectrum (top) and horizontal positions of the effective scattering positions located for the UNSIRI ($\times$), SNSIRI ($\diamond$), IDI-like ($+$), and MSIRI ($\square$) analyses (bottom) using $N_{\text{scat}} = 20$. The asterisks ($*$) are formed by the overlap of the $+$ and $\times$ symbols, thereby denoting effective scattering positions located for both the UNSIRI and IDI-like analyses. The dotted circle indicates the horizontal bounds of the radar volume, while the solid lines indicate the positions occupied by the model scatterers over the duration of the record.

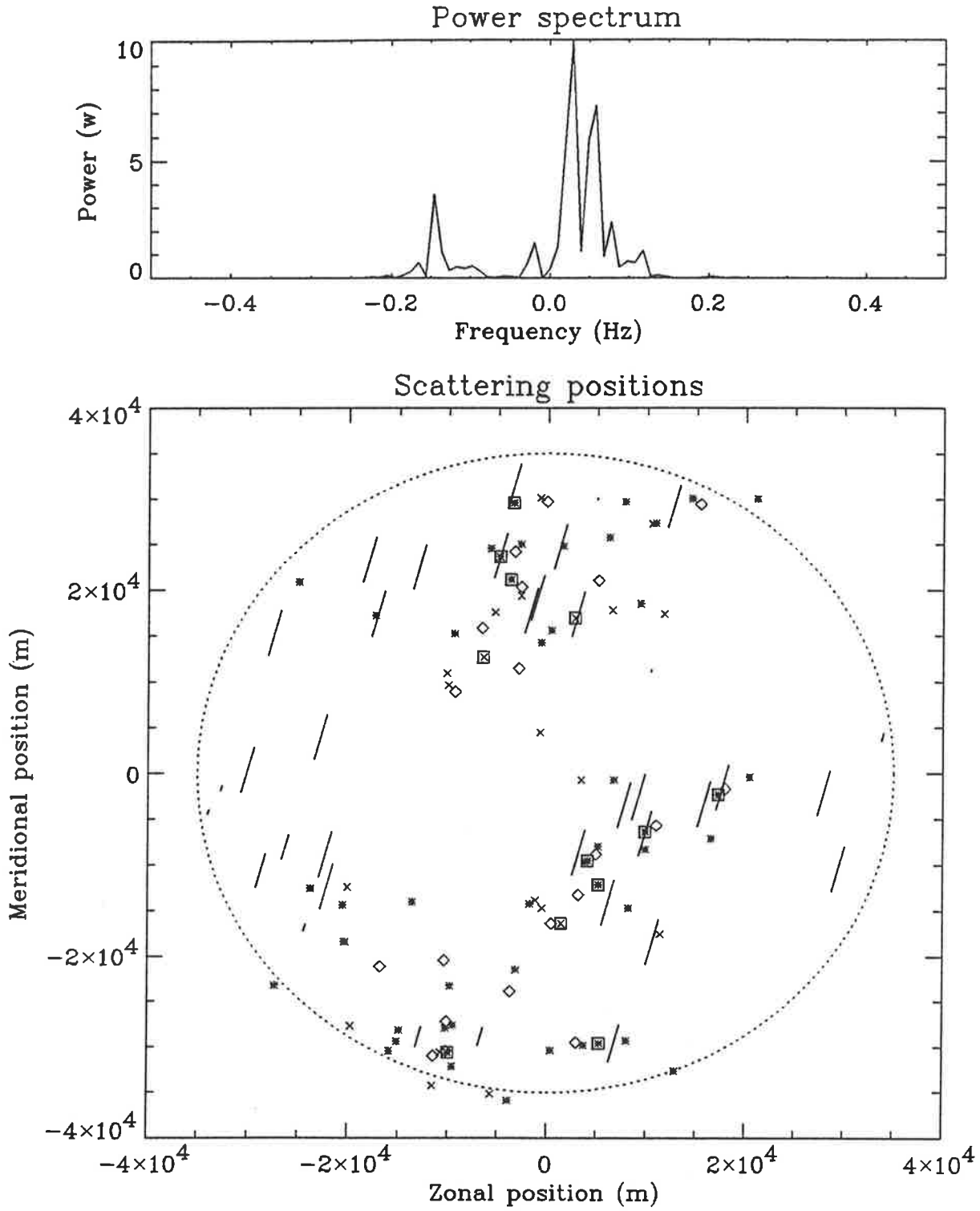

Figure 8.15: Power spectrum (top) and horizontal positions of the effective scattering positions located for the UNSIRI (×), SNSIRI (◇), IDI-like (+), and MSIRI (□) analyses (bottom) using $N_{\text{scat}} = 50$. The asterisks (∗) are formed by the overlap of the + and × symbols, thereby denoting effective scattering positions located for both the UNSIRI and IDI-like analyses. The dotted circle indicates the horizontal bounds of the radar volume, while the solid lines indicate the positions occupied by the model scatterers over the duration of the record.

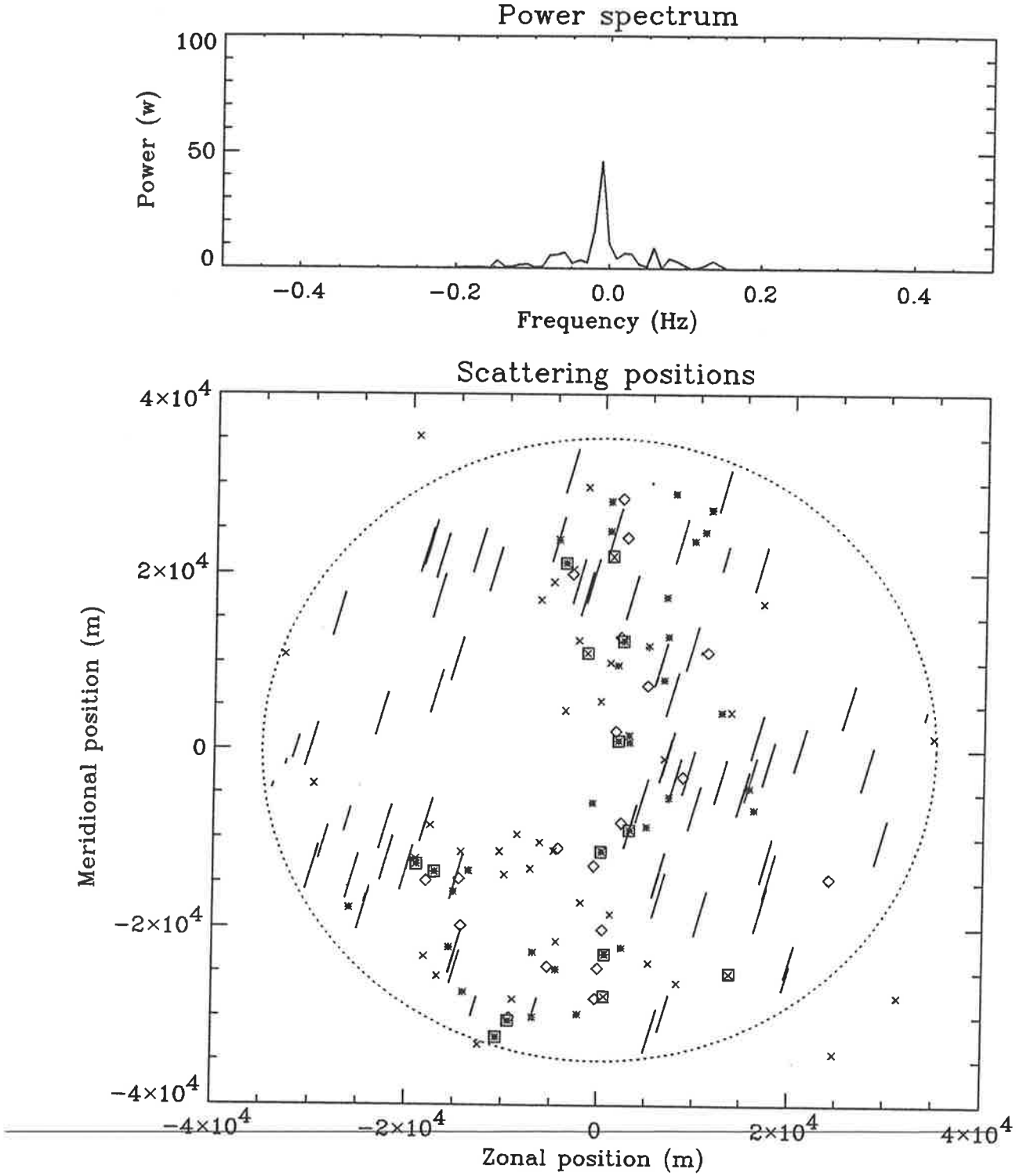

Figure 8.16: Power spectrum (top) and horizontal positions of the effective scattering positions located for the UNSIRI ($\times$), SNSIRI ($\diamond$), IDI-like ($+$), and MSIRI ($\square$) analyses (bottom) using $N_{\text{scat}} = 100$. The asterisks ($*$) are formed by the overlap of the $+$ and $\times$ symbols, thereby denoting effective scattering positions located for both the UNSIRI and IDI-like analyses. The dotted circle indicates the horizontal bounds of the radar volume, while the solid lines indicate the positions occupied by the model scatterers over the duration of the record.

The results of Figures 8.13 and 8.14 suggest that there is a reasonable overlap between the actual and effective scattering positions located by the IDI-like and MSIRI analyses for small values of N_{scat}. The MSIRI effective scattering positions located for $N_{\text{scat}} = 10$ show excellent agreement with the actual positions. The overlap however decreases rapidly as N_{scat} increases. These results may appear to contradict the results of *Adams et al.* [1985], who were able to recover their 15 scattering positions arranged in an "S" shape and their model velocity reasonably convincingly. Unlike the current analysis however, they did not include effects such as turbulence, aspect sensitivity, range gate weighting and random scatterer positioning, and used both a smaller model velocity and a smaller time series length, thereby resulting in less single-scatterer Doppler frequency spreading. As a result, their conditions are somewhat more favorable than those of the current analysis, which attempt to reproduce the volume scatter conditions that are generally encountered experimentally.

The rapid decrease in the overlap between the actual and effective scattering positions exhibited with increasing N_{scat} in Figures 8.13 to 8.16 is understandable given the increase in the ratio of N_{scat} to the number of Doppler frequency components N_f. In addition, a single scatterer may contribute to more than one Doppler frequency, thereby producing Doppler frequency spreading. This effect can be seen in the log power spectrum for $N_{\text{scat}} = 20$ illustrated in Figure 8.13, where four distinct peaks of finite width are visible. The information attributable to each frequency component may therefore be the addition of the returns from a large number of scatterers, which will be "aliased" to a single effective scattering position. There are a considerable number of UNSIRI and SNSIRI effective scattering positions exhibiting no overlap at all with the actual scattering positions, even for smaller values of N_{scat}. There are also a considerable number of UNSIRI effective scattering positions located outside the zenith bounds of the radar volume. There are considerably fewer of these "spurious" effective scattering positions for the IDI-like and MSIRI analyses, suggesting that the spurious positions may be aliased positions whose associated phase differences are precluded from the analysis by the respective single-scatterer criteria.

It is apparent from the results illustrated in Figures 8.13 to 8.16 that the effective scattering positions located for each analysis become increasingly clustered about the line passing through the zenith in direction of the model input velocity θ_{mod} as N_{scat} is increased. This is confirmed by Figure 8.17, which shows the effective scattering positions located on applying of the IDI-like technique to all 200 records of the model-generated data-set MOD-MF-IDI-NSCAT with $\nu_{\text{mod}} = 0$ ms^{-1} for N_{scat} values of 20, 50, 100 and 1000. The effective scattering

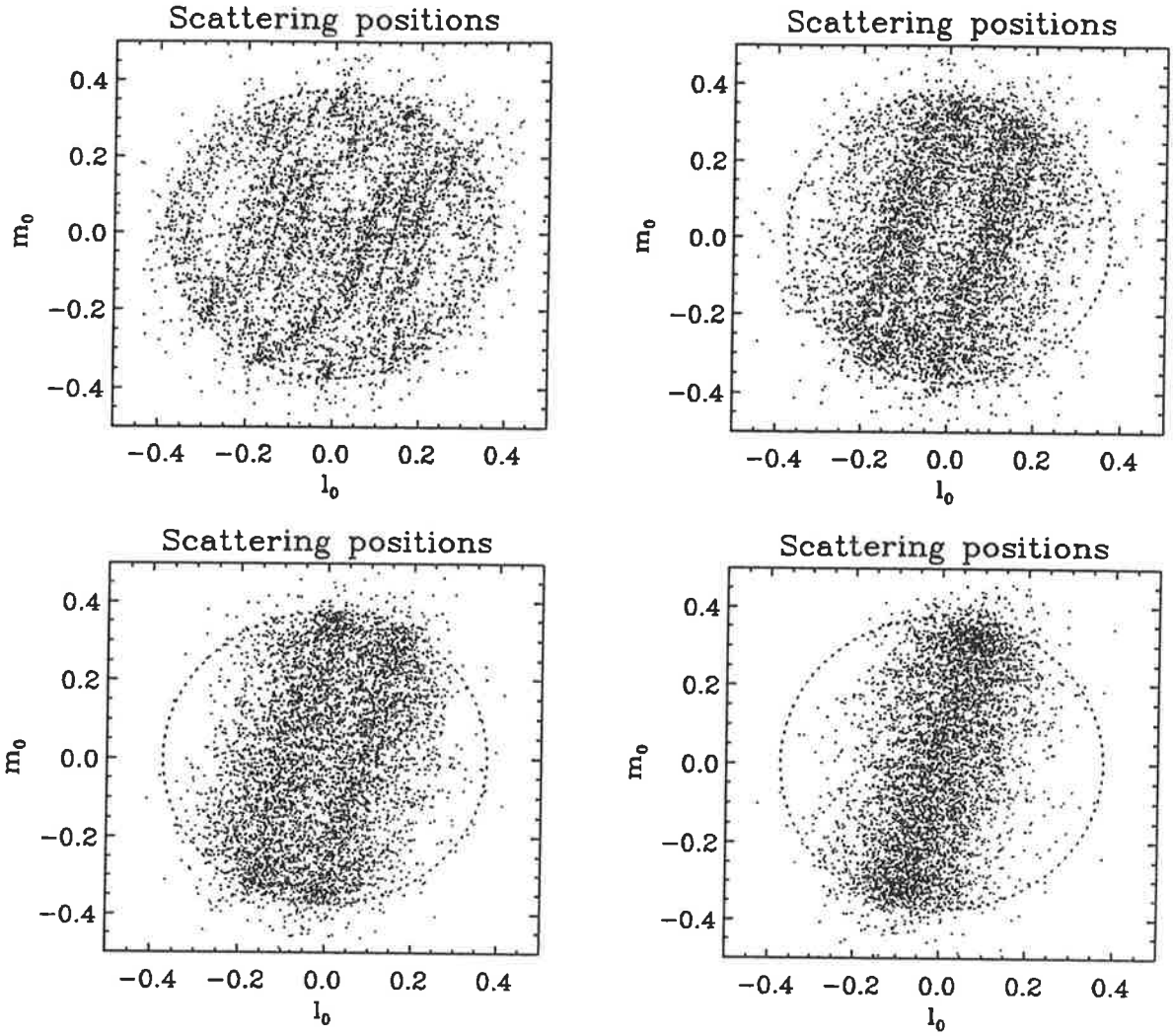

Figure 8.17: Effective scattering positions located on applying the IDI-like technique to the model-generated data-set MOD-MF-IDI-NSCAT with $\nu_{\text{mod}} = 0\text{ms}^{-1}$ using N_{scat} values of 20 (top left), 50 (top right), 100 (bottom left) and 1000 (bottom right). The effective scattering positions become increasingly clustered about the line passing through the zenith in direction of the model input velocity θ_{mod}. The dashed circle indicates the zenith bounds of the radar volume.

positions located for $N_{\text{scat}} = 20$ are randomly distributed, although there appears to be a tendency for some of the scatterers to cluster about a series of parallel lines in direction of the θ_{mod}. These parallel lines represent the actual positions occupied by the scatterers. Any scatterers leaving the enclosing volume are reinserted into the diametrically opposite position to which they left. If turbulent random motions are not employed the scatterers will therefore follow the same path after every second replacement. As N_{scat} is increased the clustering about the line passing through the zenith becomes significantly more evident, producing the band of effective scattering points predicted in section 8.3.2.

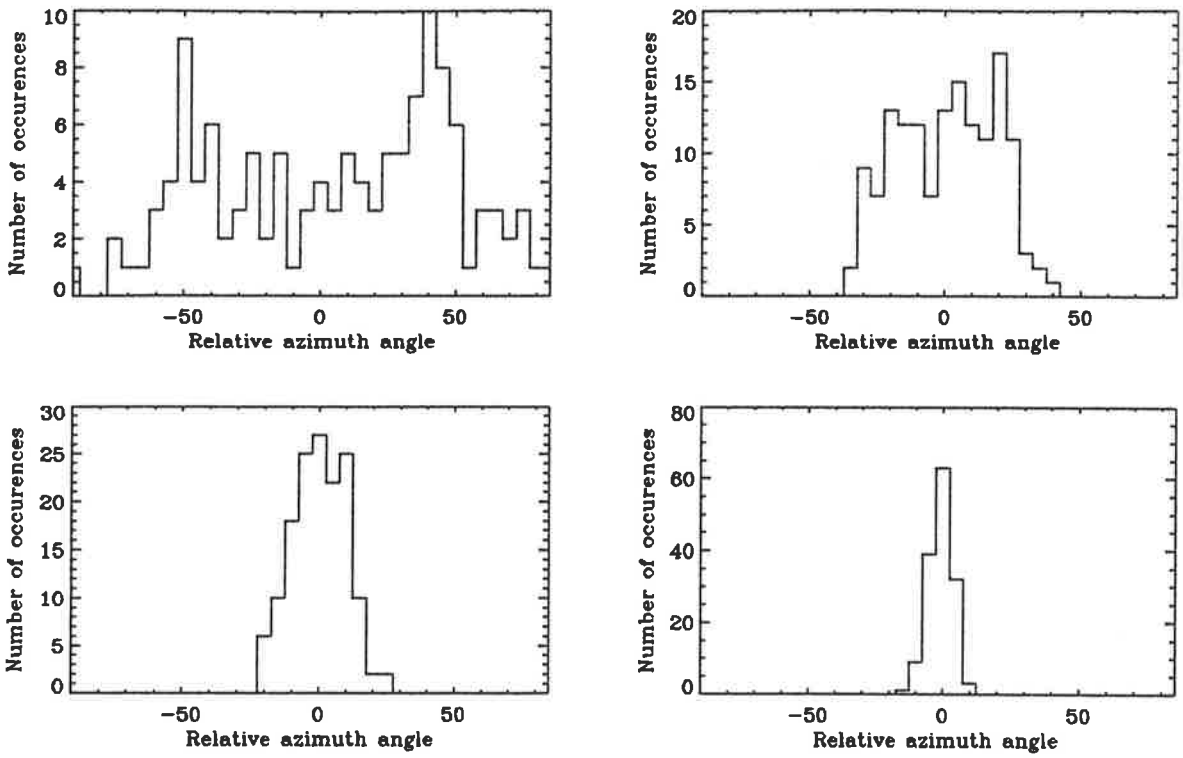

Figure 8.18: Distribution of the preferred azimuths relative to the direction of the model input velocity θ_{mod} obtained on applying the IDI-like technique to the model-generated data-set MOD-MF-IDI-NSCAT with $\nu_{\text{mod}} = 0\text{ms}^{-1}$ using N_{scat} values of 20 (top left), 50 (top right), 100 (bottom left) and 1000 (bottom right). The distributions become increasingly clustered about a difference of zero as N_{scat} increases, suggesting that the preferred azimuths becomes increasingly aligned with θ_{mod}.

The "preferred azimuth" of the effective scattering positions can be determined by applying a total regression linear fit (e.g. *Golub and Van Loan*, [1983]) to the effective scattering positions in the same manner described by *Vandepeer and Reid* [1995a]. The distribution of preferred azimuths determined for each individual record on the application of the IDI-like technique to the model-generated data-set MOD-MF-IDI-NSCAT with $\nu_{\text{mod}} = 0\ \text{ms}^{-1}$ are illustrated relative to θ_{mod} in Figure 8.18 for N_{scat} values of 20, 50, 100 and 1000. The preferred azimuths located for $N_{\text{scat}} = 20$ show little alignment with θ_{mod}. This is consistent with the results of Figure 8.14, which suggest that the IDI-like effective scattering positions located for $N_{\text{scat}} = 20$ accurately estimate the actual scattering positions which are randomly distributed throughout the radar volume and therefore have no preferred azimuth. As N_{scat} is increased the preferred azimuths show an increasing tendency to be aligned with θ_{mod}. This result is consistent with the volume scatter predictions of (8.26), which suggests that the effective scattering positions should lie along a line in the direction of the wind if the scatterers are isometric, as is the case for the data-set MOD-MF-IDI-NSCAT.

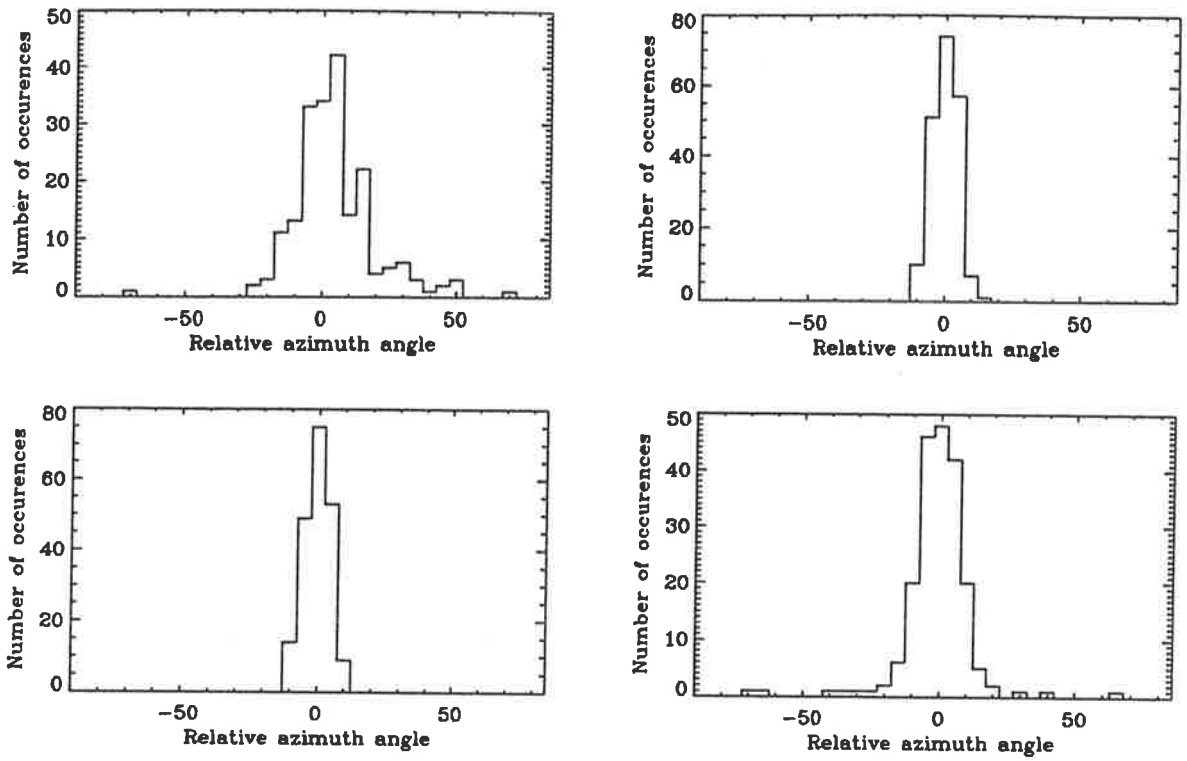

Figure 8.19: Distribution of the preferred azimuths relative to the direction of the model input velocity θ_t obtained using the model-generated data-set MOD-MF-IDI with $\nu_{\text{mod}} = 0$ ms^{-1} for the UNSIRI (top left), SNSIRI (top right), IDI (bottom left) and MSIRI (bottom left).

The distribution of the preferred azimuths determined on applying the interferometric analyses to the data-set MOD-MF-IDI with $\nu_{\text{mod}} = 0$ ms^{-1} are illustrated in Figure 8.19 relative to θ_{mod}. This data-set was generated using $N_{\text{scat}} = 1000$, and thus corresponds to the volume scatter situation. The distribution of preferred azimuths obtained for each interferometric technique is clearly centered about a difference of zero degrees. Similar distributions are also obtained for non-zero values of ν_{mod}. The widths of the IDI and MSIRI distributions are considerably smaller than the widths of the NSIRI distributions. This result suggests that the single scatterer criteria employed by these technique act to increase the agreement with the volume scatter predictions. This result is clearly sensible for the IDI-like analysis, as the phase linearity condition assumed indicative of plane wave incidence can also be obtained in the volume-scatter situation, as suggested by (8.19) and (8.22). The results of Figure 8.19 suggest that this criterion is actually selecting effective scattering positions exhibiting volume scatter characteristics as opposed to the discrete scatter characteristics for which it is employed.

The distribution of preferred azimuths obtained on applying the IDI-like analysis to the

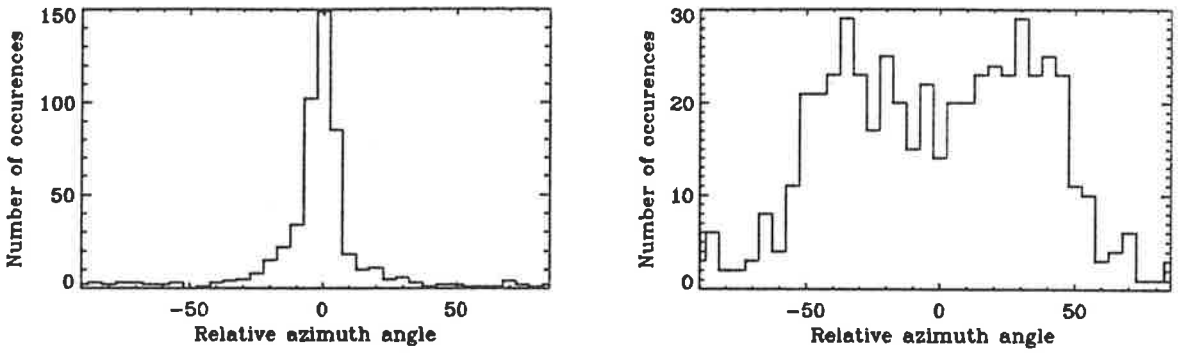

Figure 8.20: Distribution of the preferred azimuths relative to the direction α obtained by substituting the ellipsoid parameter ratios $B/A = 1$ and $H/A = 0.6$ into (8.26) (left), and relative to the direction of the model input velocity θ_t (right) obtained on applying the IDI-like analysis to the model-generated data-set MOD-MF-IDI-ROTN2.

data-set MOD-MF-IDI-ROTN2 are shown in Figure 8.20. This data-set was generated using anisometric scatterers designed to produce a characteristic ellipse with axial ratio $R_{\rm ax} = 2$ and axial rotation $\theta_{\rm ax} = 45°$. The family of ellipses of equal spatial correlation corresponding to these values of $R_{\rm ax}$ and $\theta_{\rm ax}$ are obtained by substituting the ellipsoid parameter ratios $B/A = 1$ and $H/A = 0.6$ into (8.21). The distribution of preferred azimuths shown in Figure 8.20 are plotted relative to the azimuth α obtained by substituting the ellipsoid parameter ratios into (8.26), and also relative to the direction $\theta_{\rm mod}$ of the model input velocity. The preferred azimuths obtained relative to α are closely distributed about a difference of zero degrees, thereby suggesting that (8.26) correctly estimates the preferred azimuth in the case of anisometric scatter. The preferred azimuths obtained relative to $\theta_{\rm mod}$ are almost evenly distributed between differences of $\pm 50°$, with some evidence of a bimodal distribution. This result suggests that the preferred azimuths are not necessarily aligned in the direction of $\theta_{\rm mod}$ in the anisometric scatter situation. These results further confirm the volume scatter suggestions that the preferred azimuths will not necessarily be aligned in the direction of the actual wind velocity.

The average zenith angle and radial velocity of the effective scattering positions located by applying the interferometric techniques to the model generated data-set MOD-MF-IDI are shown in Figure 8.21 as a function of the model turbulent random velocity $\nu_{\rm mod}$. This data was generated using $N_{\rm scat} = 1000$, and therefore conforms to volume scatter situation. The average zenith angle decreases with increasing $\nu_{\rm mod}$ for each technique, thereby confirming the volume scatter suggestions of (8.29). The average radial velocity meanwhile increases

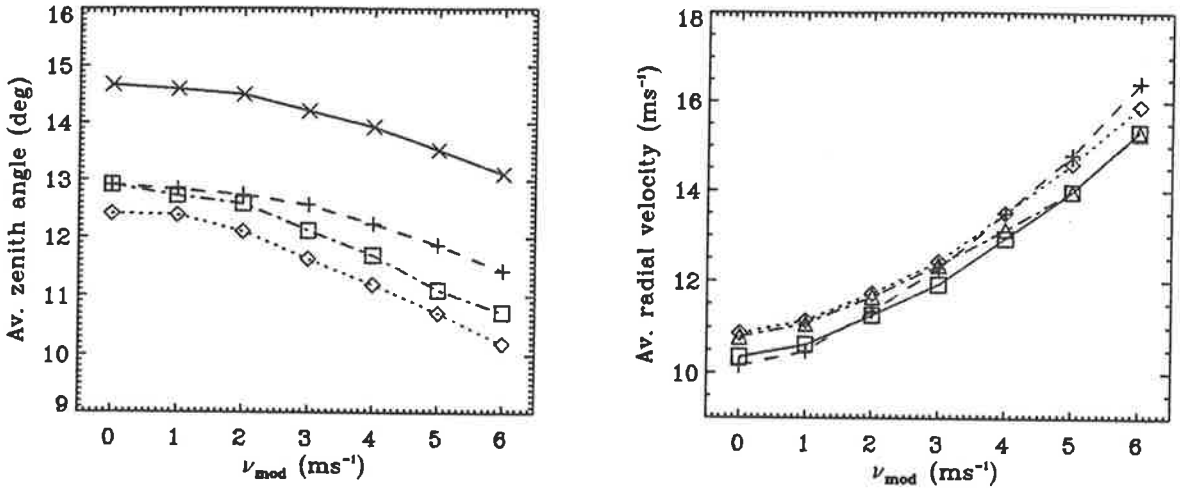

Figure 8.21: Average zenith angle (left) and absolute radial velocity (right) of the effective scattering points produced for the UNSIRI (×), SNSIRI (◇), MSIRI (□) and IDI-like (+) analyses.

with increasing ν_{mod}. This is a consequence of the beam broadening effect (e.g. *Hocking*, [1983a]), whereby the spectral width increases with the magnitude of the turbulent random motions. The spectral broadening results in the range of radial velocities employed by the analysis increasing. It follows from the results of Figure 8.21 that the magnitude of the horizontal velocity estimated by (8.5) must increase with increasing ν_{mod}, as predicted by volume scatter arguments. This effect will be discussed in the following subsection.

The agreement of the results illustrated in Figures 8.18 to 8.21 with those predicted by the volume scatter situation may appear somewhat surprising for the use of unsmoothed spectra for which the theory was not explicitly derived. The agreement can be explained as follows. The phase information associated with unsmoothed cross-spectra can be considered the sum of a component which is linear with Doppler frequency and a random component, as can be seen from the cross-spectral phases illustrated in Figure 7.5 of Chapter 7. This is verified by the fact that sufficient averaging of cross-spectra calculated from contiguous time-series records results in an average cross-spectrum with an almost linear phase variation (e.g. *Liu et al.*, [1990]). This is exactly the situation predicted by volume scatter arguments. Despite the fact that the cross-spectral phase at any particular Doppler frequency may not necessarily conform identically with predictions of volume scatter there will on average be an overall correspondence, as evidenced by the results of Figures 8.18 to 8.21.

The distributions of preferred azimuths illustrated in Figures 8.18 to 8.19 are plotted relative to the azimuth predicted by (8.26), based on the model input parameters. The distributions obtained relative to the direction of the apparent velocity θ_a are very similar,

albeit with slightly larger widths. The larger width occurs because the θ_a estimates will be distributed about the theoretical estimate provided by (8.26). Thus although these results have been plotted with respect to the actual rather than the estimated preferred azimuth, the results are no more favorable.

8.4.2 Velocity estimation in the volume scatter situation

The magnitudes of the vector averaged horizontal velocities resulting from applying the FCA and interferometric techniques to the model-generated data-set MOD-MF-IDI are shown in Figure 8.22 as a function of ν_{mod}. The FCA true velocity magnitude V_t shows excellent agreement with the model input velocity magnitude V_{mod}, compensating correctly for the effects of turbulent random motions which result in the FCA apparent velocity magnitude V_a increasing with increasing ν_{mod}. The interferometric velocity magnitudes also increase with increasing ν_{mod}, thereby confirming the volume scatter derived suggestions of *Vandepeer and Reid* [1995a] that the interferometric techniques require a correction for turbulent random motions akin to that employed by the FCA if they are to recover the correct wind velocity. The magnitudes of the average interferometric velocity V_{int} are well approximated by adapting (8.30) to yield the equation

$$V_{\text{int}} = \frac{\overline{|V_r(f)|}}{\sin \overline{\theta(f)}}, \tag{8.32}$$

where $\overline{|V_r(f)|}$ and $\overline{\theta(f)}$ denote the average absolute radial velocity and average zenith angle of the effective scattering positions. This equation will later prove useful for understanding the behavior of the interferometric velocity magnitudes as a function of the various thresholds employed by the interferometric techniques. The directions of the averaged horizontal velocities for all techniques (not shown) lie within 4° of the direction of the model input velocity.

The volume scatter situation suggests that the velocity magnitude predicted by the interferometric techniques should be equivalent to V_a (e.g. *Vandepeer and Reid*, [1995a]). The IDI-like and MSIRI velocity magnitudes shown in Figure 8.22 show good agreement with V_a for $\nu_{\text{mod}} \leq 3\text{ms}^{-1}$. For larger values of ν_{mod} the IDI-like and MSIRI velocity magnitude underestimate V_a. A number of possible causes of this underestimation will be addressed in subsection 8.4.4. The SNSIRI and UNSIRI techniques employ the same analysis technique, albeit on different spectral phase information, and should therefore be comparable. The smoothed spectral phases result in the SNSIRI effective scattering points for each Doppler

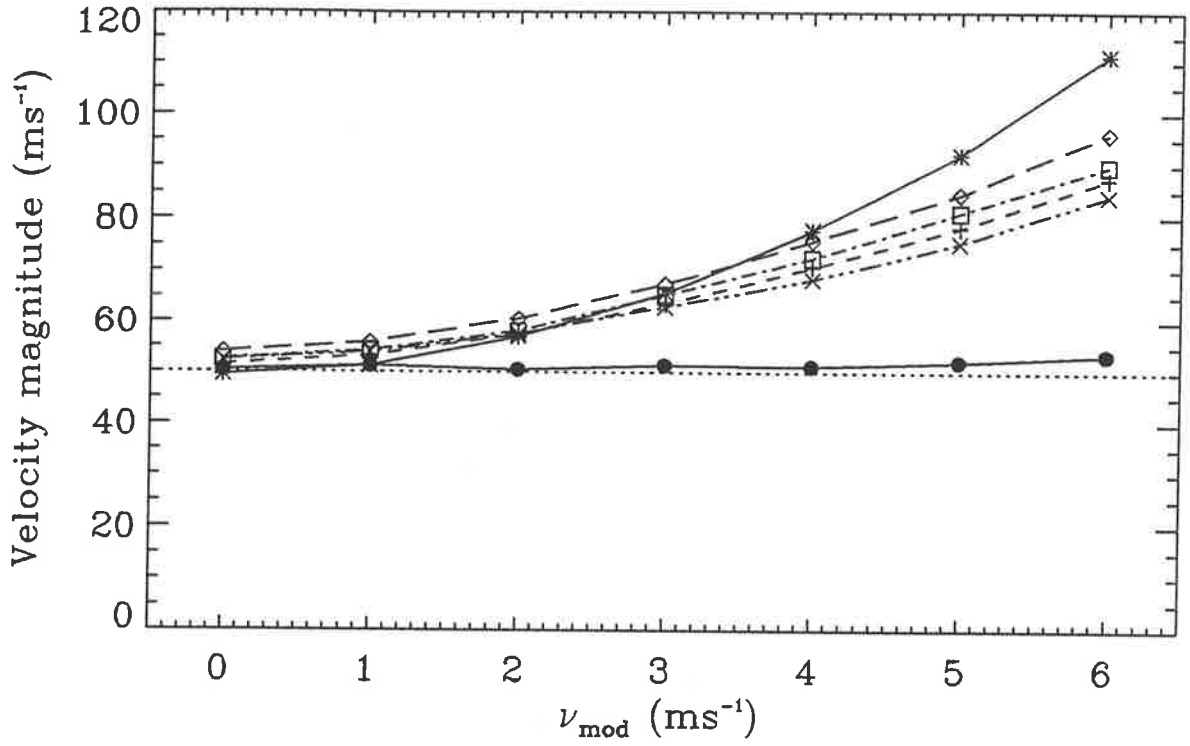

Figure 8.22: Average horizontal velocity magnitudes estimated by the FCA and interferometric techniques as a function of model turbulent velocity. FCA true (•), FCA apparent (∗), UNSIRI (×), SNSIRI (◇), IDI-like (+), MSIRI (□). The dotted line indicates the magnitude of the model input horizontal velocity.

frequency being located closer to the zenith than the UNSIRI effective scattering positions, as illustrated in Figure 8.21. Examination of (8.18) suggests this must result in the magnitude of the SNSIRI velocity being larger than the UNSIRI velocity estimate, even for the case where $\nu_{\mathbf{mod}} = 0$ ms^{-1}, where the UNSIRI velocity magnitude shows excellent agreement with $V_{\mathbf{mod}}$.

The directions of the vector-averaged horizontal velocities resulting from the application of the FCA and interferometric techniques to the model-generated data-sets MOD-MF-IDI-ROTN and MOD-MF-IDI-ROTN2 are shown in Figure 8.23. The direction of the FCA true velocity θ_t shows excellent agreement with the direction model input velocity $\theta_{\mathbf{mod}}$ for both data-sets. The direction of the FCA apparent velocity θ_a shows excellent agreement with $\theta_{\mathbf{mod}}$ for the isometric scatterer data-set MOD-MF-IDI-ROTN, but shows poor agreement with $\theta_{\mathbf{mod}}$ for the anisometric scatterer data-set MOD-MF-IDI-ROTN2. The estimates of θ_a obtained in the anisometric scatter situation are biased towards 45°, which corresponds to the direction perpendicular to the elongation of the scatterers. The behavior of the FCA in the situation of anisometric scatter has been discussed in some detail in Chapter

4 and will not be repeated here. The direction of the interferometric velocities agree well with θ_{mod} for both data-sets, thereby confirming the volume scatter suggestions deduced in Appendix G that the direction of the interferometric velocity is not influenced by scatterer anisometry. The distribution of preferred azimuths for the anisometric scatterer situation are shown in Figure 8.20, suggesting that the preferred azimuths are not necessarily aligned with $\theta_{\rm mod}$. The direction of the interferometric velocities however agrees well with θ_{mod}, thereby confirming that the effective scattering positions are not necessarily aligned with direction of the interferometric velocities.

The results of Figures 8.22 and 8.23 further confirm the volume scatter suggestions discussed in section 8.3.2, thereby raising a number important questions about the suitability of the interferometric techniques. In most instances significant turbulent random motions exist in the mesosphere, thereby suggesting that the interferometric velocity magnitudes will in general overestimate the actual wind velocity magnitudes. The issue of scatterer anisometry becomes important in the mesosphere at equatorial latitudes where the scatterers tend to exhibit East-West alignment (e.g. *Briggs*, [1977]). The results of *Lesicar* [1993] suggest that seasonal-average axial-ratios as large as 2.5 are observed at the equatorial site of Christmas Island. It is therefore quite feasible that similar axial-ratios may also be seen at Arecibo, where the AIDA campaign (e.g. *Brosnahan and Adams*, [1993]) was conducted.

8.4.3 Velocity estimation as a function of the number of model scatterers

The magnitudes of the vector averaged horizontal velocities resulting from the application of the FCA and the interferometric techniques to the model-generated data-set MOD-MF-IDI-NSCAT with $\nu_{\rm mod} = 6$ ms^{-1} are illustrated in Figure 8.24 as a function of the number of model scatterers $N_{\rm scat}$. The range of $N_{\rm scat}$ values is intended to approximately range from the discrete scatter to the volume scatter situation. The behavior of the FCA in relation to $N_{\rm scat}$ have been discussed in detail in Chapter 4. The FCA results are consistent with those inferred by the analytical model analysis of *Liu et al.* [1990], which suggests that regions of highly localized scatter will produce cross-correlation maxima time-delays differing from expected in the volume scatter situation. The FCA apparent velocity is calculated directly from the cross-correlation maxima time-delays, and clearly exhibits a distinct change from the volume scatter to the discrete scatter situation. The fall-off of the FCA velocity magnitudes for small $N_{\rm scat}$ is also accompanied by a fall-off in the data acceptance rate, as discussed in Chapter 4.

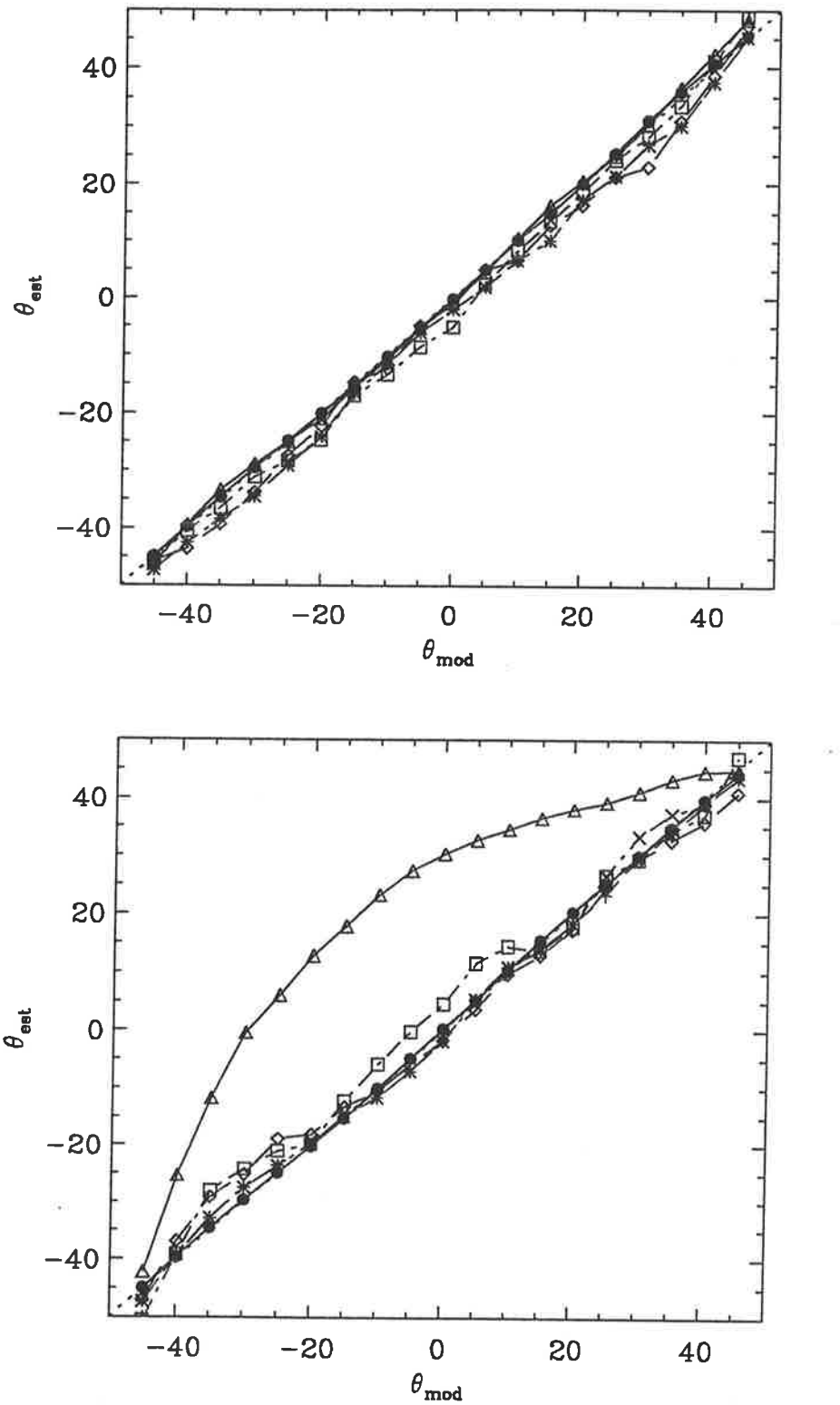

Figure 8.23: Average horizontal velocity directions θ_{est} estimated from the application of the FCA and interferometric techniques to the model-generated data-sets MOD-MF-IDI-ROTN (top) and MOD-MF-IDI-ROTN2 (bottom) as a function of the model input velocity direction θ_{mod}: FCA true (•), FCA apparent (△), UNSIRI (×), SNSIRI (◇), IDI-like (+), MSIRI (□). The dotted lines indicates $\theta_{est} = \theta_{mod}$.

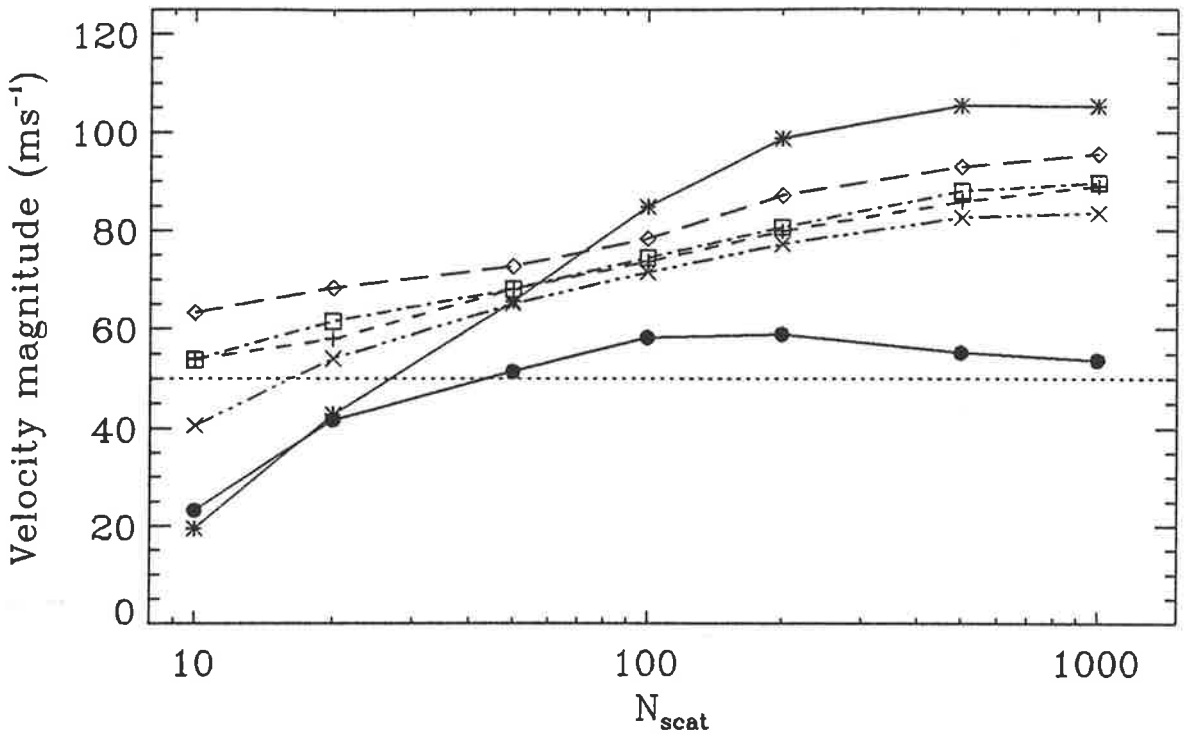

Figure 8.24: Average horizontal velocities estimated by the FCA and interferometric techniques as a function of the number of model scatterers N_{scat} for a model turbulent velocity of 6 ms^{-1}. FCA true (•), FCA apparent (∗), UNSIRI (□), SNSIRI (◇), IDI-like (+), MSIRI (△). The dotted line indicates the model input horizontal velocity.

The interferometric velocity magnitudes show an increasing tendency to agree with V_{mod} in the transition from the volume scatter to the discrete scatter situation. The IDI-like and MSIRI velocity magnitude estimates are in good agreement with V_{mod} for $N_{\mathrm{scat}} = 10$, suggesting that the IDI-like and MSIRI techniques can successfully estimate the magnitude of the actual wind velocity if there are only small number of scatterers contributing signal returns. This is of course the situation for which the interferometric techniques were designed. This result is clearly sensible in terms of the results illustrated in Figure 8.14 where the IDI-like and MSIRI effective scattering positions coincide well with the actual positions. On the other hand, the UNSIRI and SNSIRI analyses produces a number of spurious effective scattering positions which result in the estimated UNSIRI velocity magnitude underestimating V_{mod}, and the SNSIRI velocity magnitude overestimating V_{mod}. For larger values of N_{scat} the effective scattering positions tend to increasingly cluster around the azimuth predicted by volume scatter arguments, thereby producing velocity magnitudes which increase towards

those predicted by volume scatter arguments. The magnitude of the interferometric velocities obtained using $\nu_{\text{mod}} = 0$ ms^{-1} (not shown) show excellent agreement with V_{mod} for all values of N_{scat}.

The results of Figure 8.24 suggest that V_a approaches an asymptote at about $N_{\text{scat}} = 1000$. On the other hand it appears that the interferometric velocity magnitudes will continue to increase beyond $N_{\text{scat}} = 1000$, such that the asymptote will be approached at a much larger value of N_{scat}. This may partially explain the fall-off of the interferometric velocity magnitudes away from V_a seen with increasing ν_{mod}. The correlation functions employed by the FCA contain the contributions from all scatterers within the radar volume at each time-lag. The spectral phase at each Doppler frequency however contains the contributions from a much smaller number of scatterers. This result suggests that the interferometric techniques may therefore require a much larger number of scatterers than the FCA in order to attain volume scatter conditions, as indicated by the results of Figure 8.24.

8.4.4 The effects of noise on the interferometric analyses

The effects of noise upon the interferometric analyses have been simulated by adding randomly-generated Gaussian-distributed values to the real and imaginary components of the time-series. The magnitude and direction of the vector averaged horizontal velocities resulting from the application of the FCA and the interferometric techniques to the model-generated data-set MOD-MF-IDI with $\nu_{\text{mod}} = 6$ ms^{-1} are shown in Figure 8.25 as a function of the SNR of the added receiver noise. The FCA results are consistent with those presented in Chapter 5. The FCA true and apparent velocity are approximately independent of the SNR, although there is a tendency for V_t to overestimate V_{mod} for SNRs below 10 dB. The FCA employs a correction for the effects of noise as described in Appendix C. The failure to correct for the effects of receiver noise can result in V_t underestimating the actual velocity magnitude, and θ_t being biased towards the longest side of the triangle of receiving antennae employed for the analysis. These effects are detailed in Chapter 5. The interferometric velocity estimates exhibit the same biases seen in the FCA true velocity if the noise correction is not applied. The velocity magnitudes decrease with decreasing SNR, while the directions are increasingly biased towards an azimuth of $-45°$. This azimuth corresponds to the hypotenuse of the right-angled triangle formed by receiving antennae 1, 2 and 6, whose spectral phase information is employed for the analysis. The phase differences employed for the analysis however are those between antennae 1 and 2, and 1 and 6. The phase differences

between antennae 2 and 6 are not employed for the analysis.

The results of Figure 8.25 can be understood by examining the effects of noise upon the power- and cross-spectra employed by the interferometric techniques, as discussed in Appendix F. The presence of noise results in the addition of random components to the real and imaginary components of the spectrum at each Doppler frequency. This results in the presence of a "noise floor" in the power- and cross-spectral magnitude, and the addition of a random component to the cross-spectral phase at each Doppler frequency. The power threshold is employed to restrict Doppler frequencies within the noise floor from the analysis on the basis that they contribute little useful information. As the SNR is decreased the noise floor is increased, and the power threshold acts to reduce the range of Doppler frequencies employed for the analysis. The addition of the noise-induced random components to the "noise free" cross-spectral phases results in the zonal and meridional direction cosines estimated using (8.2) being "perturbed" from their noise free values. This perturbation acts to increase the average zenith angle of the effective scattering positions. The zenith angle threshold therefore acts to further decrease the number of Doppler frequencies used in the analysis.

The positional perturbations resulting from the application of the UNSIRI technique to an individual record of the model-generated data-set MOD-MF-IDI are illustrated in Figure 8.26 for various different SNRs of added receiver noise. The positional perturbations are shown only for Doppler frequencies passing the zenith angle and power thresholds, thereby also illustrating the decrease in the number of effective scattering positions obtained with decreasing SNR after the application of these thresholds. The magnitude of the positional perturbation increases with decreasing SNR. The results of Figure 8.26 suggest that the effective scattering positions can be perturbed as far as 10 km at the simulation height of 90 km for low SNRs.

The effects of the positional perturbations upon the analyses have been simulated by adding Gaussian distributed perturbations to the zonal and meridional components of the effective scattering positions prior to the velocity estimation. The effect of these perturbations upon the magnitude of the UNSIRI velocity estimate are shown in Figure 8.27, where the "displacement" indicates the standard deviation of the Gaussian distribution employed to generate the perturbations. There is a clear decrease in the magnitude of the velocity estimate as the effective scattering positions are made more random. This result suggests that any effect that acts to randomize the cross-spectral phase, and therefore, necessarily,

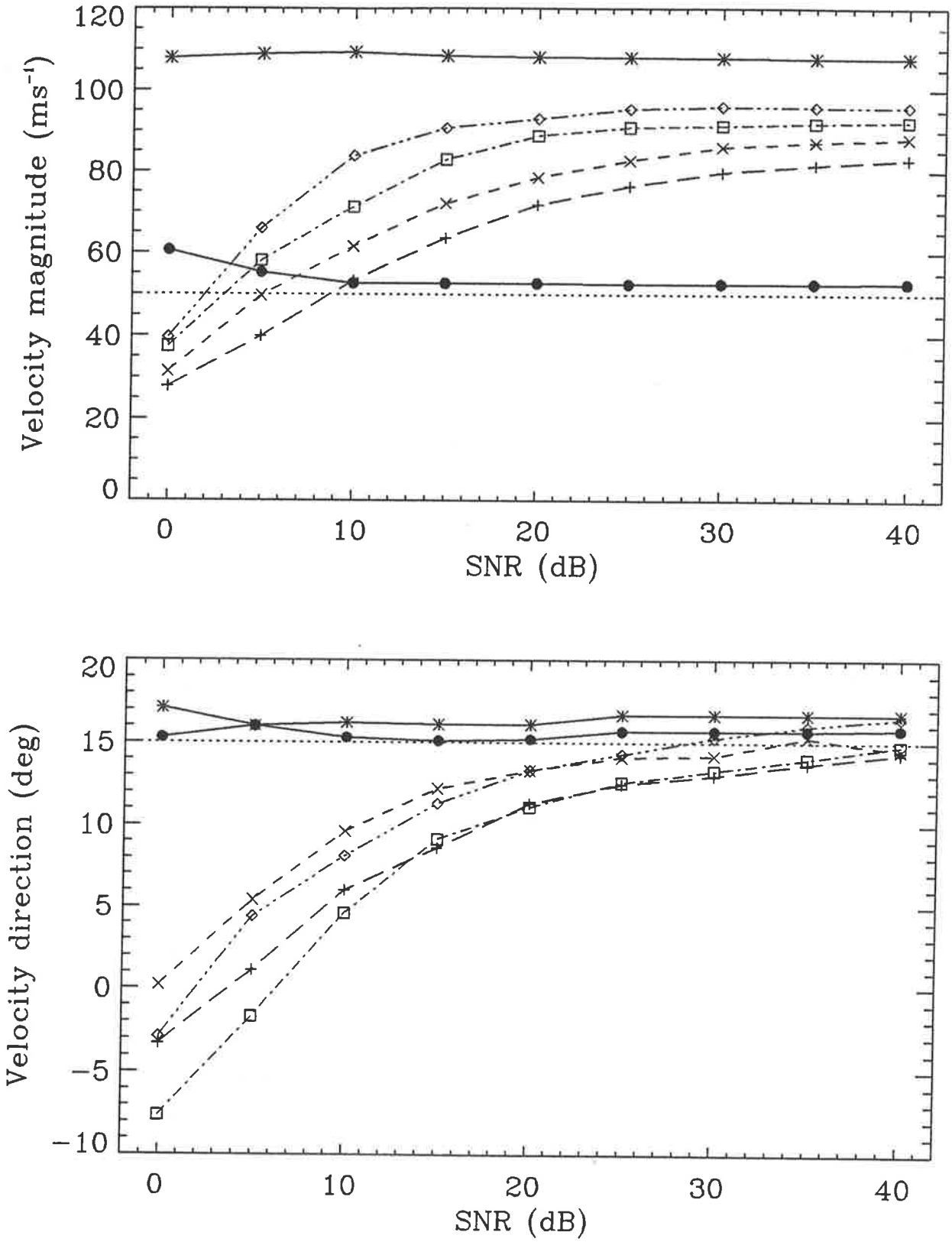

Figure 8.25: Average horizontal velocity magnitude (top) and direction (bottom) estimated on applying the FCA and interferometric techniques to the model generated data-set MOD-MF-IDI with $\nu_{\text{mod}} = 6$ ms^{-1} as a function of receiver SNR: FCA true ($\bullet$), FCA apparent ($*$), UNSIRI ($\square$), SNSIRI ($\diamond$), IDI-like ($+$), MSIRI ($\triangle$) and IDI-like using antenna spacing $D = \lambda$ (x). The dotted line on each plot indicates the model input values.

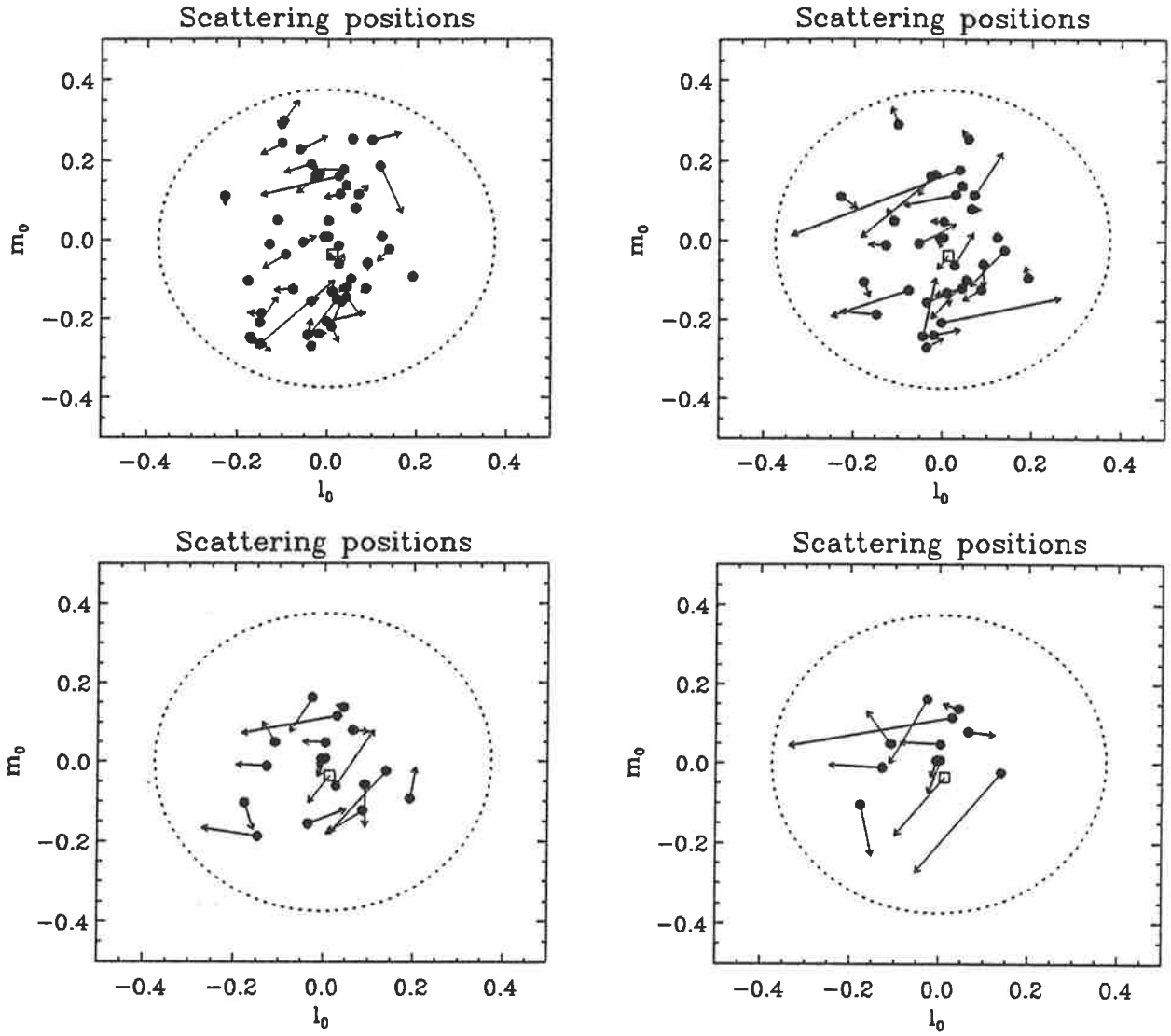

Figure 8.26: Examples of the positional perturbations resulting from the addition of receiver noise of SNR 20 dB (top left), 10 dB (top right), 5 dB (bottom left) and 0 dB (bottom right) to time-series analyzed by the UNSIRI analysis. The arrow indicates the perturbation from the original positions, which are denoted by (•). The increase in the positional perturbation with decreasing SNR is best illustrated by the effective scattering position denoted by (□).

randomize the effective scattering positions, will lead to a decrease in the magnitude of the velocity estimate. The numerical model analysis of *Sheppard and Larsen* [1992] illustrates that the effects of spatial decorrelation and turbulent random motions can result in an increase in randomness of the cross-spectral phase. The same increase in the randomness of the cross-spectral phase is also seen with increasing turbulent random motions using the data-set MOD-MF-IDI. The estimation of the interferometric velocities is reliant upon the existence of a systematic relationship between the effective scattering positions and their radial velocities. Any effect which degrades this relationship will lead to a decrease in the

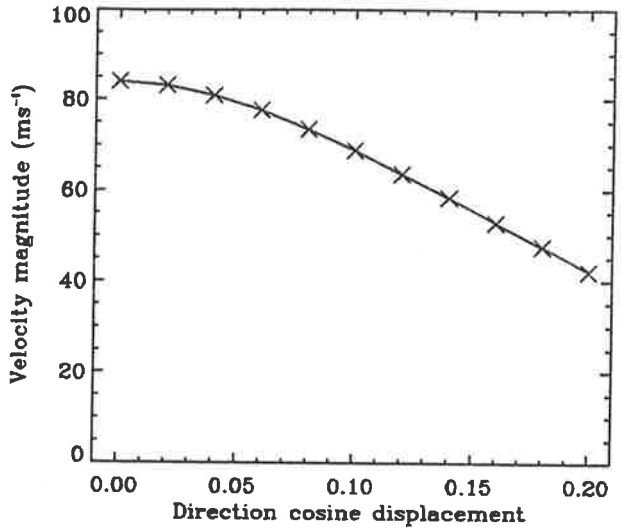

Figure 8.27: Average horizontal velocity magnitude estimated on applying the UNSIRI technique to the model-generated data-set MOD-MF-IDI with $\nu_{\text{mod}} = 6$ ms^{-1} as a function of the displacement of the direction cosines of the effective scattering positions.

magnitude velocity estimate. The noise-induced positional perturbations produce this effect, leading to the decrease in the magnitude of the interferometric velocity estimates shown in Figure 8.25.

Examination of (8.13) suggests that the magnitude of the positional perturbation resulting from any particular noise-induced phase perturbation must decrease with increasing antenna spacing, d. The results of Figure 8.27 therefore suggest that the decrease in the magnitude of the velocity estimate exhibited in Figure 8.25 should be reduced by using a larger antenna spacing. This is verified by the results of Figure 8.28, which shows the magnitudes of the interferometric velocity obtained using an antenna spacing $d = \lambda$, as opposed to the usual spacing of $d = \frac{1}{2}\lambda$ used to produce Figure 8.25. The results obtained using the larger spacing are less susceptible to the effects of noise. The use of an antenna spacing $d = \lambda$ however can result in spatial aliasing, and is therefore generally not advisable.

The signal and noise contributions to each Doppler frequency cannot be separated, suggesting interferometric techniques cannot correct for the effects of noise. This results in an effect analogous to the FCA triangle size effect, whereby the interferometric velocity decreases with decreasing antenna spacing. The magnitude of the average FCA apparent velocity however is not significantly altered by the addition of receiver noise. This may appear to be at variance with the volume scatter derived suggestion that the interferometry techniques should measure the apparent velocity. The apparent velocity is calculated directly from the delays corresponding to the cross-correlation maxima of the three calculated

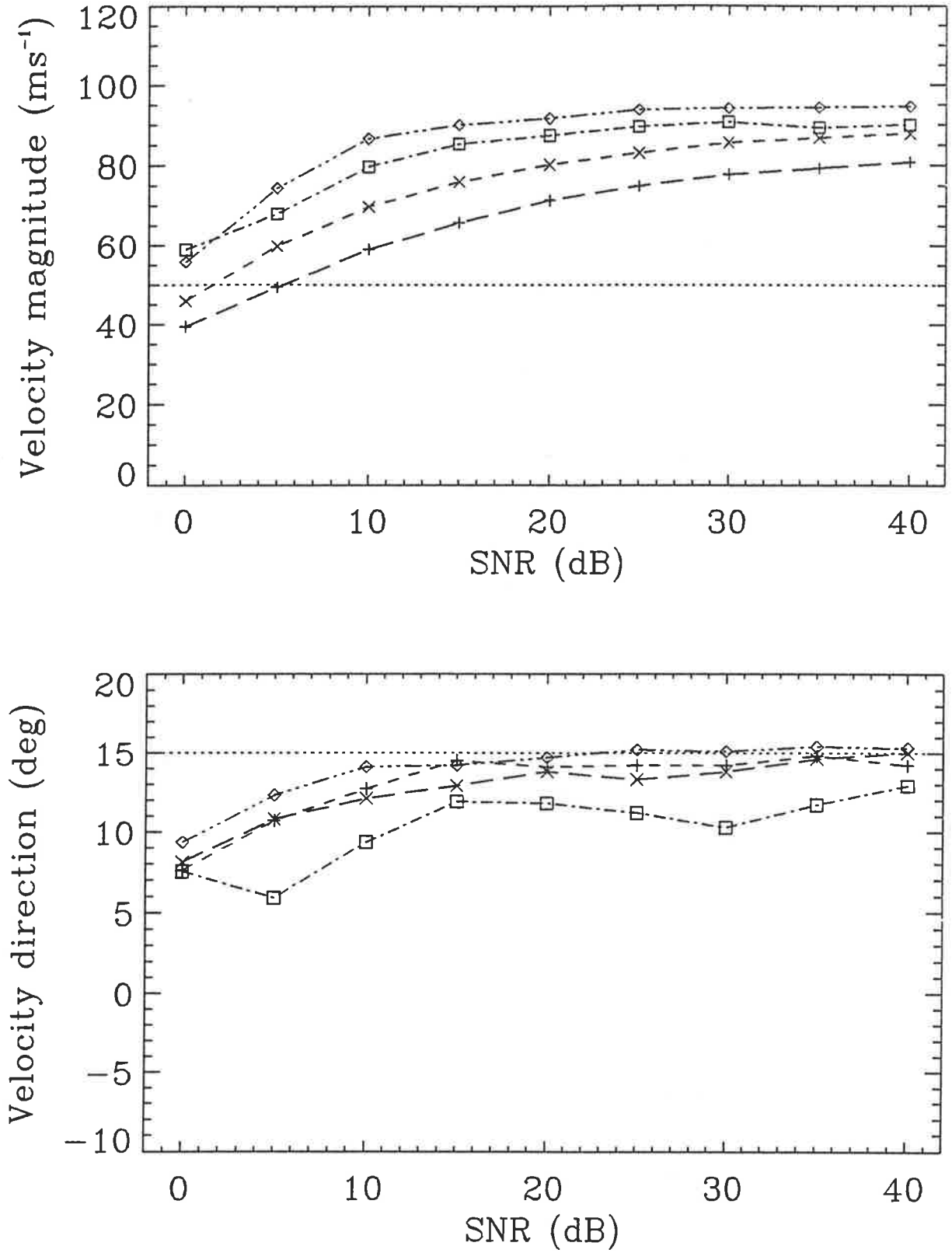

Figure 8.28: Average horizontal velocity magnitude (top) and direction (bottom) estimated on applying the interferometric techniques to the model-generated data-set MOD-MF-IDI with $\nu_{\mathrm{mod}} = 6$ ms^{-1} as a function of receiver SNR using an antenna spacing of $d = \lambda$: UNSIRI (□), SNSIRI (◇), IDI-like (+), MSIRI (△) and IDI-like using antenna spacing $D = \lambda$ (x). The dotted line on each plot indicates the model input values.

cross-correlation functions. The "shift" theorem of the Fourier transform (e.g. *Bracewell*, [1965]) indicates that the delay of the cross-correlation maxima is directly proportional to the phase slope of the corresponding cross-spectrum. This relationship has been verified experimentally by a number of authors (e.g. *Liu et al.*, [1990]; *Van Baelen and Richmond*, [1991]; *Briggs and Vincent*, [1992]). The cross-spectral phase slope is an estimate of the average phase behavior over all Doppler frequencies. As discussed above, averaging produces results that conform with volume scatter situation, even in the case of large noise-induced phase perturbations. The individual cross-spectral phases do not necessarily conform to the volume scatter situation. Noise-induced phase perturbations will further reduce the conformity. As a result, the correspondence between the FCA apparent and the interferometric velocities suggested by volume scatter arguments only really holds in the noise-free situation.

The effective scattering positions located on applying of the IDI-like technique to all 200 records of the model-generated data-set MOD-MF-IDI with $\nu_{\text{mod}} = 0$ ms^{-1} are shown in Figure 8.29 for various different SNRs of added receiver noise. The corresponding noise-free result is that illustrated in Figure 8.17 for $N_{\text{scat}} = 1000$. As the SNR is decreased the positional perturbations are increased, and the effective scattering positions are increasingly perturbed from the volume-scatter preferred azimuth predicted by (8.26). The effects of noise should therefore be taken into account in attempting to verify whether the volume scatter predictions of (8.26) hold experimentally.

The results of Figure 8.26 suggest that any effect that increases the randomness of the cross-spectral phase values at each Doppler frequency will also produce a decrease in the interferometric velocity magnitudes. The numerical model analysis of *Sheppard and Larsen* [1992] illustrates that the effects of spatial decorrelation and turbulent random motions can result in such an increase in randomness. The same increase in the randomness of the cross-spectral phase is also seen with increasing turbulent random motions using the data-set MOD-MF-IDI. This increase in the randomness may partially explain the fall-off of the interferometric velocity magnitudes away from V_a for $\nu_{\text{mod}} > 3$ ms^{-1}.

8.4.5 The effects of thresholds

The various imaging interferometry techniques employ a number of thresholds in order to select the Doppler frequencies considered appropriate to the analysis. These thresholds include zenith angle, power, phase consistency and radial velocity thresholds. The effects of these thresholds on the analysis are considered in Appendix H, illustrating that they can

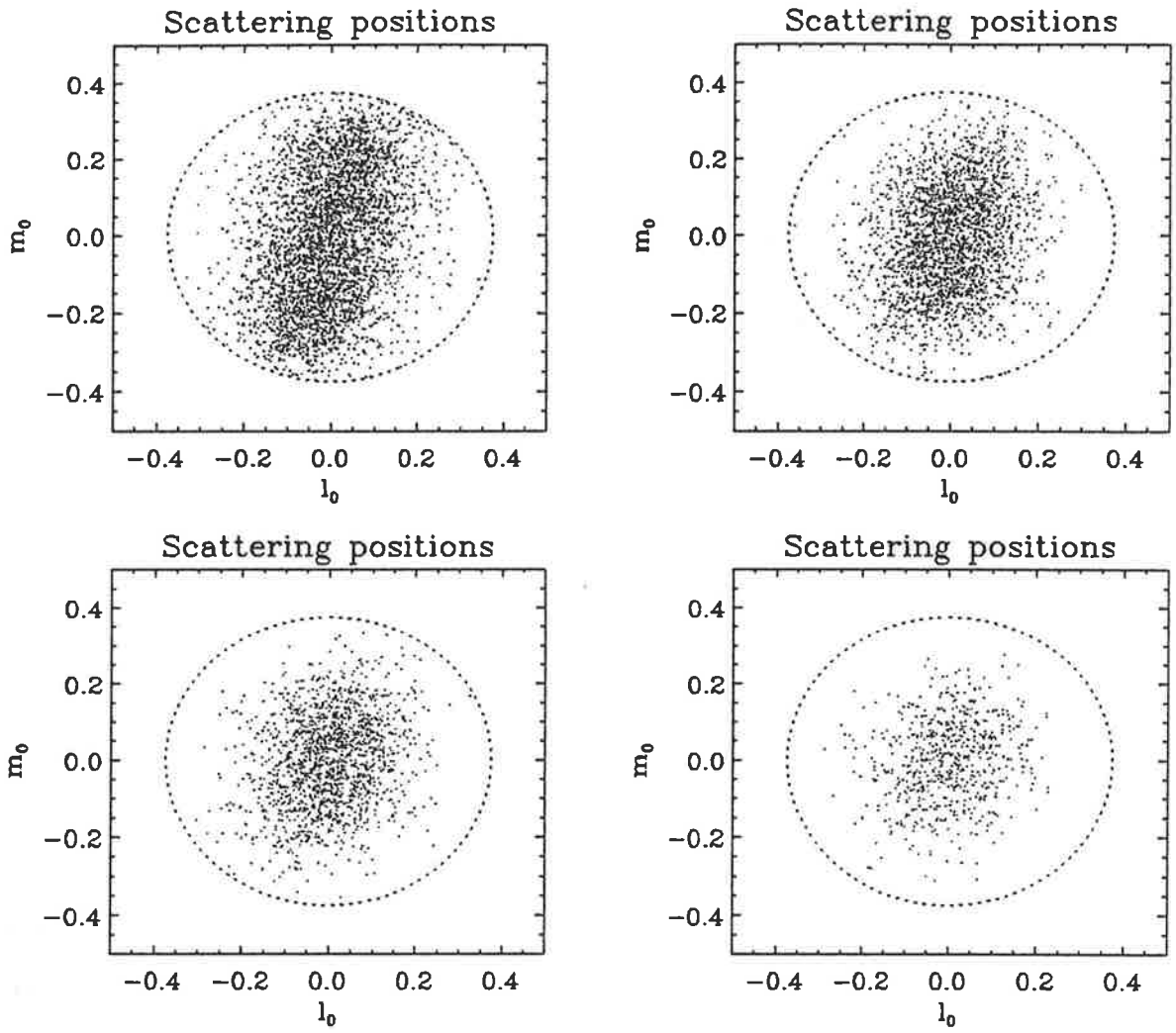

Figure 8.29: Effective scattering positions located on applying the IDI-like technique to the model-generated data-set MOD-MF-IDI with $\nu_{\text{mod}} = 0$ ms^{-1} for SNRs of 20 dB (top left), 10 dB (top right), 5 dB (bottom left) and 0 dB (bottom left). The effective scattering positions are increasingly perturbed away from the preferred azimuth predicted by volume scatter arguments. The dashed circle indicates the zenith bounds of the radar volume.

have a significant effect on the velocity estimate.

8.4.6 The multiple record analysis

The analyses described in sections 8.4.2 to 8.4.4 have been repeated using the multiple record analysis. This analysis involves combining the estimated scattering positions obtained from each of the 200 individual records into a single least squares fit to obtain the estimate of the wind velocity over the duration of the records (e.g. *Brosnahan and Adams*, [1993]). In most cases the magnitude and direction of the velocities obtained were found to be in excellent agreement with the results obtained using the individual record analysis. For instance, the

Table 8.3: Magnitude of the velocity estimates obtained for the IDI-like and MSIRI techniques for the individual and multiple record analyses

	IDI-like	MSIRI
Individual record analysis	53.9	53.8
Multiple record analysis	60.9	60.8

largest discrepancy seen in repeating the results of Figure 8.22 was less than 3%, occurring for the IDI-like technique with $\nu_{\text{mod}} = 6$ ms^{-1} where the individual record analysis gave a velocity magnitude of 87.2 ms^{-1} and the multiple record analysis gave 89.8 ms^{-1}.

The only instances where the individual and multiple record analyses produced significantly different velocity estimates was when a small number of effective scattering positions were located for the individual record analyses. In this instance the velocity estimates produced using individual records showed large variation, resulting in the vector averaged velocity obtained from the individual analysis underestimating the estimate produced from the multiple record analysis. The two major causes of the location of small numbers of effective scattering positions are the use of a small number of model scatterers, N_{scat}, and the use of smaller zenith angle thresholds. The effects of noise act to decrease the number of effective scattering positions, but do not appear to produce any further underestimation in addition to that resulting from the perturbation of the effective scattering positions. The MSIRI and IDI-like velocity magnitudes estimated using the individual and multiple record analyses for the model generated data-set with MOD-MF-IDI with $\nu_{\text{mod}} = 6$ ms^{-1} are shown in Table 8.3. The use of the individual record analysis biases the velocity magnitudes downwards by over 10%. This is a significant result, as it may suggest that the IDI-like and MSIRI techniques may not produce the correct estimate of the velocity in the presence of turbulent random motions in the discrete scatter case for which the techniques were designed.

The results obtained on applying the multiple record analysis suggest there is little or no advantage in using the technique, unless there are only a small number of effective scattering positions located for each individual record.

8.4.7 Discussion

The analysis presented in this section was approached with two fundamental aims in mind. The initial aim was to determine whether the volume scatter results predicted by *Briggs*

[1995] and *Vandepeer and Reid* [1995a] could be obtained using the radar backscatter model, which was designed primarily to simulate the volume scatter conditions for which these predictions are applicable. The results presented in 8.4.1 and 8.4.2 comprehensively illustrate that this aim has been achieved. The second aim was to compare the results obtained from the model analysis with those obtained in the rapidly growing number of experimental studies of the interferometric techniques to determine the applicability of these techniques to the various different scattering mechanisms responsible for radiowave returns. This second aim is pursued in the current subsection.

In comparing the results of the current study with those obtained experimentally it is necessary to account for a number of effects which may reduce the agreement. The interferometry results are often compared to the results obtained on applying the FCA. The results of Chapters 4 and 5 indicate that the FCA true and apparent velocities are subject to a number of biases resulting from a variety of atmospheric and instrumental effects. The interferometry techniques also apply a range of different thresholds in order to determine the suitability of each Doppler frequency to the analysis. The effects of these thresholds are discussed in Appendix H, suggesting that the techniques can be significantly influenced by the choice of thresholds. The interferometry techniques are also susceptible to the effects of receiver noise.

The NSIRI results compare well with the those obtained by *Franke et al.* [1990], as illustrated in Figure 8.7. Their antenna spacing necessitates the use of a spatial aliasing threshold of 15°. In addition, they employ a power threshold of 15 dB and a radial velocity threshold of ± 14 ms^{-1}. It is difficult to assess the effect of the radial velocity threshold without knowledge of the typical spectral widths. However, as the radial velocity will preclude effective scattering positions with larger radial velocities from the analysis it is envisaged it will play a similar role to the power threshold. The results of Appendix H suggest that the zenith angle threshold will lead to a upward bias in the magnitude of the velocity estimate with respect to the current analysis, while the power and radial velocity thresholds will lead to a downward bias. This suggests that the thresholds will overall result in only a small bias in comparison with the results of the current study. The results of *Franke et al.* [1990] suggest that UNSIRI velocity magnitude overestimates the true velocity magnitude V_t above 75 km where the SNR is high, and underestimates the V_t below 75 km where the SNR is low. This is consistent with the results of Figure 8.25. The SNSIRI results also compare well with the those of *Franke et al.* [1990] if the aforementioned effects are taken into account.

The IDI-like and MSIRI velocities also agree very well with those obtained experimentally. The IDI results of *Vandepeer and Reid* [1995a] give velocity magnitude estimates lying within the mean of V_a and V_t, and V_a itself, and therefore are in good agreement with the results of Figure 8.22. The model-generated IDI-like results may therefore appear a little larger than those obtained experimentally. However, if the effects of receiver noise are taken into account the agreement becomes very good. The IDI velocity magnitudes of *Turek et al.* [1995] and the MSIRI velocity magnitudes of *Meek and Manson* [1987] and *Brown et al.* [1995] agree well with V_a. As a result, the model-generated velocity magnitudes obtained for larger values of ν_{mod} may appear a smaller than those obtained experimentally. Despite this result it is clear that the model generated velocity magnitudes increase with increasing random motions magnitude in the same manner as V_a.

In addition to the velocity magnitude estimates described above, the model analysis also provides a number of results in good agreement with those obtained in the IDI analysis of *Vandepeer and Reid* [1995a] and the MSIRI analysis of *Brown et al.* [1995]. The agreement between the preferred azimuths predicted by (8.26) is also seen by *Vandepeer and Reid* [1995a], as shown in Figure 8.10, although the width of the relative distribution seen experimentally is significantly larger. The results of 8.4.4 suggest that the correspondence with the azimuth predicted by (8.26) decreases significantly with decreasing SNR. This must be taken into account when using experimental data, and may be the cause of the increase in the width of the distribution seen experimentally. The model results also suggest that the interferometric velocities are not influenced by the effects of pattern anisometry. This result was also found by *Brown et al.* [1995], who illustrated that the agreement between the interferometric and FCA apparent velocity decreased significantly with increasing pattern anisometry. The FCA apparent velocity is biased perpendicularly to the azimuth of pattern elongation. The results of *Brown et al.* [1995] suggest that the interferometric techniques are not subject to the same bias.

The interferometric techniques are dependent upon the discrete scatter assumption, whereby a one-to-one correspondence exists between the regions responsible for the radiowave backscatter and the Doppler frequency components. The IDI-like and MSIRI techniques employ single scatterer criteria in order to preclude Doppler frequencies contradicting this one-to-one correspondence from the analysis. The IDI-like and MSIRI analyses use identical phase information to the UNSIRI analysis, but reject Doppler frequencies on the basis of their individual single-scatterer criteria. Application of these criteria produces velocity

magnitudes lying between the UNSIRI and SNSIRI velocities, confirming the suggestion by *Franke et al.* [1990] that the single-scatterer criteria select Doppler frequencies with similar phase information to that of the smoothed spectrum. The phase information associated with the local maxima is similar to that of the smoothed spectra at the same Doppler frequency (e.g., *Franke et al.*, 1990). Similarly, the exclusion of Doppler frequencies by the phase linearity criterion constitutes a form of spectral averaging, as Doppler frequencies with phase information sufficiently removed from smoothness are excluded from the analysis (e.g., *Vandepeer and Reid*, [1995a]).

An alternative argument to that presented above is that the inclusion of Doppler frequencies failing the IDI-like and MSIRI single-scatterer criterion in the UNSIRI analysis results in a decrease in the estimated velocity. The results obtained in the current study suggests that any randomization of the effective scattering positions will lead to a decrease in the estimated velocity. The estimation of the interferometric velocities is reliant upon the existence of a systematic relationship between the effective scattering positions and their associated radial velocities. Any effect which introduces random behavior into this systematic relationship produces a decrease in the magnitude of the velocity estimate. The inclusion of Doppler frequencies failing the IDI-like and MSIRI single-scatterer criterion constitutes such an increase in randomization, as do the effects of noise, as shown in 8.4.4, and the inclusion of Doppler frequencies with low spectral power, as shown in Appendix H.

8.4.8 Notes on the interpretation of experimental results

The Doppler-selected imaging interferometry techniques are reliant on the spectral information associated with each Doppler frequency being the result of backscatter from a single discrete scattering position. Several authors have acknowledged that this situation is unlikely to hold in practice (e.g. *Brosnahan and Adams*, [1993]). The analyses of *Briggs* [1995] and *Vandepeer and Reid* [1995a] predict a number of results that will occur in the volume scatter situation. The analysis of the model-generated data presented in this Chapter has verified these predictions.

The results of section 8.4.1 suggest that the majority of the effective scattering positions located in the discrete scatter situation correspond well with the actual scattering positions. As the actual scattering positions are randomly distributed the effective scattering positions have no preferred azimuth. As the number of scatterers is increased the effective scattering

positions show less correspondence with the actual scatterers positions, and become increasingly aligned along the azimuth predicted by (8.26). It is important to stress that the failure to observe any preferred azimuth in the effective scattering positions cannot necessarily be regarded as evidence that the volume scatter situation is not applicable, or that the discrete scatter situation is applicable. The results of section 8.4.4 suggest that the presence of noise can act to randomize the effective scattering positions, therefore disguising any preferred azimuth that may exist in the absence of noise. Furthermore, any variation in the direction of the background wind may act to disguise any preferred azimuth, as the effective scattering positions will be distributed over a range of azimuths corresponding to the range of directions. The presence of internal gravity waves can produce significant fluctuations in the direction of the instantaneous wind, as is evident in the results of section 4.4.3.

The results of Figures 8.13 and 8.17 suggest that the effective scattering positions located for contiguous Doppler frequencies in the discrete scatter situation tend to form a line along the direction of motion. This occurs because the returns from individual scatterers are spread over a number of Doppler frequencies due to the finite range of positions occupied by the scatterer over the duration of the record. This result suggests a possible criterion for the verification of the discrete scatter situation. The effects of noise however will act randomize the positions of the effective scattering positions, and may therefore disguise this linear behavior. If the lifetimes of the scatterers are small there will be little Doppler spreading of individual scatterers, and therefore little evidence of this linear behavior.

The performance of the FCA in the transition between the volume scatter and discrete scatter situations is investigated in section 4.7. The results suggest a number of criteria that could be employed to verify the discrete scatter situation assumed applicable by the Doppler-selected imaging interferometry techniques. In the discrete scatter situation the FCA should produce low FCA acceptance rates, estimates of R_{ax} significantly greater than unity, and randomly distributed estimates of θ_{ax}. It is important to stress that the combination of all three of these results must occur to justify the discrete scatter hypothesis. The results of Chapter 5 suggest that large values of R_{ax} can occur if the effects of receiver saturation, coarse digitization, or differences in the characteristics of the receivers are present, or if the analysis does not employ the noise corrections outlined in Appendix C. The presence of consistent anisometric scatterer can also produce large values of R_{ax}.

The preferred azimuths obtained for the IDI analysis of *Vandepeer and Reid* [1995a] show good agreement with the predictions of (8.26). It is interesting to note however that

the agreement decreases significantly above 90 km. This results tends suggests that the discrete scatter situation may become more applicable in the region above 90 km, where total reflection returns may eventuate.

8.5 Summary and conclusions

In this chapter two different sets of "interferometry" techniques have been investigated. The mean angle of arrival (MAOA) techniques have been applied using time- and frequency-domain analyses. Comparisons involving the use of experimental data have revealed that the time- and frequency-domain analyses produce results in excellent agreement. The Doppler sorted imaging interferometry techniques have been investigated using model-generated data, and confirm the volume scatter predictions of *Briggs* [1995] and *Vandepeer and Reid* [1995a].

The MAOA corresponds to the power-weighted mean position of the radiowave backscatter. The original MAOA analyses of *Röttger and Ierkic* [1985] was performed in the time-domain, as described in section 8.2. The technique has also been shown to be applicable in the frequency-domain (e.g. *Kudeki*, [1988]; *Van Baelen et al.* [1990]; *Larsen et al.* [1992]), where, for the purposes of this thesis, it has been referred to as the phase-fitting radar interferometry (PFRI) technique. In section 8.2.1 the simple 2-dimensional FCA-based analytical model of *Briggs and Vincent* [1992] has been extended to 3-dimensions, producing formulae essentially identical to those employed by the PFRI technique. The application of this revised PFRI technique produces MAOAs in excellent agreement with the time-domain technique. The MAOA and PFRI techniques also provide formulae for the vertical velocity which correct for the situation where the MAOA is off-zenith. The formulae derived for the revised PFRI technique reveal that the vertical velocity obtained using the PFRI techniques of *Van Baelen et al.* [1990] and *Larsen et al.* [1992] is corrected using the FSA apparent velocity, which is essentially equivalent to the FCA apparent velocity. As the apparent velocity is generally assumed to be an overestimate of the actual wind velocity it therefore follows that the vertical velocity obtained using the techniques of *Van Baelen et al.* [1990] and *Larsen et al.* [1992] will actually be overcorrected.

The Doppler-selected imaging interferometry techniques are based on the determination of the locations of apparent backscatter for each individual Doppler frequency. The fundamental assumption of the analyses is that the information associated with each Doppler frequency is the result of scatter from a single discrete scattering point. The various analyses

differ in their use of selection criteria to determine which Doppler frequencies satisfy this fundamental assumption. The theoretical model of the FCA has been employed by *Briggs* [1995] and *Vandepeer and Reid* [1995] to predict the performance of the Doppler-selected imaging interferometry techniques in the volume scatter situation. A number of these predictions have been verified experimentally (e.g. *Vandepeer and Reid*, [1995]; *Brown et al.*, [1995]). The volume scatter predictions have been summarized and elaborated upon in section 8.3.2, where the effects of non-vertical velocities and off-zenith MAOAs have been considered. A number of further predictions have also been presented.

The volume scatter predictions have been investigated using the radar backscatter model in section 8.4. For smaller numbers of model scatterers the effective scattering positions located by the interferometric techniques have been shown to agree well with the actual scattering positions, while the velocity estimates show good agreement with the model input velocity. As the number of model scatterers is increased to simulate the volume scatter situation the effective scattering positions are shown to become clustered about the line predicted by the volume scatter arguments. The effective scattering positions are also shown to be brought closer to the zenith. The magnitude of the velocity estimates is shown to increase as the magnitude of turbulent motions is increased, suggesting that the interferometric techniques do not implicitly apply a correction for the effects of turbulent random motions akin to that employed by the FCA. The direction of the velocity estimates are shown to be independent of the effects of scatterer anisometry. The results also indicate that there is no advantage in combining the scattering positions obtained over a number of records into a single least squares solution unless there are very few scattering positions located for each individual record.

The effects of noise upon the interferometry techniques have also been investigated using the radar backscatter model. The results reveal that the techniques are subject to a bias analogous to the FCA triangle size effect, whereby the magnitude of the velocity decreases with increasing antenna spacing, and the direction of the velocity is biased towards the hypotenuse if a right-angled triangle of receiving antennae are employed. The results of chapter 5 suggest that the FCA triangle size effect can be avoided if the effects of noise are corrected for, if receiver saturation and coarse digitization are avoided, or if differences in the characteristics of the individual receiver are avoided. The results presented in section 8.4 however suggest that the effects of noise cannot be removed from the cross-spectral phase values, suggesting that the bias will always be present for records with low SNR. There is

reason to believe that differences in receiver characteristics may also introduce a similar bias into the interferometric velocities. This has not been investigated however as such effects cannot be properly simulated using the radar backscatter model. The various acceptance criteria employed by the interferometric analyses have also been investigated, revealing that the choice of acceptance criteria can have a significant influence of the magnitude of the velocity estimate.

The results obtained using the radar backscatter model agree well with those obtained in a number of experimental studies, such as those performed by *Meek and Manson* [1987], *Franke et al.* [1990], *Vandepeer and Reid* [1995a], and *Brown et al.* [1995]. This suggests that the discrete scatter situation assumed by the interferometric techniques may not be applicable in most instances, thereby severely questioning the applicability of the current implementation of the Doppler-selected imaging techniques.

Chapter 9

Summary and conclusions

9.1 Summary

This work presented in this thesis provides an evaluation of a number of different spaced antenna (SA) radar analysis techniques developed primarily for the estimation of parameters related to atmospheric dynamics. The motivation behind the work was to properly understand the performance of the different techniques, as well as to assess the relative advantages and disadvantages of each technique. The majority of this work was performed using the "radar backscatter model" described by *Holdsworth and Reid* [1995a] (see Appendix I), which was described in Chapter 3.

The background for the work presented in this thesis was provided in Chapter 1. A brief description of the atmosphere was provided in terms of profiles of the temperature structure and electron concentration. The observation of atmospheric dynamics using radars was discussed. The different mechanisms responsible for radiowave backscatter and the height ranges observed by different radars was presented. The history of the various SA radar analysis techniques was also discussed.

The radar backscatter model was discussed in Chapter 3. The model consists of a number of randomly distributed scatterers. Each scatterer has it's own polar diagram based on the choice of transmitted beam-width and aspect sensitivity, and therefore simulate a horizontally elongated Bragg scatterer. The model-generated data therefore simulates data received in the "volume scatter" situation. The model includes the effects of turbulent random motions, gravity wave perturbations, and finite scatterer lifetimes. The resulting time-series data was shown to exhibit the same fading characteristics seen in experimentally obtained

data, and the ground diffraction patterns were shown to exhibit the behavior expected from the simulation parameters. Standard analysis techniques were shown to accurately recover the model input values. The results also suggested that finite scatterer lifetimes and gravity waves can be mistakenly interpreted as turbulent random motions, suggesting that some care should be taken in the interpretation of experimentally determined turbulent random motions magnitudes. The spectral-width technique for the estimation of the aspect sensitivity parameter was shown to overestimate θ_s in the presence of random motions, as suggested by *Lesicar and Hocking*, [1992].

The full correlation analysis (FCA) technique was discussed in Chapter 4. The mathematical formulation of the FCA was presented using model-generated data, enabling the visualization of the development of the FCA through the progressive inclusion of the effects of a mean background wind, scatterer anisometry, and turbulent random motions. The effects of turbulent random motions and scatterer anisometry were investigated using the radar backscatter model, revealing that the FCA performs as expected. The effects of monochromatic gravity waves were also been investigated. Although the instantaneous estimate of the FCA true velocity was shown to be influenced by the wave the average velocity estimated over the period of the wave accurately predicts the model input velocity. The application of the FCA to experimentally obtained data was also presented. The effects of the sampling time upon the interpolation and fitting procedures employed by the FCA was investigated, revealing that there exists a maximum sampling time for the accurate application of the FCA. The effects of the scattering mechanism upon the FCA was investigated, revealing that the FCA can provide an acceptable estimate of the model input velocity if in excess of 12 scatterers produce signal returns. The effects of the time-series length and coherent averaging upon the FCA were investigated, revealing that the model input parameters are more predicted more accurately as the time-series length and number of averages is increased.

The triangle size effect (TSE) of the FCA was investigated in Chapter 5. The results illustrate that the magnitude of the true velocity V_t, the corrected fading time $T_{0.5}$, and the pattern scale $S_{0.5}$ increase with increasing antenna spacing. While V_t approaches an upper limit given by the magnitude of the model input velocity as the antennae spacing approaches the pattern scale, both $T_{0.5}$ and $S_{0.5}$ continue to increase as a result of selection effects. The results indicate that the TSE results from the attenuation of the cross-correlation functions. This attenuation can result from four possible causes, namely receiver noise, coarse digitization, receiver saturation, and differences in the characteristics of the receivers. While

the first three causes can be corrected for or avoided, the last cause cannot, and can therefore presents a significant problem for radars using different receiving channels for each receiving antennae. The results also illustrate a number of different directional biases.

In Chapter 6 two alternative correlation analyses were investigated. The slope fitting correlation analysis (SFCA) was investigated, revealing that the technique is essentially the isotropic scatter equivalent of the FCA. The extension to anisotropic scatter requires the parameterization of the characteristic ellipse, implying that the analysis will be subject to the same biases as the FCA triangle size effect. The application of the revised SFCA produced velocity estimates in very good agreement with the model input velocity, albeit with slightly larger error estimates than those obtained using the FCA. The spatial correlation analysis (SCA) was investigated to determine the feasibility of applying the technique with three or four receiving antennae. The three-antenna spatial correlation analysis (SCA3) requires the parameterization of the characteristic ellipse, and was shown to give very similar velocity estimates to the FCA. The four-antenna analysis (SCA4) can be applied using a square of antennae, or a "Y" configuration. The SCA4 does not require the use of zero-spatial lag, and is therefore not affected by the attenuation of the cross-correlation functions if the attenuation factors are similar. This was illustrated using experimental data collected at BP which exhibits a large FCA TSE. The SCA4 gave very similar velocity estimates to FCA applied to the largest triangle of receiving antennae, suggesting that the SCA4 avoids the TSE.

The full spectral analysis technique was investigated in Chapter 7. The FSA is the frequency-domain analogue of the FCA, employing the same mathematical formulation based on the use of spectral parameters as opposed to correlation parameters. There exist three different variations of the FSA, namely those of *Briggs and Vincent* [1992] (BVFSA), *Sheppard and Larsen* [1992] (SLFSA), and *Liu and Pan* [1993] (LPFSA). The application of the FSA techniques to experimentally obtained data produced estimates of τ'_{ij} and $\tau_{0.5}$ in good agreement with the estimates produced by the FCA, albeit with larger errors. Although the LPFSA estimate of the remaining correlation parameter exhibited good agreement with the FCA estimate, the BVFSA and SLFSA estimates exhibited poor agreement because the cross-spectral magnitude includes the effects of tails of the cross-correlation functions. As the FCA is performed solely on the main peak of the correlation functions the tails have little influence on the analysis. The cross-spectra employed by the FCA are related to the cross-correlation functions by the Fourier transform, and therefore include the effects of the

tails of the cross-correlation function. The use of coherently averaged spectra reduces the effects of the tails, such that the agreement between the BVFSA and SLFSA with the FCA increases with increasing averaging.

Two different categories of 'interferometry" techniques were presented in Chapter 8. The non Doppler-selected MAOA and PFRI techniques were first discussed. A revised PFRI technique was presented which produces results in very good agreement with the MAOA technique. The analysis indicated that the vertical velocity corrections applied by *Van Baelen et al.* [1990] and *Larsen et al.* [1992] overcorrect for the effects of off-zenith MAOAs because they effectively employ the FCA apparent velocity, which is generally assumed to be an overestimate of the actual wind velocity. The Doppler-selected imaging interferometry techniques were investigated using the radar backscatter model. The results verified the volume scatter predictions of *Briggs* [1995] and *Vandepeer and Reid* [1995], suggesting that the interferometry techniques cannot be successfully applied in the volume scatter situation.

9.2 Conclusions

The full correlation analysis (FCA) was the optimal spaced antenna techniques investigated in this thesis. The FCA was able to account for the effects of random changes in the ground diffraction pattern which resulted in the Doppler-selected imaging interferometry techniques overestimating the wind velocity. The FCA was also able to account for the effects of anisometry in the ground diffraction pattern which resulted in the velocity obtained from time-shift techniques such as the similar fades being biased perpendicularly to the azimuth of elongation of the ground diffraction pattern. The FCA was shown to correctly estimate the wind velocity in the presence of monochromatic waves if the results are averaged over the period of the wave. The FCA was also shown to produce estimates with smaller statistical errors than the full spectral analysis (FSA), which is the time-domain equivalent of the FCA, and the recently developed slope fitting correlation analysis.

In order for the FCA to perform optimally a number of factors must be taken into account. The correlation functions must be corrected for the effects of noise. This can be achieved by interpolating over the zero-lag auto-correlation to determine the "noise-free" estimate. This procedure requires the sampling time must be sufficiently short. The effects of time-series saturation and coarse digitization should also be avoided. If individual receiving channels are employed steps should be taken to minimize differences in the response between channels.

Such differences result in the attenuation of the cross-correlation functions, thereby producing the FCA triangle size effect (TSE). If the differences cannot be minimized significantly it may prove advantageous to multiplex the antennae though the same receiver. Alternatively, if the attenuation of the cross-correlation functions is similar (which should be the case in practice), the two 4-antenna spatial correlation functions can be employed to avoid the TSE. The time-series length should be made as long as feasible in order to increase the accuracy of the estimates.

9.3 Suggestions for further work

The work presented in this thesis provides a thorough investigation of a number of different spaced antenna techniques. The radar backscatter model has proven crucial to this investigation. It is envisaged that the model will remain considerably useful for the investigation of a variety of other spaced antenna and Doppler radar techniques such as those not investigated in this thesis, as well as for further investigations of the FCA. The analyses which could be investigated using the model include the post-set beam-steering, TDI, and imaging analyses described in Chapter 1. The model is also intended to be improved with the inclusion of the effects of spectrum of gravity waves, anisometric scatterers, and receiver polar diagrams. The model should also prove useful in the planning experiments to be conducted using various radar configurations, such as the upgraded BP MF radar.

The preliminary investigation of the three- and four-antenna spatial correlation analyses presented in Chapter 6 has proven very fruitful. This work should be followed up to properly determine the viability of the technique as a possible alternative to the FCA. In particular, the rejection criteria should be investigated more thoroughly, as it is clear that the embryonic version of the technique presented in Chapter 6 can produce some spurious velocity estimates.

Appendix A

Model-generated data-sets

This appendix provides the details of the model-generated data-sets employed throughout this thesis. These data-sets are referred to within the text by acronyms which indicate the origins and purpose behind the generation of the data.

- **MOD-MF-SA**

This is the standard MF SA data-set. This data was generated using the standard atmospheric, sampling, and SA polar diagram parameters outlined in Tables 3.1, 3.2, and 3.3, and Figure 3.5, with the use of isotropic turbulent velocities ranging from 0 to 6 ms^{-1} in 1 ms^{-1} intervals. 200 time-series realizations were generated for each turbulent velocity.

- **MOD-MF-IDI**

This data was generated to investigate the Doppler-selected imaging interferometry techniques. This data was generated using the same parameters for the data-set MOD-MF-SA, except for the antenna configuration, which was as shown in Figure A.1. The antennae are grouped into zonal and meridional "arms" with spacing $d = \lambda/2 = 75$ m. The transmitting antennae are centered at the position of the antenna 1.

- **MOD-MF-IDI-NSCAT**

This data-set was originally generated to investigate the effects of the number of model scatterers upon the Doppler-selected imaging interferometry techniques, and has subsequently been to investigate the effects of the number of model scatterers upon the FCA

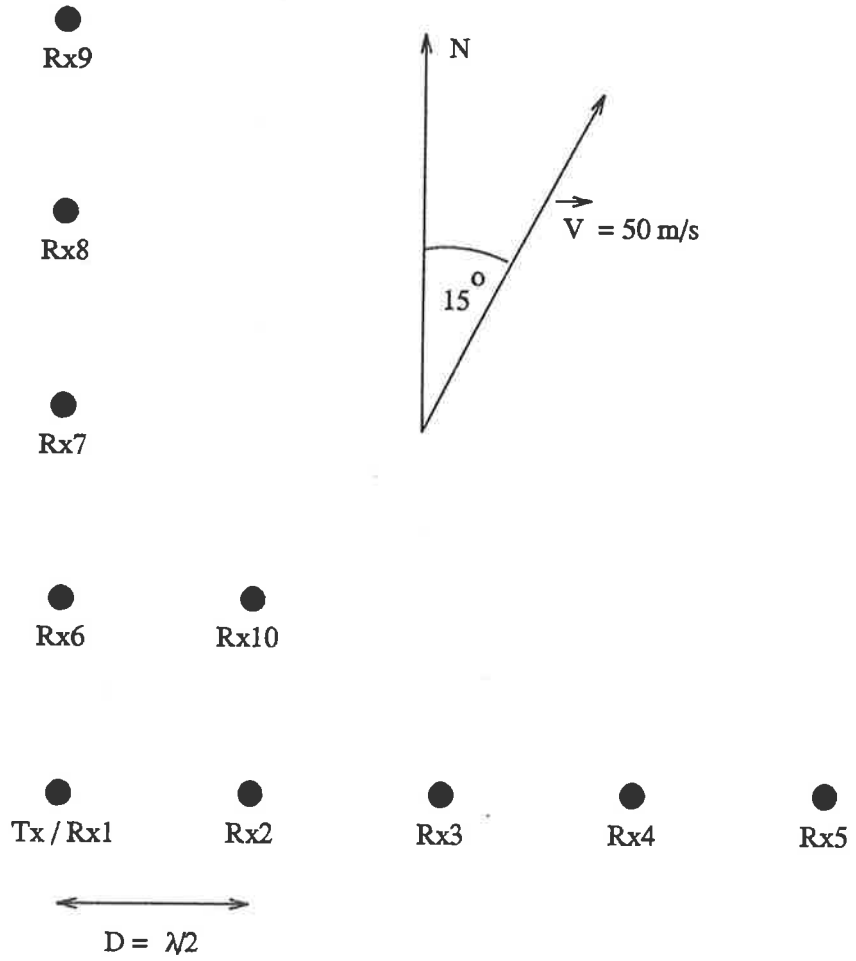

Figure A.1: Antenna configuration employed for model-generated data-set MOD-MF-IDI.

technique. The data was generated using the same model parameters as the data-set MOD-MF-IDI, using an antenna spacing of $d = \lambda = 150$ m with an isotropic turbulent velocity of 6 ms^{-1} only. The number of scatterers was varied from 10 to 1000, thereby ranging from the discrete to the volume scatter situation.

- **MOD-MF-IDI-ROTN**

This data-set was generated to determine whether the velocities estimated by the Doppler-selected imaging interferometry techniques are subject to directional biases. The data was generated using the same model parameters as the data-set MOD-MF-IDI, using model velocity directions ranging from 0° to 90° in intervals of 5°.

- **MOD-MF-IDI-ROTN2**

This data-set was generated to determine whether the velocities estimated by the Doppler-selected imaging interferometry techniques are subject to directional biases due to the effects of anisometric scatter. The data was generated using the same model parameters as the data-set MOD-MF-IDI-ROTN2, using a polar diagram elongated at an azimuth of $-45°$ with anisometry parameter $A = 2$. The ground diffraction pattern is therefore elongated at an azimuth of 45°.

- **MOD-MF-TSE**

This data was generated to investigate magnitude biases in the the FCA triangle size effect. This data was generated using the standard MF atmospheric, sampling, and SA polar diagram parameters outlined in Tables 3.1, 3.2, and 3.3. The antenna configuration employed is shown in Figure A.2. The antennae form seven equilateral triangles with spacings of 100, 150, 200, 250, 300, 350 and 400 m about a common central position which also marks the center of the transmitting antennae. 100 time-series realizations were generated.

- **MOD-MF-TSE-ROTN**

This data was generated to investigate directional biases in the FCA triangle size effect. This data was generated using the standard MF atmospheric, sampling, and SA polar diagram parameters outlined in Tables 3.1, 3.2, and 3.3, using model velocity directions ranging from 0° to 180° in intervals of 5° with no turbulent velocity. 20 time-series realizations were generated for each model velocity direction. The antenna configuration employed is shown in Figure A.3. The antennae form four equilateral and right-angled triangles. The spacings of the sides of the equilateral triangles, which are equal to the spacings of the smallest sides of the right-angled triangles, are 150, 200, 250, and 300 m. The equilateral triangles have a common midpoint which also marks the center of the transmitting antennae.

- **MOD-MF-ANISO**

This data was generated to investigate the effect of pattern anisometry upon the FCA. This data was generated using the standard MF atmospheric, sampling, and SA polar diagram parameters outlined in Tables 3.1, 3.2, 3.3, and Figure 3.5, using model velocity directions ranging from 0° to 180° in intervals of 5° with no turbulent velocity. The polar diagram was elongated at an azimuth of 90° with anisometry parameters A ranging from 1 to 3, thereby resulting in the ground diffraction pattern being elongated in the meridional

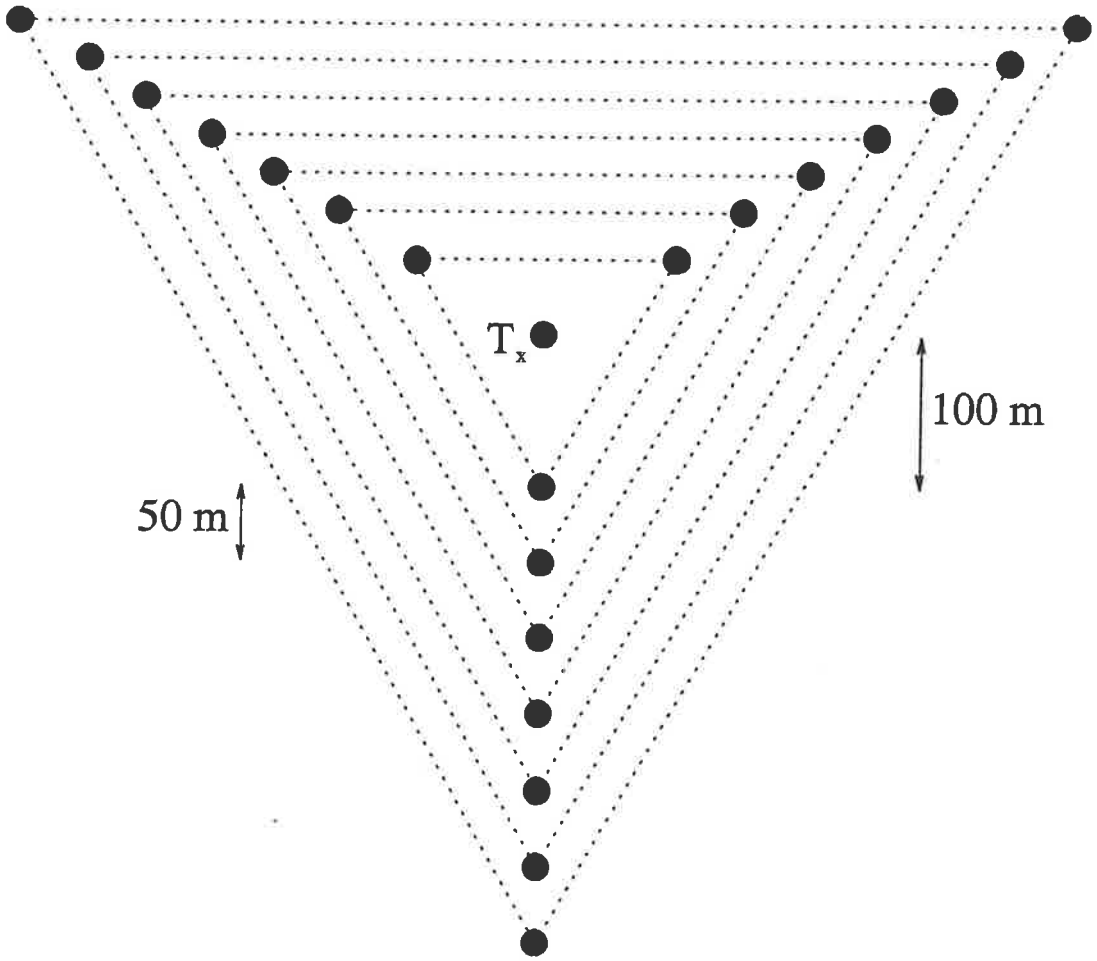

Figure A.2: Antenna configuration employed for model-generated data-set MOD-MF-TSE. The dotted lines indicate the different sized triangles used for the analysis.

direction.

- **MOD-MF-GDP**

This data was generated to produce images of the ground diffraction pattern. This data was generated using the standard MF atmospheric, sampling, and SA polar diagram parameters outlined in Tables 3.1, 3.2, and 3.3. The antenna configuration consisted of a grid of 31 by 31 antennae with spacing 50 m, covering a range 1500 m. Four data-sets were generated. The data set MOD-MF-GDP-V50 used a model velocity of magnitude 50 ms^{-1} and direction 90° with no turbulent velocity. The data-set MOD-MF-GDP-V50-T6 used a model velocity of magnitude 50 ms^{-1} and direction 90° with an isotropic turbulent velocity of 6 ms^{-1}. The data set MOD-MF-GDP-V0-T6 used a model velocity of zero and a rms velocity of 6 ms^{-1}. The data-set MOD-MF-GDP-V50-T6-AN used a model velocity of

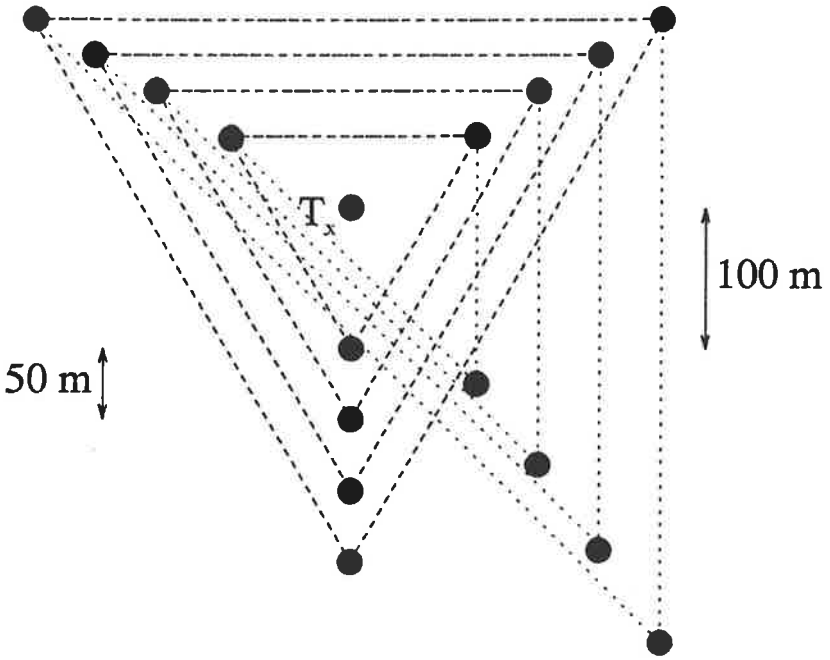

Figure A.3: Antenna configuration employed for model-generated data-set MOD-MF-TSE. The dashed lines indicates the different sized equilateral triangles, while the dotted lines indicates the different sized right-angled triangles.

magnitude 50 ms^{-1} and direction 90° with an isotropic turbulent velocity of 6 ms^{-1}, with the polar diagram elongated at an azimuth of $-45°$ with anisometry parameters $A = 2$. The resultant pattern is therefore elongated in the direction 45° clockwise from North.

- **MOD-MF-ASP-SEN**

This data-set was generated to verify the model aspect sensitivity simulation. The data was generated using the standard MF atmospheric, sampling, and SA polar diagram parameters outlined in Tables 3.1, 3.2, 3.3, and Figure 3.5, using an isotropic turbulent velocity of 0 ms^{-1} and an aspect sensitivity parameter θ_s ranging from 2 to 10 degrees, in intervals of 2 degrees. 100 time-series realizations were generated for each value of θ_s.

- **MOD-MF-TURB**

This data-set was generated to verify the model turbulence simulation. The data was generated using the standard MF atmospheric, sampling, and Doppler polar diagram parameters outlined in Tables 3.1, 3.2, 3.4, and Figure 3.5, with an isotropic turbulent velocity ν_{mod} ranging from 0 to 6 ms^{-1} in intervals of 1 ms^{-1}. 100 time-series realizations were generated for each value of ν_{mod}.

- **MOD-MF-4096**

This data-set was generated to investigate the effects of time-series length upon the FCA and FSA. The data was generated using the standard MF atmospheric, sampling, and SA polar diagram parameters outlined in Tables 3.1, 3.2, 3.3, and Figure 3.5, with isotropic turbulent velocities ν_{mod} of 0 and 6 ms^{-1} and a sample length of 4096. 50 time-series realizations were generated for each value of ν_{mod}.

- **MOD-MF-DOPP**

This data-set was generated to verify the Doppler radar simulation. The data was generated using the standard MF atmospheric, sampling, and Doppler polar diagram parameters outlined in Tables 3.1, 3.2, 3.4, and Figure 3.5, with isotropic turbulent velocities ν_{mod} of 0 and 6 ms^{-1}, and beams directed vertically, northwards and eastwards. The off-zenith beams were tilted at an angle of 10°.

- **MOD-VHF-SAMP**

This data was generated to investigate the effect of the sampling time upon the FCA. This data was generated using the standard VHF atmospheric, sampling, and SA polar diagram parameters outlined in Tables 3.1, 3.2, 3.3, and Figure 3.5, with no turbulent velocity. 100 time-series realizations were generated.

- **MOD-VHF-VEL**

This data was generated to illustrate the velocity fall-off resulting from using too a large sampling time. This data was generated using the standard VHF atmospheric, sampling, and SA polar diagram parameters outlined in Tables 3.1, 3.2, 3.3, and Figure 3.5, with model input velocity magnitudes between 10 and 60 ms^{-1} in intervals of 5ms^{-1} and no turbulent velocity. 100 time-series realizations were generated for each value of the model input velocity.

Appendix B

The time-displacement technique

The "time-displacement" technique (e.g. *Mitra*, [1949]) uses the time-displacements measured between the signals recorded by a minimum of three spaced receiving antennae to provide an estimate of the horizontal wind velocity. In the original implementation of the technique the time-displacements for each pair of receiving antennae were determined by temporally shifting one time-series record with respect to the other and determining the time "lag" where the records best resembled each other. Since the advent of modern computers these time-displacements have been calculated using the time-lags of maximum cross-correlation between the records.

Consider the situation depicted in Figure B.1 of three antennae A_i, A_j, and A_k, arranged in a right angled triangle, sampling a ground diffraction pattern propagating with velocity $\vec{V}$ at an angle ϕ clockwise from north. Let τ'_{ij} be the time-delay between the signals received at antennae A_i and A_j. In this time the vector displacement of the ground diffraction pattern is given by $\vec{V}\tau'_{ij}$. The time-delay τ'_{ij} can therefore be expressed

$$\tau'_{ij} = \frac{\xi_{ij} \sin \phi}{V}. \tag{B.1}$$

The velocity with which the pattern propagates along the zonal axis is the "trace-velocity" V_x, which is given by

$$\begin{aligned} V_x &= \frac{\xi_{ij}}{\tau'_{ij}} \\ &= \frac{V}{\sin \phi}. \end{aligned} \tag{B.2}$$

Similarly, the time-delay τ'_{ik} between the signals received at A_i and A_k with meridional separation η_{ik} will be given by

$$\tau'_{ik} = \frac{\eta_{ik} \cos \phi}{V}, \tag{B.3}$$

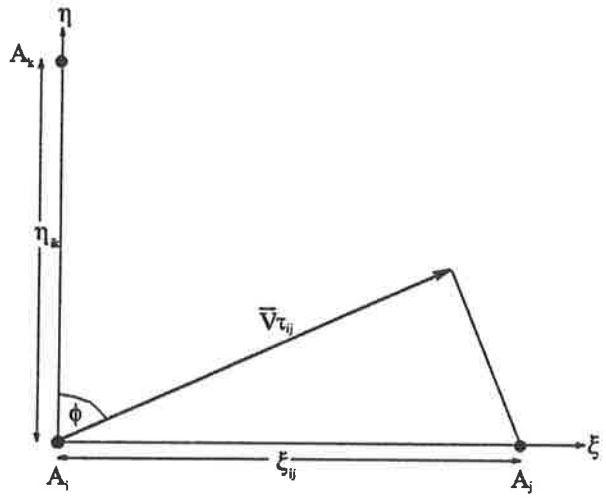

Figure B.1: Illustration of the derivation of (B.2). The lag τ_{ij} denotes the time-delay between the signals received at antennae A_i and A_j. The vector $\vec{V}\tau_{ij}$ denotes the displacement of the ground diffraction pattern (propagating with velocity $\vec{V}$) in this time interval.

with the corresponding trace velocity defined by

$$\begin{aligned} V_y &= \frac{\eta_{ik}}{\tau'_{ik}} \\ &= \frac{V}{\cos\phi}. \end{aligned} \tag{B.4}$$

Note that the trace velocities are not the components of the pattern velocity. The pattern velocity $\vec{V}$ can be calculated from the trace velocities by the geometrical construction shown in Figure B.2, yielding the equations

$$v = \frac{V_x V_y}{\sqrt{V_x^2 + V_y^2}} \tag{B.5}$$

and

$$\phi = \arctan\left(\frac{V_y}{V_x}\right) \tag{B.6}$$

For the more general case where the antenna separations are not zonally and meridionally aligned the zonal and meridional trace velocities must be determined in an alternative manner. The technique used involves defining the velocities

$$V_{\xi_{ij}} = \frac{\xi_{ij}}{\tau'_{ij}}, \tag{B.7}$$

and

$$V_{\eta_{ij}} = \frac{\eta_{ij}}{\tau'_{ij}}. \tag{B.8}$$

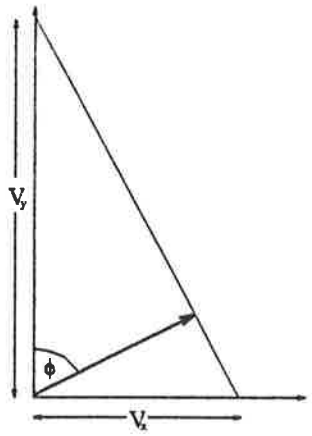

Figure B.2: Geometrical construction illustrating the calculation of the velocity $\vec{V}$ from the trace velocities V_x and V_y.

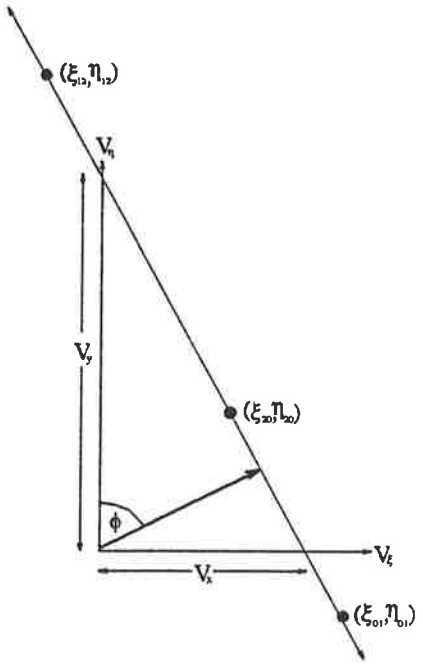

Figure B.3: Geometrical construction illustrating the calculation of the velocity $\vec{V}$ from the trace velocities V_x and V_y for the general case of non right-angled triangle.

for each antennae pair ij, where τ'_{ij} are the cross-correlation maxima delays times, and ξ_{ij} and η_{ij} denote the zonal and meridional separations of the antennae, respectively. Plotting the $(V_{\xi_{ij}}, V_{\eta_{ij}})$ pairs yields a linear variation, as illustrated in Figure B.3. In practice there may be some variation in the points so that they cannot be fitted precisely a linear fit. The trace velocities V_x and V_y are the zonal and meridional intercepts respectively of the fitted line. The velocity estimate is obtained by substituting the trace velocities into (B.5) and (B.6).

Appendix C

Correlation functions

Correlation functions are used extensively throughout this thesis. The definitions of the various correlation functions referred to are provided in this appendix. The correlation functions are defined in terms of the complex function $f(x, y, t)$ describing the ground diffraction pattern in terms of zonal and meridional coordinates x and y, respectively, and the temporal coordinate t. For the sake of simplicity, $f(x, y, t)$ is assumed to have zero mean.

C.1 The spatio-temporal correlation function

The two-dimensional spatio-temporal correlation function of $f(x, y, t)$ is defined by (e.g. *Ratcliffe*, [1956])

$$\rho(\xi, \eta, \tau) = \frac{< f(x, y, t)\, f^*(x + \xi, y + \eta, t + \tau) >}{\sqrt{< |f(x, y, t)|^2 >< |f(x + \xi, y + \eta, t)|^2 >}}, \tag{C.1}$$

where η and ξ are the zonal and meridional spatial lags, respectively, and τ is the temporal lag. The brackets $< >$ and $|\ |$ denote the average of the enclosed quantity over all spatial and temporal lags and the absolute value of the enclose quantity, respectively, while $(^*)$ denotes the complex conjugate.

In any experimental situation the function $f(x, y, t)$ will be sampled at a number of discrete positions and times. Let these discrete positions be denoted

$$\begin{aligned} x_i &= x_0 + i\triangle x, \quad i = 1, N_\xi, \\ y_j &= y_0 + j\triangle y, \quad j = 1, N_\eta, \\ t_k &= t_0 + k\triangle t, \quad k = 1, N_\tau, \end{aligned} \tag{C.2}$$

The spatio-temporal correlation function can only be evaluated at discrete positions and times given by

$$\begin{aligned} \xi_i &= i\triangle x, \quad i = -N_\xi + 1, N_\xi - 1, \\ \eta_j &= j\triangle y, \quad j = -N_\eta + 1, N_\eta - 1, \\ \tau_k &= k\triangle t, \quad k = -N_\tau + 1, N_\tau - 1. \end{aligned} \tag{C.3}$$

At the position (ξ_i, η_j, τ_k) the averaging denoted by the numerator of (C.1) can be evaluated by summing over all possible spatial and temporal lags and dividing by the total number of lags

$$< f(x,y,t)\, f^*(x+\xi_i, y+\eta_j, t+\tau_k) >= \frac{\sum_{l=1}^{N_\xi-|i|}\sum_{m=1}^{N_\eta-|j|}\sum_{n=1}^{N_\tau-|k|} f(x_l,y_m,t_n) f^*(x_l+\xi_i, y_m+\eta_j, t_n+\tau_k)}{(N_\xi-|i|)(N_\eta-|j|)(N_\tau-|k|)}. \tag{C.4}$$

After evaluating the denominator of (C.1) in an analogous manner, the spatio-temporal correlation function at position (ξ_i, η_j, τ_k) can be written

$$\rho(\xi_i,\eta_j,\tau_k) = \frac{\sum_{l=1}^{N_\xi-|i|}\sum_{m=1}^{N_\eta-|j|}\sum_{n=1}^{N_\tau-|k|} f(x_l,y_m,t_n)\, f^*(x_l+\xi_i, y_m+\eta_j, t_n+\tau_k)/(N_\tau-|k|)}{\sqrt{\sum_{l=|i|}^{N_\xi}\sum_{m=|j|}^{N_\eta}\sum_{n=|k|}^{N_\tau}|f(x_l,y_m,t_n)|^2}\sqrt{\sum_{l=0}^{N_\eta-|i|}\sum_{m=0}^{N_\xi-|j|}\sum_{n=0}^{N_\tau-|k|}|f(x_l,y_m,t_n)|^2}}. \tag{C.5}$$

The two-dimensional spatio-temporal correlation function $\rho(\xi,\tau)|_y$ at meridional position y is given by

$$\rho(\xi,\tau)|_y = \frac{< f(x,y,t)\, f^*(x+\xi,y,t+\tau) >}{\sqrt{< |f(x,y,t)|^2 >< |f(x+\xi,y,t)|^2 >}}. \tag{C.6}$$

In the discrete-sampling situation the two-dimensional spatio-temporal correlation function can be evaluated at all meridional positions y_m as defined by (C.2) using the equation

$$\rho(\xi_i,\tau_k)|_{y_m} = \frac{\sum_{l=1}^{N_\xi-|i|}\sum_{n=1}^{N_\tau-|k|} f(x_l,y_m,t_n)\, f^*(x_l+\xi_i, y_m, t_n+\tau_k)}{(N_\tau-|k|)\sqrt{\sum_{l=|i|}^{N_\xi}\sum_{n=|k|}^{N_\tau}|f(x_l,y_m,t_n)|^2}\sqrt{\sum_{l=1}^{N_\xi-|i|}\sum_{n=1}^{N_\tau-|k|}|f(x_l,y_m,t_n)|^2}}. \tag{C.7}$$

The two-dimensional spatio-temporal correlation function at zero meridional spatial lag $\rho(\xi_i, 0, \tau_k)$ can be considered the "average" of the spatial-correlation functions over all meridional spatial lags y_m, and therefore provides a statistically more reliable estimate of the two-dimensional spatial correlation function $\rho(\xi_i, \tau_k)$. The two-dimensional spatio-temporal correlation function $\rho(\eta,\tau)$ can be defined in a similar manner as described for $\rho(\xi,\tau)$.

C.2 The spatial-correlation function

The spatial correlation function of $f(x, y, t)$ at time t is defined by

$$\rho(\xi, \eta)|_t = \frac{< f(x, y, t)\, f^*(x + \xi, y + \eta, t) >}{\sqrt{< |f(x, y, t)|^2 >}}. \tag{C.8}$$

In the discrete sampling situation the spatio-temporal correlation function can be evaluated at all times t_k as defined by (C.2) using the equation

$$\rho(\xi_i, \eta_j)|_{t_k} = \tag{C.9}$$
$$\frac{\sum_{l=1}^{N_\xi - |i|} \sum_{m=1}^{N_\eta - |j|} f(x_l, y_m, t_k)\, f^*(x_l + \xi_i, y_m + \eta_j, t_k)}{(N - |k|)\sqrt{\sum_{l=|i|}^{N_\xi} \sum_{m=|j|}^{N_\eta} |f(x_l, y_m, t_k)|^2} \sqrt{\sum_{l=1}^{N_\xi - |i|} \sum_{m=1}^{N_\eta - |j|} |f(x_l, y_m, t_k)|^2}}.$$

The two-dimensional spatio-temporal correlation at zero temporal lag $\rho(\xi_i, \eta_j, 0)$ can be considered the "average" of the spatial-correlation functions over all temporal lags t_k, and therefore provides a statistically more reliable estimate of the spatial correlation function.

C.3 The auto-correlation function

The auto-correlation function for time-series measured at position $a = (x_i, y_j)$ is defined by

$$\rho_a(\tau_k) = \frac{< f_a(t)\, f_a^*(t + \tau_k) >}{< |f_a(t)|^2 >}. \tag{C.10}$$

The auto-correlation functions measured at each position are theoretically identical. As a result, the positional subscript a is usually not used, and will be dropped hereafter. In practice, small statistical differences are introduced because each position samples a different cross-section of the ground diffraction pattern. After evaluating the averaging, (C.10) can be rewritten

$$\rho(\tau_k) = \frac{\sum_{n=1}^{N_\tau - |k|} f_a(t_n)\ f_a^*(t_n + \tau_k)}{(N_\tau - |k|) \sum_{n=1}^{N_\tau} |f_a(t_n)|^2} \tag{C.11}$$

In the situation where the (C.10) is used without the denominator the function is referred to as the auto-covariance function.

C.4 The cross-correlation function

The cross-correlation function for time-series measured at positions $a = (x_i, y_j)$ and $b = (x_l, y_m)$ is defined by

$$\rho_{ab}(\tau_k) = \frac{< f_a(t)\, f_b^*(t + \tau_k) >}{\sqrt{< |f_a(t)|^2 >< |f_b(t)|^2 >}}. \tag{C.12}$$

After evaluating the averaging, (C.12) can be rewritten

$$\rho_{ab}(\tau_k) = \frac{\sum_{n=1}^{N_\tau - |k|} f_a(t_n)\ f_b^*(t_n + \tau_k)}{(N_\tau - |k|)\sqrt{\sum_{n=1}^{N_\tau} |f_a(t_n)|^2 \sum_{n=1}^{N_\tau} |f_b(t_n)|^2}}. \tag{C.13}$$

In the situation where the (C.12) is used without the denominator the function is referred to as the cross-covariance function.

C.5 The effect of noise upon the correlation functions

Let $f_i(t)$ be the time-series sampled by receiving antenna A_i. This time-series will be composed of signal $s_i(t)$ and noise $n_i(t)$ components

$$f_i(t) = s_i(t) + n_i(t). \tag{C.14}$$

As the signal and noise components are independent and have zero mean it follows that

$$< s_i(t)\ n_j^*(t+\tau) >= 0, \quad \forall\ i, j, \tau. \tag{C.15}$$

The noise component will be composed of noise which is correlated between antenna pairs $n_{ci}(t)$ such as atmospheric, mains, and man made noise, and noise which is uncorrelated between antenna pairs $n_{ui}(t)$ such as receiver or galactic noise

$$n_i(t) = n_{ci}(t) + n_{ui}(t). \tag{C.16}$$

As both correlated and uncorrelated noise components are uncorrelated over time if follows that

$$< n_i(t)\ n_i^*(t+\tau) >= 0, \quad \tau \neq 0, \tag{C.17}$$

$$< n_i(t)\ n_j^*(t+\tau) >= 0, \quad \tau \neq 0,\ i \neq j \text{ if } \tau = 0, \tag{C.18}$$

$$< n_{ci}(t)\ n_{ci}^*(t+\tau) >= 0, \quad \tau \neq 0, \tag{C.19}$$

$$< n_{ci}(t)\ n_{uj}^*(t+\tau) >= 0, \quad \forall\ i, j, \tau, \tag{C.20}$$

$$< n_{ui}(t)\ n_{uj}^*(t+\tau) >= 0, \quad \tau \neq 0,\ i \neq j \text{ if } \tau = 0. \tag{C.21}$$

The cross-correlation function for time-series $f_i(t)$ and $f_j(t)$ is given by

$$\rho_{ij}(\tau) = \frac{< f_i(t)\ f_j^*(t+\tau) >}{\sqrt{< |f_i(t)|^2 >< |f_j(t)|^2 >}}. \tag{C.22}$$

If the time-series are specified in terms of the signal and noise components, the cross-correlation function can be rewritten

$$\rho_{ij}(\tau) = \frac{< (s_i(t) + n_i(t))(s_j(t+\tau) + n_j(t+\tau))^* >}{\sqrt{< |s_i(t) + n_i(t)|^2 >< |s_j(t) + n_j(t)|^2 >}}. \quad \text{(C.23)}$$

Expanding the numerator, we obtain

$$\begin{aligned} N(\rho_{ij}(\tau)) = \; & < s_i(t)\, s_j^*(t+\tau) > \; + \; < s_i(t)\, n_j^*(t+\tau) > \; + \\ & < n_i(t)\, s_j^*(t+\tau) > \; + \; < n_i(t)\, n_j^*(t+\tau) > . \end{aligned} \quad \text{(C.24)}$$

Using (C.15), the terms $< s_i(t)\, n_j^*(t+\tau) >$ and $< n_i(t)\, s_j^*(t+\tau) >$ become zero. Expanding the last term of the numerator yields

$$\begin{aligned} < n_i(t)\, n_j^*(t+\tau) > = \; & < n_{ci}(t)\, n_{cj}^*(t+\tau) > \; + \; < n_{ci}(t)\, n_{uj}^*(t+\tau) > \; + \\ & < n_{ui}(t)\, n_{cj}^*(t+\tau) > \; + \; < n_{ui}(t)\, n_{uj}^*(t+\tau) > . \end{aligned} \quad \text{(C.25)}$$

Using (C.20) and (C.21), the last three terms on the right hand side of (C.25) become zero. Using (C.19), the first term on the right hand side becomes zero when $\tau \neq 0$. The denominator can therefore be written

$$N(\rho_{ij}(\tau)) = < s_i(t)\, s_j^*(t) > \; + \; < n_{ci}(t)\, n_{cj}^*(t+\tau) >, \quad \tau = 0, \quad \text{(C.26)}$$

$$< s_i(t)\, s_j^*(t) > \qquad \tau \neq 0. \quad \text{(C.27)}$$

Expanding the denominator, we obtain

$$D(\rho_{ij}(\tau)) = \quad \text{(C.28)}$$

$$\sqrt{< s_i(t)\, s_i^*(t) > + < s_i(t)\, n_i^*(t) > + < n_i(t)\, s_i^*(t) > + < n_i(t)\, n_i^*(t) >}$$

$$\sqrt{< s_j(t)\, s_j^*(t) > + < s_j(t)\, n_j^*(t) > + < n_j(t)\, s_j^*(t) > + < n_j(t)\, n_j^*(t) >}$$

which, using (C.15) and (C.18), reduces to

$$D(\rho_{ij}(\tau)) = \sqrt{(< |s_i(t)|^2 > \; + \; < |n_i(t)|^2 >)(< |s_j(t)|^2 > \; + \; < |n_j(t)|^2 >)} \quad \text{(C.29)}$$

The cross-correlation function can therefore be written

$$\rho_{ij}(\tau) = \frac{< s_i(t)\, s_j^*(t) > + \; < n_{ci}(t)\, n_{cj}^*(t) >}{\sqrt{(< |s_i(t)|^2 > + < |n_i(t)|^2 >)(< |s_j(t)|^2 > + < |n_j(t)|^2 >)}}, \tau = 0 \quad \text{(C.30)}$$

$$\frac{< s_i(t)\, s_j^*(t+\tau) >}{\sqrt{(< |s_i(t)|^2 > + < |n_i(t)|^2 >)(< |s_j(t)|^2 > + < |n_j(t)|^2 >)}}, \tau \neq 0. \quad \text{(C.31)}$$

The auto-correlation function for time-series $f_i(t)$ is given by

$$\rho(\tau) = \frac{< f_i(t)\, f_i^*(t+\tau) >}{< |f_i(t)|^2 >}. \tag{C.32}$$

If the time-series is specified in terms of the signal and noise components, the auto-correlation function can be rewritten

$$\rho(\tau) = \frac{< (s_i(t) + n_i(t))(s_i(t+\tau) + n_i(t+\tau))^* >}{< |s_i(t) + n_i(t)|^2 >}. \tag{C.33}$$

Expanding the numerator, we obtain

$$\begin{aligned} N(\rho(\tau)) = \; & < s_i(t)\, s_i^*(t+\tau) > \; + \; < s_i(t)\, n_i^*(t+\tau) > \; + \\ & < n_i(t)\, s_i^*(t+\tau) > \; + \; < n_i(t)\, n_i^*(t+\tau) > . \end{aligned} \tag{C.34}$$

Using (C.15), the second and third terms on the right hand side of (C.34) become zero. Using (C.17), the last term becomes zero when $\tau \neq 0$. The numerator can therefore be written

$$N(\rho(\tau)) = \; < |s_i(t)|^2 > \; + \; < |n_i(t)|^2 >, \quad \tau = 0 \tag{C.35}$$

$$< s_i(t)\, s_i^*(t+\tau) >, \qquad \tau \neq 0 \tag{C.36}$$

Expanding the denominator, we obtain

$$\begin{aligned} D(\rho(\tau)) = \; & < s_i(t)\, s_i^*(t) > \; + \; < s_i(t)\, n_i^*(t) > \; + \\ & < n_i(t)\, s_i^*(t) > \; + \; < n_i(t)\, n_i^*(t) > . \end{aligned} \tag{C.37}$$

Using (C.15), the second and third terms on the right hand side of (C.37) become zero, allowing the denominator to be rewritten

$$D(\rho(\tau)) = < |s_i(t)|^2 > \; + \; < |n_i(t)|^2 > \tag{C.38}$$

The auto-correlation function can therefore be written

$$\rho(\tau) = \quad 1, \qquad \tau = 0 \tag{C.39}$$

$$\frac{< s_i(t)\, s_i^*(t+\tau) >}{< |s_i(t)|^2 > \; + \; < |n_i(t)|^2 >}, \quad \tau \neq 0. \tag{C.40}$$

The correlation functions resulting from the addition of various different amounts of uncorrelated noise are shown in Figure C.1. The presence of noise produces a zero-lag auto-correlation "spike". The spike becomes more pronounced as the noise level is increased. This is a result of the denominator of (C.39) increasing with increasing noise-level, thereby reducing the auto- and cross-correlation at all non-zero lags.

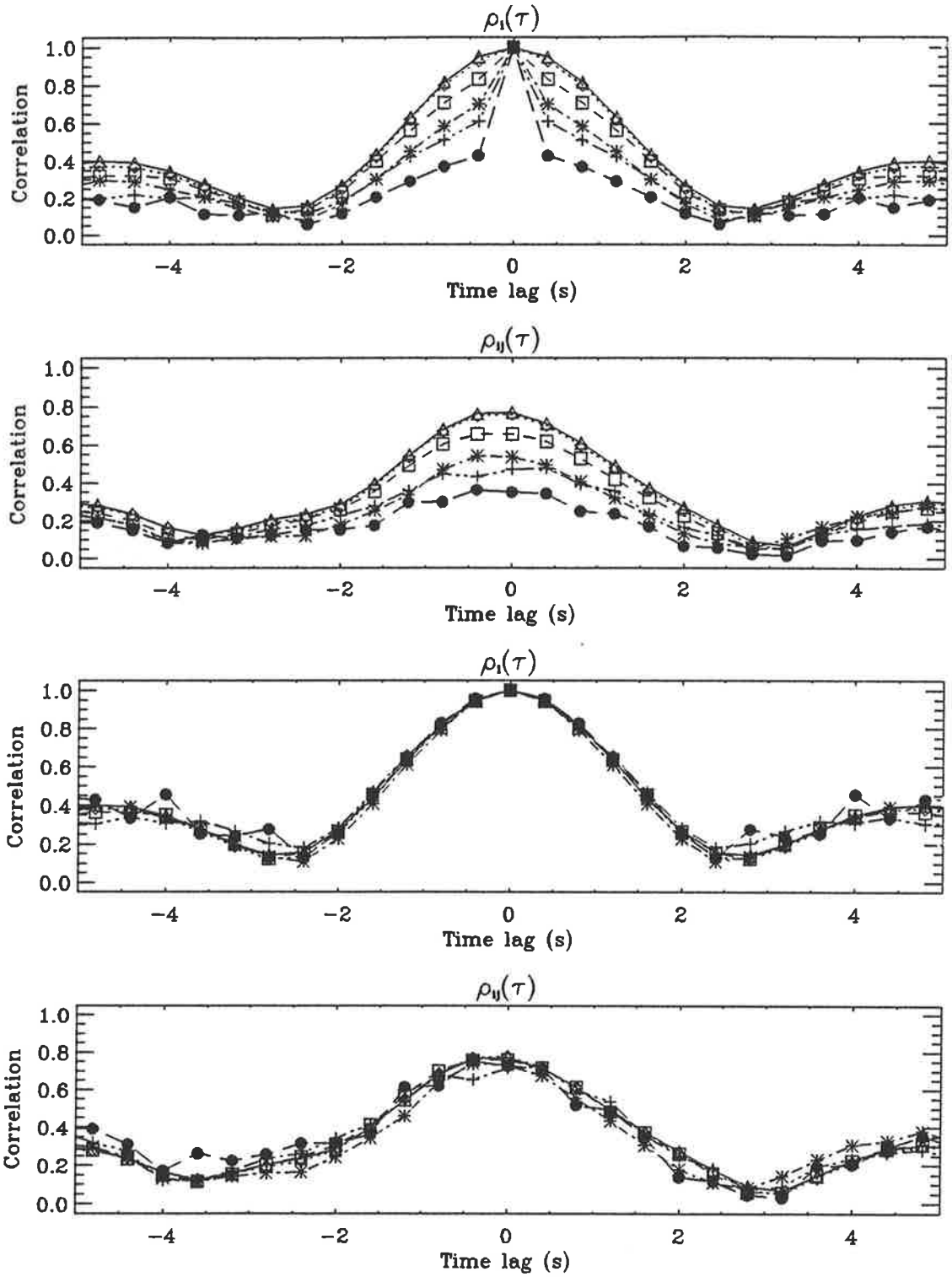

Figure C.1: Example of the effects of the addition of various different amounts of uncorrelated noise on the auto- (top left) and cross-correlation (top right) functions. The bottom plots show the corresponding noise corrected correlation functions. SNRs: 100 dB (△), 16 dB (◇), 8 dB (□), 4 dB (*), 2 dB (+), 0 dB (•).

C.6 Correction for the effects of noise

The theory of the FCA is based on the assumption that the correlation functions are "noise-free". As a result, the effects of noise must be removed from the correlation functions. This is achieved as follows. Firstly, the zero-lag auto-correlation is substituted by a "noise-free" estimate, producing the revised function

$$\rho(\tau) = \frac{< s_i(t)\ s_i^*(t+\tau) >}{< |s_i(t)|^2 > + < |n_i(t)|^2 >}. \tag{C.41}$$

This function is then renormalized by the factor

$$F_i = \frac{< |s_i(t)|^2 > + < |n_i(t)|^2 >}{< |s_i(t)|^2 >}. \tag{C.42}$$

to produce the noise-free auto-correlation function

$$\rho(\tau) = \frac{< s_i(t)\ s_i^*(t+\tau) >}{< |s_i(t)|^2 >}. \tag{C.43}$$

The zero-lag cross-correlation is substituted by a noise-free estimate, producing the revised function

$$\rho_{ij}(\tau) = \frac{< s_i(t)\ s_j^*(t+\tau) >}{\sqrt{(< |s_i(t)|^2 > + < |n_i(t)|^2 >)(< |s_j(t)|^2 > + < |n_j(t)|^2 >)}}. \tag{C.44}$$

This function is then renormalized by the factor

$$\sqrt{F_i F_j} \tag{C.45}$$

to produce the noise-free cross-correlation function

$$\rho_{ij}(\tau) = \frac{< s_i(t)\ s_j^*(t+\tau) >}{\sqrt{< |s_i(t)|^2 >< |s_j(t)|^2 >}}. \tag{C.46}$$

The results of this procedure are illustrated in Figure C.1. The noise corrected correlation functions are now almost identical to the noise-free correlation functions. As described in section 4.6, the accuracy of this procedure is limited by the sampling time. If the sampling time is too coarse there will only be a few lags on the main peak of the correlation functions. This can result in the interpolated zero-lag auto-correlation being underestimated, which will result in an over-normalization of the cross-correlation function.

C.7 Application of correlation functions

The correlation functions employed by the FCA can also be used for the determination of other useful parameters, such as radial velocity, receiver signal to noise ratios and the mean angle of arrival (MAOA) of the radiowave backscatter. The estimation of the radial velocity and the MAOA are outlined in Chapter 8.

The signal to noise ratio SNR for receiver i is usually defined as

$$\text{SNR} = 10 \log_{10} \left(\frac{< |s_i(t)|^2 >}{< |n_i(t)|^2 >} \right). \tag{C.47}$$

where $s_i(t)$ and $n_i(t)$ are the signal and noise contributions to the time-series as defined by (C.14). This equation can be rewritten

$$\text{SNR} = 10 \log_{10} \left(\frac{\rho_{nf}(0)}{1 - \rho_{nf}(0)} \right). \tag{C.48}$$

where

$$\rho_{nf}(0) = \left(\frac{< |s_i(t)|^2 >}{< |s_i(t)|^2 > + < |n_i(t)|^2 >} \right). \tag{C.49}$$

is the noise-free estimate of the zero-lag auto-correlation estimated during the noise-removal procedure.

Appendix D

The FCA rejection criteria

The FCA employs a set of rejection criteria. The error codes for the rejection criteria are shown in Table D.1. The error code zero indicates the analysis has passed all rejection criteria. The rejection of a record can be put down to at least one of three causes:

D.1 Record unsuitable for analysis

The error codes 1 and 2 result from the record being unsuitable for analysis. Such records are rejected prior to the application of the FCA.

- The error code 1 is employed in order to prevent the analysis of records with low signal level. In such instances the coarse digitization can result in the true velocity magnitude V_i being significantly underestimated, as discussed in Chapter 5.
- The error code 2 is employed to prevent the analysis of records with low SNR. This rejection criterion is applied because the corrections required for the effects of noise as outlined in Appendix C become difficult when the amplitudes of signal and noise components are comparable, as discussed in Chapter 5.

D.2 Unsuccessful correlation parameter estimation

The unsuccessful estimation of the correlation parameters can be attributed to a number of causes. It may be due to deficiencies in the correlation functions themselves, or due to errors in the fitting procedures used to estimate the correlation functions. The error codes 3 and 4 originated from real-time analysis. In order to complete the analysis of a record prior to

Table D.1: The FCA rejection criteria

Code	Explanation
0	Record accepted
1	Low signal amplitude
2	SNR < -6 dB
3	$\tau_{0.5} > 6$ s Auto-correlation above 0.5 at greatest calculated lag Oscillatory Mean auto-correlation function
4	Slow fading
5	$NTD > 0.5$
6	$K < 0$
7	Breakdown in pattern analysis
8	$V_a > 250$ ms^{-1}
9	$\lvert\theta_t - \theta_a\rvert > 40°$
10	$V_a > 4\, V_t$
11	$V_t > 1.5\, V_a$
12	Poor fit to cross-correlation function
13	$\rho_{0ij} < 0.2$
14	Poor zero-lag auto-correlation interpolation
15	Maths error

the availability of the succeeding record the correlation functions were calculated to a small number of lags. Although such time restrictions no longer exist these error codes have been maintained.

- Error code 3 results when the estimated half-width $\tau_{0.5}$ of the mean auto-correlation function exceeds 6 s. Large fading times $\tau_{0.5}$ are generally indicative of specular scatter rather than the volume scatter assumed by the FCA (see section 4.7). Specular scatter generally produces time-series with a small number of dominant frequency components, resulting in oscillatory time-series and correlation functions. In this instance $\tau_{0.5}$ is influenced by the periods of dominant frequency components rather than the fading period resulting from volume scatter. As a result, the error code 3 is employed to reject records producing either large fading times or oscillatory correlation functions.

- Error code 4 results when at least one of the cross-correlation maxima delays τ'_{ij} lies outside the calculated range of the cross-correlation functions. This usually indicates that the main peak of the corresponding cross-correlation function is subdued. This effect can occur if the pattern scale is less than the antenna spacing, such that the correlation between the time-series recorded by the antennas is small, as discussed in

Chapter 5.

- Error code 5 results if the normalized time discrepancy

$$NTD = \frac{|\sum \tau'_{ij}|}{\sum |\tau'_{ij}|} \tag{D.1}$$

exceeds 0.5. The sum of the τ'_{ij} values around a closed triangle should theoretically sum to zero. In practice, statistical variations and noise can result in the sum being non-zero. The criterion is therefore relaxed somewhat. The results of *Røyrvik* [1983] suggest that this criterion may act to select records with larger wind velocities, thereby biasing the average velocity estimate towards higher absolute values. The results of *Meek* [1984a] suggest that the number of records precluded from the analysis by this criterion increases with increasing antenna spacing. The failure to satisfy this criterion indicates that at least one of the estimated τ'_{ij} values may be incorrect. This can result if the cross-correlation function has two peaks with similar magnitude. This effect can result from abrupt changes in the wind velocity, such that two peaks are seen corresponding to the two distinct velocities, or from fringes in the ground diffraction pattern resulting from the interference of the backscatter from two or more specular scatterers (e.g. *Holmes*, [1974]; *Meek*, [1984b]).

- Error codes 12 to 17 result from the failure of the fitting routines to successfully estimate the correlation parameters. Error code 12 results if any of the τ'_{ij} estimates are nonsensical, indicating that the Gaussian fit to the cross-correlation function has failed. Error code 13 results if any of the ρ_{0ij} estimates are less than 0.2, suggesting that either that the fit has failed or that the correlation is too small to be able provide accurate FCA output. Error code 14 results if any of the interpolated zero-lag auto-covariances are less than zero. This effect can occur if the auto-correlation function has a "jagged" appearance, as is sometimes the case for low SNRs. Error code 15 results when mathematical errors occur within the fitting routines. This is an extremely rare occurrence for the analysis presented in this thesis.

D.3 Failure to satisfy theory of the FCA

The error codes 6 to 11 result from the failure of the data to satisfy the assumptions of the FCA.

- Error code 6 is employed to reject data where $K < 0$. The parameter K describes the magnitude of the random changes in the ground diffraction pattern. If there a few random changes in the pattern K will ideally be close to zero. Statistical variations may therefore result in K being less than zero. As a result, records producing small negative values of K are accepted in the analysis presented in this thesis, although $T_{0.5}$ is nonsensical. If $K < 0$, the magnitude of the apparent velocity V_a is usually smaller than the magnitude of the true velocity V_t. Preclusion of the records with error code 6 can therefore result in the FCA true velocity magnitude V_t being biased towards smaller absolute values.

- Error code 7 is employed to reject data which produces negative values of the ellipsoid parameters A and B, suggesting that FCA failed to successfully parameterize the spatio-temporal correlation function.

- Error code 8 results if the magnitude of the apparent velocity exceeds 250 ms^{-1}. This suggests that the random changes in the ground diffraction pattern are significantly larger than those expected in practice.

- Error codes 9 and 10 are employed to reject records where the correction for the effects of random changes and pattern anisometry, respectively, are inconceivably large. Error code 9 is employed to reject records where the direction of the true and apparent velocities differ by 40°. The results of section 4.4.2 suggest that such differences will only be obtained under conditions of extreme pattern anisometry which are very unlikely to occur in practice. Error code 10 is employed to reject records which suggest the random changes are significantly larger than those expected in practice. This results in the apparent velocity being overcorrected for the effects of random changes, thereby producing an underestimation of the true velocity magnitude V_t.

- Error code 11 is employed because random changes should produce apparent velocity magnitudes V_a larger than true velocity magnitudes V_t. The situation where the V_t is significantly larger than V_a suggests that the FCA failed to successfully parameterize the form of the spatio-temporal correlation function.

Appendix E

The FCA triangle size effect - directional biases

The model-generated data-set MOD-MF-TSE-ROTN has been employed to investigate the directional biases resulting from the TSE. This data-set consists of 100 time-series realizations obtained using model velocity directions ranging from 0° to 180° in 5° intervals. Both equilateral and right-angled triangles have been employed. Four different antenna spacings ranging from 150 to 350 m have been employed. For the right-angled triangles these spacings correspond to the lengths of the two shortest sides. This range of antenna spacings encompasses the average pattern scale resulting from this simulation, which is approximately 310 m.

In order to illustrate the directional biases that may result from the FCA four different plots have been employed. An example of these plots resulting from the application of the FCA to the smallest and largest equilateral triangles of antennae are illustrated in Figure E.1. The first plot is employed to illustrate the existence of any systematic bias in the direction of the average true velocity θ_t away from the direction of the model input velocity θ_{mod}. The parameter $\triangle\theta$ is defined by

$$\triangle\theta = \theta_{\text{mod}} - \theta_t. \tag{E.1}$$

If θ_t is biased towards a particular direction θ_{bias} then

$$\begin{aligned} \triangle\theta < 0 \quad &\text{if} \quad \theta_{\text{mod}} < \theta_{\text{bias}}, \text{and} \\ \triangle\theta > 0 \quad &\text{if} \quad \theta_{\text{mod}} > \theta_{\text{bias}}, \end{aligned} \tag{E.2}$$

in the region of θ_{bias}. As a result, any direction of bias can be easily be detected. These

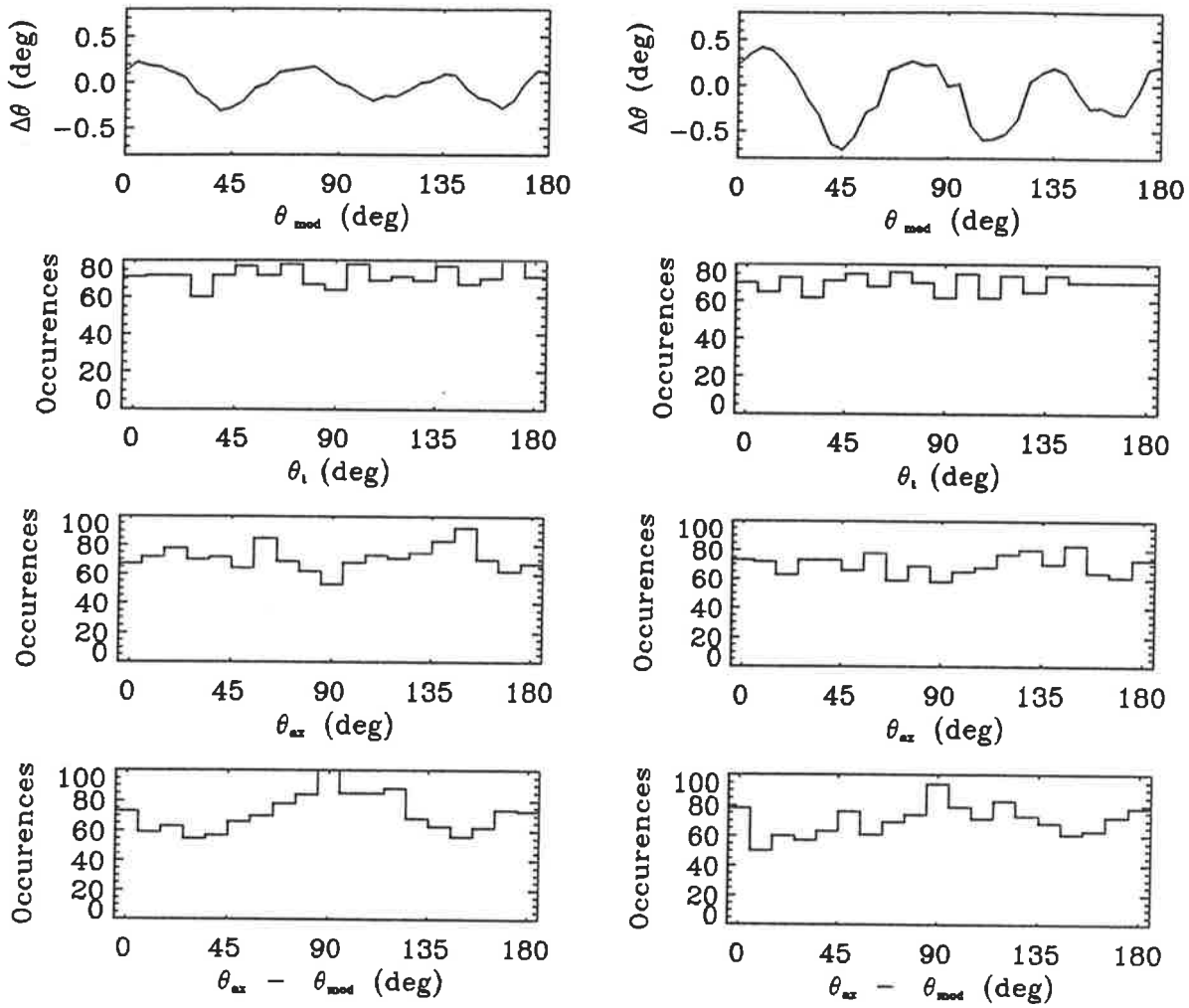

Figure E.1: Results of the application of the FCA to the smallest (left column) and largest (right column) equilateral triangles of the model-generated data-set MOD-MF-TSE-ROTN (see text for details).

results suggest there is a maximum bias of approximately 0.5° towards angles of 0°, 60° and 120°. These angles correspond azimuths perpendicular to the direction of the antenna separations. The bias appears larger for the largest spacing. The second plot shows the combined histogram of θ_t estimates for all values of $\theta_{\rm mod}$. The results suggest there is no preferred value of θ_t, despite the $\Delta\theta$ plot showing there is some bias. This result illustrates one of the advantages in using the $\Delta\theta$ plot in that small biases in θ_t are not observable in the histograms of θ_t. In addition, the $\Delta\theta$ plot reveals the direction of any biases and also allows for the situation when the FCA rejects records with a particular $\theta_{\rm mod}$. The histogram of the θ_t estimates is nevertheless still a useful tool in the determination of any biases in θ_t, as will be seen later. The third plot shows the combined histogram of $\theta_{\rm ax}$ estimates for all values of $\theta_{\rm mod}$. These results of Figure E.1 suggest there is no preferred value of $\theta_{\rm ax}$. The

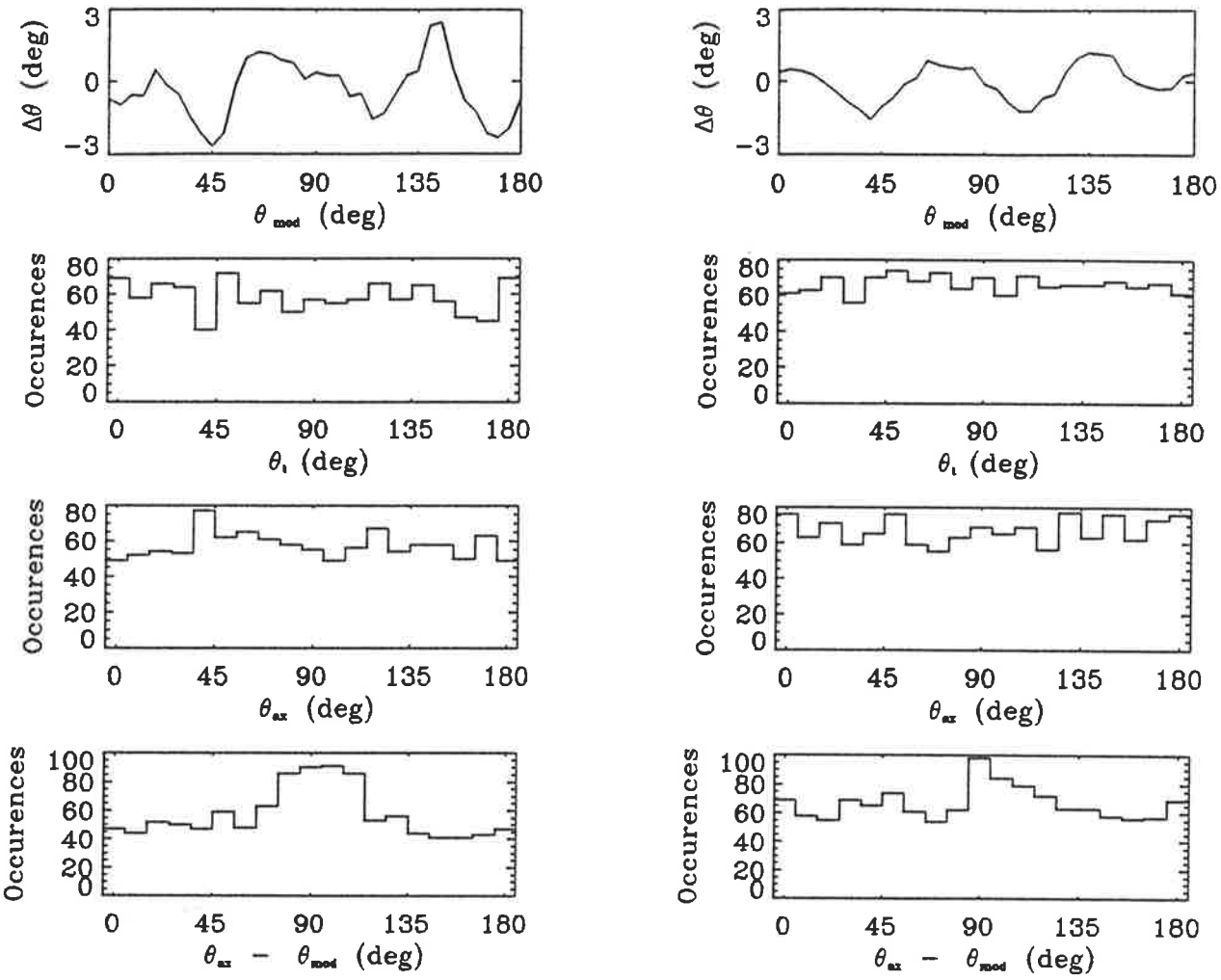

Figure E.2: Results of the application of the FCA to the smallest (left column) and largest (right column) equilateral triangles of the model-generated data-set MOD-MF-TSE-ROTN with 4 dB added noise.

final plot shows the combined histogram of $\theta_{\mathrm{ax}} - \theta_{\mathrm{mod}}$ values for all values of θ_{mod}. These results suggest there is a slight peak at 90°, suggesting that θ_{ax} is biased perpendicularly to θ_{mod}.

The corresponding results for the application of the FCA to the smallest and largest equilateral triangles with 4 dB of added noise are illustrated in Figure E.2. The $\triangle\theta$ plot reveals a θ_t bias of the same form as seen in Figure E.1 but larger, producing a maximum bias of approximately 3°. The histogram of θ_{ax} values also show more evidence of a bias perpendicular to θ_{mod}, while the histograms of θ_t and θ_{ax} show no apparent bias. The corresponding results for the application of the UFCA are shown in Figure E.3. The θ_t bias is comparable to that seen for the FCA. The $\triangle\theta$ plot reveals a θ_t bias of the same form as for the FCA. The histogram of θ_{ax} values show a clear bias perpendicular to θ_{mod}. This

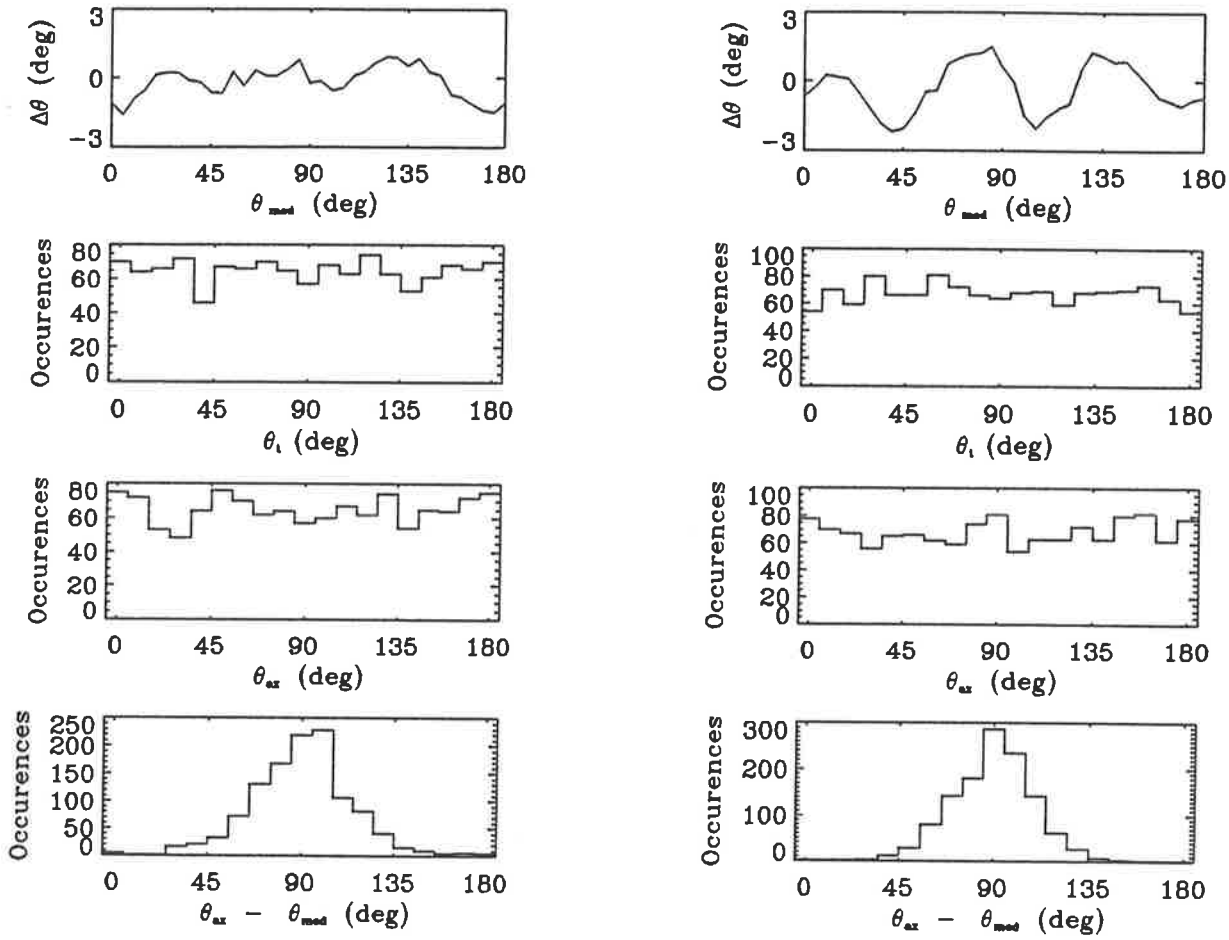

Figure E.3: Results of the application of the UFCA to the smallest (left column) and largest (right column) equilateral triangles of the model-generated data-set MOD-MF-TSE-ROTN with 4 dB added noise.

result is consistent with the suggestions of *Meek* [1990] that the failure to correct for noise biases θ_{ax} perpendicularly to θ_t, as in this case $\theta_t \approx \theta_{mod}$. The magnitude of this bias is comparable for both antenna spacings, suggesting that the bias is in fact independent of the antenna spacing. The histograms of θ_t and θ_{ax} show no apparent bias. These result suggests that the failure to correct for the effects of noise does not produce any significant bias in the direction of the true velocity if the antennae are arranged in an equilateral triangle.

The results of the application of the FCA to the smallest and largest right-angled triangles are illustrated in Figure E.4. The $\triangle\theta$ plot reveals that θ_t appears biased towards angles of 45°, 112.5° and 157.5°. These angles correspond to azimuths perpendicular to the direction of the antenna separations, as was the case for the equilateral triangle. For the largest triangle the only bias evident is towards 45°. The histogram of θ_t suggests there is a minima

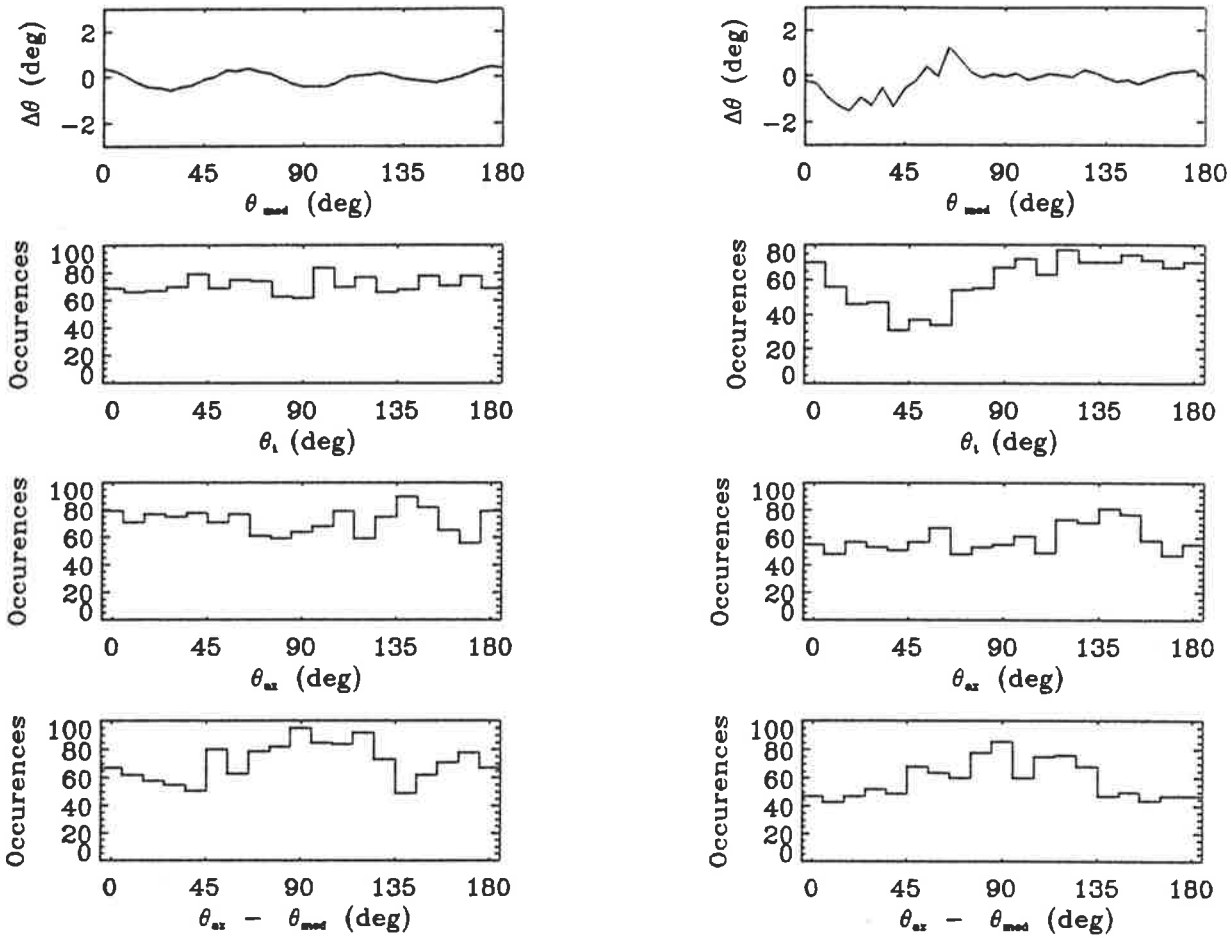

Figure E.4: Results of the application of the FCA to the smallest (left column) and largest (right column) right-angled triangles of the model-generated data-set MOD-MF-TSE-ROTN.

at 45° for the largest triangle, perpendicular to the angle of the hypotenuse (135°). This minima is a result of a minima in the acceptance rate for records where $\theta_{\mathrm{mod}} = 45°$, as shown in in Figure E.5. The majority of these records are rejected by criteria 4 and 5, which the results of the section 5.2 suggest are the most prevalent rejections when the antenna spacing is comparable to the pattern scale, as it the case for the largest spacing in this analysis. The histogram of $\theta_{\mathrm{ax}} - \theta_{\mathrm{mod}}$ values again suggests that θ_{ax} is biased perpendicularly to θ_{mod}. The histogram of θ_{ax} suggests there are no biases evident. For the smallest triangle there is a minima in the histogram of θ_t at 45°, which is perpendicular to the angle of the hypotenuse (135°). This may suggest some bias towards of the θ_t towards the hypotenuse.

The corresponding results for the application of the FCA to the smallest and largest right-angled triangles with 4 dB of added noise are illustrated in Figure E.6. The $\triangle\theta$ plot

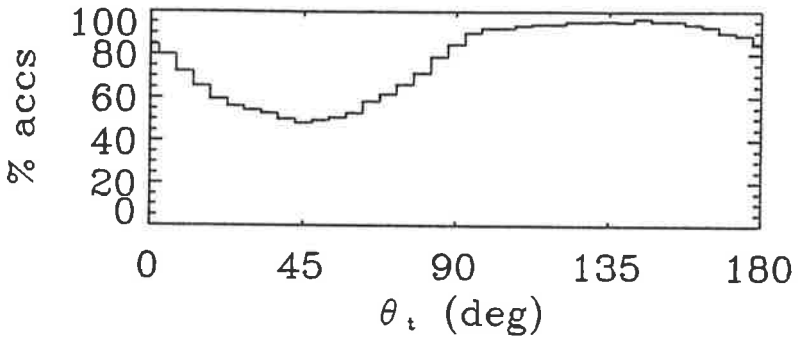

Figure E.5: Acceptance rate for the application of the FCA to the largest right-angled triangle of the model-generated data-set MOD-MF-TSE-ROTN.

reveals that θ_t is biased towards angles of 45°, 112.5° and 157.5° for the largest triangle only. For the smallest triangle the θ_t values are biased towards the hypotenuse at 135°, with a maximum bias of almost 4°. The histograms of θ_t values both show minima at 45°. The minima for the largest triangle again results from a minima in the acceptance rate. The minima for the smallest triangle however appear to be a result of the bias of the θ_t values towards the hypotenuse. The histogram of θ_{ax} values shows no bias. The histogram of $\theta_{\mathrm{ax}} - \theta_{\mathrm{mod}}$ values again reveals that θ_{ax} is biased perpendicularly to θ_{mod}.

The corresponding results for the application of the UFCA are shown in Figure E.7. The $\triangle\theta$ plots reveal a large bias towards the hypotenuse at 135°. This bias is also evident in the histograms of θ_t. The size of this bias increases with decreasing spacing. The maximum bias for the smallest and largest triangles are 25° and 12°, respectively. Thus, although the spacings of the largest triangle exceeds the pattern scale the bias is still seen. This is despite the results of the magnitude bias which suggest that the magnitude of the true velocity V_t is not biased if the antenna spacing is comparable to the pattern scale. The θ_{ax} values are also biased, but the sense of the bias is dependent on the antenna spacing. For the smaller spacing θ_{ax} is predominantly biased towards the direction of the hypotenuse, although there is also evidence of bias perpendicular to θ_{mod}. For the larger spacing θ_{ax} is predominantly biased perpendicular to θ_{mod}, although there is also evidence of bias towards the direction of the hypotenuse. These results are consistent with the prediction of *Meek* [1990] that the failure to correct for noise biases θ_{ax} towards the hypotenuse, and that this bias should decrease with with increasing antenna spacing. However, as this bias decreases the other bias predicted by *Meek* [1990], that the failure to correct for noise biases θ_{ax} perpendicularly

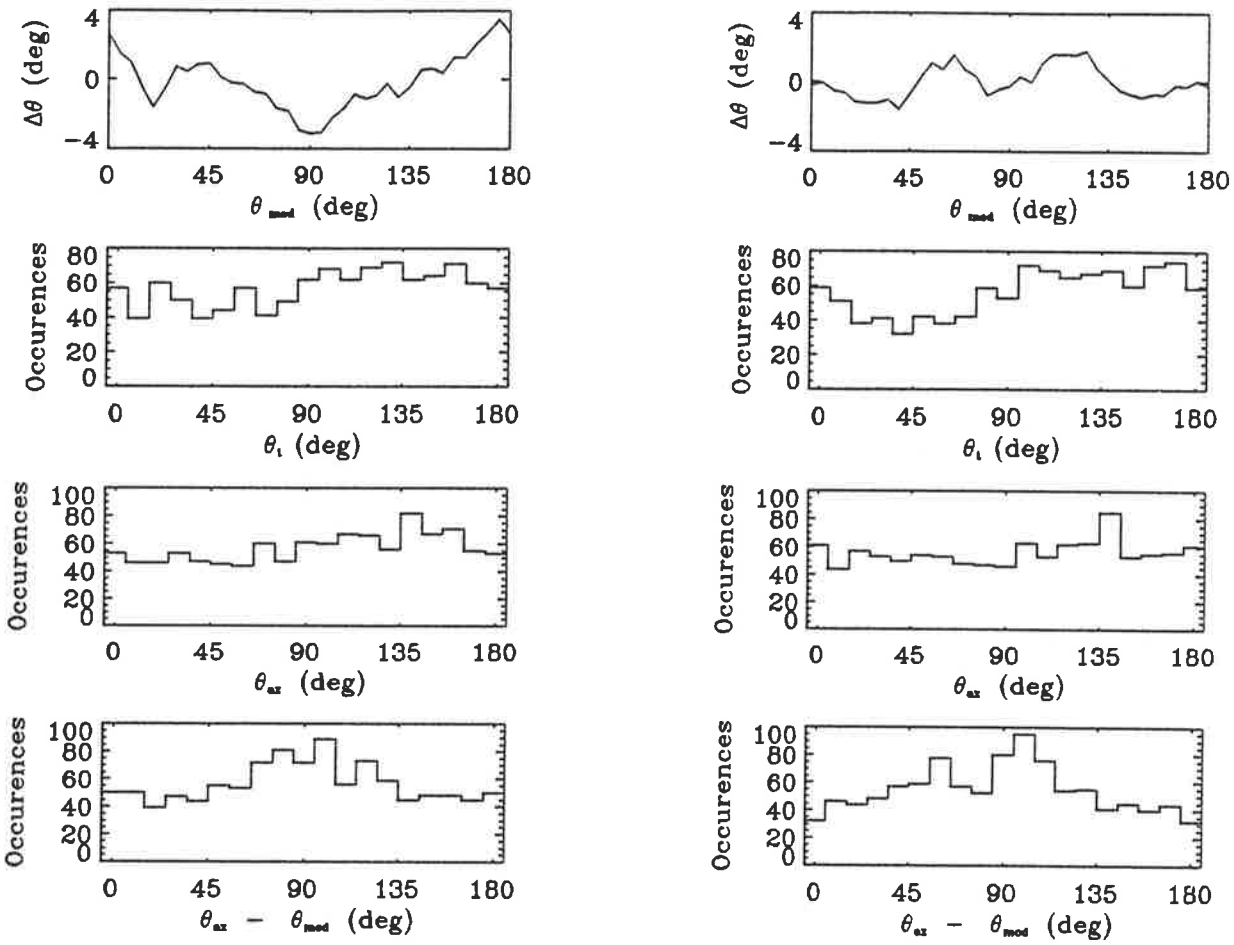

Figure E.6: Results of the application of the FCA to the smallest (left column) and largest (right column) right-angled triangles of the model-generated data-set MOD-MF-TSE-ROTN with 4 dB added noise.

to θ_t, becomes predominant.

The bias of the UFCA estimates of θ_t towards the hypotenuse for a right-angled triangle of antennae can be understood by considering equation (5.2). This equation was derived using a one-dimensional formulation of the spatial correlation function. As a result, it is not directly applicable to the components of the two-dimensional ground diffraction pattern as it does not include for the effects of spatial-decorrelation, which is the decrease in correlation resulting from the different antennae measuring different cross-sections of the ground diffraction pattern. The decrease in correlation resulting from spatial decorrelation is considerably less significant than the decrease in correlation resulting from increasing the antenna spacing (e.g. *Sheppard and Larsen*, [1992]), suggesting that (5.2) will still provide a reasonable estimate of velocity component along the line of each antenna pair as a function

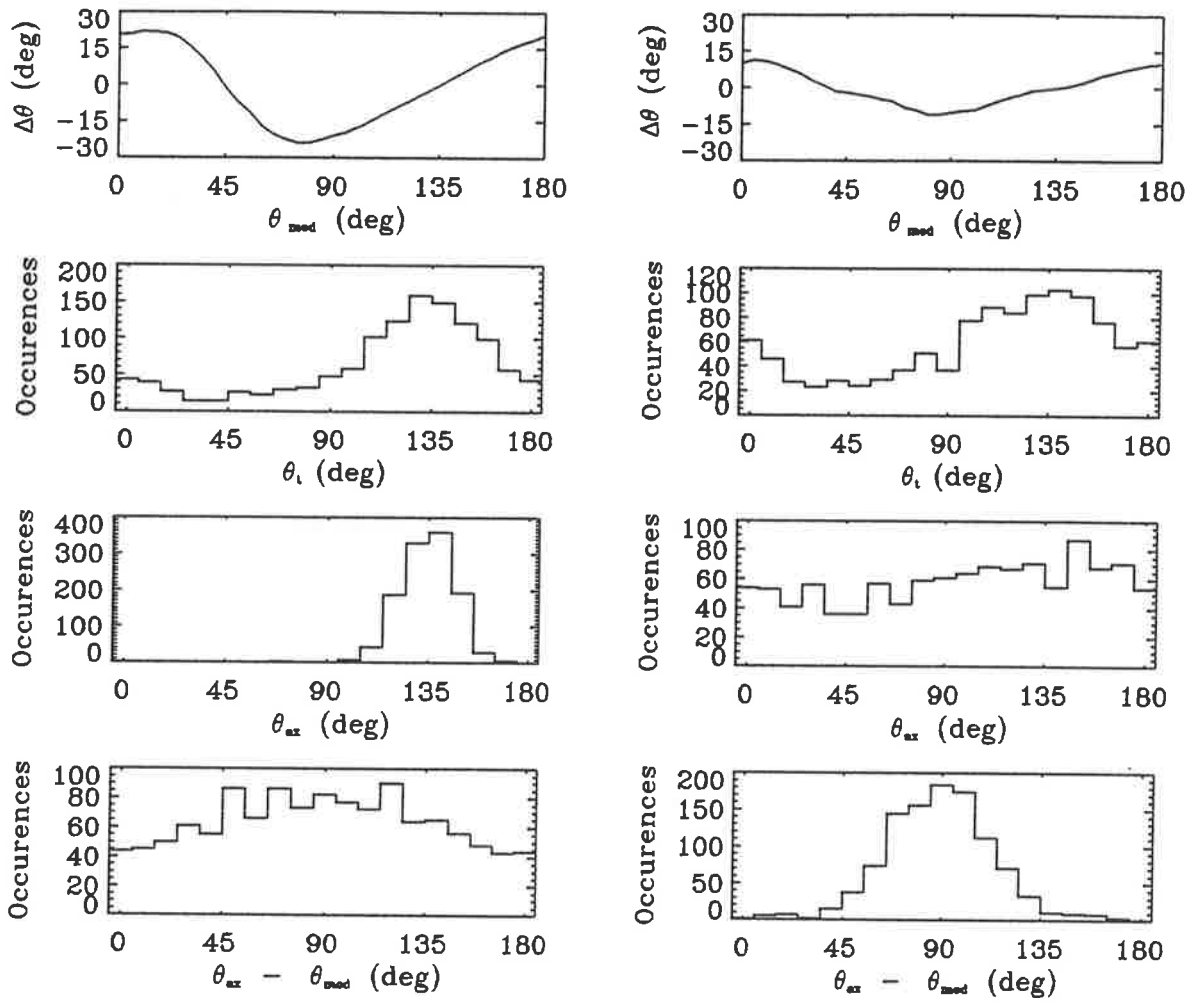

Figure E.7: Results of the application of the UFCA to the smallest (left column) and largest (right column) right-angled triangles of the model-generated data-set MOD-MF-TSE-ROTN with 4 dB added noise.

of the separation of the antenna. Because the antenna separation along the hypotenuse is greater than the antenna separation along the legs of the triangle it follows from (5.2) that the ratio V_t/V_{t0} will be greater along the hypotenuse than along the legs. As a result, the velocity component along the hypotenuse will be greater than the velocity components along the legs. If the component of the wind velocity along the hypotenuse is significant it follows that θ_t will be biased towards the hypotenuse. On the other hand, if the component of the wind velocity along the hypotenuse is small θ_t will only show a small bias. These results are apparent in the $\triangle\theta$ plots of Figure E.7. The form of (5.2) also suggests that the bias will decrease as the antenna spacing is increased, although there will always be some bias. An identical argument can be applied using (5.4) to show that $\theta_{\rm ax}$ will also be biased towards

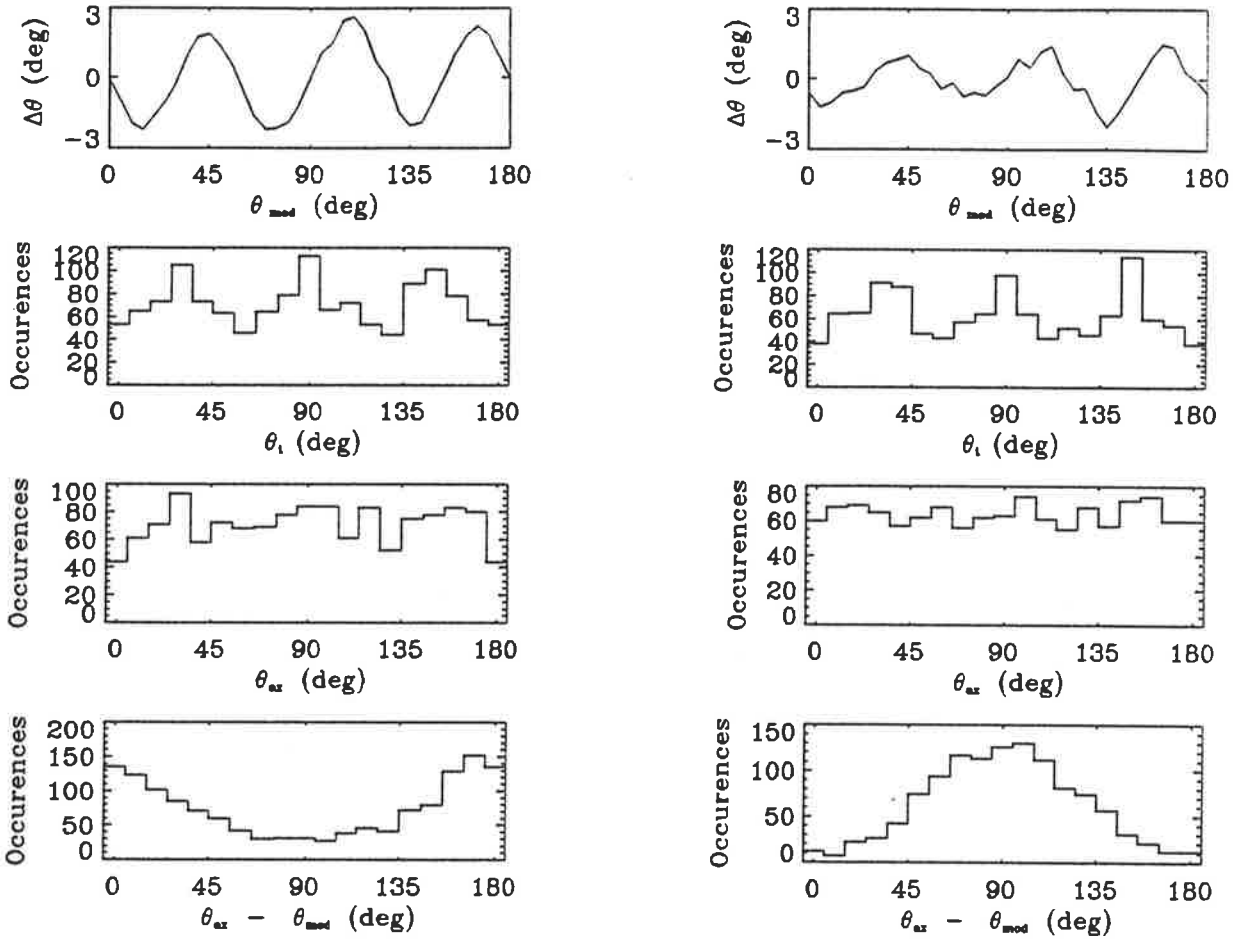

Figure E.8: Results of the application of the UFCA to the smallest (left column) and largest (right column) equilateral triangles of the model-generated data-set MOD-MF-TSE-ROTN for a saturation percentage of 100%.

the hypotenuse, and that that the bias will decrease as the antenna spacing is increased.

The bias of the UFCA estimates of θ_t towards the hypotenuse contradicts the results of *Benyon and Wright* [1969], who found that θ_t was biases perpendicular to the hypotenuse. This is a puzzling result. The fact that *Benyon and Wright* [1969] found θ_{ax} was biased towards the hypotenuse suggests that the spatial-correlation function extrapolated to below unity at zero spatial lag. This suggests the results should be directly applicable to what is seen on applying the UFCA to records with added receiver noise.

The results of section 5.2 suggest that magnitude biases will be seen for time-series data with coarse digitization or saturation regardless of whether the noise correction is applied or not. The results of applying the FCA to the smallest and largest equilateral triangles using data with a saturation percentage of 100% are shown in E.8. The $\Delta\theta$ plots reveal that

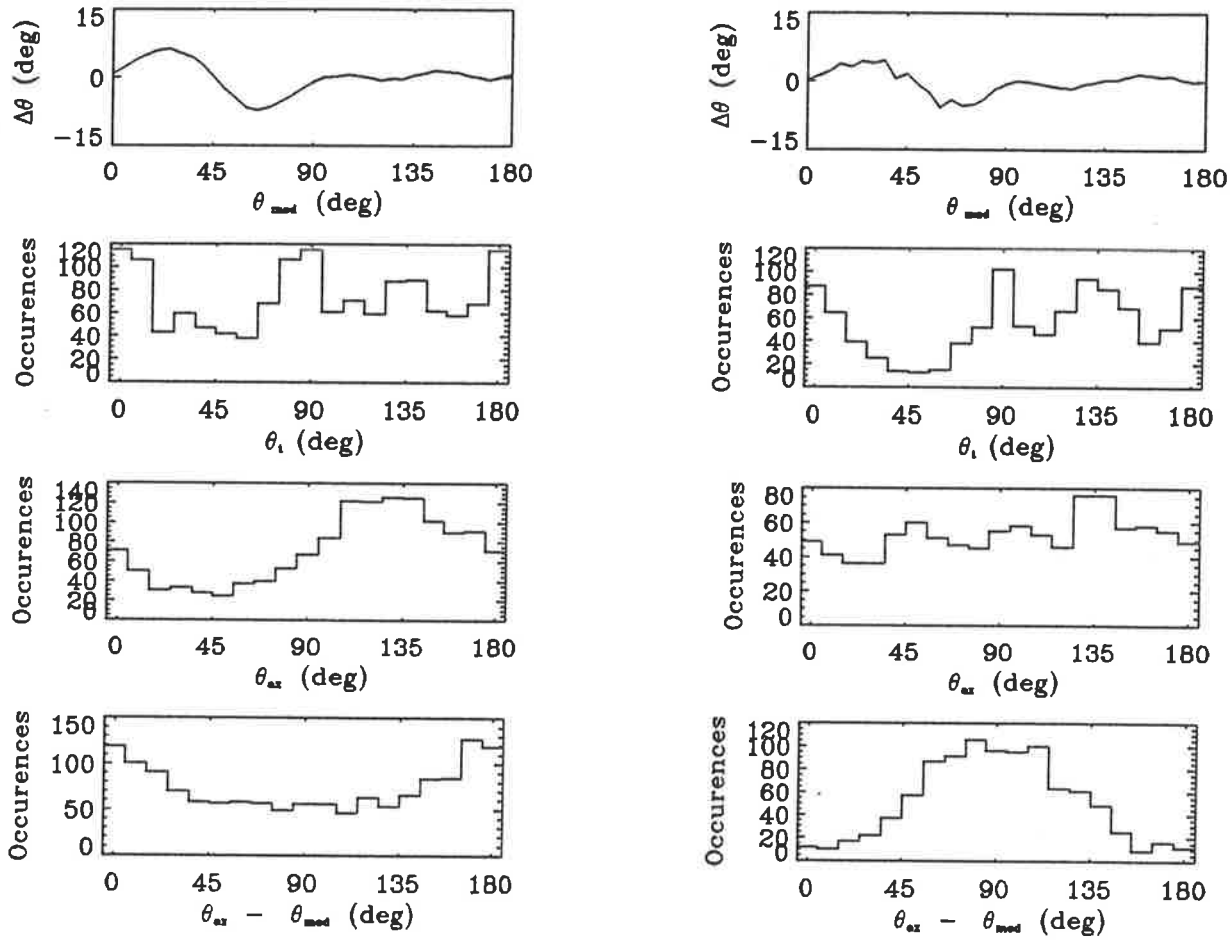

Figure E.9: Results of the application of the UFCA to the smallest (left column) and largest (right column) right-angled triangles of the model-generated data-set MOD-MF-TSE-ROTN for a saturation percentage of 100%.

θ_t is biased along the directions of the antenna spacings of 30°, 90° and 150°. The bias is largest for the largest spacing. The maximum bias for the largest spacing is approximately 6°. The histograms of θ_{ax} values show biases towards the same directions as θ_t for the smallest spacing, and no apparent bias for the largest spacing. The corresponding results for smallest and largest right-angled triangles are shown in Figure E.9. The $\Delta\theta$ plots suggests the θ_t values are biased towards 0°, which is along the direction of one of the antenna pairs. The histogram of θ_t values suggests that biases are also seen along the direction of the the remaining antenna pairs at 90° and 135°. The histogram of θ_{ax} values suggests θ_{ax} is biased towards the direction of the antenna pairs for the smallest spacing, and biased towards the hypotenuse for the largest spacing.

The results of Figures E.8 and E.9 illustrate the maximum biases that can result from

coarse digitization and saturation. The corresponding results for smaller saturation percentages and larger numbers of digitization levels (not shown) suggest that there are significant directional biases for saturation percentages above 60%, and if less than 8 digitization levels are used.

Appendix F

Spectra

Spectra are used extensively throughout this thesis. The definitions of the various spectra referred to are provided in this appendix.

F.1 Definition of the spectra

Consider the case of a time-series $f_i(t)$ recorded by a particular receiving antenna A_i. The amplitude spectrum $F_i(f)$ is given by the Fourier transform of $f_i(t)$

$$F_i(f) = \int_{-\infty}^{\infty} f_i(\tau) \exp(-j2\pi f\tau) d\tau, \tag{F.1}$$

where $j = \sqrt{-1}$.

The power spectrum $W_i(f)$ of $f_i(t)$ is given by

$$W_i(f) = |F_i(f)|^2 \tag{F.2}$$

$$= F_i^*(f) F_i(f). \tag{F.3}$$

where $*$ denotes the complex conjugate. The power spectrum is a real function.

The normalized cross spectrum of the time-series $f_i(t)$ and $f_j(t)$ recorded by receiving antenna A_i and A_j is defined by (e.g., *Briggs and Vincent* [1992])

$$W_{ij}(f) = \frac{F_i^*(f) F_j(f)}{\sqrt{\int_{-\infty}^{\infty} |F_i(f)|^2 df \int_{-\infty}^{\infty} |F_j(f)|^2 df}}. \tag{F.4}$$

The normalized cross-spectrum is a complex function.

F.2 The effect of noise upon the power-spectra

Consider the situation occurring in practice where the time-series $f_i(t)$ is composed of signal $s_i(t)$ and noise $n_i(t)$ components

$$f_i(t) = s_i(t) + n_i(t). \tag{F.5}$$

Substituting (F.5) into (F.1) yields

$$\begin{aligned} F_i(f) &= \int_{-\infty}^{\infty} (s_i(\tau) + n_i(\tau)) \exp(-j2\pi f\tau) d\tau, & \text{(F.6)} \\ &= S_i(f) + N_i(f) & \text{(F.7)} \end{aligned}$$

where

$$\begin{aligned} S_i(f) &= \int_{-\infty}^{\infty} s_i(\tau) \exp(-j2\pi f\tau) d\tau & \text{(F.8)} \\ N_i(f) &= \int_{-\infty}^{\infty} n_i(\tau) \exp(-j2\pi f\tau) d\tau & \text{(F.9)} \end{aligned}$$

are the amplitude spectra of the signal and noise components, respectively. The majority of noise encountered in radar systems is "white" noise. This noise is distributed over a wide range of spectral frequencies, thereby producing a "noise floor".

In the presence of noise the power-spectrum $W_i(f)$ can be rewritten

$$\begin{aligned} W_i(f) &= |(S_i(f) + N_i(f))|^2 & \text{(F.10)} \\ &= (S_i(f) + N_i(f))^*(S_i(f) + N_i(f)) & \text{(F.11)} \\ &= S_i^*(f)S_i(f) + N_i^*(f)N_i(f) + N_i^*(f)S_i(f) + N_i^*(f)N_i(f) & \text{(F.12)} \\ &= |S_i(f)|^2 + |N_i(f)|^2 + K_i(f), & \text{(F.13)} \end{aligned}$$

where $|S_i(f)|^2$ and $|N_i(f)|^2$ are the power-spectra attributable to the signal and noise contributions respectively, and

$$\begin{aligned} K_i(f) &= S_i^*(f)N_i(f) + S_i(f)N_i^*(f). & \text{(F.14)} \\ &= 2\,\mathrm{Re}(S_i(f))\,\mathrm{Re}(N_i(f)) + 2\,\mathrm{Im}(S_i(f))\,\mathrm{Im}(N_i(f)), & \text{(F.15)} \end{aligned}$$

where "Re" and "Im" represent the real and imaginary components of the arguments respectively. The total spectral power W_{ipow} can be obtained by integrating $W_i(f)$ over all Doppler frequencies.

$$\begin{aligned} W_{ipow} &= \int_{-\infty}^{\infty} (|S_i(f)|^2 + |N_i(f)|^2 + K_i(f)) df & \text{(F.16)} \\ &= S_{ipow} + N_{ipow} + K_{ipow}, & \text{(F.17)} \end{aligned}$$

where

$$S_{\text{ipow}} = \int_{-\infty}^{\infty} |S_i(f)|^2 df \tag{F.18}$$

is the total signal spectral power

$$N_{\text{ipow}} = \int_{-\infty}^{\infty} |N_i(f)|^2 df \tag{F.19}$$

is the total noise spectral power, and

$$K_{\text{ipow}} = \int_{-\infty}^{\infty} K_i(f) df. \tag{F.20}$$

The contributions of the signal and noise components to the power-spectra of (F.10) are illustrated in Figure F.1, which shows the power-spectra obtained using various different SNRs of added Gaussian distributed random noise components for a record of the model-generated data-set MOD-MF-SA. The signal power-spectra $|S_i(f)|^2$ is effectively given by the SNR = 100 dB case. As the SNR is decreased the power-spectrum $W_i(f)$ diverges from $|S_i(f)|^2$ as the terms $|N_i(f)|^2$ and $K_i(f)$ become more prominent. The $|N_i(f)|^2$ term manifests itself by the introduction of a "noise floor". The $K_i(f)$ term manifests itself by changing the features of the main peak of the spectrum away from $|S_i(f)|^2$. Because the noise term $n_i(t)$ is random it follows that the real and imaginary components of the amplitude spectrum $N_i(f)$ are also random, with a mean value of zero. It therefore follows that the $K_i(f)$ are also random, with a mean value of zero. This result suggests $K_{\text{ipow}} = 0$.

The noise-level N_{ilev} can be determined by estimating the average noise power at Nyquist frequency f_N. If a sufficiently small sampling time is employed $S_i(f_N) = 0$, so that $W_i(f_N) = N_i(f_N)$. The total noise power can then be determined by

$$N_{\text{ipow}} = 2 f_N N_{\text{ilev}}. \tag{F.21}$$

If the noise-level N_{ilev} is removed from the spectrum the total power of the resulting spectrum $W_i'(f)$ will be given by

$$W'_{\text{ipow}} = S_{\text{ipow}} + K_{\text{ipow}}, \tag{F.22}$$

Because the resulting spectrum is Gaussian W'_{ipow} can be estimated using a Gaussian fit using the equation

$$W'_{\text{ipow}} = \sqrt{\pi} W'_{0i} f_{e^{-1}}, \tag{F.23}$$

where W'_{0i} is the maximum and $f_{e^{-1}}$ is the e^{-1} half width of the fitted Gaussian.

The estimates of W'_{ipow} obtained using (F.23) after the removal of the noise-level for power-spectra determined using the model-generated data-set MOD-MF-SA are shown in

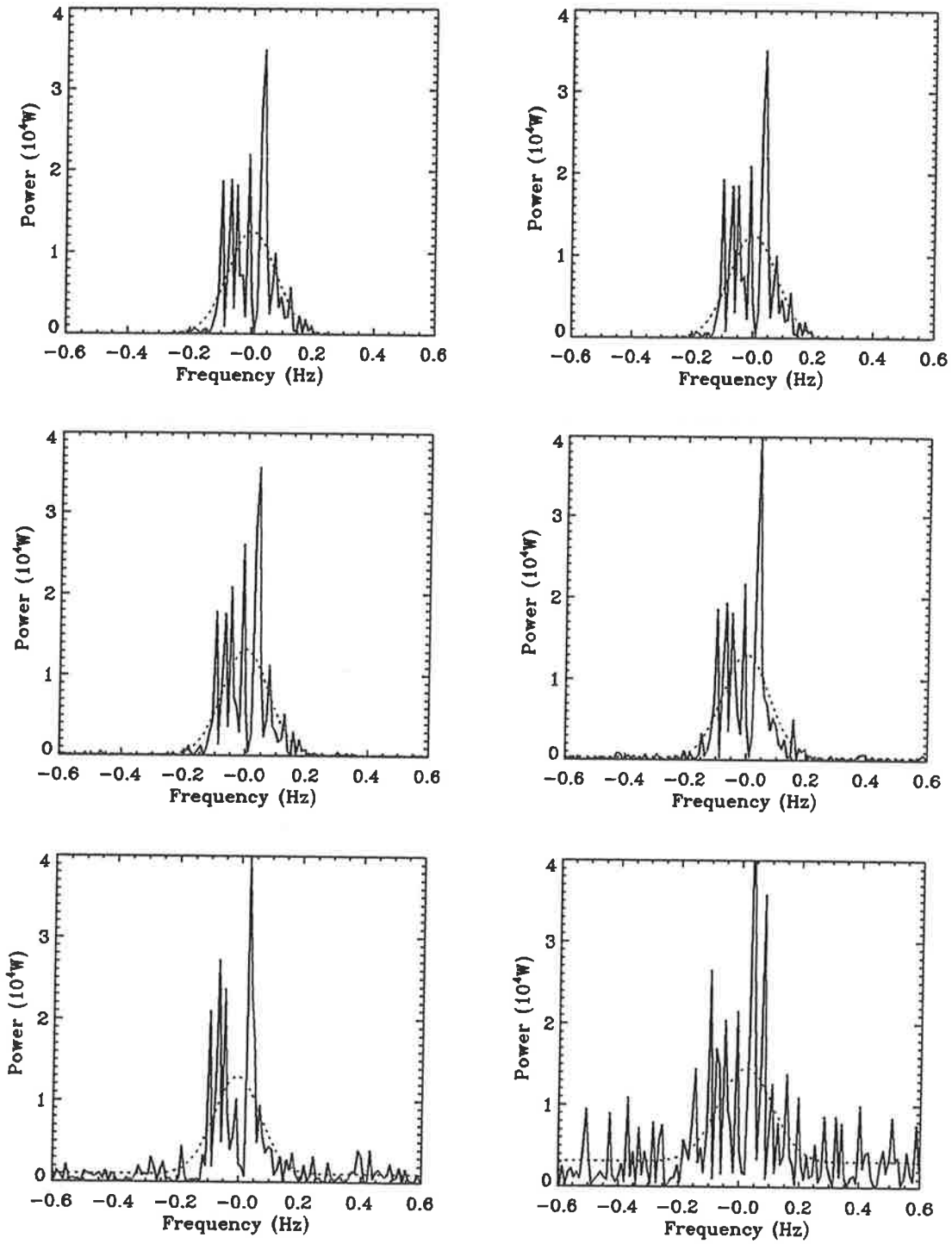

Figure F.1: Example of power-spectra obtained using various SNRs of added noise: 100 dB (top left), 20 dB (top right), 10 dB (middle left), 5 dB (middle right), 0 dB (bottom left) and -5 dB (bottom right). The dotted line indicates the Gaussian fit to each spectrum.

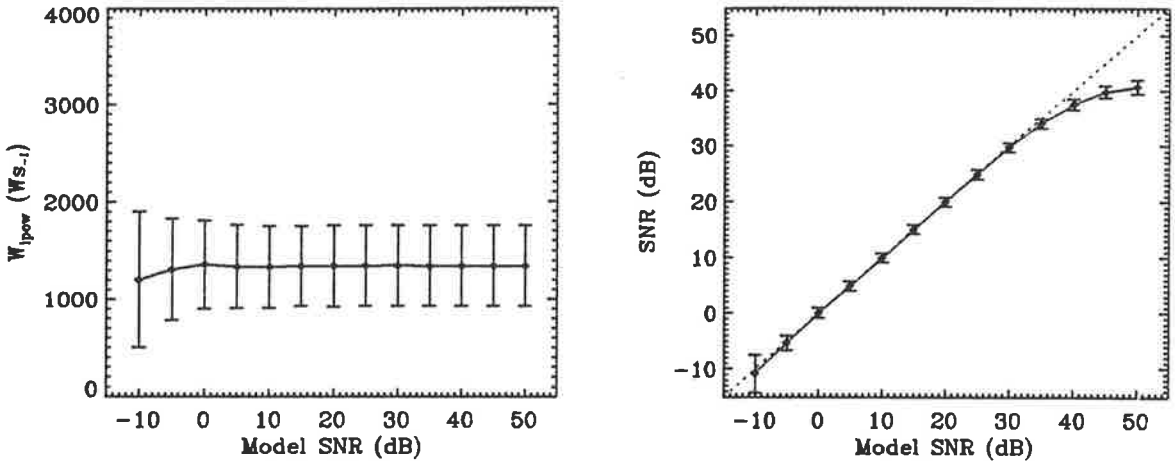

Figure F.2: Illustration of the variation of the spectral parameters determined from the cross-spectrum for various different SNRs.

Figure F.2 as a function of SNR. These results suggest that the estimate of W'_{ipow} is almost constant for SNRs exceeding 0 dB, thereby confirming that $K_{ipow} \approx 0$. There is a small decrease for SNRs below 0 dB, where $N_{ipow} \geq S_{ipow}$. In this instance the features of the power-spectra are changed significantly by the effects of noise, as can be seen in Figure F.1. There is also a small increase in the standard deviation of the estimates at SNRs below 0 dB. These results suggest that the properties of the signal spectrum can be successfully determined by removing the noise-level from the power-spectrum.

F.2.1 Estimation of the SNR

The SNR of the time-series recorded by the receiving antenna A_i is defined by

$$SNR = 10 \log_{10} \left(\frac{S_{ipow}}{N_{ipow}} \right). \tag{F.24}$$

where S_{ipow} and N_{ipow} are the total signal and noise powers as defined by (F.18) and (F.21). Because $K_{ipow} \approx 0$, S_{ipow} can be determined from the parameters obtained from the Gaussian fit to W'_{ipow}, as specified by (F.23).

The estimates of the SNR obtained using (F.24) for power-spectra determined using the model-generated data-set MOD-MF-SA are shown in Figure F.2 as a function of SNR. These results illustrate that the SNR is successfully estimated for all values of the model SNR above 30 dB. The fall-off with increasing SNR above 30 dB may be the result of two effects. The use of finite length time-series records for the determination of the power-spectra may result in "spectral leakage" from the main peak of the spectrum out into the tails (e.g.

Bracewell, [1965]). The use of 256 level digitization may also produce "digitization noise". These effects may produce a noise-level which exceeds the noise-level that would be induced by the added noise. As a result, the noise-level estimation procedure would measure this noise-level, thereby producing the fall-off seen in Figure F.2.

F.3 The effect of noise upon the cross-spectra

The effect of noise upon the cross-spectra can be understood by determining the effects upon the numerator and denominator separately. The numerator of the cross-spectrum $N(W_{ij}(f))$ is given by

$$N(W_{ij}(f)) = (S_i(f) + N_i(f))^*(S_j(f) + N_j(f)) \quad \text{(F.25)}$$

$$= S_{ij}(f) + N_{ij}(f) + K_{ij}(f), \quad \text{(F.26)}$$

where

$$S_{ij}(f) = S_i^*(f)S_j(f) \quad \text{(F.27)}$$

is the unnormalized signal cross-spectrum, and

$$N_{ij}(f) = N_i^*(f)N_j(f), \quad \text{(F.28)}$$

$$K_{ij}(f) = S_i^*(f)N_j(f) + S_j^*(f)N_i(f). \quad \text{(F.29)}$$

As the terms $S_{ij}(f)$, $N_{ij}(f)$ and $K_{ij}(f)$ are all complex, the cross-spectrum is also complex. The components of the terms $N_{ij}(f)$ and $K_{ij}(f)$ are both randomly distributed about zero. It therefore follows that the product of either of these quantities with any other quantity besides itself must integrate to zero.

The denominator of the cross-spectrum $D(W_{ij}(f))$ is given by

$$D(W_{ij}(f)) = \sqrt{\int |S_i(f) + N_i(f)|^2 df \int |S_j(f) + N_j(f)|^2 df}. \quad \text{(F.30)}$$

The first term on the right hand side can be expanded to give the expression

$$D_i = \sqrt{\int |S_i(f) + N_i(f)|^2 df} \quad \text{(F.31)}$$

$$= \sqrt{\int (S_i^*(f)S_i(f) + S_i^*(f)N_i(f) + S_i(f)N_i^*(f) + N_i(f)N_i^*(f))df} \quad \text{(F.32)}$$

$$= \sqrt{\int S_i^*(f)S_i(f)df + \int S_i^*(f)N_i(f)df + \int S_i(f)N_i^*(f)df + \int N_i^*(f)N_i(f)df} \quad \text{(F.33)}$$

$$= \sqrt{\int |S_i(f)|^2 df + \int |N_i(f)|^2 df + \int S_i^*(f)N_i(f)df + \int S_i(f)N_i^*(f)df}. \quad \text{(F.34)}$$

As is the case for the power spectra, the last two terms on the right hand side cancel to zero, giving the expression

$$D_i = \sqrt{\int |S_i(f)|^2 df + \int |N_i(f)|^2 df} \quad \text{(F.35)}$$

$$= \sqrt{S_{\mathbf{ipow}}(f) + N_{\mathbf{ipow}}(f)}. \quad \text{(F.36)}$$

This term is the the square root of the integrated power-spectrum for the receiving antenna A_i, $W_{\mathbf{ipow}}$. The cross-spectrum is therefore be given by

$$W_{ij}(f) = \frac{S_{ij}(f) + N_{ij}(f) + K_{ij}(f)}{\sqrt{W_{\mathbf{ipow}}(f) W_{\mathbf{jpow}}(f)}}, \quad \text{(F.37)}$$

In order to determine the signal contribution to the cross-spectrum in the presence of noise the noise-terms must be removed from the denominator of (F.37). This can be achieved by substituting the signal powers $S_{\mathbf{ipow}}$ calculated using (F.23) for the total powers $W_{\mathbf{ipow}}$, yielding the "renormalized" cross-spectrum

$$W'_{ij}(f) = \frac{S_{ij}(f) + N_{ij}(f) + K_{ij}(f)}{\sqrt{S_{\mathbf{ipow}} S_{\mathbf{jpow}}}}. \quad \text{(F.38)}$$

This is effectively equivalent to multiplying the cross-spectrum by the renormalizing factor

$$F_i = \sqrt{\frac{W_{\mathbf{ipow}} W_{\mathbf{jpow}}}{S_{\mathbf{ipow}} S_{\mathbf{jpow}}}}. \quad \text{(F.39)}$$

This factor is identical to the factor used to renormalize the auto- and cross-correlation functions in the presence of noise, given by C.42 as discussed in Appendix C.

The full spectral analyses developed by *Briggs and Vincent* [1992] and *Sheppard and Larsen* [1992] require the determination of the total signal cross-spectral power $S_{ij\mathbf{pow}}$ from the cross-spectrum magnitude. The magnitude of the renormalized cross-spectrum is given by

$$|W'_{ij}(f)| = \frac{|S_{ij}(f) + N_{ij}(f) + K_{ij}(f)|}{\sqrt{S_{\mathbf{ipow}} S_{\mathbf{jpow}}}} \quad \text{(F.40)}$$

$$= \frac{\sqrt{|S_{ij}(f)|^2 + |N_{ij}(f)|^2 + L_{ij}(f)}}{\sqrt{S_{\mathbf{ipow}} S_{\mathbf{jpow}}}} \quad \text{(F.41)}$$

where

$$L_{ij}(f) = S^*_{ij}(f) N_{ij}(f) + S^*_{ij}(f) W_{ij}(f) + N^*_{ij}(f) S_{ij}(f) + N^*_{ij}(f) W_{ij}(f) + W^*_{ij}(f) S_{ij}(f) + W^*_{ij}(f) N_{ij}(f) + W^*_{ij}(f) W_{ij}(f) \quad \text{(F.42)}$$

The term $L_{ij}(f)$ is similar to the term $K_i(f)$ for the power spectra in that it contributes to all frequencies but integrates to zero. This follows because as previously discussed, the product of either $N_{ij}(f)$ or $K_{ij}(f)$ with any other quantity besides themselves integrates to zero. The total power of the renormalized cross-spectrum magnitude W'_{ijpow} can be obtained by integrating $|W'_{ij}(f)|$ over all Doppler frequencies

$$W'_{ijpow} = \frac{\int_{-\infty}^{\infty} \sqrt{|S_{ij}(f)|^2 + |N_{ij}(f)|^2 + L_{ij}(f)}\, df}{\sqrt{S_{ipow} S_{jpow}}}. \tag{F.43}$$

The presence of the square-root inside the integrand precludes this expression being separated into signal S_{ijpow}, noise N_{ijpow} and cross-term L_{ijpow} contributions. The noise contribution could be excluded by removing $|N_{ij}(f)|^2$ from the square of F.40.

The contributions of the signal and noise components to the cross-spectral magnitude and phase for one antenna pair of an individual record of the model-generated data-set MOD-MF-SA are shown in Figures F.3 and F.4 for various different SNRs. The effects upon the cross-spectrum magnitude are essentially identical to the effects upon the power-spectrum as shown in Figure F.1. The effects upon the phase are to increases the variability of the phase estimates, therefore disguising the general linear behavior exhibited in the phase in the situation where there is no noise present.

Although the effects of noise upon the cross-spectrum magnitude appear similar to the effects of noise upon the power-spectra the form of (F.43) suggests that the effects of noise cannot be removed from the cross-spectrum by removing the noise-level. However, for large SNRs this removal is an adequate correction. This is justified by the results of Figure F.5, which shows the average values of W'_{ijpow} obtained using the noise removed cross-spectral magnitude for one antenna pair for all records of the model-generated data-set MOD-MF-SA. These results suggest that the average values are approximately constant for SNRs below 5 dB. For SNRs below 5 dB the estimate of W'_{ijpow} decreases with decreasing SNR's. This result suggests that the effects of noise can be removed successfully by removing the noise-level for SNRs exceeding 5 dB.

The full spectral analysis developed by *Liu and Pan* [1993] requires the integration of $S_{ij}(f)$ over all Doppler frequencies to determine the zero-lag cross-correlation ρ_{0ij} for each antenna pair.

$$\rho_{ij}(0) = \int_{-\infty}^{\infty} S_{ij}(f) \tag{F.44}$$

Because the terms $N_{ij}(f)$ and $K_{ij}(f)$ are randomly distributed about zero it follows that

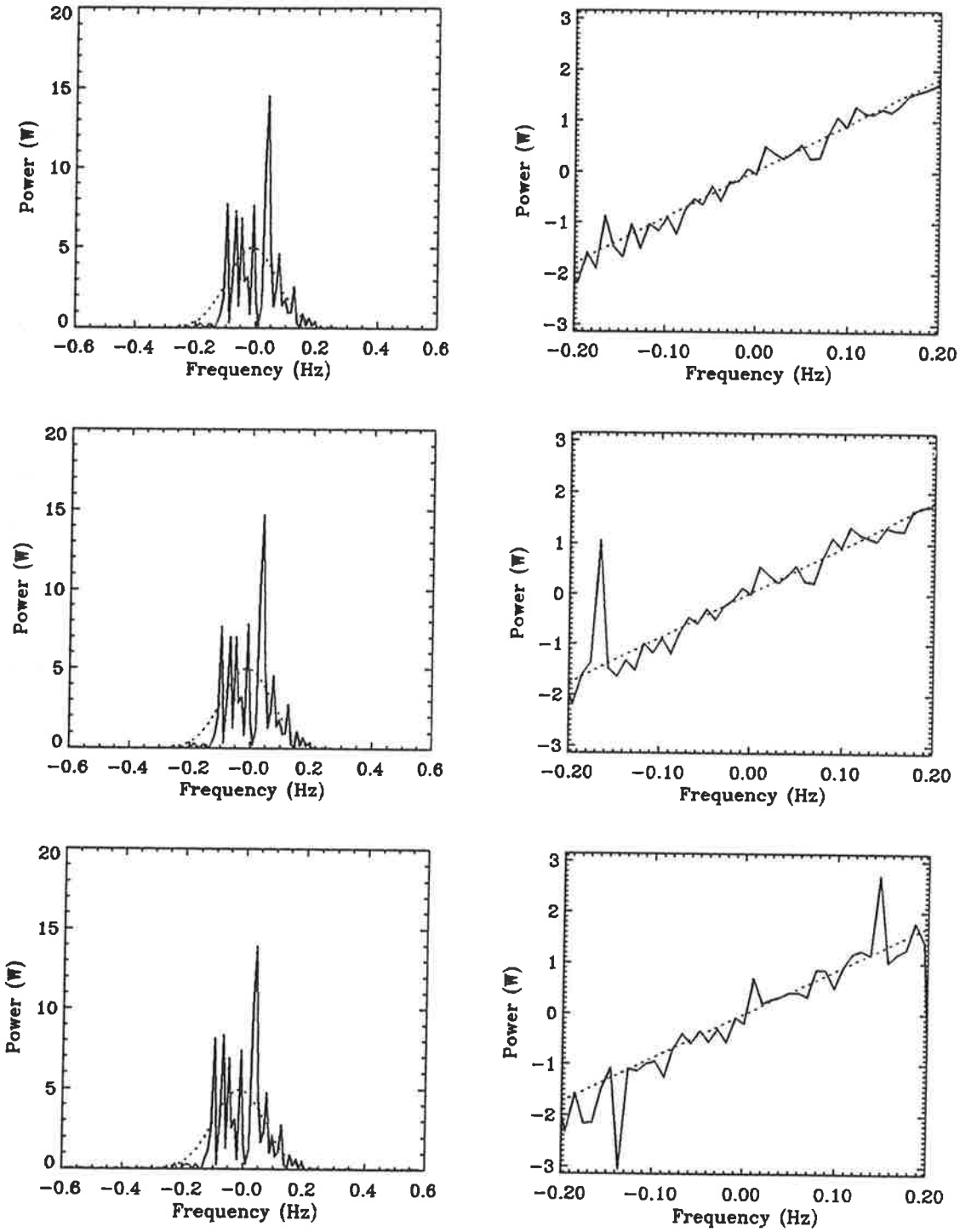

Figure F.3: Example of cross-spectral magnitude (left) and phase (right) obtained using various SNRs of added noise: 100 dB (top), 20 dB (middle) and 10 dB (bottom). The dotted lines indicates the Gaussian and linear fits.

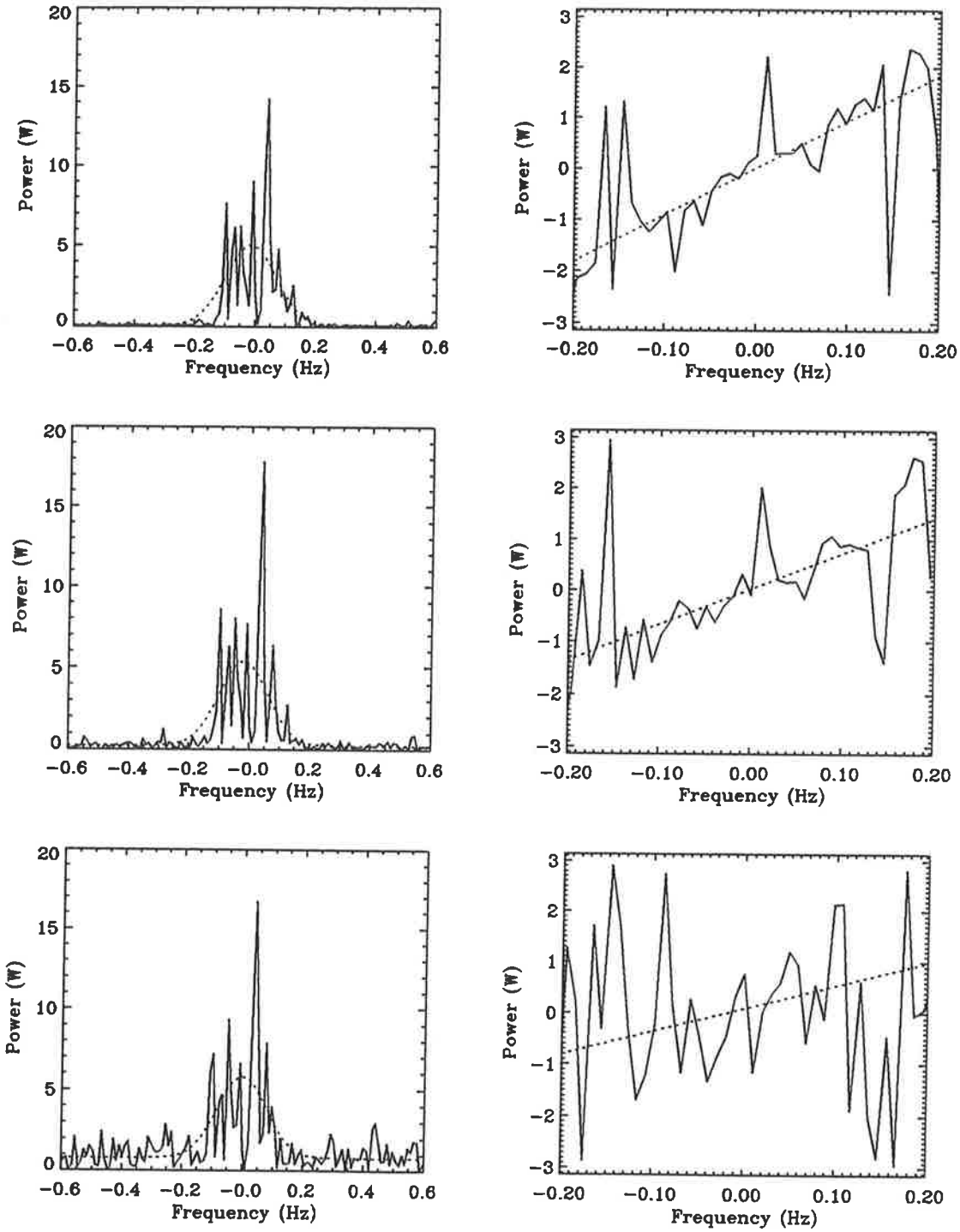

Figure F.4: Example of cross-spectral magnitude (left) and phase (right) obtained using various SNRs of added noise: 5 dB (top), 0 dB (middle) and -5 dB (bottom). The dotted lines indicates the Gaussian and linear fits.

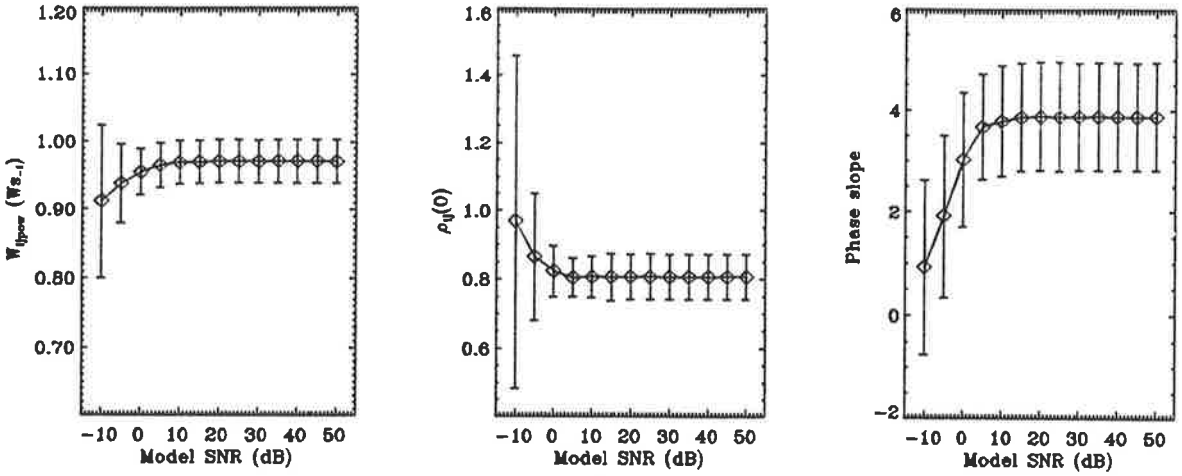

Figure F.5: Illustration of the variation of the spectral parameters determined from the cross-spectrum for various different SNRs.

they should integrate to zero. As a result, ρ_{0ij} can be determined using the equation

$$\rho_{ij}(0) = \int_{-\infty}^{\infty} W_{ij}(f), \tag{F.45}$$

thereby removing the need for the removal of the effects of noise. This is somewhat confirmed by the results of Figure F.5, which show the average values of $\rho_{ij}(0)$ as a function of SNR obtained using the cross-spectra for one antenna pair of the model-generated data-set MOD-MF-SA. These results suggest that the average values are approximately constant for SNRs below 5 dB. For SNRs below 5 dB the estimates of $\rho_{ij}(0)$ increase with decreasing SNR's. This effect occurs because the noise component becomes more dominant, such that the signal contributions cannot be successfully determined.

The average value of the phase slope obtained from the cross-spectra determined for one antenna pair for all records of the model-generated data-set MOD-MF-SA are shown in Figure F.5. These results suggest that the average values are approximately constant for SNRs below 5 dB. For SNRs below 5 dB the estimates of decrease with decreasing SNR. This is because the phase becomes more random, thereby increasing the probability that the slope of the fitted line will be closer to zero lag.

F.4 Summary

The results of Figure F.2 suggest that the properties of the signal contributions to the power-spectra can be successfully estimated for SNRs as low as 10 dB. However, the results of Figure F.5 suggest signal contributions to the cross-spectra can only be successfully estimates for

SNRs above 5 dB. It therefore follows that the FSA techniques should be limited to time-series records with SNRs greater than 5 dB. This may restrict the range coverage if individual time-series records are employed, as is the case for the analysis of *Briggs and Vincent* [1992]. On the other hand, there should be no problem meeting the 5 dB criterion if coherently averaged spectra are used, as is the case for the analysis employed by *Liu and Pan* [1993] and *Sheppard and Larsen* [1993].

Appendix G

The direction of the interferometric velocity

Although *Vandepeer and Reid* [1995] were able to derive a relatively simple analytical expression for the magnitude of the interferometric velocity in the volume scatter situation, attempts to derive a corresponding equation for the direction of the interferometric velocity have proven somewhat difficult. However, it is possible to deduce that the direction of the interferometric velocity must be equivalent to the direction of the actual wind velocity. The process of deduction is described below.

Consider the situation where the MAOA is centered on the zenith (i.e. $l_0 = m_0 = 0$) and the vertical velocity $w = 0$. In this case $v_{r_0} = 0$. The radial velocity $v_r(f)$ for each Doppler frequency f can then be expressed

$$v_r(f) = ul(f) + vm(f) = -\frac{\lambda f}{2}, \tag{G.1}$$

where u and v are the meridional components of the interferometric velocity, and λ is the radar wavelength. The direction cosines can be expressed by

$$l(f) = \frac{-\lambda(aV_x + hV_y)f}{aV_x^2 + bV_y^2 + 2hV_xV_y + k}, \text{ and} \tag{G.2}$$

$$m(f) = \frac{-\lambda(bV_y + hV_x)f}{aV_x^2 + bV_y^2 + 2hV_xV_y + k}, \tag{G.3}$$

where V_x and V_y are the zonal and meridional components of the ground diffraction pattern velocity.

Substituting (G.2) and (G.3) into (G.1) yields

$$-\frac{\lambda f}{2} = \frac{-\lambda u(aV_x + hV_y)f - \lambda v(bV_y + hV_x)f}{aV_x^2 + bV_y^2 + 2hV_xV_y + k}. \tag{G.4}$$

Canceling the factor λf from both sides multiplying both sides by the denominator yields

$$aV_x^2 + bV_y^2 + 2hV_xV_y + k = 2(u(aV_x + hV_y) + v(bV_y + hV_x)) \tag{G.5}$$

Collecting like terms into the coefficients for a, b, h and k yields

$$aV_x(V_x - 2u) + bV_y(V_y - 2v) + 2h(V_xV_y - uV_y - vV_x) + k = 0. \tag{G.6}$$

Consider the case where there are no random changes in the pattern, such that $k = 0$. In this case (G.6) can be rewritten

$$aV_x(V_x - 2u) + bV_y(V_y - 2v) + 2h(V_xV_y - uV_y - vV_x) = 0. \tag{G.7}$$

The ellipsoid parameters a and b are by definition positive. If the spatial correlation function of the ground diffraction pattern is elongated with axial-rotation $90° < \theta_{ax} < 180°$ it follows that h is also positive. In this case, it follows that (G.7) will only be satisfied if the coefficients of a, b, and h are zero. This yields the equations

$$u = V_x/2, \text{and} \tag{G.8}$$

$$v = V_y/2. \tag{G.9}$$

The choice of the x and y axes is arbitrary. If the axes were chosen such that the x-axis was reversed the same result would be obtained if the spatial correlation function of the ground diffraction pattern was elongated with axial-rotation $0° < \theta_{ax} < 90°$. It therefore follows that (G.8) and (G.9) must hold for all possible elliptical orientations of the spatial correlation function. This result suggests that the interferometric velocity will be equal to the actual wind velocity in the absence of turbulent random motions. In this case the apparent velocity magnitude will be equal to the magnitude of the actual wind velocity, while the direction will be biased perpendicular to the direction of elongation of the characteristic ellipse.

In the case where turbulent motions are present $k > 0$. In this case the direction cosines l and m are brought closer to the zenith in the same proportion. As the radial velocities associated with each Doppler frequency are constant it follows that u and v must increase in the same proportion, inversely proportional to l and m. It therefore follows that the direction of the interferometric velocity will not be altered by the effects of turbulent motions, suggesting that the direction of the interferometric velocity is identical to the direction of the actual wind velocity for all values of k.

Appendix H

Thresholds and the imaging interferometric analyses

The various imaging interferometry techniques employ a number of thresholds in order to select the Doppler frequencies considered appropriate to the analysis. These thresholds include zenith angle, power, phase consistency and radial velocity thresholds. This subsection focuses on the influence of these thresholds upon the interferometric analyses.

H.1 Zenith angle threshold

The various imaging interferometry techniques employ some form of zenith angle threshold for a variety of different reasons. A lower limit threshold was employed by *Meek and Manson* [1987] in order to minimize ambiguities associated with the correction for the phase differences between receivers. An upper limit threshold was employed by *Adams et al.* [1985,1986], *Meek and Manson* [1987] and *Franke et al.* [1990] in order to minimize the effects of spatial aliasing. An upper limit was employed by *Brosnahan and Adams* [1993] to preclude effective scattering positions outside the first minima in the transmitter polar diagram from the analysis.

The magnitude of the vector-averaged horizontal velocities obtained as a function of zenith angle threshold for the application of the interferometric techniques to the model-generated data-set MOD-MF-IDI with $v_{\mathrm{mod}} = 6$ ms^{-1} are shown in Figure H.1. The UNSIRI velocity magnitude increases as the zenith angle threshold is decreased. On the other hand, the SNSIRI, IDI-like and MSIRI velocity magnitudes increase with decreasing zenith angle

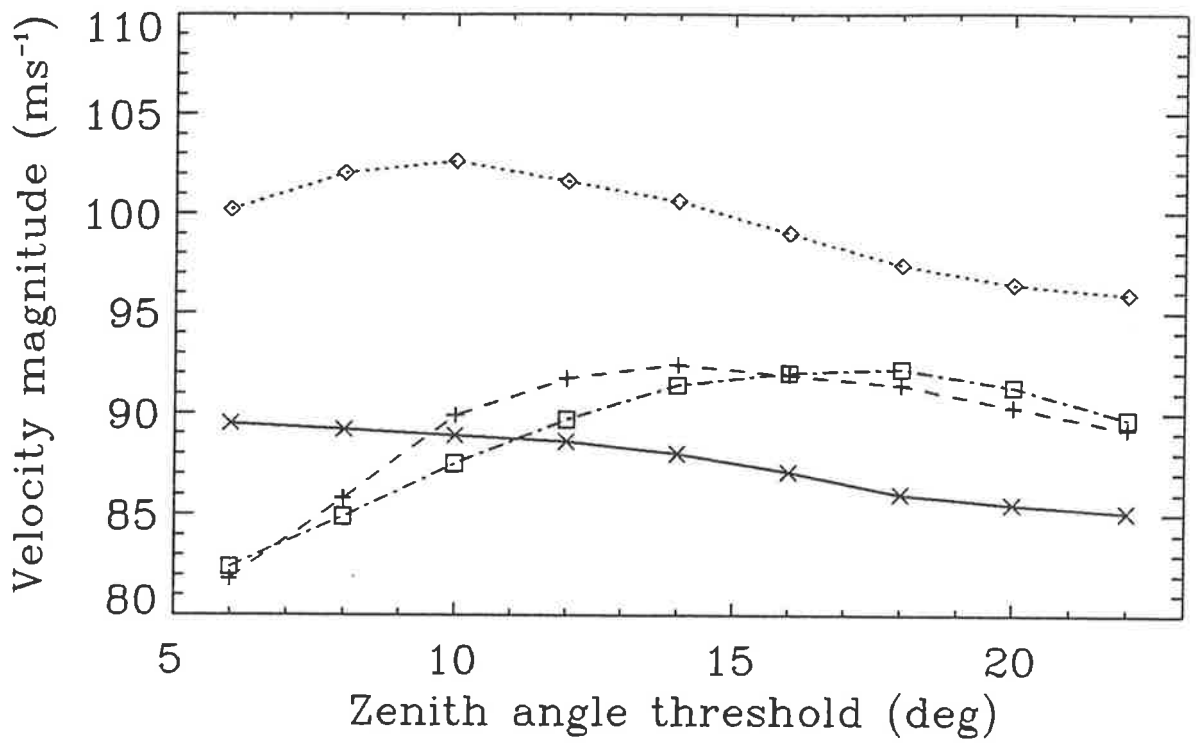

Figure H.1: Average horizontal velocities estimated by the interferometric techniques as a function of zenith angle threshold for a model turbulent velocity of 6 m s^{-1}. UNSIRI (□), SNSIRI (◇), IDI-like (+) and MSIRI (△).

threshold up to an upper limit, and then decrease with decreasing zenith angle threshold. At smaller zenith angle thresholds the UNSIRI velocity magnitude is larger than the IDI-like and MSIRI velocity magnitudes. This effect occurs despite the arguments presented in section 8.3 that the UNSIRI velocity magnitude is smaller than the IDI-like and MSIRI velocity magnitudes due to the inclusion of the effective scattering positions failing the single scatterer criterion employed by the IDI-like and MSIRI techniques in the UNSIRI analysis.

The cause of the velocity magnitude decrease can be understood by examining the effects of the zenith angle threshold upon the average of the magnitude of the individual velocity estimates, $\overline{V_{\rm int}}$, and the standard deviation of the direction of the individual velocity estimates, $\Delta\theta_{\rm int}$, as illustrated in Figure H.2. These results indicate $\overline{V_{\rm int}}$ increases with decreasing zenith angle. This effect occurs because the average zenith angle of the effective scattering positions decreases slower than the average absolute radial velocity as the zenith angle threshold is decreased. This effect is illustrated for the UNSIRI and IDI-like analyses in Table H.1. The value of $\Delta\theta_{\rm int}$ also increases with decreasing zenith angle threshold. This effect occurs because the number of effective scattering positions is decreased as the zenith

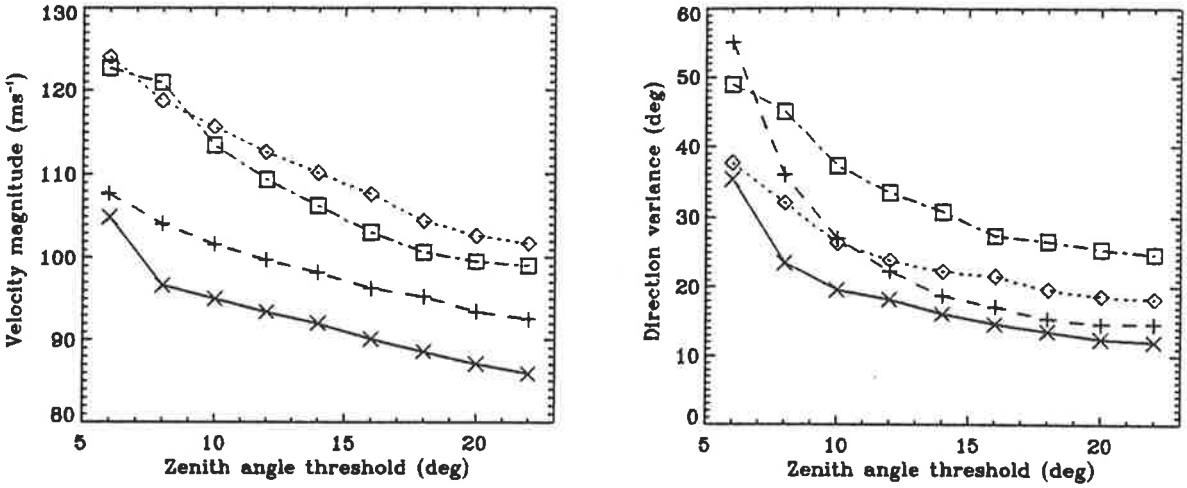

Figure H.2: Average horizontal velocities estimated by the interferometric techniques as a function of zenith angle threshold, for a model turbulent velocity of 6 ms^{-1}. UNSIRI (□), SNSIRI (◇), IDI-like (+) and MSIRI (△).

Table H.1: Relationship between estimated velocity, average zenith angle and average radial velocity for different values of the zenith angle threshold for the UNSIRI and IDI-like analyses.

	UNSIRI		IDI-like	
	10°	22°	10°	22°
Average zenith angle, deg	6.0	10.4	6.0	11.0
Average radial velocity, m s^{-1}	9.4	13.4	9.6	15.9
Average of the magnitude of velocity estimates, m s^{-1}	95.0	85.9	100.6	92.5

angle threshold is decreased, thereby resulting in an increase in the error of the velocity estimate. An increase in $\Delta\theta_{\text{int}}$ will lead to a decrease in the magnitude of the average velocity estimate. For smaller zenith angle thresholds the increase in $\Delta\theta_{\text{int}}$ overrides the increase in $\overline{V_{\text{int}}}$ for the SNSIRI, IDI-like and MSIRI analyses, thereby leading to a decrease in the magnitude of the velocity estimate as the zenith angle threshold is decreased.

The increase in the magnitude of the velocity estimates seen with decreasing zenith angle in Figure H.1 have also been reported by *Brosnahan and Adams* [1993]. This behavior was reduced by the implementation of a two-step process involving the use of the multiple record technique, as described in section 8.3. This process involved estimating the vertical velocity using effective scattering positions within 5° of the zenith, and then estimating the horizontal velocity using scattering positions within $3 - 16°$ of the zenith together with the estimated vertical velocity. This process is difficult to implement for the individual record analysis

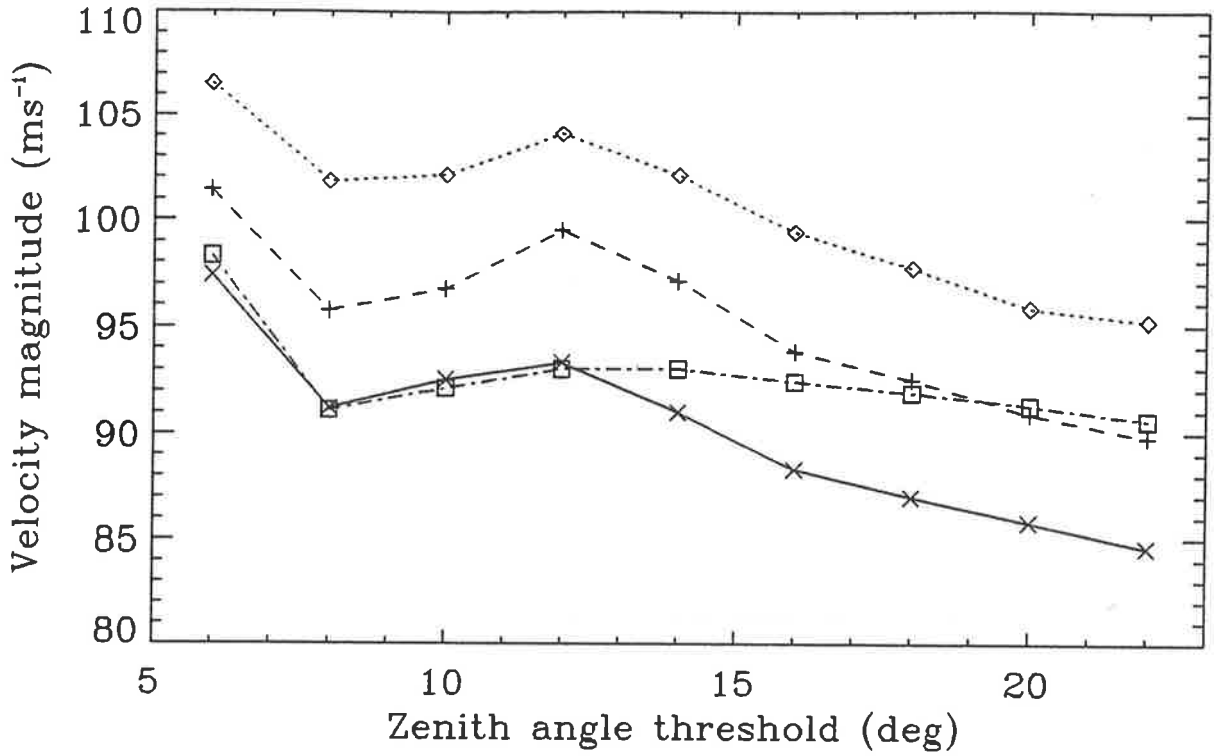

Figure H.3: Average horizontal velocities estimated by the interferometric techniques as a function of zenith angle threshold, for a model turbulent velocity of 6 ms^{-1}. UNSIRI (□), SNSIRI (◇), IDI-like (+) and MSIRI (△).

employed to produce the results illustrated in Figure H.2 and H.3 due to the small number of effective scattering positions. The magnitude of the velocity estimates obtained on applying this two-step process for the multiple record analysis of the interferometric techniques to the model generated data-set MOD-MF-IDI with $\nu_{\mathrm{mod}} = 6$ ms^{-1} are shown in Figure H.3 as a function of the zenith angle threshold. There is a general increase in the magnitude of the velocity estimate as the zenith angle threshold is decreased. There is also an odd effect seen for the NSIRI and IDI-like analyses where the magnitude of the velocity estimate decreases in the same fashion for zenith angle thresholds of $8 - 12°$. The source of this effect has not been established.

These results impact upon the use of spatial-aliasing thresholds. The results of Figures H.1 and H.3 indicate that the zenith-angle threshold can have a significant influence upon the velocity estimate.

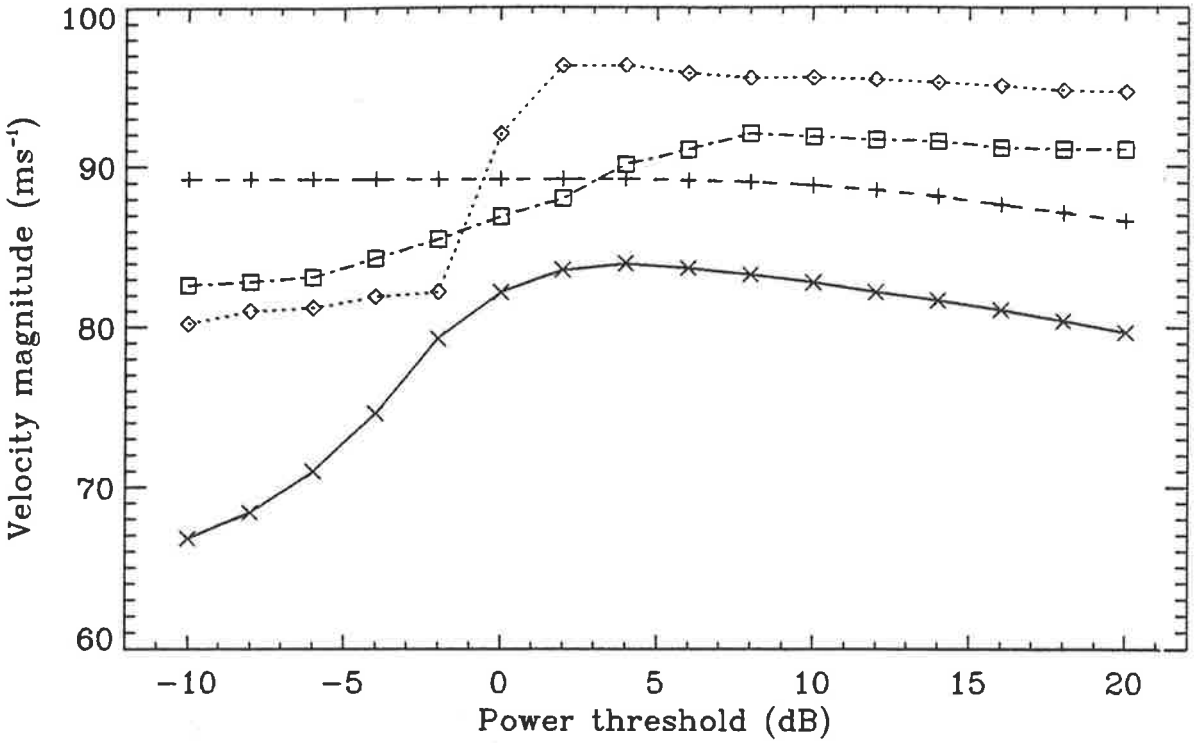

Figure H.4: Average horizontal velocities estimated by the interferometric techniques as a function of power threshold for a model turbulent velocity of 6 ms^{-1}. UNSIRI (×), SNSIRI (◇), IDI-like (+), MSIRI (□).

H.2 Power threshold

The majority of the imaging interferometry techniques employ some form of power threshold to preclude Doppler frequencies within the spectral tails from the analysis on the basis that they contribute little or no useful information. The IDI analysis of *Brosnahan and Adams* [1993] found that the effective scattering positions located using Doppler frequencies with low spectral power tended to cluster about the zenith. The close proximity of these scattering positions and the large distribution of the associated radial velocities prohibited an effective analysis, thereby necessitating their preclusion from the analysis.

The magnitude of the vector-averaged velocities resulting from the application of the interferometric techniques to the model-generated data-set MOD-MF-IDI with $\nu_{\text{mod}} = 6$ ms^{-1} are shown in Figure H.4 as a function of the power threshold. The general trend is that the estimates decrease with increasing power threshold above about 5 dB, and decrease with decreasing power threshold below about 5 dB. The decrease above about 5 dB results from the spectra being cut-off at progressively smaller Doppler frequencies. The resulting decrease in the average radial velocity is larger than the decrease in the average zenith angle, thereby

Table H.2: Relationship between estimated velocity, average zenith angle and average radial velocity for different values of the power threshold for the UNSIRI and IDI-like analyses.

	UNSIRI		IDI-like	
	4 dB	20 dB	4 dB	20 dB
Average zenith angle, deg	10.96	10.4	11.0	10.4
Average radial velocity, m s^{-1}	15.0	13.4	16.0	14.7
Magnitude of velocity estimate, m s^{-1}	84.0	79.4	89.3	86.6

resulting in a decrease in the magnitude of the average velocity. This behavior is summarized for the UNSIRI and IDI-like analyses in Table H.2.

The decrease in the magnitude of the velocity estimates seen with decreasing power threshold below 5 dB results from the inclusion of Doppler frequencies within the tails of the spectrum in the analysis. The additional effective scattering positions produced by these Doppler frequencies are randomly distributed within the ± 1 domain of the zonal and meridional direction cosines. This effect is illustrated in Figure H.5, which shows the effective scattering positions located on applying the UNSIRI and IDI-like analyses to all 200 records of the model-generated data-set MOD-MF-IDI with $\nu_{\text{mod}} = 6$ ms^{-1}, using Doppler frequencies with spectral powers *below* the 5 dB power threshold. These positions represent the effective scattering positions introduced into the analyses in the absence of a power threshold. The majority of the UNSIRI positions will be precluded from the analysis by the zenith angle threshold. The estimation of the interferometric velocities is reliant upon the existence of a systematic relationship between the effective scattering positions and their radial velocities. Any effect which degrades this relationship will lead to a decrease in the magnitude velocity estimate. The inclusion of the spurious effective scattering positions which pass the zenith angle threshold will therefore produce a decrease in the magnitude of the interferometric velocity estimate. Only 13 of the UNSIRI effective scattering positions pass the IDI-like phase consistency criteria. This is consistent with the results of Figure H.4 which illustrates that the magnitude of the velocity estimated by the IDI technique is constant for power thresholds below about 6 dB. The decrease in the MSIRI velocity magnitude is significantly smaller than for the NSIRI analyses because the local maxima criterion precludes the majority of Doppler frequencies from the tails of the spectrum from the analysis. The MSIRI analysis of *Meek and Manson* [1987] employs an additional "maxima threshold" precluding Doppler frequencies 30 dB below the largest spectral power from the analysis. The use of this maxima threshold in

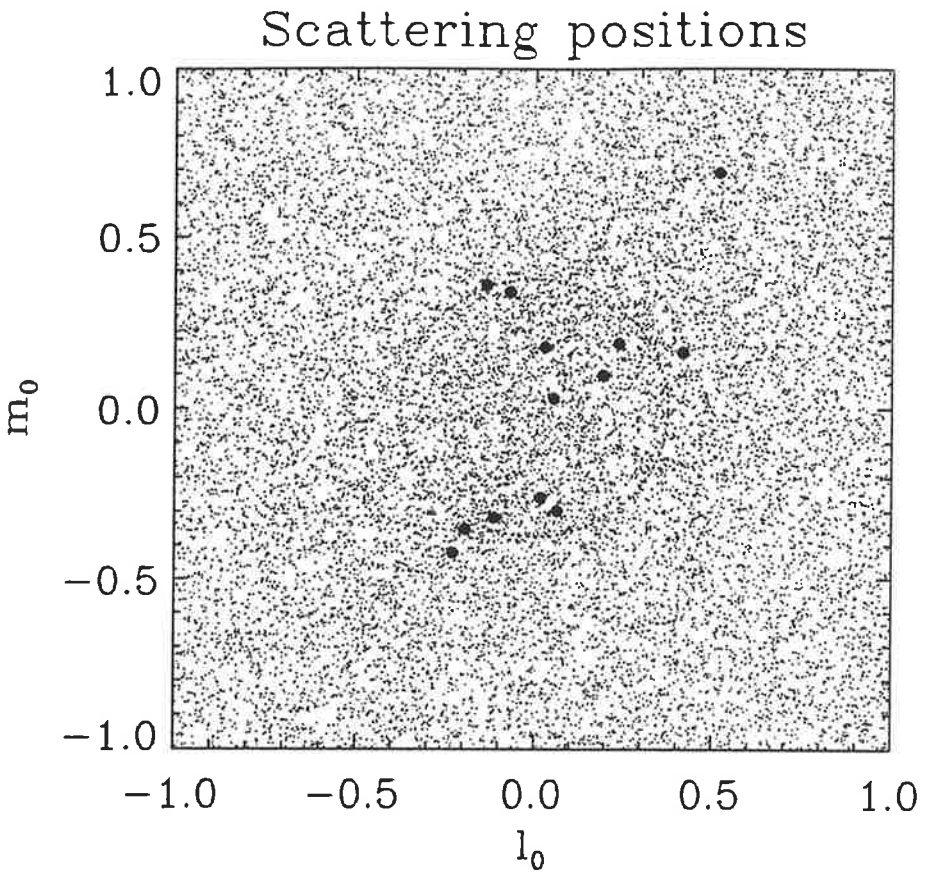

Figure H.5: Effective scattering positions located using Doppler frequencies with spectral powers below the 5 dB power threshold on applying the UNSIRI (·) and IDI-like (•) analyses to the model-generated data-set MOD-MF-IDI with $\nu_{\text{mod}} = 6$ ms^{-1}. The dotted circle denoted the bounds of the radar volume.

the current analysis overrides the power threshold, producing a MSIRI velocity magnitude of 89.4 ms^{-1} for all values of the power threshold.

There is no evidence of the clustering effect described by *Brosnahan and Adams* [1993] in either the UNSIRI and IDI-like effective scattering positions illustrated in Figure H.5. Although the IDI-like analyses of *Adams et al.* [1985,1986] do not employ a power threshold the results of Figure H.4 justify the use of a power threshold in the IDI analysis in the absence of any clustering effects. The absence of any power threshold will result in a significant increase in computation time due to the application of the phase consistency criterion to Doppler frequencies within the spectral tails which contain little or no useful information. The results of Figure H.5 suggest that very few of these Doppler frequencies will pass the IDI-like phase consistency criterion, suggesting that they should be precluded from the analysis prior to the phase consistency check. This is effectively the role played by the power threshold in the current IDI-like analysis.

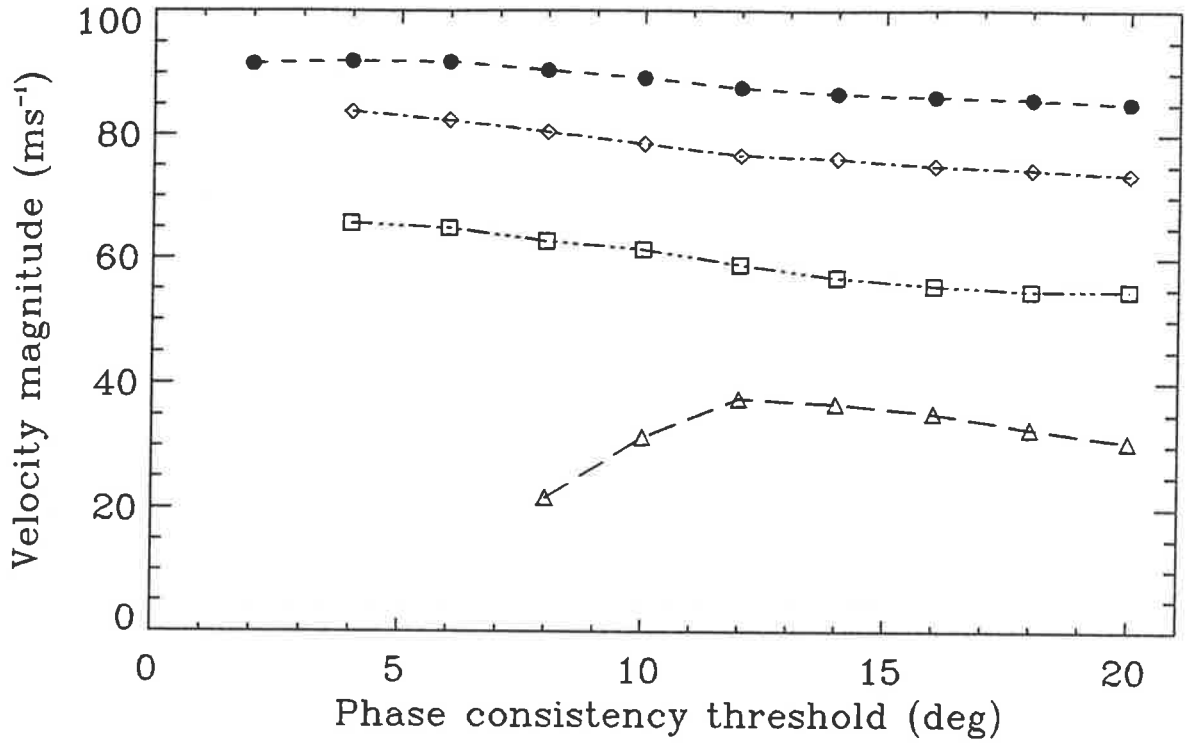

Figure H.6: Magnitude of the average horizontal velocities obtained on the application of the IDI-like technique to the model-generated data set MOD-MF-IDI with $v_{\rm mod} = 6$ ms^{-1} as a function of phase consistency threshold for the case of no added noise (•), and added noise with SNR 20 dB (◇), 10 dB (□) and 0 dB (△).

H.3 Phase consistency threshold

The phase linearity check employed by the IDI requires a goodness of fit threshold to determine whether the phase variation along each arm of the interferometer is linear, and therefore consistent with plane wave incidence. The goodness of fit parameter employed is arbitrary. The RMS difference between the actual and fitted phase variation used by *Adams et al.* [1985,1986] is used in current analysis, while the χ^2 parameter is used by *Vandepeer and Reid* [1995a].

The magnitude of the vector-averaged horizontal velocity resulting from the application of the IDI-like technique to the model-generated data-set MOD-MF-IDI with $v_{\rm mod} = 6$ ms^{-1} are illustrated in Figure H.6 as a function of the phase consistency threshold for various different SNRs of added receiver noise. The lowest value of the phase threshold for each plot indicates the value below which only a small number of acceptances occurred. The velocity magnitudes increase with decreasing phase threshold for larger values of the phase thresholds. This effect occurs because the analysis is progressively rejecting Doppler frequencies which

do not conform with the volume scatter situation. The velocity magnitudes either level-off or decrease with decreasing phase threshold for smaller values of the phase thresholds because the variance in the direction of the individual velocity estimates increases. This effect occurs because progressively fewer Doppler frequencies pass the phase consistency threshold, resulting in a larger error in the velocity estimate.

The minimum phase threshold decreases with decreasing SNR because the addition of noise results in the phases being perturbed from their noise free values, thereby resulting in increasingly fewer cases satisfying the same phase consistency threshold than for the noise free case. This result suggests that the phase consistency criteria should possibly be varied with height as appropriate to the expected SNR. Use of a constant phase threshold may therefore preclude Doppler frequencies with useful information from the analysis procedure.

Appendix I

A simple model of atmospheric backscatter: Description and application to the full correlation analysis of spaced antenna data

This is a reprint of a paper by David A. Holdsworth and Iain M. Reid, published in *Radio Science, 30*(4), 1263-1280, 1995.

Radio Science, Volume 30, Number 4, Pages 1263–1280, July–August 1995

A simple model of atmospheric radar backscatter: Description and application to the full correlation analysis of spaced antenna data

David A. Holdsworth and Iain M. Reid

Department of Physics and Mathematical Physics, University of Adelaide, Adelaide, Australia

Abstract. A model has been developed for simulating the effects of backscatter from scatterers advected with a mean background wind. This model has been designed to be as simple yet as realistic as possible, allowing the simulation of both spaced antenna and Doppler radars, and includes features such as aspect sensitivity, gravity wave perturbations, and turbulent motions. The model simulates the characteristics of radar backscatter very well at both MF and VHF. Results of the application of the full correlation analysis to model data generated for the spaced antenna configuration are presented, revealing good agreement with the model input velocity. The effects of the sampling time upon the full correlation analysis are investigated, suggesting an upper limit for the successful application of the technique. The triangle size effect of the full correlation analysis is also investigated, confirming that the major cause is the failure to properly compensate for the effects of noise. The application of techniques for the estimation of turbulent velocities and aspect sensitivity from model-generated data have also proven successful.

1. Introduction

The conventional technique for the estimation of atmospheric wind velocities using spaced antenna (SA) radars is the full correlation analysis (FCA) [e.g., *Briggs*, 1984]. The FCA is applied to SA data obtained both at VHF in the lower atmosphere (2-20 km) [e.g., *Vincent et al.*, 1987] and at MF/HF in the upper mesosphere and lower thermosphere (60-100 km) [e.g., *Vincent and Lesicar*, 1991]. Comparisons between the FCA velocities and direct measurements are possible using radiosonde (2-20 km) [e.g., *Vincent et al.*, 1987] and rocket (60-100 km) [e.g., *Vincent et al.*, 1979] measurements. The FCA velocities can also be compared with the results of alternative techniques such as Doppler radar [e.g., *Reid*, 1988], meteor drifts [e.g., *Cervera and Reid*, this issue], and interferometry [e.g., *Franke et al.*, 1990; B. G. W. Vandepeer and I. M. Reid, On the spaced antenna and imaging Doppler interferometer techniques, submitted to *Radio Science*, 1994]. Needless to say, these techniques may have systematic velocity biases themselves.

It is generally considered that the FCA velocity underestimates the actual wind velocity by approximately 5-10%, as suggested by intercomparisons with both meteor drift winds [e.g., *Stubbs*, 1973] and high-resolution Doppler imaging (HRDI) derived winds [e.g., *Burrage et al.*, 1993]. This may be a result of several possibilities, including the "triangle size effect" [e.g., *Golley and Rossiter*, 1970], filtering of the fluctuations in the backscattered signal [e.g., *Chandra and Briggs*, 1978], resulting, for example, from the use of coherent integration, saturation of the time series, and undersampling.

The present model has been developed to al-

Copyright 1995 by the American Geophysical Union.

Paper number 95RS00645.
0048-6604/95/95RS-00645$08.00

low the comparison of results obtained using various techniques with known model inputs. Partial motivation for this work has been provided by *Hines et al.* [1993], who suggested that MF radars may be in error because they measure the phase speed of gravity wave perturbations within the volume illuminated by the radar, rather than the background wind velocity. Additional motivation is the desire to more fully understand the analysis of radar data from SA and Doppler experiments, both at MF and VHF.

Similar model analyses have previously been conducted exclusively for SA techniques for a variety of different purposes, none of which will be repeated in this paper [e.g., *Pfister*, 1971; *Pitteway et al.*, 1971; *Wright and Pitteway*, 1978; *Meek and Reid*, 1984; *Van Baelen et al.*, 1989; *Sheppard and Larsen*, 1992; *Sūrūcū et al.*, this issue]. The present model incorporates features from some of these models such as gravity wave perturbations and turbulent motions, and additional features such as aspect sensitivity effects and a "constant range" scattering volume, used to overcome any spurious effects that may result from the "constant height" scattering volume used in the aforementioned models. The basis of the model is presented in section 2. The analysis of model generated data is presented in section 3 in order to validate the model. Model-generated data are utilized in section 4 to analyze the effects of the sampling time upon the FCA, and in section 5 to analyze to triangle size effect. A brief summary and suggestions for future work are presented in section 6.

2. The Atmospheric Radar Backscatter Model

2.1. Basis of the Model

The atmospheric radar backscatter model has been developed to be as simple and versatile as possible, allowing the application of a number of techniques such as SA, Doppler, and interferometry. The model is programmed in interactive data language (IDL), requiring few simplifications in order to produce convenient computational times when run on a DEC Alpha.

The "radar volume" is defined according to a beam-pointing angle, an "effective" beam width, and a range gate extent. In this model the radar volume is enclosed within a cylindrical volume, hereafter referred to as the "enclosing" volume, throughout which a number of scattering locations are initially randomly positioned. These scatterers represent regions of refractive index irregularity, as opposed to physical objects. At each sampling time the complex returns from each scatterer are added, and the scattering positions are updated, based on specified values of the mean background wind, turbulent motions, and gravity wave perturbations. Scatterers updated to positions outside the enclosing volume are readmitted in the same manner as described by *Meek and Reid* [1984], maintaining a constant number of scatterers.

The effective beam width is defined by the largest angle from the beam-pointing angle resulting in a returned power equal to some specified ratio P_0 of the maximum power returned within the beam, based on the specified value of aspect sensitivity. This is calculated using the equation

$$P(\theta) = \exp\left(-\left(\frac{\sin\theta}{\sin\theta_s}\right)^2\right) \exp\left(-\left(\frac{\sin\theta - \sin\theta_a}{\sin\theta_b}\right)^2\right), \quad (1)$$

where θ_a is the beam pointing angle, θ_b is the e^{-1} beam width, and θ_s is the aspect sensitivity [e.g., *Reid*, 1988]. This aspect sensitivity simulates scatterers which are more extended horizontally than vertically. Thus although individual scattering positions are used, the model is not a "point scatterer model." It corresponds to a random array of diffracting irregularities, each of which has a polar diagram corresponding to θ_s, and thus corresponds to a "volume scatter model." The θ_s values used can be converted into length-to-height (L/h) ratios of the scat-

terers [e.g., *Lesicar and Hocking*, 1992] by the equation

$$\left(\frac{L}{h}\right)^2 = \left(\frac{\lambda}{8\pi^2 \sin^2 \theta_s} + 1\right), \qquad (2)$$

where λ is the radar wavelength. Typical average weekly mesospheric L/h values of between 3 and 5 have been obtained using the Adelaide 2-MHz radar [*Lesicar and Hocking*, 1992], corresponding to average weekly θ_s values ranging from 6° to 14°.

The enclosing volume is selected in order to comfortably encompass the extent of the radar volume, as illustrated in the model geometry plot of Figure 1. The initial scattering positions are obtained by generating uniform random three-dimensional positions within the enclosing volume.

2.2. Generating the Model Time Series

At each sampling time the complex returns from all scatterers within the radar volume are added. Each scatterer is assigned a reflectivity ratio p within the range [0.5, 1.0] in relation to the maximum reflectivity value within the radar volume. The amplitude of the complex return from the ith scatterer a_i, located at a zenith angle θ_i, is given by

$$a_i = p_i R_i \sqrt{P(\theta_i)}, \qquad (3)$$

where $P(\theta_i)$ is obtained from (1), and R_i is a triangular range weighting function varying linearly from unity in the middle of the range gate to zero at the edges of the range gate. The inclusion of the aspect sensitivity and range gate function implies no spurious effects are generated by a scatterer leaving the radar volume, as the amplitude of the complex return from this scatterer is small due to the close proximity of the radar volume boundary. The phase of the complex return from the ith scatterer is given by

$$\phi_i = 2\pi \left(\frac{|\vec{r}_{ti}| + |\vec{r}_{ri}|}{\lambda}\right), \qquad (4)$$

where $|\vec{r}_{ti}|$ is distance between the transmitter and the ith scatterer, $|\vec{r}_{ri}|$ is distance between the relevant receiver and the ith scatterer, and λ is the radar wavelength.

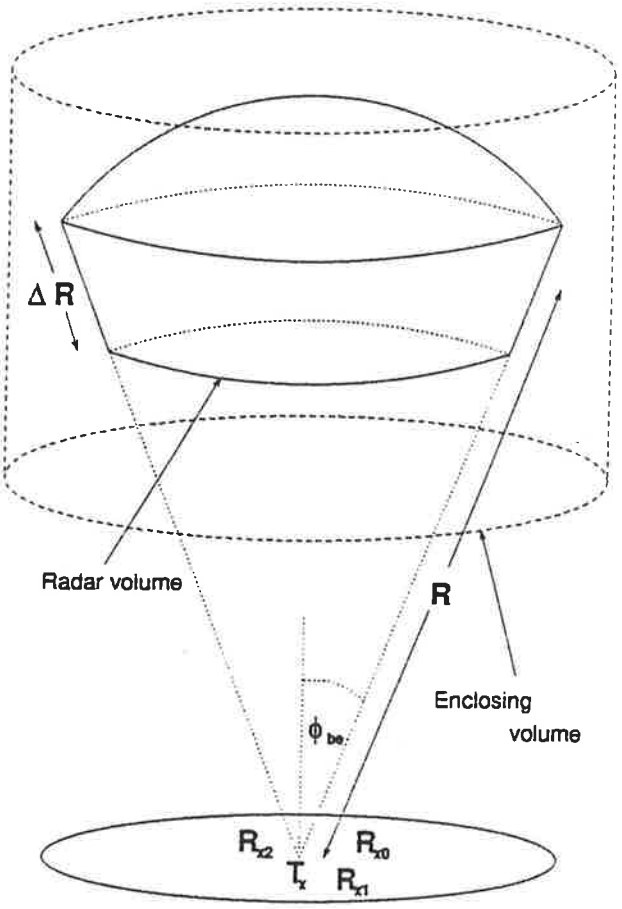

Figure 1. Radar volume enclosed within cylindrical enclosing volume, where θ_{be} is the effective beam width, R is the range, and ΔR is the range gate width.

The triangular range weighting function employed is not ideal, as artificial partial reflection components may result due to the discontinuity in the first derivative at the middle of the range gate and, to a lesser extent, at the edges of the range gate. This function has subsequently been replaced by a Gaussian range weighting function, thereby removing the discontinuity at the middle of the range gate. The Gaussian range weighting function still results in an unavoidable discontinuity at the edges of the range gate. The range cutoff is set in an analogous manner to the zenith cutoff.

2.3. Updating the Scattering Positions

The position of the ith scatterer after the $n+1$th update of position $\vec{r}_{i,n+1}$ is given by

$$\vec{r}_{i,n+1} = \vec{r}_{i,n} + (\vec{V} + \vec{V}_{\mathrm{gw}}(\vec{r}_{i,n}) + \vec{V}_{\mathrm{turb}}(\vec{r}_{i,n}))\Delta t, \quad (5)$$

where $\vec{V}$ is the mean background wind velocity, $\vec{V}_{\mathrm{gw}}(\vec{r}_{i,n})$ is the gravity wave perturbation velocity at $\vec{r}_{i,n}$, $\vec{V}_{\mathrm{turb}}(\vec{r}_{i,n})$ is the turbulent velocity at $\vec{r}_{i,n}$, and Δt is the sampling time. The gravity wave velocity perturbations have been implemented in the same manner as in the model of *Meek and Reid* [1984], which was used to analyze the effects of short-period gravity waves upon FCA. At any position $\vec{r}_i$ the velocity perturbation is given by

$$\vec{V}_{\mathrm{gw}}(\vec{r}_i) = \vec{v}'_{\mathrm{gw}} \cos(\omega t + \vec{k} \cdot \vec{r}_i), \quad (6)$$

where $\vec{v}'_{\mathrm{gw}}$ is the gravity wave perturbation velocity, $\vec{k}$ the direction of propagation, and ω the angular frequency. The effects of gravity waves upon the FCA will not be covered in the present paper.

Turbulent motions are simulated as follows. A three-dimensional vector $\vec{v}'$ is generated for each scatterer, with components generated according to Gaussian distributions with specified horizontal and vertical root-mean-square (rms) values. The turbulent velocity for the ith scatterer is then given by

$$\vec{V}_{\mathrm{turb}}(\vec{r}_{i,n}) = \sum_{j=0}^{N-1} \vec{v}'_j \exp - \left(\frac{|\vec{r}_{i,n} - \vec{r}_{j,n}|}{S_{\mathrm{turb}}} \right)^2, \quad (7)$$

where S_{turb} is the "turbulent scale factor". This simulation allows the turbulent motions to evolve so that no abrupt changes are seen. Examples of the horizontal and vertical turbulent velocity fields are shown in Figure 2. If the density within the radar volume is assumed constant the continuity equation is satisfied to within 2% when using a rectangular volume of the scale of the interscatterer spacing about each scattering position.

It appears that this turbulent motion simulation is a significant improvement on the simulations of *Wright and Pitteway* [1978] and *Sheppard and Larsen* [1992]. Turbulent motions are simulated in the model of *Sheppard and Larsen* [1992] by generating a different set of three-dimensional normally distributed random turbulent velocity components for each positional update. In the duration of the sampling time the turbulent velocity of an individual scatterer can therefore reverse direction. In addition to the obvious poor approximation of this simulation, such abrupt changes in the turbulent velocity result in "spikes" at zero lag in the auto- and cross-correlation functions. Since the spike in the autocorrelation function is usually used to estimate the signal-to-noise ratio (SNR) in the FCA, this is an undesirable effect. Such effects are not seen in the current model.

Wright and Pitteway [1978] simulate two-dimensional turbulent motions using either the same technique as *Sheppard and Larsen* [1992] ("explicit random motions"), or by giving each scatterer a fixed turbulent velocity ("fixed direction motions"). However, instead of using normally distributed random turbulent velocity components, *Wright and Pitteway* [1978] use uniformly distributed components, raised to various different powers between 0 and 1, in order to produce various different distributions. The latter technique does not produce zero-lag correlation spikes but does allow the possibility that scatterers with different turbulent velocities can overlap.

If the updated position for a particular scatterer lies outside the enclosing volume the scatterer is readmitted at the opposite horizontal position to that occupied at the previous sampling time. On readmission of a scatterer, both the random reflectivity and the turbulent velocity $\vec{v}'$ associated with the scatterer are regenerated, as the readmitted scatterer is considered to be a different scatterer to that leaving the enclosing volume.

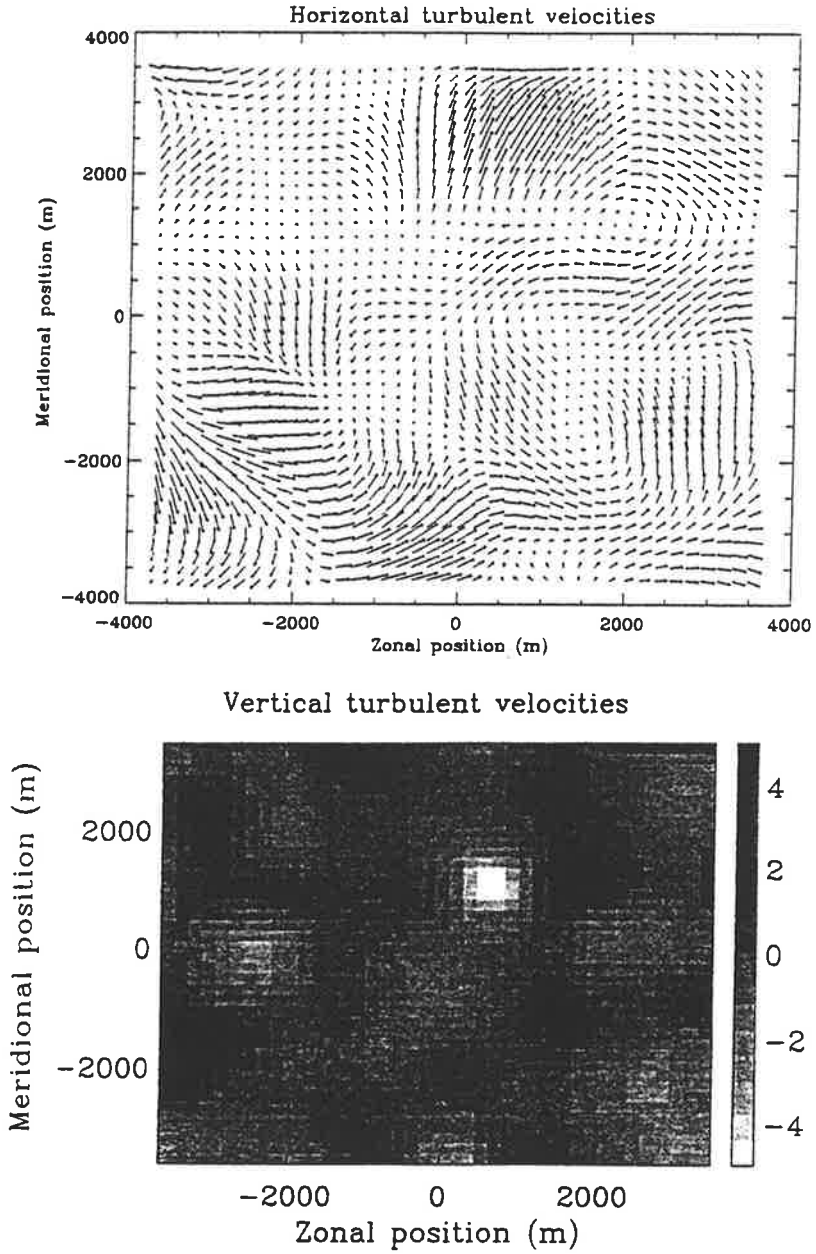

Figure 2. Examples of subsets of the constant height horizontal and vertical turbulent velocity fields obtained using the MF simulation with $\nu_{mod} = 5$ m s^{-1}. The longest arrow on the horizontal field corresponds to a velocity magnitude of 12 m s^{-1}.

2.4. Model Parameters

The model has been used to approximate the general conditions appropriate to MF and VHF SA radars. The relevant parameters used in this paper unless otherwise indicated are shown in Table 1, and will hereafter be referred to as the MF and VHF simulation parameters. As various noise sources seen in actual radar systems are not present in the model, no coherent averaging is necessary, and each multiantenna receiving array can be simulated by a single an-

Table 1. MF and VHF Simulation Parameters

Model parameter	MF mode	VHF mode
Radar Frequency, Hz	1.98	54.1
Range, km	90	10
Range resolution, km	2	0.5
Transmitter beam width, deg	15	2.5
Beam pointing angle, deg	0	0
Receiver beam-width, deg	∞	∞
Receiver spacing, m	200	50
Sampling time, s	0.4	0.125
Time series length	256	256
Number of scatterers	600	200
Aspect sensitivity, deg	10	4
Cut-off power ratio P_0	0.05	0.0 5
Wind speed, m s^{-1}	50	20
Wind direction (E of N), deg	15	15
Turbulent rms velocity, m s^{-1}	5	0.5

tenna position with the appropriate polar diagram. Each sample is therefore the representation of the complex voltage induced at the particular sampling time and antenna position rather than the coherent average over the complex voltages induced over number of pulses and antenna positions. These simplifications have been tested and found to not significantly alter the results obtained. Gaussian-distributed receiver noise of a specified SNR may be added to the time series afterwards to simulate the effects of receiver noise. The importance of filtering of the time series by the application of coherent integration will be addressed in later work.

Because the polar diagrams of the receiving antennae are generally significantly larger than the angular polar diagrams of the backscatter for both the MF and VHF radars, the model receiver beam width is set to be infinite. The receiving antennae form the vertices of an equilateral triangle, at azimuth angles 60°, 180°, and 300° east of north from the transmitter, located at the center of the triangle. The aspect sensitivity values used for each height are based on the values given by *Reid* [1990] for MF radars in the 60-100 km height region and *Hocking et al.* [1986] for VHF radars in the 2-20 km region. An example of the complex time series produced by the MF simulation parameters is illustrated in Figure 3.

3. Analysis of Model-Generated Data

3.1. The Full Correlation Analysis

The full correlation analysis (FCA) is used to estimate atmospheric wind velocities from the ground diffraction pattern resulting from the atmospheric backscatter of a transmitted signal by refractive index irregularities. The pattern is generally sampled at three spatially separated positions. The basic assumption of FCA is that contours of equal spatial-temporal correlation of the ground diffraction pattern can be approximated by a family of ellipses [e.g., *Briggs*, 1984] of the general form

$$\rho(\xi,\eta,\tau) = \rho(A\xi^2 + B\eta^2 + C\tau^2 + 2H\xi\eta + 2(F\xi + G\eta)\tau), \quad (8)$$

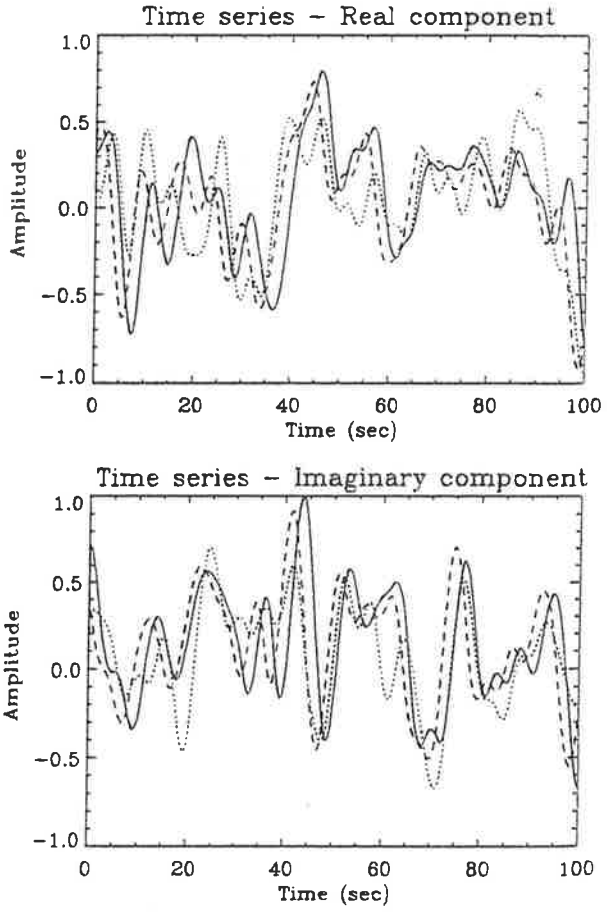

Figure 3. Real and imaginary components of model-produced time series using the MF simulation parameters shown in Table 1.

where ξ and η are the spatial dimensions and τ is the temporal dimension. Complex auto- and cross-correlation functions are calculated from the complex voltages induced at each receiver. Two velocity estimates are produced: the "apparent" and "true" velocities. The apparent velocity is calculated directly from the time delays corresponding to the cross-correlation function maxima, and is usually an overestimate of the actual velocity, as it incorporates the effects of random changes in the ground pattern resulting from turbulent fading. The true velocity is corrected for this effect and is therefore generally considered the better estimate of the actual velocity. FCA also provides information on the characteristics of the ground diffraction pattern.

The basic calculations employed by FCA are as follows. The three auto- and cross-covariance functions are calculated from the three-receiver time series. The autocovariance at zero-lag includes the effects of noise. This is removed by using an interpolation over zero-lag. The most commonly used interpolations are parabolic and cubic spline. In the real-time radar FCA programs used by the Adelaide group a cubic spline interpolation is used, using the first, second, and third lags of the autocovariance functions. The zero-lag autocovariances are then used to normalize the auto- and cross-covariance functions to produce the auto- and cross-correlation functions, denoted $\rho_i(\tau)$ and $\rho_{ij}(\tau)$, $(i,j) = (1,2,3)$, respectively. The cubic spline interpolation is also used to interpolate over the zero-lag cross-correlation to remove the effects of noise seen simultaneously in each of the three receivers.

Having calculated the correlation functions, the relevant parameters can be determined. The cross-correlation maxima ρ_{0ij} and their corresponding lag times τ'_{ij} are determined by fitting a Gaussian over the three lags either side of the maxima. The half width of the mean autocorrelation function is then determined by fitting a Gaussian over those lags exceeding the minimum value of the three cross-correlation maxima and 0.5, producing the fading time $\tau_{0.5}$. Finally, the lags τ_{ij} where the mean autocorrelation function equals the zero-lag cross correlations are determined analytically by the equation

$$\tau_{ij}^2 = \tau_{ij}'^2 - \tau_{ij}''^2, \tag{9}$$

where τ''_{ij} are the lags where the mean autocorrelation function equals the cross-correlation maxima, given by

$$\tau''_{ij} = \sqrt{\frac{-\ln \rho_{ij\max}}{\ln 2}}\,\tau_{0.5}. \tag{10}$$

Having calculated these parameters, the "ellipse parameters" ($A, B, C, F, G,$ and H from (8)) can be calculated, from which the various FCA outputs can be determined. These outputs include the apparent $\vec{V}_a$ and true velocity $\vec{V}_t$, the fading time in the reference frame of the mean background wind $T_{0.5}$, and parameters describing the ground diffraction pattern in terms of the elliptical formulation of the FCA describe in (8), such as the pattern scale (the square root of the product of the major and minor axes), the pattern orientation (angle subtended by the major axis), and the axial ratio (ratio of the major to minor axis).

3.2. Application of the FCA to Model-Generated Data

In the absence of turbulent motions or gravity waves the atmospheric refractive index irregularities propagate with the mean background wind. In this case the true and apparent velocity should almost be equal. The fading time in the frame of the pattern $T_{0.5}$ should be large, as the only change in the pattern in this frame is due to the variation in reflectivity of the individual scatterers as they propagate across the field of the transmitted beam.

These conditions can be simulated using the model without turbulent motions or gravity wave perturbations. The model was run using the MF simulation parameters, with horizontal and vertical turbulent rms velocities ranging from 0 to 6 m s^{-1}. The resultant average FCA outputs over 200 realizations are illustrated in Figure 4, where the error bars denote the standard devi-

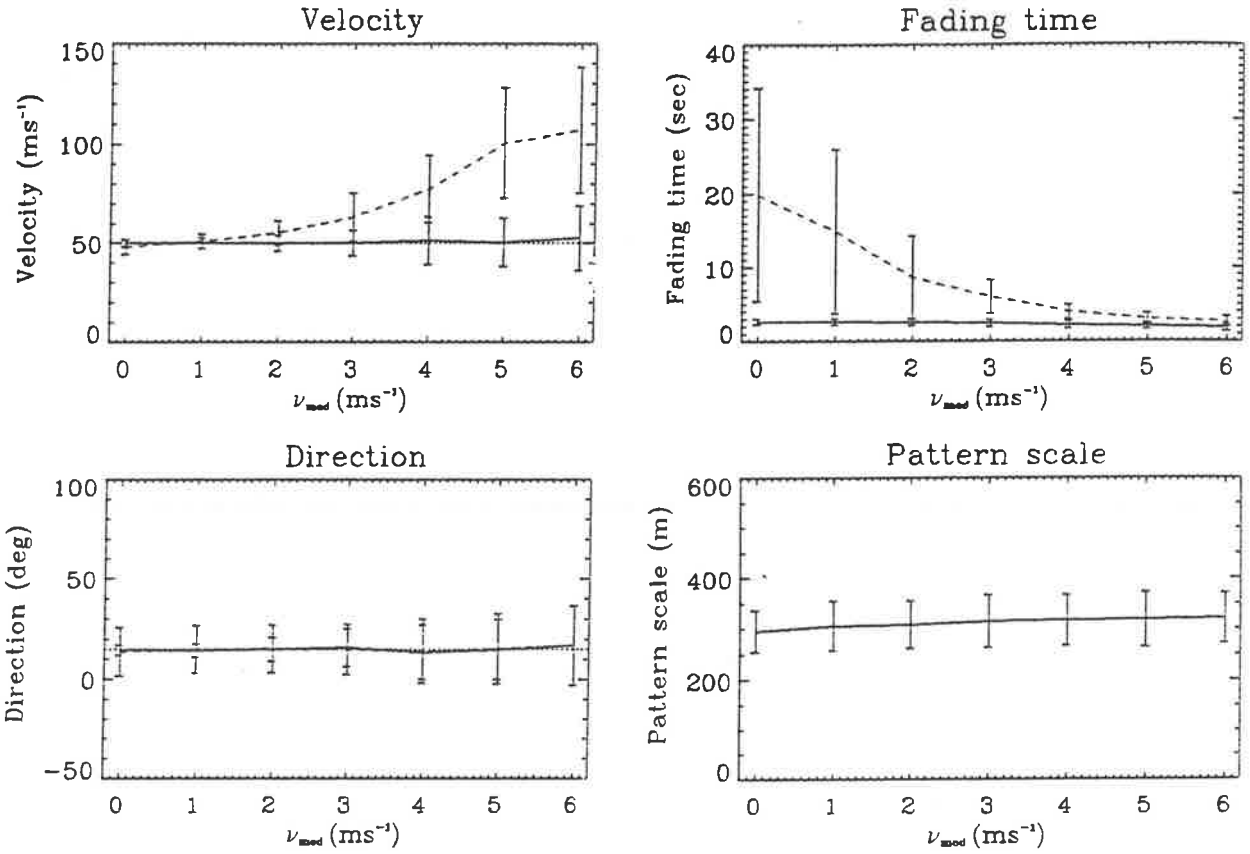

Figure 4. The FCA outputs as a function of ν_{mod} for the MF simulation. The solid and dashed lines on the velocity and direction plots indicate the vector averaged true and apparent outputs, respectively, while the dotted lines indicate the model input values. The solid and dashed lines on the fading time plot indicate the fading times in the frame of the receiving antennae and the frame of the pattern, respectively.

ation of the distributions. Without turbulent motions $\vec{V}_a \approx \vec{V}_t$, and $T_{0.5}$ is large. With increasing turbulent motions, $|\vec{V}_a|$ increases, and $T_{0.5}$ and $\tau_{0.5}$ decrease, as expected. The true speed $|\vec{V}_t|$ is essentially constant, accurately reproducing the magnitude of the model velocity, and also revealing that the FCA is compensating correctly for the effects of turbulent fading. The true and apparent directions accurately reproduce the model velocity direction.

3.3. Turbulent Velocity Estimations From Model-Generated Data

The turbulent motions simulation has been analyzed by comparing the model rms turbulent velocity ν_{mod} with values estimated by the techniques of *Briggs* [1980] and *Hocking* [1983]. The turbulent rms velocity predicted by *Briggs* [1980] is given by

$$\nu_{\mathrm{fca}} = \frac{\lambda\sqrt{\ln 2}}{4\pi T_{0.5}}, \tag{11}$$

and can therefore be determined during the application of FCA. The turbulent vertical rms velocity predicted by the "spectral width" method of *Hocking* [1983] is given by

$$\nu_{\mathrm{sp}} = \frac{\lambda}{2\sqrt{2\ln 2}}\sqrt{f_{0.5}^2 - f_{\tau 0.5}^2}, \tag{12}$$

where $f_{0.5}$ is the "turbulent" power spectrum half width and $f_{r0.5}$ is the theoretical "nonturbulent" power spectrum half width. The experimental application of this technique requires the use of a narrow transmitting beam and a short pulse width in order to eliminate the effects of wind shear broadening. These conditions have been simulated by the model using the MF simulation parameters with a vertically transmitted beam width of 2° and range gate extent of 500 m. This is essentially a Doppler radar configuration. The nonturbulent power spectrum half width was calculated by running the model with a zero rms turbulent velocity.

Figure 5 shows the relationship between the model input turbulent velocity ν_{mod} and the average values of ν_{fca} and ν_{sp} over 200 realizations. The nonzero value of ν_{fca} obtained when $\nu_{\text{mod}} = 0$ can be explained by taking into account the fact that the value of $T_{0.5}$ used to derive (11) is assumed to be solely due to turbulent fading. However, as discussed above the variation in the reflectivity of the individual scatterers as they propagate through the beam contributes to $T_{0.5}$, as alluded to by *Briggs* [1984]. This effect results in ν_{fca} overestimating ν_{mod} when ν_{mod} is small. As ν_{mod} is increased turbulent fading gradually becomes the major contributor to $T_{0.5}$, and $\nu_{\text{fca}} \approx \nu_{\text{mod}}$. These results suggest that the turbulent motions simulation employed by the model approximates actual turbulent motions satisfactorily.

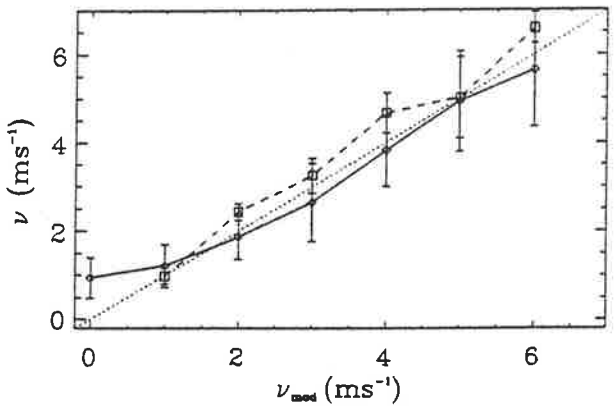

Figure 5. Estimated ν as a function of ν_{mod} for the MF simulation. The solid line indicates the FCA estimated values, while the dashed line indicates the spectral width estimated values. The error bars indicate the standard deviations of the distributions.

3.4. Aspect Sensitivity Estimations From Model-Generated Data

The aspect sensitivity simulation has been analyzed by comparing the model aspect sensitivity with the results obtained using two techniques described by *Lesicar and Hocking* [1992]. The "spectral width" method relates the FCA fading time $\tau_{0.5}$ to the e^{-1} width of the effective polar diagram θ_{sb} (in degrees) by the equation (after some manipulation)

$$\theta_{sb} = \frac{7.6\lambda}{|\vec{V}|\tau_{0.5}}, \tag{13}$$

where λ is the radar wavelength, and $\vec{V}$ is the horizontal wind velocity. The "spatial correlation" method relates the FCA pattern scale S and axial ratio r to θ_{sb} (in degrees) by the equation (after some manipulation)

$$\theta_{sb} = \frac{15.2\lambda\sqrt{r}}{S}. \tag{14}$$

Using (1), the aspect sensitivity θ_s can be estimated by

$$\sin^{-2}\theta_s = \sin^{-2}\theta_{sb} - \sin^{-2}\theta_b, \tag{15}$$

where θ_b is the beam width.

The model was run using the MF simulation parameters without turbulent motions, using a number of different aspect sensitivities. Figure 6 shows the average predicted θ_s values for both techniques as a function of the model aspect sensitivity $\theta_{s\text{mod}}$, over 100 realizations. These results suggest the aspect sensitivity simulation approximates the realistic case well.

As illustrated in Figure 4 the presence of turbulent motions results in an decrease in $\tau_{0.5}$ and a small increase in the pattern scale. As a result, the spectral width estimate of θ_s will be greater than that calculated without turbulent motions, while the spatial correlation estimate

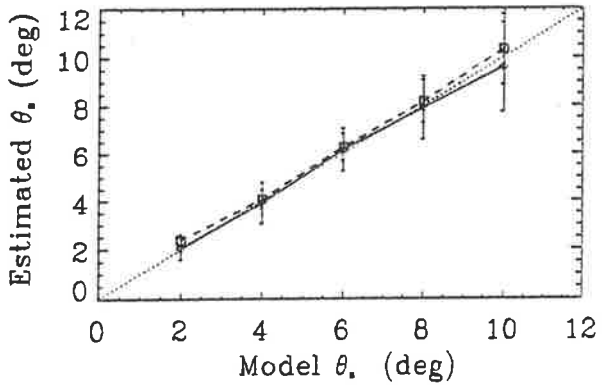

Figure 6. Estimated θ_s as a function of θ_{smod} for the MF simulation. The solid line indicates the results estimated using the spatial correlation technique, while the dashed line indicates the results estimated using the spectral width technique. The error bars indicate the standard deviations of the distributions.

will be slightly smaller. These results are consistent with those obtained by *Lesicar and Hocking* [1992] who found that the spectral width estimate produced values up to 2° larger than the spatial correlation estimate.

Because the scatterers are isotropic and homogeneously distributed throughout the radar volume, there should be no preferred pattern orientation, and the distribution of the axial ratio of the ellipses describing the ground diffraction pattern should be centred close to unity. Figure 7 shows histograms of the pattern rotation and axial ratio for the combined results used to produce Figure 4. These results clearly indicate there is no preferred pattern orientation, and the peak in the axial ratio distribution is close to unity. The small bias of the axial ratio distribution from unity is a statistical effect, related to the fact that the contours describing the spatial correlation of the ground diffraction pattern are very unlikely to be perfectly circular.

3.5. Summary of Analysis of Model-Generated Data

The results of subsections 3.2 to 3.4 illustrate that standard analysis techniques are able to recover the input model velocity, turbulent velocity, and aspect sensitivity satisfactorily. It must however be pointed out that certain model parameters required manipulation in order to produce the results anticipated. For instance, the scattering density must exceed a certain minimum in order to produce suitable FCA results. This is clearly sensible in terms of FCA being a "volume scatter" method. If there are only a small number of scatterers used in the model then only a small volume of the radar volume will be occupied. It was also found that if the zenith angle power cut off ratio P_0 is too large that velocity overestimations could occur. This has been attributed to the resultant sharp power cutoff seen on the scatterer leaving the radar volume, resulting in the Doppler frequency being overestimated due to spurious high-frequency

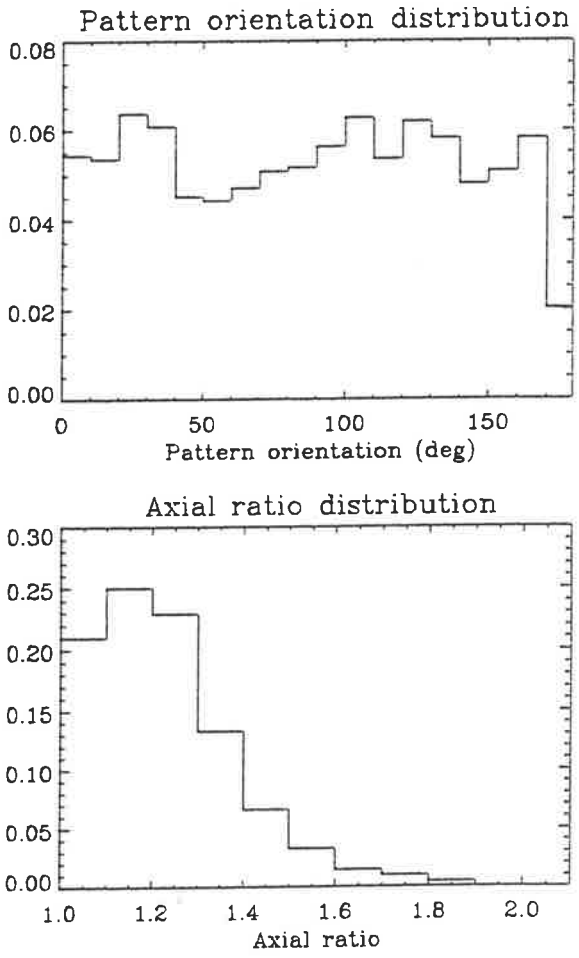

Figure 7. Distribution of pattern rotation and axial label for the MF simulation.

components resulting from the cutoff. This result suggests that the returns from large zenith angles may have a significant impact upon the FCA.

The model was originally run using the radar volume as the enclosing volume. On a scatterer leaving the radar volume it was replaced in the same manner as a scatterer leaving the enclosing volume of the present model. However, it was found that on using a vertically transmitted beam that the mean scattering position was biased off-zenith in the direction opposite to the motion of the scatterers. This resulted in underestimated horizontal velocities and predominantly negative vertical velocities from the FCA.

4. Effect of Sampling Time Upon the FCA

4.1. Zero-Lag Interpolation

The effectiveness of the techniques used to extract the correlation parameters have been analyzed using a range of sampling times. The cubic spline zero-lag autocovariance interpolation was investigated using autocovariance functions calculated using the VHF simulation parameters, without the addition of either turbulent motions or noise. In this instance the interpolated value should equal the zero-lag autocovariance. Figure 8 shows the average interpolated zero-lag autocovariance (normalized by the actual zero-lag autocovariance) over 100 realizations using from three to five lags either side of zero-lag, over a range of sampling times. The interpolated value decreases with sampling time as the first lag either side of zero-lag used for the interpolation is pushed further along the main lobe of the autocovariance function and hence is not a good indicator of the zero-lag autocovariance. For smaller sampling times the interpolated value obtained using four lags is significantly closer to unity than that obtained using three lags, although there appears little advantage in using greater than four lags. However, as the sampling time increases the improvement decreases. This is because the extra lags used in the fits are outside the main lobe of the autocovariance function and hence do not contribute any additional useful information to the interpolation.

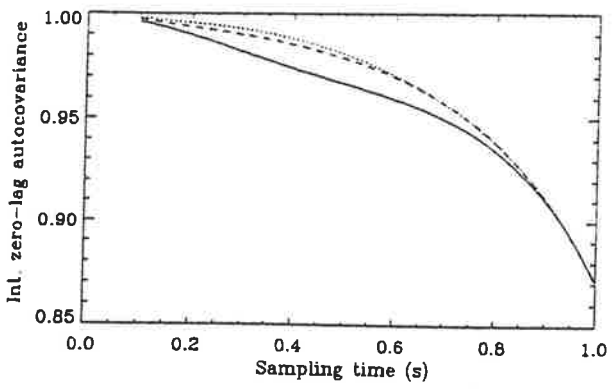

Figure 8. Average cubic spline interpolated zero-lag autocovariance using 3 (solid line), 4 (dotted line), and 5 (dashed line) lags either side of zero-lag for the VHF simulation.

Another method of interpolating the zero-lag autocovariance is by using even-order quadratic interpolations. The order of the interpolation is limited by the number of lags used in the fit. Such interpolations should only use lags within the main lobe of the autocovariance function, as spurious higher order polynomial powers may be introduced if oscillations in the tails are included in the fit. The average interpolated values obtained over 100 realizations using even order quadratic interpolations over four lags either side of zero-lag are illustrated in Figure 9, in addition to the four-lag cubic spline interpolated values. Only the sixth-order polynomial interpolation outperforms the cubic spline interpolation but still reveals a clear underestimation in the interpolated value.

These results have several consequences for the FCA. The underestimation of the zero-lag autocovariance results in the mean autocorrelation function being flatter about zero-lag. This subsequently results in an overestimation of the fading time $\tau_{0.5}$. The SNR is given by the ratio of the interpolated zero-lag autocovariance to the difference between the interpolated and original zero-lag autocovariance, usually specified in dB. The interpolation underestimation will therefore

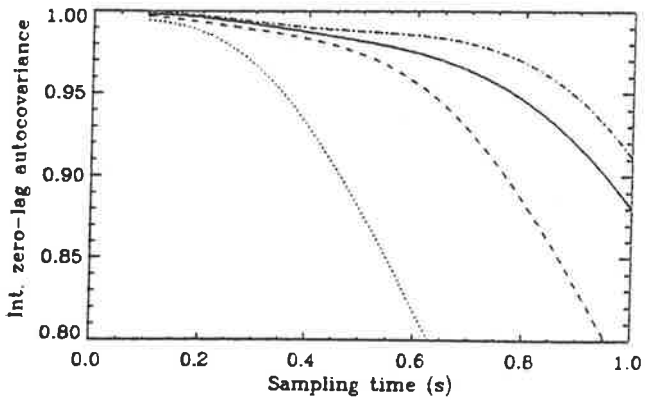

Figure 9. Average second- (dotted line), fourth- (dashed line), and sixth-order (dash-dotted line) polynomial interpolated zero-lag autocovariance using 4 lags either side of zero-lag for the VHF simulation. The solid line indicates the 4-lag cubic spline interpolated zero-lag autocovariance.

result in an underestimation of the SNR. The behavior of the average fading time and the SNR as a function of sampling time for the three-lag cubic spline interpolation and four-lag sixth-order polynomial interpolation over 100 realizations of the VHF simulation with 20 dB added receiver noise are shown in Figure 10.

The same cubic spline interpolation procedure is also used to interpolate the zero-lag cross-correlation to correct for any noise seen simultaneously in each of the three receivers. If the cross-correlation maxima is close to zero-lag there will be a similar underestimation in the interpolated zero-lag value. This could result in either the cross-correlation maxima being incorrectly estimated, the lag corresponding to the maxima being incorrectly estimated, or both of these effects.

4.2. Cross-Correlation Gaussian Fit

The Gaussian fits used to determine ρ_{0ij} and τ'_{ij} from the cross-correlation functions were also investigated, using cross-correlation functions determined using the VHF simulation parameters, without using the interpolated zero-lag autocovariances for normalization. Figure 11 shows the average fitted ρ_{0ij} over 100 realizations for various sampling times. The falloff for lags exceeding 0.5 s results from lags within the tail of the cross-correlation function being used in the fit. The Gaussian fit is compromised between fitting the main lobe of the correlation function and the nonzero tails. The estimated location of the maxima τ'_{ij} for individual cross-correlation functions can also be affected by this problem, although the average τ'_{ij} is independent of the sampling time.

There is no simple solution to this problem. The cubic spline interpolation used to estimate the zero-lag autocovariance is unsuitable because it does not locate the position of τ'_{ij}. High even-order polynomial fits are susceptible to oscilla-

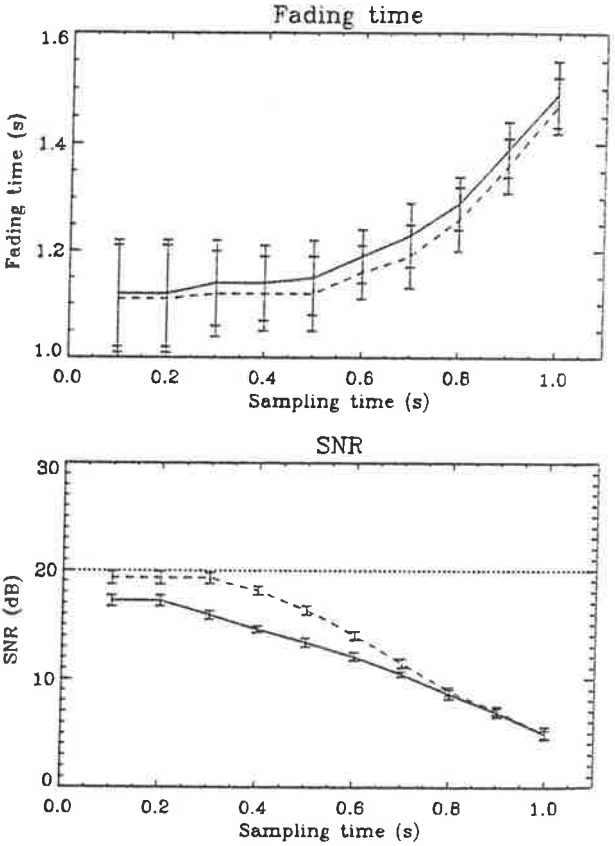

Figure 10. Variation of fading time and SNR as a function of sampling time for the VHF simulation. The solid line indicates the results of the three-lag cubic spline interpolation, while the dashed line indicates the results of the four-lag sixth-order polynomial interpolation. The dotted line on the SNR plot specifies the model input SNR. The error bars indicate the standard deviations of the distributions.

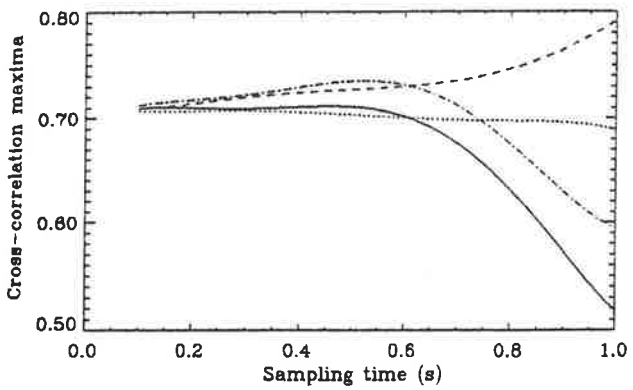

Figure 11. Average fitted cross-correlation maxima as a function of sampling time for the MF simulation. The solid and dotted lines indicate the values obtained using the current and revised fitting techniques, while the dot-dashed and dashed lines correspond to the values resulting when the interpolated zero-lag autocovariance underestimation is taken into account.

tions in the tails of the correlation functions, and are therefore unsuitable. The most appropriate solution is to limit the Gaussian fit to lags within the main lobe of the cross-correlation function. As a result of the small number of lags used in such a fit for higher sampling times ρ_{0ij} and τ'_{ij} are not accurately estimated. The average ρ_{0ij} obtained using this technique is shown in Figure 11. This is a clear improvement on the results obtained using the current six-lag fit, although there is still some underestimation.

The cross-correlation functions are normalized using the interpolated zero-lag autocovariances. As the sampling time is increased these interpolations become smaller, implying that the cross-correlation functions are larger than expected. The effect of this normalization upon ρ_{0ij} is illustrated in Figure 11.

4.3. Combined Effects of Interpolations and Fits Upon the FCA

It is difficult to assess the role each individual correlation parameter has on the analysis. As a result of the effects illustrated in the previous two subsections it is useful to determine a set of conditions for the optimal performance of the FCA.

The average true velocity obtained using the VHF simulation over 100 realizations using the current zero-lag interpolations and cross-correlation fits, hereafter referred to as the "current FCA," is shown as a function of sampling time in Figure 12. The true velocity follows the behavior of ρ_{0ij}, showing an increasing overestimation due to the increasing zero-lag autocorrelation underestimation at small sampling times, before falling off at sampling times exceeding 0.5 s. As discussed previously, this falloff can be corrected by using a revised Gaussian fit limited to the main lobe of the cross-correlation function. The results of using this revised fit, together with the four-lag sixth-order polynomial zero-lag autocovariance interpolation, and hereafter referred to as the "revised" FCA, are also shown in Figure 12.

The true velocity overestimation resulting from the zero-lag autocovariance overestimation is harder to compensate for. If the zero-lag autocovariance is used in preference to the interpolated value to normalize the cross-correlation functions, velocity underestimations can occur [e.g., *Meek*, 1989], as will be shown in section 5. It is therefore necessary to establish a maximum sampling time $\Delta t_{\max}$ for which the FCA can be

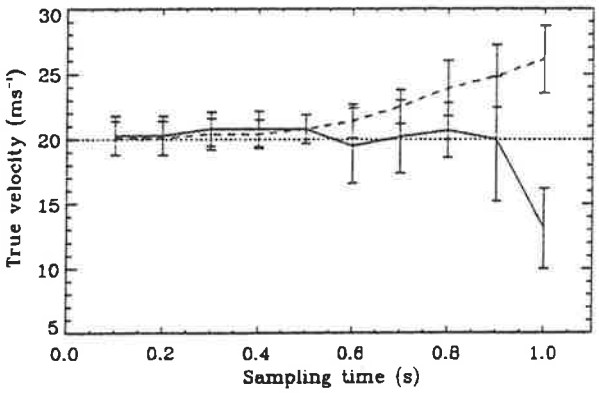

Figure 12. True velocity as a function of sampling time for the VHF simulation. The solid line indicates the velocity obtained using the current fit, while the dashed line indicates the velocity obtained using the revised fit. The dotted line indicates the model input velocity. The error bars indicate the standard deviations of the distributions.

expected to perform satisfactorily. As $\tau_{0.5}$ is the half width of the mean autocorrelation function it seems sensible to express Δt_{max} in terms of this quantity. The fading times corresponding to the velocity variations seen in Figure 12 are those shown in Figure 10, which suggests that $\tau_{0.5} \rightarrow 1.1$ s as $\Delta t \rightarrow 0$ s. If a maximum variation from the model velocity of 10% is assumed acceptable, then Figure 12 suggests $\Delta t_{max} = 0.7$ s for both the velocity overestimation resulting from the interpolation underestimation of the zero-lag autocovariance, and the velocity underestimation resulting from the underestimation of the cross-correlation maxima when using the tails of the function in the Gaussian fit. This result suggests a maximum sampling time given by the relationship

$$\Delta t_{max} = 0.63\tau_{0.5}. \quad (16)$$

In the case of no turbulent motions, (13) and (14) can be substituted into (16) to yield

$$\Delta t_{max} = \frac{4.8\lambda}{|\bar{V}|}[\arcsin((\sin^{-2}\theta_s + \sin^{-2}\theta_b)^{-1/2})]^{-1} \quad (17)$$

where λ is the radar wavelength, θ_s is the aspect sensitivity in degrees, and θ_b is the beam width in degrees. Because θ_s and θ_b are in degrees the result of the arcsin must also be specified in degrees. The maximum velocity magnitude V_{max} for the acceptable performance of FCA can be expressed as a function of sampling time Δt by the equation

$$V_{max} = \frac{4.8\lambda}{\Delta t}[\arcsin((\sin^{-2}\theta_s + \sin^{-2}\theta_b)^{-1/2})]^{-1}. \quad (18)$$

These equations can be used to estimate the sampling time and velocity limits for specific radars. Given known values of λ, θ_b, and the expected maximum θ_s for the height range probed by the radar, (17) can be used to determine Δt_{max} using the maximum expected velocity, and (18) can be used to determine V_{max} using the sampling time. Because conditions of maximum velocity and maximum aspect sensitivity do not generally coincide, Δt_{max} and V_{max} derived by these formulae are somewhat underestimated. However, turbulent motions are not accounted for in these formulae. Turbulent motions would result in a decrease in both Δt_{max} and V_{max}, thereby compensating for the initial underestimation. For the Adelaide VHF radar of wavelength $\lambda = 5.5$ m and beam width $\theta_b \approx 2°$, covering a height range of 2-20 km, the maximum θ_s encountered will be approximately 10° [e.g., *Hocking et al.*, 1986], while the maximum wind velocity encountered will be of the order of 80 m s^{-1} [e.g., *Van Baelen et al.*, 1990]. Substitution of these parameters into (17) yields $\Delta t_{max} = 0.17$ s, which is significantly smaller than the effective sampling time after coherent integration of 0.5 s currently used, and $V_{max} = 27$ m s^{-1}. For the Adelaide MF radar of wavelength 150 m and beam width $\theta_b \approx 20°$, covering the height range 60-100 km, the maximum expected aspect sensitivity will be $\approx 10°$ [e.g., *Reid*, 1990], while the maximum expected velocity will be ≈ 150 m s^{-1}. These parameters yield $\Delta t_{max} = 0.54$ s, which exceeds the effective sampling time of 0.4 s.

The velocity falloff seen in Figure 12 can be used to explain some results which indicate that the FCA may underestimate the wind velocity. Figure 13 illustrates the average true velocity as a function of the model velocity over 100 realizations for the VHF simulation parameters, using the current FCA with a sampling time of 0.5 s. Below model velocities of 30 m s^{-1} the true velocity accurately estimates the model velocity. However, at velocities above this there is a falloff. Such falloffs are also seen in some comparisons of VHF radar velocities calculated using FCA with radiosonde wind velocities data. In particular, Figure 5 of *Vincent et al.* [1987] and Figure B.3 of *Rajopadhyaya* [1994] appear to show this effect. Both of these results were produced using a sampling time of 0.5 s, the latter using the current FCA technique. Similar underestimations at large velocities have also been

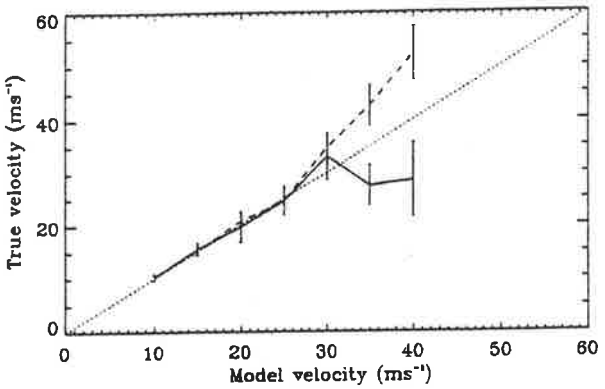

Figure 13. True velocity as a function of model velocity for the VHF simulation. The solid line indicates the velocity obtained using the current fit, while the dashed line indicates the velocity obtained using the revised fit. The dotted line indicates equal model and true velocities. The error bars indicate the standard deviations of the distributions.

seen at VHF by *Van Baelen et al.* [1990]. In general, the fall-off velocity will be greater than shown in Figure 13. These results were obtained using a constant θ_s value of 3°, corresponding to a pattern scale of 50 m. However, larger velocities are usually seen at heights where $\theta_s < 3°$, thereby increasing the fall-off velocity, as derived from (18).

5. The Triangle Size Effect

The triangle size effect was first described by *Golley and Rossiter* [1970]. They found that the true velocity increased with antenna spacing up to a limiting value supposedly equal to the actual wind velocity. This limiting velocity was obtained when the triangle spacing was approximately equal to the actual pattern scale. The calculated pattern scale was also found to increase with antenna spacing, while little variation was seen in the apparent velocity. This effect has been attributed to a number of possible causes, including antenna coupling [*Fedor and Plywaski*, 1972], digitization [*Golley and Rossiter*, 1970], and random noise [e.g., *Meek*, 1989]. The effect has also recently been seen in the analysis of real data [e.g., *Meek*, 1989; *Van Baelen et al.*, 1990] and simulated data [*Van Baelen et al.*, 1989].

The model was used to generate a set of 200 time series using the MF simulation parameters. Seven different antenna spacings were used, with the pattern scale lying between the last two spacings. The effects of digitization and receiver noise were later simulated. The FCA was run with and without the cubic spline interpolation of the zero-lag autocovariance. The latter case follows the analysis outlined by *Meek* [1989], whereby no correlation function renormalization is used to correct for the presence of noise, and will hereafter be referred to as the MFCA.

The results of applying the FCA and MFCA

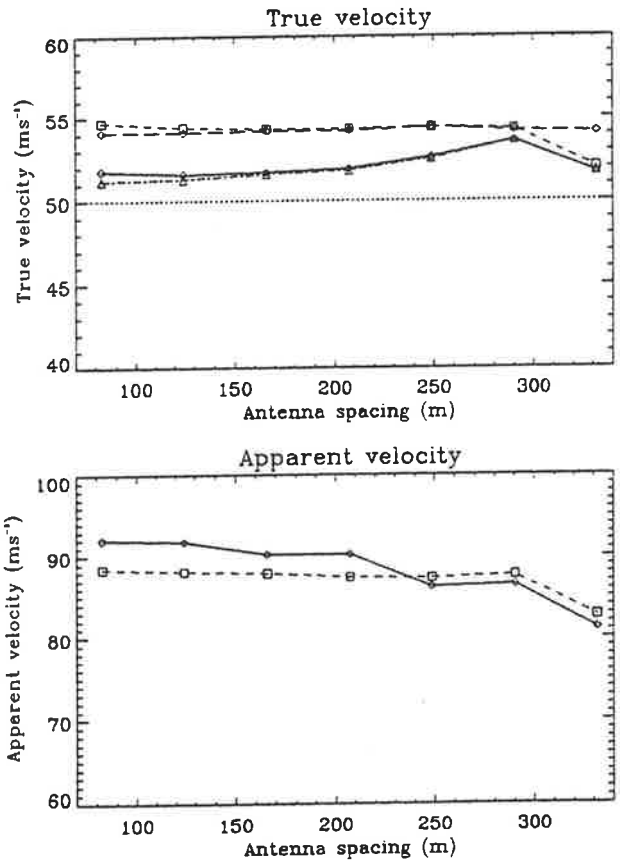

Figure 14. Vector averaged true (top) and apparent velocity (bottom) as a function of antenna spacing for the FCA (solid lines) and MFCA (dot-dashed lines) analyses. The postanalysis criteria FCA (dashed lines) and MFCA (long-dashed lines) velocities are also indicated. The dotted line indicates the model input velocity.

to time series without digitization or noise are illustrated in Figure 14. There is a small increase in the average true velocity as the antenna spacing is increased, corresponding to approximately 5% over a range of 200 m. This velocity increase is substantially smaller than the increase seen in the analysis of real data, and it is therefore unlikely that this is the sole cause of the triangle size effect. At spacings exceeding the pattern scale the true velocity decreases with increasing antenna spacing. This appears to be the result of an increase in the variance of the true velocity direction reducing the vector average magnitude. There is also a 15% decrease in the apparent velocity over the range of spacings. This effect was not encountered by *Golley and Rossiter* [1970], but appears to be seen in recent analyses of real data [e.g., *Van Baelen et al.*, 1990, Figure 7b, most heights] and simulated data [e.g., *Van Baelen et al.*, 1989, Figure 2]. There appears to be little difference in the true velocity results of FCA and MFCA. Because the only difference between the FCA and MFCA is the normalization, they produce the same apparent velocity.

In order to minimize any biases that may occur due to the rejection criteria used in FCA [e.g., *Briggs*, 1984], the same analysis as above was repeated, using only the results where acceptances occurred for both the smallest and largest spacings for each FCA analysis. This will hereafter be referred to as the "postanalysis criteria," and is similar to that used in the *Meek* [1989] triangle size effect analysis. The results of applying this criteria to the FCA and MFCA results are shown in Figure 14. The average true velocity is now constant over the range of spacings smaller than the pattern scale, while the apparent velocity decrease has been reduced to approximately 3% over the same range. This suggests the results produced without using the postanalysis criteria are significantly biased by the FCA acceptance criteria. Again, there appears to be little difference in the results of FCA and MFCA.

The effects of time series digitization were then analyzed by digitizing the time series into 256, 128, 64, and 32 bit time series. The results of applying the FCA and MFCA to the 32 bit time series and using the postanalysis criteria are shown in Figure 15, along with the FCA results obtained without digitization. These results suggest digitization causes an underestimation smaller than 1%, but no triangle size effect.

The effects of receiver noise were then analyzed by adding random Gaussian distributed values to the time series. The expected velocity variation as a function of receiver noise for the MFCA is given by [*Meek*, 1989]

$$\frac{V_0}{V} = 1 + \frac{2\triangle S_0^2}{D^2}, \tag{19}$$

where $\triangle$ is the "noise parameter", V_0 and S_0 are the "noise free" true velocity and pattern scale, V is the resultant underestimated true velocity, and D is the antenna spacing. The results of applying the FCA and MFCA to time series with various SNRs of added receiver noise are shown in Figure 16. There appears to be little difference in the FCA results obtained with and without added noise. However, there is a clear underestimation in the MFCA results obtained with added noise of the form described by (19). The true velocity underestimation is encountered for MFCA because the effects of noise are not compensated for. Correct compensation for noise

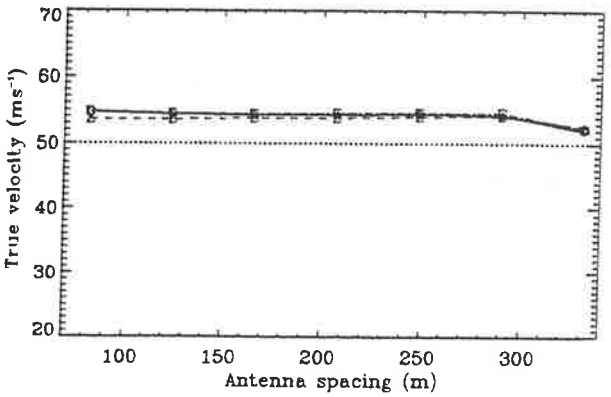

Figure 15. Vector averaged true velocity as a function of antenna spacing for the FCA (solid line) and 32 bit digitized FCA (dashed line) and MFCA (dot-dashed lines) analyses using the postanalysis criteria. The dotted line indicates the model input velocity.

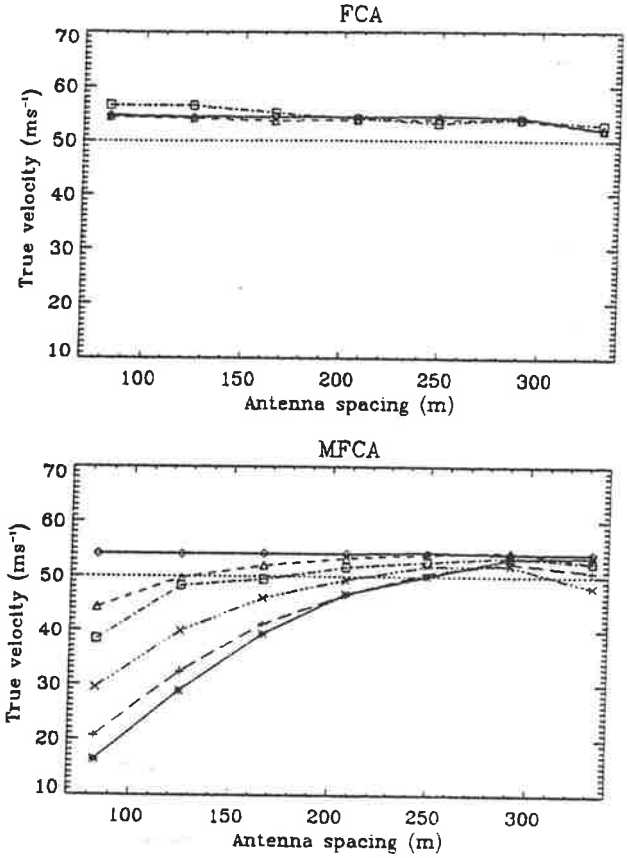

Figure 16. Vector averaged FCA (top) and MFCA (bottom) true velocity as a function of antenna spacing for various levels of receiver noise. For FCA plots: no added noise (solid line), 20 dB (dashed line), 10 dB (dot-dashed line). For MFCA plot: no added noise (thick solid line), 20 dB (dashed line), 16 dB (dot-dashed line), 12 dB (triple dot-dashed line), 8 dB (long-dashed line), 4 dB (solid line). The dotted line indicates the model input velocity.

effects as used in FCA removes this underestimation. However, as shown in section 4, and as acknowledged by *Meek* [1989], difficulty will occur when the main lobe of the autocovariance function is not sufficiently sampled, resulting in an underestimate of the zero-lag autocovariance.

The results obtained here suggest two causes of the FCA triangle size effect. The major contribution results when the effects of noise are not accounted for. As previously discussed, when a suitably small sampling time is used the correction for noise is both straightforward and reliable. The other, minor contributor to the triangle size effect is the FCA acceptance criteria.

6. Summary and Suggestions for Further Work

A simple volume scatter model has been introduced and successfully implemented. Several analysis techniques have been used to successfully recover the model input parameters, thereby verifying both the model and the individual techniques. The problem of undersampling the ground diffraction pattern has been discussed, and a parameter denoting the maximum sampling time in order to eliminate such problems has been established. The triangle size effect has been addressed, with the major cause attributed to not accounting for noise effects.

The only obvious omission from the present model is the dynamical contributions resulting from a spectrum of gravity waves. This omission is currently being addressed. Plans for future work involve the analyses of the performance of Doppler and interferometric techniques. Because the model scattering locations are known, they can be compared with the positions located by interferometry in a similar manner to that employed by *Adams et al.* [1985].

Acknowledgments. The authors gratefully acknowledge discussions with R. A. Vincent, D. F. Scroop and T. T. Guy. This work has been supported by Australian Research Grants A69231890 and A69031462, by the University of Adelaide, and by the Department of Physics and Mathematical Physics. David Holdsworth is supported by the Defence Science and Technology Organization, Australia.

References

Adams, G. W., D. P. Edwards and J. W. Brosnahan, The imaging Doppler interferometer: Data analysis, *Radio Sci., 20*, 1481-1492, 1985.

Briggs, B. H., Radar observations of atmospheric winds and turbulence: A comparison of techniques, *J. Atmos. Terr. Phys., 42*, 823-833, 1980.

Briggs, B. H., The analysis of spaced sensor records by correlation techniques, *Handbook for MAP*, vol. 13, pp. 166-186, SCOSTEP Secr., Univ. of Ill., Urbana, 1984.

Burrage, M. D., W. R. Skinner, A. R. Marshall, P. B. Hays, R. S. Leiberman, S. J. Franke, D. A. Gell, D. A. Ortland, Y. T. Morton, F. J. Schmidlin, R. A. Vincent and D. L. Wu, Comparison of HRDI wind measurements with radar and rocket observations, *Geophys. Res. Lett., 20*, 1259-1262, 1993.

Cervera, M. A., and I. M. Reid, Comparison of simultaneous wind measurements using colocated VHF meteor radar and MF spaced antenna radar systems, *Radio Sci.*, this issue.

Chandra, H., and B. H. Briggs, The effect of filtering on ionospheric drift parameters determined by full correlation analysis, *J. Atmos. Terr. Phys., 40*, 541-548, 1978.

Fedor, L. S., and W. Plywaski, The interpretation of ionospheric radio drift measurements, IV, The effects of signal coupling among spaced sensor channels, *J. Atmos. Terr. Phys., 34*, 1285-1303, 1972.

Franke, P. M., D. Thorsen, M. Champion, S. Franke, and E. Kudeki, Comparisons of time- and frequency-domain techniques for wind velocity estimation using multiple-receiver MF radar data, *Geophys. Res. Lett., 17*, 2193-2196, 1990.

Golley, M. G., and D. E. Rossiter, Some tests of methods of analysis of ionospheric drift records using an array of 89 aerials, *J. Atmos. Terr. Phys., 32*, 1215-1233, 1970.

Hocking, W. K., On the extraction of atmospheric turbulence parameters from radar backscatter Doppler spectra, I, Theory, *J. Atmos. Terr. Phys., 45*, 89-102, 1983.

Hocking, W. K., R. Rüster, and P. Czechowsky, Absolute reflectivities and aspect sensitivities of VHF radio wave scatterers measures with the SOUSY radar, *J. Atmos. Terr. Phys., 48*, 131-144, 1986.

Hines, C. O., G. W. Adams, J. W. Brosnahan, F. T. Djuth, M. P. Sulzer, C. A. Tepley, and J. S. Van Baelen, Multi-instrument observations of mesospheric motions over Arecibo: Comparison and interpretations, *J. Atmos. Terr. Phys., 55*, 241-287, 1993.

Lesicar, D., and W. K. Hocking, Studies of the seasonal behavior of the shape of mesospheric scatterers using a 1.98 MHz radar, *J. Atmos. Terr. Phys., 54*, 295-309, 1992.

Meek, C. E., Triangle size effect in spaced antenna wind measurements *Radio Sci., 25*, 641-648, 1990.

Meek, C. E., and I. M. Reid, A simple model for testing the effects of gravity-wave-produced vertical oscillations of scattering irregularities on spaced-antenna, horizontal drift measurements, *Handbook for MAP*, vol. 14, pp. 131-133, SCOSTEP Secr., Univ. of Ill., Urbana, 1984.

Pfister, W., The wave-like nature of inhomogeneities in the E-region, *J. Atmos. Terr. Phys., 33*, 999-1025, 1971.

Pitteway, M. L. V., J. W. Wright, and L. S. Fedor, The interpretation of ionospheric radio drift measurements, III, Validation of correlation analysis by computer simulation, *J. Atmos. Terr. Phys., 33*, 635-660, 1971.

Rajopadhyaya, D. K., Meteorological studies using a VHF radar, Ph.D. thesis, Univ. of Adelaide, Adelaide, Aust., 1994.

Reid, I. M., MF Doppler and spaced antenna radar measurements of upper middle atmosphere winds, *J. Atmos. Terr. Phys., 50*, 117-134, 1988.

Reid, I. M., Radar observations of stratified layers in the mesosphere and lower thermosphere (50-100 km) *Adv. Space Res., 10(10)*, 7-19, 1990.

Sheppard, E. L., and M. F. Larsen, Analysis of model simulations of spaced-antenna/radar interferometer measurements, *Radio Sci., 27*, 759-768, 1992.

Sūrūcū, F., S. J. Franke and E. Kudeki, On the influence of specular reflections in MF radar wind measurements, *Radio Sci.*, this issue.

Stubbs, T. J., The measurement of winds in the D-region of the ionosphere by the use of partially reflected radio waves, *J. Atmos. Terr. Phys., 35*, 909-919, 1973.

Van Baelen, J. S., A. D. Richmond, S. K. Avery, T. Tsuda, S. Kato, and S. Fukao, SAD and interferometry analysis with the MU radar: Simulations and preliminary results, *Handbook for MAP*, vol. 28, pp. 416-423, SCOSTEP Secr., Univ. of Ill., Urbana, 1989.

Van Baelen, J. S., T. Tsuda, A. D. Richmond, S. K. Avery, S. Kato, S. Fukao and M. Yamamoto, Comparison of VHF Doppler beam swinging and spaced antenna observations with the MU radar: First results, *Radio Sci., 25*, 629-640, 1990.

Vincent, R. A., T. J. Stubbs, P. H. O. Pearson, K. H Lloyd and C. H. Low, A comparison of partial reflection drifts with winds determined by rocket measurements, *J. Atmos. Terr. Phys., 39*, 813-821, 1977.

Vincent, R. A., P. T. May, W. K. Hocking, W. G. Elford, B. H. Candy, and B. H. Briggs, First results with the Adelaide VHF radar: Spaced antenna studies of tropospheric winds, *J. Atmos. Terr. Phys., 49*, 353-366, 1987.

Vincent, R. A., and D. Lesicar, Dynamics of the equatorial mesosphere: First results with a new generation partial reflection radar, *Geophys. Res. Lett., 18*, 825-828, 1991.

Wright, J. W. and M. L. V. Pitteway, Computer simulations of ionospheric radar drift measurements and their analysis by correlation methods, *Radio Sci., 13*, 189-210, 1978.

D. A. Holdsworth and I. M. Reid, Department of Physics and Mathematical Physics, University of Adelaide, Adelaide, 5005, Australia. (e-mail: dholdswo@physics.adelaide.edu.au and dah@mod.dsto.gov.au; ireid@physics.adelaide.edu.au)

(Received May 20, 1994; revised August 22, 1994; accepted September 15, 1994.)

Appendix J

Spaced antenna analysis of atmospheric radar backscatter model data

This is a reprint of a paper by David A. Holdsworth and Iain M. Reid, published in *Radio Science, 30*(5), 1417-1433, 1995.

Radio Science, Volume 30, Number 5, Pages 1417–1433, September–October 1995

Spaced antenna analysis of atmospheric radar backscatter model data

David A. Holdsworth and Iain M. Reid

Department of Physics and Mathematical Physics, University of Adelaide, Adelaide, Australia

Abstract. A simple computer model of atmospheric radar backscatter is used to investigate and compare various spaced antenna (SA) techniques, including the full correlation analysis (FCA) and a number of imaging interferometry techniques. The results illustrate that the FCA true velocity proves to be an excellent estimate of the model input velocity for all magnitudes of model turbulent motions. On the other hand, the interferometric velocities increase as the magnitude of the turbulent motions are increased, providing a poor estimate of the model input velocity for large turbulent motion magnitudes. Maps illustrating the interferometry-estimated scattering positions superimposed upon the actual model scatterer positions reveal the estimated positions to be inaccurate. The estimated positions are shown to approach the zenith as the magnitude of the turbulent motions increases, confirming the volume scatter derived suggestions of Briggs (1995). Furthermore, the estimated positions have a preferred azimuth angle agreeing with volume scatter derived suggestions. The effects of receiver noise upon the interferometric techniques are investigated, revealing an effect analogous to the FCA triangle size effect whereby the estimated velocity decreases with increasing noise level. The effects of the thresholds used to preclude individual Doppler frequencies from the analyses are illustrated. The results are in excellent agreement with the experimental results obtained in a number of different studies.

1. Introduction

The conventional and most commonly used technique for the estimation of atmospheric wind velocities using spaced antenna (SA) radar data is the full correlation analysis (FCA) [e.g., *Briggs*, 1984]. The FCA is applied to SA data obtained both at VHF in the lower atmosphere (2-20 km) [e.g., *Vincent et al.*, 1987] and at MF/HF in the upper mesosphere and lower thermosphere (60-100 km) [e.g., *Vincent and Lesicar*, 1991]. The FCA produces two velocity estimates, namely the "apparent" and "true" velocities. The true velocity is usually considered the better estimate of the actual velocity, as it includes a correction for the effects of random changes and anisotropy in the ground diffraction pattern.

In recent years there has been considerable interest in estimating wind velocities using spectral analyses. A number of full spectral analysis (FSA) techniques have been developed [e.g., *Briggs and Vincent*, 1992; *Sheppard and Larsen*, 1992; *Liu and Pan*, 1993]. These techniques are frequency domain analogues of the FCA, using the same mathematical formulation based on spectral rather than correlation parameters. As a result the FCA and FSA produce very similar velocity estimates. Additionally, a number of interferometry techniques have been developed. These techniques can be separated into "imaging" and "non imaging" techniques. The imaging techniques can be further separated into "Doppler-sorted" [e.g., *Adams et al.*, 1985; *Meek and Manson*, 1987; *Franke et al.*, 1990]

Copyright 1995 by the American Geophysical Union.

Paper number 95RS01888.
0048-6604/95/95RS-01888$08.00

and "non-Doppler-sorted" [e.g., *Vandepeer and Reid*, 1995b] techniques. The Doppler-sorted techniques rely on locating discrete scattering positions for each Doppler frequency based on spectral phase information and can provide an estimate of the wind velocity for each record. The non-Doppler-sorted techniques locate the mean angle of arrival [e.g., *Röttger and Ierkic*, 1985] of the scatter for each record, requiring a minimum of three records to produce a wind velocity estimate. The records used are usually obtained using one vertical and at least two orthogonal off-vertical beams. The non imaging techniques [e.g., *Van Baelen et al.*, 1991] estimate the wind velocity directly from the phase information. The full spectral analysis (FSA) is sometimes referred to as a nonimaging interferometric technique. The FSA apparent velocity is estimated in the same manner as the velocity estimated by the alternative nonimaging techniques. The alternative nonimaging techniques can therefore be considered Fourier equivalents of the technique used to determine the FCA apparent velocity [e.g., *Van Baelen et al.*, 1991]. As a result of this Fourier equivalence, the nonimaging techniques are not addressed in this paper. The FCA and Doppler-sorted imaging interferometric techniques are presented in section 2, along with some discussion of the various experimental results obtained.

While comprehensive model analyses have previously been conducted for the FCA [e.g., *Wright and Pitteway*, 1978; *Meek and Reid*, 1984; *Sürücü et al.*, 1995; *Holdsworth and Reid*, 1995], the only analogous analysis for any imaging interferometric technique appears to be that performed by *Adams et al.* [1985]. A particular advantage of applying Doppler-sorted imaging interferometry to model-generated data is that the actual scattering locations are known, thereby allowing the investigation of the idea of fictitious scattering locations proposed by *Briggs* [1995]. The model of *Adams et al.* [1985] used a limited number of scatterers. They found that the imaging Doppler interferometry (IDI) technique estimated both the scattering positions and model velocities accurately. The considerably more realistic model of *Holdsworth and Reid* [1995] has been used to produce the results of this paper. The basis of this model is discussed in section 3. The results of applying the FCA and imaging interferometry techniques to model-generated data are shown in section 4, while the consequences of these results are discussed of section 5.

2. Analysis Techniques

2.1. The Full Correlation Analysis

The full correlation analysis (FCA) of spaced antenna (SA) data is used to estimate atmospheric wind velocities from the ground diffraction pattern resulting from atmospheric radio wave backscatter. The basic assumption of FCA is that contours of equal spatiotemporal correlation of the ground diffraction pattern can be approximated by a family of ellipsoids [e.g., *Briggs*, 1984] of the general form

$$\rho(\xi,\eta,\tau) = \rho(A\xi^2 + B\eta^2 + 2H\xi\eta + (F\xi + G\eta)\tau + C\tau^2), \quad (1)$$

where ξ and η are the spatial dimensions and τ is the temporal dimension. The pattern is generally sampled at three spatially separated positions. Complex auto- and cross-correlation functions are calculated from the complex voltages sampled at each antenna. The apparent velocity is calculated directly from the time delays corresponding to the cross-correlation function magnitude maxima and is usually an overestimate of the actual velocity as it incorporates the effects of random changes and anisotropy in the ground pattern resulting from turbulent fading. The true velocity is corrected for these effects and is generally considered the better estimate of the actual velocity. The FCA also provides information on the characteristics of the ground diffraction pattern.

Comparisons between the FCA true velocity and both the meteor drift winds [e.g., *Cervera and Reid*, 1995] and high-resolution Doppler imaging (HRDI) derived winds [e.g., *Burrage et al.*, 1993] suggest the FCA true velocity may un-

derestimate the actual wind velocity by approximately 5-10%. Possible causes for this underestimation include the "triangle size effect" [e.g., *Golley and Rossiter*, 1970], low-pass filtering resulting from the use of coherent integration [e.g., *Chandra and Briggs*, 1978], receiver saturation, and spatial undersampling of the ground diffraction pattern. In addition, *Hines et al.* [1993] have suggested that MF radars may measure the phase speed of gravity wave perturbations within the radar volume as opposed to the background wind velocity.

2.2. Doppler-Sorted Imaging Interferometry

The Doppler-sorted imaging interferometry techniques use a two-step process first proposed by *Pfister* [1971]. The first step involves using the phase differences between three or more spaced receiving antennae at each available Doppler frequency f_i to determine the positions of apparent radio wave scatter. These positions will hereafter be referred to as the "effective scattering positions," following the terminology of *Briggs* [1995]. Given a phase difference ϕ_i between two antennae with separation D, the zenith angle θ_i of apparent scatter in the $Z - D$ plane is determined by

$$\theta_i = \arcsin\left(\frac{\phi_i \lambda}{2\pi D}\right), \tag{2}$$

where λ is the radar wavelength. A minimum of three receiving antennae are required to completely define the effective scattering position, specified by the radial direction unit vector $\hat{r}_i$. The second step involves the least squares estimate of the mean wind field velocity $\vec{V}$ over all available Doppler frequencies using

$$V_{ri} = \vec{V} \cdot \hat{r}_i, \tag{3}$$

where V_{ri} is the radial velocity associated with the Doppler frequency f_i. The "phase difference" between two antennae at a particular Doppler frequency is equivalent to the "cross-spectral phase" at that Doppler frequency. In accordance, these two terms will be used interchangeably throughout the remainder of this paper.

Because the various Doppler-sorted imaging interferometry techniques differ in the analysis applied, the taxonomy introduced by *Vandepeer* [1993] is used in this paper to distinguish between them. Both the imaging Doppler interferometer (IDI) introduced by *Adams et al.* [1985] and the magnitude-selected imaging radar interferometer (MSIRI) introduced by *Meek and Manson* [1987] use unsmoothed spectra to obtain velocities agreeing best with the FCA apparent velocity. The nonselected imaging radar interferometer (NSIRI) introduced by *Franke et al.* [1990] produces velocities agreeing with the FCA true velocity when using unsmoothed spectra (UNSIRI) and velocities agreeing with the FCA apparent velocity when using smoothed spectra (SNSIRI).

The fundamental assumption of the imaging interferometric analyses is that the information available at each Doppler frequency results from a single discrete scattering location. If two or more scattering locations contribute to the same Doppler frequency the resultant effective scattering position will not necessarily coincide with either of the actual scattering positions. This effect is referred to as "aliasing" [e.g., *Adams et al.*, 1985]. The three imaging interferometric techniques applied in this paper differ in their use of criteria to determine whether the spectral information for each Doppler frequency satisfies the conditions for scatter from a single discrete scattering location. The IDI technique [e.g. *Adams et al.*, 1985, 1986; *Brosnahan and Adams*, 1993] uses two orthogonal rows of receiving antennae. Doppler frequencies exhibiting sufficiently linear phase variation along both rows of antennae are assumed indicative of plane-wave incidence, and therefore scatter from a single discrete location. These Doppler frequencies are subsequently used in the analysis. The phase differences between antennae used in (2) are determined from a linear fit to the spectral phases along each arm. The MSIRI technique of *Meek and Manson* [1987] uses three

receiving antennae. Doppler frequencies with simultaneous local maxima in the power spectra calculated for each receiving antennae are assumed indicative of scatter from a single discrete location and subsequently used in the analysis. Use of an extra receiving antenna in order to calculate the normalized phase discrepancy as further indication of scatter from a single discrete location is suggested but not employed in their velocity analysis, despite the statements of *Franke et al.* [1990]. The NSIRI technique used by *Franke et al.* [1990] uses three receiving antennae, employing no single-scatterer criterion.

It is also important that the effective scattering positions are unambiguously resolved. However, with certain combinations of antenna spacings and radar wavelengths it is possible that some zenith angles are not unambiguously resolved. For instance, a spacing of $D = \lambda$ results in the zenith angles of all effective scattering points lying within 30° of the zenith, despite the fact that some of the actual scattering location may lie outside this zenith angle. This effect is referred to as "spatial aliasing" [e.g., *Franke et al.*, 1990], and can be eliminated by using antenna spacings less than $D = (1/2)\lambda$ [e.g., *Adams et al.*, 1985]. It is generally impossible to determine whether a located position has been spatially aliased. It is therefore often considered necessary to preclude effective scatterering positions with zenith angles exceeding a calculated spatial aliasing threshold from the analysis, even though not all of these effective scatterering positions are necessarily spatially aliased.

There has been little attempt to theoretically analyze the imaging interferometric techniques. This is a result of the difficulty in theoretically modeling unsmoothed cross spectra [e.g., *Franke et al.*, 1990]. The theoretical model analysis of *Liu et al.* [1990] predicts that (2) is applicable in the absence of turbulent motions if the information for each Doppler frequency is due to scatter from individual highly localized regions within the radar volume. This analysis also predicts that the FCA will not estimate the correct wind velocity in this situation. Conversely, in the volume scatter situation where the FCA is applicable this analysis predicts that imaging interferometry will not estimate the correct wind velocity. In assuming a volume scatter situation *Briggs* [1995] has shown that the effective scattering positions lie along a straight line not necessary aligned with the direction of the background wind and are therefore fictitious. This analysis also suggests that the effective scattering positions approach the zenith as the magnitude of the turbulent motions increases. As a result, the horizontal wind velocity component inferred from the radial velocity must increase as the magnitude of the turbulent motions increases. These results have been elaborated upon by *Vandepeer and Reid* [1995a], who have shown that the imaging interferometric velocity estimated under the volume scatter assumption is equal to the FCA apparent velocity. This suggests that the imaging interferometric techniques do not implicitly employ a correction for turbulent motions akin to that used to produce the FCA true velocity. Furthermore, the work of *Briggs* [1995] suggests that volume scatter will produce a linear phase variation along a line of equally spaced receiving antennae. This is exactly the situation assumed by the IDI to be indicative of scatter from a single scattering position.

The volume scatter predicted results are difficult to relate to the "noisy" cross-spectral phase variations obtained for unsmoothed spectra. However, the IDI-like analysis of *Vandepeer and Reid* [1995a] indicates that the distributions of effective scattering positions are elongated in the direction predicted by the volume scatter arguments of *Briggs* [1995]. The MSIRI analysis of *Brown et al.* [1995] also indicates that the agreement between the FCA apparent and MSIRI velocities is significantly greater than the agreement between the FCA true and MSIRI velocities for large FCA-estimated values of turbulent motions. In such instances the apparent velocity is usually significantly greater than the true velocity because the apparent velocity is not corrected for the effects of turbulent motions.

3. Application of the Radar Backscatter Model

3.1. The Radar Backscatter Model

The radar backscatter model employed in this paper is extensively described by *Holdsworth and Reid* [1995]. As such, only a brief description will be provided in this paper. The model has been developed to be as simple and versatile as possible, allowing the effective analysis of a number of different estimation techniques. The model is programmed in Interactive Data Language (IDL), producing convenient computational times when run on a DEC Alpha.

The basis of the model is as follows. A "radar volume" is defined according to a selected beam-pointing angle, beam width, and range gate. The radar volume is encompassed within in a cylindrical "enclosing" volume, throughout which a number of scatterering locations are positioned. These "scatterers" represent regions of refractive index irregularity as opposed to physical objects. At each sampling time the backscattered complex signal returns from scatterers within the radar volume are combined, with the amplitudes of the returns determined by the polar diagram associated with transmission, reception, and aspect sensitivity, and a range gate weighting function. The scattering positions are then updated, based on specified values of the mean background wind, turbulent motions, and gravity wave perturbations. Scatterers updated to positions outside the enclosing volume are readmitted through the surface opposite the one they left.

As discussed by *Holdsworth and Reid* [1995], the model simulates the characteristics of radar backscatter very well at both MF and VHF. The application of the FCA to model-generated data reveals excellent agreement between the true velocity and the model input velocity. In addition, standard techniques for the estimation of aspect sensitivity and turbulent velocities produce estimates in excellent agreement with the model input values.

3.2. Model Parameters

The model has been used to approximate the general configuration of an MF SA radar suitable for the application of the FCA and the three imaging interferometric techniques under examination. The relevant model parameters are shown in Table 1. Unless otherwise specified, these parameters are used to produce all results presented in this paper. The atmospheric parameters are intended to simulate the volume scatter situation. The antenna spacing of $D = (1/2)\lambda$ produces no spatial aliasing. The enclosing volume is chosen to be approximately four times the volume of the radar volume. Because the angular polar diagrams of receiving antennae are generally significantly larger than the angular polar diagrams of the backscatter for MF radars, the model receiver beam width is set to be infinite. As various noise sources seen in actual radar systems are not present in the model, no spatial or temporal coherent averaging is employed, so that a multiantenna receiving array is simulated by a single antenna position with the appropriate polar diagram, and each sample is the representation of the complex voltage induced at the particular sampling time.

The selected antenna configuration is shown in Figure 1. The MSIRI, NSIRI, and FCA tech-

Table 1. Simulation Parameters Employed for Model Data Generation

Model Parameter	Value
Radar frequency, MHz	2
Range, km	90
Range gate size, km	4
Transmitter e^{-1} half beam width, deg	15
Beam pointing angle, deg	0
Receiver e^{-1} half beam width, deg	∞
Receiver spacing, m	75 ($\frac{1}{2}\lambda$)
Sampling time, s	0.4
Time series elements	256
Time series length, s	102.4
Number of scatterers	1000
Aspect sensitivity, deg	10
Mean horizontal wind speed, m s^{-1}	50
Mean horizontal wind direction (E of N), deg	15
Mean vertical wind speed, m s^{-1}	0
Isotropic turbulent rms velocity, m s^{-1}	6

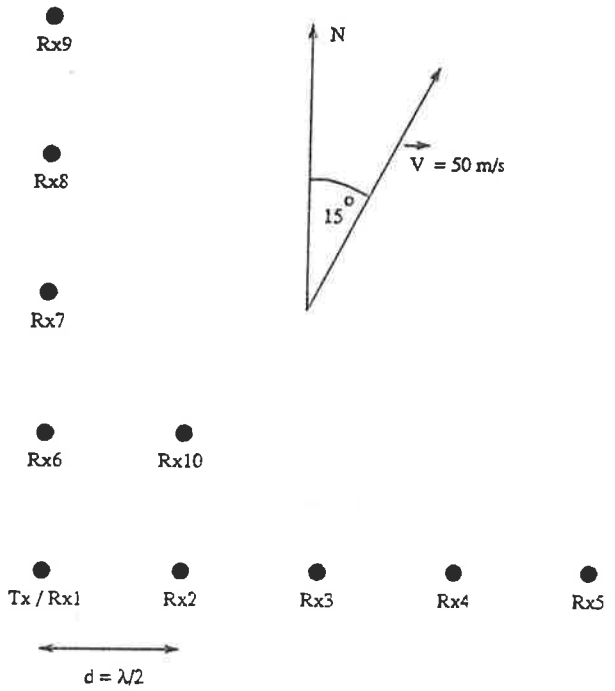

Figure 1. Receiver configuration employed for analyses.

niques are applied to data from antennae 1, 2, and 6. This configuration may not appear ideal for the FCA, as *Golley and Rossiter* [1970] have illustrated that for antennae arranged in a right-angled triangle, the FCA true velocity is biased toward the direction of the largest side of the triangle of antennae. However, our recent analyses of model-generated data indicates that this effect is eliminated if receiver noise is properly accounted for in the FCA, as is the case in this paper. The IDI technique is applied using antennae 1-5 as the zonal arm of the interferometer, and antennae 1 and 6-9 as the meridional arm. The actual phase differences between antenna pairs 1,2 and 1,6 are used in place of the phase differences estimated by the linear fit. We therefore refer to this as the "IDI-like" technique. The purpose of this choice is so the technique uses the same phase information as the MSIRI and NSIRI techniques, thereby allowing a direct comparison of the effects of the individual single-scatterer criterion employed. The velocity estimates resulting from applying the IDI-like technique do not differ significantly from those obtained using the IDI technique.

3.3. Application of Analysis Techniques

The interferometry procedures applied in this paper are kept as similar as possible to those used by *Adams et al.* [1985], *Meek and Manson* [1987], and *Franke et al.* [1990]. The only common acceptance criterion used in each technique is that Doppler frequencies with spectral power less than 5 dB above the noise floor are precluded from the analysis. This criterion is employed to exclude Doppler frequencies within the spectral tails with no apparent useful information from the analysis. The same criterion is applied by *Meek and Manson* [1987] and *Franke et al.* [1990], using thresholds of 5 dB and 15 dB, respectively. No zenith angle thresholds are used. No lower zenith angle threshold is required, as the receiver phase information is known exactly. Upper limit spatial-aliasing thresholds are employed by *Adams et al.* [1985,1986], *Meek and Manson* [1987], and *Franke et al.* [1990]. Such a threshold is not required for the current analysis as the antenna spacing of $(1/2)\lambda$ eliminates spatial aliasing. The IDI analysis of *Brosnahan and Adams* [1993] uses an upper limit to exclude zenith angles outside the first minima in the transmitter polar diagram.

The additional criteria employed are those specific to each particular technique. The IDI-like technique uses Doppler frequencies where the rms error of the linear fit to the phase variation along each antenna arm is less than 10°. The phase-unwrapping algorithm described by *Adams et al.* [1985] is employed in this process. The MSIRI technique uses Doppler frequencies where simultaneous local maxima are seen in all three power spectra. The NSIRI techniques use no additional criteria. Spectral smoothing for the SNSIRI technique is performed in the same manner used by *Franke et al.* [1990], whereby individual time series are divided into four segments, and the cross spectra obtained from each segment are averaged to produce an averaged, or

smoothed, cross spectrum. Since the model uses only one range gate, no range correction is used. Because the model does not incorporate velocity gradients this should not affect the analysis. Doppler frequency weighting is not used. The effects of weighting are discussed thoroughly by *Brosnahan et al.* [1993] and *Meek and Manson* [1987]. All results presented in this paper are the average of the results of the application of the techniques to 200 individual time series realizations.

4. Analysis Results

4.1. Effective Scattering Point Determination

Typical examples of the power spectra obtained and the horizontal effective scattering positions located from an individual 2-min record using the UNSIRI and IDI-like techniques are shown in Figure 2. The four plots correspond to the use of 20, 50, 100, and 1000 scatterers within the enclosing volume, respectively. On average, approximately 25% of these scatterers will occupy parts of the radar volume, thereby producing signal returns. The solid lines indicate the actual locations occupied by the scatterers during the 2-min record, while the dotted circle indicates the horizontal bound of the radar volume.

There is clearly little overlap between the actual and estimated positions. This is understandable for a large number of scatterers, as there will be significantly more scatterers than Doppler frequency components to contribute to. In addition, a single scatterer may contribute to more than one Doppler frequency, as illustrated in the 20-scatterer plot in Figure 2, where the three distinct peaks correspond to the backscatter from three individual scattering locations. The information attributable to each frequency component may therefore be the addition of the returns from a number of scatterers, which will be aliased to a single effective scattering point. Figure 2 indicates that there is little overlap, even for smaller numbers of scatterers. This appears to contradict the results of *Adams et al.* [1985], who recover their 15 scattering positions arranged in an "S" shape and their model velocity reasonably convincingly. Unlike the current analysis they did not include effects such as turbulent motions, aspect sensitivity, range gate weighting and random scatterer positioning, and they used both a smaller model velocity and a smaller time series length, thereby resulting in less single-scatterer Doppler frequency spreading. As a result, their conditions are considerably more favorable than those of the current analysis, which attempts to reproduce conditions that are generally encountered experimentally. Despite these results, the velocity estimates shown in section 4.2 are clearly sensible. This is despite the fact outlined by *Meek and Manson* [1987] that effective scattering points resulting from aliasing do not necessarily propagate with the same speed as the individual scattering positions responsible for the aliasing. Some of the UNSIRI effective scattering positions lie outside the zenith bounds of the radar volume, while very few of the IDI-like positions do so. This suggests that the majority of these "outside positions" are rejected as aliased positions by the IDI-like single-scatterer criterion. The SNSIRI and MSIRI analyses also produce very few outside positions.

The average zenith angle of all effective scattering positions located over 200 records for each interferometric technique as a function of the model turbulent velocity is shown in Figure 3a. The average zenith angle decreases as the turbulent velocity increases, as suggested by the volume scatter arguments of *Briggs* [1995]. Because the model scatterers are isotropic and homogeneously distributed throughout the radar volume the volume scatter situation also suggests that the effective scattering positions should lie along a line in the direction of the wind [e.g., *Briggs*, 1995]. Figure 3b illustrates the distribution of preferred azimuths relative to the model input velocity inferred from total regression linear fits to the effective scattering positions located by applying the UNSIRI analysis to 200 records using a model turbulent velocity of 6 m

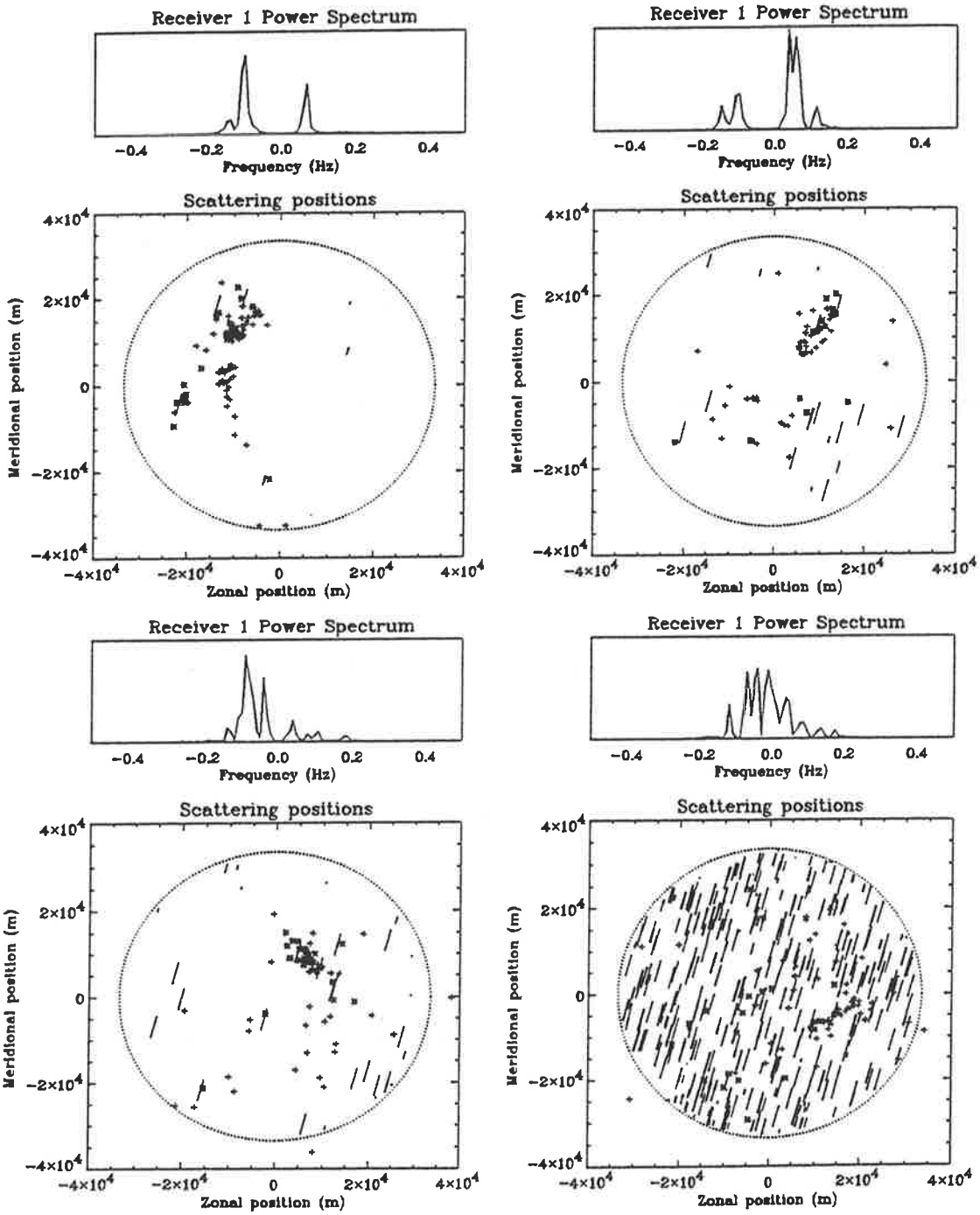

Figure 2. Power spectra and horizontal positions of effective scattering points produced for the UNSIRI (pluses) and IDI-like (crosses) analyses, using 20 (top left), 50 (top right), 100 (bottom left), and 1000 (bottom right) scatterers within the model enclosing volume. An asterisk denotes points located for both techniques.

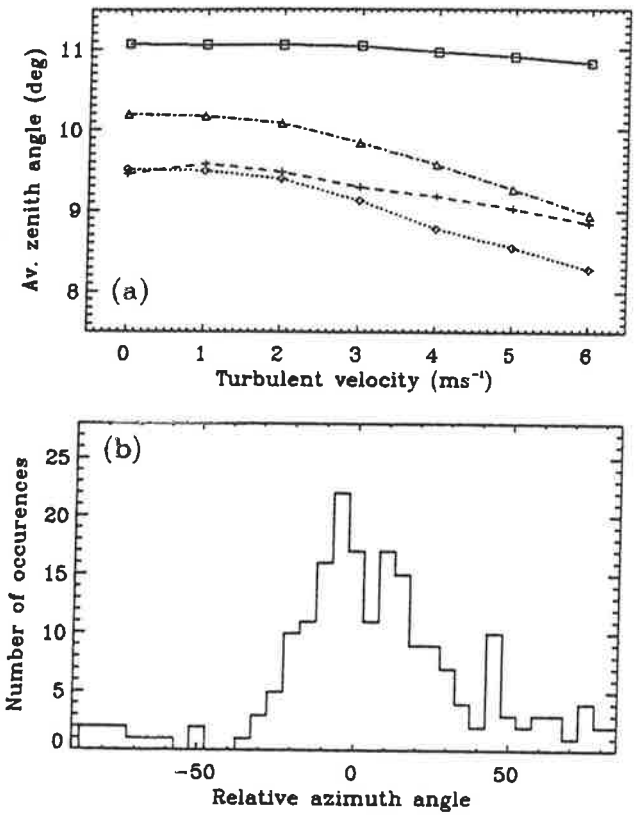

Figure 3. (a) Average zenith angle of effective scattering points produced for the UNSIRI (squares), SNSIRI (diamonds), MSIRI (triangles), and IDI-like (pluses) analyses. (b) Distribution of azimuth angles inferred from total regression linear fit to the UNSIRI estimated effective scattering points relative to the model input velocity for a model turbulent velocity of 6 m s^{-1}.

s^{-1}. The distribution is clearly centered about a difference of 0°, thereby confirming the volume scatter predictions.

The agreement of these results with those predicted by the volume scatter situation may appear somewhat surprising for the use of unsmoothed spectra for which the theory was not explicitly derived. This can be explained as follows. The phase information associated with unsmoothed cross spectra can be considered the sum of a component which is linear with Doppler frequency and a random component. This is verfied by the fact that sufficient averaging of cross spectra calculated from contiguous time records results in an average cross spectrum with almost linear phase variation [e.g., *Liu et al.*, 1990]. This is exactly the phase behavior predicted by volume scatter arguments. The individual unsmoothed cross-spectral phases for each Doppler frequency do not necessarily conform to the volume scatter situation, but sufficiently averaged individual cross-spectral phases over either time or Doppler frequency will show greater conformity. The distribution of the azimuth angles located by the UNSIRI technique can be viewed as an indication of the number of Doppler frequencies satisfying the volume scatter scenario.

4.2. Velocity Determination

The magnitudes of the vector-averaged horizontal velocities resulting from applying the FCA and interferometric techniques to model-generated data are shown in Figure 4, as a function of the rms velocity of the model turbulent motions. The FCA true velocity shows excellent agreement with the model input velocity, compensating correctly for the effects of turbulent motions which result in the FCA apparent velocity increasing as the turbulent velocity increases. The interferometric velocities also increase as the turbulent velocity increases. This confirms the suggestion of *Vandepeer and Reid* [1995a], that the imaging interferometric techniques require a correction for turbulent motions akin to that employed by the FCA if they are to recover the correct wind velocity. The directions of the averaged horizontal velocities for all techniques (not shown) lie within 4° of the direction of the model input velocity.

The volume scatter situation suggests that the velocity predicted by the imaging interferometric techniques should be equivalent to the FCA apparent velocity [e.g., *Vandepeer and Reid*, 1995a]. The IDI-like and MSIRI velocities show good agreement with the apparent velocity. The SNSIRI and UNSIRI techniques employ the same analysis, albeit on different spectral phase information, and should therefore be comparable. The smoothed spectral phases result in

the SNSIRI effective scattering points for each Doppler frequency being located closer to the zenith than the UNSIRI effective scattering points, as illustrated in Figure 3a. Examination of (3) suggests this must result in the SNSIRI velocity estimate being larger than the UNSIRI velocity estimate, even in the absence of turbulent motions where the UNSIRI shows some agreement with the model input velocity. This is despite the fact that the effects of averaging as discussed above may be expected to enhance the agreement with the volume scatter predictions.

4.3. Effect of Varying the Number of Model Scatterers

The magnitudes of the vector-averaged horizontal velocities resulting from using various different numbers, N, of model scatterers are shown in Figure 5, for a model turbulent velocity of 6 m s^{-1}. The number of scatterers is intended to approximately range from the discrete scatter to the volume scatter situation. The FCA results are consistent with those inferred by the theoretical model analysis of *Liu et al.* [1990], who illustrated that regions of highly localized scatter produce cross-correlation maxima time delays differing from the volume scatter situation. The FCA apparent velocity is calculated directly from the cross-correlation maxima time delays and clearly exhibits a distinct change from the volume scatter to the discrete scatter situation. The fall-off of the FCA velocities for small N is accompanied by a fall-off in the data acceptance rate. The FCA true velocity accurately estimates the model input velocity if more than of 100 scatterers are employed, corresponding to approximately 25 or more scatterers contributing signal returns. The interferometric results suggest that a correction for the effects of turbulent motions is required even in the discrete scatter situation. The decreasing interferometric velocities estimated with decreasing N result because the variance in the individual velocity directions increases, while the average magnitude of the individual velocity estimates is almost constant.

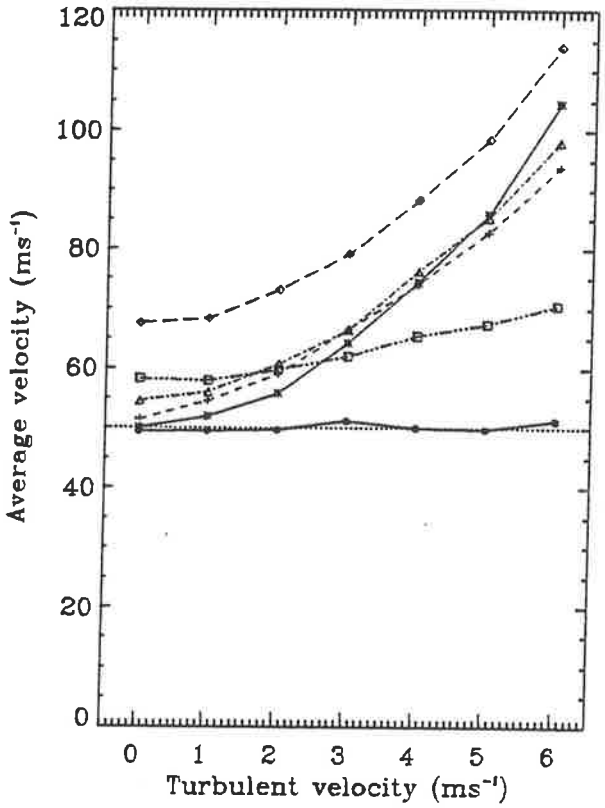

Figure 4. Average horizontal velocities estimated by the FCA and interferometric techniques as a function of model turbulent velocity. FCA true (solid circles), FCA apparent (asterisks), UNSIRI (squares), SNSIRI (diamonds), IDI-like (pluses), MSIRI (triangles). The dotted line indicates the model input horizontal velocity.

4.4. Effect of Receiver Noise

The effects of receiver noise have been simulated by adding randomly generated Gaussian-distributed values to the real and imaginary components of the time series. The magnitude of the resulting vector-averaged horizontal velocities as a function of SNR are shown in Figure 6a, for a model turbulent velocity of 6 m s^{-1}. The FCA velocities are almost constant, while the interferometric velocities decrease significantly with increasing receiver noise, or decreasing SNR. The FCA true velocity is corrected for the effects of receiver noise by interpolating over the zero-lag autocovariance [e.g.,

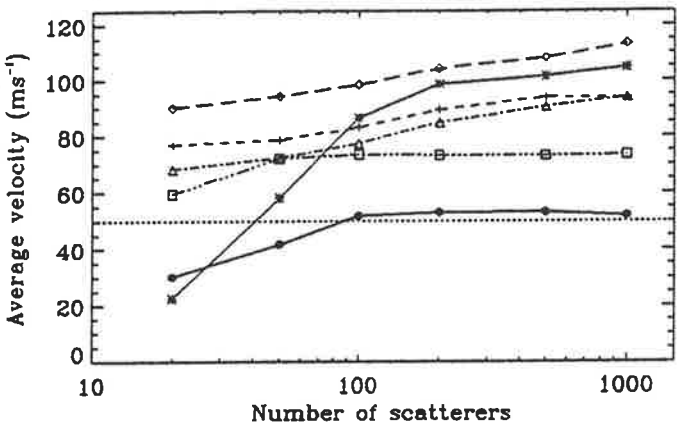

Figure 5. Average horizontal velocities estimated by the FCA and interferometric techniques as a function of the number of model scatterers for a model turbulent velocity of 6 m s^{-1}. FCA true (solid circles), FCA apparent (asterisks), UNSIRI (squares), SNSIRI (diamonds), IDI-like (pluses), MSIRI (triangles). The dotted line indicates the model input horizontal velocity.

Briggs 1984]. Failure to correct for receiver noise in the FCA can result in an underestimation of the true velocity [e.g., *Holdsworth and Reid*, 1995]. This effect results in the "triangle size effect" [e.g., *Golley and Rossiter*, 1970; *Meek*, 1990], whereby the true velocity increases with increasing triangle spacing up to a limit equivalent to the noise-corrected true velocity.

The presence of noise results in the addition of random values to the noise-free cross-spectral phases at all Doppler frequencies. As suggested by (2), the presence of noise results in the zonal and meridional zenith angle components being perturbed from their noise-free values. This perturbation does not significantly alter the average zenith angle of the effective scattering positions, and is thus distinct from the effects of turbulent motions which result in a systematic zenith angle decrease. The results of applying Gaussian-distributed perturbations to the noise-free zonal and meridional zenith angle components of the effective scattering positions located by applying the UNSIRI and IDI-like analyses for a model turbulent velocity of 6 m s^{-1} are illustrated in Figure 6b. The zenith angle displacement indicates the standard deviation of the Gaussian distribution used to generate the zenith angle component perturbations. There is a clear decrease in the estimated velocity as the effective scattering positions are made more random. Equation (2) suggests the perturbations will decrease with increasing antenna spacing, D. This is verified by the results obtained using the IDI-like technique with antenna spacing $D = \lambda$, rather than the usual spacing of $D = (1/2)\lambda$, seen in Figure 6a. The velocity obtained using $D = \lambda$ is less succeptable to the effects of noise, thereby suggesting that the noise-induced phase alteration results in smaller zenith angle perturbations. The noise-induced phase variations are smaller for Doppler frequencies with large spectral powers. As illustrated in Figure 6a, the MSIRI technique is the most robust of the interferometric techniques for small additions of noise because only those Doppler frequencies associated with local maxima are used.

The signal and noise contributions to each Doppler frequency cannot be separated, suggesting imaging interferometric techniques cannot correct for the effects of noise. The presence of noise therefore results in an effect analogous to the FCA triangle size effect, whereby the interferometric velocity decreases with decreasing antenna spacing. The average FCA apparent velocity is not significantly altered by the addition of receiver noise. This result appears at

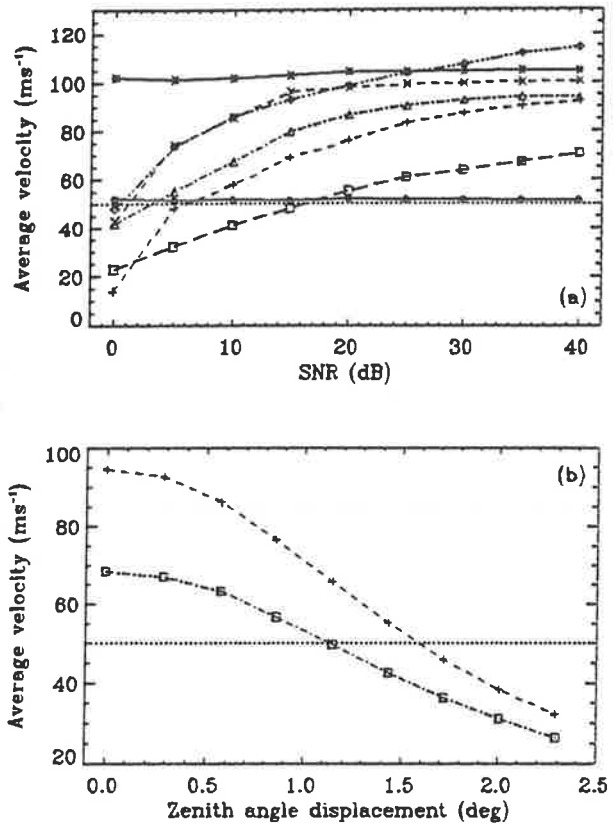

Figure 6. (a) Average horizontal velocities estimated by the FCA and interferometric techniques as a function of receiver SNR for a model turbulent velocity of 6 m s^{-1}. FCA true (solid circles), FCA apparent (asterisks), UNSIRI (squares), SNSIRI (diamonds), IDI-like (pluses), MSIRI (triangles) and IDI-like using antenna spacing $D = \lambda$ (crosses). (b) Average horizontal velocity estimated as a function of zenith angle displacement for the UNSIRI (squares) and IDI-like (pluses) analyses. The dotted line in both plots indicates the model input horizontal velocity.

variance with the volume scatter derived suggestion of *Vandepeer and Reid* [1995a] that the imaging interferometry techniques should measure the apparent velocity. The apparent velocity is calculated directly from the delays corresponding to the cross-correlation maxima of the three calculated cross-correlation functions. The "shift" theorem of the Fourier transform [e.g., *Bracewell*, 1965] indicates that the delay of the cross-correlation maxima is directly proportional to the phase slope of the corresponding cross spectrum. This relationship has been verified experimentally by many authors [e.g., *Liu et al.*, 1990]. The cross-spectral phase slope is an estimate of the average phase behavior over all Doppler frequencies. As discussed above, averaging produces results that conform better with volume scatter situation, even in the case of large noise-induced phase perturbations. However, the individual cross-spectral phases do not necessarily conform to the volume scatter situation. Noise-induced perturbations in the phase will further reduce the conformity. As a result, the correspondence between the FCA apparent and the imaging interferometric velocities suggested by volume scatter arguments can only be considered to hold in the absence of receiver noise.

4.5. Effect of Zenith Angle Threshold

The magnitude of the vector-averaged interferometric horizontal velocities obtained as a function of zenith angle threshold for a model turbulent velocity of 6 m s^{-1} are shown in Figure 7. The velocity variation is a result of two competing effects. The first effect is that the magnitude of the individual velocity estimates increases with decreasing zenith angle threshold. A similar behavior was noted by *Brosnahan*

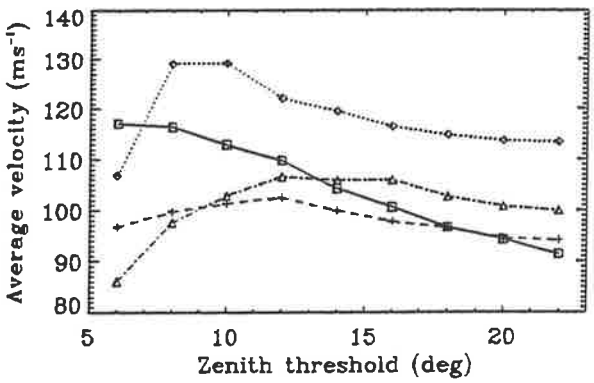

Figure 7. Average horizontal velocities estimated by the interferometric techniques as a function of zenith angle threshold for a model turbulent velocity of 6 m s^{-1}. UNSIRI (squares), SNSIRI (diamonds), IDI-like (pluses) and MSIRI (triangles).

and Adams [1993] and eliminated by the implementation of a two-step process. This process involved the estimation of the vertical velocity using effective scattering positions close to the zenith and the estimation of the horizontal velocity using this calculated vertical velocity and effective scattering positions located off zenith. Such a process is difficult to implement for the analysis of individual time series records as performed here, as there are often too few effective scattering points close to the zenith. The second effect is that the variance of the individual velocity direction estimates increases with decreasing zenith angle threshold.

This result impacts upon the use of spatial-aliasing thresholds. Figure 7 indicates that use of a zenith angle threshold equal to the radar volume cutoff of 22° does not significantly bias the SNSIRI, MSIRI, and IDI-like velocities from the values obtained without using a zenith angle threshold, as shown in Figure 4 for a model turbulent velocity of 6 m s^{-1}. This result suggests that no significant bias will be introduced for these analyses if the required spatial-aliasing threshold exceeds the zenith angle corresponding to the first minima in the transmitter polar diagram. However, if the threshold is well within the first minima the velocity will be biased positively. The application of any zenith angle threshold to the UNSIRI analysis will result in a significant positive velocity bias. This result can be explained as follows. Volume scatter arguments suggest that effective scattering points with large zenith angles are produced by larger Doppler frequencies. However, smaller Doppler frequencies can produce large zenith angles in the UNSIRI analysis, presumably due to the use of Doppler frequencies with aliasing. As a result, the application of a zenith angle threshold decreases the average zenith angle, but does not appreciably affect the average radial velocity. This behavior is summarized in Table 2. Equation (3) suggests that application of a zenith angle threshold for the UNSIRI analysis must therefore result in the estimated velocity increasing.

4.6. Effect of Power Threshold

The magnitude of the vector-averaged interferometric velocities estimated as a function of the power threshold for a model turbulent velocity of 6 m s^{-1} is shown in Figure 8. The general trend is that the velocities decrease with increasing power thresholds above about 0 dB and decrease with decreasing power thresholds below about 0 dB. The decrease above about 0 dB results from the spectra being cut-off at a progressively smaller Doppler frequencies. This does not significantly alter the average zenith angle of the effective scattering positions, but excludes larger radial velocities from the least squares fit of (3). This behavior is summarized for the UNSIRI and IDI-like analyses in Table 3. The decrease below 0 dB results from the use of noisy Doppler frequencies. The additional effective scattering points resulting from the inclusion of noisy Doppler frequencies will be randomly distributed, thereby resulting in an increase in the average zenith angle of the effective scattering positions, and therefore a decrease in the estimated velocity.

There is only a small decrease for the IDI-

Table 2. Relationship Between Estimated UNSIRI Velocity, Average Zenith Angle and Average Radial Velocity for Different Values of Zenith Angle Threshold

	Zenith Angle Threshold, deg	
	22	90
Average zenith angle, deg	9.1	12.0
Average radial velocity, m s^{-1}	21.5	21.9
Velocity estimate, m s^{-1}	101.9	68.7

UNSIRI, nonselected radar interferometry using unsmoothed spectra

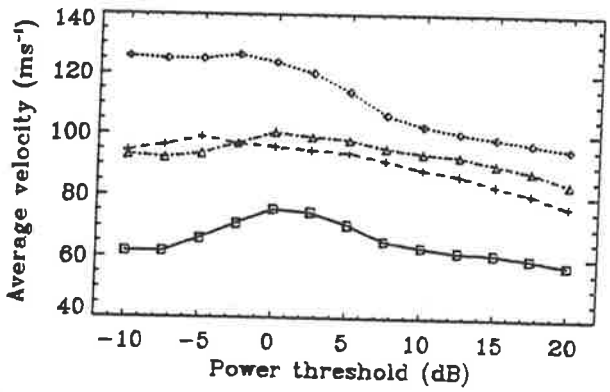

Figure 8. Average horizontal velocities estimated by the interferometric techniques as a function of power threshold for a model turbulent velocity of 6 m s^{-1}. UNSIRI (squares), SNSIRI (diamonds), IDI-like (pluses), MSIRI (triangles).

like and MSIRI-like techniques below about 0 dB. This is not unexpected, as there is only a small statistical probability that noisy Doppler frequencies will pass either single-scatterer criteria and hence be used in the analysis. The single-scatterer criteria can therefore be considered to play a similar role to the noise threshold, selecting Doppler frequencies within the main lobe of the cross spectrum. As a result, the IDI-like and MSIRI analyses effectively use a different range of radial velocities to the NSIRI analyses, which do not employ single-scatterer criterion, as summarized in Table 3. The larger radial velocities used by the NSIRI analyses for small noise thresholds results in a positive velocity bias in relation to the IDI-like and MSIRI analyses. For small turbulent velocities the larger radial velocities used result in the UNSIRI velocity exceeding both the IDI-like and MSIRI velocities, as illustrated in Figure 4. The power threshold required to employ a similar range of radial velocities in each analysis varies as a function of the turbulent velocity, which acts to increase the width of the spectra.

4.7. Comparison of Imaging Interferometric Techniques

The magnitudes of the vector-averaged horizontal velocities resulting from applying "revised" interferometric analyses are shown in Figure 9. The revised analyses use different power thresholds for each turbulent velocity in order to employ a similar range of radial velocities, and thereby allow an unbiased comparison of the velocities estimated by each technique. The IDI-like and MSIRI analyses use identical phase information to the UNSIRI analysis, but reject Doppler frequencies on the basis of their individual single-scatterer criteria. Application of these criteria produce velocities between the UNSIRI and SNSIRI velocities, confirming the suggestion by *Franke et al.* [1990] that the single-scatterer criteria selects Doppler frequencies with similar phase information to the SNSIRI analysis. The phase information associated with the local maxima is similar to that of the smoothed spectra at the same Doppler frequency [e.g., *Franke et al.*, 1990]. Similarly, the exclusion of spectral phases by the phase linearity criterion is a form of spectral averaging, as Doppler frequencies with phase information sufficiently removed from smoothness are excluded from the analysis [e.g., *Vandepeer and Reid*, 1995a]. An alternative description is that the inclusion of Doppler frequencies failing the single-scatterer

Table 3. Relationship Between Estimated Velocity, Average Zenith Angle and Average Radial Velocity for Different Values of the Power Threshold for the UNSIRI and IDI-Like Analyses

	UNSIRI		IDI-like	
	0 dB	15 dB	0 dB	15 dB
Average zenith angle, deg	10.5	10.1	9.2	8.6
Average radial velocity, m s^{-1}	30.7	11.6	26.4	12.8
Velocity estimate, m s^{-1}	77.6	61.9	104.8	90.6

UNSIRI, nonselected radar interferometry using unsmoothed spectra; IDI, imaging Doppler interferometry.

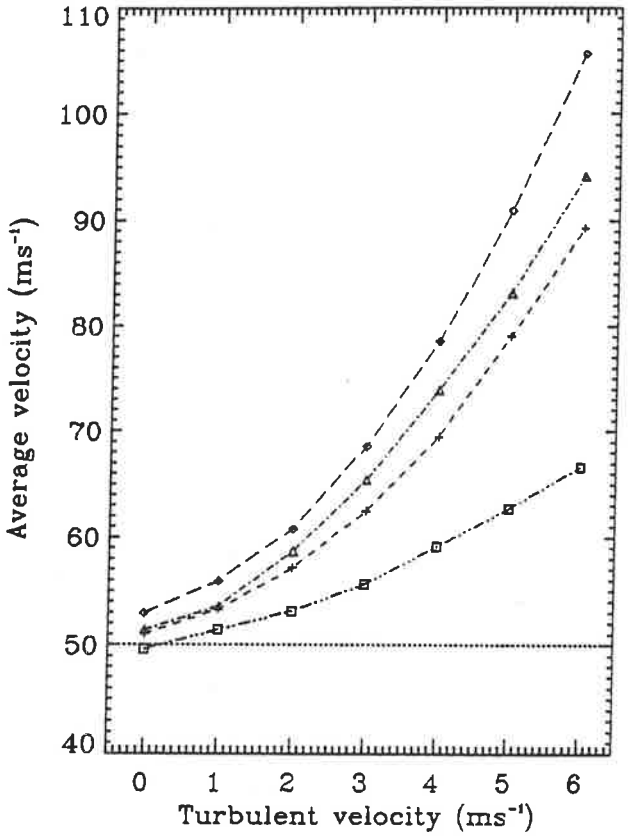

Figure 9. Average horizontal velocities estimated by the revised interferometric techniques as a function of model turbulent velocity. UNSIRI (squares), SNSIRI (diamonds), IDI-like (pluses), MSIRI (triangles). The dotted line indicates the model input horizontal velocity.

criteria in the analysis results in a decrease in the estimated velocity. This may be related to the effect of position randomization shown in Figure 6b, whereby perturbations in the effective scattering positions result in a decrease in the estimated velocity. The positions of aliased effective scattering points are indeed random, because the positions depend upon the locations of the scatterers contributing to the aliasing, which will most likely be randomly distributed throughout the radar volume.

The UNSIRI results compare well with the those of *Franke et al.* [1990]. Their antenna spacing necessitates the use of a spatial aliasing threshold. As seen in Figure 6a, zenith angle thresholds result in a positive velocity bias. This bias is counteracted by the 15-dB power threshold used and effects of noise. both of which result in a negative velocity bias. The radial velocity threshold of 14 m s^{-1} employed may also result in a negative velocity bias in an analogous fashion to the power threshold. Their finding that the UNSIRI velocity is smaller than the FCA true velocity for lower SNRs is also consistent with Figure 7a, where the UNSIRI velocity is shown to decrease with noise while the FCA true velocity remains constant. The SNSIRI results also compare well with the those of *Franke et al.* [1990] if the aforementioned effects are taken into account.

The IDI-like and MSIRI velocities agree very well with those obtained experimentally. The IDI results of *Vandepeer and Reid* [1995a] give velocity estimates within the mean of the FCA true and apparent velocities and the apparent velocity itself. The model-generated IDI-like results may therefore appear a little larger than those obtained experimentally. However, if the effects of receiver noise are taken into account the agreement becomes very good. The model-generated MSIRI velocity is slightly smaller than the experimentally obtained estimates of *Meek and Manson* [1987] and *Brown et al.* [1995], whose results agree well with the FCA apparent velocity. This discrepancy may result from the spatial aliasing thresholds used in the experimental analyses.

5. Conclusions

A simple computer model has been used to illustrate that the volume scatter derived predictions of *Briggs* [1995] and *Vandepeer and Reid* [1995a] appear to be satisfied by the imaging interferometric techniques. The interferometric velocities increase as the turbulent velocity increases. Furthermore, the effective scattering positions are shown to approach the zenith as the turbulent velocity increases and have a preferred azimuth angle agreeing with that predicted by volume scatter arguments. The tech-

niques are also sensitive to both zenith angle and power thresholds, suggesting that such thresholds should be applied with care. The techniques also produce an effect analogous to the FCA triangle size effect, whereby the presence of receiver noise results in the estimated velocity decreasing with decreasing triangle spacing. However, unlike the FCA, the effects of noise cannot be accounted for. The velocity results obtained using model data agree very well with those obtained experimentally by a number of different authors.

Acknowledgments. The authors would like to thank B. G. W. Vandepeer, C. E. Meek, Z. Goss and A. U. C. Clubb for useful discussions relevant to this work. This work has been supported by Australian Research Council grants A69231890 and A69031462 and by the University of Adelaide. David Holdsworth is supported by the Defence Science and Technology Organization, Australia.

References

Adams, G. W., D. P. Edwards, and J. W. Brosnahan, The imaging Doppler interferometer: Data analysis, *Radio Sci., 20*, 1481-1492, 1985.

Adams, G. W., J. W. Brosnahan, D. C. Walden, and S. F. Nerney Mesospheric observations using a 2.66 MHz radar as an imaging Doppler interferometer, *J. Geophys. Res., 91*, 1671-1683, 1986.

Bracewell, R., *The Fourier Transform and its Applications*, McGraw-Hill, New York, 1965.

Briggs, B. H., The analysis of spaced sensor records by correlation techniques, in *Handbook for MAP*, vol. 13, pp. 166-186, SCOSTEP Secr., Univ. of Ill., Urbana, 1984.

Briggs, B. H., On radar interferometric techniques in the situation of volume scatter, *Radio Sci., 30*(1), 109-114, 1995.

Briggs, B. H., and R. A. Vincent, Spaced-antenna analysis in the frequency domain, *Radio Sci., 27*, 117-129, 1992.

Brosnahan, J. W., and G. W. Adams, The MAPSTAR imaging Doppler interferometer: Description and first results, *J. Atmos. Terr. Phys., 55*, 203-228, 1993.

Brown, W. O. J., G. J. Fraser, S. Fukao and M. Yamamoto, Spaced antenna and interferometric velocity measurements with MF and VHF radars, *Radio Sci., 30*(4), 1281-1292, 1995.

Burrage, M. D., et al., Comparison of HRDI wind measurements with radar and rocket observations, *Geophys. Res. Lett., 20*, 1259-1262, 1993.

Cervera, M. A., and I. M. Reid, Comparison of simultaneous wind measurements using colocated VHF meteor radar and MF spaced antenna radar systems, *Radio Sci., 30*(4), 1245-1261, 1995.

Chandra, H., and B. H. Briggs, The effect of filtering on ionospheric drift parameters determined by full correlation analysis, *J. Atmos. Terr. Phys., 40*, 541-548, 1978.

Franke, P. M., D. Thorsen, M. Champion, S. Franke, and E. Kudeki, Comparisons of time- and frequency-domain techniques for wind velocity estimation using multiple-receiver MF radar data, *Geophys. Res. Lett., 17*, 2193-2196, 1990.

Golley, M. G., and D. E. Rossiter, Some tests of methods of analysis of ionospheric drift records using an array of 89 aerials, *J. Atmos. Terr. Phys., 32*, 1215-1233, 1970.

Hines, C. O., G. W. Adams, J. W. Brosnahan, F. T. Djuth, M. P. Sulzer, C. A. Tepley and J. S. Van Baelen, Multi-instrument observations of mesospheric motions over Arecibo: Comparison and interpretations, *J. Atmos. Terr. Phys., 55*, 241-287, 1993.

Holdsworth, D. A., and I. M. Reid, A simple model of atmospheric radar backscatter: Description and application to the full correlation analysis of spaced antenna data, *Radio Sci., 30*(4), 1263-1280, 1995.

Liu, C. H, and C. J. Pan, New observational techniques for studying the dynamics of the middle atmosphere using the Chung Li VHF radar, *J. Atmos. Terr. Phys., 55*, 1055-1066, 1993.

Liu, C. H, J. Röttger, C. J. Pan and S. J. Franke, A model for spaced antenna observational mode for MST radars, *Radio Sci., 25*, 551-563, 1990.

Meek, C. E., Triangle size effect in spaced antenna wind measurements *Radio Sci., 25*, 641-648, 1990.

Meek, C. E., and A. H. Manson, Mesospheric motions observed by simultaneous medium-frequency interferometer and spaced antenna experiments, *J. Geophys. Res., 92*, 5627-5639, 1987.

Meek, C. E., and I. M. Reid, A simple model for testing the effects of gravity-wave-produced vertical oscillations of scattering irregularities on spaced-antenna, horizontal drift measurements, in *Handbook for MAP*, vol. 14, pp. 131-133, SCOSTEP Secr., Univ. of Ill., Urbana, 1984.

Pfister, W., The wave-like nature of inhomogeneities in the E-region, *J. Atmos. Terr. Phys., 33*, 999-1025, 1971.

Röttger, J., and H. M. Ierkic, Postset beam steering and interferometer applications of VHF radars to study winds, waves and turbulence in the lower and middle atmosphere, *Radio Sci., 20*, 1461-1480, 1985.

Sheppard, E. L., and M. F. Larsen, Analysis of model simulations of spaced-antenna/radar interferometer measurements, *Radio Sci., 27*, 759-768, 1992.

Sürücü, F., S. J. Franke, and E. Kudeki, On the influence of specular reflections in MF radar wind measurements, *Radio Sci.,30*(4) 1229-1244, 1995.

Van Baelen, J. S., A. D. Richmond, T. Tsuda, S. K.

Avery, S. Kato, S. Fukao, and M. Yamamoto, Radar interferometry technique and anisotropy of the echo power distribution: First results, *Radio Sci.*, *26*, 1315-1326, 1991.

Vandepeer, B. G. W., A new MF Doppler radar for upper atmospheric research, Ph.D. thesis, Univ. of Adelaide, Adelaide, Aust., 1993.

Vandepeer, B. G. W., and I. M. Reid, On the spaced antenna and imaging Doppler interferometer techniques, *Radio Sci.*,*30*(4), 885-901, 1995a.

Vandepeer, B. G. W., and I. M. Reid, Some preliminary results obtained with the new Adelaide MF Doppler radar, *Radio Sci.30*(4), 1191-1203, 1995b.

Vincent, R. A., and D. Lesicar, Dynamics of the equatorial mesosphere: First results with a new generation partial reflection radar, *Geophys. Res. Lett.*, *5*, 825-828, 1991.

Vincent, R. A., P. T. May, W. K. Hocking, W. G. Elford, B. H. Candy and B. H. Briggs, First results with the Adelaide VHF radar: Spaced antenna studies of tropospheric winds, *J. Atmos. Terr. Phys.*, *49*, 353-366, 1987.

Wright, J. W., and M. L. V. Pitteway, Computer simulations of ionospheric radar drift measurements and their analysis by correlation methods, *Radio Sci.*, *13*, 189-210, 1978.

D. A. Holdsworth and I. M. Reid, Department of Physics and Mathematical Physics, University of Adelaide, Adelaide, 5005, Australia. (e-mail: dholdswo@physics.adelaide.edu.au;ireid@physics.adelaide.edu.au)

(Received October 25, 1994; revised June 13, 1995; accepted June 19, 1995.)

References

Adams, G. W., D. P. Edwards, and J. W. Brosnahan, The imaging Doppler interferometer: Data analysis, *Radio Sci., 20*(6), 1481-1492, 1985.

Adams, G. W., J. W. Brosnahan, D. C. Walden, and S. F. Nerney Mesospheric observations using a 2.66 MHz radar as an imaging Doppler interferometer, *J. Geophys. Res., 91*(A2), 1671-1683, 1986.

Appleton, E. V., On some measurements of the equivalent height of the atmospheric ionized layer, *Proc. Royal Soc. Lond., A126*, 542-569, 1930.

Appleton, E. V., and M. A. F. Barnett, On some direct evidence for downward reflection of electric rays, *Proc. Royal Soc. Lond., A109*, 621-624, 1926.

Awe, 0., Errors in the correlation between time-series, *J. Atmos. Terr. Phys., 26*, 1239-1255, 1964.

Balsley, B. B., and K. S. Gage, The MST radar technique: Potential for middle atmosphere studies, *Pure. App. Geophys., 118*, 452-493, 1980.

Balsley, B. B., W. Ecklund, and D. C. Fritts, VHF echoes from the high-latitude mesosphere and lower thermosphere, *J. Atmos. Sci., 40*, 2451-2466, 1983.

Benyon, W. J. G., and J. C. Wright, Ionospheric drift measurements on adjacent aerial arrays, *J. Atmos. Terr. Phys., 31*(1), 119-134, 1969.

Berkefeld, K. , Time domain interferometry wind estimations at mesospheric heights, Honours thesis, Univ. of Adelaide, Adelaide, Aust., 1994.

Bracewell, R., *The Fourier Transform and its Applications*, McGraw-Hill, New York, 1965.

Brasseur, G., and S. Solomon, *Aeronomy of the middle atmosphere, chemistry and physics of the stratosphere and mesosphere*, 2nd ed., Reidel, Dordrecht, Holland, 1986..

Brennan, D. G., *Statistical methods in radio wave propagation*, Edited by W. C. Hoffman, Pergamon Press, Oxford, 1960.

Briggs, B. H., On the analysis of moving patterns in geophysics - I. Correlation analysis, *J. Atmos. Terr. Phys., 30*, 1777-1788, 1968.

Briggs, B. H., Ionospheric drifts, *J. Atmos. Terr. Phys., 39*, 1023-1033, 1977.

Briggs, B. H., Radar observations of atmospheric winds and turbulence: A comparison of techniques, *J. Atmos. Terr. Phys., 42*, 823-833, 1980.

Briggs, B. H., The analysis of spaced sensor records by correlation techniques, in *Handbook for MAP*, vol. 13, pp. 166-186, SCOSTEP Secr., Univ. of Ill., Urbana, 1984.

Briggs, B. H., Radar measurements of aspect sensitivity of atmospheric scatterers using spaced-antenna correlation techniques, *J. Atmos. Terr. Phys., 54*(2), 153-162, 1992.

Briggs, B. H., Observations of atmospheric dynamics using radar techniques, *Aust. J. Phys., 46*, 127-147, 1993.

Briggs, B. H., The spaced receiver technique, *J. Atmos. Terr. Phys, 56*(7), 831-834, 1994.

Briggs, B. H., On radar interferometric techniques in the situation of volume scatter, *Radio Sci., 30*(1), 109-114, 1995.

Briggs, B. H., W. G. Elford, D. G. Felgate, M. G. Golley, D. E. Rossiter, and J. W. Smith, Buckland Park aerial array, *Nature, 223*(5213), 1321-1325, 1969.

Briggs, B. H., and N. E. Holmes, Ionospheric observations using an ultrasonic image-forming technique, *Nature, 243*, 111-112, 1973.

Briggs, B. H., and A. D. Maude, Spaced sensor observations of pattern motion, *J. Geophys. Res., 83*(A11), 5309-5311, 1978.

Briggs, B. H., G. J. Phillips and D. H. Shinn, The analysis of observations on spaced receivers of the fading of radio signals, *Proc. Phys. Soc., 63B*, 106-121, 1950.

Briggs, B. H., and R. A. Vincent, Spaced-antenna analysis in the frequency domain, *Radio Sci., 27*(2), 117-129, 1992.

Brosnahan, J. W., and G. W. Adams, The MAPSTAR imaging Doppler interferometer: Description and first results, *J. Atmos. Terr. Phys., 55*, 203-228, 1993.

Brown, G. M., and J. W. Chapman, An investigation of the ground diffraction pattern of radio waves reflected by the ionosphere, *J. Atmos. Terr. Phys., 34*, 1445-1454, 1972.

Brown, W. O. J., G. J. Fraser, S. Fukao and M. Yamamoto, Spaced antenna and interferometric velocity measurements with MF and VHF radars, *Radio Sci., 30*(4), 1281-1292, 1995.

Burrage, M. D., et al., Comparison of HRDI wind measurements with radar and rocket observations, *Geophys. Res. Lett., 20*, 1259-1262, 1993.

Cervera, M. A., and I. M. Reid, Comparison of simultaneous wind measurements using colocated VHF meteor radar and MF spaced antenna radar systems, *Radio Sci., 30*(4), 1245-1261, 1995.

Cervera, M. A., Meteor observations with the upgraded Buckland Park pencil beam VHF radar, Ph.D. thesis, Univ. of Adelaide, Adelaide, Aust., to be submitted 1996.

Chandra, H., and B. H. Briggs, The effect of filtering on ionospheric drift parameters determined by full correlation analysis, *J. Atmos. Terr. Phys., 40*, 541-548, 1978.

Chilson, P. B., C. W. Ulbrich, M. F. Larsen, R. D. Palmer, S. Fukao, M. Yamamoto, and T. Nakamura, The effects of particle size distributions on cross-spectral phase measurements in spatial interferometry, *Radio Sci., 30*(4), 1065-1083, 1995.

Churnside, J. H., and H. T. Yura, Velocity measurement using laser speckle statistics, *Appl. Opt., 20*, 353903541, 1981.

Costa, E., and P. F. Fougere, Cross-spectral analysis of spaced-receiver measurements, *Radio Sci., 23*(2), 129-139, 1988.

Costa, E., P. F. Fougere, and S. Basu, Cross-correlation analysis and interpretation of spaced receiver measurements, *Radio Sci., 23*(2), 141-162, 1988.

Doviak, R. J., R. J. Lataitas, C. L. Holloway, and J. Van Baelen, A generalized theoretical analysis of cross-correlation and cross-spectra for spaced-antenna wind profilers, NCAR Technical note NCAR/TN-407+STR, National center for atmospheric research, Boulder, Colorado, 1995.

Farley, D. T., H. M. Ierkic, and B. G. Fejer, Radar interferometry: A new technique for studying plasma turbulence in the ionosphere, *J. Geophys Res., 86*(A3), 1467-1472, 1981.

Fedor, L. S., A statistical approach to the determination of three-dimensional ionospheric drifts, *J. Geophys. Rev., 60*(21), 5401-5415, 1967.

Fedor, L. S., and W. Plywaski, The interpretation of ionospheric radio drift measurements, IV, The effects of signal coupling among spaced sensor channels, *J. Atmos. Terr. Phys., 34*, 1285-1303, 1972.

Felgate, D. G., On the point source effect in the measurement of ionospheric drifts, *J. Atmos. Terr. Phys., 32*, 241-245, 1970.

Felgate, D. G., and M. G. Golley, Ionospheric irregularities and movements observed with a large aerial array, *J. Atmos. Terr. Phys., 33*, 1353-1369, 1971.

Felgate, D. G., A. N. Hunter, S. P. Kingsley, and H. G. Muller, Comparative studies of E-region ionospheric drifts and meteor winds, *Planet. Space Sci., 23*(3), 389-400, 1975.

Flock, W. L., and B. B. Balsley, VHF radar returns from the D-region of the equatorial ionosphere, *J. Geophys. Res., 72*(21), 5537-5541, 1967.

Fooks, G. F., Ionospheric drifts measurements using correlation analysis: methods of computation and interpretation of results, *J. Atmos. Terr. Phys., 27*, 979-989, 1965.

Franke, P. M., D. Thorsen, M. Champion, S. Franke, and E. Kudeki, Comparisons of time- and frequency-domain techniques for wind velocity estimation using multiple-receiver MF radar data, *Geophys. Res. Lett., 17*(12), 2193-2196, 1990.

Fraser G. J., The measurement of atmospheric winds at altitudes of 64-120 km using ground based radio equipment,, *J. Atmos. Sci., 22*, 217-218, 1965.

Fraser G. J., Partial reflection spaced antenna wind measurements, in *Handbook for MAP*, vol. 13, pp. 233-247, SCOSTEP Secr., Univ. of Ill., Urbana, 1984.

Gage, K. S., and B. B. Balsley, On the scattering and reflection mechanisms contributing to clear air radar echoes from the troposphere, stratosphere and mesosphere, *Radio Sci., 15*, 243-258, 1980.

Gardner, F. F., and J. L. Pawsey, Study of the ionospheric D-region using partial reflections, *J. Atmos. Terr. Phys., 3*, 321-344, 1953.

Golley, M. G., and D. E. Rossiter, Some tests of methods of analysis of ionospheric drift records using an array of 89 aerials, *J. Atmos. Terr. Phys., 32*, 1215-1233, 1970.

Golub, G. H., and C. F. Van Loan, *Matrix computations*, John Hopkins University Press, Baltimore, MD., [1983]

Gregory, J. B., Ionospheric reflections from heights below the E-region, *Aust. J. Phys., 9*, 324-342, 1956.

Harper, R. M., Preliminary measurements of the ion component of the incoherent scatter spectrum in the 60-90 km range over Arecibo, *Geophys. Res. Lett., 5*(9), 784-786, 1978.

Harper, R. M., and W. E. Gordon, A review of radar studies of the middle atmosphere, *Radio Sci., 15*(2), 195-211, 1980.

Hines, C. O., G. W. Adams, J. W. Brosnahan, F. T. Djuth, M. P. Sulzer, C. A. Tepley and J. S. Van Baelen, Multi-instrument observations of mesospheric motions over Arecibo: Comparison and interpretations, *J. Atmos. Terr. Phys., 55*, 241-287, 1993.

Hines, C. O., and R. R. Rao, Validity of three-station methods of determining ionospheric motions, *J. Atmos. Terr. Phys., 30*, 979-993, 1968.

Hocking, W. K., On the extraction of atmospheric turbulence parameters from radar backscatter Doppler spectra, I, Theory, *J. Atmos. Terr. Phys., 45*, 89-102, 1983a.

Hocking, W. K., Mesospheric turbulence intensities measured with a HF radar at 35°S II, *J. Atmos. Terr. Phys., 45*, 103-114, 1983b.

Hocking, W. K., R. Rüster, and P. Czechowsky, Absolute reflectivities and aspect sensitivities of VHF radio wave scatterers measures with the SOUSY radar, *J. Atmos. Terr. Phys., 48*, 131-144, 1986.

Hocking, W. K., P. T. May, and J. Röttger, Interpretation, reliability and accuracies of parameters deduced by the spaced antenna method in middle atmosphere applications, *Pageoph, 130*(2/3), 265-299, 1989.

Holdsworth, D. A., and I. M. Reid, A simple model of atmospheric radar backscatter: Description and application to the full correlation analysis of spaced antenna data, *Radio Sci., 30*(4), 1263-1280, 1995a.

Holdsworth, D. A., and I. M. Reid, Spaced antenna analysis of atmospheric radar backscatter model data, *Radio Sci., 30*(5), 1417-1433, 1995b.

Holmes, N. E., An ultrasonic image former for ionospheric studies, Ph.D. thesis, Univ. of Adelaide, Adelaide, Aust., 1993.

Kelleher, R. F., Some statistical properties of the ground diffraction patterns of vertically reflected radio waves, *J. Atmos. Terr. Phys., 28*(2), 213-223, 1966.

Kudeki, E., Radar interferometer observations of mesospheric echoing layers at Jicamarca, *J. Geophys. Res., 93*(D5), 5413-5421, 1988.

Kudeki, E., and R. F. Woodman, A post-statistics steering technique for MST radar applications, *Radio Sci., 25*(4), 591-594, 1990.

Kudeki, E., P. K. Rastogi, and F. Sürücü, Systematic errors in radar wind estimation: implications for comparative measurements, *Radio Sci., 28*(2), 169-179, 1993.

Larsen, M. F., and J. Röttger, VHF radar measurements of in-beam incidence angles and associated vertical-beam radial velocity corrections, *J. Atmos. Oceanic Technol., 8*, 477-490, 1991.

Larsen, M. F., R. D. Palmer, S. Fukao, R. F. Woodman, M. Yamamoto, T. Tsuda, and S. Kato, An analysis technique for deriving vector winds and in-beam incidence angles from radar interferometer measurements, *J. Atmos. Oceanic Technol., 9*(1), 3-14, 1992.

Lataitas, R. J., S. C. Clifford, and C. L. Holloway, An alternative method for inferring winds from spaced-antenna radar measurements, *Radio Sci., 30*(2), 463-467, 1995.

Lesicar, D., Study of the structure of partial reflection radar scatterers and their application in atmospheric measurements, Ph.D. thesis, Univ. of Adelaide, Adelaide, Aust., 1993.

Lesicar, D., and W. K. Hocking, Studies of the seasonal behavior of the shape of mesospheric scatterers using a 1.98 MHz radar, *J. Atmos. Terr. Phys., 54*, 295-309, 1992.

Liu, C. H, and C. J. Pan, New observational techniques for studying the dynamics of the middle atmosphere using the Chung Li VHF radar, *J. Atmos. Terr. Phys., 55*(7), 1055-1066, 1993.

Liu, C. H, J. Röttger, C. J. Pan and S. J. Franke, A model for spaced antenna observational mode for MST radars, *Radio Sci., 29*(4), 551-563, 1990.

Low, D. J., Some applications of a VHF wind profiler to studies in mesoscale and dynamic meteorology, Ph.D. thesis, Univ. of Adelaide, Adelaide, Aust., to be submitted 1996.

McAfee, J. R., K. S. Gage and R. G. Strauch, Examples of vertical velocity comparison from collocated VHF and UHF wind profilers, *Radio Sci., 29*(4), 879-880, 1994.

McAfee, J. R., K. S. Gage and R. G. Strauch, Vertical velocities at Plateville, Colorado: An intercomparison of simultaneous measurements by the VHF and UHF profilers, *Radio Sci., 30*(4), 1027-1042, 1995.

Manning, L. A., O. G. Villiard, V. M. Peterson, Meteoric echo study of upper atmospheric winds, *Proc. I. R. E., 38*, 877, 1950.

May, P. T., Statistical errors in the determination of wind velocities by the spaced antenna technique, *J. Atmos. terr. Phys., 50*, 21-32, 1988.

Meek, C. E., An efficient method for analysing ionospheric drifts data, *J. Atmos. Terr. Phys., 42*, 835-839, 1980.

Meek, C. E., Criteria for optimum spacing of spaced antennas, in *Handbook for MAP*, vol. 14, pp. 139-143, SCOSTEP Secr., Univ. of Ill., Urbana, 1984a.

Meek, C. E., Problems and solutions in analyzing partial-reflection drift data by correlation techniques, in *Handbook for MAP*, vol. 14, pp. 297-299, SCOSTEP Secr., Univ. of Ill., Urbana, 1984b.

Meek, C. E., Triangle size effect in spaced antenna wind measurements, *Radio Sci., 25*(4), 641-648, 1990.

Meek, C. E., and J. Soiferman, A real-time ionospheric drift system, Technical report, Atmos. Dyn. group, Inst. of space and atmos. stud., Univ. of Sask., Saskatoon, Sask., Canada, 1979.

Meek, C. E., and A. H. Manson, Mesospheric motions observed by simultaneous medium-frequency interferometer and spaced antenna experiments, *J. Geophys. Res., 92*(D5), 5627-5639, 1987.

Meek, C. E., A. H. Manson, and N. D. Lloyd, Progress in MF radar measurements at Saskatoon, in *Handbook for MAP*, vol. 28, pp. 467-470, SCOSTEP Secr., Univ. of Ill., Urbana, 1989.

Meek, C. E., and A. H. Manson, Angle-of-arrival oscillations in the mesosphere as seen by medium frequency (MF) radar, *J. Atmos. Terr. Phys., 54*(3), 277-293, 1992.

Meek, C. E., and I. M. Reid, A simple model for testing the effects of gravity-wave-produced vertical oscillations of scattering irregularities on spaced-antenna, horizontal drift measurements, in *Handbook for MAP*, vol. 14, pp. 131-133, SCOSTEP Secr., Univ. of Ill., Urbana, 1984.

Megaw, E. C. S., Fundamental radio scatter propagation theory, *Inst. Elec. Eng. Proc., 104*, (C6), 441-456.

Mitra, S. N., A radio method of measuring winds in the ionosphere, *Proceedings of the institute of electrical engineers, 96*, 441-446, 1949.

Pan, C. J., and C. H. Liu, A model for oblique spaced antenna technique for the mesosphere-stratosphere-troposphere radars and its applications, *Radio Science, 27*(2), 131-144, 1992.

Pawsey, J. L., Further investigations of the amplitude variations of downcoming wireless waves, *Proc. Cambridge Phil. Soc., 31*, 125, 1935.

Pfister, W., The wave-like nature of inhomogeneities in the E-region, *J. Atmos. Terr. Phys., 33*, 999-1025, 1971.

Phillips, G. J., and M. Spencer, The effects of anisometric amplitude patterns in the measurement of ionospheric drifts, *Proc. Phys. Soc., 68B*, 481-492, 1955.

Pitteway, M. L. V., J. W. Wright, and L. S. Fedor, The interpretation of ionospheric radio drift measurements, III, Validation of correlation analysis by computer simulation, *J. Atmos. Terr. Phys., 33*, 635-660, 1971.

Ratcliffe, J. A., Some aspects of diffraction theory and their application to the ionosphere, *Reports on Progress in Physics, 19*, 188-267.

Rajopadhyaya, D. K., Meteorological studies using a VHF radar, Ph.D. thesis, Univ. of Adelaide, Adelaide, Aust., 1994.

Reid, I. M., Radar studies of atmospheric gravity waves, Ph.D. thesis, Univ. of Adelaide, Adelaide, Aust., 1984.

Reid, I. M., MF Doppler and spaced antenna radar measurements of upper middle atmosphere winds, *J. Atmos. Terr. Phys., 50*, 117-134, 1988.

Reid, I. M., Observations of gravity wave scales, fluxes, and saturation during MAP, in *Handbook for MAP*, vol. 27, pp. 87,103, SCOSTEP Secr., Univ. of Ill., Urbana, 1989.

Reid, I. M., Radar observations of stratified layers in the mesosphere and lower thermosphere (50-100 km) *Adv. Space Res., 10*(10), 7-19, 1990.

Reid, I. M., P. Czechowsky, R. Rüster, and G. Schmidt, First VHF radar measurements of mesopause summer echoes at mid-latitudes, *Geophys. Res. Lett., 16*(2), 135-138, 1989.

Reid, I. M., B. G. W. Vandepeer, S. C. Dillon, and B. M. Fuller, The new Adelaide medium frequency Doppler radar, *Radio Sci., 30*(4), 1177-1189, 1995.

Rishbeth, H., and O. K. Garriot, Introduction to ionospheric physics, International geophysics series,vol. 14, Academic Press, New York, 1969

Rishbeth, H., and A. P. Van Eyken, EISCAT: early history and the first ten years of operation, *J. Atmos. Terr. Phys., 55*(4/5), 525-542, 1993.

Rossiter, D. E., Coupling between aerials used for measuring ionospheric drifts, *Nature, 228*, 1299-1300, 1970

Röttger, J., Investigations of the lower and middle atmosphere dynamics with a spaced antenna drifts radar, *J. Atmos. Terr. Phys., 43*, 277-292, 1981.

Röttger, J., The MST radar technique, in *Handbook for MAP*, vol. 13, pp. 187-232, SCOSTEP Secr., Univ. of Ill., Urbana, 1984.

Röttger, J., The interpretation of MST radar echoes: The present knowledge of the scattering/reflection and the irregularity generation mechanism, in *Handbook for MAP*, vol. 28, pp. 68-82, SCOSTEP Secr., Univ. of Ill., Urbana, 1989.

Röttger, J., and R. A. Vincent, VHF radar studies of tropospheric velocities and irregularities using spaced antenna techniques, *Geophys. Res. Lett., 5*(11), 917-920, 1978.

Röttger, J., and H. M. Ierkic, Postset beam steering and interferometer applications of VHF radars to study winds, waves and turbulence in the lower and middle atmosphere, *Radio Sci., 20*(6), 1461-1480, 1985.

Röttger, J., C. H. Liu, J. K. Chao, A. J. Chen, Y. H. Chu, I.-J. Fu, C. M. Huang, Y. W. Kiang, F. S. Kuo, C. H. Lin, and C. J. Pan, The Chung-Li VHF radar: Technical layout and a summary of initial results, *Radio Sci., 25*(4), 487-502, 1990.

Röttger, J., C. H. Liu, J. K. Chao, A. J. Chen, C. J. Pan, and I.-J. Fu, Spatial interferometer measurements with the Chung-Li VHF radar, *Radio Sci., 25*(4), 503-515, 1990.

Røyrvik, O., Spaced antenna drift at Jicamarca, mesospheric measurements, *Radio Sci., 18*(3), 461-476, 1983.

Sato, T., Radar principles, *Lecture notes: International school on atmospheric radars*, ed. S. Fukao, Kyoto, 1988.

Sheppard, E. L., and M. F. Larsen, Analysis of model simulations of spaced-antenna/radar interferometer measurements, *Radio Sci., 27*(5), 759-768, 1992.

Sheppard, E. L., M. F. Larsen, R. D. Palmer, S. Fukao, M. Yamamoto, T. Tsuda, and S. Kato, A statistical comparison of spaced antenna and spatial interferometry wind estimation, *Radio Sci., 28*(4), 585-593, 1993.

Steel, D. I., and W. G. Elford, The height distribution of radio meteors: Comparison of observations at different frequencies on the basis of standard echo theory, *J. Atmos. Terr. Phys., 53*, 409-417, 1991.

Stubbs, T. J., The measurement of winds in the D-region of the ionosphere by the use of partially reflected radio waves, *J. Atmos. Terr. Phys., 35*, 909-919, 1973.

Sürücü, F., E. Kudeki, and P. K. Rastogi Systematic errors in spaced antenna wind estimators under inhomogeneous flow conditions, *Radio Sci.,30*(4) 837-876, 1995a.

Sürücü, P. M. Franke, and E. Kudeki, On the use of software beam synthesis in multiple-receiver MF radar wind estimation, *Radio Sci.,27*(6) 775-782, 1992.

Sürücü, F., S. J. Franke, and E. Kudeki, On the influence of specular reflections in MF radar wind measurements, *Radio Sci.,30*(4) 1229-1244, 1995b.

Turek, R. S., K. L. Miller, R. G. Roper, and J. W. Brosnahan, Mesospheric wind studies during AIDA act '89: morphology and comparison of various techniques, *J. Atmos. Terr. Phys.,57*(11) 1321-1343, 1995.

Van Baelen, J. S., A. D. Richmond, S. K. Avery, T. Tsuda, S. Kato, and S. Fukao, SAD and interferometry analysis with the MU radar: Simulations and preliminary results, *Handbook for MAP*, vol. 28, pp. 416-423, SCOSTEP Secr., Univ. of Ill., Urbana, 1989.

Van Baelen, J. S., T. Tsuda, A. D. Richmond, S. K. Avery, S. Kato, S. Fukao and M. Yamamoto, Comparison of VHF Doppler beam swinging and spaced antenna observations with the MU radar: First results, *Radio Sci., 25*, 629-640, 1990.

Van Baelen, J. S., and A. D. Richmond, Radar interferometry technique: three-dimensional wind measurement theory, *Radio Sci., 26*(5), 1209-1218, 1991.

Van Baelen, J. S., A. D. Richmond, T. Tsuda, S. K. Avery, S. Kato, S. Fukao, and M. Yamamoto, Radar interferometry technique and anisotropy of the echo power distribution: First results, *Radio Sci., 26*(5), 1315-1326, 1991.

Vandepeer, B. G. W., A new MF Doppler radar for upper atmospheric research, Ph.D. thesis, Univ. of Adelaide, Adelaide, Aust., 1993.

Vandepeer, B. G. W., Private communication, 1995.

Vandepeer, B. G. W., and I. M. Reid, On the spaced antenna and imaging Doppler interferometer techniques, *Radio Sci.,30*(4), 885-901, 1995a.

Vandepeer, B. G. W., and I. M. Reid, Some preliminary results obtained with the new Adelaide MF Doppler radar, *Radio Sci.30*(4), 1191-1203, 1995b.

Vincent, R. A., Ionospheric irregularities in the E-region, *J. Atmos. Terr. Phys., 34*, 1881-1989, 1972.

Vincent, R. A., and D. Lesicar, Dynamics of the equatorial mesosphere: First results with a new generation partial reflection radar, *Geophys. Res. Lett., 5*, 825-828, 1991.

Vincent, R. A., P. T. May, W. K. Hocking, W. G. Elford, B. H. Candy and B. H. Briggs, First results with the Adelaide VHF radar: Spaced antenna studies of tropospheric winds, *J. Atmos. Terr. Phys., 49*, 353-366, 1987.

Vincent, R. A., and J. Röttger, Spaced antenna VHF radar observations of tropospheric velocities and irregularities, *Radio Sci., 15*(2), 319-335, 1980.

Vincent, R. A., T. J. Stubbs, P. H. O. Pearson, K. H Lloyd and C. H. Low, A comparison of partial reflection drifts with winds determined by rocket measurements, *J. Atmos. Terr. Phys., 39*, 813-821, 1977.

Vincent, R. A., D. A. Holdsworth, I. M. Reid, and M. A. Cervera, Spaced-antenna wind measurements: The effects of signal saturation, Proceedings of "Wind observations in the middle atmosphere" workshop, Paris, 1994.

Wang, T., G. R. Ochs, and R. S. Lawrence, Wind measurements by the temporal cross-correlation of the optical scintillations, *Appl. Opt., 20*, 4073-4081, 1981.

Woodman, R. F., Inclination of the geomagnetic field measured by an incoherent scatter technique, *J. Geophys. Res., 76(1)*, 178-184, 1971.

Woodman, R. F., High-altitude resolution stratospheric measurements with the Arecibo 430-MHz radar, *Radio Sci., 15(2)*, 417-422, 1980.

Woodman, R. F., and A. Guillen, Radar observations of winds and turbulence in stratosphere and mesosphere, *J. Atmos. Sci., 31*, 493-505, 1974.

Wright, J. W., M. Glass and A. Spizzichino, The interpretation of ionospheric radio drift measurements - VIII. Direct comparisons of meteor radar winds and Kinesonde measurements: mean and random motions, *J. Atmos. Terr. Phys, 38*, 713-729, 1976.

Wright, J. W., and M. L. V. Pitteway, Computer simulations of ionospheric radar drift measurements and their analysis by correlation methods, *Radio Sci., 13*, 189-210, 1978.